

NASA Technical Memorandum 81776

NASA-TM-81776 19800007750

Reports of Planetary Geology Program, 1979-1980

FOR REFERENCE

NOT TO BE TAKEN FROM THIS ROOM

JANUARY 1980

NASA

NASA Technical Memorandum 81776

Reports of Planetary Geology Program, 1979-1980

**Compiled by P. Wirth, R. Greeley, and R. D'Alli
NASA Office of Space Science
Washington, D.C.**



**National Aeronautics
and Space Administration**

**Scientific and Technical
Information Branch**

1980

Foreword

This is a compilation of abstracts of reports from Principal Investigators of NASA's Office of Space Science, Division of Lunar and Planetary Programs Planetary Geology Program.

The purpose is to provide a document which succinctly summarizes work conducted in this program. Each report reflects significant accomplishments within the area of the author's funded grant or contract.

No attempt has been made to introduce editorial or stylistic uniformity; on the contrary, the style of each report is that of the Principal Investigator and may best portray his research. Bibliography information will be included in a separately published document.

Full reports of selected abstracts were presented to the annual meeting of Planetary Geology Principal Investigators at Arizona State University, Tempe, Arizona, January 14-16, 1980.

J. M. Boyce
Acting Discipline Scientist
Planetary Geology Program

TABLE OF CONTENTS

Foreword	iii
 CHAPTER 1. ASTEROIDS, COMETS AND SATELLITES	
Planetary Studies. H. Alfvén and D. A. Mendis	3
Asteroid Collisions and Evolution. D. R. Davis, C. R. Chapman, R. Greenberg, and S. J. Weidenschilling	5
Search for Planet-crossing Asteroids with the Palomar 122-CM Schmidt Camera	8
E. M. Schoemaker, S. J. Bus, J. G. Williams, and E. F. Helin	
Comet Encke: Precession of the Spin Axis, Nongravitational Motion, and Sublimation	11
F. L. Whipple (and Z. Sekanina)	
The Shapes, Volumes and Mean Densities of Phobos and Deimos	12
J. Veverka, P. Thomas, J. Gradie, and G. Goguen	
Dynamical Studies of Phobos and Deimos: Groove Origin and Ejecta Dynamics	14
D. R. Davis, S. J. Weidenschilling, C. R. Chapman, R. Greenberg, and K. Housen	
 CHAPTER 2. STRUCTURE, TECTONICS AND STRATIGRAPHY	
Origin of Lunar Grabens and Constraints on the Total Expansion of the Moon	19
M. P. Golombek and G. E. McGill	
The Gravity Anomalies of Oceanus Procellarum	22
J. L. Whitford-Stark	
Irregularities of Lunar Basin Structure	25
D. E. Wilhelms	
Normal Faults on Mercury: Examples in the Kuiper Quadrangle.	28
D. H. Scott, J. R. Underwood Jr, and R. A. De Hon	
Inter crater Plains of Mercury.	31
M. A. Leake	
Plains-forming Materials of the Kuiper Quadrangle of Mercury	34
R. A. De Hon, D. H. Scott, and J. R. Underwood Jr	

CHAPTER 2. STRUCTURE, TECTONICS AND STRATIGRAPHY (continued)

Relative Ages of the Smooth Plains and Caloris Related Terrain of Mercury	37
J. A. Watkins	
Mars Stratigraphic Studies.	40
D. H. Scott	
Layered Materials of the Ridged Plains of Mars.	41
R. A. De Hon	
Photogeologic Studies of the Cerberus Albedo Feature of Mars	43
A. L. Chaikin, T. A. Maxwell, and F. El-Baz	
Martian Color/Albedo Units: Viking Lander 1 Stratigraphy vs. Orbiter Color Observations	46
E. L. Strickland III	
Two Mars Years: Viking Lander Imaging Observations	48
K. L. Jones and S. K. LaVoie	
Classification of Analysis of Rocks at the Viking Lander Sites	51
J. B. Garvin, D. Grinspoon, J. W. Head, P. Helfenstein, P. Lucey, P. J. Mouginis-Mark, E. A. Robinson, and L. Viglienzzone	
Geomorphic Mapping of Dry Valley Systems on Mars.	54
V. R. Baker	
Pits, Streets, Platea, Towers, and Marginal Plains on Mars	57
G. A. Brook	
Studies of the Martian Polar Caps	60
A. D. Howard	
Simulations of Stratigraphy of Martian Polar Layered Deposits	63
J. A. Cutts	
Patterns of Ridges and Scarps on Mars	66
J. F. Eppink and R. S. Saunders	
Tectonic Features of Southeast Tharsis.	68
J. B. Plescia, L. E. Roth, and R. S. Saunders	
Tharsis: An Alternative Explanation	71
S. C. Solomon and J. W. Head	
Early Volcanic-Tectonic Province: Coprates Region of Mars.	74
R. S. Saunders, L. E. Roth, G. S. Downs, and G. Schubert	

CHAPTER 2. STRUCTURE, TECTONICS AND STRATIGRAPHY (continued)

Thermal Histories of Mars, Including Convection and Core Formation.....	77
G. F. Davies	
An Analysis of Martian Gravity Over Three Shield Volcanoes.....	79
J. C. Smith, R. J. Phillips, and S. Ritke	
Planetary Fracture Patterns; Influence of Inheritance on Stress Analysis.....	80
G. E. McGill	
Origins of Regional Scale Lineament Swarms as Suggested by Fracture Domain Analysis of Italy	83
D. U. Wise, R. Funiciello, M. Parotto, and F. Salvini	
Research Activity of the Planetology Branch of the Laboratorio Astrofisica Spaziale - 1979	86
R. Bianci, A. Carusi, A. Coradini, M. Coradini, C. Federico, E. Flamini, M. Fulchignoni, G. Magni, M. Poscolieri, and G. Valsecchi	

CHAPTER 3. CRATERING AS A PROCESS, LANDFORM AND DATING METHOD

A Global Study of Primary Crater Ejecta Morphology on Mars: A Progress Report.....	93
K. R. Blasius, J. A. Cutts, and W. J. Roberts	
Impact Cratering in Viscous Targets	95
R. Greeley, D. E. Gault, D. B. Snyder, V. Sisson, P. H. Schultz, and J. E. Guest	
Emplacement of Martian Rampart and Pedestal Ejecta Blankets.....	96
P. Mutch and A. Woronow	
Ejecta Emplacement for Martian Fluidized Ejecta Craters.....	99
P. J. Mouginis-Mark	
On the Origin of Martian Pedestal, Lobate, and Multilobate Ejecta Deposits	102
A. Woronow and P. Mutch	
Crater Studies in the Northern Plains of Mars: Thickness Estimates of Fluidized Ejecta Deposits	105
P. J. Mouginis-Mark and D. L. Carey	
Gravity and Target Strength: Controls on the Morphologic Transition from Simple to Complex Impact Craters	108
R. J. Pike, D. J. Roddy, and D. W. G. Arthur	

CHAPTER 3. CRATERING AS A PROCESS, LANDFORM AND DATING METHOD (continued)

Crater Distributions and the Evolution of the Lunar Farside Highlands	111
C. A. Wood and A. W. Gifford	
Resurfacing History of Mars - Crater Flux Models and Thermal History Models	114
R. E. Arvidson	
Time Sequence of Martian Geologic Features	119
K. Hiller and G. Neukum	
Dating Methodology of Small, Homogeneous Crater Populations Applied to the Tempe-Utopia Trough Region of Mars.	122
D. Wise and G. Milkowski	
Meteoroid Impact into Short-Period Comet Nuclei - I: The Process	125
M. J. Cintala	
Meteoroid Impact into Short-Period Comet Nuclei - II: The Results.	128
M. J. Cintala	

CHAPTER 4. GEOCHEMISTRY, VOLATILES AND REGOLITH

Evolution of the Martian Atmosphere and Interaction with the Regolith	133
J. B. Pollack	
Mars Atmosphere-Regolith Simulation Experiment.	134
R. S. Saunders, F. P. Fanale, and J. B. Stephens	
Volatile Loss and Thermal Stability of Martian Analog Clay and Sulfur Minerals	135
E. K. Gibson, M. A. Urbancic, and F. F. Andrawes	
Experimental Evidence Against the UV Photodehydration of Goethite (α -FeOOH)	138
R. V. Morris and H. V. Lauer Jr	
The Evidence Against UV Photostimulated Oxidation of Magnetite	141
R. V. Morris and H. V. Lauer Jr	
The H ₂ O Mass Balance on Mars: Implications for a Global Supermafrost Groundwater Flow System	144
S. M. Clifford and R. L. Huguenin	
Additional Experimental Evidence for the Photostimulated Oxidation of Magnetite on Mars	147
R. Huguenin, J. Danielson, and S. Clifford	

CHAPTER 4. GEOCHEMISTRY, VOLATILES AND REGOLITH (continued)

Alteration Products of Frost Weathering on Mars	149
K. J. Miller, R. L. Huguenin, and J. Danielson	
Chemical Environments of Martian Oases	151
K. J. Miller and R. L. Huguenin	
Additional Remote Sensing Evidence for Oases on Mars	153
R. L. Huguenin and S. M. Clifford	
Phase Equilibria of the Martian Mantle	156
E. S. Patera and J. R. Holloway	
Analogue and Simulation Studies of Martian Chemical Weathering: The Formation of Evaporite Minerals	159
D. J. Prestel and D. S. McKay	
Recent (?) Surface Alterations from Subsurface Sources in the Olympus Mons Area	162
E. C. Morris	
Carbochlorination of Common Silicates: Implications for the Composition of the Martian Surface	164
R. J. Williams and T. E. Erstfeld	
Viking Surface Sampler Diurnal Temperatures	166
H. J. Moore, R. E. Hutton, R. F. Scott, R. W. Shorthill and C. R. Spitzer	
Study of Libyan Desert Glass Site, SW Egypt: June 1979	169
J. R. Underwood Jr and R. Giegengack	

CHAPTER 5. VOLCANIC PROCESSES AND LANDFORMS

The Volcanic Resurfacing History of Mars	173
P. D. Spudis and R. Greeley	
Origin of the Olympus Mons Aureole and Perimeter Scarp	176
R. M. C. Lopes, J. E. Guest, and C. J. N. Wilson	
Lava Flow Maps of the Tharsis Province on Mars	179
D. H. Scott, G. G. Schaber, K. C. Horstman, and A. L. Dial Jr	
Tempe-Mareotis Volcanic Province of Mars	181
C. A. Hodges	
The Domes and Associated Flow Lobes in Arcadia Planitia, Mars	184
C. A. Hodges	

CHAPTER 5. VOLCANIC PROCESSES AND LANDFORMS (continued)

Small Volcanic Constructs in Utopia Planitia	187
A. Woronow	
The Tempe Volcanic Province: An Analog to the Eastern Snake River Plains?	189
J. B. Plescia	
Quantitative Morphology of Volcanoes: Recent Results for Earth and Mars	192
R. J. Pike, R. Jordan, and F. J. Schafer	
Problems Associated with the Identification of Magma Composition from Volcanic Landforms	195
J. L. Whitford-Stark	
Are Calc-alkalic Volcanic Rocks Unique to Earth?	198
W. E. Elston, J. C. Aubele, L. S. Crumpler, and D. B. Eppler	
Estimates of Lava-flow Velocities using Lava Trees	201
H. J. Moore and R. Kachadoorian	
Viscosity of Basaltic Lavas: Comparison of Theoretical Models and Experimental Measurements	204
M. Settle	
Scale Model Simulation of Lava Flows	207
M. B. Womer, R. Greeley, J. D. Iversen, and J. Kremer	
Scale Model Simulations of Mare Basalts	210
M. B. Womer, R. Greeley, and J. D. Iversen	

CHAPTER 6. AEOLIAN PROCESSES AND LANDFORMS

Mars: Origin of the Global Dust Storms	215
R. L. Huguenin, S. M. Clifford, and R. Greeley	
The Effects of Topography, Albedo and Thermal Inertia Variations on the Generation of Mesoscale Martian Wind Patterns: A Comparative Study of the Snake River Plain, Idaho and the Martian Surface	217
R. L. Rankin, A. R. Peterfreund, R. Greeley, and G. Eckerman	
Mars: Some Mechanisms of Contrast Change Inferred from Behavior of Wind Streaks	219
P. Thomas and J. Veverka	
Surface Characterization of Wind Streaks on Mars	221
A. R. Peterfreund	

CHAPTER 6. AEOLIAN PROCESSES AND LANDFORMS (continued)

Distribution of Eolian Mantle on Martian Canyon Rims	223
P. J. Mouginis-Mark and J. W. Head	
Threshold Windspeeds for Sand on Mars: Wind Tunnel Simulations.	226
R. Greeley, R. N. Leach, B. R. White, J. D. Iversen, and J. B. Pollack	
Effect of Interparticle Force and Reynolds Number on Wind Threshold Speed	228
J. D. Iversen, B. R. White, R. Greeley, R. Leach, and J. B. Pollack	
Pitted and Fluted Rocks - Viking Comparisons.	231
J. F. McCauley, C. S. Breed, M. J. Grolier, M. I. Whitney, and A. W. Ward	
Ventifacts: Models for Wind Erosion on Any Scale	236
M. I. Whitney	
Studies of the Coatings on Sand Grains from the Gilf Kebir, Southwest Egypt.	238
D. J. Prestel, J. E. Wainwright, and F. El-Baz	
Mars: Simulation of Surface Wind Abrasion.	241
R. Greeley and S. H. Williams	
"Aggregate" Parameters and Martian Aeolian Abrasion.	244
D. H. Krinsley, T. Fillers, and E. Patera	
Inventory of Wind-formed Features on Mars: An Eolian Atlas.	246
C. S. Breed, A. W. Ward, J. F. McCauley, and N. Witbeck	
Eolian Features of the North Polar Region on Mars: Comparison with Earth.	249
C. S. Breed, J. F. McCauley, and M. J. Grolier	
"Zig-zag" Dunes on Mars and Earth	252
R. S. U. Smith	
Maintenance of Barchan Size in the Southern Algodones Dune Chain, Imperial County, California	253
R. S. U. Smith	
Topographically Controlled Dune Systems on Earth and Mars	255
C. K. McCauley and W. J. Breed	
Dunes Related to Obstacles on Earth and Mars: Observation and Simulation.	257
H. Tsoar and R. Greeley	

CHAPTER 6. AEOLIAN PROCESSES AND LANDFORMS (continued)

Experimental Modeling of Erosional Windforms II	260
A. W. Ward and R. Greeley	

CHAPTER 7. MASS MOVEMENT, FLUVIAL, PERIGLACIAL, AND OTHER SURFACE PROCESSES AND LANDFORMS

Survey of Martian Fluvial Features	265
M. H. Carr	

Origin of Mars Fluvial Features: Analysis for Fluids of Stress and Temperature Dependent Rheology	268
D. E. Thompson and J. E. Laity	

Martian Outflow Channels Sculptured by Glaciers	271
B. K. Lucchitta and D. M. Anderson	

Mars Catastrophic Flooding Analog: Analysis of Debris Transport in Variable Viscosity Fluids.	274
D. E. Thompson	

An Analysis of the Modes of Sediment Transport in Rivers with Application to the Erosion of the Martian Outflow Channels	276
P. D. Komar	

Fluvial and Glacial Processes, Central Arctic Slope, Alaska	277
J. Boothroyd and B. S. Timson	

Global Inventory of Glacial and Periglacial Features on Mars, A Progress Report.	281
B. K. Lucchitta and E. T. Mohr	

Thermokarst on Mars	283
L. Rossbacher and S. Judson	

Some Terrestrial Analogs to Dry Valley Systems on Mars	286
V. R. Baker	

Debris Flows and Debris Avalanches in the Large Martian Channels	289
D. Nummedal	

Sapping: Network Structure in Terrestrial and Martian Valleys	292
D. C. Pieri, M. C. Malin, and J. E. Laity	

Sapping Processes in Tributary Valley Systems	295
J. E. Laity, D. C. Pieri, and M. C. Malin	

Sapping: Analog Studies on Earth and Mars.	298
M. C. Malin, J. E. Laity, and D. C. Pieri	

CHAPTER 7. MASS MOVEMENT, FLUVIAL, PERIGLACIAL, AND OTHER SURFACE PROCESSES AND LANDFORMS (continued)

- Studies of Fluvial, Eolian, and Sapping Processes in Iceland 300
M. C. Malin

CHAPTER 8. REMOTE SENSING OF PLANETARY SURFACES: INTERPRETATIONS AND TECHNIQUES

- Radar, Visual and Thermal Characteristics of the Tharsis-Memnonia-Amazonis Lava Flows on Mars 305
G. G. Schaber

- Correlations Between Earth-based Radar and Martian Landforms Imaged by the Viking Orbiters 308
P. J. Mouginis-Mark, S. H. Zisk, and G. H. Pettengill

- Scattering of Light from Particulate Surfaces. V. A Simple, Approximate Photometric Function for Surfaces of Arbitrary Albedo 311
J. Goguen and J. Veverka

- The Photometric Function of the New Dust Deposit at the Viking Lander 2 Site. 313
E. A. Guinness

- Lunar Geochemical Anomalies Detected by Orbital Remote Sensing 316
B. R. Hawke, P. D. Spudis, and P. E. Clark

- Application of the G-Mode Cluster Analysis Technique to Multispectral Data Sets 319
M. Poscolieri

- Optical Power Spectrum Analysis of Martian Terrains. 323
R. W. Wolfe

CHAPTER 9. GALILEAN SATELLITES

- Thermal Evolution of Europa, Ganymede and Callisto 329
R. T. Reynolds, P. M. Cassen, and S. J. Peale

- Volcanic Eruptions on Io 331
R. G. Strom, R. J. Terrile, H. Masursky, and C. Hansen

- Volatile Evolution: The SO₂ Regime of Io. 334
F. P. Fanale

- Photometric Studies of the Satellites of Jupiter Using Voyager Imaging Data. 336
J. Veverka, S. Squyres, P. Thomas, D. Simonelli, and D. Morrison

CHAPTER 9. GALILEAN SATELLITES (continued)

Phase Functions of Water Frosts and Ice.	338
N. G. Purves and C. B. Pilcher	
Basin Peak-ring Spacing on Ganymede and Callisto: Implications for the Origin of Central Peak and Peak Rings	339
J. M. Boyce	
Amalthea: Analysis of Voyager Imaging Data	343
J. Veverka, P. Thomas, J. Gradie, D. Morrison, and M. Davies	
Volume Changes in Ganymede and the Origin of Grooved Terrain	345
S. Squyres and E. M. Shoemaker	
Impact Heating of H ₂ O Ice Targets: Applications to Outer Planet Satellites	347
M. J. Cintala, J. W. Head, and E. M. Parmentier	

CHAPTER 10. PLANETARY CARTOGRAPHY, GEODESY, AND GEOLOGIC MAPPING

Improved Accuracy of Coordinates of Features on Mars.	353
M. E. Davies	
The Control Networks of the Galilean Satellites	354
M. E. Davies	
Photogrammetric Application to Planetary Mapping.	355
S. S. C. Wu	
Precise Mars Relative Altitudes	358
D. W. G. Arthur	
An Interactive Computer System for Extracting Topographic Data from Viking Orbiter Stereo Digital Imagery	359
S. W. Lee	
Relative Elevations in the Valles Marineris Chaos	362
L. E. Roth, G. S. Downs, R. S. Saunders, and G. Schubert	
Viking Lander Interactive Computerized Video Stereophotogrammetry: Accomplishments and Prospects	365
S. Liebes Jr and E. C. Levinthal	
Geologic Mapping in the Southwest Equatorial Region of Mars	368
J. S. King	
Evolution of the Geological Map of Kuiper Quadrangle of Mercury	369
J. R. Underwood Jr, D. H. Scott, and R. A. De Hon	

**CHAPTER 10. PLANETARY CARTOGRAPHY, GEODESY, AND GEOLOGIC MAPPING
(continued)**

Mars Geologic Map, 1:15 Million Scale	372
D. H. Scott	

CHAPTER 11. WORKSHOPS AND SPECIAL PROGRAMS

Planetary Studies at the Hawaiian Volcano Observatory	375
D. Dzurisin	

SAR Interpretation Course for VOIR Photogeologists	376
G. L. LaPrade	

The Planetary Geology Associates Project: A Progress Report	377
R. E. D'Alli	

Application of BIRP (Automated Picture Search) to Viking Orbiter Data - The Ubiquity of Martian Dunes	378
R. E. Arvidson, L. K. Bolef, and E. A. Guinness	

Author Index	383
--------------------	-----

ABSTRACTS RECEIVED AFTER DEADLINE

Intra-crater Formations as Revealed in Survey Mission Imaging Data	391
N. Evans	

Plots and Mosaics of Survey Mission Coverage.	392
N. Evans, S. Dueck, G. Johnston, and P. Scribner	

Transportation and Deposition of Particulate Material on the Surface of Mars: Inferences From Sand Sheet Deposits in the Western Desert of Egypt	393
T. A. Maxwell and F. El-Baz	

Condensates at the Viking 2 Lander Site.	396
S. D. Wall	

Polar Ice Inventory - A Progress Report	399
H. Masursky, A. L. Dial, and M. Strobell	

Fluvial History of the Chryse Basin - A Progress Report	402
H. Masursky, A. L. Dial, and M. Strobell	

Constraints on the Density of the Martian Mantle.	404
K. A. Goettel	

1. The first part of the paper is devoted to a general discussion of the problem of the existence of solutions of the system of equations

(1)
$$\frac{dx}{dt} = A(x)u, \quad \frac{dy}{dt} = B(x)y,$$

where $A(x)$ and $B(x)$ are matrices depending on x , and u is a vector function.

2. In the second part, we consider the case when the matrix $A(x)$ is constant.

3. In the third part, we consider the case when the matrix $B(x)$ is constant.

4. In the fourth part, we consider the case when the matrix $A(x)$ is constant and the matrix $B(x)$ is constant.

5. In the fifth part, we consider the case when the matrix $A(x)$ is constant and the matrix $B(x)$ is constant.

6. In the sixth part, we consider the case when the matrix $A(x)$ is constant and the matrix $B(x)$ is constant.

7. In the seventh part, we consider the case when the matrix $A(x)$ is constant and the matrix $B(x)$ is constant.

8. In the eighth part, we consider the case when the matrix $A(x)$ is constant and the matrix $B(x)$ is constant.

9. In the ninth part, we consider the case when the matrix $A(x)$ is constant and the matrix $B(x)$ is constant.

10. In the tenth part, we consider the case when the matrix $A(x)$ is constant and the matrix $B(x)$ is constant.

11. In the eleventh part, we consider the case when the matrix $A(x)$ is constant and the matrix $B(x)$ is constant.

12. In the twelfth part, we consider the case when the matrix $A(x)$ is constant and the matrix $B(x)$ is constant.

13. In the thirteenth part, we consider the case when the matrix $A(x)$ is constant and the matrix $B(x)$ is constant.

14. In the fourteenth part, we consider the case when the matrix $A(x)$ is constant and the matrix $B(x)$ is constant.

15. In the fifteenth part, we consider the case when the matrix $A(x)$ is constant and the matrix $B(x)$ is constant.

16. In the sixteenth part, we consider the case when the matrix $A(x)$ is constant and the matrix $B(x)$ is constant.

17. In the seventeenth part, we consider the case when the matrix $A(x)$ is constant and the matrix $B(x)$ is constant.

18. In the eighteenth part, we consider the case when the matrix $A(x)$ is constant and the matrix $B(x)$ is constant.

19. In the nineteenth part, we consider the case when the matrix $A(x)$ is constant and the matrix $B(x)$ is constant.

20. In the twentieth part, we consider the case when the matrix $A(x)$ is constant and the matrix $B(x)$ is constant.

Chapter 1

ASTEROIDS, COMETS AND SATELLITES

PLANETARY STUDIES, Hannes Alfvén and D. A. Mendis, Department of Electrical Engineering and Computer Science and the Center for Astrophysics and Space Science, University of California, San Diego, La Jolla, CA 92093 -- Recent observations of narrow rings around Uranus and Jupiter have lent further support to the essential validity of the hydromagnetic-planetesimal model for the formation of planets and satellites (Alfvén and Arrhenius, 1976). In order to develop a consistent model of the evolution of matter streams in a magnetized plasma environment we need to study in detail the physical and dynamical processes associated with the dust in such an environment. This is because the dust is thermodynamically coupled to the plasma via exchange of charge, mass, momentum and energy (Mendis, 1979a). This year we have initiated such a study within the framework of the present-day planetary magnetospheres and the heliosphere since its predictions can be verified by direct observations. In particular, we have studied the detailed physics and dynamics of interplanetary dust entering the Jovian magnetosphere (Mendis, 1979b; Hill and Mendis, 1979a, 1979b). These studies have been successful in describing the presently observed distribution of micrometeoroid dust within the Jovian magnetosphere and have thereby underscored the crucial role played by electromagnetic forces in the orbital evolution. We are extending these studies to the heliosphere. We propose detailed calculations of the orbits of these charged micrometeoroids in the combined gravitational, electric and radiative field within the heliosphere with a view of evaluating their distributions, as well as their modulations with solar cycle. We are also extending these studies to the primitive heliosphere. On the one hand, we expect that the additional electromagnetic perturbation on the dust in primitive pre-planetary matter streams will provide the essential ingredient for the continuous scrambling of orbits necessary for their eventual evolution into one or more larger bodies, rather than a thin disc. On the other hand, physical processes associated with the dust-plasma interactions seem to give a natural explanation to the regular density variation in the terrestrial planets as well as the Galilean satellites of Jupiter. We have also begun investigation of the late stages of "jet stream" evolution when a gravitating body is present (Hill, 1979).

References

- Alfvén, H. A. and Arrhenius, G., 1976, Evolution of the Solar System, NASA SP-345.
- Mendis, D. A., 1979a, Dust in Cosmic Plasma Environments, Astrophys. and Space Sci. (in press).

- Mendis, D.A., 1979b, Dust-Magnetospheric Interactions, COSPAR Space Research, Vol. XIX (Ed. M. J. Rycroft), Pergamon Press, p. 423.
- Hill, J.R. and Mendis, D.A., 1979a, Charged Dust in Outer Planetary Magnetospheres. I. Physical and Dynamical Process, The Moon and the Planets, 21, 3.
- Hill, J.R. and Mendis, D.A., 1979b, Charged Dust in Outer Planetary Magnetospheres. II. Trajectories and Spatial Distribution, The Moon and the Planets (in press).
- Hill, J.R., 1979, Jet Stream Evolution in the Presence of a Gravitating Body in the Stream (under preparation).

ASTEROID COLLISIONS AND EVOLUTION

Davis, Donald R., Clark R. Chapman, Richard Greenberg, and S.J. Weidenschilling, Planetary Science Institute, Tucson, Arizona 85719

Collisions affect asteroids in many ways. Energetic collisions serve both to destroy large asteroids and create smaller ones. They expose, on asteroid surfaces, materials originally buried at great depth. Collisions modify asteroid spins and may be largely responsible for asteroid shapes. Hirayama families are thought to be the result of past major inter-asteroidal collisions. Dynamical processes proposed for depleting Kirkwood gaps and for transporting asteroid fragments into Earth-crossing orbits to fall as meteorites usually invoke collisions. If collisions serve to fragment and disrupt even the largest asteroids on time scales comparable with the age of the solar system, then the present asteroid population itself may be a collisional remnant of a vastly greater early population. On the other hand, if the efficiency of disruption by collision is relatively low, some traits of asteroidal sizes and properties may still reflect early processes of accretion.

During the past year, we have made considerable progress in understanding the collisional evolution of asteroids. Much of our work was reported a few months ago at the 1979 meeting of Planetary Geology Principal Investigators in Providence, R.I. (Chapman *et al.*, 1979). In the intervening few months, as we await the beginning of our F.Y. 80 program, we have obtained updated results summarized here.

We have developed two numerical models for simulating asteroid collisional evolution. These programs have similar collisional physics, but emphasize different aspects of asteroid collision evolution process. One program, which is an improved version of the model described by Chapman and Davis in 1975, models the collisional evolution of the size frequency distributions of two interacting populations having different material properties; however, the populations have a fixed distribution of collision speeds. The other program computes both the size-frequency evolution and changes in the mean impact speed due to collisions among bodies of a population described by a single set of material properties.

The chief conclusions from our 1979 research are:

1. Collisional lifetimes, the mean time between collisions that remove at least 50% of a body's mass, of most asteroids larger than 50 km diameter are comparable to or greater than the age of the solar system. Hence, present collision lifetimes do not distinguish whether such asteroids are original condensations or fragments of larger bodies.

2. Most hypothetical initial C asteroid populations, except those with numerous bodies larger than 300 km diameter, collisionally evolve to the present belt in 4.5 Gy. The major part of the asteroid population is in collisional equilibrium.
3. Most asteroids larger than 100 km diameter probably are fractured throughout much of their volume; i.e., they have developed a megaregolith.
4. It is predicted that the rotation rate for large, gravitationally bound asteroids should be the equilibrium value between infrequent large collisions tending to spin up asteroids and numerous small collisions which dampen rotation. The prediction agrees with the observed mean rotation rate only if most (50-100%) of the collisional kinetic energy is converted into kinetic energy of ejecta, an unexpectedly large percentage. Results from rotational studies confirm those from collision evolution modeling; namely that for power-law distributions with a population index (incremental diameter) <4 , the initial population could not have been appreciably more numerous than the present belt population.
5. The current asteroidal encounter speed may be due to (a) gravitational stirring by massive Jupiter-scattered planetesimals, or (b) gravitational resonances with Jupiter which swept through the asteroid zone during early stages of solar system formation.
6. The large mean eccentricities and inclinations of asteroids, resulting in an average encounter speed of 5 km sec^{-1} , did not result from collisions between reasonable populations of early asteroids and Jupiter-scattered planetesimals (JSP). For most plausible distributions, the high encounter speed ($3.5\text{-}20 \text{ km sec}^{-1}$) between asteroids and JSP would have collisionally destroyed the asteroid population before there could have been a significant change in the mean orbital elements of asteroids.

Our work on early asteroid evolution suggests the following scenario. Accretion was proceeding in a high-mass-density population of proto-asteroidal planetesimals, colliding with each other at low velocities. Perhaps a Mars mass or even an Earth mass existed in the asteroid zone. Later, accretion was terminated and collisional erosion began when encounter speeds were augmented by one or more mechanisms associated with the rapid formation of Jupiter. Perhaps Jupiter planetesimals collided with and fragmented, or swept out, many asteroidal planetesimals. Alternatively, the largest Jupiter-scattered bodies gravitationally stirred up the asteroids so they began to collide destructively with themselves. Collisional destruction over the age of the solar system ground down most of the asteroidal mass to dust, which was removed from the asteroid zone. The largest present asteroids have survived battered but largely intact, since the end of the accretion era. At smaller sizes an increasing fraction of asteroids are fragments from major collisional events involving larger bodies. The smallest asteroids are overwhelmingly of fragmental origin.

For more complete discussion of our research, see our review chapter in the Asteroid Colloquium volume (Davis et al., 1979).

REFERENCES: Chapman, C.R., D.R. Davis, and R. Greenberg (1979), NASA-TM 80339, 6-8; Davis, D.R., C.R. Chapman, R. Greenberg, and S.J. Weidenschilling (1979), in Asteroids (ed. T. Gehrels and M. Matthews, Univ. of Arizona Press), in press.

SEARCH FOR PLANET-CROSSING ASTEROIDS WITH THE PALOMAR 122-CM
SCHMIDT CAMERA

Shoemaker, Eugene M., Bus, Schelte J., Williams, James G., and
Helin, Eleanor F., California Institute of Technology, Pasadena,
California 91125

Initial work was carried out in 1978 and 1979 to search for planet-crossing asteroids with large aperture Schmidt cameras. We report here preliminary results from a single field photographed by Shoemaker, Helin and Bus with the Palomar 122-cm Schmidt on four consecutive nights in early November 1978 and from follow-up positions obtained from four plates with the same telescope taken on the nights of November 28/29 and 29/30 by Charles T. Kowal, as part of his on-going solar system survey.

The original $6.6^\circ \times 6.6^\circ$ search field was centered on $\alpha = 05^h 00^m 13^s$ and $\delta = +23^\circ 04' 27''$; both our search field and the fields taken by Kowal were centered very close to the ecliptic. Baked IIIa-J plates were exposed with a Wratten 2c filter on Nov. 5.31979 - 5.36127, Nov. 6.34375 - 6.38542, Nov. 7.27048 - 7.32256, and Nov. 8.31250-8.36458. On the third and fourth nights the exposures were gated for ten minutes near the ends of the exposures. From these latter plates three well defined positions were obtained for relatively bright asteroids, one at the beginning of exposure, one at the beginning of the gate, and one at the center of the trail recorded after gating.

All four plates were scanned during the observing run with a hand lens for fast moving objects; none were found. After return to Pasadena, the plate with a gated exposure taken on the third night was examined by microscope for trailed images. Asteroids found by this method were then identified, where possible, with the aid of a blink comparator on plates taken on preceding and following nights. Positions (beginnings and ends of trails) for all objects found on more than one plate were then measured; approximate orbits and ephemerides were calculated for objects found on three or more plates, in order to identify these objects on the plates taken by Kowal in late November. After measurement of the positions of identified objects on the late November plates preliminary orbits were then obtained from ~ 25 day arcs.

Positions for a total of 232 asteroids were measured from the early November plates and reported to the Minor Planet Center. Positions were obtained on four plates for 205 asteroids, on three plates only for 20 asteroids, on 2 plates only for 6 asteroids, and on 1 plate only for one asteroid. Six of the measured objects are numbered asteroids, three have been identified with unnumbered asteroids with previously published orbits, and one is an asteroid discovered in the Palomar-Leiden Survey that became numbered during the course of our work. Remaining are 145 asteroids for which we have obtained new orbits based on ~ 25 day arcs. Apparent visual magnitudes of most of the 145 remaining asteroids are in

the range 15 to 21. Statistics for the 145 orbits (based on three positions) are given in figure 1.

The asteroids with osculating perihelion distances in the range 1.70 - 1.90 AU are of special interest as possible Mars crossers. For 13 such objects we have calculated improved orbits, based on all the observed positions, and studied the secular perturbations from the improved orbits. The results are listed in the table below:

Asteroid	Δ_4 AU	ω deg	Ω deg	i deg	q AU	e	a AU
1978VR8	-0.13	15.05	138.47	1.578	1.791	0.222	2.302
1978VL4	-0.06	201.58	229.76	4.107	1.776	0.231	2.309
1978VC6	+0.04	87.56	244.08	9.679	1.736	0.340	2.630
1978VU10	+0.05	69.65	257.07	1.926	1.767	0.226	2.283
1978VW5	+0.06	124.77	213.97	2.125	1.777	0.242	2.343
1978VV6	+0.06	274.91	47.25	2.822	1.783	0.208	2.252
1978VM7	+0.06	88.79	241.38	6.360	1.783	0.305	2.567
1978VB6	+0.06	25.69	244.88	23.572	1.859	0.202	2.329
1978VS9	+0.08	286.65	55.26	3.897	1.798	0.190	2.220
1978VB9	+0.09	342.63	54.21	3.365	1.851	0.209	2.339
1978VQ4	+0.11	76.95	227.01	4.111	1.853	0.164	2.217
1978VE7	+0.12	170.28	176.15	0.759	1.383	0.213	2.335
1978VG8	+0.14	282.08	62.53	4.302	1.870	0.270	2.561

The column headed Δ_4 gives the closest approach to Mars. Asteroids 1978VR8 and 1978VL4, for which Δ_4 is negative, are Mars crossers. After improved orbits have been calculated and studied for all 145 asteroids for which we obtained ~ 25 day arcs, it is likely that one or two additional Mars crossers will be recognized.

As more than 6 percent of the numbered asteroids are Mars-crossing, the yield of Mars crossers from 145 randomly selected new asteroids would be expected to be about 10. Our yield is less than this primarily because many of the possible Mars crossers found on the early November search field have predicted positions that do not fall on Kowal's late November plates. Among 32 new objects found with predicted positions outside the region photographed by Kowal, about a dozen are possibly planet-crossing. It is necessary to photograph a large area on the second lunation to recover the majority of planet crossers; we have attempted to secure this coverage, whenever possible, in our search programs with large Schmidt cameras.

Among other objects of interest, about 1 percent of the new asteroids found are members of the Eos family, about 4 percent are members of the Coronis family, and about 5 percent are members of the Themis family. Asteroid 1978VB6 (see table) is a Phocaea.

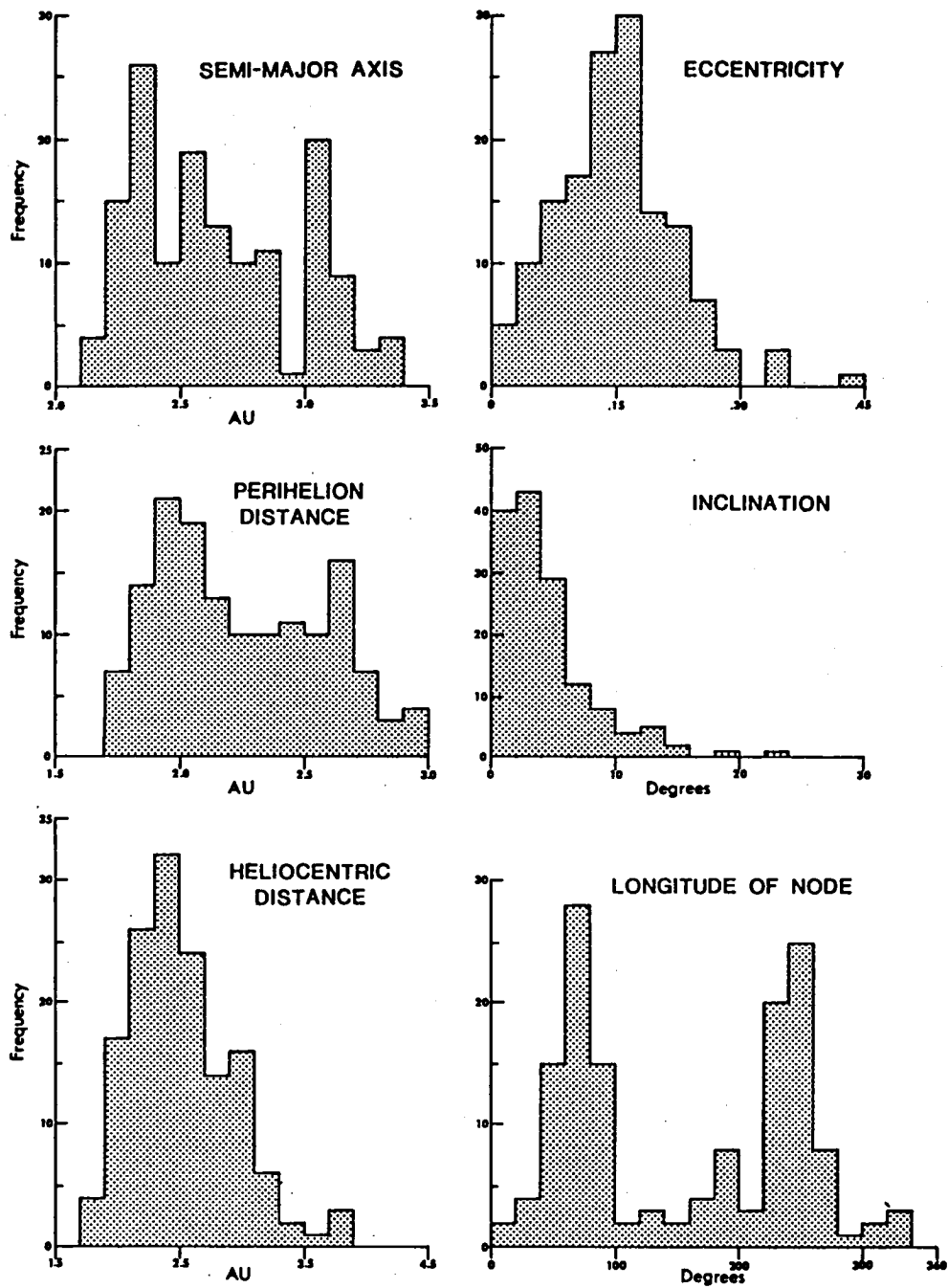


Figure 1. Distribution of semi-major axis, eccentricity perihelion distance, inclination, heliocentric distance and longitude of the node for 145 new asteroids discovered with the Palomar 122-cm Schmidt camera. Preliminary orbits are based on 24 to 25 day arcs.

Comet Encke: Precession of the Spin Axis, Nongravitational Motion, and Sublimation. F. L. WHIPPLE (& Z. SEKANINA), Center for Astrophys. - We assume that the nucleus of P/Encke is an oblate spheroid rotating about its minor axis. The observed light curve enables us to calculate the jet force from sublimation both as a torque, which causes precession of the spin axis, and as a force transverse to the radius vector, which perturbs the orbital motion. The large latitudinal variation in the sublimation rate derived from the peculiar light curve is important. Starting with the polar axis and lag angle in sublimation as derived by Sekanina, we iterate the integration over 59 perihelion passages, 1786-1977, to fit the nongravitational transverse force A_2 determined previously from orbital calculations and to derive the precession of the spin axis. The iterated fit of A_2 is better than 1/3 the mean A_2 scatter in the 17 multiple apparitions. We derived numerically four major parameters: (1) and (2) coordinates of the direction of the polar axis, (3) the lag angle (assumed constant), and (4) the ratio of rotation period to radius for an assumed oblateness. A fifth parameter involves the sublimation rate and a momentum-transfer coefficient. An independent validation lies in the excellent agreement in the derived lag angle (to $<1^\circ$) and the starting polar direction (to 4°) between our solution and Sekanina's earlier, entirely independent, results. Even more striking is the satisfactory prediction of the changing position angles of asymmetrical fan comas from 1805 to 1904, not included in his study. The calculated spin axis almost flips over between 1786 and 1977, turning more than 100° in longitude and almost 30° in latitude. The obliquity crossed the 90° mark near 1700, reached a maximum of 103° in the 1850's and dropped below 90° after 1950. The basic period of revolution should begin to increase about 1990. The rotation axis appears to have been virtually fixed for hundreds of revolutions before 1700, the currently more active polar hemisphere pointing toward the sun near perihelion. We suggest that ejected meteoroidal debris accumulated on the other hemisphere, insulating it to reduce its activity. We derive a tentative rotation period of 6^h33^m (circa 1900) by Whipple's halo method from four apparitions in 1838-71 and five in 1937-70. A possible spinup rate is some 21 minutes per century. The required mass loss by sublimation is about 0.09 percent of the comet's mass per revolution, and the mass and oblateness of the nucleus are estimated at less than 10^{16} grams and less than 4 percent, respectively.

The Shapes, Volumes and Mean Densities of Phobos and Deimos. J. Veverka,
P. Thomas, J. Gradie, J. Goguen, Cornell University.

We have reestimated the volumes of the two satellites using Viking images allowing for the actual shapes and without assuming that the satellites are triaxial ellipsoids. Silhouettes of Phobos and Deimos are shown in Figures 1 and 2. The irregular shapes of the satellites suggest that they were formed by fragmentation from larger parent bodies and the presence of ridges continuous over most of each satellite show that they are not reaccumulations of fragmented debris as has been suggested by Harris (1978).

We estimate that the actual volume of Phobos is $5050 \pm 400 \text{ km}^3$, a value similar to that used by Tolson *et al.* (1978) in estimating the density of Phobos, but smaller than that found by Turner (1978) or Duxbury (1979). For Deimos we estimate a volume of $950 \pm 150 \text{ km}^3$, substantially lower than that given by Duxbury (1979) on the basis of a triaxial model.

These volumes combined with mass estimates for the satellites given by Christensen *et al.* (1977) and by Duxbury (1979) yield the mean densities around 2 gm/cm^3 for both satellites (Table 1).

If the mean densities are really close to 2 gm/cm^3 (note the large error bars) then the best explanation is that these objects are made of low density carbonaceous chondrite material. We have constructed models in which the satellites consist entirely of regolith to see whether the constituent material can have a density much in excess of the mean density of the satellites. Assuming that under self-gravity this regolith displays the compaction characteristics of lunar soils and of laboratory materials, it is difficult to construct the satellites of materials whose mean density is significantly higher than the mean density of the objects.

TABLE 1: BULK PROPERTIES OF PHOBOS AND DEIMOS

	Phobos	Deimos
Axes (radii)		
a (km)	13.5	7.5
b	10.5	6.0
c	9.0	5.0
Mass (10^{16} gm)	9.6 ± 2.0	2.0 ± 0.7
Volume (km^3)		
Duxbury*	5200 ± 600	1300 ± 300
Thomas†	5050 ± 400	950 ± 150
Density (gm/cm^3)		
Duxbury	1.9 ± 0.4	1.5 ± 0.6
Thomas	1.9 ± 0.4	2.1 ± 0.5

* Volume of model ellipsoid.

† Volume allowing for departures from model ellipsoid.

References

- Duxbury, T. (1979). Personal communication.
- Harris, A. W. (1977). Bull. Am. Ast. Soc. 9, 519.
- Christensen, E. J., Born, G. H., Hildebrand, C. E., and Williams, B. G. (1977). Geophys. Res. Lett. 11, 555-557.
- Tolson, R. H., Duxbury, T. C., Born, G. H., Christensen, E. J., Diehl, R. E., Farless, D., Hildebrand, C. E., Mitchell, R. T., Molko, P. M., Morabito, L. A., Palluconi, F. D., Reichert, R. J., Taraji, H., Veverka, J., Neugebauer, G., and Findlay, J. T. (1978). Preliminary results of the first Viking close encounter with Phobos. Science 199, 61-64.
- Turner, R. (1978). Icarus 33, 116-140.

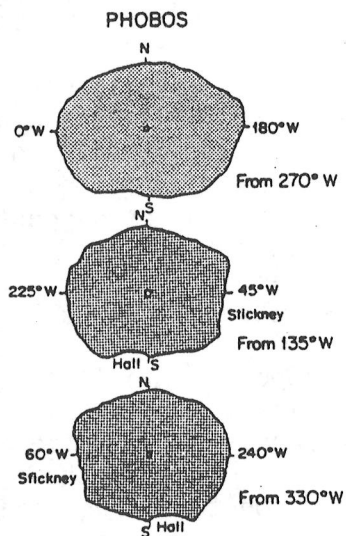


FIGURE 1. Silhouettes of Phobos based on Viking images.

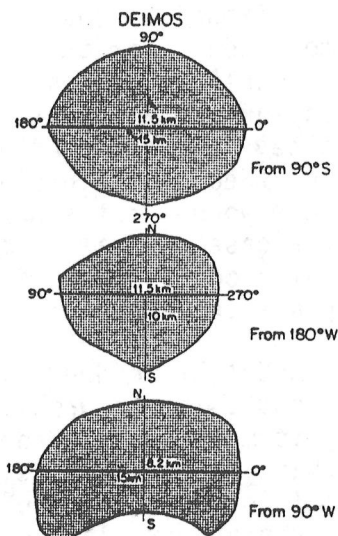


FIGURE 2. Silhouettes of Deimos based on Viking images.

DYNAMICAL STUDIES OF PHOBOS AND DEIMOS: GROOVE ORIGIN AND EJECTA DYNAMICS

Davis, Donald R., S.J. Weidenschilling, Clark R. Chapman, Richard Greenberg, Planetary Science Institute, Tucson, Arizona 85719; Kevin Housen, University of Arizona Lunar and Planetary Laboratory Tucson, Arizona 85721.

Spacecraft imagery of Phobos and Deimos, showing the unusual grooves on Phobos as well as the strikingly different surface appearances of the two satellites, presents us with new data with which to learn about the surfaces of small bodies. We describe here initial results of dynamical studies pertinent to groove origin together with the unusual ejecta trajectories and dynamical environment that exists in this satellite system.

Detailed studies of the groove system by Thomas (1978) and Thomas *et al.* (1978) show that the grooves are most prominent near the large crater Stickney. However, analysis of groove plane orientations indicates that many of them are parallel to principal planes of the approximate triaxial ellipsoidal shape of Phobos. Various hypotheses have been advanced to account for these grooves, including (a) tidal stresses due to nearby Mars (Soter and Harris, 1977), (b) aerodynamic drag stress during capture of Phobos (Pollack and Burns, 1977), (c) fractures from the Stickney forming impact (Thomas *et al.*, 1978), and secondary cratering chains (Head and Cintala, 1979). The first model predicts that grooves are young, but superimposed craters on grooves suggest that this is not the case. Tidal or aerodynamic stresses do not explain the association of grooves with Stickney. Impact fractures do not account for groove plane orientation controlled by the shape of Phobos.

A recent model by Weidenschilling (1979) proposes a modification of the impact hypothesis for groove origin. In this scenario, prior to the Stickney-forming event, Phobos was synchronously rotating in an orbit larger than its present one. The Stickney impact broke the synchronous rotational lock and started Phobos rotating about a random axis. The non-synchronous rotation, coupled with Phobos' irregular shape and the tidal gravity field of Mars, generated a time varying stress field throughout the volume of Phobos' interior which gave rise to the grooves. This model assumes that material weakened by fracturing from Stickney yielded along planes of maximum shear stress which were controlled by the shape of Phobos. Most Stickney ejecta would have been deposited over the surface, either by direct ballistic emplacement or by recapture from circum-Mars orbit, long before the non-synchronous rotation of Phobos was damped out. Hence, grooves could have been formed or regenerated subsequent to blanketing by Stickney ejecta.

Dynamical calculations using a realistic model for the satellite environment have been carried out in order to explore the plausibility of a

secondary impact origin for the grooves by Stickney ejecta. Impact loci for particles launched from Stickney in different directions and with varying speeds were calculated using a rotating, triaxial ellipsoid to represent Phobos and including the effect of Mars gravity. Calculations have been carried out both at the present distance of Phobos from Mars as well as at greater orbital distances that Phobos may have had in the past. Figure 1 illustrates impact loci at the time when Phobos was located midway between the current position and the Mars-synchronous orbit distance. Calculations at other distances and using non-synchronous rotation rates for Phobos produce impact patterns that only marginally resemble groove orientations. The best approximation to the observed groove pattern was found assuming that Phobos is far from Mars. At best, however, impact loci are consistent with only a fraction of the observed grooves; no impact loci have been found which match the grooves lying in planes which are far removed from the center of Phobos. While secondary impacts may explain some groove features, it appears necessary to seek other mechanisms also in order to understand all groove orientations.

The unusual dynamical environment of Phobos, due principally to its proximity to Mars, produces non-intuitive ejecta distribution patterns. Not only does the escape speed vary with location over the surface, but also with direction from any particular point on the surface. Furthermore, the distance that a particle travels also depends on location and initial direction, so that non-escaping ejecta from an impact would not be uniformly deposited in all directions. Ejecta distribution patterns for material launched with speeds up to 7 m/s from two sites on the surface of Phobos are shown in Figure 2. Material ejected from (0N,315E) approximately the location of the center of Stickney, shows a highly asymmetric distribution; material launched in the prograde direction (relative to the rotation of Phobos) travels further than material ejected with the same speed in the retrograde direction. The dominant cause of this asymmetry is the Coriolis force which tends to deflect particles traveling in the prograde direction away from the surface, while those moving in the retrograde sense are bent toward the surface. The effect of this force increases with increasing ejecta flight times.

Can these dynamical calculations of ejecta distributions be related to observed distributions of ejecta on Phobos? Thomas (1978) finds only two craters on Phobos that show possible evidence of ejecta as "blankets" - the hummocky area east of Stickney and a bright, rayed crater near 0°, 230°. However, inferences regarding ejecta distribution patterns and regolith thickness on Phobos and Deimos are too inconclusive for meaningful comparison with theoretical predictions at this time.

REFERENCES: Head, J.W., and M.J. Cintala (1979), NASA TM 80339, 19-21; Pollack, J.B., and J.A. Burns (1977), BAAS 9, 518-519; Soter, S., and A. Harris (1977), Nature 268, 421-422; Thomas, P. (1978), Dissertation, Cornell University; Thomas, P., J. Veverka and T. Duxbury (1978), Nature

273, 282-284; Weidenschilling, S.J. (1979), Nature, in press.

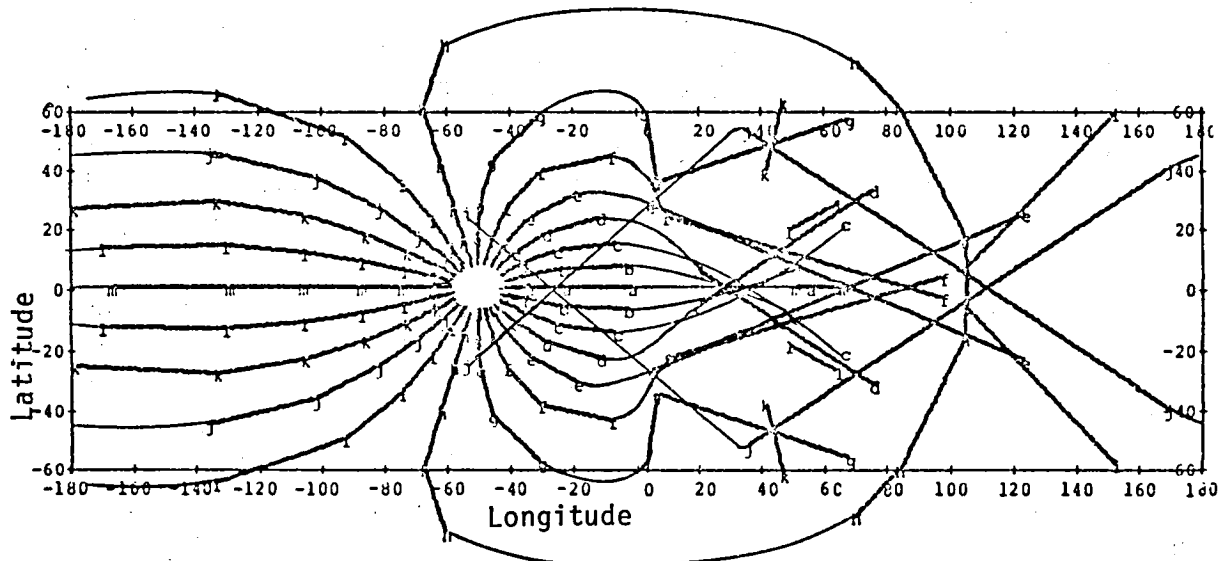


FIGURE 1: Ejecta distribution pattern from Stickney with Phobos located midway between current position and synchronous orbit distance

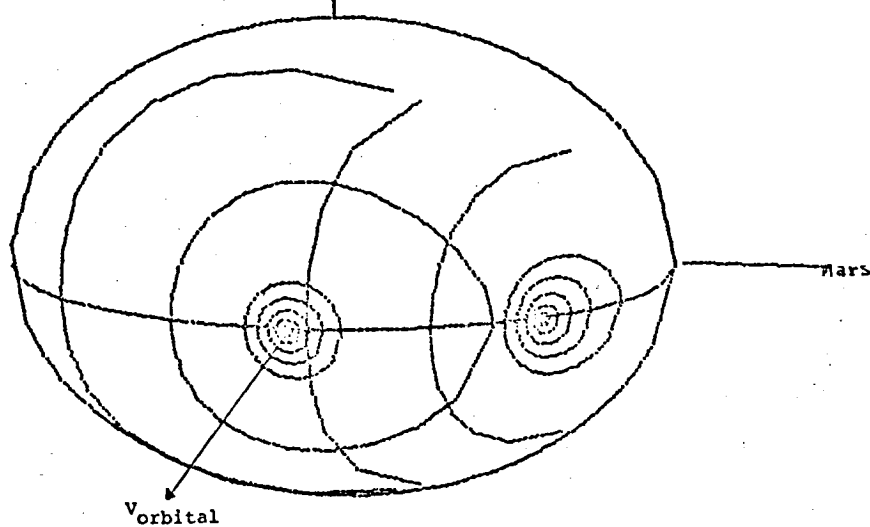


FIGURE 2: Ejecta impact distributions for three primary impacts on Phobos at (0N,270E), (0N,315E). Impact contours are calculated for ejecta velocities of 0.5, 1.0, 1.5, 2.0, 2.5, 5.0 and 7.0 m/s respectively in going from innermost to ourtermost contours and the initial launch angle was 45° from the surface normal. Variations in the ejecta distributions reflect the differences in the effective surface gravity at different points on Phobos. Non-closure of contours indicates that particles escaped in those directions.

Chapter 2

STRUCTURE, TECTONICS AND STRATIGRAPHY

ORIGIN OF LUNAR GRABENS AND CONSTRAINTS ON THE TOTAL EXPANSION OF THE MOON

Golombek, Matthew P. and George E. McGill, Dept. of Geology/Geography,
Univ. of Massachusetts, Amherst 01003

Straight and arcuate lunar rilles can provide reasonable estimates of the tensile stress and strain that have affected near-surface rocks (1, 6, 7). Furthermore, because the age of these grabens is known (2), the inferred stresses and strains constrain theories of lunar thermal evolution. Solomon and Head (6, 7) have suggested a model of lunar thermal history that is consistent with the age of the grabens. We believe that their approach is unusually interesting because of this effort to satisfy geological constraints. However, we also believe that the grabens provide an even more severe constraint on lunar thermal history.

In a study of the geometry of major lunar grabens, Golombek (1) determined that the increase in surface area of the Moon implied by these grabens could be satisfied by an increase in the lunar radius (ΔR) of ~ 20 m. If smaller and geometrically more uncertain structures are included (e.g., 2), the figure for ΔR may be increased to ~ 55 m. These numbers are not strictly dependent on any of the geometric details developed by Golombek (1), nor are they dependent on his underlying mechanical model (3). The only assumptions necessary are that the faults bounding these grabens dip $\sim 60^\circ$, and that the bulk of the global expansion is expressed as visible faults. The first assumption is supported by a wealth of observation, theory, and experiment; the second, though more debatable, is reasonable because elastic expansion or brittle failure of the coherent rocks of the elastic lithosphere will impose an extension on the overlying megaregolith which, because of its very low tensile strength, will respond by failure along faults and not be simple elastic expansion. Expansion is determined by simply estimating the average structural depth of each graben and calculating the average increase in width. Multiplying this by the graben length gives the surface area increase; ΔR is then calculated from the total area increase for all grabens. This yields a maximum ΔR because deformation of the lithosphere is assumed to be entirely elastic; if open tension cracks are formed in the lithosphere the grabens could be due, in part, to drainage of megaregolith into these cracks, thus allowing an even smaller ΔR (1).

The model by Solomon and Head (6, 7) predicts the occurrence of peak lunar volume near the end of graben formation at 3.6 ± 0.2 byBP (2). In addition, the model predicts times of expansion or contraction before and after the period of graben formation (Fig. 1); predictions that can be checked against observable surface geology. The fact that almost all lunar grabens appear as fresh, relatively unmodified features implies that they formed over a geologically short time interval. It is interesting, but probably coincidental (Fig. 1), that the thermal expansion curve of Solomon and Head (6, 7) predicts the appropriate ΔR (~ 55 m) to account for the observed grabens in about 150my before peak volume. But

where are the grabens corresponding to the much greater expansion predicted for the immediately preceding few hundred my? Terminal bombardment cannot have destroyed all of them. In particular, there should be more grabens older than existing grabens but younger than 3.9 byBP (end of terminal bombardment) than there are existing grabens. These hypothetical grabens may have been modified by impact but they should still be recognizable. The only way to account for their absence is to assume either that they were buried by younger basalts, or to conclude that the Moon did not expand significantly in the critical time interval. Although burial of grabens by basalt flows is observed on the Moon, the cumulative length of grabens which must be covered since heavy bombardment is roughly 4 times the length now present. This possibility seems highly unlikely considering that: 1) most lunar grabens occur peripheral to basins where basalt cover is thin and discontinuous, 2) some basins probably preserve nearly their entire record of extensional faulting (e.g., Humorum), and 3) some graben clusters occur entirely in highland regions (e.g., Petavius). This leaves us with the conclusion that the Moon has not expanded as much as suggested in Figure 1.

If the visible grabens can be explained by a ΔR of only a few 10's of meters, it is of interest to ask if any ΔR is necessary. As has been noted (e.g., 5) most grabens are areally related to the mare basins. Solomon and Head (6, 7) explain this as due to the superposition of local stresses due to basin subsidence on global tension resulting from expansion. However, it is possible that the entire observed extension implied by the grabens is due to bending of a thick lithosphere around the periphery of the mare basins.

Assume a rough correspondence between the position of the grabens and the position of the anticlinal flexure. Assume also that the flexure can be approximated by a circular arc of large radius of curvature (fig. 2). From the geometry of Figure 2:

$$\theta = L/(\rho + 0.5T) \approx \alpha \quad (1)$$

where L = arc length \approx width of graben belt, ρ = radius of curvature, θ = central angle subtended by L , T = thickness of elastic lithosphere, and α = maximum angle of dip of flexed surface. But the "fiber strain", ϵ_f , of a flexed beam or plate is, to first order, equal to the distance from the "neutral fiber" of the flexure divided by the radius of curvature. Thus, for the top of the elastic lithosphere:

$$\epsilon_f \approx 0.5T/\rho \quad (2)$$

and:

$$\epsilon_f \approx T\alpha/(2L - T\alpha) \quad (3)$$

Measurements of inclined layers in the Serenitatis Basin sensed by the Apollo 17 Sounder (4) suggest that α may be as high as 3.5° . Tipped craters around Mare Humorum indicate dips of $\sim 1.1^\circ$. Mare Humorum provides an excellent test because it is a small basin bounded by relatively large concentric grabens (i.e., Rimae Hippalus); if these grabens can be explained by gentle flexing alone, then the grabens associated with larger basins will be even easier to explain. For Humorum, L may be taken either as the actual width of a graben set (~ 50 km) or as the width of a concentric zone containing all associated grabens (~ 190 km). Some results are:

<u>T(km)</u>	<u>L(km)</u>	<u>α(radians)</u>	<u>ϵ_f</u>	<u>$\Delta L = \epsilon_f \cdot L$</u>	<u>ΔL(measured from grabens)</u>
50(7)	50	.019	.0096	480m	470m(1)
50(7)	190(7)	.019	.0025	475m	470m(1)

Even though the two models yield almost the same total extension (ΔL), the implied stresses differ, with $L=190\text{km}$ yielding the more believable values of tensile stress for reasonable values of Young's modulus. Increasing α increases ΔL , but also results in unrealistically high stresses.

The total expansion implied by lunar grabens is about an order of magnitude less than predicted by the model of Solomon and Head (6, 7). In fact, the grabens can be explained as entirely due to bending strains peripheral to sagging mare basins. A small amount of global expansion remains possible, but is not required. Perhaps the model for thermal evolution can be modified to predict either less expansion or a more complex curve of ΔR vs. time such that much more of the desired expansion is accomplished earlier, coincident with terminal bombardment.

- (1) Golombek, M.P., J. Geophys. Res., 84, 4657-4666, 1979.
- (2) Lucchitta, B.K., & J.A. Watkins, Proc. 9th LPC, 3459-3472, 1978.
- (3) McGill, G.E., NASA Tech. Mem. 79729, 100-102, 1978.
- (4) Phillips, R.J., & T.A. Maxwell, Lun. Plan. Sci. IX, 890-892, 1978.
- (5) Quaide, W., Icarus, 4, 374-389, 1965.
- (6) Solomon, S.C., & J.W. Head, J. Geophys. Res., 84, 1667-1683, 1979.
- (7) Solomon, S.C., & J.W. Head, Rev. Geophys. Space Physics, in press.

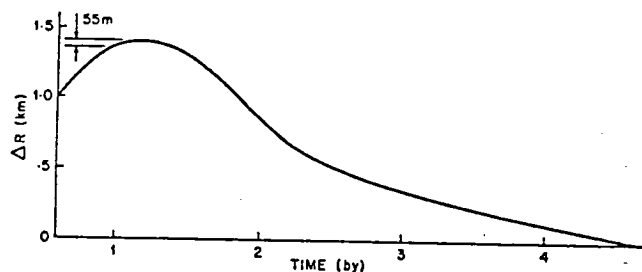


Fig. 1 Thermal model of the moon relating ΔR , the change in radius to time (6,7). Peak lunar volume occurred near 3.6 byBP when graben formation ceased (2). Plotted with this curve is the maximum ΔR necessary for the formation of all lunar grabens $\sim 55\text{m}$. This plot coupled with the observation that most lunar grabens appear in a similar state of degradation indicates that graben formation occurred during a limited ($\sim 150\text{my}$) period in lunar history. Grabens are not evident on surfaces corresponding to the expansion portion of this curve previous to this time.

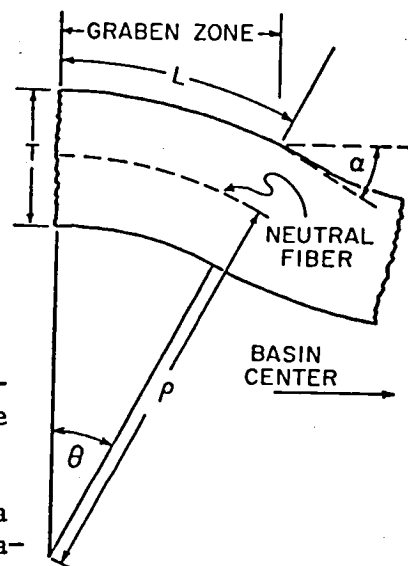


Fig. 2 Idealized geometry of basin periphery.

THE GRAVITY ANOMALIES OF OCEANUS PROCELLARUM

Whitford-Stark, J.L., Dept. of Geological Sciences, Brown Univ., Providence, RI 02912

Sjogren *et al.*¹ noted that, in Procellarum, the gravity structure calculated from the line of sight accelerations of the Apollo 16 subsatellite (Fig. 1) did not correlate with any visible surface features. Later, Scott² by combining data from several missions defined linear gravity anomalies within Procellarum; highs corresponding to mare ridges and lows to intervening topographic lows. Scott also noted that a westward shift of 1 to 2° of the gravity axes would produce a better correlation. Recent detailed mapping of Procellarum by Whitford-Stark and Head³ has defined four major lithostratigraphic basaltic units. Comparison of figures 1a and 1b indicate a correlation between the youngest, medium to high titanium basalts and the strong positive gravity anomalies. This correlation is more pronounced over the entirety of Procellarum as illustrated in Fig. 2b and Fig. 1 of Whitford-Stark and Head.⁴

Morphological criteria^{3,5} indicate the western part of Fig. 1 to be more deeply flooded than the eastern and therefore it should have a stronger positive gravity anomaly rather than a weaker anomaly. This discrepancy can perhaps be reconciled if it is assumed that the older, intermediate basalts of the western portion have undergone, at least partial, isostatic equilibration whereas the younger basalts have not. It would require a thickness of about 400 m of basalt with a density of $3.0 \times 10^3 \text{ kg/m}^3$ to produce a 50 milligal anomaly. This thickness is the estimated average thickness of Procellarum basalts.⁶ It was during the deposition of the sequence of intermediate basalts that the tectonic rilles near the mare/highland boundary and the major mare ridges terminated formation. The younger titanium basalts contain no tectonic rilles and only minor ridges. Thus by the end of deposition of the intermediate basalts, the lunar crust was not responding to the basalt load as dramatically as earlier.⁷ In fact, the pre-existing ridges acted to channel and confine the youngest Procellarum flows.⁶

Employing the simplified relationship of Haskell⁸

$$t_e \approx \frac{20\eta}{\rho g \ell}$$

(where t_e is equilibration time, η is the crustal viscosity, ρ is the density, g is gravity and ℓ is the half length) with the values for Procellarum ($\ell = 275 \times 10^3 \text{ m}$, $\rho = 3.0 \times 10^3 \text{ kg/m}^3$, $g = 1.62 \text{ m/s}^2$ and t_e as the age of the intermediate basalts estimated at $3.3 \pm 0.3 \text{ b.y.}$ ³) gives an estimated crustal viscosity of approximately 7.0×10^{25} poise. This is of the same order of magnitude as that derived by Kunze⁹

GRAVITY ANOMALIES OF OCEANUS PROCELLARUM

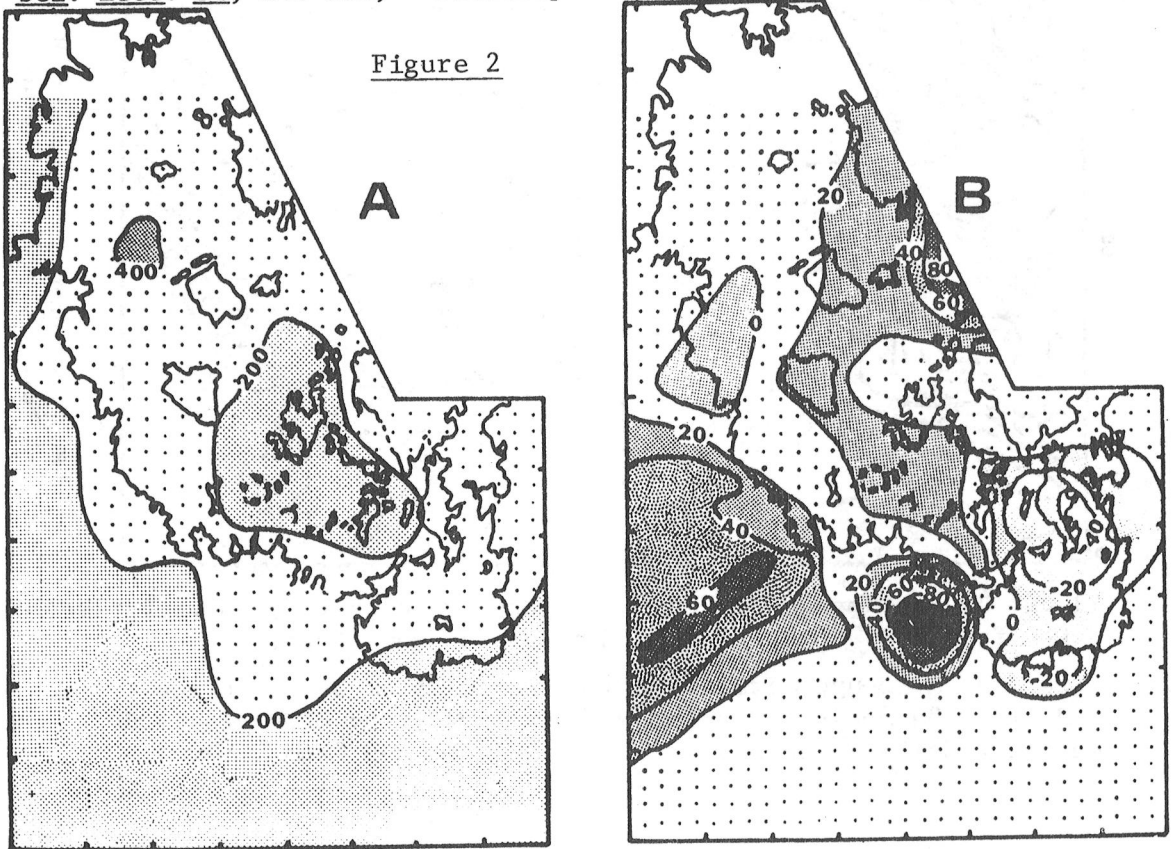
Whitford-Stark, J.L.

($1.6 \pm 0.3 \times 10^{25}$ poise) for the lunar mare crust on the basis of settling trends of mare craters. The non-isostatic behavior of the youngest Procellarum basalts could reflect a rapid increase in sub-mare crustal viscosity following the deposition of the intermediate basalts.

Other prominent gravity-geology correlations of figures 1 and 2 are the negative anomalies of young craters and highland material and the positive anomalies of Humorum, Imbrium and Orientale. Particularly interesting in the linear positive anomaly to the southwest of Procellarum (Fig. 2b). This correlates with Rima Sirsalis which also has an associated magnetic anomaly¹⁰ and has been interpreted as a major structural feature of Procellarum;³ probably a dike intruded fault.

References: ¹Sjogren W.L. et al. 1974, *The Moon* 9, 115-128; ²Scott D.H. 1974, *PLSC-5*, 3025-3036; ³Whitford-Stark J.L. and Head J.W. 1979, Submitted to *J. Geophys. Res.*; ⁴Whitford-Stark J.L. and Head J.W. 1978, *Lunar & Plan. Sci.* IX, 1250-1252; ⁵DeHon R. 1979, *Lunar & Plan. Sci.* X, 274-276; ⁶Pieters C.M. et al. 1979, Submitted to *J. Geophys. Res.*; ⁷Solomon S.C. and Head J.W. 1979, *J. Geophys. Res.* 84, 1667-1682; ⁸Haskell N.A. 1937, *Am. J. Sci.* 33, 22-28; ⁹Kunze A.W.G. 1974, *Phys. Earth Plan. Int.* 14, 1-12; ¹⁰Anderson K.A. et al. 1977, *Earth Plan. Sci. Lett.* 34, 141-151; ¹¹Frontispiece, *PLSC-5*; ¹²Frontispiece, *PLSC-7*.

Figure 2



GRAVITY ANOMALIES OF OCEANUS PROCELLARUM

Whitford-Stark, J.L.

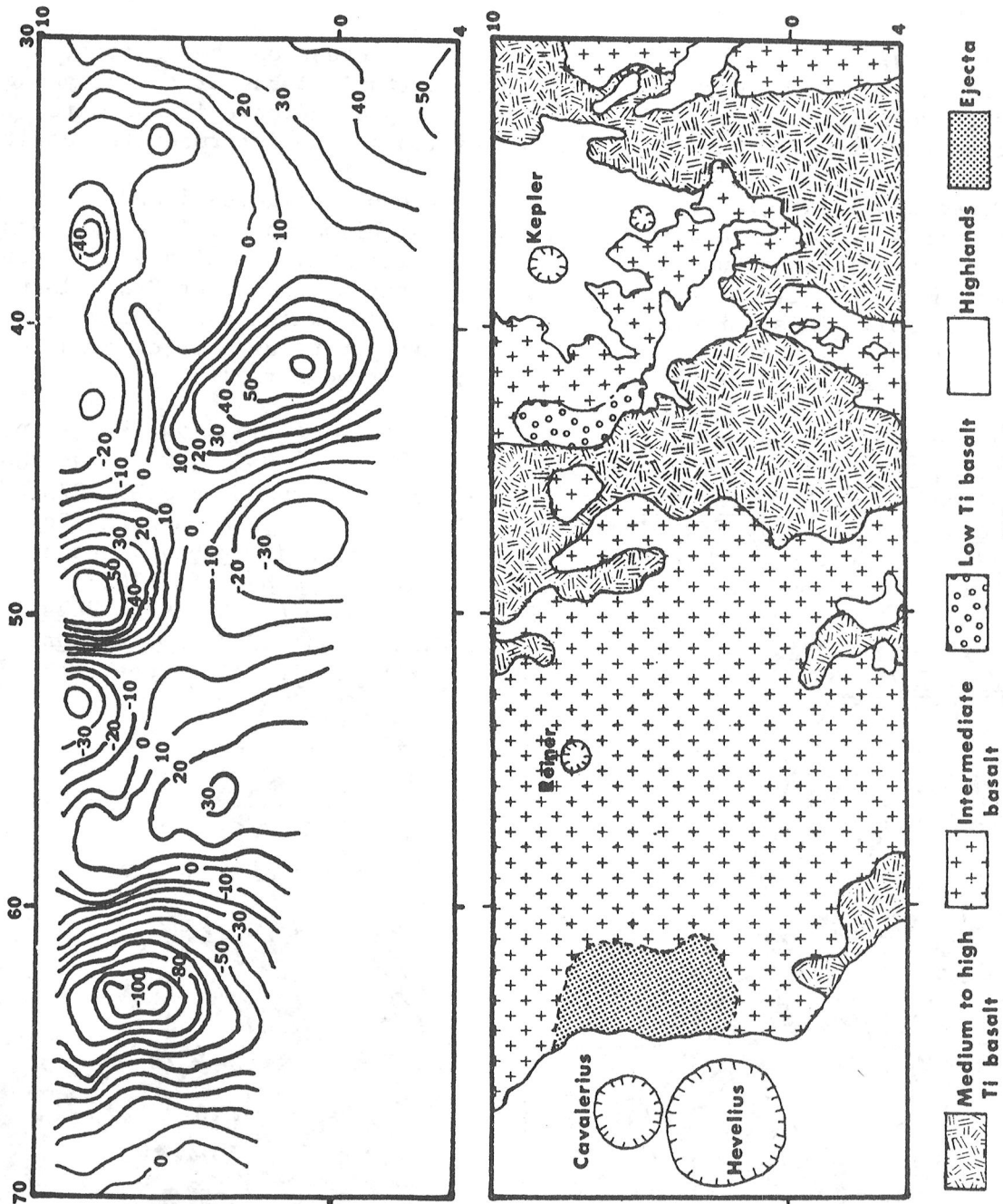


Figure 1

Figure 1. A. Gravity structure of part of southern Oceanus Procellarum taken from (1). B. Geological map of the same area.

Figure 2. A. Bouger gravity map of Procellarum based on twelfth degree and order harmonic. Taken from (11). B. Gravity of Procellarum at 100 km altitude based on 350 surface disks. Taken from (10).

IRREGULARITIES OF LUNAR BASIN STRUCTURE

Wilhelms, Don E., U.S. Geological Survey, Menlo Park, CA 94025

Most previous reviews of ringed impact basins have stressed regularities of ring spacing and morphologic similarities to craters (1-9). Ring spacing and overall complexity do seem to increase approximately with basin size (2-9), and deposits of basin ejecta generally resemble those of craters. Irregularities and asymmetries, however, also characterize basins. In this abstract I describe some departures from ideal ring form and ejecta pattern that may shed light on the still-vexing problems of ring origin and size of the excavated cavity.

Interior: Well-exposed basins the size of Hertzprung (570 km) and larger display irregular or chaotic interior morphology that replaces the regular ring structure in some sectors. For example, much of the north half of the figure-8-shaped Humboldtianum double or triple basin (10) consists of irregular, ragged hills apparently at the level of the surrounding terrain. Even the otherwise annular Orientale contains a jumbled zone in which ring structure is weakly evident. Morphologies both of these irregular zones and of the better defined peak rings of basins (4) are more nearly consistent with origin by forceful uplift (1,9,11,12) than with passive postexcavation adjustments (2,4,5,7). The uplift may have been oscillatory--one of the earliest mechanisms proposed for ring origin (1,11) and recently revived (12).

Topographic rim and exterior: Rings that bound the topographic basin--and that are considered alternatively as the boundary of the excavation (9,13,14) or as exterior scarps (7,10,15-17)--also depart from perfect concentricity and regular morphology. For example, Imbrium is bounded by a single, massive topographic rim in the south and southeast (Montes Carpatius and Apenninus), but the continuation of Montes Apenninus apparently splits into two segments in Montes Caucasus (fig. 1). One segment continues as the rugged Montes Alpes, which is the apparent inner boundary of the knobby Alpes Formation. The other continues as the scarp-like but massif-lined north shore of Mare Frigoris, which is the apparent inner boundary of lineated deposits and secondary-impact grooves. Therefore the Imbrium basin rim is single in the south and double in the north. The division occurs at an outward bend in Montes Caucasus, whose summit is lineated at an angle that is oblique to the scarp but radial to the center of the Carpatius-Apenninus-Alpes circle (lat. 33°N, long. 17°W). The Serenitatis rim may have blocked expansion of the Imbrium basin in the Apenninus-southern Caucasus sector during the excavation, while the Frigoris sector expanded farther because of more favorable target-material properties. The northern pair of rings resembles the Rook-Cordillera pair of Orientale (3-9,15,16) in respect to summit morphologies, relative positions, and ejecta type.

The irregularities of the outer rings may be interpreted as the result of either differential deformation or differential excavation. The purely deformational model that is most nearly consistent with clear geologic relations at Orientale (superposition of ejecta on the Cordillera ring; 9,15,16) involves downward and inward movement, during cratering, of a deformed zone outside the excavation (15,16). In this model, the curved Caucasus scarp of Imbrium formed during cratering and was struck grazing blows by projectiles from a cavity bounded by Montes Alpes. I suggest, alternatively, that deformed material was also ejected from the outer zones of Imbrium (Alpes-Frigoris shelf) and Orientale (Rook-Cordillera shelf; 9). Experimental analogs suggest that spalling or other deformation ahead of the expanding excavation differentially preconditioned the outer zones for subsequent ejection (18). Differential deformation and differential excavation are both consistent with the postulate that the main excavated cavity is gravity-scaled ($1/4$ root) whereas the outer zone is strength-scaled ($1/3$ root) the differences in the two dimensions become increasingly significant in high-energy impacts (17,19). The inner, gravity-scaled cavity (Alpes-Apenninus-Carpatus; Rook) may be the source of most ejecta, but the shelves contribute their share in easily stripped zones of large basins, and their outer boundary (Frigoris-Apenninus-Carpatus; Cordillera) is the excavation boundary. Crisium may have been excavated to a 530-km radius in some sectors.

Ejecta blanket: The best observed basin-ejecta blankets and secondary-crater fields are asymmetric (Orientale (16), Schrödinger, Imbrium, Nectaris, Hertzsprung, Korolev, Humboldtianum). Their map patterns are elongated N-S or NW-SE. These patterns (also observed in crater ejecta) are consistent with basin formation by oblique impacts from directions perpendicular to the elongations (16,20,21). Shallower depths of energy release than for craters are indicated by the linear geometry of "sculpture" (1,11) and of such secondary-crater chains as those of Schrödinger.

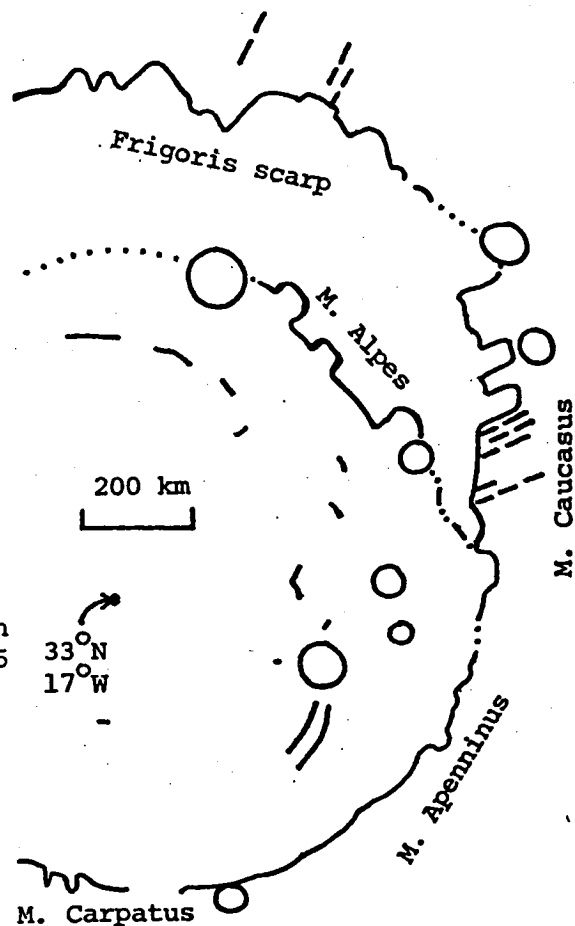
Discussion and conclusions: The general picture of ringed basin structure seems to be one of irregularities superposed on an overall, more regular pattern dictated by impact magnitude. Oblique impacts apparently produced the asymmetric ejecta and may also have caused the interior and exterior irregularities, perhaps because their energy is coupled into the target material from a sloping zone (21). Layering of target materials is an attractive explanation for departures from the regular scheme including (a) the peak-in-ring-in-rim configuration of the otherwise craterlike Antoniadi and Compton (9), (b) two pulses of ejecta from large basins (lineated Hevelius and knobby Montes Rook types at Orientale; 9,15,16,22), (c) interplanetary differences in basin morphology, (d) partial rimlike morphologies of nested basin rings (9,13,14), (e) diverse development of interior sectors of a basin, and (f) differential deformation or excavation of outer zones.

(1) Baldwin, R.B., 1949, *The Face of the Moon*; 1963, *The Measure of the Moon*: Univ. Chicago Press. (2) Hartmann, W.K. and Kuiper, G.P., 1962, *Comm. Lunar and Planet. Lab. no. 12*. (3) Stuart-Alexander, D.E. and Howard, K.A., 1970, *Icarus* 12, 440-456. (4) Hartmann, W.K. and Wood, C.A., 1971, *The Moon* 3, 3-78. (5) Howard, K.A., Wilhelms, D.E. and Scott, D.H., 1974, *Rev. Geophys. Space Phys.* 12, 309-327. (6) Moore, H.J., Hodges, C.A. and Scott, D.H., 1974, *Proc. 5th LSC*, 71-100. (7) Head, J.W., 1974, *The Moon* 11, 327-356; 1977, *in* (23), 563-573. (8) Wood, C.A. and Head, J.W., 1976, *Proc. 7th LSC*, 3629-3651. (9) Wilhelms D.E., Hodges, C.A. and Pike, R.J., 1977, *in* (23), 539-562; Hodges, C.A. and Wilhelms, D.E., 1978, *Icarus* 34, 294-323. (10) Lucchitta, B.K., 1978, *USGS Map I-1062*. (11) Baldwin, R.B., 1972, *Phys. Earth Planet. Interiors* 6, 327-339; 1974, *Proc. 5th LSC*, 1-10. (12) Dence, M.R. and Grieve, R.A.F., 1979, *Lunar and Planet. Sci. X*, 292-294. (13) Oberbeck, V.R., 1975, *Rev. Geophys. Space Phys.* 13, 337-362. (14) DeHon, R.A., 1978, *Lunar and Planet. Sci. IX*, 232-234. (15) McCauley, J.F., 1977, *Phys. Earth Planet. Interiors* 15, 220-250. (16) Scott, D.H., McCauley, J.F. and West, M.N., 1977, *USGS Map I-1034*. (17) Croft, S.K., 1979, *Lunar and Planet. Sci. X*, 245-247. (18) *In* (23), p. 40, 96-97, 893, 989, 1004. (19) Dence, M.R., Grieve, R.A.F. and Robertson, P.B., *in* (23), 266-268. (20) Moore, H.J., 1976, *USGS Prof. Paper 812-B*. (21) Gault, D.E. and Wedekind, J.A., 1978, *Proc. 9th LPSC*, 3843-3875. (22) *In* (23), p. 52-58, 71-100, 1089-1100. (23) Roddy, D.J., Pepin, R.O. and Merrill, R.B., eds., *Impact and Explosion cratering*: Pergamon Press.

Fig. 1. Sketch of Imbrium basin rings based on Orbiter 4-M-115

- Ring crest
- Inferred connection
- Linear groove
- Superposed crater

(North at top)



NORMAL FAULTS ON MERCURY: EXAMPLES IN THE KUIPER QUADRANGLE

Scott, D. H., U.S. Geological Survey, Flagstaff, Arizona 86001,
Underwood, J. R., Jr., Dept. of Geology, Kansas State University,
Manhattan, Kansas 66506, and De Hon, R. A., Dept. of Geosciences,
Northeast Louisiana University, Monroe, Louisiana 71209

Linear scarps resembling those formed by normal faults occur in several areas on Mercury. Around large basins, particularly Caloris, these scarps form radial or subradial straight-walled valleys similar to some of those around the Orientale and Imbrium Basins on the Moon (1,2). Whether these features are faults and grabens of tectonic origin or represent sculpture produced by gouging of low-angle ejecta and overlapping secondary craters is difficult to tell, as distinguishing criteria are usually absent. Some scarps, however, are not associated with basins and appear comparatively fresh and young (3). They do not have lobate fronts with rounded crests that are characteristic of lava flows and thus probably are fault scarps. Unlike the Moon, where rilles cross rugged highlands and smooth plains alike, the flatness of the mercurian terrain and consequent small deviations of the fault traces provide little information on the inclinations of their planes.

In the Kuiper quadrangle, scarps interpreted as normal faults have been mapped in smooth plains material covering the floors of relatively young (class 4) craters (4,5). These faults clearly offset the plains material, and their traces are also discernible in places on the walls of some craters where they are inclined in directions consistent with normal displacements. In the 75-km-diameter crater centered near lat 19° S, long 31°, two branches of a northwest-trending fault are nearly linear and parallel but discontinuous at the crater's central peaks (fig. 1). Plains on the southwest side of the faults are lower than those on the northeast. The northwest branch of the fault intersects the crater wall within a shadow zone, but the scarp is still faintly visible as a brighter line extending upward along the wall with the geometry indicative of a fault plane dipping to the southwest. The southeast fault branch appears in the crater wall as a slight declivity. There, too, the change in direction of the fault trace from crater floor to wall reflects normal displacement.

Another young crater about 70 km in diameter located near lat 16° N, long 30° also shows a northwest-trending fault across its central floor and walls, similar to the preceding example. Here, however, there is less deviation in the surface trace of the fault from floor to wall, probably indicating a more steeply dipping plane. At other places within Kuiper and other quadrangles of Mercury, scarps transect crater walls and adjacent terrain but maintain their linearity, and thus may represent high-angle normal, reverse, or vertical faults (6).

A few depressions on Mercury resemble broad rilles or rift valleys and are partly bounded along their length by scarps. One of these in the Kuiper quadrangle, Santa Maria Rupes, shows opposing low-relief scarps across a wide valley in its northern part and is mapped as a graben (5). Another prominent scarp in the Discovery quadrangle, appropriately named "Discovery Rupes", is several hundred kilometers long and has a lobate and rounded front. It has been interpreted to be a thrust fault on the basis of its morphology (7). However, where this feature transects a crater located near lat 54° S, 38°, the feature consists of two opposing scarps separating a long, depressed region having the appearance of a graben.

Normal faults on Mercury are much less numerous than on the Moon. Their occurrence, however, in relatively young plains material may signify a late period of crustal extension in the evolutionary history of the planet.

REFERENCES

- 1) Scott, D. H., McCauley, J. F., and West, M. N., 1977, Geologic map of the west side of the moon: U.S. Geol. Survey Misc. Geol. Inv. Map I-1034.
- 2) Scott, D. H., 1972, Structural aspects of Imbrium sculpture, in Apollo 16 Preliminary Science Report, U.S. Nat. Aeronautics and Space Admin. SP-315, p. 29-31 to 29-33.
- 3) Atlas of Mercury, 1978, U.S. Nat. Aeronautics and Space Admin. SP-423, p. 53, figs. 3-27 and 3-28; p. 93, figs. 8-17.
- 4) Scott, D. H., De Hon, R. A., and Underwood, J. R., Jr., 1976, The geology of the Kuiper quadrangle of Mercury (abs.), in Papers Presented to the Conference on Comparisons of Mercury and the Moon, Lunar Science Institute Publication 262, p. 31.
- 5) De Hon, R. A., Scott, D. H., and Underwood, J. R., Jr., 1980, Geologic map of the Kuiper quadrangle of Mercury: U.S. Geol. Survey Misc. Geol. Inv. Map I-1233, in press.
- 6) Atlas of Mercury, 1978, U.S. Nat. Aeronautics and Space Admin. SP-423, p. 35, fig. 2c.
- 7) Strom, R. G., Trask, N. J., and Guest, J. E., 1975, Tectonism and volcanism on Mercury: J. Geophys. Res., v. 80, no. 17, p. 2478-2507.

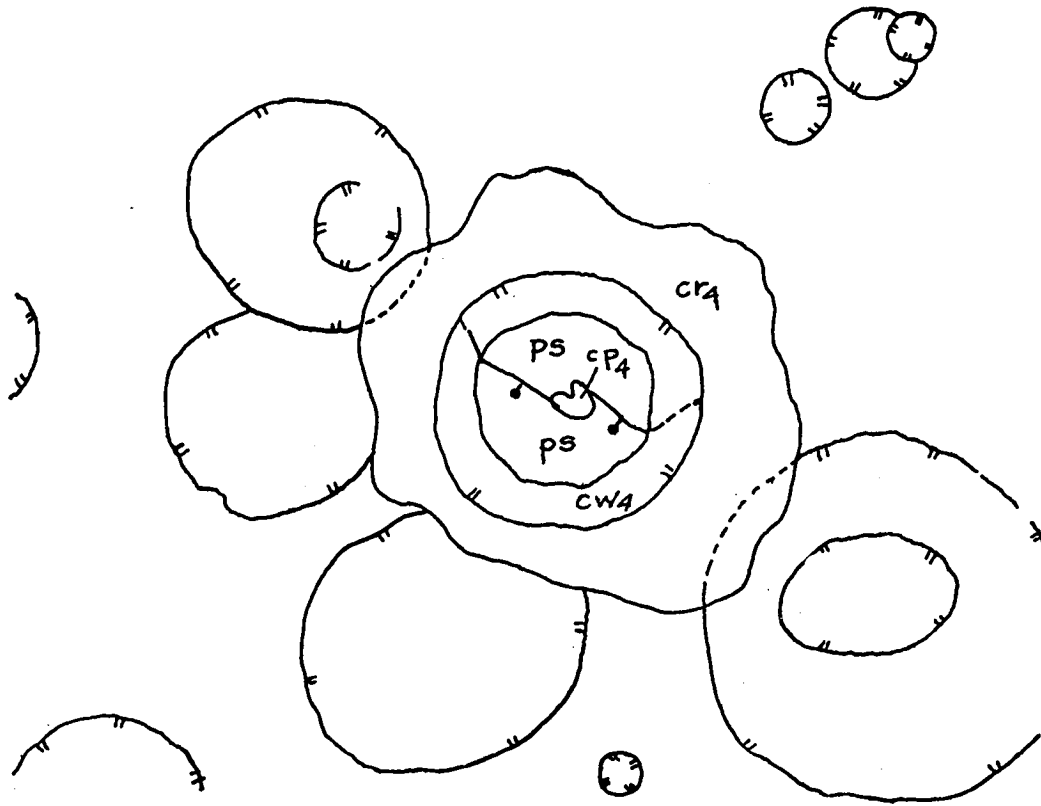


Figure 1.--Normal fault cutting walls and floor of crater. Rimcrests of older and/or smaller craters in area are shown by conventional symbol. Letter symbols; ps, smooth plains, cp₄, cw₄, and cr₄ indicate central peak, wall, and rim respectively of class 4 crater.

INTERCRATER PLAINS OF MERCURY

Leake, Martha A., Lunar and Planetary Laboratory, University of Arizona, Tucson, AZ, 85721

Following the Mariner 10 flybys of Mercury, a study was undertaken to define and constrain the nature and origin of the intercrater plains. This study consisted of geologically mapping Mercury's incoming side and of determining crater statistics of heavily cratered terrain and surrounding intercrater regions. The smooth plains of the incoming side and the lunar intercrater plains in the southern highlands were studied similarly. The major product of this research is a geological terrain map of the incoming side of Mercury employing five units each of crater and plains materials to sizes as small as 40 km. Map units are extended into the hilly and lineated terrain establishing map continuity and enabling a determination of the relative age of this area. Plains units are assigned an age based on the relative ages of the craters which they embay or which are superposed on them, a method used in the forthcoming USGS maps of Mercury's quadrangles. Relative ages of craters were derived from their degradational state patterned after that system used by the Lunar and Planetary Lab for lunar craters; class 1 craters are freshest and class 5 most degraded (1). For example, plains within class 2 craters or superposed on C2 ejecta blankets, and cratered by C1 craters or their secondaries, are designated P2 plains. The relative ages of the oldest plains units are still ambiguous; they may overlie or underlie the oldest C5 craters. An additional category, C5', designates the vague, ancient, circular depressions, often buried by P5 material. The P5 through P3 plains generally comprise the intercrater plains mapped by Trask and Guest (2); most of the P1 and P2 units are textural equivalents of the smooth plains occupying large areas of the outgoing side. Table 1 lists the crater classes and plains units, their descriptions and the percentage of map area covered by each.

The hilly and lineated area forms a critical link between relative ages established on the outgoing and incoming sides. Rather than designate this area as a separate unit or deposit, it was treated as a region disturbed by some distinct event. To determine the relative age of this disturbance, plains and crater units were continued into this region from the surrounding area. Sections of rims of class 3 craters are modified where they extend into the hilly and lineated area; exterior to this boundary, the rims are intact. Class 1 and 2 craters superposed on this surface are unmodified. Furthermore, smooth plains in this zone are undisturbed and fill older, heavily disrupted craters such as Petrarch. Hummocky P3 material fills some craters of classes 3, 4, and 5 northeast of Petrarch. These stratigraphic relations suggest that the disturbance occurred sometime between the formation of class 2 and 3 craters. Independently, in geological mapping of the H-3 and H-8 quadrangles, McCauley et al. (3) find that the Caloris impact occurred between the formation periods of (LPL) class 2 and 3 craters. This agreement of relative ages lends support to the proposal by Schultz and

Gault (4) that the hilly and lineated terrain was disrupted by seismic waves which were generated by the Caloris impact and then focused on its antipodal area.

Using the Caloris impact at the end of the class 3 period as a "time horizon," craters and plains units of the geologic map were dated relative to the Caloris event. Paleogeologic maps were constructed by grouping units of class 1 and 2 as Post-Caloris features, units of class 3 as "Caloris" features, and units of classes 4, 5, and 5' as Pre-Caloris features. Large basins of 100 to 400 km in diameter and ubiquitous plains dominate the Pre-Caloris surface. Since some plains even bury the C5' structures and their underlying surfaces, the intercrater plains are not primordial. The "Caloris" surface also consists of mostly pre-Caloris material, but is labelled separately to emphasize the continuing plains emplacement and fairly heavy cratering which preceded the Caloris impact. By contrast, the Post-Caloris surface is sparsely populated with craters and plains. Many of the smooth plains are isolated, remote from younger craters, interspersed with older plains deposits, or lie in Pre-Caloris craters and basins. This distribution makes it unlikely that the smooth plains were formed strictly by ballistic deposition of ejecta. The paleogeologic maps and measurements of the existing plains' area (Table 1) confirm that plains formation on the incoming side generally decreases with time, falling off extensively after the C3 cratering period. The percentage of the mapped area ($A = 1.0284 \cdot 10^7 \text{ km}^2$) covered by different ages of plains, both exterior and interior to craters, was compared to the percentage area covered by the craters. This latter value is an upper limit to crater areal coverage determined by summing the values of crater "density" $p = (\pi D^2 N \cdot 100) / (4A)$ over all diameters $> 40 \text{ km}$ for each class of crater. D is the geometric mean of the diameter bin; N is the number of craters in that bin. In general, the percentage of area covered by craters also declines with decreasing age, although not in a manner to suggest plains formation by ejecta deposition alone. Gault et al. (5) have noted that the extent of the continuous ejecta blanket and secondary crater field around mercurian craters is more limited than around lunar craters. Trask and Strom (6) have noted that some craters are relatively well preserved near the rims of later basin-sized impacts, indicating that the resurfacing potential of mercurian craters is not extensive. Table 1 shows that intercrater plains P3 through P5 cover nearly 44% of the map surface while only 30% is covered by craters of the same ages. If the resurfacing potential of existing craters is small, then many more basins than are visible are required to create this amount of intercrater material through deposition of ejecta. Contribution of surface material from a third source, which is most likely volcanic, is indicated.

The three competing theories of the origin of Mercury's plains are: (a) a primordial surface remaining after global melting and solidification, (b) basin ejecta and melt deposits, and (c) volcanic deposits. It is

doubtful that the oldest intercrater plains (P4 and P5) represent a primordial surface because their formation spans a range of time overlapping Mercury's heavy bombardment represented by class 4 and 5 craters. Furthermore, parts of the oldest plains unit (P5) buries craters even older than class 5. Extensive areas of younger intercrater plains (P3) were apparently emplaced near the end of heavy bombardment. As noted above, resurfacing by ballistic deposition must be supplemented by other materials and processes. Arguments for plains formation by volcanism include the extensive nature of the intercrater plains, the lack of source basins for these plains as well as for isolated smooth plains filling older craters, and tentative volcanic features. Strom (7) and Dzurisin (8) and others suggest that the crater Renoir contains volcanic material; that hypothesis is supported in this analysis. On the incoming side and adjacent quadrangles, such as H-15 and H-12, domical structures, large sinuous valleys headed in craters, rimless depressions, and flat, inundated craters with radiating tectonic features may be sites of past volcanic activity, some of which are quite ancient. Ridges like Mirni Rupes may be, as suggested by Dzurisin (8), fissures along which extensive plains deposits were extruded.

In summary, complex and varied origins are indicated for the plains of Mercury's incoming side. A primordial surface is unlikely. Instead, there appears to be a subtle interplay of volcanic and ballistic processes at work; it is likely that the intercrater plains represent a volcanic surface interbedded with ballistic ejecta from basins, disrupted by basin secondaries and smaller craters.

References:

1. Arthur, et al., 1963, *Comm. Inner Planet. Lab* 2, pp. 71ff.
2. Trask, H.J. and Orest, J.E., 1975, *J.G.R.* 80, pp. 2461-2477.
3. McCauley et al., 1979, *Icarus*, in press.
4. Schultz, P.E. and Gault, D.E., 1976, *Geol. Soc. 15*, pp. 479-480.
5. Gault, et al., 1975, *J.G.R.* 80, pp. 2444-2460.
6. Trask, H.J. and Strom, R.G., 1976, *Icarus* 28, pp. 559-563.
7. Strom, et al., 1975, *J.G.R.* 80, pp. 2476-2507.
8. Dzurisin, D., 1978, *J.G.R.* 83, pp. 4883-4906.

Table 1: Description of the Geological Map of Mercury's Incoming Side

Era	Plains/Crater Class	Brief Description of Materials	% of mapped area covered ^a
Post-Caloris	P1	Very smooth plains material	0.85 (0.01, 0.94) ^b
	C1	Fresh and/or rayed craters	1.3 ^c
	P2	Smooth plains material where thick, rougher where thin, burying rough topography	9.3 (3.3, 6.0)
Caloris	C2	Moderately fresh craters	5.4
	P3	Moderately smooth to hummocky plains	14.4 (11.4, 3.0)
	C3	Moderately subdued craters, rounded rims	10.0
Pre-Caloris	P4	Moderately rough to hilly intercrater plains	11.4 (9.8, 1.5)
	C4	Subdued, dissected craters	12.5
	P5	Very rough, knobby and pitted plains	18.6 (18.5, 0.1)
	C5	Highly subdued craters	7.6
	C5'	Ancient circular depressions; vague rims	10.5
	Hilly and Lineated	Hilly and lineated material, large massive hills and troughs	0.06

a. Total mapped area A = $1.0284 \cdot 10^7$ km²

b. In parentheses are % area of exterior and interior plains, respectively.

c. Crater area percentage = $\Sigma(\pi D^2 N \cdot 100) / (4A)$ for each crater class over all diameter bins of geometric mean bin size D340 km, N craters per bin.

PLAINS-FORMING MATERIALS OF THE KUIPER QUADRANGLE OF MERCURY. R. A. De Hon, Northeast Louisiana University, Monroe, LA 71209, D. H. Scott, U. S. Geol. Survey, Flagstaff, AZ 86001, and J. R. Underwood, Jr., Kansas State University, Manhattan, KS 66506.

Surface Characteristics. Plains-forming materials (units pc and ps) occur over 27% of the Kuiper quadrangle (fig. 1). The older of these units is a cratered plains material that has a surface exposure of approximately 16% of the region. The cratered plains material (unit pc) is relatively flat with broad ridges and lobate scarps that resemble those of the lunar maria. The albedo is intermediate compared to that of other mercurian units, but higher than the lunar maria. Smooth plains material (unit ps) occurs in 11% of the region. These occurrences are generally as small patches with few or no distinctive characteristic surface features. The surface is flat and smooth with a few lobate scarps and relatively small ridges that more nearly resemble flow fronts and mare ridges on the moon. The albedo is similar to that of the cratered plains material.

Location and Distribution. Both plains units appear to be located at lower elevations in the quadrangle and occupy crater and basin floors or broad irregular lowlands within the subdued terra (unit ts). At least some of the cratered plains material occupies roughly circular areas which may represent impact basins which have lost almost all distinguishing characteristics because of their advanced stage of degradation and superposed younger materials (fig. 1). Smooth plains material is chiefly restricted to crater interiors or relatively small low lying areas within regions of cratered plains material.

Thickness. Rough estimates of the thickness of the plains materials, based on exposed rims of partially buried craters, indicate maximum thicknesses of 1050 m in basins, whereas thickness of 700 - 800 m are more common in irregular patches. Plains-forming materials within the inner basins of Renior and Homer are approximately 800 - 1000 m thick, indicating that the basins are not especially deep. Mare fill within lunar basins of comparable size is generally 1250 - 1800 m thick (1), but most lunar basins are more completely flooded.

Age. Contacts between plains materials and subjacent units range from sharp to gradational. Embayment relations are especially clear, in places, between smooth plains and older units including crater rims, smooth and rough terra, and even cratered plains material. Smooth plains material covers the floors of craters of all ages,

but in places this material is overlapped by crater materials or secondaries from c_5 , c_4 , and rarely by c_3 craters. Cratered plains material embays or floods craters in classes c_1 and c_2 and some c_3 craters; crater plains material is overlain by some c_3 and younger craters. Thus both units taken together may have a relatively wide age range. It is difficult to obtain reliable crater counts on the cratered plains material because primary and secondary craters cannot everywhere be separately distinguished. The crater density of the cratered plains material is higher than that of the smooth plains and lower than the terra materials. The smooth plains material has a cumulative crater frequency of about $7.5 \times 10^2 / 10^6 \text{ km}^2$ for craters larger than 2.5 km diameter which is comparable to that of the lunar maria near the Apollo 11 landing site (2,3). Neither of the plains materials represent a single, short episode of deposition, rather the materials were emplaced episodically over a long time.

Origin. Mercurian plains exhibit morphologic features and areal distributions that are somewhat similar to those of both the maria and smooth plains materials of the moon. Mercurian plains-forming materials may have diverse origins, but they are presumed to be chiefly volcanic. Surface characteristics that support a volcanic origin include: partially buried rather than mantled craters, embayments into older terrain; and mare ridge-like structures and lobate scarps confined to plains materials. Also, for the smooth plains, at least. There is no clear association with impact craters of comparable age and sufficient size to indicate an ejecta origin. No unambiguous volcanic vents or constructs exist within the Kuiper quadrangle, hence the style of lava emplacement appears to be more like that of the moon than Mars.

Unlike lunar mare material, mercurian plains materials were emplaced throughout a long period of the planet's history. A long history of volcanism is probably related to the planet's large size, long duration of core separation and near surface melting. Although the mercurian plains are interpreted to be chiefly volcanic, they may have diverse origins. A long history of concurrent volcanism and impact may result in interbedded impact breccias and lava flows. Some plains, like the lunar plains at the Apollo 16 site, may consist of breccias emplaced as impact ejecta.

References. (1) De Hon, R. A. (1979) Lunar and Planet. Sci. X, Houston, TX, 274-276. (2) Greeley, R. et al (1970) The Moon, v. 2, 10-77. (3) Neukum, G. et al (1975) The Moon, v. 12, 201-229.

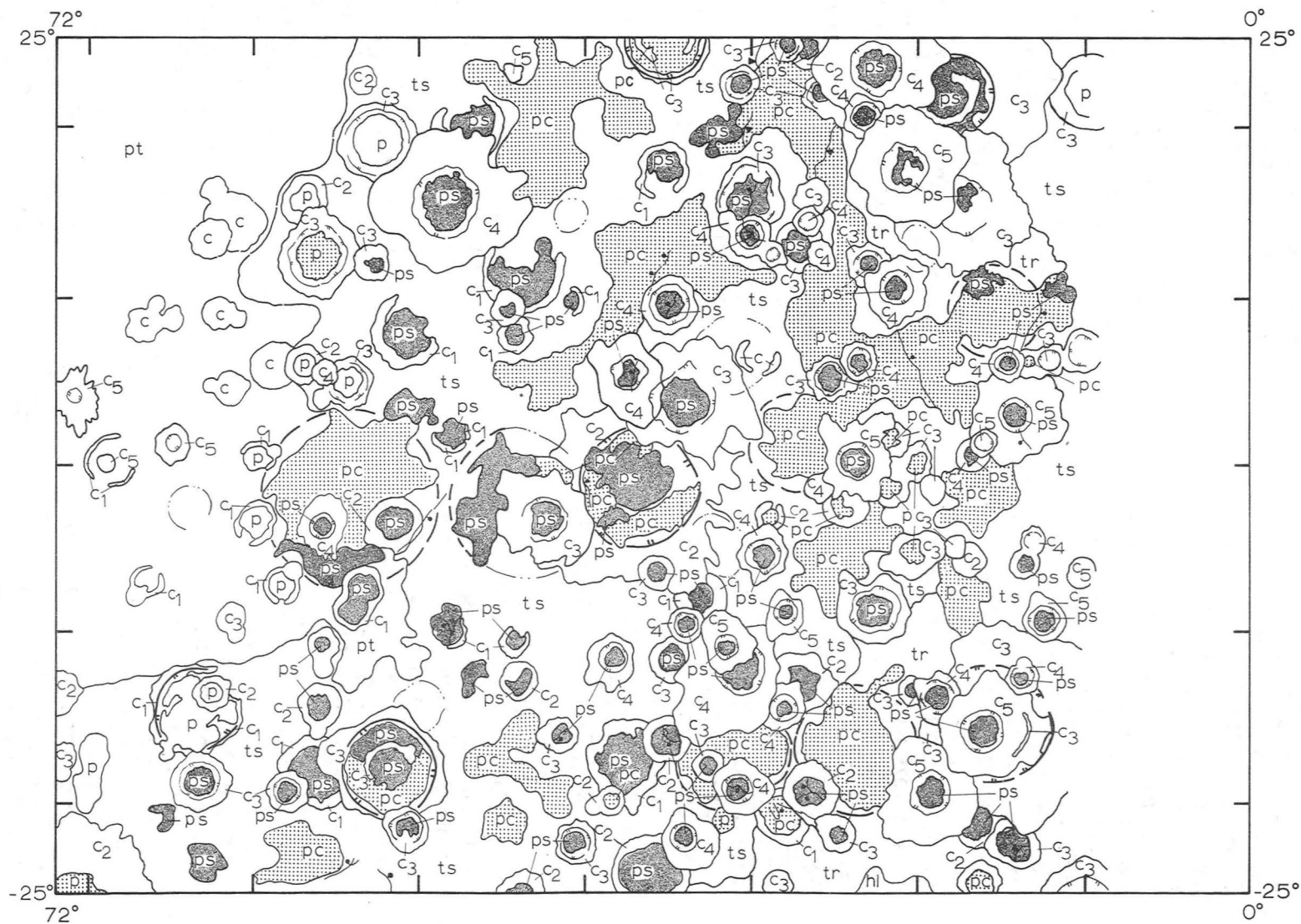


FIGURE 1. Distribution of plains-forming materials in the Kuiper quadrangle.

RELATIVE AGES OF THE SMOOTH PLAINS AND CALORIS RELATED TERRAIN OF MERCURY

Watkins, J. A., Lunar and Planetary Laboratory, University of Arizona, Tucson, AZ 85721

The distribution of crater densities, diameter-frequency distributions, and morphologic crater types on the smooth plains and Caloris related terrain were investigated to determine the chronology of these geologic units. Areas of smooth plains as described by Trask and Guest (4) and terrain related to the Caloris forming impact (Van Eyck [cvl]; Odin [ho]; and Caloris Montes [ccm] formations as described by McCauley et al.; 2) were plotted on Mercury quadrangle maps. Regions excluding those with large numbers of secondary craters or poor lighting were divided into cells of approximately 50×50 or equivalent size depending upon the areal extent of the geologic units. Excluding obvious secondaries, all craters greater than 10 km were recorded for each cell, and each crater was classified according to the morphologic scheme of Wood et al. (6). The very few class 3 craters that were observed on the Caloris related terrain were combined with class 2 craters for simplification of data and analysis.

The areal density and statistical uncertainty were calculated for each cell and recorded on a matrix covering the plotted areas with points at approximately 50° intervals. Additional points were interpolated and the entire array was smoothed using a running average with a 3×3 neighborhood after a method similar to that of Eliason and Soderblom (1). This gave an average statistical noise of about 22%. The resulting array was plotted on a map of the outgoing hemisphere of Mercury and contour lines between density intervals were drawn.

Initial comparison of the diameter-frequency distribution was done using Scheffe's multiple comparison test. This test is well suited for pairwise comparisons of several independent samples involving small numbers (Pollard; 3). Scheffe's multiple comparison test on all data indicated that 90% of all cells on Caloris related terrain had diameter-frequency distributions that were the same at the 99.5% confidence level. The diameter-frequency distributions on Caloris related terrain were different from that of the smooth plains at the same confidence level. At least three different diameter-frequency distributions are present on the smooth plains as determined by Scheffe's test at the 99.5% confidence level. The variation of crater densities on the smooth plains is 1:4 and this distribution is not unimodal. The crater density data further indicate that some areas of smooth plains have crater densities greater than Caloris related terrain while other smooth plains areas have lower crater densities. The smooth plains older than Caloris are located farthest away from that basin. The Caloris related terrain crater densities were uniform. Any model proposed to explain these data must fit the crater density and diameter-frequency data simultaneously, and must obtain areal homogeneity of diameter-frequency distributions on areas of a given crater density.

A four stage model of smooth plains formation provides the best fit to the density and diameter-frequency data. The model features smooth

plains of four different relative ages, tentatively labeled sp I-IV, and provides a minimum of 80% areal homogeneity of diameter-frequency distributions within each density interval. The Kolmogorov-Smirnov test indicates that sp I and sp IV, respectively the oldest and youngest units, each have a different diameter-frequency distribution, both of which differ from sp II and sp III which have the same diameter-frequency distribution.

The distribution of relative ages of smooth plains according to the model and the location of Caloris related terrain is shown in figure 1. The resolution of the smooth plains part of the map is about 600 km², thus the smallest areas on the map are near the resolution limit and should be considered with extreme caution. The diameter-frequency distribution of cells in each density interval were summed to obtain adequate statistics for diameter-frequency curves. Linear regression fits of the power function, $N=KD^{\alpha}$, were obtained for each diameter-frequency distribution and were verified by the Kolmogorov-Smirnov test at the 99% confidence level. The Caloris related terrain could only be fit by two functions covering the diameters from 10-25 km and 35-55 km. The observed and calculated cumulative diameter-frequency curves are shown in figure 2. In an attempt to estimate the relative ages of the smooth plains and Caloris related terrain, the density of craters at 10 km were calculated from the linear regression fits. The observed and calculated densities and percent class 2 craters are shown in table 1.

The results of these data indicate that the smooth plains were emplaced in four major stages at the end of the period of heavy bombardment. The following sequence is indicated: a period of smooth plains formation (sp I), the Caloris forming impact, two major periods of smooth plains formation the later ending contemporaneously with a period of small crater obliteration on the Caloris related terrain, and a final stage of smooth plains formation. Finally, the areal distribution of smooth plains of various relative ages and the relative age relationship to the Caloris related terrain suggest a volcanic origin of smooth plains in agreement with the interpretation of Strom et al. (5).

References:

- (1) Eliason, E. M., and Soderblom, L. A. (1977) Proc. Lunar Sci. Conf. 8th, p. 1163-1172.
- (2) McCauley, J. F., Guest, J. E., Trask, N. J., Schaber, G. G., Greeley, R., Gault, D. E. and Holt, H. E. (1979) Jour. Res. of the U. S. Geological Survey (in press).
- (3) Pollard, J.H. (1977) Numerical and Statistical Techniques, Cambridge Univ. Press, London.
- (4) Trask, N. J., and Guest, J. E. (1975) Jour. Geophys. Res., 80, p. 2461-2477.
- (5) Strom, R. G., Trask, N. J., and Guest, J. E. (1975) Jour. Geophys. Res., 80, p. 2478-2507.
- (6) Wood, C. A., Head, J. W., and Cintala, M. J. (1977) Proc. Lunar Sci. Conf. 8th, p. 3503-3520.

Table 1

	Smooth Plains				Caloris Terrain		
	sp I	sp II	sp III	sp IV	ct hi ^a	ct lo ^b	Total
Observed [*] Density (10 ⁻⁴ craters/ km ²)	1.75 ± 0.28	1.32 ± 0.10	0.71 ± 0.06	0.33 ± 0.10			0.76 ± 0.08
Calculated [*] Density (10 ⁻⁴ craters/ km ²)	2.2 ± 0.3	1.6 ± 0.2	0.8 ± 0.1	0.4 ± 0.3	2.1 ± 0.3	0.8 ± 0.1	0.7 ± 0.2
Percent Class Z (s)	29 ± 11	36 ± 4	35 ± 4	44 ± 23	60 ± 11	29 ± 15	48 ± 4

^{*}) Densities calculated for all craters greater than 10 km per square km. Standard error is given for observed values; standard deviation of values calculated from data points is given for the calculated densities.

a) Caloris associated terrain high diameter population; all craters greater than 30 km comprise this population.

b) Caloris associated terrain low diameter population; all craters less than 25 km comprise this population.

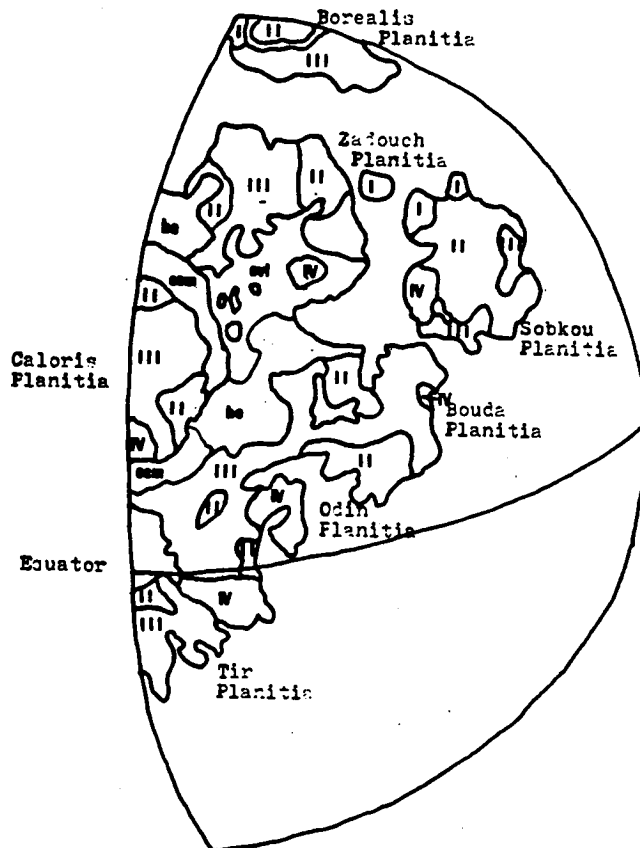


Figure 1

Distribution of major relative age (crater density) units on the smooth plains and Caloris associated terrain. Note that older sp units are located away from the Caloris units.

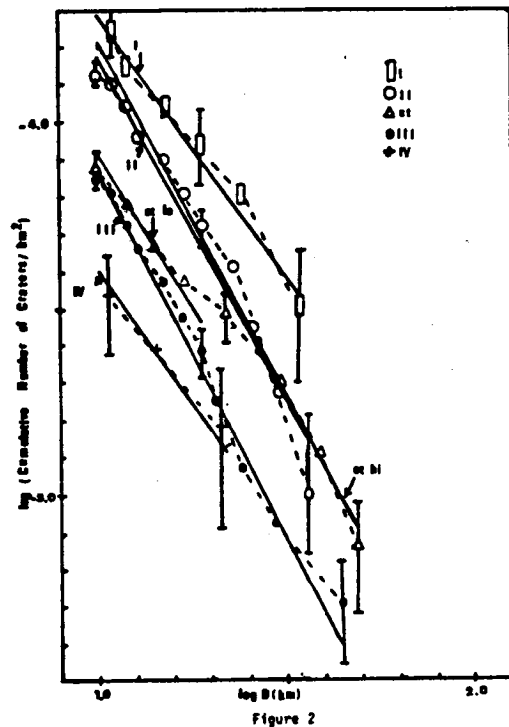


Figure 2

Cumulative diameter - frequency curves from smooth plains units and Caloris associated terrain. Dashed lines connect data points for individual surfaces and straight solid lines are calculated from linear regression fits to the data. Note the sharp bend in the Caloris terrain diameter frequency curve at about 20 km. Key to symbols: I - sp I, II - sp II, III - sp III, IV - sp IV, ct - Caloris terrain, ct hi - Caloris terrain high diameter population, ct lo - Caloris terrain low diameter population.

MARS STRATIGRAPHIC STUDIES

Scott, D. H., U.S. Geological Survey, Flagstaff, Arizona 86001

Stratigraphic studies in the northern lowland plains of Mars have shown that they consist of lava flows in various stages of erosion and mantling by eolian material. In several places near the south boundary of the plains, the lava flows embay the older highland rocks (1). Viking images reveal a wide variety of surface textures and albedo contrasts within the broad categories of plains units mapped from Mariner 9 pictures. Although these morphologic and color variations are seldom sharp and boundaries appear to be gradational, the plains have been subdivided in places into smaller, more definitive units (2). The plains material that is most difficult to subdivide and interpret lies mostly north of 50° N and appears as a mottled light and dark zone that nearly encircles the planet. The origin of these plains is unknown but they may be the eroded remnants of highland material that have survived an episode of crustal separation and volcanism.

A photogeologic study of Hebes Chasma has been started and will be extended to other chasmata throughout the Valles Marineris system. High-resolution Viking Orbiter 1 images enlarged to about 1:250,000 scale were used for the mapping. Topographic profiles across Hebes Chasma were made using preliminary elevation data from the Flagstaff Field Center of the U.S. Geological Survey. Work in progress by Christine Peterson (University of Texas) shows that Hebes Chasma may have been formed contemporaneously with some of the younger lava flows from Olympus Mons more than 3000 km to the northwest. The lava plains bordering the chasma are much older, possibly correlative in time with those around Sinai Planum. Within Hebes Chasma, a high central plateau rises some 5 km above the floor. Its origin is unknown but four possibilities are considered: a) the plateau may be a remnant of the adjacent plains isolated by faulting and erosion, b) it may consist of lake beds that accumulated in a subsiding basin, c) it may have been formed by eolian deposits, or d) pyroclastic deposits.

REFERENCES

- 1) Scott, D. H., 1978, *Icarus*, 34, p. 479-485.
- 2) Scott, D. H., 1979, *Lunar and Planetary Sci. Conf.*, X, Proc. (in press).

LAYERED MATERIALS OF THE RIDGED PLAINS OF MARS. R. A. De Hon, Department of Geosciences, Northeast Louisiana University, Monroe, LA 71209.

Geologic mapping of any planetary surface rests on a fundamental supposition that the surface is composed of discernible material units. Stratigraphic analysis is primarily based on the principles of superposition of distinctive patterns of distribution and transection of pre-existing patterns by younger structural or erosional patterns (1). Superposition is usually recognized as imbricate patterns of distinctive surface characteristics. Only rarely does planetary imagery provide direct observation of multiple layers of materials in a vertical sequence. On Mars, stratification may be assumed to exist by virtue of multiple processes and episodes of erosion and deposition that have shaped the surface. Direct evidence of stratigraphic layering observed in Mariner 9 images include apparent layering in the walls of Vallis Marineris (2) and layered polar deposits (3).

Viking Orbiter images reveal a possible occurrence of stratification south of Chasma Coprates near 20°S ; 54°W . Viking frames 610A25, 610A26, 610A27, 610A42, 610A44 and 610A46 provide images of the contact between mare-like plains-forming materials and an older sculptured terrain. The older trough-and-furrow material consists of an elevated region characterized by a moderately undulating surface crossed by numerous subdued troughs and furrows (2). The younger ridged plains material is characterized by numerous elongate and sinuous ridges on an otherwise smooth plain which resembles the lunar maria (2). The regional pattern as seen in Mariner 9 images is interpreted as a diapiric uplift of the trough-and-furrow material after deposition of the ridged plains materials (2). At Viking resolution, a northward trending, scalloped scarp separates the older material of the west from the younger plains to the east. Westward facing scarps and smooth, eastward sloping, v-notched surfaces that have developed in the plains material suggest the development of cuestas or homoclinal ridges. The development of two, and in some places three, subparallel ridge crests resembles multiple homoclinal ridges which developed in inclined layered materials.

Widely scattered partially buried craters provide thickness estimates within the ridged plains material that vary from 200 m to greater than 2000 m. While some estimates may reflect variations in subsurface topography, other estimates may indicate crater formation on intrabasalt surfaces; hence, the ridged plains material probably represents multiple flows emplaced over a moderate time span.

The existence of a cuesta at the contact suggests that the plains-forming materials were at one time continuous across the region or at least overlapped further onto the older terrain. The pattern is similar to homoclinal ridges of dipping strata around the flanks of uplifted domes or plugs. The pattern suggests uplift of the older furrowed terrain, followed by erosional removal of the overlying material to form the present scarp and expose multiple dip slopes within the ridged plains material. Removal of material in this region is apparently complete as no debris mantle obscures the sinuous ridges of the plains. Elsewhere in the region, at 16°N; 80°W, a smaller diapiric exposure of the trough-and-furrow material is surrounded by smooth plains which do not display sinuous ridges. This region may retain a part of the erosional debris mantle.

References

- (1) Wilhelms, D. E. (1972) Geologic Mapping of the Second Planet. Interagency Report: Astrogeol. 55, 1-36.
- (2) McCauley, J. F. (1978) Geologic Map of the Coprates Quadrangle of Mars. U. S. Geol. Survey Misc. Inves. Map I-897.
- (3) Cutts, J. A. (1973) Nature and Origin of Layered Deposits of the Martian Polar Regions. Journ. Geophys. Res., 78, 4231-4249.

PHOTOGEOLOGIC STUDIES OF THE CERBERUS ALBEDO FEATURE OF MARS

A.L. Chaikin, T.A. Maxwell and F. El-Baz, Center for Earth and Planetary Studies, National Air and Space Museum, Smithsonian Institution, Washington, D.C. 20560

Studies of Viking images of the Cerberus low-albedo feature (12°N , 205°W) have given new information on its relationship to other surficial units in the Elysium quadrangle and on the nature of its dark surface. Numerous volcanic flows can be seen within Cerberus which originate in the Elysium Mons/Albor Tholus volcanic complex. These flows, trending N-S, cross into Cerberus from the higher albedo plains to the north, mapped as "rolling plains" and "plains" units by Scott and Allingham (1976). The flows appear unchanged in morphology as they cross into Cerberus, but they change in albedo from that of the bright plains to that of Cerberus. Many of the flows continue south into the "plains" unit again, with an accompanying change from low to high albedo (Fig. 1). The presence of these flows in Cerberus, mapped as "streaked plains", means that Cerberus does not owe its low albedo simply to an exposure of older, dark plains which predate light Elysium volcanics. In addition, parts of the highlands unit which borders Cerberus on the east are also dark. These highlands predate all plains units in the Elysium quadrangle (Scott and Allingham, 1976).

Two possible models are proposed to account for the low albedo of Cerberus: 1) The streaked plains, as well as the highlands, rolling plains, and plains units of Scott and Allingham (1976) all are composed of dark materials. Any visible dark surface, therefore, would be an exposure of bedrock. Sometime after the emplacement of the youngest flows from the Elysium volcanic complex, the whole area was mantled by bright dust. Areas which now appear dark have been stripped of this thin, bright cover to reveal the dark substrate, or 2) Sometime after the emplacement of the youngest flows, much of the region was mantled by a dark deposit. Pyroclastic materials from the Elysium Mons or Albor Tholus or both could have been responsible. Malin (1976) has suggested that pyroclastic activity could have occurred at some time in the history of Elysium Mons. The apparent freshness of the flows within Cerberus means that this deposit would have to be fairly thin.

Viking IRTM results give some clues to the nature of the surface material within Cerberus but do not rule out either of the above models. Cerberus was found to occupy a zone of relatively high thermal inertia (Peterfreund et al., 1977). The highest values of thermal inertia obtained within Cerberus are consistent with either a mixture of 32% rocks and 78% fine grained material, or a deposit with a mean grain size of 600 microns. Other possibilities are allowed by the data, however (Kieffer et al., 1977).

Either model implies that the dark area exposed within Cerberus is only part of a much more extensive dark surface, mantled by a thin

layer of bright dust. Changes in the outline of Cerberus have been observed which are consistent with redistribution of this layer during Martian dust storms (Chaikin et al., 1979). This dust layer could conceivably be thin enough in places to cause a high albedo surface without masking the thermal signature of the underlying high-inertia material. This would account for the discrepancies observed between the distribution of high thermal inertias and low-albedo surfaces in the area.

It is possible that topographic controls on regional atmospheric circulation determine Cerberus' general shape and position in a zone which is particularly susceptible to deflation. Because such controls are not subject to change, it seems unlikely that the albedo patterns would disappear entirely or shift gradually to an entirely new location.

References

- Chaikin, A.L., El-Baz, F. and Maxwell, T.A. (1979) Comparison of Mariner 9 and Viking Imagery of the Cerberus Albedo Feature. Reports of Planetary Geology Program, 1978-1979, p. 279-281.
- Kieffer, H.H., Martin, T.Z., Peterfreund, A.R., and Jakosky, B.M. (1977) Thermal and Albedo Mapping of Mars During the Viking Primary Mission. JGR, v. 82, n. 28, p. 4249-4291.
- Malin, M.C. (1976) Age of Martian Channels. JGR, v. 81, n. 26, p. 4825-4845.
- Peterfreund, A.R. and Kieffer, H.H. (1977) Thermal Inertia of the Elysium Region of Mars. Lunar and Planetary Science VIII, LPI, Houston, p. 765-767.
- Scott, D.H. and Allingham, J.W. (1976) Geologic Map of the Elysium Quadrangle of Mars. U.S. Geological Survey, Geol. Series Map I-935 (scale 1:5,000,000).

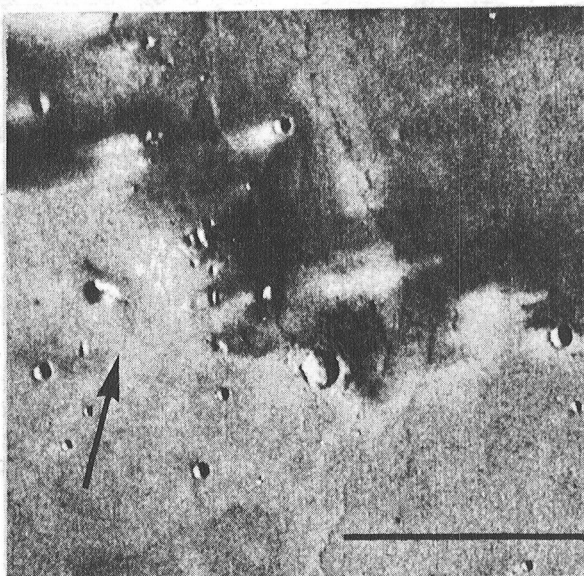


Figure 1. Viking frame 631A24 showing volcanic flows within Cerberus which extend into the bright plains to the south, going from dark to light as they do so. Arrow points north; scale bar is 50 km.

Martian Color/Albedo units: Viking Lander 1 Stratigraphy
vs. Orbiter color Observations, E. L. Strickland III, McDonnell
Center for the Space Sciences, Washington Univ., St. Louis, Mo.
63130

Several distinct soil stratigraphic units have been recognized in color-enhanced Viking Lander images of both landing sites. They are identified on the basis of color, texture, surface morphology, and contact relations (1). At the Viking 1 site, a thin, discontinuous, bright, relatively "red" soil is the uppermost unit. It is probably underlain by another thin patchy layer: "green-blue" soil. "Blue" drift soils, generally covered by the "red" and "green-blue" soils, cover much of the site. Viking 1 landed straddling the edge of one of these drifts. A unique patch of crust-like "orange-red" soil was exposed at the edge of the drift, where retrorocket exhaust apparently scoured away a few centimeters of "blue" drift soil. The "blue" drift soil, and probably the "orange-red" soil, rest on the lowermost unit: rocky "blue" soil. A sixth soil unit, "dark red" soil, caps the "big Joe" boulder near the lander, and surrounds several nearby boulder clusters. Its stratigraphic position is not well defined, but it probably lies below the "blue" drift soil and above the rocky "blue" soil. Soils observed at the Viking 2 site, nearly halfway around the planet, greatly resemble those seen at the first site. Soil units similar to these are probably widely distributed on Mars.

A study of color-enhanced Viking Orbiter images of regions near the Chryse basin (Viking 1 site), suggests that some of the soil units observed at this site can be observed from orbit, and may extend for thousands of kilometers. Chryse Planitia, at 2 kilometer resolution, has a uniformly "red" high-albedo surface. These observations were made during the extended mission, when the Viking 1 site's soils were covered with a thin, bright "red" dust, deposited during the first winter (2). Dark albedo features to the northwest, at the mouth of Kasei Vallis, show mostly "blue" and some "green-blue" colors. The Lunae Planum highlands to the west are nearly as red as Chryse, but are much darker. To the east of Chryse, in Oxia Palus, dark "blue" crater streaks are surrounded by bright "red" borders on a dark "red" intercrater plain. Features in both of these regions can be interpreted- -though not uniquely- -in terms of the stratigraphy at the Viking 1 site. The simplicity and lateral continuity of these color/albedo features, over more than 1000 kilometers, suggest that these probably are the same units observed at the Viking 1 landing site.

Unambiguous indications of stratigraphic relations between units are rarely available in Orbiter color imagery at 1 km./pixel resolution. To obtain more information on the contact relations between the color/albedo units seen in the color images, several higher resolution, black and white images of selected features were databased. The procedure removes reseau marks, bit errors, vidicon shading, illumination angle variations, and projects the image into mercator map format. Approximate albedos of surface units can be determined from these images. These images greatly aid interpretation of relations between units observed in the lower resolution color images.

In the Oxia Palus region, in Becquerel crater (8.4°W, 21.3°N), dark "blue" soils form dune masses and featureless dark "blue" patches. The dunes are not well resolved at 75 m/pixel, but appear to have maximum dimensions of about 300 meters. Surrounding the dune fields, and extending downwind (southwest) from them, are areas with higher albedo and weaker "blue" coloring. These two units are surrounded by a higher albedo "red" border. The intermediate albedo "blue" unit probably consists of an unresolved patchwork of small (≤ 75 m.) "blue" drifts resting on the brighter "red" unit. The dark "red" unit surrounding the bright "red" border is then interpreted as the lowermost unit. This interpretation is supported by a 2-dimensional plot of "redness" vs. "brightness" for streaks extending from two craters south of Becquerel. The intermediate albedo "blue" unit clearly lies on a mixing line between the dark "blue" and brighter "red" units. The two "red" units also appear to mix at kilometer resolution, while there is an unoccupied gap between the dark "blue" and darker "red" soils, indicating that they are not in direct contact. A fourth unit: "diffuse red", forms diffuse bright crescents in the upwind walls of craters, and diffuse bright streaks downwind of several small craters. This unit is brighter than the other "red" units, and may be the uppermost unit in this region. In this and other regions examined in this preliminary survey, the observed color/albedo features show little relation to underlying geologic structures. The stratigraphic units involved probably represent thin, relatively mobile soils resting on possibly unobserved bedrock and "bedsoils".

* Colors referred to are relative to scene averages, as displayed in the color enhanced images.

E. L. Strickland, III, Soil stratigraphy and rock coatings observed in color-enhanced Viking Lander images. Tenth Lunar and Planetary Science Conference Proceedings, in press.

E. A. Guinness, et al., Color changes at the Viking landing sites over the course of a Mars year. J. Geophys. Res. in press.

TWO MARS YEARS: VIKING LANDER IMAGING OBSERVATIONS -

Kenneth L. Jones and Susan K. LaVoie, Jet Propulsion Laboratory, Pasadena, CA.

On 24 April, 1980, Viking Lander 1 completes its second Mars year; on June 9, VL-2 completes its second Mars year. Both spacecraft are continuing to collect both imaging and meteorological data. VL-1 is returning data via the direct-link mode at the rate of a single image per week. VL-1 operations will continue until the spacecraft ceases to function, possibly several more years. VL-2 is sending back a substantial amount of imaging data approximately once per month via relay-links through the remaining orbiter. Since VL-2 is dependent upon the remaining orbiter, operations are expected to terminate sometime during the summer of 1980. Processed images from both spacecraft are being prepared for distribution to NSSDC and to the Regional Planetary Imaging Facilities.

Changes at the Lander Sites

The opportunity to image the surface of Mars for a second complete year has allowed us to test the working hypothesis of our "One Mars Year" paper (1) - that the first Mars year observed by the Landers should be treated as "typical", at least in the sense that both the types of changes and the magnitudes of the changes should be considered normal. VL-2 images document the formation of a condensate layer nearly identical to the first year's. VL-1 images reveal the appearance of a new landslide slump. There have been no dust storms similar to the two seen during the first year. There has been no new accumulation of dust at either site, and the dust that was deposited during the first year has remained undisturbed by eolian activity. These changes enable us to infer possible limits on the range of yearly variations. We conclude that the first year is indicative of an average year except that with observable frequency (~ 10 yr) the lander sites are swept by winds capable of redistributing a substantial amount of the bright surface dust layer.

Darkening over the VL-2 Site

Between VL-2 sols 816 ($L_S=196$) and sol 824 ($L_S=200$), the optical depth at the VL-2 site increased from an average between 0.2 and 0.8 to an average between 1.0 and 1.4. One year earlier, a similar darkening reached a peak intensity (>2.2) on VL-2 sol 161 ($L_S=203$). During the first year, an equivalent increase was seen concurrently by VL-1, reaching a maximum (>2.5) on VL-1 sol 210 ($L_S=206$). Since a darkening had been seen at both sites, and since the increase in the optical depth had occurred during a single sol, the first year's increase was attributed to a global dust storm that had been seen by the Viking Orbiters to have originated in the Martian equatorial regions.

Unfortunately, the relay-link containing the VL-1 data from the equivalent period during the second year was not received due to tracking station non-availability. Images on VL-1 sols 841 ($L_S=185$) and 920 ($L_S=232$) which bracket the time period neither support nor contradict the hypothesis that a dust storm may have occurred. However, the increase in the optical depth seen at VL-2 during the second year was more gradual than during the first year and did not reach as great a maximum. What was seen at the VL-2 site may have resulted from small dust storms that introduced dust into the atmosphere in smaller amounts than during the first year. Alternatively, the increase might have been associated with the formation of the polar hood. A unique answer to these alternatives may not be able to be determined from lander imaging data alone.

Absence of a Global Dust Storm

During the first year, the dust storm described above was followed by a second global dust storm some 65 sols later that was also seen by both landers and was more intense than the first storm had been. During the second Mars year, no dust activity other than the event just described was documented by either lander. Although sun diode optical depth data was not acquired, a reference test chart image that was repeated on a 12 sol cycle clearly shows no sky darkening. Also, unlike the first year, no new deposition of a bright surface dust layer was observed. The suggestion is that the first year's dust accumulation at both sites was linked to the first year's dust storm activity rather than transport from local sources.

Whale Rock Slump at the VL-1 Site

The "One Mars Year" paper (1) discusses a small landslide slump feature near the large boulder known as "Big Joe". Since the Big Joe slump formed near (~ 8 m) the spacecraft, and since there were no equivalent features in the scene, any arguments about the time implications of such a change could only be conjectural.

A second slump, near the rock called "whale rock", formed between VL-1 sols 767 ($L_S=147$) and 771 ($L_S=149$). While the appearance of the feature would be far from definitive without the Big Joe slump for comparison, the sharply defined edge of the feature suggest an equivalent formational mechanism. Indeed, in another drift location nearby a series of fractures can be seen, previously non-existent, that suggest that yet another slump may be in its incipient stages. All of these features occur in the lee tails of topographic features, suggesting eolian origins.

The distance (~ 25 m) to the new slump and the long time (770 sols) between touchdown and slump formation suggest that a lander-related origin is unlikely. Instead, both of these features are now interpreted as significant evidence that dust accumulations at the VL-1 site are routinely redistributed by eolian activity. Equivalent features, formed by the accumulation of a surface dust layer, should be scattered about the landscape unless they are removed on a time scale equivalent to the time the landers have been on the Martian surface. This year's absence of a global dust storm is taken as one extreme of the yearly variation in eolian activity. A storm capable of obliterating small artifacts such as the two slumps, as well as depositing a substantial (~ 1 cm) layer of residual dust, is proposed as the other extreme. The 1971 global dust storm seen by Mariner 9 may have been such an event.

Surface Condensates at the VL-2 Site

Around VL-2 sol 886 ($L_S=239$), a thin layer of bright condensates again began to form at the Utopia Site. As before, the condensates accumulated very slowly, reaching a maximum thickness around sol 955 ($L_S=287$). Subsequent images show that starting around sol 960 ($L_S=291$) the condensates were beginning to disappear. The latest images processed at the time of this writing (sol 1033, $L_S=335$) again suggest a very slow sublimation rate as the condensates return to the atmosphere. Temperature data suggests, as during the first year, that CO_2 is a significant contributor to condensate formation. The slow disappearance again suggests that H_2O is the dominant residual condensate. However, the role that dust may play as an agent of H_2O transport needs to be reconsidered. It was suggested in our previous paper that, although dust storms themselves did not seem to directly related to the rate of condensate formation, dust transport from the equatorial regions was the likely medium by which solid H_2O was trans-

ported to the lander site. It may be possible to determine from images to be acquired by VL-2 early in 1980 whether "absolutely no dust" or "only small amounts of dust" have accumulated at the site. Small amounts of dust may be consistent with our earlier hypothesis. No dust may imply that either or both H₂O and CO₂ accumulated on the surface directly from the vapor phase - i.e. as frost.

Reference:

Jones, K.L., R.E.Arvidson, E.A.Guinness, S.L.Bragg, S.D.Wall, C.E.Carlston, and D.G.Pidek, One Mars Year: Viking Lander Imaging Observations, Science, 204, pp. 799-806, 25 May, 1979.

CLASSIFICATION AND ANALYSIS OF ROCKS AT THE VIKING LANDER SITES

Garvin, J.B.; Grinspoon, D.; Head, J.W.; Helfenstein, P.; Lucey, P.;
Mouginis-Mark, P.J.; Robinson, E.A.; and Viglienzone, L.*, Dept.
of Geological Sciences, Brown Univ., Providence, RI 02912
(*NASA Summer Intern)

The characterization of rock origin and composition from the images returned by the Viking landers represents an integral phase of martian data analysis. Utilizing a digitizing table, a preliminary study to:
1) assess camera resolution effects in rock size distributions and
2) derive a suitable rock morphology classification scheme, has been completed. Rock locations and sizes were calculated from two high-resolution mosaics: Lander 1 L1C1 11A156/027 AM Q3 + Q4 and Lander 2 L2C1 21A147/020 AM Q3 + Q4.

A total of 848 rocks were included in the data set for Lander 1 and 551 rocks for Lander 2. Only camera inclination angles between -10° and -40° from the horizontal were considered to preclude excessive rock distortions in the nearfield and inherent inaccuracies in monoscopic ranging in the farfield due to local topographic undulations. Fig. 1 demonstrates that the size distributions at the two sites are remarkably similar. At VL-1 the mean rock size is 51 mm, that at VL-2, 61 mm. Sorting values in the vicinity of 1.0 (phi values) were derived; these are representative of moderately to poorly sorted sediments. A critical question is whether the size distributions are in fact genuine, or simply controlled by resolution limits in the smaller rock size range. Table 1 shows that the mean phi values do increase as rocks closer to the cameras are considered. However, the distributions have very low skewness values; i.e., they are very nearly symmetric. Assuming an originally symmetric distribution and a pronounced resolution effect, one would expect there to be a marked surplus of coarse material at great ranges. This is not observed. Our conclusion, which concurs with previous analyses,^{1,2} is that the size distributions are truly bimodal, with the second mode in the silt/dust size range.

Present work in our Mars rock analysis program involves an image processing system consisting of a PDP-11/03 CPU, a Grinnell display controller, Conrac color and monochrome monitors, a tape drive, and a disk drive. Raw lander images are displayed, contrast stretched, and magnified; and individual rocks are traced (using a track-ball) and monoscopically ranged. An interactive package permits the collection and reduction of morphological data designed to characterize the origin, composition and degree of weathering of the rock populations.

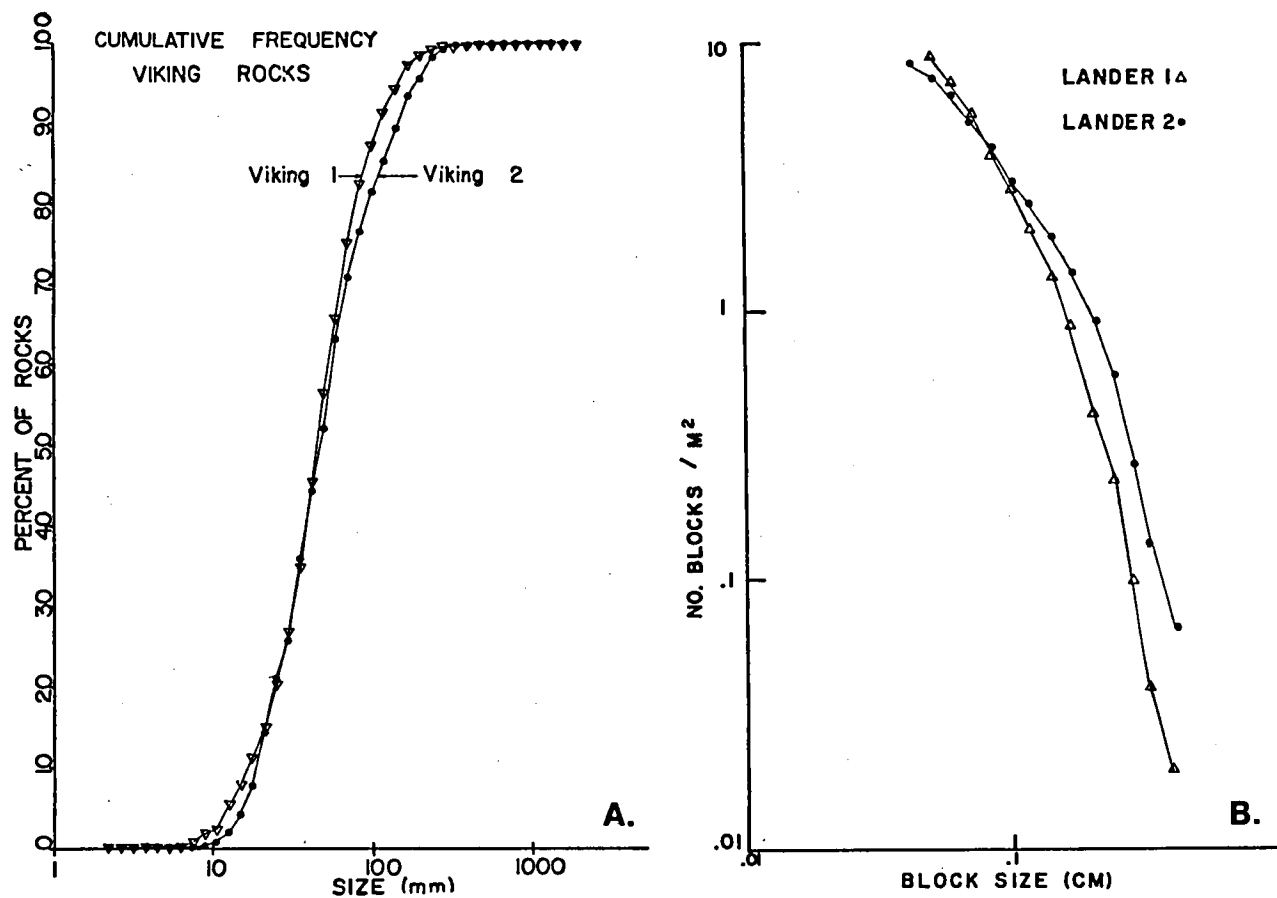


Fig. 1: A) Cumulative size frequency distributions for sampled rocks at the two lander sites. B) Rock distributions expressed as the number of rocks of a given size or smaller per square meter. Note that both figures indicate that the two landing sites have comparable rock size distributions.

CLASSIFICATION AND ANALYSIS OF ROCKS AT VIKING LANDER SITES

Garvin, J.B. et al.

TABLE 1: ROCK SORTING AND SKEWNESS DISTRIBUTIONS FOR THE SAMPLE ROCKS

Camera	Inclination Angle	Mean (mm)	Sorting (phi)	Skewness	No. Rocks
V.L. 1	-10° to -40°	51	1.0	0.04	848
	-10° to -20°	67	0.9	0.07	531
	-20° to -30°	37	0.9	0.04	213
	-30° to -40°	23	1.0	0.09	104
V.L. 2	-10° to -40°	61	1.1	0.04	551
	-10° to -20°	73	0.9	0.14	334
	-20° to -30°	47	1.1	0.20	156
	-30° to -40°	39	1.2	0.04	61

References:

¹Binder A.B. et al. 1977, J. Geophys. Res. 82, 4439-4451.

²Moore H.J. et al. 1977 J. Geophys. Res. 82, 4497-4523.

Geomorphic Mapping of Dry Valley Systems on Mars. Victor R. Baker, North Australia Research Unit, Australian National Univ., P.O. Box 39448, Winnellie, N.T. 5789 Australia, and Dept. Geological Sciences, Univ. of Texas, Austin, TX 78712.

Geomorphic mapping procedures were previously developed for analyzing the large outflow channels of Mars (1, 2). These procedures are here modified for application to the smaller dry valley systems of the old cratered terrains on Mars. Dry valley systems were mapped in the southeastern Margaritifer Sinus Quadrangle (Figure 1), the central Thaumasia Quadrangle, and the Nirgal Vallis regions. The dry valley systems of these regions have previously been described as gullies (3), arroyos (4), runoff channels (5), dendritic channels (6), fine channels (7), and furrowed terrain (8). This report follows the terminology of Pieri and Sagan (9). A consensus on the origin of Martian dry valleys is as elusive as one on their name.

Mapping in Margaritifer Sinus (Figure 1) distinguishes large dry valleys with broad floors ("major channels") from small filamentous "channels" that are less easily resolved on the Viking imagery. Many of the latter types drain outward from crater rims. Crater types are classified by the degree of crater rim degradation. One crater category (C₃) applies to craters that have been modified by the valley-forming processes.





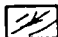

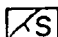

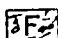
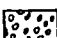

Very high resolution Viking frames from the Thaumasia region show valley forms that have been considerably modified, either by heavy cratering or by alas-type permafrost processes. Such regions pose severe problems for genetic mapping and for determination of post-valley crater densities.

Mapping of Nirgal Vallis was compiled from Viking Frames 466 A49 through 466 A68. Nirgal Vallis displays detailed wall and floor morphology consistent with valley modification by mass movement processes. Tributaries to the main valley are unusually short and terminate in cirquelike valley heads. Several hanging valleys also occur.

Features of probable fluvial origin could not be discerned on the floor of Nirgal Vallis. However, one reach (Frame 466 A61) contains several midvalley ridges that are uniformly spaced and oriented transverse to the valley axis. These features could possibly be large transverse bars. However, a single, isolated occurrence of such features should remain suspect.

References: (1) Kochel R.C. and Baker V.R. (1979) N.A.S.A. Tech. Memo. 80339, p. 338-340. (2) Baker V.R. and Kochel R.C. (in press) J. Geophys. Res. (3) Milton D.J. (1973) J. Geophys. Res. 78, p. 4037-4047. (4) Hartmann W.K. (1974) J. Geophys. Res. 79, 3951-3957. (5) Sharp R.P. and Malin M.C. (1975) Geol. Soc. Amer. Bull. 86, p. 593-609. (6) Masursky H. *et al.* (1977) J. Geophys. Res. 82, p. 4016-4038. (7) Scott D.H. and Carr M.H. (1978) U.S. Geol. Survey Map I-1083. (8) Mutch T.A. *et al.* (1976) The Geology of Mars, Princeton Univ. Press. (9) Pieri D. and Sagan C. (1978) N.A.S.A. Tech. Memo. 79729, p. 268.

EXPLANATION

- | | |
|--------------------------------------------------------------------------------------------------------------|--------------------------------------------------------------------------------------------------------------------------|
|  Hilly and cratered region |  Relatively young crater (raised rim) |
|  Major channels |  Older crater (degraded rim) |
|  Small filamentous channels |  Crater modified by channel processes |
|  Scarps of various origins |  Very old crater (buried, degraded rim) |
|  Fretted terrain |  Crater rims and hummocky margins |
|  Slumps | |

All mapped craters are C₁ unless otherwise noted

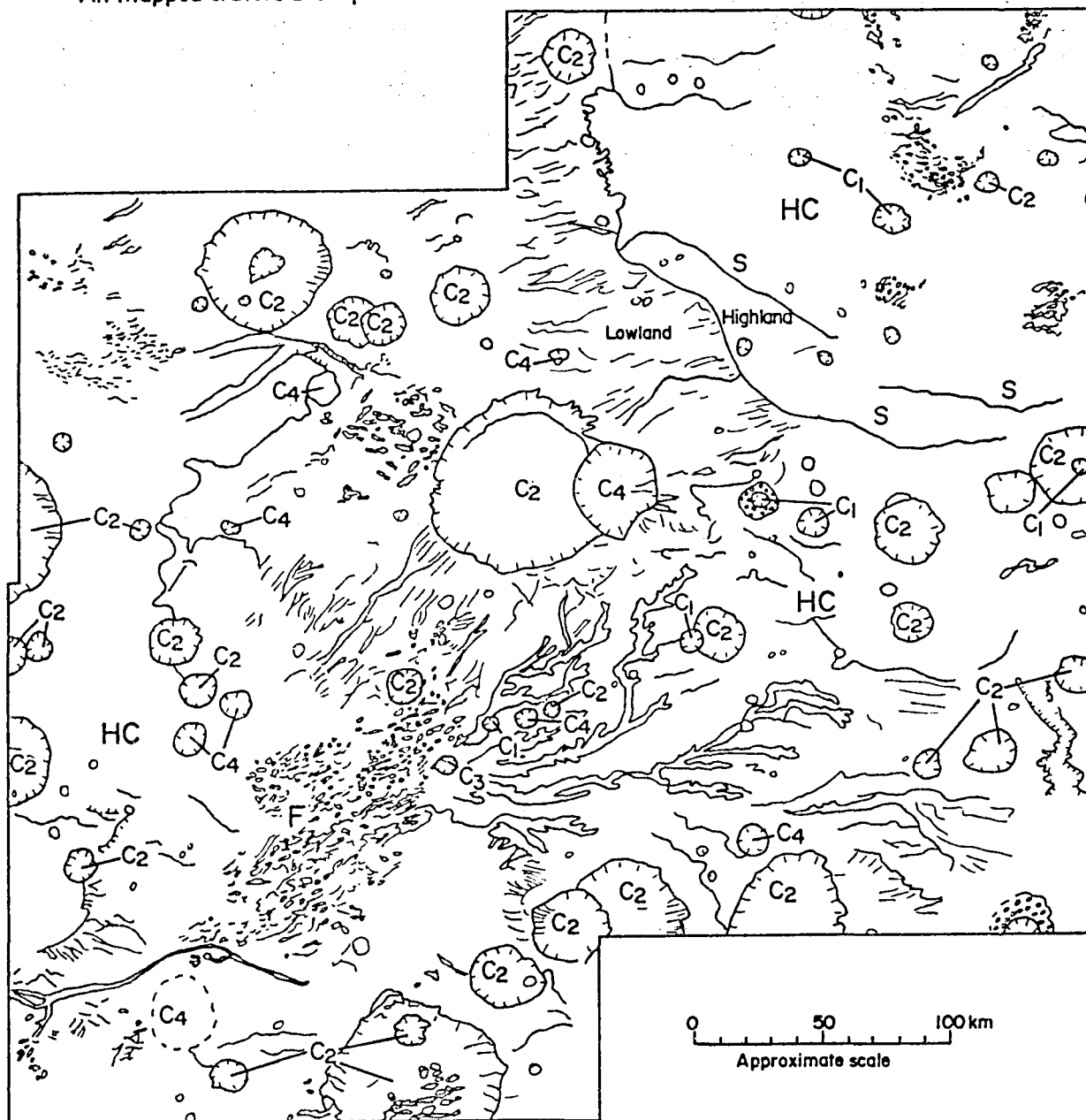


Figure 1. Geomorphic map showing dry valley (channel) systems in the southeastern portion of the Margaritifer Sinus Quadrangle of Mars (MC-19). The mapping is from Viking Frames 084 A46 and 084 A47 and is approximately centered at Lat. 21°S., Long. 9°W.

PITS, STREETS, PLATEA, TOWERS, AND MARGINAL PLAINS ON MARS

Brook, George A., Department of Geography, University of Georgia,
Athens, Georgia 30602

On Earth rock labyrinths originate as parallel, en echelon, or intersecting narrow grabens, or develop where fault and joint networks are selectively eroded. Labyrinths frequently contain both downfaulted and erosional elements. Closed labyrinths contain closed depressions, open labyrinths are part of graded fluvial networks.

Almost all deep closed terrestrial labyrinths are formed by solution of karst rocks. The channelled scablands of eastern Washington in basalt, and the Antarctic Wright Dry Valley labyrinth in dolerite are the only known deep erosional labyrinths in non-carbonate rocks. The channelled scablands were produced by catastrophic flood erosion (Baker 1978). The origin of the Wright Valley labyrinth is not known. Catastrophic flood erosion, glacial erosion, and subglacial meltwater erosion have been suggested. An origin involving salt weathering with removal of weathered products by wind appears to be the most likely explanation of this landscape (Selby and Wilson 1971).

No matter how they have formed, terrestrial closed labyrinths contain the same relief elements: pits, streets, platea, towers, and marginal plains. Furthermore there is a simple developmental sequence (Brook and Ford 1978). Strings of elliptical, vertical-walled pits develop in intersecting fracture systems. Pits gradually enlarge and coalesce so that steep-walled linear depressions or streets are formed. As streets deepen and widen, intervening rock ridges are dissected and ultimately destroyed. Angular closed depressions called platea are produced which frequently contain residual rock towers. As platea increase in number and size, the landscape is reduced to a series of isolated rock towers separated by broad marginal plains.

Open labyrinths on Earth are well developed in a limestone, sandstone, and shale sequence at Bryce Canyon National Park, Utah; in sandstones at Arches National Park, Utah; and in volcanic rhyolites in the Chisos Mountains, Texas, and the Chiricahua Mountains, Arizona. In each area the labyrinths form part of a stream channel network. Linear, joint-controlled channel segments which often intersect at high angles, box valleys, and buttes are the open labyrinth equivalents of streets, platea, and towers.

A terrestrial labyrinth containing both downfaulted and erosional relief elements occurs in the Needles District, Canyonlands National Park, Utah. Numerous parallel and en echelon grabens 100-600 m wide, 0-100 m deep, and several kilometers long, closely resemble erosional streets. Grabens are deeper and wider at their midpoints and therefore form

structural closed depressions. Graben floors are covered by alluvium, aeolian deposits, and rubble derived from graben wall collapse (McGill and Stromquist 1979). Upland surfaces between grabens are underlain by massive, well jointed sandstone. Selective erosion of fractures has produced a series of upland open labyrinths with streets, platea, and towers within a closed graben labyrinth.

Closed labyrinths on Mars are generally much larger than those on Earth but have virtually identical form. In the southeast portion of Memnonia Southeast Quadrangle, for example, a depression 90 km long and 10-15 km wide has developed in the old cratered surface. The eastern one-third of the depression is formed of two intersecting craters; the western two-thirds is an angular platea with residual rock towers 0.5-10 km in diameter. Walls of the platea are structurally controlled. West of the depression are strings of elliptical pits developed in regional fractures.

Noctis Labyrinthus and Valles Marineris are the largest rock labyrinths on Mars; together they extend a distance of more than 3,000 km. Both downfaulted and erosional relief elements are evident. Noctis Labyrinthus is a network of intersecting troughs (Sharp 1973a) tens of kilometers wide and hundreds of kilometers long at the summit of the Tharsis-Syria Rise; the labyrinth is 1,000 km across. East of Noctis Labyrinthus the Mariner valleys are troughs up to 200 km wide, several hundred kilometers long, and several kilometers deep. Some of these, such as Ius Chasma and Melas Chasma, are interconnected; others are entirely closed depressions (e.g. Hebes Chasma and Juventae Chasma).

Strings of pits or catenas are found on upland surfaces surrounding Noctis Labyrinthus and Valles Marineris. South of Coprates Chasma and parallel to it are three catenas, the longest is 350 km long. Other strings occur east of Ophir Chasma and south of Tithonius Chasma. All are developed in regional fractures. Sharp (1973a), Mutch *et al.* (1976), and Blasius *et al.* (1977) agree that strings of pits evolve into narrow, linear troughs. Mutch *et al.* (1976) also argue that where parallel troughs develop, slope recession gradually erodes the intervening upland surfaces. This has occurred in Coprates Chasma. At the western end of the chasma a plateau remnant 60 km long and 5 km wide is preserved as the crest of a narrow ridge separating two troughs. Where Coprates Chasma joins Eos and Capri Chasma, a second ridge is in a more advanced stage of evolution; receding slopes have intersected so that no plateau remnants remain. If Martian troughs have developed in the manner described, they are really huge platea formed by erosion acting along vertically and horizontally persistent regional fractures which surround the Tharsis uplift.

Headward erosion along vertical fissures at the western end of Kasei Vallis, north of Lunae Planum, has produced one of the best examples of

an open labyrinth on Mars. Open and closed rock labyrinth relief elements are also evident in areas of pitted, etched, and fretted terrain (Sharp 1973b, c).

Karst labyrinths on Earth vary in size by a factor of one thousand but all were produced by the same process--solution. The fact that Martian pits, streets, and platea are up to one hundred times larger than the largest equivalent forms on Earth does not, therefore, preclude a similar origin. There is no consensus on the origin of labyrinths on Mars but it is possible that most were etched out by chemical and/or mechanical weathering processes, which reduced the bedrock along fractures to clay-, silt-, or sand-sized particles. These weathering products may then have been removed by wind.

References

- Baker, V. R. (1978). The Spokane flood controversy and the Martian outflow channels. *Science*, 202: 1249-1256.
- Blasius, K. R., Cutts, J. A., Guest, J. E., and Masursky, H. (1977). Geology of the Valles Marineris: First analysis of imaging from the Viking I Orbiter primary mission. *J. Geophys. Res.*, 82: 4067-4091.
- Brook, G. A. and Ford, D. C. (1978). The origin of labyrinth and tower karst and the climatic conditions necessary for their development. *Nature*, 275: 493-496.
- McGill, G. E. and Stromquist, A. W. (1979). The grabens of Canyonlands National Park, Utah: Geometry, mechanics, and kinematics. *J. Geophys. Res.*, 84: 4547-4563.
- Mutch, T. A., Arvidson, R. E., Head, J. W., Jones, K. L. and Saunders, R. S. (1976). *The Geology of Mars*. Princeton Univ. Press, Princeton, N.J.
- Selby, M. J. and Wilson, A. T. (1971). The origin of the labyrinth, Wright Valley, Antarctica. *Geol. Soc. Amer. Bull.*, 82: 471-476.
- Sharp, R. P. (1973a). Mars: Troughed terrains. *J. Geophys. Res.*, 78: 4063-4072.
- Sharp, R. P. (1973b). Mars: Fretted and chaotic terrains. *J. Geophys. Res.*, 78: 4073-4083.
- Sharp, R. P. (1973c). Mars: South polar pits and etched terrain. *J. Geophys. Res.*, 78: 4222-4230.

Studies of the Martian polar caps, A. D. Howard, University of Virginia, Department of Environmental Sciences, Charlottesville, Va. 22903.

Study of the topography and deposits of the polar areas is crucial for the understanding of the recent geologic and climatic history of Mars. Studies underway at the University of Virginia are focusing on detailed analysis of polar topography, stratigraphy, and eolian features. We are using several interrelated techniques of analysis:

1). Detailed mapping of landforms, deposits, and eolian features of the polar caps. This comprehensive mapping will be quantitatively analyzed (by digitizing) to provide statistical information on the topography and deposits and their relationships to latitude, longitude and dominant wind directions. From images taken during the martian summer we are mapping the following major terrain types: Distinctly and indistinctly layered terrain, featureless terrain, the underlying "basement", stripped layers, dunes, and grooves. In addition, we are mapping conformable and unconformable boundaries between units, wind directions from frost streaks, grooves, and dunes, and the frost cover. From images taken during the martian early spring with complete frost cover we are mapping trough edges and bottoms, the crests and bottoms of the "wavy" topography, and the underlying basement.

2). Local stratigraphic studies. The stratigraphy of the layers and ice in local areas of critical interest are being mapped in detail. One result of such mapping has been to demonstrate an abundance of unconformities in the layered deposits of the North Pole, both within the layers and at the trough-bottom ice-layer contact (Howard, 1979). We have recently discovered the first direct evidence for ablational retreat of the polar scarps. In some places where scarps in layered terrain rise directly from the underlying sparsely cratered plains, low, morain-like ridges parallel the scarp on the cratered unit (see, for example, the high-resolution spring images 566B61,63,65,67,69,70, 79). Although these ridges are suggestive of morain systems, they do not necessarily indicate flow or sliding of the ice and layered terrain; rather, they may be ablational dust accumulated at the base of the scarp as it retreated.

3). Quantitative stratigraphic correlations and photometric slope determinations. We are constructing brightness transects across scarps in layered terrain from photometrically corrected digital picture listings by the projection and averaging of adjacent pixel values. These transects are used for detailed quantitative correlation as well as for photoclinometric determination of slope gradients using early spring images. Figure 1 compares a summer and early spring transect across a southwest-facing scarp at approximately 79.35 N

and 332.41 W, shown on 078B23 and 566B75, respectively. The early spring image was used to determine slope gradients and the topographic profile under the assumption of a continuous frost cover of uniform albedo. Using reasonable photometric functions for snow and for the atmospheric optical thickness, the scarp is found to have an average gradient of about 3 degrees and a maximum gradient of about 6 degrees, which seems consistent with the photogrammetric determinations of Dzurisin and Blasius (1975). Comparison of the spring with the summer transects reveals that the strong definition of layers in many summer images is due to the differential defrosting of steeper slope segments, leaving slightly less steep slope segments partially frosted. This, of course, results in contrast reversal from spring to summer (Fig. 1). However, compositional factors also appear to determine the extent of summertime ablation, because the relatively steep basal slopes of the scarp have remained largely frosted while overlying, gentler slopes have defrosted (Fig. 1). The difference in defrosting behavior may be due to a contrast in heat capacity or thermal conductivity of the layered deposits, or to a difference in microtopography of the surface which would differentially trap the winter frost or protect it from ablation. Such microtopographical differences would, in turn, be due to differences in layer properties.

References

- Howard, A.D., 1979, The martian poles: studies of topography, stratigraphy, and geologic evolution. in Reports of Planetary Geology Program, 1978-1979, NASA Tech. Mem. 80339, p. 103-105.
- Dzurisin, D. and Blasius, K.R., 1975, Topography of the polar layered topography of Mars. Jour. Geophys. Res. 80, 3286-3306.

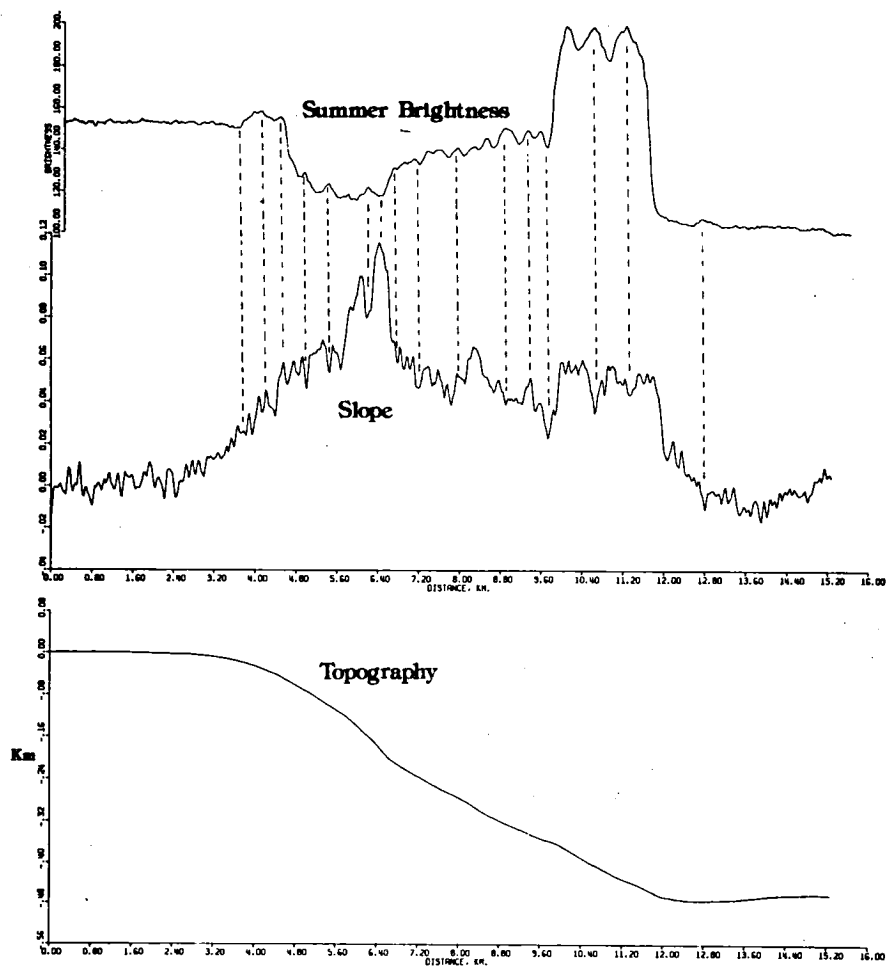


Figure 1. Transect analysis of a polar scarp across layered terrain. Top profile is brightness during the summer, when the scarp is partially defrosted. Bottom two profiles show the slope gradients and topography determined photometrically from an early spring image. Vertical dashed lines correlate the two transects.

SIMULATIONS OF STRATIGRAPHY OF MARTIAN POLAR LAYERED DEPOSITS

Cutts, James A., Planetary Science Institute, Science Applications, Inc., Pasadena, California 91101

Polar layered deposits on Mars are now widely thought of as the geological expression of long term quasi-periodic variations in orbital and axial elements of the planet (Murray et al, 1972; Howard, 1977; Toon, 1979,; Ward, 1979; and Pollack et al, 1979). However, quantitative models of the layered structure of the polar deposits have never been attempted. Here I consider a simple model of this process and make some quantitative predictions of the thicknesses of sequential layers formed during the last 10 million years.

The model considered here is an elaboration of some previously published ideas (Cutts, 1973; Cutts et al, 1976; Cutts et al, 1979). The essence of the model is that; 1) the deposits form by accumulation of dust, 2) dust accumulation is identical each year when a function $F(\theta, e)$ of the obliquity (θ) and the eccentricity (e) exceeds a threshold F_c and is zero when $F(\theta, e)$ falls below F_c , and 3) a layer is established when $F(\theta, e)$ is below threshold for a period greater than T_L . The illustrated example (Fig. 1) shows how a series of layers is generated.

Several different function forms for $F(\theta, e)$ have been experimented with. In the example illustrated in Fig. 2 the function has the dimensional form of a wind surface stress

$$F(\theta, e) = \rho(\theta) [v(e)]^2 \quad (1)$$

where $\rho(\theta) = \rho_0 \exp (C_0 + C_1\theta + C_2\theta^2)$
and $v(e) = v_0 (1 + D_1e)$

ρ_0 , C_0 , C_1 , C_2 , v_0 , D_1 have been selected to match dependences of atmospheric density (e) and diurnal tidal wind velocity (v) reported by Ward (1974) and Leovy and Zurek (1979). Behavior appears to be dominated by the obliquity variations and, as Fig. 2 shows, layer thicknesses are quite uniform and insensitive to the choice of threshold.

When the values of the parameters in equation (1) are manipulated so that eccentricity is the primary forcing function layer thicknesses are found to be highly variable and rather sensitive to the choice of threshold. These models are likely to prove useful in interpreting the types of polar photogeologic data reported by Howard (1980) in this document.

REFERENCES

Cutts, J.A., *JGR*, v. 78, No. 20, 10 July 1973, pp. 4231-4291. Cutts, J.A., Blasius, K.R., Briggs, G.A., Carr, M.H., Greeley, R., and Masursky, H., *Science*, v. 194, 17 Dec. 1976, pp. 1329-1337. Cutts, J.A., Blasius, K.R., and Roberts, W.J., *JGR*, v. 84, No. B6, 10 June 1979, pp. 2975-2994. Howard, A.D., *Icarus*, 34, 1978, pp. 581-599. Leovy, C.B., Zurek, R.W., *JGR*, v. 84, No. B6, 10 June 1979, pp. 2956-2968. Murray, B.C., Malin, M.C., *Science*, v. 182, 2 Nov. 1973, pp. 437-443. Pollack, J.B., *Icarus*, 37, 1979, pp. 479-553. Toon, O.B., *Second Inter. Colloquium on Mars*, 15-18 Jan. 1979, p. 84. Ward, W.R., Murray, B.C., and Malin, M.C., *JGR*, v. 79, No. 24, 20 Aug. 1974, pp. 3387-3410. Ward, W.R., *JGR*, v. 84, No. B1, 10 Jan. 1979, pp. 237-241.

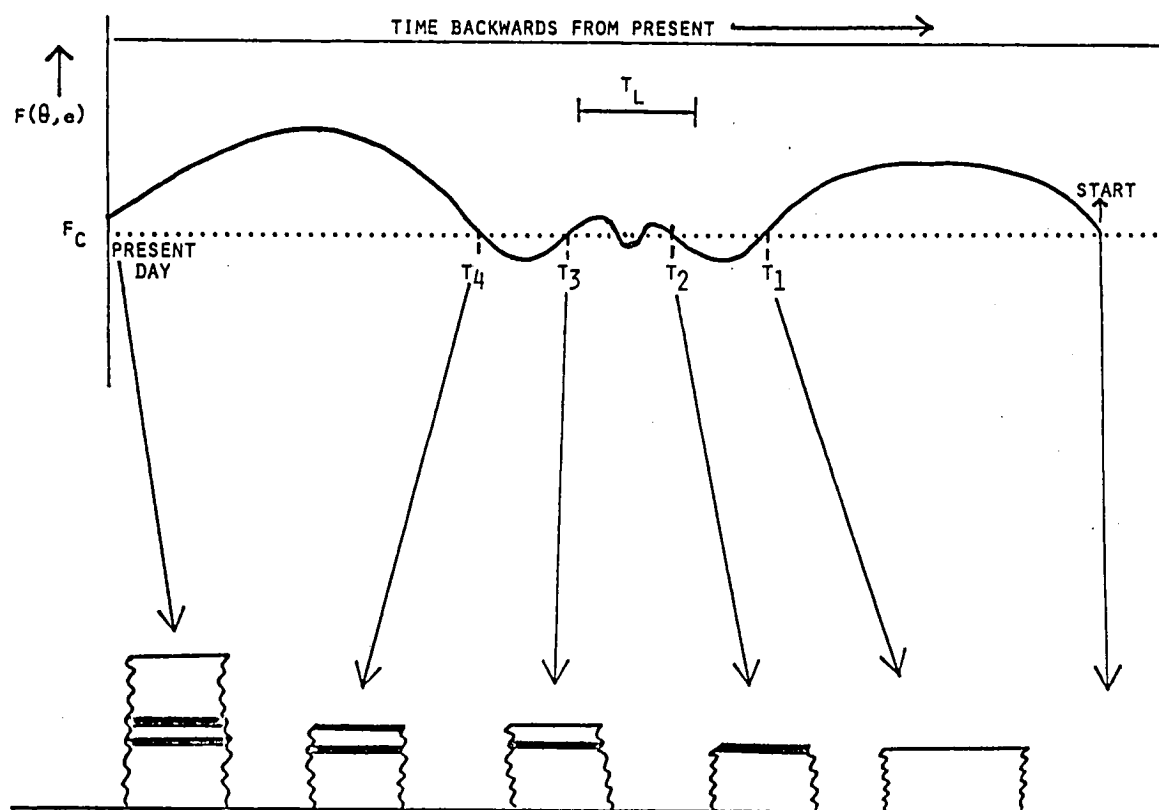


Figure 1: STRATIGRAPHIC CROSS SECTIONS
AT FIVE SUCCESSIVE TIMES IN THE MODEL
FOR FORMATION OF POLAR STRATIGRAPHY

FIGURE 1: Model Formation of Polar Stratigraphy: Stratigraphic Cross Sections at Five Successive Times.

Figure 2
TIME BACKWARD FROM PRESENT IN MILLIONS OF YEARS

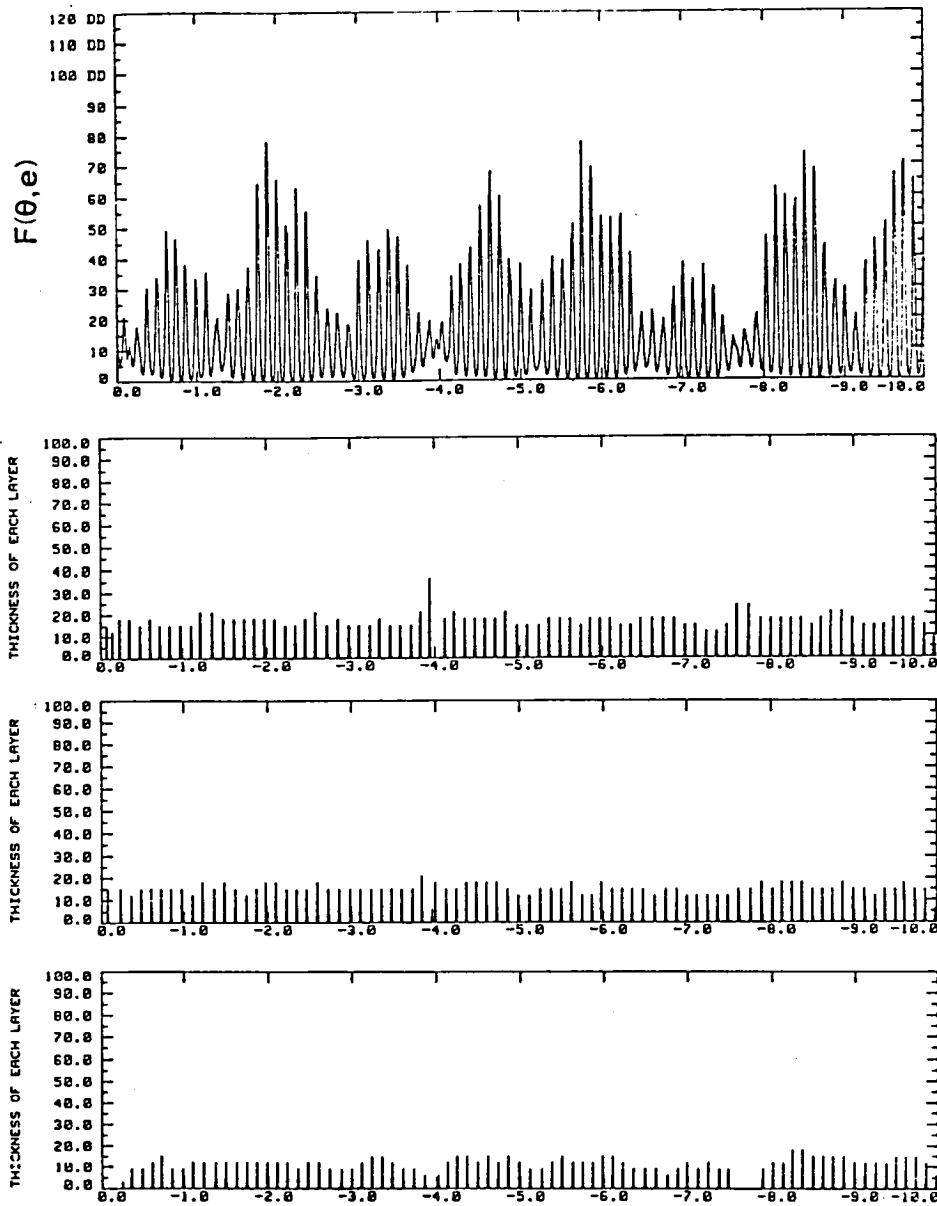


FIGURE 2: Martian polar stratigraphy for the past 10^7 years computed for the value of $F(\theta, e)$ described in equation 1. The top curve shows $F(\theta, e)$ for the past 10^7 years. The three curves below that show layer thicknesses generated for the threshold $F_c = 8, 10, \text{ and } 15$ respectively. Layer thicknesses are quite uniform although quite sensitive to the choices of threshold.

PATTERNS OF RIDGES AND SCARPS ON MARS

Eppink, J.F., Jet Propulsion Laboratory, 4800 Oak Grove Drive,
Pasadena, California 91103 /Department of Geological
Sciences, University of Southern California,
Los Angeles, California 90007,
Saunders, R.S., Jet Propulsion Laboratory, 4800 Oak Grove Drive
Pasadena, California 91103.

Surface patterns of deviatoric compressive stresses associated with crustal loading centered on Tharsis have been modeled by Phillips and Lambeck (1). They noted that many ridges are orthogonal to the modeled compressive stress trajectories. Systematic global mapping of ridges and scarps (2) has been undertaken in an effort to examine the correlation of ridges and modeled stresses.

Ridge mapping was undertaken for each martian quadrangle using computer searches of Viking orbiter imagery to insure maximum coverage of each quadrangle. To date 21 of the 30 quadrangles have been surveyed covering nearly all of the planet south of 30°N latitude. Mapping reveals numerous occurrences of ridges and scarps in locations other than previously mapped ridged plains (3). Ridges and scarps are found to occur throughout highland cratered terrain, where they generally occur on intercrater plains of limited areal extent. Locally ridges lie wholly within craters or transect crater walls. The global geometric configuration formed by the ridges shows a striking degree of orthogonality to modeled compressive stresses of Phillips and Lambeck (1). This is especially true in regions adjacent to Tharsis. In regions farther from Tharsis the correlation is weaker.

This orthogonal relationship of ridges and compressive stresses associated with Tharsis loading is most noticeable to the east of Tharsis. Here, from 30°N to nearly 30°S latitude and centered on 70° longitude, plains of numerous well-developed parallel ridges form a broad arcuate band up to 1400 km wide and are oriented normal to modeled compressive stress trajectories. South of Tharsis below 30°S latitude and stretching from 45° to 180° longitude ridges also correlate very well with modeled compressive stresses. Compressive stresses are radial to Tharsis in this region whereas the ridges are oriented circumferentially. To the west of Tharsis between 30°N and 40°S latitude and as far west as 210° longitude modeled compressive stresses strike approximately east-west. Once again ridges display an orthogonal configuration striking approximately north-south. On the Tharsis plateau itself in the area of maximum compressive stress, ridges are absent (except within the calderas of the Olympus and Pavonis Montes) and may be covered by volcanic lavas.

On the opposite side of the planet from Tharsis at $\sim 290^\circ$ longitude agreement between ridge orientations and modeled compressive stress trajectories is less certain. In equatorial latitudes ($\pm 30^\circ$) of this area modeled stress trajectories are oriented predominantly north-south. Parallel ridges of this same area trend north and northwest and are at best highly oblique to modeled stresses. Ridges such as those of Hesperia Planum (20°S , 250°) are anastomosing reflecting a major northwest trend and a minor northeast trend. In southern latitudes (below 30°S) modeled compressive stress trajectories rotate clockwise from an east-west orientation at 230° longitude to $\sim \text{N}15\text{W}$ at 310° longitude. Ridge orientations do not fit this pattern and instead trend in various nonorthogonal directions.

The extent to which geometric configurations of ridges fit this model of deviatoric compressive stresses implies that the ridges have a structural origin and are a tectonic expression crustal failure due to Tharsis loading. Ridges remote from Tharsis may be influenced by a differing stress regime.

References:

- (1) Phillips, R.J., and K. Lambeck, 1979, Gravity fields of the terrestrial planets- Long wavelength anomalies and tectonics, Reviews Geophys. & Space Phys., in press.
- (2) Martian ridge morphologies are discussed by Luchitta, B.K. and J. L. Klockenbrink, 1979, Ridges and scarps in the equatorial belt of Mars, in Lunar and Planetary Science X p. 31-33.
- (3) Scott, D.H. and Carr, M.H., 1977, U.S. Geological Survey Misc. Inv. Map I-1083.

TECTONIC FEATURES OF SOUTHEAST THARSIS

Plescia, J.B., Roth, L.E. and Saunders, R.S., Jet Propulsion
Laboratory, 4800 Oak Grove Drive, Pasadena, California 91103

Radar topography of Mars has been obtained over the past several years during each opposition (1). This topography has allowed a more detailed understanding of several structures of the equatorial belt. Two features, in particular, will be discussed here, the Claritas Fossae region and the Coprates Rise.

Claritas Fossae is an elongate piece of ancient crust at approximately 110° longitude, which is surrounded by younger volcanic plains. Relative relief with the adjacent plains varies from 0 km at -14.5° latitude, to nearly 2 km at -20° , (Figure 1). The absolute elevation, relative to the reference areoid (2), is fairly constant along the strike. The observation that the absolute elevation of this old piece of crust is constant and does not increase northward, may indicate that much of Tharsis plateau is constructional rather than a crustal uplift.

Claritas Fossae has apparently acted as a barrier for lavas extending away from both Arsia Mons and the Syria Rise volcanic region. This effect is evident in the images of the southeast flank of Arsia Mons where flows can be seen to be deflected by the Claritas Fossae horst. The thickness of the lavas increases along the western side of the horst as reflected in an increase of elevation northward. At -14.5° the flows from Arsia Mons appear to have capped the western reaches of Claritas Fossae, as there is no relative relief between the Fossae and the flows. This would imply a thickness of at least 2 km for the lavas in this areas.

Along the eastern margin, relative relief with respect to the Syria plains is constant at about 1 km. To the south, beginning at -18° , a graben has developed, with an average width of about 100 km. This graben can be traced southward into Thaumasia for a distance of over 1800 km. The southernmost radar track which crosses this feature, indicates a graben depth of 2 km relative to the adjacent plains.

A second major structural feature observed are a series of tilted fault blocks between 50° and 75° longitude. (Figure 2), south of Coprates Chasma, and termed the Coprates Rise. Topographic ridges are observed at three longitudes; 65° , 59° and 52° . All of the ridges strike north-south and have asymmetric slopes. In all three cases, the eastern flank of the Rise exhibits a steeper slope than the western side. The ridges at 65° and 59° rise 1.8-2.0 km above the surrounding plains. These two ridges are separated by a plains unit which lies about 500m below the

ridge crests. Along the eastern side of the 59° ridge, a steep slope is observed with approximately 2 kilometers of relief across it. A second north-south trough occurs along 55° . To the east of this trough, the elevation crests in the region of 52° . Due to limited latitude coverage by radar the north-south extent of these ridges could not be determined; however, they can be seen in orbiter images to dive below younger plains to the north, while to the south, they merge with the Thaumasis highlands. The troughs at 55° and 62° are both floored by ridged plains units, appreciably younger than the ridges. The ridges themselves are composed of heavily cratered crust, Regional slopes are about 0.2° to the west, while eastern slopes are much steeper, reaching 2.5° .

The interpretation here is that this structure represents blocks of older crust which have been tilted to the west by some tectonic process. The size of the blocks appears to decrease to the west, with the westernmost block being approximately 500 km across, the central block 350 km across, and the eastern block 200 km across. A second area of similar faulting, Figure 3, occurs to the west of the Tharsis region, at about 165° longitude. Here the fault block has the opposite orientation, being tilted eastward. This raises the interesting possibility that these tilted blocks may be related to the tectonism of the Tharsis region. A second possibility is that these blocks represent the rim of some ancient impact basin centered on the Tharsis region.

References:

- (1) Down, G.S., Reichley, P.E., Green, R.R. (1975). Icarus 26, 273-312.
- (2) Standish, E.M. (1973). Astom Astrophys , 26, 463-466.

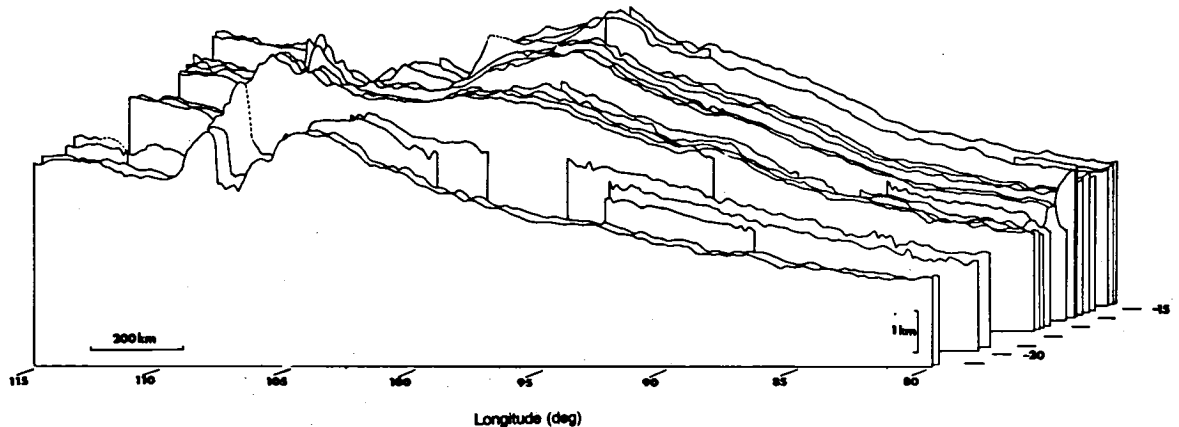


Figure 1. Topography around the summit of the Syria Rise and the Claritas Fossae horst. Vertical exaggeration 100X. 22 Goldstone radar scans between latitudes -14.23° and -21.19°

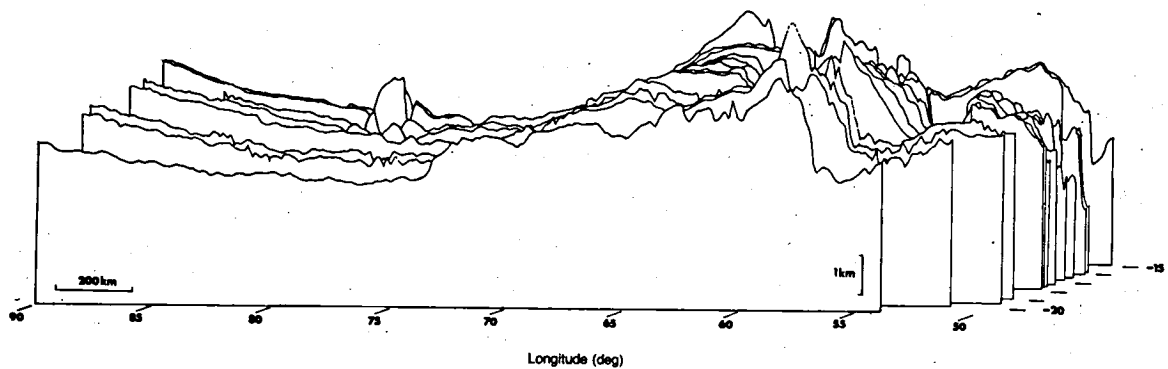


Figure 2. Topography of the Coprates Rise. Vertical exaggeration 100X. 19 Goldstone radar scans between the latitudes of -14.23° and -21.19°

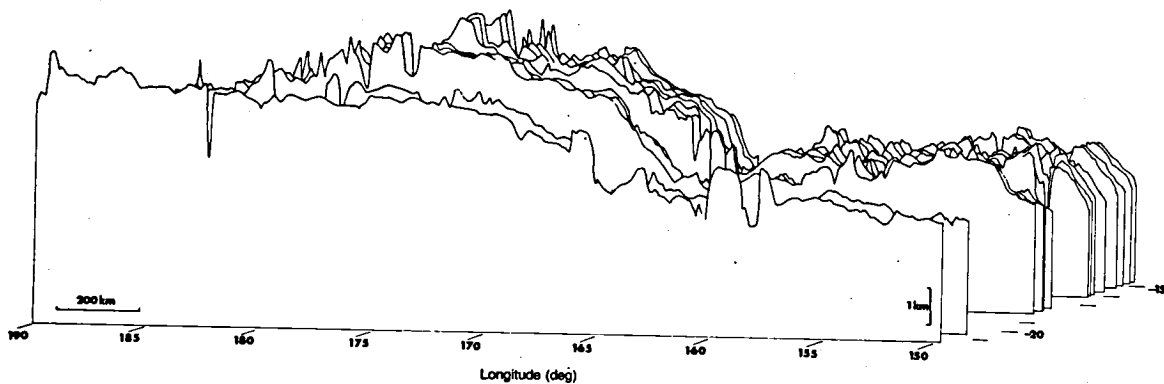


Figure 3. Topography of cratered highlands in Memnonia. Vertical exaggeration 100X. 15 Goldstone radar scans between latitudes -14.50° and -21.19° .

THARSIS: AN ALTERNATIVE EXPLANATION

Sean C. Solomon¹ and James W. Head²

¹Dept. of Earth and Planetary Sciences, Massachusetts Institute of Technology, Cambridge, MA 02139

²Dept. of Geological Sciences, Brown University, Providence, RI 02912

The Tharsis region of Mars, by virtue of its large scale and its complex and extended history of volcanic and tectonic activity, is a focal point for discussions of Martian geologic evolution. The traditional explanation of Tharsis [1,2] is that broad updoming of the lithosphere caused by a thermal or chemical anomaly in the mantle led to fracturing and to the volcanic emplacement of thin plains units and later of the large shields. Evidence cited in support of this model includes the broad topographic high of the Tharsis region, the large elevation of surface units mapped as relatively old on the basis of density of craters and fractures, and the generally radial trends to most extensional fractures in and near the Tharsis area.

We offer in this paper an alternative explanation for the events of the Tharsis region. In briefest terms, the explanation contains three elements: (1) The elastic lithosphere of Mars throughout much of its history has been heterogeneous in thickness (i.e., in temperature). Stress due both to global and local causes was concentrated in zones of thin lithosphere, foremost among which was (perhaps a small fraction of) the Tharsis region, preferentially concentrating fracturing in such areas. (2) Intense fracturing was conducive to local volcanism. The heating associated with volcanism maintained a locally thin elastic lithosphere, thus insuring that further fracturing and volcanism would be concentrated in the same area. (3) Tharsis topography was produced primarily by volcanic construction. The topographic and gravity highs have been supported against complete isostatic compensation by the strength of a broadly thick (if locally thin) lithosphere.

There is strong evidence for the existence of lateral variations in the thickness of an elastic lithosphere on Mars from the apparent flexural response of the lithosphere to local volcanic loads [3]. In particular, there appears to have been a dichotomy in lithospheric thickness that is insensitive to load age, with thin (25-50 km) elastic lithosphere indicated for the regions immediately surrounding large shield volcanoes in major volcanic provinces (Tharsis Montes, Elysium Mons), and a thick elastic lithosphere (>100 km) for regions at greater distances from volcanic province centers (Isidis basin, Olympus Mons). A similar case for contemporaneous heterogeneities in elastic lithosphere thickness on the Moon has been made from the local tectonic response to mascon loading [4].

We hypothesize that Tharsis (and Elysium) was the site of locally thin lithosphere dating from a time shortly after crustal formation. Concentration of stress due to such global causes as warming and expansion of the deep Martian interior [5] combined with locally generated stress to produce early fracturing. The history of faulting in the Tharsis region has been characterized by several major episodes of extensional faulting, each with a generally preferred direction for fault trends [2,6,7]. In particular, early Tharsis faults showed dominantly N-S trends, and later faults showed mostly NE-SW trends [6]. Thus at any given time in the Tharsis region, the pattern of major extensional faults was not clearly radial. That the faulting was an expression simply of global (thermal) and local (loading) stress is therefore at least as plausible an explanation as regional doming.

The most straightforward explanation for regional doming, the explanation generally invoked for large scale doming on the Earth, is thermal expansion associated with an anomalously vigorous mantle heat source [1]. Doming by thermal expansion is nearly an isostatic process, leading to at most modest gravitational anomalies unless a great thickness of mantle material is involved in the heating. While an isostatic model for Tharsis is possible [8], the required lateral temperature contrast rules out a strictly thermal explanation.

The Elysium area is a smaller scale analog to the Tharsis region [9]. The analogy includes both topographic and gravity highs [10], evidence for a locally thin elastic lithosphere near Elysium Mons [3], and a fracture system with a stronger regional than radial trend [11]. A thermal doming explanation for the Elysium topographic and gravity anomalies can be excluded: because of the comparatively great age of Elysium volcanic activity compared to Tharsis [2], any thermal anomaly beneath Elysium should have substantially decayed. The anomalies, however, have clearly persisted. While a chemically anomalous mantle beneath Elysium (and Tharsis) could account for the gravity and topography [2], at least an equally likely explanation is that the Elysium topography is constructional in origin and has been supported since emplacement by a regionally thick elastic lithosphere.

We have thus been led to consider the hypothesis that much of the topographic anomaly of Tharsis is also constructional in origin. The great shields are clearly constructional and are largely supported by lithospheric strength. While the youngest volcanic plains in the Tharsis region may be relatively thin (<1 km), the thickness of earlier volcanic units is not well constrained. The comparatively old, high standing surfaces in the Tharsis area, by this hypothesis, may be the still exposed surfaces of volcanic constructs from an early episode of Tharsis activity, perhaps dating as far back as near the time of termination of heavy bombardment.

As an alternative to an updoming model for Tharsis, we therefore propose a model incorporating zones of locally thin lithosphere capable of concentrating stress and lithospheric failure, closely associated volcanism and fracturing maintaining the locally thin lithosphere by positive feedback, and an evolving topographic construct built by the successive addition of volcanic units and supported by a regionally thick lithosphere. By this model, the topographic and gravity highs in Tharsis and Elysium are primarily constructional and permanent. The concentration of fracturing and volcanism in distinct provinces follows naturally from the notion of heterogeneities in lithosphere structure. Fracturing is in response to global and local sources of stress and reflects lithospheric strength, so that radial fracture trends are not required.

A major distinction between the explanation for Tharsis offered here and all earlier explanations [12] is that no special or anomalous properties need to be attached to the mantle beneath major Martian volcanic provinces. The location of volcanism on Mars is governed primarily by the sites of easiest access of magma to the surface. In this respect, Tharsis may be similar to mid-ocean ridges on the Earth. The mid-Atlantic ridge and the east Pacific rise are major volcanic centers and are nearly stationary in a hotspot reference frame, yet no anomalous characteristic is attributed to the mantle beneath them. The mantle beneath ocean ridges, and beneath Tharsis in the model proposed here, plays a passive rather than an active role.

The model for Tharsis evolution proposed here, like all other simple models, may fail to account for all of the details of a complex regional history. Nonetheless we feel the model offers an attractive alternative to regional doming and merits further critical testing by both geophysical and geological data.

References:

- [1] M.H. Carr, J. Geophys. Res., 79, 3943-3949, 1974.
- [2] D.U. Wise et al., Icarus, 38, 456-472, 1979.
- [3] S.C. Solomon et al., NASA TM 80339, 60-62, 1979.
- [4] S.C. Solomon and J.W. Head, Rev. Geophys. Space Phys., in press, 1980.
- [5] S.C. Solomon and J. Chaiken, Proc. Lunar Sci. Conf. 7th, 3229-3243, 1976.
- [6] J.B. Plescia et al., Geophys. Res. Lett., in press, 1979.
- [7] H. Frey, J. Geophys. Res., 84, 1009-1023, 1979.
- [8] N.H. Sleep and R.J. Phillips, Geophys. Res. Lett., in press, 1979.
- [9] M.C. Malin, Geol. Soc. Amer. Bull., 88, 908-919, 1977.
- [10] W.L. Sjogren, Science, 203, 1006-1010, 1979.
- [11] D.H. Scott and M.H. Carr, U.S.G.S. Map I-1083, 1978.
- [12] R.J. Phillips, NASA TM 79729, 334-336, 1978.

EARLY VOLCANIC-TECTONIC PROVINCE: COPRATES REGION OF MARS

Saunders, R. S., Roth, L. E., and Downs, G. S., Jet Propulsion Laboratory, California Institute of Technology, Pasadena, CA 91103;
Schubert, G., Department of Earth and Space Sciences, University of California, Los Angeles, CA 90024.

Features of an elevated region south of Coprates Chasma may have implications for regional volcanic and tectonic history. The elevated region lies south of Coprates Chasma and near the eastern margin of the ridged plains [1] of Coprates quadrangle (MC-18). McCauley [2] has recognized the existence of this region and considered it to comprise a geologic unit equivalent to the cratered plateau material which underlies the Ridged Plains material and is exposed to the east. The region coincides with the crest of a topographic high recently identified [3] in the Goldstone Mars radar scans [4] extending between longitudes 57° and 80° (here termed the Coprates Rise, see Fig. 1). Within this elevated region a possible volcanic feature occurs at -18.4° latitude and 59.7° longitude. The illumination and shadowing (Viking Orbiter frames 610A24, 26) reveal an impact modified conical mountain 80 km in diameter with a 22 km diameter summit crater. The flanks display a sinuously channeled texture. We would interpret this feature as a shield volcano with radiating lava channels on its flanks. A similar feature occurs about 200 km south (-20.5° lat., 60.5° long.). This mountain is more irregular than the first one. It is about 60 km in diameter and has an indistinct summit caldera.

The elevated region is embayed by material of the Ridged Plains and apparently existed as a topographic high prior to emplacement of that material. The east side of the rise is marked by a steep linear ridge that extends from near the rim of Coprates Chasma for approximately 1000 km to the south along longitude 57° W. The eastern slope drops 2 km to the east over a distance of approximately 50 km. The slope is cut by numerous fractures and channels, some of which may have carried the material (presumably as lava) that formed the ridged plains. The steepest slopes here contain numerous aligned triangular facets that point uphill. There appears to be a structural control, but in many places the alignment of the facets suggests that resistant layers such as those exposed in Coprates Chasma to the north have been etched out by some erosional process.

If the faces on the slope result from erosion of layered material, then the layers dip in the same direction as the slope at an angle that somewhat exceeds the slope. This would indicate that the topographic rise is tectonic in origin, possibly a monoclinial fold, rather than a volcanic pile. The local topography appears to form a segment of a circle of elevated pre-ridged plains topography that extends down to

latitude -35° . The circular aspect suggests also that the topography may represent the remnants of an early impact basin. Apparently this elevated region was a local source for some of the plains volcanics.

References

- [1] Scott, D. H. and Carr, M. H. (1978). Geologic Map of Mars. USGS Map I-1083. Scale 1:25,000,000.
- [2] McCauley, J. F. (1978). Geologic map of the Coprates Quadrangle of Mars. USGS Map I-897. Scale 1:5,000,000.
- [3] Roth, L. E., Downs, G. S., Saunders, R. S., and Schubert, G. (1979). Submitted to Icarus.
- [4] Downs, G. S., Reichley, P. E., and Green, R. R. (1975). Icarus 26, 273-312.

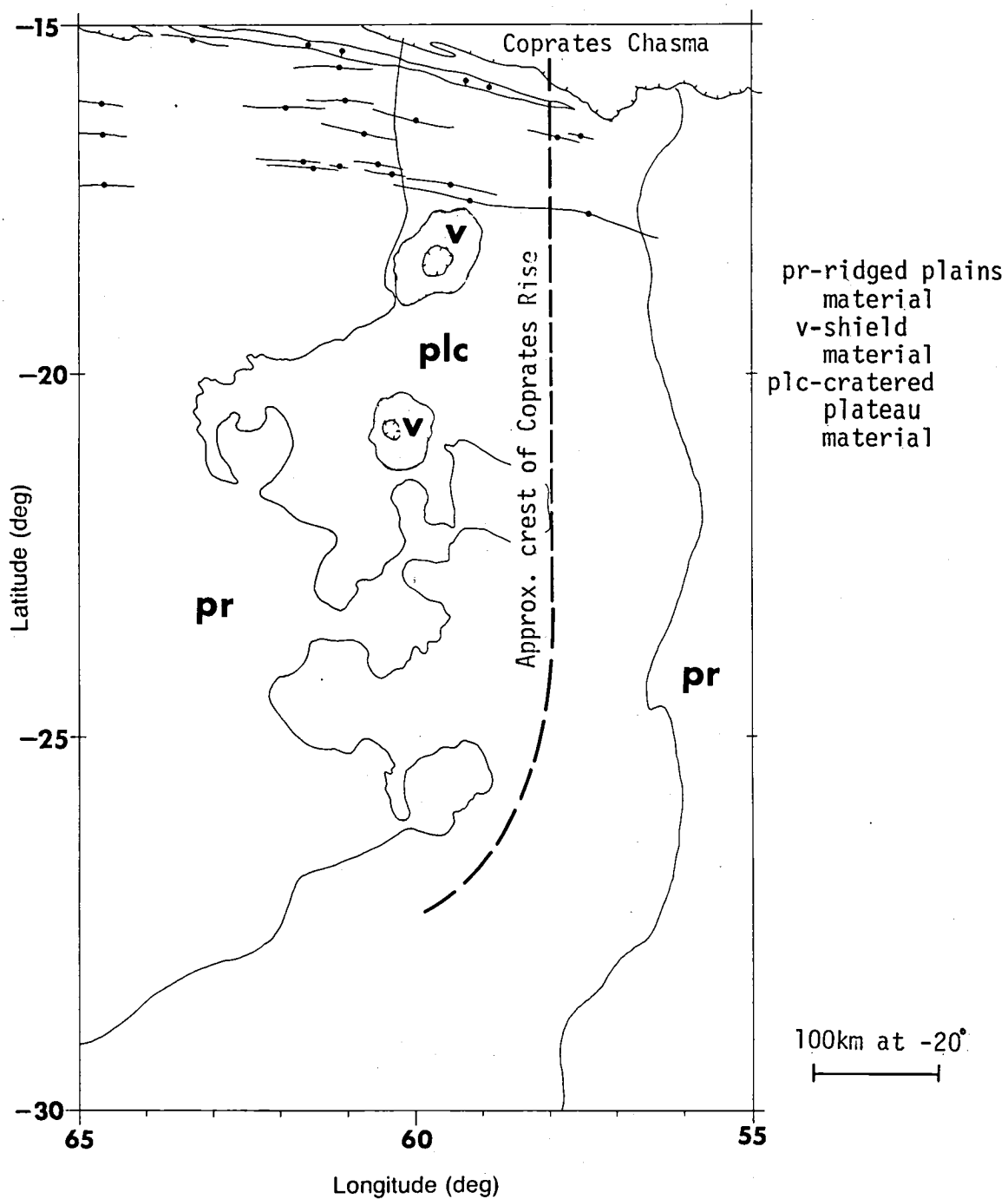


Fig. 1. Geology of the Coprates Southeast Quadrangle of Mars. (USGS Map M2M-22/56 CM, 1979, I-1184, MC-18 SE).

THERMAL HISTORIES OF MARS, INCLUDING CONVECTION AND CORE FORMATION

Davies, Geoffrey F., Dept. of Earth and Planetary Sciences and
McDonnell Center for Space Sciences, Washington University,
St. Louis, Missouri 63130.

Convective models of the thermal history of Mars have been used to explore the relationships between initial temperature, core separation and the formation of Mars' crust. The results favor initial mean temperatures at least 80% of the present value, and peak heat fluxes comparable to those in modern earth ocean basins.

Core separation would have released sufficient energy to raise Mars' mean temperature by up to 300°K (Solomon, 1979), and would thus be a significant event in Mars' thermal history. As a first approximation, this energy is included in the models as a heat source with various assumed distributions in time. Convective heat transport through the interior is assumed, and is modeled through a simple, approximate relation between heat flux, temperature difference and viscosity. The assumed strong temperature dependence of the viscosity is the dominant factor governing the surface heat flux. Accretional and other early heating mechanisms are included implicitly through the initial mean temperature. Radioactive heating is included explicitly, with chondritic U and Th abundances (15 and 60 ppb) and $\text{K/U} = 2 \times 10^4$. Conductive loss of near-surface accretional heat is not adequately treated, so the formation of the primitive crust cannot be addressed.

Arvidson, Goettel and Hohenberg (1979) have concluded from an analysis of crater populations that the early phase of formation of primitive crust (southern cratered terrain), was followed by a second phase in which the northern cratered plains, fretted terrains and "cratered terrain plains" were formed. If a constant cratering flux is assumed, the second phase would have peaked about 1.5 Gy ago, but if the more realistic cratering flux of Neukum and Wise (1976) is assumed, it would have peaked earlier than 3.5 Gy ago. It is hypothesized here that the second phase was related to a maximum in heat transport from the Martian interior.

Models have been calculated in which the duration of core formation varies from 50 My to 3 Gy and in which the rate of release of core energy either is constant or growing exponentially with time. Subsequent thermal history is insensitive to the mode of core formation. Models which become fully convective yield a present heat flux of about 30 mW/m^2 , about 50% greater than present heat production and in reasonable agreement with the value of 35 mW/m^2 obtained by Toksöz and Hsui (1978) from a full finite-amplitude convection calculation.

The time of peak heat flow depends mainly on the initial temperature. Models with peak heat flow within the last 2 Gy require initial mean temperatures between 50% and 20% of the present value. Solomon (1979)

achieved this result with a somewhat higher initial mean temperature, but his model did not include convective heat transport. Such late-peaking models are not favored since they would require a nearly constant cratering flux (Arvidson et al., 1979). Arvidson et al. (1979) also note that many extensional tectonic features may be related to the Tharsis uplift, and that many compressional tectonic features have been identified in Viking pictures, implying the possibility of significant cooling and contraction of Mars.

Models in which peak heat flows were reached earlier than 3.5 Gy ago require initial mean temperatures of at least 80% of the present value. The precise timing of the peak in these models is controlled by the time of core formation. A consistent feature of these models is that peak heat fluxes are greater than 80 mW/m^2 . These are comparable to modern heat fluxes in earth's ocean basins (which average 100 mW/m^2), and raise the question of why, or whether, plate tectonics did not operate on Mars.

REFERENCES

- Arvidson, R. E., Goettel, K. A., and Hohenberg, C. M., submitted for publication (1979).
- Neukum, G., and Wise, D., Science, 194, 1381-1387 (1976).
- Solomon, S. C., Phys. Earth Planet. Interiors, 19, 168-182 (1979).
- Toksöz, M. N., and Hsui, A. T., Icarus, 34, 537-547 (1978).

AN ANALYSIS OF MARTIAN GRAVITY OVER THREE SHIELD VOLCANOES

Smith, John Carl, Phillips, Roger J., and Ritke, Steven, Jet Propulsion Laboratory, Pasadena, California 91103

Using Viking Orbiter II data an analysis has been made of the gravity anomalies over Arsia Mons, Pavonis Mons and Ascraeus Mons. A disk of fixed size was placed at the location of each volcano and the disk's mass was fit to the data of orbits 600, 638, 676 and 677. For each volcano the solved for mass was roughly 7% of the mass estimated strictly from topographic data. This result is thus indicative of substantial amounts of compensation occurring under each volcano. This is in distinct opposition to the results from Olympus Mons, which indicate that the volcano is relatively poorly compensated.

Given the linear alignment of these volcanoes one might expect some deep-seated structure connecting the three; however, the data is fit quite well by three distinct disks with no connecting density anomaly and thus it seems somewhat unlikely that any connecting density structure exists between the volcanoes.

Several modes of compensation exist, and the data at present is probably unable to distinguish between the different processes involved. However, if one assumes that the compensation is a result entirely of lithospheric flexure then it is possible from these answers to get a rough estimate of the lithospheric thickness. Results of such calculations and their uncertainty due to uncertainties in the topography will be presented.

PLANETARY FRACTURE PATTERNS; INFLUENCE OF INHERITANCE ON STRESS ANALYSIS

McGill, George E., Dept. of Geology/Geography, University of
Massachusetts, Amherst, MA 01003

To determine stress orientations from fracture patterns, it is first necessary to demonstrate that the fracture sets used are about the same age before it is reasonable to infer that they result from a single system of principal stresses (Donath, 1962). One major source of age uncertainty is the very real possibility that some (or perhaps all) of the fracture orientations present in near-surface rocks are in fact inherited from older, underlying rocks. Hodgson (1961), in a brief reconnaissance study of fracture patterns at various stratigraphic levels in the Grand Canyon, reported evidence suggesting significant correlation between basement fracture trends and fracture trends in overlying Paleozoic sedimentary rocks. The problem that this creates for fracture analysts was succinctly stated by Hodgson (1961, p. 97): "If the fracture pattern seen today in the sedimentary rocks is 'Precambrian', the direction or disposition of the forces producing this pattern must be referred to the Precambrian also and an attempt to establish a direct genetic relation between the major elements of the joint pattern and post-Vishnu folding or faulting would be questionable."

In dealing with the question of inheritance, we must distinguish between large-scale, individual planar structures such as major faults, and smaller, outcrop-scale fractures (joints and small faults) that we may think of as "penetrative" on a macro scale. There is abundant evidence that large, individual basement structures may be reactivated even if principal stress orientations have changed. Some of the better examples of such fault reactivation come from the Grand Canyon itself (Huntoon, 1976). But is it possible for outcrop-scale joint patterns to be inherited, and then for this inherited anisotropy to influence major fracture patterns developed by younger stress systems? Hodgson believed that his evidence from the Grand Canyon supported inheritance of joint orientations, but most of his stations are located along the Kaibab trail, and thus many of them are very close to one or more faults (Fig. 1), some of which exhibit clear evidence for post-Paleozoic reactivation. My intent is to carry out a much more systematic comparison of Precambrian and Paleozoic fractures involving: 1) comparison of fracture patterns in basement and immediately overlying Tapeats Sandstone (Cambrian) at stations as close together as possible and also as far from faults as possible; 2) determination of the inherent variability of the Precambrian and Paleozoic fracture patterns by collecting data from more than one place in the Canyon; and 3) investigation of the exposed contact between Tapeats and basement in search of direct evidence for or against upward propagation of individual joints.

Sufficient progress has been made on phase 1) to present some tentative ideas; much more work is needed before the other phases can be discussed. Two students at Northern Arizona University, Martha Hall and Susan Beard,

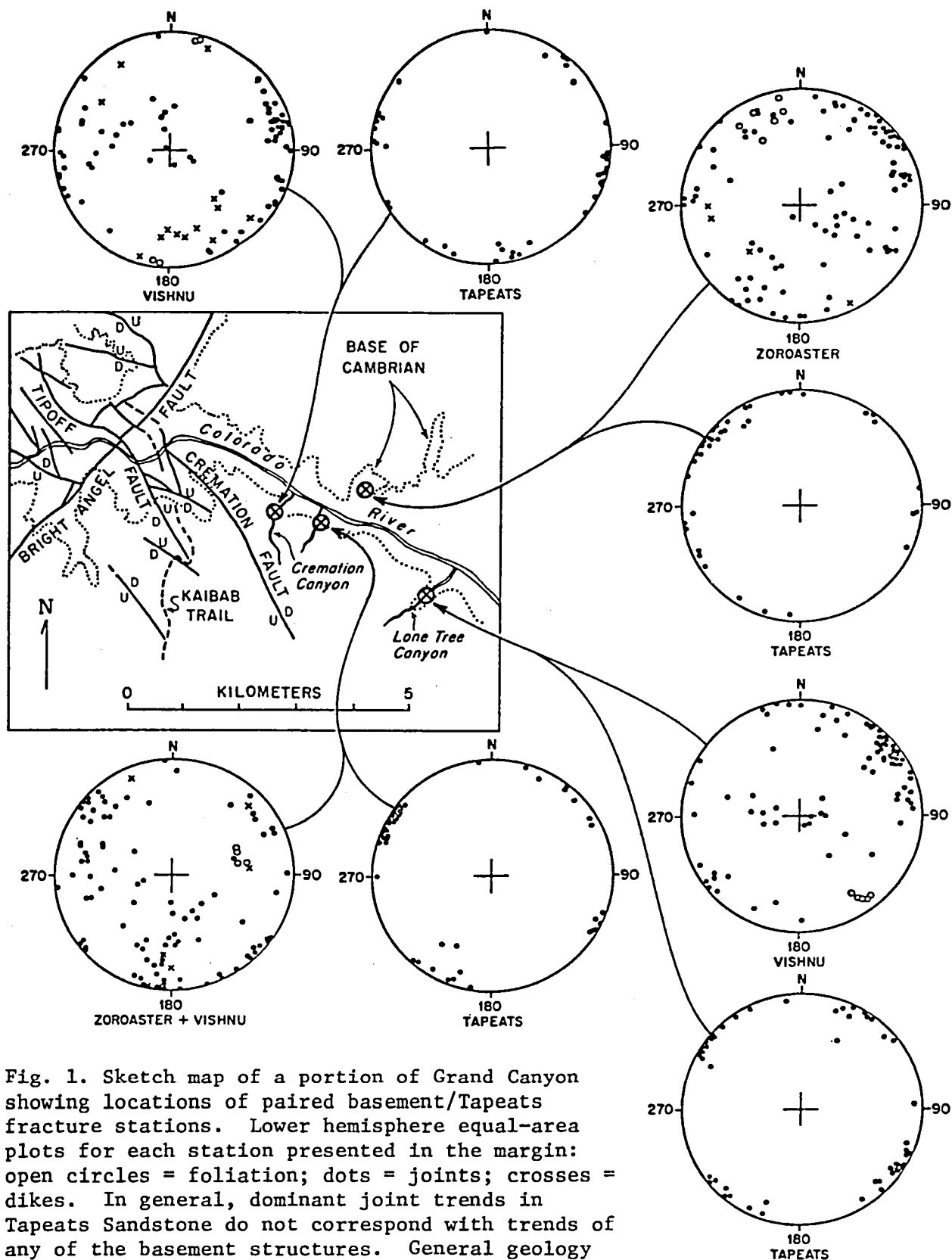


Fig. 1. Sketch map of a portion of Grand Canyon showing locations of paired basement/Tapeats fracture stations. Lower hemisphere equal-area plots for each station presented in the margin: open circles = foliation; dots = joints; crosses = dikes. In general, dominant joint trends in Tapeats Sandstone do not correspond with trends of any of the basement structures. General geology from Geologic Map of the Grand Canyon National Park.

devised an almost identical project completely independently. This report involves only my own data; final analysis and publication will involve all three of us using merged data.

Figures 1-3 summarize findings from a 3 km stretch of Canyon upstream from the Kaibab trail where several small tributary canyons cut the Tonto Platform, exposing Vishnu Formation or Zoroaster Granite on their floors and Tapeats Sandstone on their walls. These small canyons are ideal places for comparison studies because they are distant from faults, basement and Tapeats exposures are close together, and access is easy.

As figure 1 demonstrates, there is little correspondence between azimuths of dominant joint sets recorded for Tapeats stations and the azimuths of joints, foliation, or dikes in the associated basement stations. A comparison of lumped data is presented in contour form in figure 2. Figure 3 is a comparison of azimuths of only the steeply dipping joints plotted as simple histograms. My preliminary conclusion is that significant inheritance of the Paleozoic joint pattern from underlying basement cannot be supported with these data.

Donath, F.A., 1962, Geol. Soc. America Bull., 73, 1-16.
 Grand Canyon Natural History Association, 1976, Geologic map of the Grand Canyon National Park, Arizona.
 Hodgson, R.A., 1961, Amer. Ass. Petrol. Geol. Bull., 45, 95-97.
 Huntoon, P.W., 1976, in Breed, W.J. and Roat, E., ed., Geology of the Grand Canyon, Flagstaff, Museum of Northern Arizona, p. 82-115.

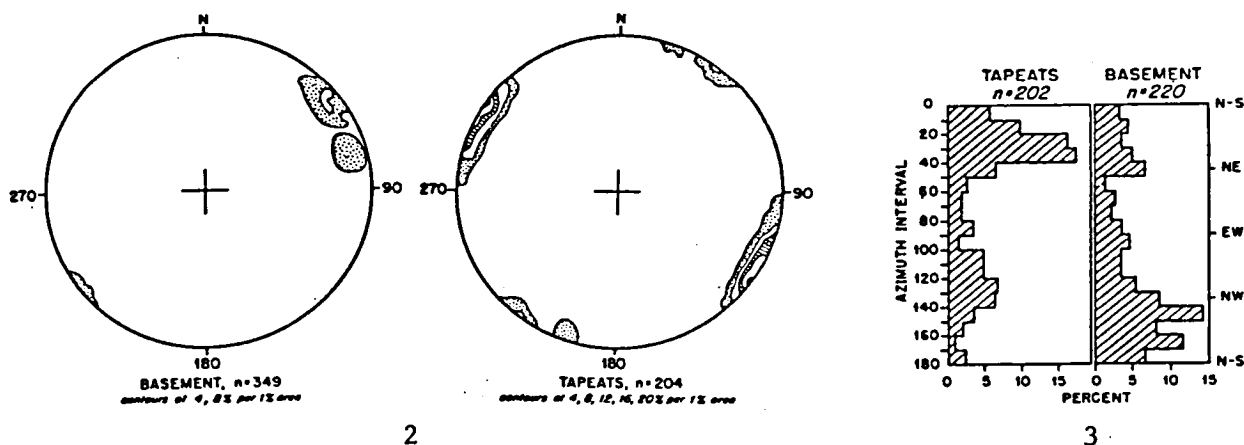


Fig. 2. Lower hemisphere equal-area contour plots (% of poles per 1% area of net) of all joints from the four localities (Fig. 1).

Fig. 3. Histograms of % of all steeply dipping joints (dip $\geq 70^\circ$) vs. azimuth for basement and Tapeats stations (Fig. 1).

ORIGINS OF REGIONAL SCALE LINEAMENT SWARMS AS SUGGESTED BY FRACTURE DOMAIN ANALYSIS OF ITALY

(1) (2) (2) (2)
D.U. Wise, R. Funicello, M. Parotto and F. Salvini, (1) Dept. of Geology/
Geography, Univ. of Mass., Amherst, MA 01003; Institute di Geologic,
Univ. of Rome, Italy.

With the advent of satellite imagery of other planets and satellites as well as the Earth, it has become generally acknowledged that linear patterns related in some way to fracturing are ubiquitous features of almost all planetary crusts. On Earth many individual lineaments have been related to specific faults and fracture zones. Some martian and lunar lineaments are obvious horst and grabens but both bodies have other "grid" systems of more complex nature. Indeed, the nature, origin and tectonic settings of most swarms of lineaments characteristic of planetary and large terrestrial surfaces continue to elude us. The origins and meanings of these lineament arrays remain among the most poorly understood structural aspects of planetary crusts.

Lineament detection is not among the more precisely controlled of geologic observations. The variety of observations and interpretations is so great that it is sometimes considered an artform termed "Linesmanship" (Wise 1976). Reasons for difficulties in working with lineament arrays are numerous but include enhancement or suppression in various lighting conditions, observer reproducibility and illusion, albedo effects, scale effects for differing lengths of lineament classes, and difficulties with the "ground truth" about the lineaments. To avoid some of these difficulties, the present study was restricted to topographic lineaments visible on raised relief maps of Italy illuminated from various azimuths.

The reproducibility question is examined in Fig. 1 for the Island of Sicily. Three different observers analyzed the same relief map images shadowed from four different directions. The results were digitized and converted to azimuth-frequency histograms. The peaks of these were automatically fitted with gaussians, the azimuths and strengths of which are indicated on Fig. 1, as 1, 2, 3. Four published sets of Sicily lineament data by other authors based on photo and satellite imagery were treated in the same way as shown on Fig. 1, (4,5,6,7). We conclude that for Sicily, the orientations of lineament swarms derived by relief map methods, at the very least, are as reliable and reproducible as the results from lineament studies based on more traditional imagery.

In all a total of 7063 topographic lineaments were drawn for all Italy using shadowing techniques on raised relief maps. The Italian relief map lineament data for 100 km diameter circular areas were computer digested with automatic gaussian fitting techniques to produce 88 overlapping computer-smoothed windrose plots covering all Italy. Orientation peaks, correlatable from windrose to windrose, were used to map 41 separate lineament domains. Clues to the age and origin of the lineament sets were sought by

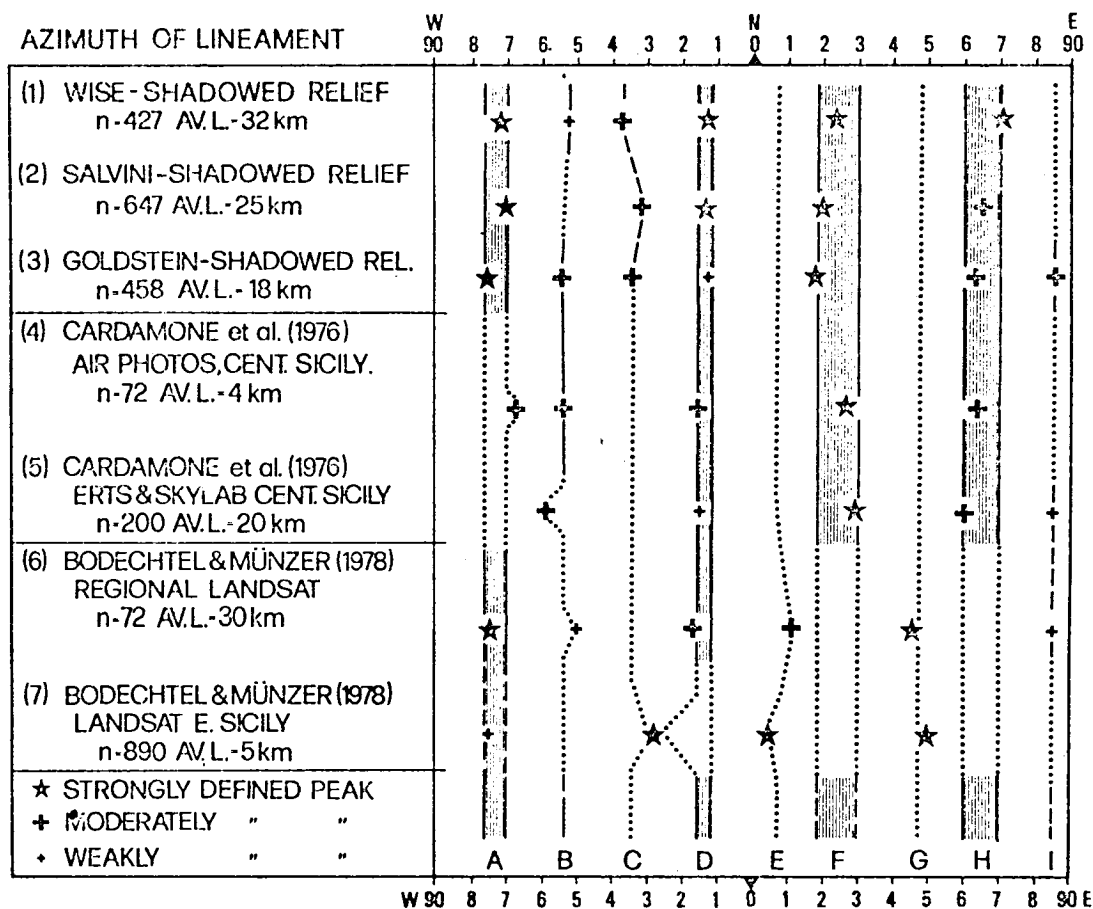


Fig. 1 Reproducibility test of lineament swarm orientations drawn for Sicily by various observers and methods.

of these domain boundaries and orientations with domains and orientations of better known tectonic elements from a new brittle tectonic map of Italy prepared especially for this study. Many of the domain boundaries are traceable into adjacent seas as similarly oriented fault domains mappable by marine geophysics. Among the most common relationships are lineament domains corresponding in strike and areal distribution to broad arches, basins, or regional flexures. Other domains correlate with regional fault systems, most commonly of normal displacement. One lineament domain, interpreted as being presently active, corresponds closely in orientation with recent fault scarps and in distribution with present seismic energy release patterns of the Appennines. A lineament swarm model (Fig. 2) is proposed for the origin of these features, in which long, deep fracture swarms open by very small amounts perpendicular to sigma 3 (least compression axis). Only locally is the extension great enough to produce

normal faulting. Dilatency in the zone permits enhanced joint development in the near-surface rocks with tectonic heredity influencing the production of a variety of local joint orientations in the zone. Joint sets parallel or normal to the zone need not even appear. Consequent localization of erosional processes along these zones of better joint development explains the unusual prominence of such subtle structural features in the regional topographic grain. The extent to which these observations and mechanisms apply to other regions and other planets is debatable but for this volcanic and tectonically youthful land a lineament swarm origin by extension seems indicated.

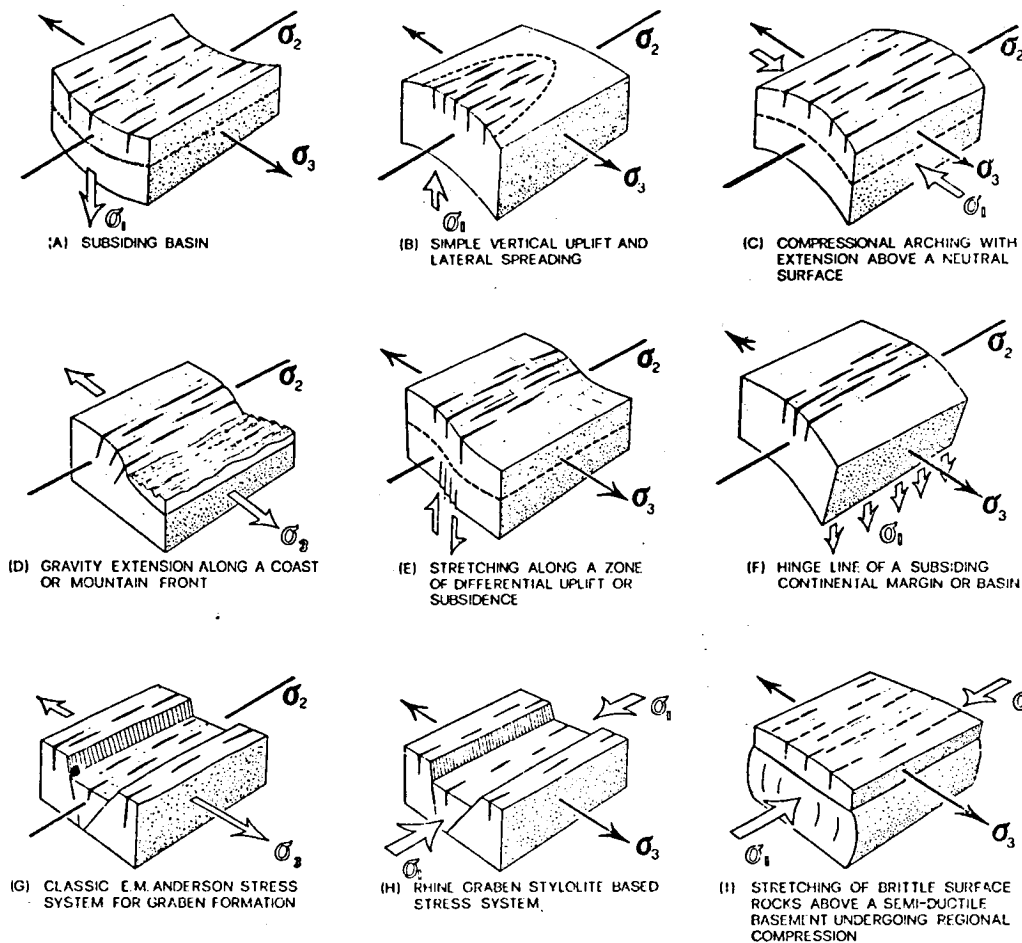


Fig. 2. Possible tectonic settings for Italian lineament swarm development. Note σ_3 normal to lineament.

References: Bodechtel, J. and U. Munzer, 1978, Satellite lineaments of the central Mediterranean Region, p. 339-340 in Alps, Apennines, Hellenides, Interunion Comm. on Geodyn. Sci Rept. 38. Cardamone, et al, 1976, Study of regional linears of central Sicily by satellite imagery, Tectonophysics 33, 81-96. Wise, D.U., 1976, Linesmanship: guidelines to a thriving geologic artform, p. 635-636, Utah Geol. Assoc. Publ. No. 5.

RESEARCH ACTIVITY OF THE PLANETOLOGY BRANCH OF THE
LABORATORIO ASTROFISICA SPAZIALE - 1979 -

P.Bianchi, A.Carusi, A.Coradini, M.Coradini, C.Federico, E.Flamini,
M.Fulchignoni, G.Magni, M.Poscolieri, G.Valsecchi.

ORIGIN OF THE SOLAR SYSTEM

The study of the accumulation processes of the primordial solar Nebula has been developed taking also into account the role of melted grains.

The results obtained have been published in "The Moon and the Planets".

Furthermore, the hydrodynamics of grains in the Solar Nebula has been investigated. In fact, during the collapse it can be assumed that the solid components of the nebula (grains) and the gaseous ones are well mixed because of the turbulence. When the turbulence decays, at the end of the collapse, a dynamical separation of the two fluids can appear.

Preliminary results about these topics have been published in the Expanded Abstracts of the 9th. Lunar and Planetary Science Conference (Houston, Tx, March 1978).

The general results can be summarized as follows:

Formation of planetesimals from the dusty component of the protosolar nebula has been widely accepted. The most probable driving mechanism can be found in the gravitational instabilities. They cannot occur in the gaseous component of a small mass nebula, because the densities required are very high and temperatures of the nebula, formation of a thin dusty disk and fragmentation of such disk because of gravitational instabilities have been investigated. On the other hand, a high mass protosolar nebula can be gravitationally unstable regardless of grains sedimentation, at least in the external regions, but the problem of blowing off the excess off mass (T-Tauri wind) remains. The sedimentation of grains through the gas has been studied in some details. During sedimentation, instability of the gas-dust configuration against axisymmetric perturbations has been checked.

We have assumed that grains, strongly affected by gas, settle through a quiescent medium, i.e. the gas is nearly in hydrostatic equilibrium. Moreover, falling down of grains to the midplane does not appreciably modify the vertical structure of the gas. The presence of turbulence in the gas strongly influences the general

behaviour of the sedimentation, but a sufficiently energetic source to sustain turbulence has not been clearly understood yet. The gravitational instability mechanism is very efficient to stop the grain motion, i.e. the characteristic viscous slowing down time is much less than mean grain-grain collision time. The system can be considered as a heavy gas with mass equal to the sum of the gas and dust masses and with thermodynamical properties due to the gas only. The dispersion relationship is corrected taking into account the flatness of the disk. Unstable wavelengths are selected by the condition of being less than the characteristic scale length of the physical parameters involved. The evolution of density distribution of grains and the onset of gravitational instabilities has been studied for three models of nebula, from low ($.01 M_{\odot}$) to high ($2 M_{\odot}$) disk masses. It comes out that a grain/gas fluid makes it possible to obtain planetesimals via gravitational instabilities, with masses larger than those obtained in previous works. Moreover, in low mass nebula models high values of sedimentation are required, which are inhibited by the presence of turbulence, at least in the inner regions of the nebula. In the external regions, quiescence of gas is a less strong constraint and dusty planetesimals can form. In the high mass model, appearance of primordial giant protoplanets at several A.U. cannot be avoided, and this presumably influences the formation of the inner planetesimals.

DYNAMICS OF THE SOLAR SYSTEM.

Studies concerning the evolutions of orbits of minor bodies of the solar System during a close encounter with Jupiter have been carried out. The general research, concerning 3000 close encounters of minor bodies belonging to 3 different populations (an asteroidal one, a cometary one and an intermediate one), has been carried out and the conclusions have been published in international journals; in addition, the study of the satellite-capture phenomena during planetary close encounters has been started.

The first conclusion of this work have been presented at the IAU Symposium n.81, held in Tokio. The results of a research concerning the effect of a close encounters with Jupiter on a population of planet-crossers of the inner planets have been presented at the annual meeting of NASA Planetary Principal Investigator held in Tucson.

Two more lines of research have been carried on: the first is concerned with the effects of the presence of the Galilean satellites of Jupiter during a deep close encounter

between that planet and a minor body; the second is concerned with the general problem of the evolution of orbits of minor bodies, due to planetary perturbations and to planetary close encounters in various regions of the Solar System. Finally it has been shown that close encounters between Jupiter and minor bodies are generally more efficient if the initial orbit of the small body is nearly tangent to that of the planet. An analysis of available data allows us to identify the class of nearly orbits for which the effects are significant.

PLANETARY SURFACES

Researches on planetary surface features have been carried out, both theoretically and experimentally utilizing Mariner 10 and Viking imagery.

Crater distributions of the Mercury surface have been compiled; main goals of this work were: 1) determination of a statistical index to discriminate secondaries in crater fields; 2) the analysis of the behaviour of cumulative and relative distributions of large craters in different areas; 3) the comparison between distributions of peculiar crater (peak craters, lava filled craters, terraced craters, etc.) in different areas.

The definition of the entropy of a cratered surface is given in analogy with the entropy of the information theory. The saturation, defined as the ratio between the area covered by craters of diameters D and the total observed area, is adopted as a measure of the probability find a portion of a planetary surface covered by craters of a given diameter.

The meaning of such new function is discussed in comparison with statistical approaches to the study of the cratering.

Applications to Mercury are discussed.

The role of the permafrost in the martian soil has been studied from a thermodynamical point of view.

An outstanding result of the Viking mission has been the detection, both photographic and instrumental of water vapor in the martian environment. The only possible "tank" for the water, where no evidence of surface frost has been detected, is the soil which could contain unexpected amounts of water.

On the Earth, the mixture of water ice and soil, called permafrost, is continuously present in the northern hemisphere in a latitude belt of about 40° around the pole.

A comparative morphology analysis of periglacial terrestrial and martian terrain suggest the permafrost can play an important role in forming many surficial structure in the volcanic region of Tharsis.

A study of the thermodynamics which regulate the processes of thawing and freezing of the layer of permafrost on Mars has been carried out.

The equation of the heat propagation has been solved, under martian conditions, both in the case of periodic (daily, seasonal and longer) variations of the surface temperature, and in the case of an anomalous heating of the ground. Such an extra heating could be caused by the presence of a lava flow or by energy released during a meteoritical impact.

Distributions of the temperature and a function of the depth and time have been computed.

Possibility of formation of water lenses at some depth in the martian underground has been also checked in order to get a reservoir of liquid water, to be considered as responsible for some collapse features visible on the Viking Orbiters photographs.

On the basis of Mariner 9 data the hypsometric curve of Mars has been computed and drawn.

For the construction of the hypsometric curve of Mars the topographic map of Mars produced by the U.S.G.S. Astrogeology Center, Flagstaff (Az) has been utilized. All the areas delimited by isolines and geographical grid have been measured, then summing all the contributions given by the areas included between the same isolines. Such measurements have been effectuated by the means of a solid-state optic image analyzer.

A comparative study of the hypsometric curve of the Earth and the Moon shows that on Mars several processes of vertical differentiation of the crust started but did not develop completely owing to the exhaustion of the endogenic processes which determine the surficial dynamics of a planet.

A model for the evolution of the Martian crust is discussed to justify the shape of the hypsometric curve.

Finally, the formation of the sodium cloud and the regolith on Io during micrometeorite impacts has been studied.

Almost full penetration of the second mode of the micrometeorites distribution in the interplanetary space ($M > 10^{-8}$ gr) across the Io atmosphere has been found out numerically. The impact velocities turned out to be close to the

initial ones, and are sufficient for the generation of the contrary intensive ion-atom fluxes from the Io topsoil. If the satellite surface contains at least 1% of sodium, the flux of Na ions and excited sodium atoms should be conform with Na (D) - line emission from Io. Even if the extension of the topsoil unflooded by lava is not large, owing to its high specific surface ($\text{m}^2 \text{gr}^{-1}$), the interaction between the topsoil itself and the atmosphere can be considered having the same importance of interaction between terrains, covered by lava, and the atmosphere.

A statistical approach to the study of lunar sample chemical analyses data have been continued developing the G-mode analysis and applying that method both to Moon rocks and glassy particles analyses.

Such new technique allows to cluster samples without a detailed knowledge of the instrumental errors. This new method is called "central" one. Moreover a statistical method to classify new samples when a general classification has already been obtained was studied and a computer algorithm was performed.

A particular interest has been also devoted to educational activities during 1978. All the members of the "Reparto di Planetologia" are coauthors of a book entitled "La Planetologia", edited by Newton Compton (Roma) - in late 1978. In the book the main results and the discoveries in the exploration of the planets, since the last 10 years, by sovietic and american space missions, are summarized in a easy-reading but scientifically precise way.

By the same token a divulgative laboratory experience on cratering has been carried out to show students the morphology and the physical aspects of the formation of a craters. Such experimental work has been furtherly developed, in strict cooperation with highschool students trying to obtain a set of laboratory experiments capable of clearing up some of the main problems of the formation and evolution of the Solar System.

Chapter 3

CRATERING AS A PROCESS, LANDFORM, AND DATING METHOD

A GLOBAL STUDY OF PRIMARY CRATER EJECTA MORPHOLOGY ON MARS: A PROGRESS REPORT

Blasius, K.R., Cutts, J.A., and Roberts, W.J., Planetary Science
Institute, 283 So. Lake Ave., Suite 218, Pasadena, Calif. 91101

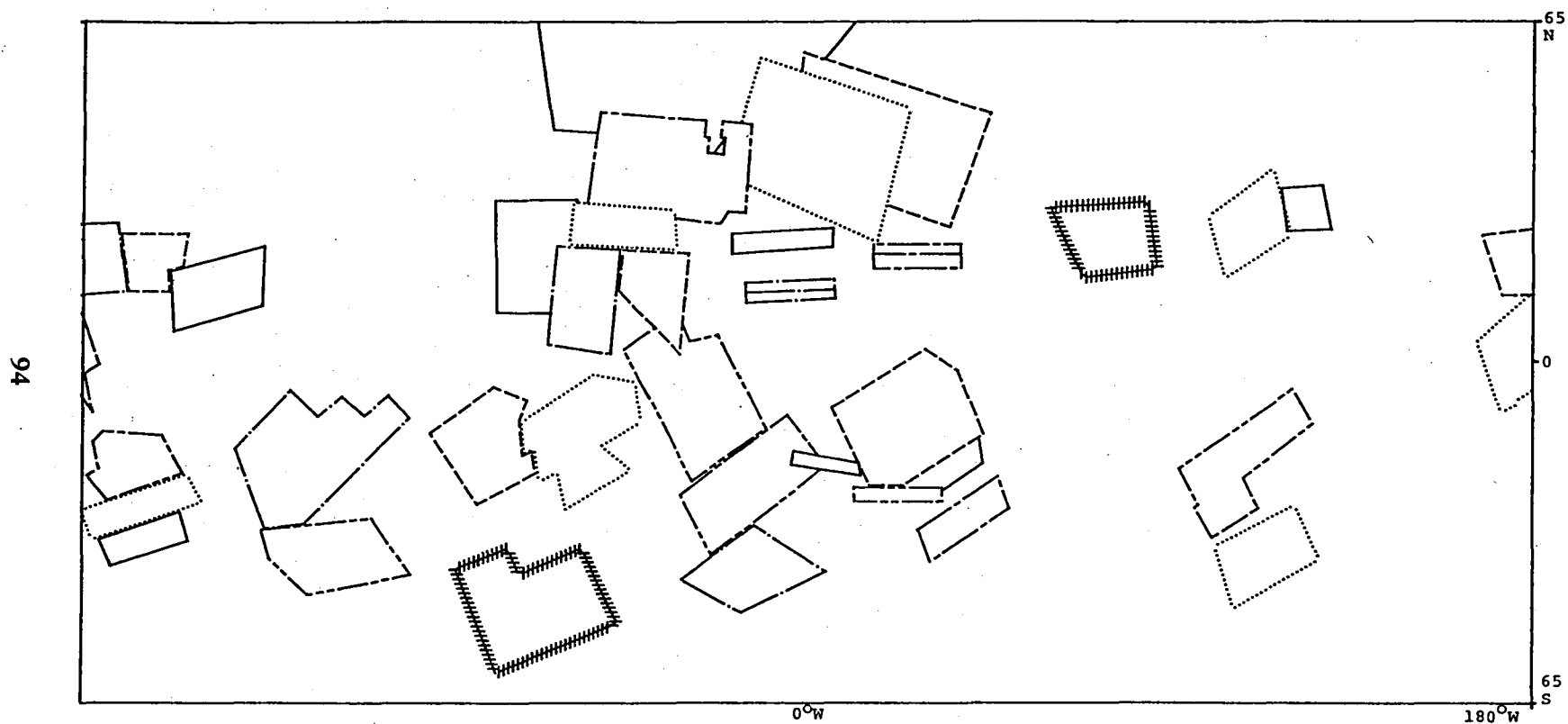
The varied crater ejecta flow features which are unique to Mars (Carr et al., J.G.R. 82: 4055-65) attest to the occurrence of processes on that planet which do not occur on the moon and Mercury. Several studies of the distribution of ejecta morphologies over different latitudes, altitudes, and geologic units claim discovery of significant (but apparently contradictory) relationships (Allen, Icarus, 1979, 39: 111-123; Mouginis-Mark, NASA TM80339, 1979, 144-146, 147-149; Johansen, Proc. 2nd Colloq. on Planetary Water and Polar Process., 1978, pp. 109-110).

The goal of this investigation is to establish the observational evidence for varied crater ejecta morphologies in a way which will better support discrimination between proposed mechanisms of formation. We are gathering new morphometric data on crater ejecta deposits and have tried to define a new system of qualitative classification which imposes fewer constraints than previous studies on trends and associations which might emerge from data (Cutts, J.A. et al., NASA TM 80339, 1979, 111-113). We are also using the geographically most complete and uniform data set for Mars, the Viking orbiter medium resolution mapping coverage.

The collection of data involves three steps: 1) Acquire and record on magnetic tape geometrical control point data and other fundamental data relevant to a single mosaic strip, note control point locations on plastic overlays, 2) on the same plastic overlays identify and record characteristics of craters with extensive visible ejecta deposits, 3) record on magnetic tape, through the use of a NUMONICS digitizer, the positions of geometric control points, positions and sizes of craters and their ejecta characteristics.

Figure 1 is a map of areas (except for polar regions) for which we have now gathered data through step 3.

Figure 1.



IMPACT CRATERING IN VISCOUS TARGETS

Greeley, Ronald, Department of Geology, Arizona State University, Tempe, AZ; Donald E. Gault, Murphys Center for Planetology, Murphys, CA; David B. Snyder, Department of Geology, Arizona State University, Tempe, AZ; Virginia Sisson, Department of Geology, Princeton University, Princeton, NJ; Peter H. Schultz, Lunar Science Institute, Houston, TX; and John E. Guest, University of London Observatory, London.

Martian multilobed craters - alias ejecta flow craters, "splosh" craters, and rampart craters - have been suggested to involve fluidization of ejecta as a result of entrained water, melted and/or vaporized ice, or aerodynamically decelerated ejecta. Some outer planet satellites appear to be composed partly of ice and ice-silicate mixtures; impact craters formed in these materials may have markedly different morphologies from impact craters on rocky surfaces. To determine the effects that target viscosity and yield strength may have on the formation and morphology of craters, a series of 61 experiments was carried out at the NASA-Ames Vertical Gun Facility in which target viscosities and impact energies were varied: 42 shots involved mixtures of potters clay and silica oil; 19 shots involved clay and water. Viscosities ranged from 72 to 2750 poise, and yield strengths ranged from 1.3 to 3.40 Nt/m². Preliminary assessments of the results show that: 1) The viscosity of the target material governed the preservation of ejecta deposits and crater form. Although in very fluid materials the crater was not preserved as a distinct topographic feature, the outline of the transient crater was visible. With increasing viscosity, topographic relief also increased. Thus, the depth-to-diameter ratio of some craters may be as much a function of target properties as of age. 2) Lobes of ejecta were emplaced by the collapse of a central peak, as observed in high speed motion pictures; as it collapsed, it sent a surge of ejecta over the rim. In higher energy impacts and/or less viscous targets, the central peak oscillated, with each oscillation sending a progressively smaller surge of ejecta over the rim developing multiple flow lobes. 3) In some experiments, the oscillating central peak "froze" in a negative position, resulting in a central depression. 4) Immediately after some shots, the target material in and near the impact zone actively degassed; evidently the impact released volatiles from the clay-water and clay-oil mixtures. The effect was two-fold: in 74% of the impacts there was a marked decrease in target viscosity (measured *in situ* before and after impact); and the post-impact fluidized material smoothed out irregularities in the floor of some of the craters, giving a "flooded" appearance. 5) Multilayer targets influence the ejecta morphology: a thin, "dry" layer (i.e. "regolith" or an icy crust) on top of the viscous mixture retarded the emplacement of ejecta, whereas a thin fluid (water) layer on top of the mixture lubricated the ejecta and enhanced flow. Although these observations are qualitative and exploratory, the implications for Mars and the icy satellites warrant additional study in which extrapolations to full-scale martian craters will be attempted through dimensionless parameters.

EMPLACEMENT OF MARTIAN RAMPART AND PEDESTAL EJECTA BLANKETS

Mutch, P. & Woronow, A., Lunar & Planetary Lab, U. of Az., Tucson, AZ 85721

The distinctive splash-like ejecta-blanket morphology of Martian rampart craters probably indicates that their emplacement was in a fluidized state due to entrained gases (1). The origin of Pedestal craters is more ambiguous. Although they have been attributed to erosion (2,3), they may be basically primary structures with only moderate erosion.

Figures 1 through 3 are log-log plots of ejecta blanket area vs crater area (A_c - A_e plots) for MC-18. The simple linear regression lines fitted to all of the data in Figures 1, 2, and 3 have slopes of $1.27 \pm .03$, $1.38 \pm .04$, and $1.06 \pm .07$ respectively. The data in Figure 1 appear to exhibit two intersecting linear trends, a line with slope of about 1.5 for craters with areas greater than 30 km^2 and a line with slope of about 1.0 for craters with areas less than 30 km^2 . Regression lines for each of these segments actually have slopes of $1.46 \pm .04$ and $0.9 \pm .1$ respectively. More importantly, the large Lobate and Multilobate craters ($A_c > 30 \text{ km}^2$) follow a slope of $1.50 \pm .05$ while all Pedestal craters follow a slope of $1.06 \pm .07$.

These data were compared with six models, each having a different set of physical constraints. Models constraining maximum ejecta thickness to a single value independent of crater size predict the results found for the larger rampart craters. Ballistic emplacement, without subsequent flow, and constant surface-slope models do not satisfy these data, but do predict the results found for the smaller rampart craters and all of the Pedestal craters.

Therefore, we interpret the data in Figures 1 through 3 to indicate that the dominant physical process which yields the observed ejecta-blanket morphologies of rampart craters is different for craters larger and smaller than approximately 6 km diameter ($A_c = 30 \text{ km}^2$). The ejecta of Pedestal craters is physically different, during emplacement, from that of rampart craters. The ejecta of the larger Rampart craters was probably considerably fluidized during its emplacement. However, the ejecta must resist being piled beyond some maximum height at which the column weight is sufficient to initiate penecontemporaneous internal deformation and flow resulting in the extensive sets of lobes.

The slope of $0.9 \pm .4$ appropriate to rampart craters of less than approximately 6 km diameter mimics ballistic and angle-of-repose emplacement models, even though the ejecta blankets do not appear to be normal ballistically-emplaced blankets, but instead have lobes. These ejecta blankets were probably very fluid, but never exceeded the critical column height necessary to produce significant internal failure and flow. Their surfaces may be near the maximum slope which a material of their viscosity could sustain.

Pedestal craters also follow the "ballistic" models. This suggests that Pedestal ejecta blankets are also primary structures that fall naturally into the sequence Multilobate-Lobate-Pedestal. The lack of lobate flow in the Pedestal class could reflect the fact that the major source of volatiles is at some substantial depth below the surface. Pedestal craters, being predominantly small in size, did not excavate to that depth; therefore, their ejecta was substantially more viscous and could not flow into lobes. The source of volatiles apparently varies in depth between approximately 0.8 and 1.6 km.

The larger Lobate-ejecta and Multilobate-ejecta craters in MC-18 satisfy physical models for ejecta emplacement which constrain the maximum ejecta thickness, implying that substantial volumes of material have participated in viscous flow, probably initiated by internal failure under loading by the ejecta itself. The rampart craters smaller than about 6 km diameter do not follow the same scheme. While their morphologies indicate a dominance of nonballistic emplacement, extensive late-stage flow has probably not occurred because critical column heights were not reached. Pedestal-ejecta blankets are probably primary structures as well. The ejecta was relatively volatiles poor, compared to that for rampart craters, but still contains sufficient volatiles to allow local flows to level the surface and cover up any ballistic morphologies on the deposits.

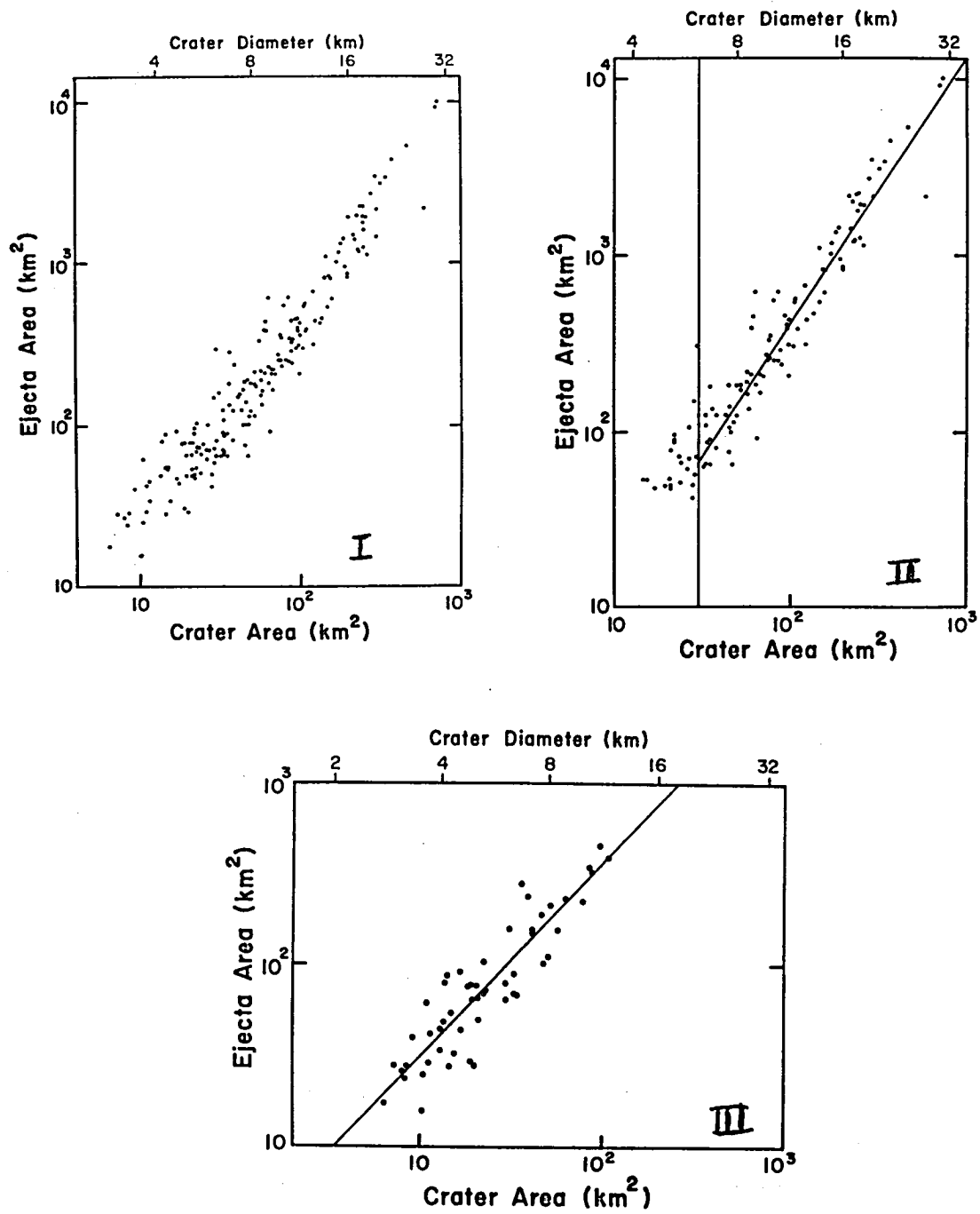
REFERENCES: (1) Carr et al., JGR, 82, 4055, 1977. (2) McCauley, JGR, 78, 4123, 1973. (3) Arvidson et al., Icarus, 27, 503, 1976.

Figure 1: Ac-Ae plot for all measured craters: Lobate, Multilobate, and Pedestal classes.

Figure 2: Ac-Ae plot for all measured Lobate and Multilobate craters. The plotted regression line of slope $1.50 \pm .05$ is fitted to only those craters with Ae > 30 km².

Figure 3: Ac-Ae plot for all measured Pedestal class

craters. The plotted regression line has a slope of $1.06 \pm .07$.



EJECTA EMPLACEMENT FOR MARTIAN FLUIDIZED EJECTA CRATERS

Mouginis-Mark, P.J., Dept. of Geological Sciences, Brown Univ., Providence, RI 02912

The unique "fluidized" character of morphologically fresh ejecta blankets associated with martian impact craters has been attributed to the influence of subsurface ice or water within the target at the time of the cratering event.¹⁻⁴ While several attempts are being made to investigate the spatial distribution of related crater morphologies,³⁻⁵ the emplacement sequence and mode of deposition for the ejecta materials remains poorly understood. Consequently, attempts are currently underway to compare the morphological characteristics of craters in the size range 2-50 km diameter that possess single (Type 1) and double (Type 2) continuous ejecta deposits.^{4,6,7,8}

Both Type 1 and Type 2 craters possess an areally extensive ejecta deposit that is characterized by distal ridges and has a surface morphology indicative of ground-flow during the late-stages of emplacement.^{1,9,10} A reanalysis of data pertaining to the maximum ejecta range (normalized to the parent crater radius)^{4,7} reveals that despite close morphological similarities, the ejecta surrounding Type 2 craters consistently travelled further from the parent crater center than the ejecta of Type 1 craters. Cumulative percentage frequency plots of the maximum ejecta range for both types of crater are presented in Fig. 1A for three physiographic provinces identified by Scott and Carr¹¹ (hilly and cratered, and cratered plateau materials are here combined in the unit "ancient terrain"). Implicitly, it is assumed that if the outer unit of Type 2 craters was emplaced by the same mechanism as the Type 1 deposit, the cumulative curves should be similar: clearly this is not true.

A Kolmogorov-Smirnov two-sample statistical test indicates that the probability of the cumulative curves for each target material being representative of the same population can be rejected at the 99.9% confidence level. However, if the range of Type 1 craters is increased by 0.8 radii (Fig. 1B) (i.e., hypothesizing that some factor makes Type 2 deposits more mobile, despite a common mode of origin) the test is unable to distinguish between the samples at the 75% confidence level.

Analysis of high resolution Viking images of the 25 km crater Arandas (43°N, 14°W) leads to an hypothesis for the different ejecta travel distances of Type 1 and Type 2 ejecta. Fig. 2 illustrates (between pts. "A") a series of massive ridges¹ that have formed on the inner ejecta deposit "upstream" of a pre-existing crater (B). Detailed examination of this image reveals a series of longitudinal grooves radiating from Arandas that are superimposed upon the surface of these ridges. Previous interpretations compared these ridges to surface patterns observed

MARTIAN FLUIDIZED EJECTA CRATERS

Mouginis-Mark, P.J.

on the Sherman Glacier Landslide:^{1,10,12} it was inferred that they were produced during the emplacement of the inner ejecta unit and were formed by shearing taking place between substreams of the ejecta flow. The linear nature of the Arandas grooves indicates that they cross the ridges unaltered, however, and hence were not formed contemporaneously with the ridges during the time of abutment of the inner ejecta unit against crater "B." This inner ejecta unit is interpreted to be a remnant of the overturned crater rim flap,^{8,10} and it is concluded here that this rim material was emplaced prior to the more extensive outer unit of Type 2 craters, which overrode the inner unit during terminal collapse of the ejecta cloud, scouring the material already deposited.⁸

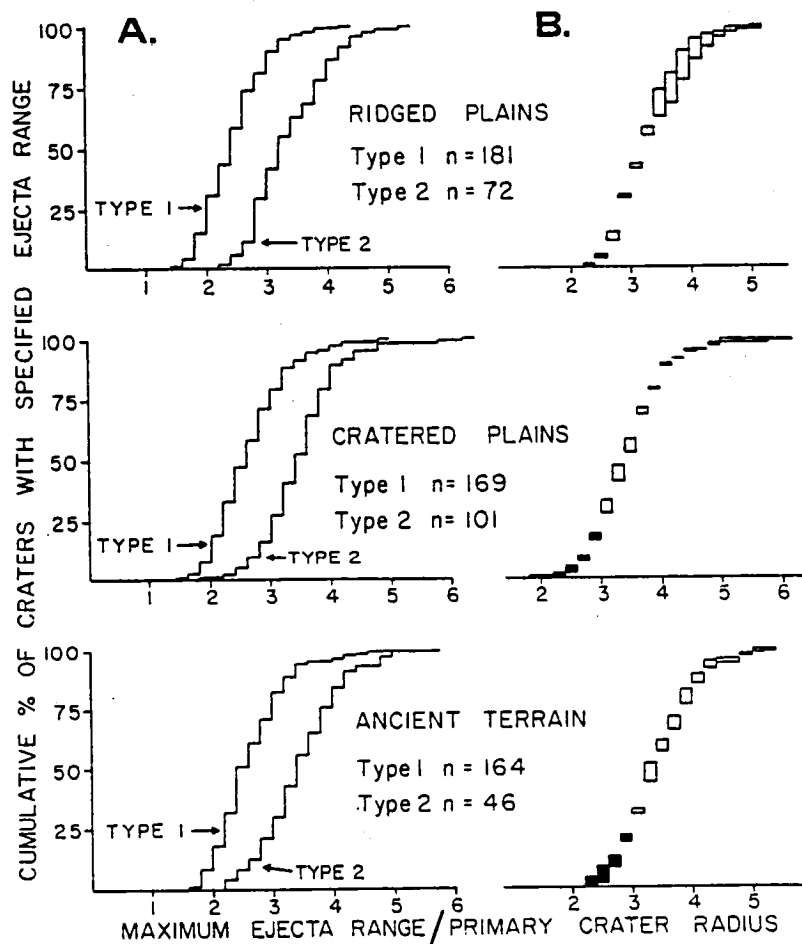


Fig. 1: A) Cumulative percentage frequency curves for two crater types on three target materials. "n" gives size of each sample. B) Residual curves produced by increasing Type 1 curve by 0.8 crater radii and subtracting this curve from that of Type 2 craters. Solid boxes illustrate where Type 2 curve is greater than adjusted Type 1 curve, open boxes where Type 1 curve is greater than Type 2.

Mouginis-Mark, P.J.

Schultz (1979, pers. comm.) has also suggested this emplacement sequence, which offers an explanation for the more mobile ejecta of Type 2 craters revealed in Fig. 1A. Numerical modelling (currently in progress) of ejecta ground flows, based on the terrestrial models of Sparks *et al.*,¹³ indicates that the increased energy associated with a ground flow falling over the edge of the inner Type 2 unit would be capable of producing the observed increased travel distances providing the inner unit is approximately 40-100 meters thick. These ejecta thicknesses agree well with estimated values for Arandas.¹⁴ Consequently, ongoing analysis will be concentrated toward understanding the flow characteristics and rheological properties that are consistent with the surface flow of martian ejecta materials.

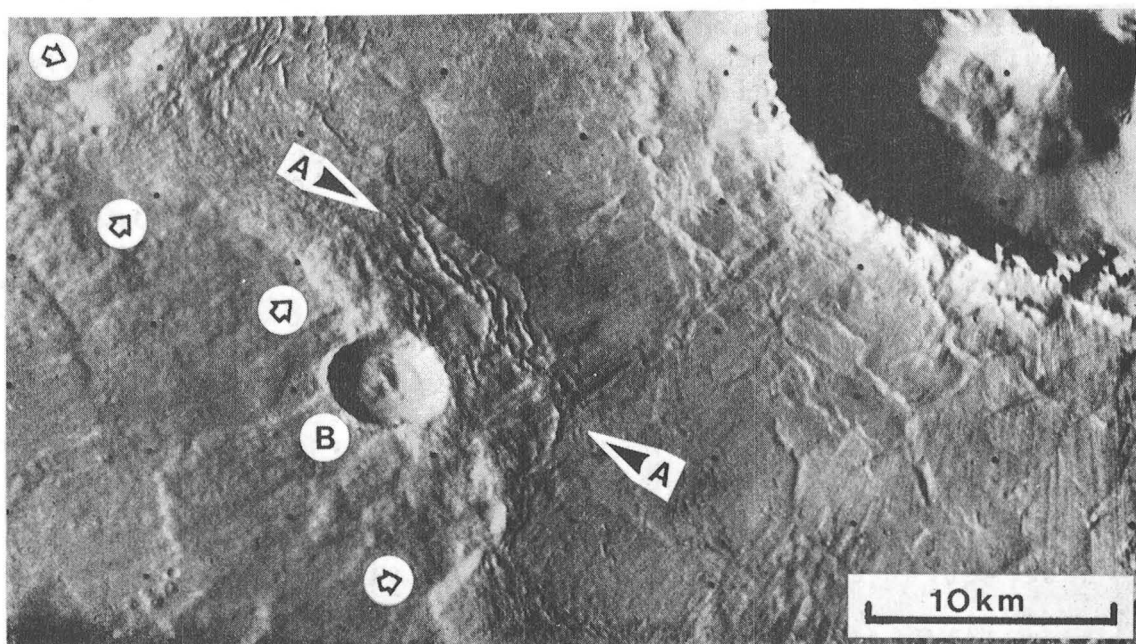


Fig. 2: Inner ejecta deposit southwest of Arandas. Ejecta boundary delineated by small arrows. Points "A" mark ends of massive ridges abutted against crater "B." Viking frame 32A28.

- References: ¹Carr M.H. *et al.*, 1977, *J. Geophys. Res.* 82, 4055-4065. ²Boyce J.M. 1979, NASA TM-80339, 114-118. ³Johansen L.A. 1979, NASA TM-80339, 123-125. ⁴Mouginis-Mark P.J. 1979, *J. Geophys. Res.*, in press. ⁵Cutts J.A. *et al.*, 1979, NASA TM-80339, 111-113. ⁶Mouginis-Mark P.J. 1979, submitted to *Geophys. Res. Lett.* ⁷Mouginis-Mark P.J. 1979, NASA TM-80339, 144-146. ⁸Mouginis-Mark P.J. 1979, PLPSC-10, in press. ⁹Head J.W. and Roth R. 1976, *Symp. Plan. Crater Mech.* (abs), LSI, 50-52. ¹⁰Schultz P.H. and Gault D.E. 1979, *J. Geophys. Res.*, in press. ¹¹Scott D.H. and Carr M.H. 1978, USGS Map I-1083. ¹²Shreve R.L. 1966, *Science* 154, 1639-1643. ¹³Sparks R.S.J. *et al.* 1978, *J. Geophys. Res.* 83, 1727-1739. ¹⁴Mouginis-Mark P.J. and Carey D.L., 1980, this vol.

ON THE ORIGIN OF MARTIAN PEDESTAL, LOBATE, AND MULTILOBATE EJECTA DEPOSITS

Woronow, A. & Mutch, P., Lunar & Planetary Lab, U. of AZ., Tucson, Az 85721

Mutch and Woronow (1979) have proposed a sequence of models of ejecta emplacement in order to explain their measurements on martian Pedestal, Lobate, and Multilobate ejecta deposits in quads MC 17 and MC 18. The fact that somewhat different physical circumstances are invoked for each class of ejecta deposit makes their model distinctive from those models which rely on an evolutionary track to carry craters from one class to another. For instance, if Pedestal craters result from the erosion and removal of ejecta from around Lobate craters (which in turn could be the remains of eroded Multilobate craters), then a continuum of morphologies should exist. Or, if the physical processes which created these morphologies as primary structures grade slowly into each other, a continuum would again be expected. Here we will present evidence that no true continuum of ejecta blanket morphologies exists, but instead, Pedestal, Lobate, and Multilobate deposits have distinct attributes with intermediate forms being the exception.

A useful scheme for quantifying ejecta geometries must avoid problems of arbitrariness and also assign a single index to all similar ejecta blankets, regardless of wide variations in their size. Fortunately, a procedure that is well understood mathematically, and applicable, though certainly under-utilized, already exists. Consider the relationship

$$P^{(1/h)} / A^{(1/2)} = K \quad (1)$$

For our particular case, P is the perimeter of an ejecta blanket, A is the area it covers, and H and K are constants which describe the ejecta blanket's geometry. H is known as the "Hausdorff dimension", (Mandelbrot, 1977). H will take on values $1.0 \leq H \leq 2.0$, depending on how crenulated the ejecta margin is. K will also be affected by the attributes of the crenulations, but K also senses a broader scale geometry (e.g. circularity or ellipticity of the entire ejecta deposit). Regardless of size, ejecta borders with similar geometries will be satisfied by Equation 1 with similar values of H and of K .

To demonstrate that the various classes of ejecta do not form a continuum, we need, then, only show that the values

of H and K are distinct for each class. Figures 1a, b, and c are plots of ejecta perimeter as a function of ejecta blanket area for Pedestal, Lobate and Multilobate classes respectively. In each figure the solid curve is the regression to Equation 1. Clearly, the functional form of Equation 1 closely describes the data. Table 1 gives the values fitted to each ejecta class, along with R^2 , the fraction of the sum of squares explained by the regression. The high values of R^2 for each regression imply high significance, but an exact test is not possible in the nonlinear model. The errors for H and K cited in Table 1 are only approximate.

TABLE 1

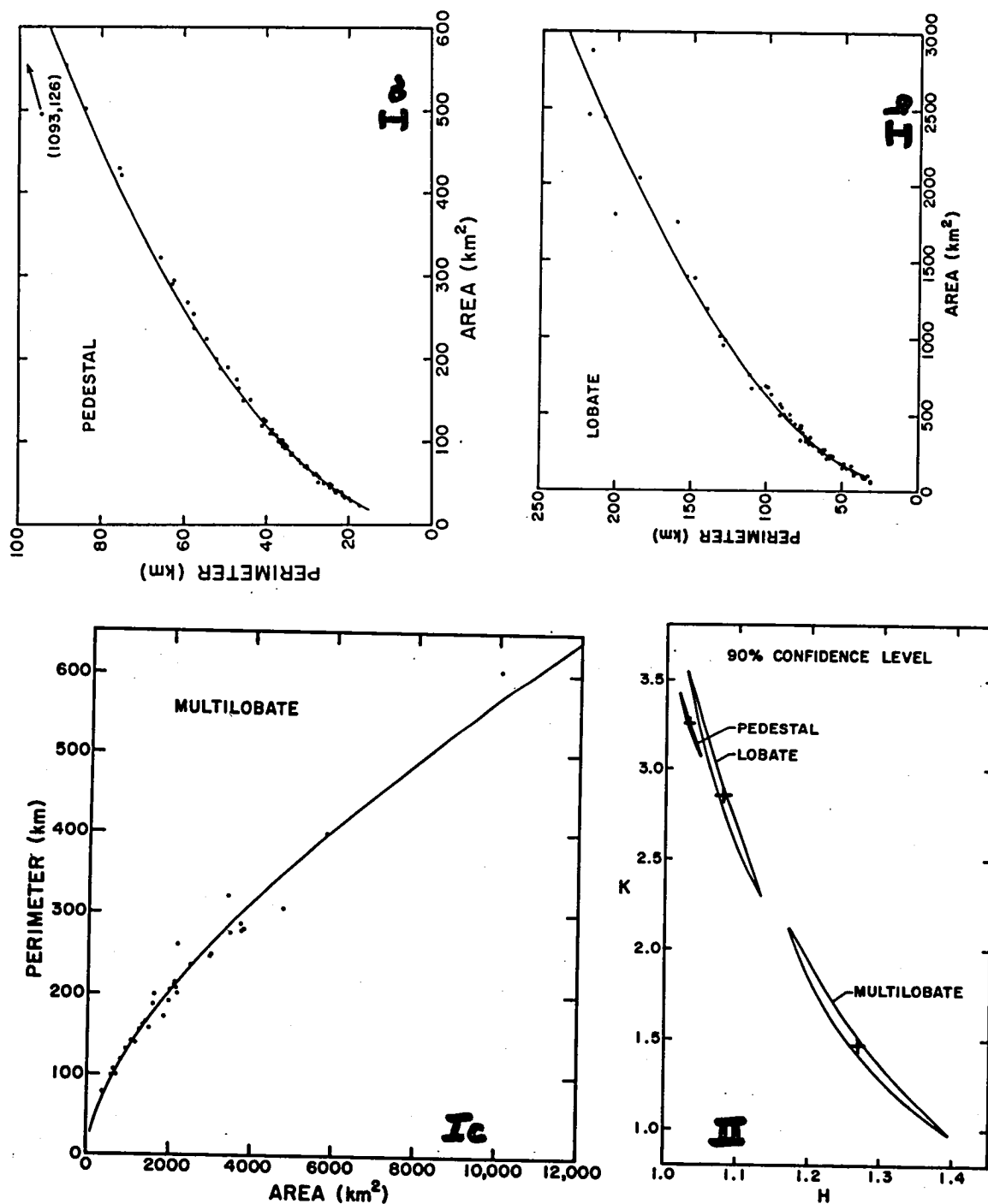
Class	H	K	R ²
Pedestal	1.032 ± <1%	3.249 ± 2%	.9998
Lobate	1.079 ± <1%	2.852 ± 14%	.9972
Multilobate	1.270 ± <1%	1.470 ± 53%	.9941

Figure 2 shows the 90% confidence regions around the regression values of H and K. All three regions are disjoint. If these ejecta types were merely names attached to a true continuum of types, then the continuous variations in H and K would stretch these confidence regions until considerable overlap occurred. Because K reflects the gross planar geometry of the ejecta deposit, which can vary widely due to such effects as the obliquity of the impact, it is less important in determining the similarities or differences among classes. H describes the geometry and degree of crenulation of the margin, which is more likely the result of the physical state of the ejecta (e.g. viscosity, velocity, momentum); therefore, H best determines whether a continuum of morphologies exists or not. Table 1 shows that the values of H for each class are clearly distinct--no continuum exists. An erosional evolution of classes is unlikely, as is a smooth gradational relationship for primary structures. Most likely Pedestal, Lobate, and Multilobate craters result from distinct and different physical circumstances.

REFERENCES: (1) Mandelbrot, B.B. (1977), Fractals Form, Chance, and Dimension. Freedman & Co. (2) Mutch, P. & Woronow, A. (1979), Emplacement of Martian Rampart and Pedestal Ejecta Blankets. Submitted to Icarus.

Figure 1: Ejecta area vs ejecta perimeter for each of the morphologic classes. The curves drawn through the data are the regressions to Equation 1.

Figure 2: The 90% confidence intervals around H and K for each of the morphologic classes.



CRATER STUDIES IN THE NORTHERN PLAINS OF MARS: THICKNESS ESTIMATES OF FLUIDIZED EJECTA DEPOSITS.

Mouginis-Mark, P.J. and Carey, D.L.*, Dept. of Geological Sciences,
Brown Univ., Providence, RI 02912 (*NASA Summer Intern)

Subsurface volatiles are generally described as the main agent responsible for the production of the fluidized ejecta deposits surrounding impact craters on Mars.^{1,2,3} Interpreting the global distribution of craters with different fluidized ejecta morphologies^{2,3,4} depends critically on understanding the flow processes, rheological properties and volumes of material incorporated within individual ejecta deposits. We have initiated a series of crater studies designed to provide pertinent data for the interpretation of ejecta emplacement processes related to impact events in a variety of target materials. The first stage of this program concentrates on craters lying within Acidalia Planitia (30-60°N, 0-50°W). Theoretical models,^{5,6} photogeological interpretations of surface features suggestive of periglacial processes^{7,8} and the abnormally extensive crater ejecta deposits^{3,9} indicate that this area was probably abnormally rich in volatiles at the time the craters were formed. Because target material characteristics are considered important in the formation of martian ejecta blankets,^{3,10} this region is therefore intended to be the "volatile-rich end member" of our series of materials within which fluidized ejecta craters were formed.

Estimates of ejecta thickness and volumes are considered relevant to the problem of interpreting the erosional/depositional flow characteristics of the ejecta. The deposits may have acquired a significant amount of locally derived material during the surface-flow stage that would, in turn, alter the original particle distribution, thermal conditions and volatile component of the excavated material. A possible terrestrial analogue supporting this hypothesis is the Ries Crater, West Germany, which displays radial scouring of bedrock beyond the crater rim¹¹ and a greater proportion of locally derived material with increasing radial distance from the crater.¹²

Excellent Viking images (frames 9A42, 32A28-32; resolution ~40 m/pixel; sun angle ~75° from normal) permit shadow length measurements to be made of several ejecta flow heights associated with the 25 km diameter, Type 2 fluidized ejecta crater,³ Arandas (43°N, 14°W). Twin concentric ejecta deposits surround Arandas, the inner of which is interpreted to be part of the crater's overturned rim flap that was subsequently overridden by the areally more extensive outer ejecta deposits.¹³ Table 1 presents the height measurements, which were derived utilizing techniques described by Cintala *et al.*¹⁴ The location of each data point is illustrated in Fig. 1. Typically, these measurements indicate that

MARS CRATER STUDIES

Mouginis-Mark, P.J. and Carey, D.L.

the inner ejecta unit rises 40-110 meters above the surrounding material, while the distal ridges of the outer unit average 80 meters high.

Planimetric measurements¹⁵ from an 8x10" orthographic image (frame 673B52) indicate that the surface areas of the Arandas ejecta deposits are 3860 km² for the inner deposit and 6230 km² for the outer deposit. This implies that a total deposit volume of 650-925 km³ may be distributed around Arandas as a direct consequence of the impact event.

Estimates of the cavity volume for Arandas are difficult to derive due to the presence of a large central peak, an unknown true rim height above the pre-impact surface, and the degree of crater infilling due to eolian processes. Our best estimates for crater diameter, depth and rim height (24.9 km, 2.9 km and 0.5 km, respectively) with an assumed flat floor 12.5 km wide would predict a cavity volume¹⁶ of ~600 km³, remarkably close to the volume estimate for the surrounding ejecta deposits. This similarity may be fortuitous, because comparable analyses of lunar craters have shown the problems inherent in calculating crater cavity volume,¹⁷ the role of structural uplift¹⁸ and infilling by fall-back ejecta.¹⁹ To these unknowns must be added the loss of ejecta volume due to volatilization of ice or water from the cavity and ejecta bulking during emplacement for martian cratering events. The observation that the ejecta deposit and cavity volumes for Arandas are quite similar suggests that locally derived material may only represent a small component of the ejecta deposit, although basic problems relating to the validity of these volume estimates remain unresolved.

Current analysis is attempting to derive ejecta thicknesses for the central part of each deposit and expand our data base of fluidized craters in the size range 5-50 km diameter that have twin ejecta deposits and flat floors. Such an approach will facilitate our determinations of crater cavity and ejecta volumes and enable a comparison of craters in volatile-rich and volatile-poor target materials to provide more confident estimates of ejecta mixing with pre-existing terrain during the process of ejecta flow.

References: ¹Carr M.H. et al. 1977, *J. Geophys. Res.* 82, 4055-4065. ²Johansen L.A. 1979, NASA TM-80339, 123-125. ³Mouginis-Mark P.J. 1979, *J. Geophys. Res.*, in press. ⁴Allen C.C. 1979, *Icarus* 39, 111-123. ⁵Fanale F.P. 1976, *Icarus* 28, 179-202. ⁶Farmer C.B. and Doms P.E. 1979, *J. Geophys. Res.* 84, 2881-2888. ⁷Carr M.H. and Schaber G.G. 1977, *J. Geophys. Res.* 82, 4039-4054. ⁸Guest J.E. et al. 1977, *J. Geophys. Res.* 82, 4111-4120. ⁹Mouginis-Mark P.J. 1979, NASA TM-80339, 144-146. ¹⁰Schultz P.H. and Gault D.E. 1979, *J. Geophys. Res.*, in press. ¹¹Chao E.C.T. 1974, *PLSC-5*, 35-52. ¹²Pohl J. et al. 1977, in *Impact and Explosion Cratering*, Pergamon Press, NY, 343-404. ¹³Mouginis-Mark P.J. 1980, this volume. ¹⁴Cintala M.J. et al. 1976, *LSI Contr.* 262, 5. ¹⁵Carey D.L. 1979, unpubl. data. ¹⁶Pike R.J. 1967, *J. Geophys. Res.* 72, 2099-2105. ¹⁷Moore H.J. et al. 1974, *PLSC-4*, 71-100. ¹⁸Settle M. and Head J.W. 1977, *Icarus* 31, 123-135. ¹⁹Settle M. 1979, *Icarus*, in press.

TABLE 1.
SHADOW LENGTH ESTIMATES OF EJECTA THICKNESSES

Pt.No.	Frame No.	Height $\pm 1\sigma^*$	# Meas- urements	Loca- tion
1	32A29	67.8 \pm 5.7	7	OED
2	32A30	193.3 \pm 14.7	5	PBC
3	32A29	127.2 \pm 7.6	8	PBC
4	32A29	81.1 \pm 5.9	8	OED
5	32A31	68.9 \pm 4.9	8	OED
6	32A30	55.8 \pm 2.4	5	IED
7	32A31	95.8 \pm 6.2	8	OED
8	32A31	106.6 \pm 5.8	8	OED
9	32A31	107.4 \pm 4.8	8	OED
10	32A30	42.0 \pm 2.4	5	IED
11	32A30	493.7 \pm 9.5	5	RCH
12	32A30	504.4 \pm 9.5	5	RCH
13	32A30	388.9 \pm 10.6	5	RCH
14	32A30	53.4 \pm 1.3	5	IED
15	32A32	51.8 \pm 4.6	6	OED
16	32A32	120.6 \pm 11.0	6	OED
17	9A42	107.3 \pm 9.6	7	IED
18	32A30	50.8 \pm 3.3	5	IED
19	9A42	77.8 \pm 4.4	7	IED
20	9A42	67.4 \pm 1.9	7	OED
21	9A42	46.9 \pm 3.8	7	OED
22	9A42	74.0 \pm 5.5	7	OED
23	32A28	417.0 \pm 9.0	6	PBC

OED-outer ejecta deposit
PBC-depths of partially buried craters
IED-inner ejecta deposit
RCH-rim crest height
* σ is one standard deviation.
Heights are in meters.

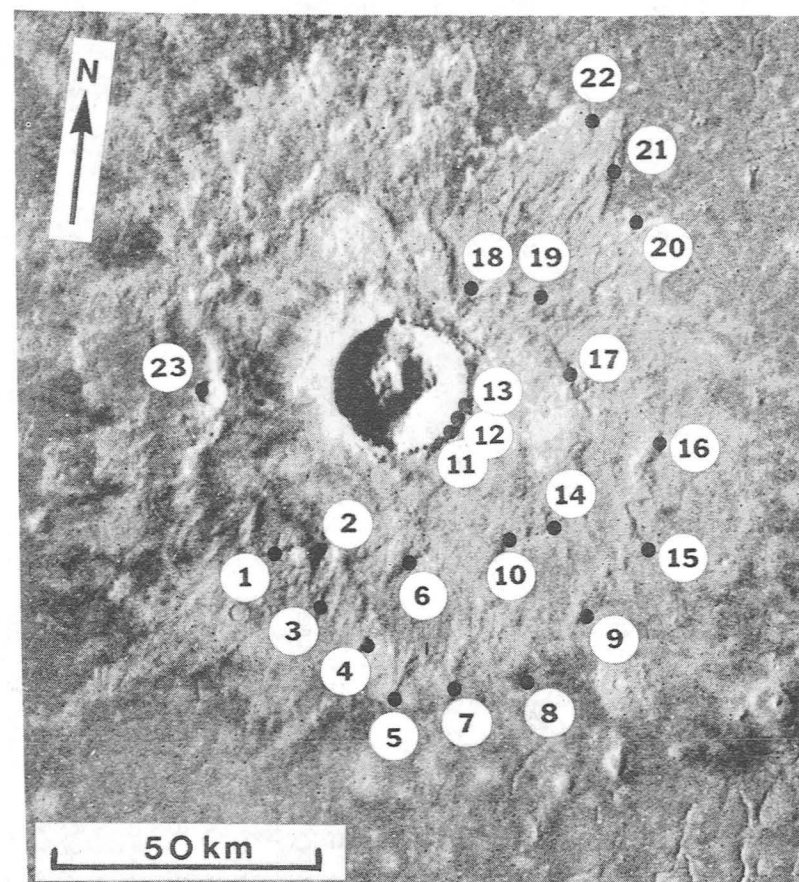


Fig. 1: Locations of height measurements given in Table 1. Viking frame no. 673B52.

GRAVITY AND TARGET STRENGTH: CONTROLS ON THE MORPHOLOGIC TRANSITION
FROM SIMPLE TO COMPLEX IMPACT CRATERS

R. J. Pike, D. J. Roddy, and D. W. G. Arthur, U.S. Geological Survey,
Menlo Park, CA 94025 and Flagstaff, AZ 86001

As the scope of study of impact craters broadens to include the Jovian satellites, a sound basis of comparison for depth/diameter (d/D) and other descriptive aspects of craters on all the inner planets is essential. A reliable d/D relation for Mars, which is needed to complement those for craters on Earth, Mercury, and the Moon, has not yet been agreed upon. We have calculated two linear d/D relations from 57 craters between 0.5 km and 19 km across depicted on three U.S. Geological Survey contour maps derived from photogrammetry of Viking Orbiter pictures. No other photogrammetric data have resulted from our inventory of martian craters. After reviewing the nine other available d/D distributions for impact craters on Mars, we judge the new photogrammetric results acceptable, if preliminary, models for martian craters. The d/D relation for simple craters ($n = 49$):

$$d = 0.16 D^{1.00} \quad (1)$$

(where d and D are in km, correlation coefficient, r , = +0.92; standard error of the estimate of depth on diameter, s , = +0.044 km and -0.035 km; and standard error of the slope is ± 0.063), may be more accurate than that for complex craters ($n = 8$):

$$d = 0.41 D^{0.33} \quad (2)$$

(where $r = +0.83$, $s = +0.05$ km and -0.04 km, and slope error = ± 0.09).

The d/D distribution for the relatively deep, simple craters on Mars generally resembles that for small impact craters on Mercury, the Moon, Earth, and Phobos, but the distribution for the shallow, complex craters differs substantially: it is located midway between those for large craters on Earth and Mercury (Figure 1). The d/D inflection does not occur at the same diameter range for craters on all bodies. Inflection of the martian d/D relation at about 4 km crater diameter is consistent with a size-dependent morphologic transition from simple to complex craters at about 6 km to 7 km diameter.

We have determined that average depths of complex craters on the first four of the five planets, which correlate with from 9 to 23 other size-related aspects of crater morphology, vary inversely with gravitational acceleration at the planetary surface, g . Phobos and Deimos do not have sufficiently high g for complex impact craters to form. The inverse correlation suggests that g is an overriding control on the development of the morphologic transition.

We define D_t , the crater size that best characterizes the simple-to-complex transition, as the geometric mean of several constituent crater diameters at which specific differences in morphology are observed. This figure is about 19 km on the Moon, 16 km on Mercury, 6 to 7 km on Mars, and 3.2 km on Earth. D_t varies inversely with g for the four planets. We have found that dispersion in the statistical dependence of D_t upon g drops by at least 100 % if g is divided by v_∞ , the approach velocity of one of the most likely types of impacting bodies, asteroids. This relation suggests that v_∞ could be an important factor in modulating the control of g on the transition size, D_t .

Dispersion in the inverse $D_t:g$ relation could be equally well explained by variable target-strength, whereby Mercury is a much "harder" target than average localities on both Earth and Moon, and Mars is a "softer" target. The model derives from D_t contrasts between meteorite craters formed in sedimentary rock and those formed in crystalline rock on Earth (Grieve and Robertson, 1979). Evidence for pervasive volatiles in the surface rocks of Mars and for possibly dense surface rocks on Mercury is consistent with this hypothesis (Figure 2).

Predictions of D_t values on Venus (about 4 km) and the large satellites Ganymede, Callisto, Europa, and Titan (about 15 km to 40 km) made from both mean $D_t:g$ and $D_t:g/v_\infty$ regressions yield roughly comparable values. However, the soft-target $D_t:g$ model (Figure 2) predicts substantially lower D_t values than either the mean $D_t:g$ model or the $D_t:g/v_\infty$ model. Testing these D_t estimates is well within the capabilities of current spacecraft-mission results and those anticipated from future planetary probes. We measured diameters of small impact craters that contain central peaks on Voyager I images of Ganymede and Callisto. Preliminary medial values of D_t for these two bodies (13 km and 15 km, respectively) are more consistent with the low values predicted from the soft target hypothesis (15 km and 23 km, respectively) than with the higher values estimated from the approach-velocity model (27 km and 29 km, respectively). Our results do not necessarily exclude v_∞ as a control on crater morphology, but they tend to shift the burden of proof to that model rather than to the target-strength hypothesis.

References

- Grieve, R.A.F., and Robertson, P.B., 1979, The terrestrial cratering record I. Current status of observations: *Icarus*, v. 38, p. 212-229.
- Malin, M.C., and Dzurisin, D., 1977, Landform degradation on Mercury, the Moon, and Mars: evidence from crater depth/diameter relationships, *J. Geophys. Res.*, v. 82, p. 376-388.
- Pike, R.J., 1974, Depth/diameter relations of fresh lunar craters: revision from spacecraft data, *Geophys. Res. Letts.*, v. 1, p. 291-294.

- Pike, R.J., 1977, Size-dependence in the shapes of fresh impact craters on the Moon, in *Impact and Explosion Cratering*, Roddy et al., eds., Pergamon, N.Y., p. 489-509.
- Pike, R.J., and Arthur, D.W.G., 1979, Simple to complex impact craters: the transition on Mars, N.A.S.A. Tech. Memo. 80339, p. 132-134.
- Thomas, P.C., 1978, The morphology of Phobos and Deimos, Ph.D. thesis, Cornell Univ., Ithaca, N.Y., 272 p.

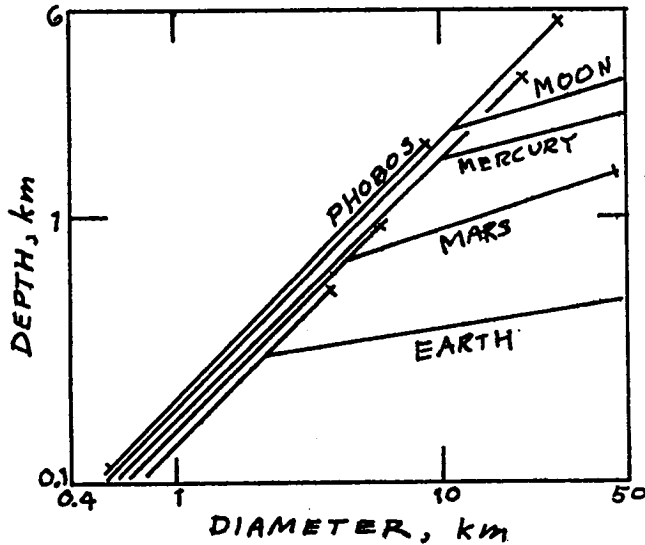
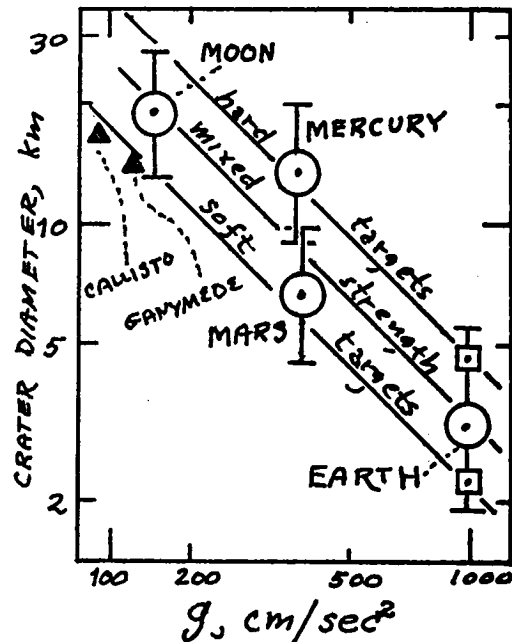


Figure 1.

Depth versus diameter for simple (steep slope) and complex (gentle slope) impact craters on five planets. Lines are least-squares fits. Martian curves are equations (1) and (2), this paper; lunar curves are from Pike (1974); Mercurian curves are from Malin and Dzurisin, 1977; terrestrial curves mostly from data in Pike (1977); curve for Phobos from data of Thomas (1978).

Figure 2.

The $D_t:g$ relation (Pike and Arthur, 1979) incorporating the modulating effects of target strength. Upper square on "Earth" data bar: D_t in crystalline rocks; lower square: D_t in sedimentary rock. Extrapolated lines slope at -1.0. Observed estimates of D_t for impact craters on Ganymede and Callisto are consistent with the very low crustal strengths predicted for these bodies.



CRATER DISTRIBUTIONS AND THE EVOLUTION OF THE LUNAR FAR SIDE HIGHLANDS

Wood, C.A* and Gifford, A.W., National Air and Space Museum, Smithsonian Institution, Washington, DC 20560; * also at Geophysics Branch, Goddard Space Flight Center, Greenbelt, MD 20771.

The highlands of the Moon appear to be a large, relatively homogeneous unit formed by intense impact cratering of a global anorthosite crust. There is little evidence for the action of other geologic processes within the highlands except for volcanic flooding of some basins. In an attempt to test if the highlands are as structurally homogeneous as this model implies we have examined the mapped distribution of large craters on the farside and limb regions of the Moon. Our results are preliminary due to the inhomogeneities of the data set, but the observed crater density variations appear to reflect both the distribution of basins as well as other unidentified surface modification processes.

We have counted all craters with diameters > 25 km that are individually mapped on the 1:5m geologic charts of the farside and limb regions of the Moon (1,2,3). The crater counts are subdivided into $20^{\circ} \times 20^{\circ}$ squares which allows construction of crude contour maps of crater density (Fig. 1). A word of caution is necessary before interpretation of these maps. Although each crater > 20 km is shown on the Geologic Map of the East Side of the Moon (1, and El Baz, pers. comm.), we are not certain that the other two maps (2,3) have the same level of completeness, and in fact a previous analysis of plains unit distribution (4) found some systematic differences between the three farside charts. Thus our present results are preliminary.

CRATER DENSITY: The number of craters per $20^{\circ} \times 20^{\circ}$ square varies from 0 to 59. Areas with the lowest crater density (< 10) have been rejuvenated relatively recently in lunar cratering history, either by lava flows (Procellarum and Crisium) or by deposition of impact basin ejecta (Orientale). Intermediate crater densities are commonly associated with older basins (within the South Polar-Aitken basin, and around Moscovien-se, Humboldtianum, Sharonov-Dante, Korolev, and Hertzsprung). Other basins (Australe, Smythii, Lomonosov-Fleming, Al-Khwarizmi-King, Mendel-eev, and Apollo) appear to be too old, too small, or too unflooded by lava to affect crater density. Regions with the highest crater density (> 25) are far from large basins.

RELATIVE AGE RATIO: More detailed information on the evolution of the highland crust can be gained by dividing the number of young (Copernican and Eratosthenian) and intermediate (Imbrian) age craters in each square by the number of ancient (Nectarian and Pre-Nectarian) craters (Fig. 2). Ronca and Green (5) used a similar but more complex ratioing of young and old craters to define a geomorphologic index for the nearside of the Moon. For convenience our ratio is termed the relative age ratio (RAR).

Two-thirds of the area shown in Figure 2 (72% of the entire lunar equatorial zone) have RAR values < 1 ; i.e. these areas have not been resurfaced recently or extensively enough to eliminate significant numbers of old craters. Areas where $RAR > 1$ are dominated by young craters - near Orientale RAR averages 3.6, with most older craters destroyed or blanketed by ejecta. The interior of the South Polar-Aitken basin is also well defined, with $RAR > 1$, as are small regions between Moscoviense and Sharonov-Dante, and near Humboldtianum.

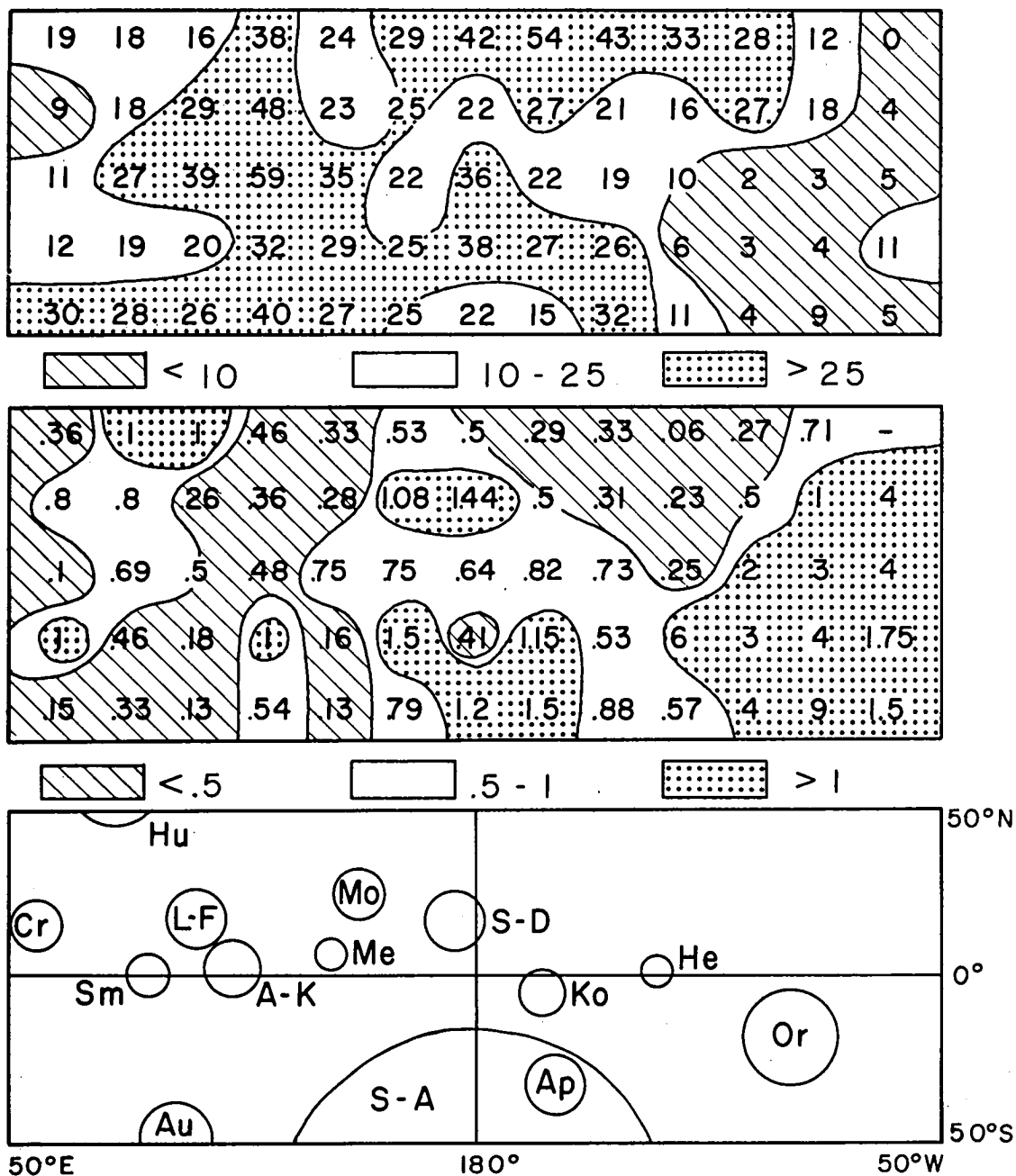
Ancient craters outnumber young ones more than 2 to 1 ($RAR < 0.5$) for 37% of the area shown in Figure 2; these surfaces are the oldest and least altered by recent volcanism and ejecta deposition.

DISCUSSION AND CONCLUSIONS: Because of limitations of the data and the large area over which they are averaged, only coarse patterns in crater distribution can be documented. None-the-less, it is clear that many crater density variations can be explained in terms of crater destruction near impact basins. Our results confirm and extend Ronca's (6) observation that highlands on the lunar near side are severely modified near basins and are progressively less altered away from basins.

The contours in Figures 1 and 2 do not agree totally with mapped geologic units. The most notable conflict occurs in the north-central region of the lunar farside. Most of this region is mapped as a single unit - Irregular Terra (2) - but the northern portion of the region has twice the crater density as the southern portion (Fig. 1) and RAR values imply that large numbers of older craters have been destroyed in the southern area. Crater statistics thus identify this as a region where processes unrelated to obvious basin ejecta deposition or mare-albedo volcanism have operated. Refined crater statistics, based on the forthcoming Lunar and Planetary Lab catalog of farside craters, may clarify the location and nature of this discontinuity in farside highlands crater patterns.

Our data also illustrate that, although most of the rim structure of the South Polar-Aitken basin is obscure, its existence is clearly indicated by crater frequency and RAR contours. Thus basins appear to preserve crater density anomalies long after rim morphology is subdued.

REFERENCES: (1) D.E. Wilhelms and F. El-Baz; USGS Map I-948, 1977. (2) D. E. Stuart-Alexander; USGS Map I-1047, 1978. (3) D.H. Scott, J.F. McCauley, and M.N. West; USGS Map I-1034, 1977. (4) A.W. Gifford and F. El-Baz; Papers Presented to Conf. Lunar Highland Crust, 21-23; Lunar & Planetary Inst. Contr. 394; 1979. (5) L.B. Ronca and R.R. Green; Geol. Soc. Am. Bull. 81, 337; 1970. (6) L.B. Ronca; The Moon (ed. Urey and Runcorn), 43-54; 1972.



CAPTIONS: Fig. 1 (top): Total number of craters per 20° x 20° square, as mapped in references 1-3.

Fig. 2 (middle): Ratio of number of young to old craters in each 20° x 20° square (RAR = Relative Age Ratio).

Fig. 3 (bottom): Schematic map of major basins.

RESURFACING HISTORY OF MARS - CRATER FLUX MODELS AND THERMAL HISTORY MODELS

Arvidson, Raymond E., McDonnell Center for the Space Sciences,
Washington University, St. Louis, Missouri 63130

Figure 1 is a way to examine the distribution of retention ages for craters on Mars. We plot, in a manner similar to Condit (1978), the abundance of craters that are between 4 to 10 km in diameter as a gray tone image. The data were derived from the Brown University Mariner 9 A-frame crater catalog. The size range of 4 to 10 km was chosen to give good statistics and because this size range consists almost totally of fresh-appearing craters (Soderblom et. al., 1974). As such, the display provides an indication of the geographic distribution of the relative timing of cessation of major obliteration for time periods after formation of any primitive cratered terrain crust (Soderblom et. al., 1974). These data probably reflect both the geographic and temporal distribution of extensive volcanic activity. The greatest abundances of 4-10 km craters occur in cratered terrain, while the smallest abundances are found in the higher latitude northern plains, the Hellas basin (45° S. lat.; 290° W. long.), and the Tharsis plateau. The data are not valid over the higher latitude plains nor over Hellas because of obscuration by haze. However, within $\pm 30^\circ$ in latitude of the equator, the data provide a valid indication of the distribution of ages, largely of volcanic units.

Figure 2A is an alternative presentation of the crater data shown in Figure 1 that are located within $\pm 30^\circ$ lat. of the equator. In this figure we have shown the fractional area covered by various abundances of 4 to 10 km diameter craters. Fractional area was obtained by first determining the number of 4 to 10 km diameter craters that fell within a 5° solid angle about a given latitude, longitude intersection. By examining intersections spaced at 5° latitude and longitude increments, we were able to obtain 936 estimates of the 4 to 10 km crater abundance. The fractional area occupied by a given abundance is then simply the number of estimates obtained for that abundance divided by 936.

The technique in essence is similar to the "averaging circle" used by structural geologists to contour piercing point densities on an equal area net. In our case, the circle was 5° in diameter. The choice of a 5° circle and a 5° latitude, longitude spacing was driven by: (1) the need to examine small areas so as not to average together distinct geologic units, and (2) the amount of computer time needed to cover the whole equatorial region.

Higher latitudes were excluded from the analysis shown in Figure 2A because of the complexity of the origin of plains in these regions. As shown in numerous Viking Orbiter frames, the northern mid to high latitude plains probably have a polygenetic origin, involving aeolian erosion and sedimentation, volcanism, tectonism, and periglacial phenomena, such as

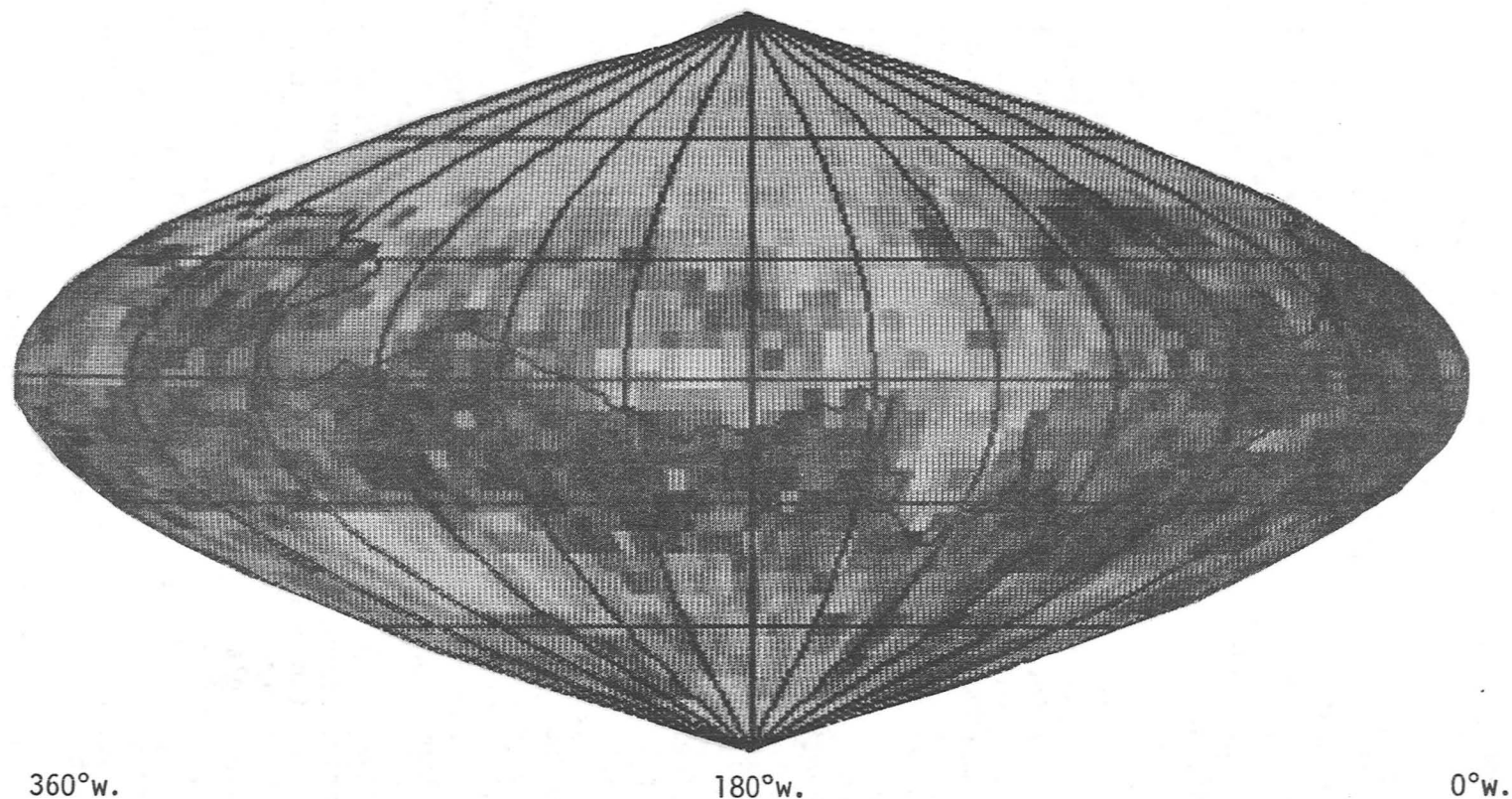


Figure 1 - Sanson-Flamsteed projection of the abundances of craters with diameters between 4 to 10 km, shown as a gray tone map. The darkest patches correspond to an abundance of 50 craters within a 2.5° solid angle of a given latitude and longitude. The brightest patches correspond to the smallest crater abundances. This crater size interval was chosen to give good statistics and to provide an indication of the relative stratigraphy of various geologic units. The 4-10 km crater population within cratered terrain records cessation of intercrater plains formation. These units are stratigraphically the oldest, although there is considerable overlap with cratered plains, fretted terrain, and older plains.

freeze-thaw cycling (Guest et. al., 1977; Carr and Schaber, 1977). In contrast, the equatorial region of Mars seems to have been stripped of loose material (McCauley et. al., 1973), while retaining a large number of pristine volcanic features (Arvidson et. al., 1979). For instance, the region surrounding the Viking Lander 1 site contains a population of fresh craters extending down to the resolution limit of about 100 m, indicating that only meters of erosion have occurred since emplacement of these volcanic materials (Arvidson et. al., 1979). As such, the equatorial regions provide a first-order record of the timing and spatial distribution of volcanic activity.

The intent of Figure 2A is to illustrate the rate of resurfacing of Mars as a function of time. If the cratering rate had remained constant during all of the time it took to accumulate all the 4 to 10 km craters on Mars, then the shape of the histogram in Figure 2A would not change if the abscissa were replaced with an age axis. To illustrate the effect that various assumptions about the cratering history have on the resurfacing history, we: (1) reformatted the data in Figure 2A to the cumulative percent surface area covered by crater abundances less than some value, (2) substituted an age, t , for the crater abundances, based on both a constant cratering rate model, and on the flux model of Neukum and Wise (1976), and (3) differentiated the cumulative percent surface area covered by ages less than t , with respect to t , to determine the rate of areal resurfacing versus time. Results are shown in Figure 2B. In each case, the maximum resurfacing rate corresponds stratigraphically to times when the plains within cratered terrain overlap with cratered plains (ridged plains of Scott and Carr, 1978), and with some of the older undifferentiated plains. The constant flux model results in a maximum resurfacing rate between 1 to 1.5 billion years ago, along with a prolonged period of volcanism. The Neukum and Wise (1976) flux model forces 75% of the planet to have been resurfaced between about 3.5 to 4.0 billion years ago. With their model, plains within cratered terrain, and the cratered plains formed extremely rapidly and occupy a very narrow time span. Other plains extend over most of geologic time, forming at a very slow rate.

The Neukum and Wise (1976) flux model assumes that Mars and the Moon have the same flux of impacting objects scaled for impact velocity and gravitational effects between the two bodies. The result is that Mars would accumulate craters at 0.28 times that of the moon. The reason that cratered terrain plains and cratered plains form so quickly in their model is that these terrains have crater abundances that place them in the time period corresponding to the tail end of the early heavy bombardment. The exact cratering history of Mars is unknown, although recent work by Wetherill (1975) and Shoemaker (1977) suggested that the relative encounter probabilities for impacting objects are similar for the terrestrial planets. This suggests that the Neukum and Wise (1976) flux is probably good to within a factor of two (Wise, 1979, personal communication). To the extent to which the maximum resurfacing rate corresponds to extensive mantle differentiation and planetary peak radius, the two flux models used

to generate the curves in Figure 2B suggest vastly different thermal histories for Mars. Work by Solomon and Chaiken (1976), where Mars is assumed to accrete cold and in a homogeneous manner, suggests a resurfacing history somewhat akin to the constant flux model, while the thermal history suggested by Toksöz and Hsui (1978) would correspond to a flux history intermediate between the Neukum and Wise (1976) and the constant flux model. We could not find a thermal evolution model in the existing literature that would lead to the massive resurfacing period between 3.5 to 4.0 billion years ago that can be inferred from the Neukum and Wise (1976) flux model. This research was supported by Planetary Geology Program Grant NSG-7087 and Mars Data Analysis Grant NSG-7545.

References

- Arvidson, R.E., E.A. Guinness, and S.W. Lee, 1979, Differential aeolian redistribution rates on Mars, Nature, V. 278, pp. 533-535.
- Carr, M.H. and G.G. Schaber, 1977, Martian permafrost features, J. Geophys. Res., V. 82, pp. 4039-4054.
- Condit, C.D., 1978, Distribution of 4 to 10 km diameter craters to global geologic units of Mars, Icarus, V. 34, pp. 465-478.
- Guest, J.E., P.S. Butterworth, R. Greeley, 1977, Geological observations in the Cydonia region of Mars from Viking, J. Geophys. Res., V. 82, pp. 4111-4120.
- McCauley, J.F., 1973, Mariner 9 evidence for wind erosion in the equatorial and mid-latitude regions of Mars, J. Geophys. Res., V. 78, pp/ 4123-4138.
- Neukum, G. and D. Wise, 1976, Mars: A standard curve and a possible new time scale, Science, V. 194, pp. 1381-1387.
- Scott, D.H., M.H. Carr, 1978, Geologic map of Mars, U.S. Geol. Survey, Misc. Inves. I-1083.
- Shoemaker, E.M., 1977, Astronomically observable crater-forming projectiles, in Impact and Explosion Cratering, D.J. Roddy, R.O. Pepin, R.B. Merrill, eds., Pergamon Press, pp. 617-628.
- Soderblom, L.A., C.D. Condit, R.A. West, B.M. Herman and T. J. Kreidler, 1974, Martian planet-wide crater distributions-implications for geologic history and surface processes, Icarus, V. 22, pp. 239-263.
- Solomon, S.C. and J. Chaiken, 1976, Thermal expansion and thermal stress in the moon and terrestrial planets: Clues to early thermal history, Proc. 7th Lunar Sci. Conf., V. 3, pp. 3229-3243.
- Toksöz, M.N. and A.T. Hsui, 1978, Thermal history and evolution of Mars, Icarus, V. 34, pp. 537-547.

Wetherill, G.W., 1975, Late heavy bombardment of the moon and terrestrial planets, Proc. Lunar Sci. Conf. 6, pp. 1539-1561.

Wise, D.U., M.P. Golombek, and G.E. McGill, 1979, Tharsis province of Mars-Geologic sequence, geometry and a deformation mechanism, Icarus, in press.

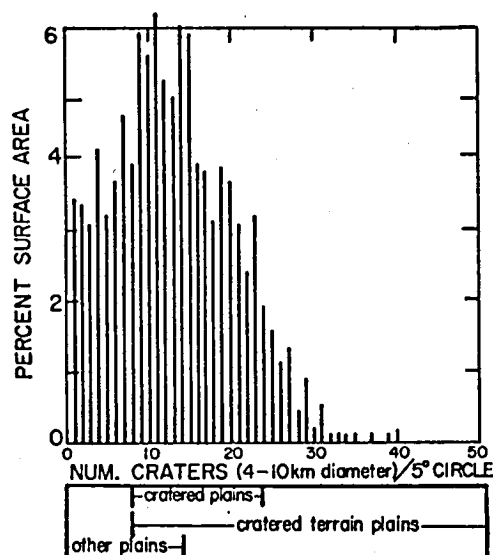


Fig. 2A

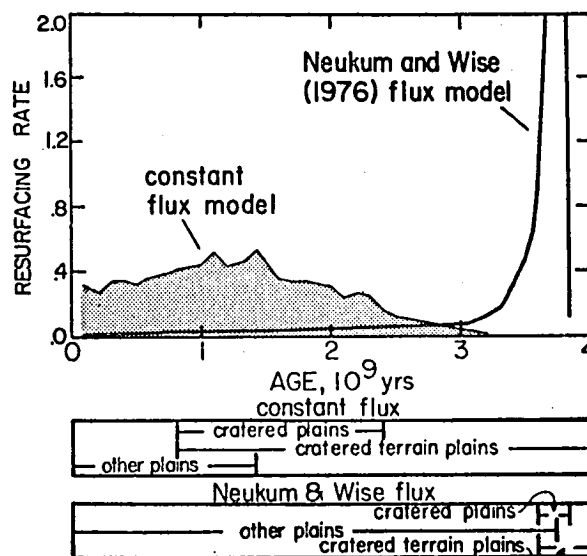


Fig. 2B

Figure 2 - The left-hand graph (Fig. 2A) illustrates the present area occupied by various crater abundances, for craters 4-10 km in diameter. The data is for regions with $\pm 30^\circ$ in latitude about the equator, where volcanic landforms are dominant. The peak in surface area corresponds to crater abundances where plains within cratered terrain, the cratered plains, and other plains, overlap. The right-hand graph (Fig. 2B) indicates the rate of resurfacing (percent area/billion years) versus time, based on a constant cratering rate model and on the Martian cratering history of Neukum and Wise (1976). The constant flux model is consistent with volcanic activity peaking between 1 to 1.5 billion years ago, while the Neukum and Wise (1976) model requires 75% of the surface to have formed between 3.5 to 4.0 billion years ago.

TIME SEQUENCE OF MARTIAN GEOLOGIC FEATURES

Hiller, Konrad, and Neukum, Gerhard, Institut für Allgemeine und Angewandte Geologie, Ludwig-Maximilians-Universität, 8000 München 2, W-Germany

From our own work and that of other groups we have compiled crater count data of a variety of geologic features on Mars. Our aim is to establish a time sequence of the main activities like volcanism, erosion and to some extent tectonism.

We have classified the volcanic constructs in a scheme based primarily on location and also morphology rather than petrological criteria (Plescia & Saunders, 1979). Five groups were separated and named after one characteristic volcanic construct of the area:

The Tyrrhena group includes Tyrrhena Patera, Hadriaca Patera and Tempe Patera (feature at 62°W, 44°N named by Plescia & Saunders, 1979). This group comprises intensely channelled, low and broad constructs that are located in the highlands.

Members of the Elysium group are volcanoes of the Elysium province with Elysium Mons, Hecates Tholus, and Albor Tholus. Apollinaris Patera is included because of proximity and morphological similarity although not directly part of this region.

The Uranus group covers the small size volcanic constructs of the Tharsis province like Uranus Tholus, Uranus Patera, Ceraunus Tholus, Ulysses Patera, Tharsis Tholus, Biblis Patera, and Jovis Tholus.

The prominent Tharsis shield volcanoes Olympus Mons, Ascraeus Mons, Pavonis Mons, and Arsia Mons set up the Olympus group.

Alba Patera although located at the edge of the Tharsis bulge and despite its close connection to the development of this region (Wise et al., 1979) was set aside as an own group because of its unique morphology/size/age characteristics.

The following periods of activity of the different groups can be deduced from fig. 1:

<u>Crater Frequency</u>	<u>total(10^{-6}km^{-2})</u>	<u>main activity(10^{-6}km^{-2})</u>
Tyrrhena group:	17000-4000(1100)	10000-6000
Elysium group:	10000-1000	6000-2000
Uranus group:	10000- 600	4000-1700
Olympus group:	1000- 60	600- 130
Alba Patera:	2000- 170	2000- 300

Examining the times of main activity in the individual group one could speculate on a time-versus-area correlation but the data are much too scarce to prove this idea at present time.

Data from Fig. 1, Wise et al. (1979) and Hiller & Neukum (1979) are displayed in a rough and qualitative manner in Fig. 2. Data for the erosional features are from a compilation by Hiller & Neukum (1978). For the better comparison of the different time sequences an absolute age scale, an updated version of Neukum & Wise (1976) was used. On the basis of the Soderblom chronology (Soderblom et al., 1974; Soderblom, 1977) ages younger than $3.8 \cdot 10^9$ years would differ substantially. But this discrepancy affects all data in the same way and therefore is of no importance for the comparison of a number of individual time sequences.

Fig. 2. shows that the area of crust formation and early tectonism ($>4.1 \cdot 10^9$ years ago) was followed by a period of intense activities of every kind. During this unique time span (between 4.0 and $3.3 \cdot 10^9$ years ago) endogenic activities like the emplacement of the vast plains lavas, the construction of volcanoes in several regions and of different morphology/chemistry, and the fracturing of Tharsis as much as exogenic effects like the retreat of the scarp bordering the highlands in the north and the erosion of channel systems occurred. It seems to be likely that some kind of a global process caused this time of hyperactivity.

After those events basically only the shield volcanism of the Tharsis region continued until very recent times (recent in any current absolute age model).

References: Blasius K.R. (1976) *Icarus* 29, pp 343; Carr M. (1976) *NASA TMX* 3364, pp 152; Carr M. et al. (1977) *JGR* 82, pp 3985; Crumpler L.S. and Aubele J.C. (1978) *Icarus* 34, pp 496; Hiller K. & Neukum G. (1978) *NASA TM* 79729, pp 91; Hiller K. & Neukum G. (1979) *NASA TM* 80339; Malin M.C. (1976) *JGR* 81, pp 4825; Masursky H. et al. (1977) *JGR* 82, pp 4016; Neukum G. & Wise D.U. (1976) *Science* 194, pp 1381; Neukum G. et al. (1977) *NASA TM* 79729; Plescia J.B. & Saunders R.S. (1979) *subm. LPSC* 10th; Squyres S.W. (1978) *Icarus* 34, pp 600; Wise D.U. et al. (1978) *NASA TM* 79729; Wise D.U. et al. (1979) *Icarus* 38, pp 456.

AGES OF MARTIAN VOLCANOES

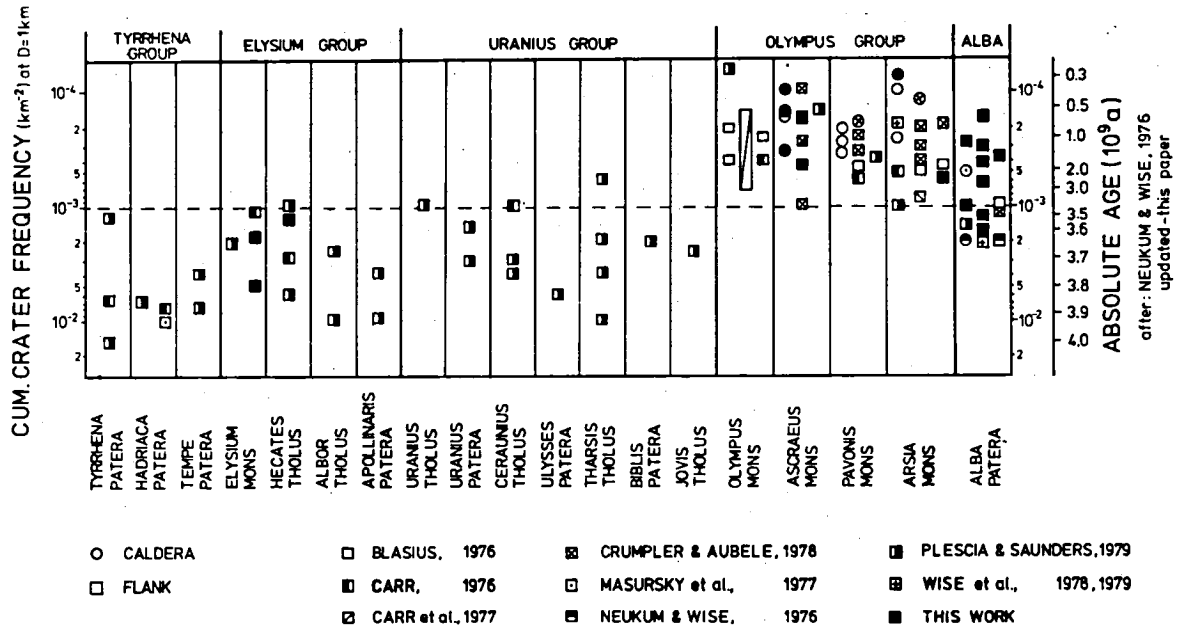


fig. 1

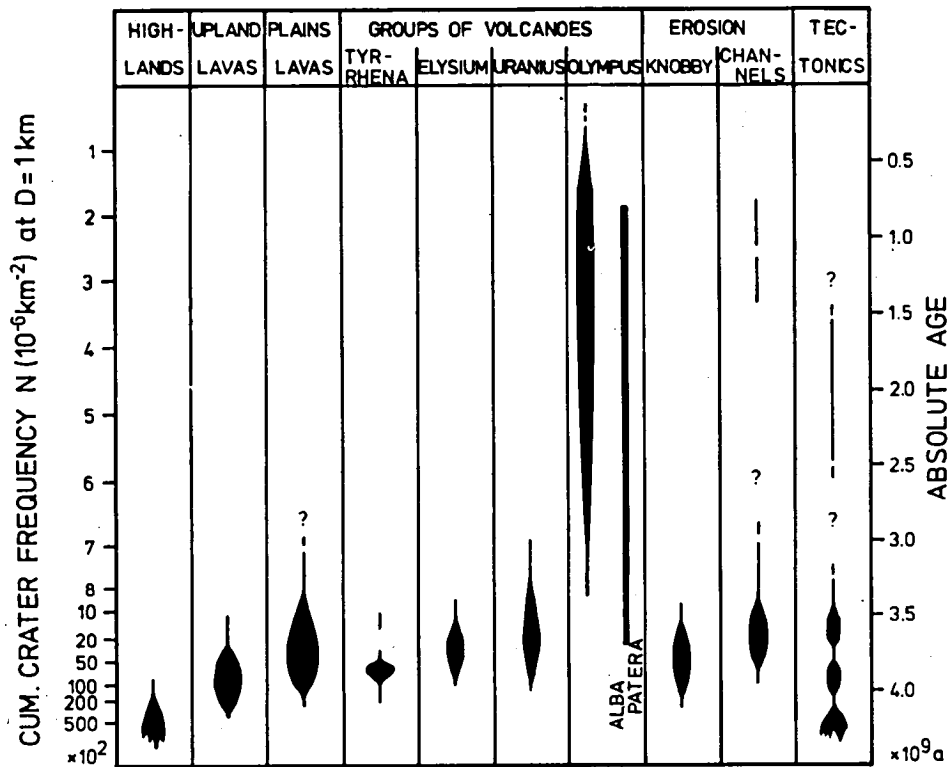


fig. 2

DATING METHODOLOGY OF SMALL, HOMOGENEOUS CRATER POPULATIONS APPLIED TO
THE TEMPE-UTOPIA TROUGH REGION OF MARS

Donald Wise and George Milkowski, Dept. of Geology/Geography, Univ. Mass,
Amherst, MA 01003

Within the Loyal Order of Crater Observers (LOCO), a long philosophic battle has been waged. One group prefers to lump data over large areas to build a massive statistical base. The other prefers to make more subtle distinctions on small geologic map units and work around the statistical limitations of the resulting small populations. Widespread misunderstandings of the precisions inherent in this second method continue to exist, even among many who use it. This paper is an attempt to demonstrate the possibilities of this technique on a small and relatively simple area of Mars. This area, a lowland trough, lies between the Tempe Plateau and Utopia Patera regions of Mars. The trough materials show little faulting and lie unconformably across Tempe and Utopia terrains having several intensities of fault development. Peeking through both these terrains are small patches and/or larger crater remnants of still older terrains. The geologic map pattern is one of "islands" of older units of several ages and scales projecting through "oceans" of several ages of younger fill. Crater counts lumping of many of these "islands" and "oceans" into a single cumulative crater plot would inevitably produce an irregular curve with bumps and variable slopes depending on the extent to which the several ages of surfaces entered into the total statistics.

For a geologic unit of given age, craters smaller than some minimum size are obliterated by erosion or covered by younger units. Thus, of the total population of craters produced on that surface only the large size segment of the total production curve retains a memory of the age of that geologic unit. The method is to select and outline areas with relatively homogeneous crater density in some size range. The resulting crater curve in that size range should be related to the age of that geologic map unit with a minimum of dilution of the curve by older or younger crater populations. For the present study approximately 50 homogeneously cratered small areas were outlined and counted. The cumulative curves, corresponding to the crater size ranges on which the homogeneity of the areas was originally defined, are presented in Fig. 1. The method requires that data from many curves of various size ranges be brought to a common base, usually the 1 km intersection. By using this method of small areas of homogeneous populations for Mariner data, Neukum and Wise (1976) cobbled together an approximation of a standard production curve for martian craters (Fig. 1). This curve is then used to project data from the preserved crater sizes on any geologic unit to a 1 km intersection. It has been pointed out to us that real crater curves are far more variable than the standard curve, that variable secondary craters so dilute the smaller size data as to make the curve worthless, and that the curve flattens markedly below a half km (personal communications, Anonymous, 1976, 1977, 1978, 1979). The reader can judge from Fig. 1 the appropriateness of these comments to this area.

The size range of homogeneously cratered small areas are contrasted with their crater numbers or ages in Fig. 2. For a given age a veil with approximate slope of +1 obscures craters below a certain size. The slope of this veiling curve is an indicator of average rates of erosion or of burial in this region of Mars. Areas with greater than average thickness of covering units truncate their data somewhat to the right of the veiling line. From the plot it is clear that dates representative of any given crater number are preserved only in craters above some given diameter range. Fig. 2 also shows clusterings of crater numbers in the vertical dimension, the most obvious being in the 2500-3000 range. All of the lines of Fig. 2 can be projected to the left of the figure and their distribution smoothed by a running average to produce Fig. 3. Checking the peaks of Fig. 3 against the geologic map units from which the numbers were derived shows that the 2500 unit dates the lightly faulted plains unit of the Tempe-Utopia trough. Clusters of crater numbers around values of 5000 represent heavily fractured terrain beneath the regional unconformity, indicating that a major faulting episode took place between about 3000 and 5000. Several older units appear to be extensions of the type Lunae Planum area and show even higher intensity of faulting. In this type Lunae Planum, other studies by us suggest there are three ages of units commonly lumped into the term "Lunae Planum". We refer to them as Lunae Planum A, B, and C or old, middle, and young. There, they yield approximate ages of 20,000, 10,000 and 5,000. In the Tempe-Utopia trough these same numbers appear for older units which we correlate with Lunae Planum units. Caution is needed in interpreting times of faulting in that nearby areas have intense fractures of about 1000 and 5000-10,000.

The methods described above provide a numerical framework for dating major depositional and structural events. Typical error bars on curves of individual small areas suggest ranges of values within a factor of 2 but it is highly debatable just what the tradition $\pm\sqrt{n}$ really signifies. The requirement of finding homogeneously cratered areas commonly limits crater populations to small exposures of geologic units with 50(\pm 30) significant craters. With these minimal statistics no great faith can be attached to the crater age for any single small area. However, a recurring age for different small outcrops of the same geologic unit significantly increases the probability that this recurring age approximates the correct one. The statistics might be improved in this method by lumping all the dates near 2500 into a composite curve but the range of dates to be combined is an arbitrary decision which would be reflected in a changed slope of the final curve. There is probably more loss and smearing of data by that method than by the method of smoothing the results with a running average as done in Fig. 3 to obtain the typical crater number range of the best preserved, most widespread geologic units.

Doing this type of dating requires that the geologic analyses be done with very close linkage to the crater measurements. One must look back at each area to ask why its curve looks the way it does, what survivor craters and what cover are present. Little reliance can be placed on any single crater

plot. Instead the cumulative effects of small segments of the best data must stand as the most likely ages of major units and events. The method is tedious but it permits a dating finesse linked to specific units not readily obtainable with "broad brush" lumping statistics.

Reference: Neukum, G. and D. Wise, 1976, Mars: A standard crater curve and possible new time scale, Science, 194, p. 1381-1387.

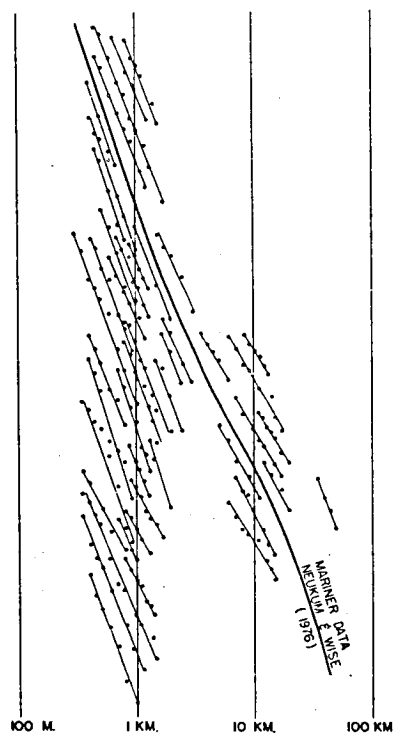


Fig. 1 (above). Slopes of cumulative crater curves for size ranges used to define homogeneously cratered small areas in the Tempe-Utopia region. Vertical scale same as horizontal scale but position arbitrary.

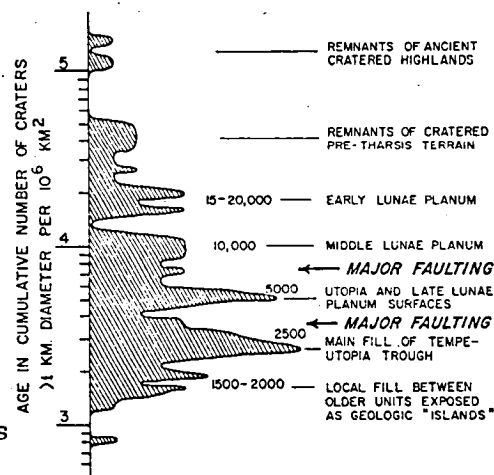
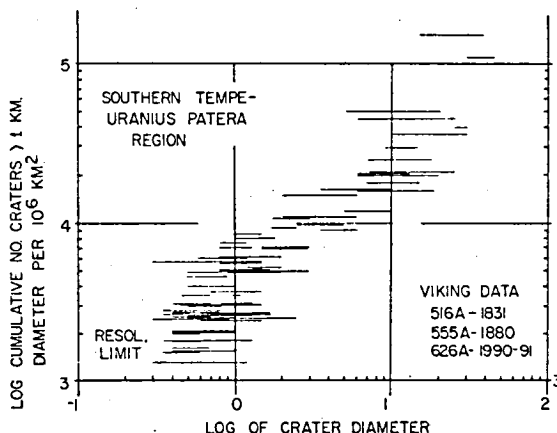


Fig. 2 (right top). Crater number or age versus diameter range of homogeneously cratered populations in the Tempe-Utopia region. Data are resolution limited at 300-500 meters.

Fig. 3 (right bottom). Histogram of the frequency of crater numbers from the Tempe-Utopia trough region (Fig. 2) smoothed by a running average.

METEOROID IMPACT INTO SHORT-PERIOD COMET NUCLEI-I: THE PROCESS

Cintala, Mark J., Dept. of Geological Sciences, Brown Univ., Providence, RI 02912.

A number of approaches to the problem of evaluating collision rates lead to the conclusion that the impact flux is significantly higher in the asteroid belt than in the sunward regions of the Solar System.^{1,2} Among the consequences of the higher impact flux should be more rapid mixing of asteroid regoliths³ and shorter collisional lifetimes of bodies within this volume of space.² The purpose of this study is to investigate the effects which such an impact environment might have on the nuclei of short-period comets.

The Comet Nucleus - If comet nuclei were accreted through the action of their own gravitational fields, the probability of negligible internal heating (e.g., through radioisotopic decay) should have left them with substantial porosity and meager intrinsic strength. Spectroscopic and photographic observations point to H₂O ice as a major cometary constituent, along with minor quantities of other volatiles,⁴ and it is probable that nonvolatile (i.e., at ~300 K) solids comprise an important mass fraction of these objects.⁴ Various deduced, estimated, and/or calculated physical properties of these bodies allude to characteristics grossly similar to those of terrestrial snow (Table 1). Comet nuclei are small by planetary standards, ranging from a few to tens of kilometers in diameter;⁵ it is possible that very rare nuclei approach dimensions on the order of 100 km.^{5,6} This paper assumes a model short-period comet nucleus with physical properties similar to those of H₂O snow confined to an orbit totally within the asteroid belt.

Meteoroid Impact into Comet Nuclei - Numerous experiments designed to study the phenomenology of fragment impact into snow have been performed, revealing that such events result in craters characterized by larger depth/diameter ratios and little lateral excavation, with the projectile ultimately located at or near the apex of the crater.⁷ Swinzow⁸ has provided penetration depths for 0.55 cm metal cubes (steel, aluminum, and a hybrid) into snow ($\rho = 0.41 - 0.42 \text{ g/cm}^3$) at relatively low impact velocities ($\lesssim 1.3 \text{ km/s}$). A least-squares fit to his data ($n = 22$) gives

$$L/d = 0.2\rho_o^{1.045} V_1^{0.349} \quad (1)$$

where L is the depth of penetration, d and ρ_o are the projectile length and density, respectively, and V_1 is the impact velocity, all in CGS units; this fit has a standard error of estimate of ± 0.0054 , from an initial expressions of the form $\log_{10} x = \log_{10} a + b \log_{10} y + c \log_{10} z$. The cumulative flux per cm^2 per second used here is that given by Housen et al.,³ viz.,

Cintala, M.J.

$$N = km^\alpha = 4.74 \times 10^{-17} m^{-0.833} \quad (2)$$

where m is the projectile mass in grams. Use of this equation in evaluating the mass flux $[\phi(t)]$ between the limits M (largest meteoroid which can be stopped by the nucleus) and m_0 (smallest particle which can be retained against devolatilization-induced gas drag) yields

$$\phi(t) = \frac{k\alpha}{\alpha+1} (m_0^{\alpha+1} - M^{\alpha+1}) \quad (3)$$

If the rate of change of radius (λ) of the idealized spherical nucleus due to volatile loss were constant, its time-dependent surface area would be

$$A(t) = 4\pi R_c^2(t) = 4\pi(R_0 - \lambda t)^2 \quad (4)$$

where R_0 is the initial radius. The total mass of debris acquired by the nucleus from time 0 to the time of total devolatilization T would then be given by

$$M_T = \int_0^T \phi(t) A(t) dt \quad (5)$$

Taking for m_0 Whipple's⁹ expression for the largest particle that can be ejected from a nucleus through gas drag, a perihelion distance of 2.0 A.U., a devolatilization rate of 2.8×10^{-6} cm/s and a final (volatile-free) nuclear radius of $0.07 R_0$ (both derived from estimates of Sekanina⁵), an average impact velocity of 5 km/s,² and using eq. (1) to establish M , eq. (5) becomes

$$M_T = 3.5 \times 10^{-10} (0.139 R_0^{3.501} - 1.204 \times 10^3 R_0^{2.499}) \text{ [grams]} \quad (6)$$

Total Accumulated Mass - The results of eq. (6) for nuclei of various initial radii are illustrated in Fig. 1; also presented is the total accumulated mass normalized to that of the cometary solids (assumed $\rho = 3.0$ g/cm³) remaining after devolatilization. While the values for the latter might seem small, they are brought into perspective by noting that the lunar maria comprise only $\sim 4 \times 10^{-5}$ to 4×10^{-4} of the total lunar mass.^{10,11} The final surface area of the nucleus can be used to determine the average mass accumulated per final unit area, giving

$$\mu = 5.85 \times 10^{-9} (0.139 R_0^{1.501} - 1.204 \times 10^3 R_0^{0.499}) \text{ [gms/cm}^2\text{]} \quad (7)$$

This can be translated into an effective surface layer thickness $h(p)$ by

$$h(p) = \frac{\mu}{\rho(1-p)} \text{ [cm]} \quad (8)$$

where p is the porosity of the surface layer. The results of eq. (8) for various initial nuclear radii and surface layer porosities are illustrated in Fig. 2.

Associated Processes - As the duration of a comet's residence in the asteroid belt grew, the nucleus would suffer a steadily increasing num-

Cintala, M.J.

ber of impacts. Concurrent loss of ejecta from these events along with solar irradiation-induced volatilization would decrease the dimensions of the nucleus. The accumulated projectiles (and fragments derived from them by spallation during their penetration) would eventually re-surface and, provided they were sufficiently large to resist ejection by gas drag, would remain there unless removed by a subsequent impact event. These fragments would complement the role of original cometary solids in insulating the remaining volatile reservoir,⁹ thus reducing cometary activity. Finally, the completely devolatilized core would consist of original cometary matter (of as yet uncertain composition), coated with a regolith rich in foreign (i.e., added) material.

References: ¹Anders E. (1975) *Icarus* 24, 363-371. ²Chapman C.R. and Davis D.R. (1975) *Science* 190, 553-556. ³Huelsen K.R. et al. (1979) *Icarus* 39, 317-331. ⁴Whipple F.L. (1977) In *Comets, Asteroids, Meteorites: Interrelations, Evolution, and Origins*, A.H. Delsemme, ed., The Univ. Of Toledo, pp. 51-56. ⁵Sekanina Z. (1971) In *Physical Studies of Minor Planets*, T. Gehrels, ed., NASA SP-267, pp. 423-428. ⁶Roomer E. (1966) *Mem. Soc. Roy. Sci. Liège, Ser. 5, 12*, 21-28. ⁷Johnson P. R. (1977) U. S. Army Cold Regions Res. Engin. Lab. Report 77-6, 29 pp. ⁸Swinzow G.K. (1977) In *Proc. Fuse/Amun./Environ. Sym.*, Battelle Mem. Inst., Dayton, Ohio. ⁹Whipple F.L. (1951) *Astron. J.* 113, 464-474. ¹⁰Horz F. (1978) *Proc. Lunar Sci. Conf. 9th*, 3311-3331. ¹¹Head J.W. (1975) In *Origins of Mare Basalts and Their Implications for Lunar Evolution*, Lunar Sci. Ins. (Houston), pp. 61-65.

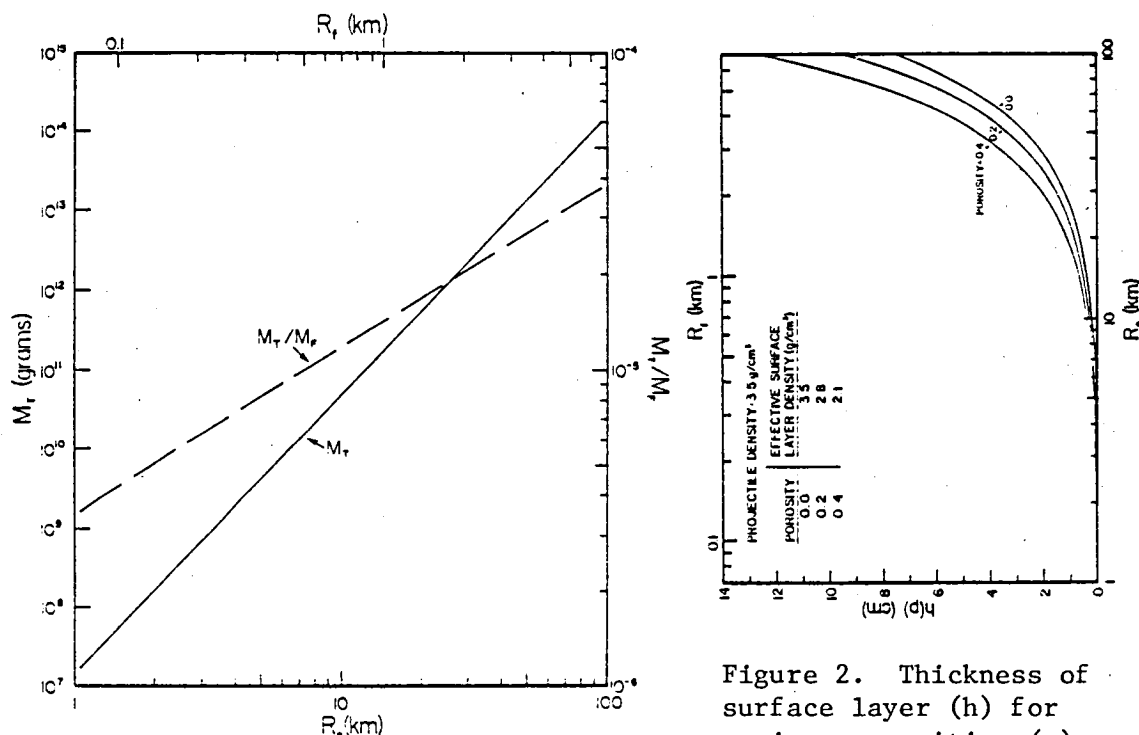


Figure 1. Total mass (M_T) accumulated by a short-period comet as a function of initial (R_0) and final (R_f) nucleus radii. M_f is the final devolatilized nucleus' mass.

Figure 2. Thickness of surface layer (h) for various porosities (p) as a function of R_0 and R_f , assuming that the layer consisted only of debris collected by the nucleus from the asteroid belt.

METEOROID IMPACT INTO SHORT-PERIOD COMET NUCLEI-II: THE RESULTS

Cintala, Mark J., Dept. of Geological Sciences, Brown Univ., Providence, RI 02912

In part I of this study it was shown that, provided H₂O snow can be taken as a reasonable approximation to the impact behavior of material comprising comet nuclei, short period comets (which generally spend a large fraction of each orbital period within the asteroid belt; see Table 1) would collect significant quantities of asteroidal debris as a result of collisions with meteoroids. Among the results of this process would be (1) a favorable environment for the formation of polymict brecciated meteorites, (2) regoliths with non-unique reflectance spectra, and (3) a reasonably gentle mechanism by which meteorites could be placed into Earth-crossing orbits.

Polymict Brecciated Meteorites - Polymict brecciated meteorites in terrestrial collections have been attributed to low-velocity collisions between asteroids and meteoroids, such that fragments of the projectile are incorporated into a groundmass of target material.^{1,2} Insofar as low velocity impacts should occur in the asteroid belt, this is a reasonable suggestion. A burned-out comet nucleus with a multicomponent regolith, however, could also act as a source of such meteorites. By direct analogy with lunar polymict breccias,³ shock lithification of a variegated target on a devolatilized nucleus would yield indurated fragments without requiring projectile incorporation into the final product. Fine-grained material can be compacted irreversibly and lithified by shock stresses between ~20 to 100 kbar.^{4,5} Since these shock intensities are realized at expected asteroidal impact velocities, considerable volumes of such a regolith could be lithified as a natural consequence of the evolution of a former comet nucleus (Fig. 1). Subsequent removal of such breccias from the parent body would thus make them candidate meteorites, particularly if the initial orbit were Earth-crossing.

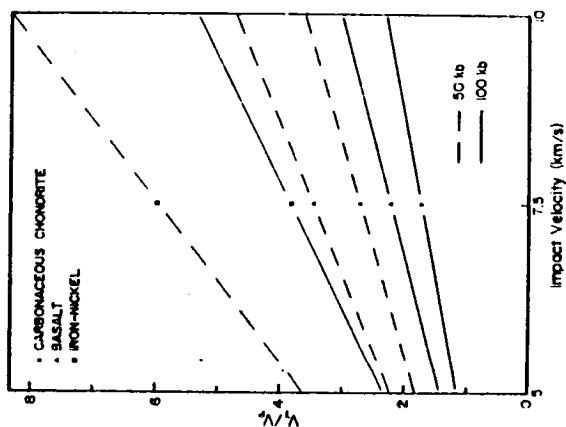
Reflectance Spectra of Apollo and Amor Asteroids - For dynamical reasons, Apollo (Earth-crossing) and Amor (Mars-crossing) asteroids are often interpreted to be the devolatilized cores of former short-period comets.^{6,7} While primordial cometary solids are usually considered to be carbonaceous chondritic in composition, the fraction of the known Apollo asteroids which exhibit "C-type" spectra is small.⁷ Instead, the studied Earth-crossers are, for the most part, characterized by "S-type" spectra,^{8,9} which are generally interpreted to be indicative of silicate and/or silicate-metal assemblages.^{8,9,10} A definitive match between this broad spectral type and a single known meteorite composition, however, has not yet been established.⁹ A regolith of compositionally random debris admixed with original cometary "dust," on the other hand,

METEOROID IMPACT INTO SHORT-PERIOD COMET NUCLEI-II: THE RESULTS

Cintala, M.J.

would exhibit a distinctive reflectance spectrum in the sense that no correlation with a single meteorite type would be found. Thus, the difficulty in finding agreement between telescopic and laboratory spectra could be indicative of the multicompositional nature of the surfaces of these bodies. It is noted that this process could also apply to bodies which are now classified as main belt asteroids; spectral "mixing models" might provide information regarding the validity of this hypothesis.

Comet-Meteorite Orbital Relationships - Orbital and dynamical investigations of fireballs favor some relationships between short-period comets and meteoroids.¹¹ While suggestions have been made regarding the cometary origins of meteorites,¹² doubt has been cast upon these hypotheses due to strong chemical and petrologic arguments to the contrary.¹³ These difficulties can be avoided if the meteoroids were acquired by the comets during their passages through the asteroid belt. Even if the material comprising the nuclei had shock behavior similar to solid H₂O ice,¹⁴ basalt-like (i.e., stony) meteorites would suffer minor damage at the expected impact velocities (Fig. 2), which is consistent with that exhibited by a large fraction of the sampled stony meteorites.¹⁵ Insofar as minor heating of meteoroids should occur at these shock stresses, it is expected that loss of rare gases would be minimal. While some investigators have expressed concern over a nucleus' ability to rid itself of sizeable particles by gas drag during periods of devolatilization,⁶ Figure 3 illustrates that substantial chunks of solid debris can be ejected by this process,¹⁶ thus placing them into independent orbits. Since the active lifetimes of short-period comets are so brief in comparison to meteorite exposure ages,¹⁵ this mechanism should be consistent with cosmic ray data.



References: Wilkening L.L. and Clayton R.W. (1974) *Geochim. Cosmochim. Acta*, 38, 937-943. Wilkening L.L. (1977) in (17), 389-396. Simonds C. S. (1977) *Am. Jour. Sci.*, 273, 428-439. Ahrens T.J. and Cole D.M. (1974) *Proc. Lunar Sci. Conf.*, 2th, 2, 2333-2345. Kieffer S.W. (1975) *The Moon*, 11, 301-320. Matherill G.W. (1978) in (18), 17-39. Shoemaker E.M. and Selin C.F. (1978) in (18), 161-173. Gaffey M.J. and McCord T.B. (1977) in (17), 199-218. Zellner B. and Rowell E. (1977) in (17), 183-197. Chapman C.R. (1976) *Geochim. Cosmochim. Acta*, 40, 701-719. Matherill G.W. (1974) *Ann. Rev. Earth Planet. Sci.*, 2, 303-321. Spik E.J. (1966) *Adv. Astron. Astronnav.*, 2, 301-336. Anders E. (1971) in *Physical Studies of Minor Planets*, T. Gehrels, ed., NASA SP-267, 429-440. Anderson G.D. (1968) *U.S. Army Cold Regions Res. Eng. Lab. Research Report 237*, 50 pp. Anders E. (1964) *Space Sci. Rev.*, 1, 583-714. Whipple F.L. (1951) *Astron. J.*, 112, 464-472. Delamere A.W. (1977) *Comets, Asteroids, Meteorites: Interrelations, Evolution, and Origins*, The Univ. of Toledo, 587 pp. Gehrels T. (1971) *Physical Studies of Minor Planets*, NASA SP-267, 687 pp.

Figure 1. Volumes of fragmental target material (V_T) which would be subjected to shock stresses sufficient to cause lithification during the impact of various projectile types. V is the projectile volume.

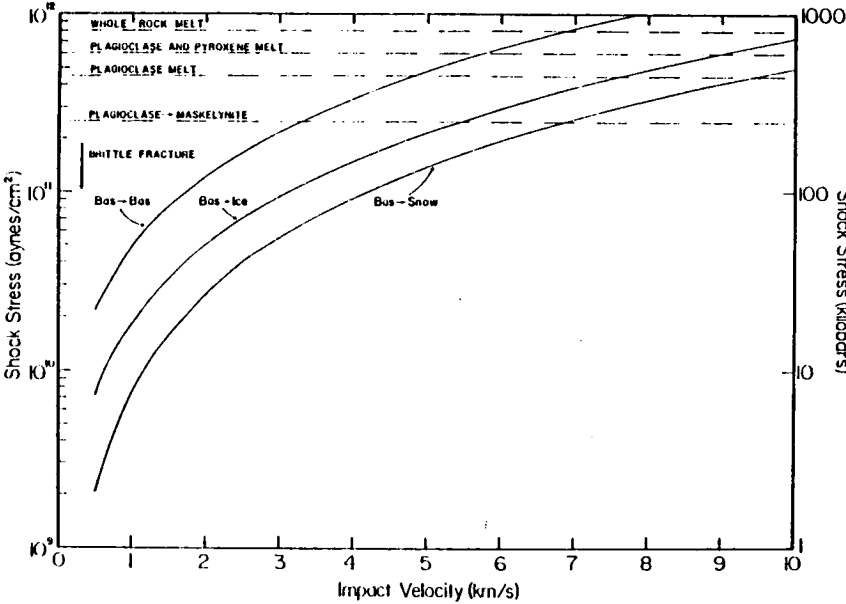


Figure 2. Shock stresses expected for stony projectiles impacting H₂O snow and ice (v_{comet}) and basalt (v_{asteroid}) targets. Stresses at which the indicated petrographic effects would obtain are from Schaal and Hörz (1977) PLSC 8, p. 1697.

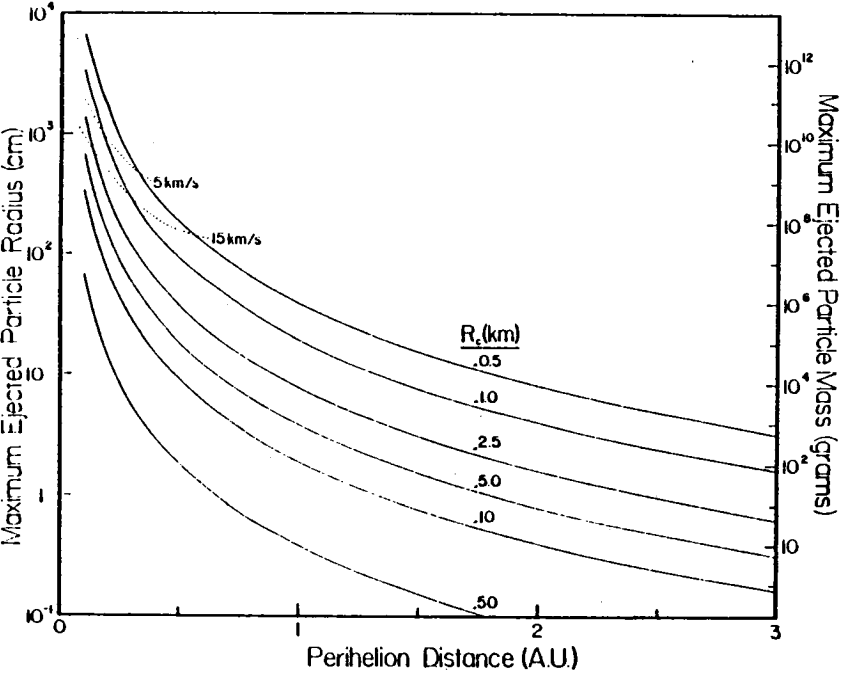


Figure 3. Sizes and masses of stony fragments which could be removed by gas drag from comet nuclei of various radii (R_c) as a function of perihelion distance. Dotted lines represent the largest particles that can be stopped by the nuclei at the indicated impact velocities.

Comet	Period (years)	q (A.U.) ^a	Eccentric Anomaly at 2.2 A.U. (radians)	Fraction of Period spent beyond 2.2 A.U.
Encke	3.30	0.34	1.559	0.772
Encke-Winnecke	6.04	1.04	1.509	0.851
D'Aleut	6.87	1.32	0.923	0.865
Brooks	6.94	1.87	0.621	0.892

^a2.2 A.U. is taken to be the inner limit of the asteroid belt. From (14).

Chapter 4

GEOCHEMISTRY, VOLATILES, AND REGOLITH

Comparison of the volatile inventories of Mars, the Earth, and Venus imply that their atmospheres are derived almost entirely from the release of volatiles contained in the material that formed these bodies, rather than from gases captured from the solar wind or primordial nebula subsequent to planet formation or from the impact of volatile rich asteroids and comets. In order to understand the increase in the amount of non-radiogenic rare gases from the Martian to the Venus atmosphere, it is necessary to postulate that rare gases were incorporated into planet forming grains at times when there was a large pressure gradient in the solar nebula, but that the temperature gradient was small.

The volatile inventories have been fit quantitatively with a model that allows for pressure difference in the solar nebula and differences in the efficiency of outgassing at early and later epochs. The division of volatile release into two different periods corresponds to release during accretion and global internal differentiation on the one hand and more local volcanism on the other hand, by analogy to lunar chronology. All major volatiles, except for radiogenically derived gases such as ^{40}Ar , are entirely available for release during the early epoch. In the case of Mars, we find efficiencies for early and late outgassing of about 1/10 and 1/20 of that for the Earth. Hence, Mars' small inventory of rare gases is due in part to pressure differences in the nebula and in part to a less efficient outgassing. Altogether, Mars outgassed about 2 bars of CO_2 , 100 mb of N_2 , and 100 meters of H_2O .

Absolute age dating for the Moon and relative age dating of the Moon and Mars imply that the early epoch of outgassing, when most of Mars' volatile inventory was released, occurred during the first billion years of its history. Additional juvenile volatiles were released episodically in association with major igneous events. In contrast to the Earth, there has been little recycling of volatiles between the atmosphere and crust. Hence, the atmospheric pressure of Mars has more or less monotonically declined with time.

At an intermediate epoch when the atmospheric mass was still quite large (~ 1 bar of CO_2) and the solar luminosity was somewhat larger than its initial value, a strong greenhouse effect may have occurred, which generated the numerous water carved gullies. But such a clement condition may have accelerated the loss of the atmosphere due to an enhanced rate of both fine grained regolith formation and carbonate rock formation. At the present epoch the atmospheric pressure is sufficiently low so that the quasi-periodic exchange of gas between the atmosphere and regolith, driven by obliquity oscillations, results in a strong modulation of dust storm activity on a time scale of 10^5 - 10^6 years, thus leading to the formation of layered terrain in the polar regions.

MARS ATMOSPHERE-REGOLITH SIMULATION EXPERIMENT

Saunders, R.S., Fanale, F.P. and Stephens, J.B., Jet Propulsion
Laboratory, 4800 Oak Grove Drive, Pasadena, California 91103

We have designed, fabricated and tested the Mars Atmosphere-Regolith Simulation Chamber. We have designed, fabricated and tested an Aeolian Clay (Air) Classifier System which is currently being used to fill the chamber with dried 1μ to 10μ montmorillonite clay. This classifier is the subject of a new Technology Report and may be patented by NASA in the future.

We intend to study the rate at which CO_2 penetrates the regolith in response to variations in atmospheric pressure in order to determine whether or not the regolith could buffer the atmospheric variations in pressure on a seasonal time scale. We intend to also do analogous experiments with inert gases in order to evaluate the importance of adsorption of CO_2 on the cold simulated Mars regolith, and the effect on the rate of CO_2 permeation of the soil. The chamber is instrumented in such a way that any thermal effects of atmosphere-regolith exchange may be evaluated, and has been designed to minimize wall thermal effects. Later we will study the effect of any CO_2 - regolith interaction on possible water vapor migration within the regolith and exchange between the atmosphere and the regolith. We are considering possible application to other areas such as frost formation if the first series of experiments proves to be fruitful.

We have initiated a cooperative effort with University of California at Irvine to parametrically calibrate their computer model for soil heat transfer and gas diffusion. This calibrated model will allow computer modeled interpolation of martian soil properties and behavior within the boundaries of the experiment parametric space.

VOLATILE LOSS AND THERMAL STABILITY OF MARTIAN ANALOG CLAY AND SULFUR MINERALS

Gibson, Everett K., SN7, Geochemistry Branch, NASA-JSC, Houston, TX 77058
Urbancic, Mike A., Chem. Dept., U. of Illinois, Urbana, IL and
Andrawes, Fikry F., Lockheed Electronics Co., Inc., Houston, TX.

The bulk chemical composition of the Martian surface materials at the VI and V2 sites is consistent with a mixture of the Fe-rich clay minerals and magnesium sulfate or the isochemical equivalent of such a mixture (Clark et al., 1976, 1977; Baird et al., 1976; Toulmin et al., 1977). It has been suggested (Gooding, 1978; Gooding and Keil, 1978; Clark, 1978, 1979) that processes operate within the Martian regolith for the formation of clay and sulfur-bearing minerals. In order to determine the nature of the thermal stabilities and volatile release profiles of candidate minerals present in the Martian regolith along with developing the data base of mineral stabilities which can be used in the design of future flight experiments, we have measured the thermal stability and volatile release profiles of analog clay and sulfur-bearing minerals.

Mineral samples were studied using thermogravimetric analysis (TGA) techniques in which samples were heated at controlled rates under atmospheres including N₂, CO₂ and air and pressures from 760 to 10 mm. The identity of the decomposition products were made from comparisons with previously determined gas release profiles for the same suite of minerals using mass spectrometry or gas chromatography.

Clay minerals: Clay minerals studied were the following: montmorillonite, nontronite, bentonite, kaolinite and dickite. Thermal stability curves for these minerals are given in Figs. 1-6.

a. Montmorillonite and nontronite clays: The montmorillonite clay was the American Petroleum Institute (API) reference clay #27 (Fig. 1). At temperatures below 150°C, adsorbed water was lost from the clay. At 600°C, structural water was lost. No significant differences were noted in the thermal stability of the clay sample at 1 atm. N₂ or CO₂. Nontronite clay from Allentown, PA (obtained from Ward's Scientific) was found to lose between 14.7 and 20.0% adsorbed water upon heating to 150°C under N₂ and CO₂ respectively (Fig. 2). Greater water loss occurred below 150°C for samples studied under N₂. Loss of structural water from the nontronite began to occur at 400°C (200° lower than for the montmorillonite clay). It appears that the addition of iron to the montmorillonite clay structure causes the loss of structural water to occur at a lower temperature. In order to examine the water vapor adsorption characteristics of nontronite, a sample which had previously been heated to 1000°C was exposed to the Houston humidity for 6 days and reexamined (Fig. 3). The heated sample gained 15.0% by weight adsorbed water. This observation is consistent with the previous observation of Fanale and Cannon (1979) regarding the water adsorption properties of nontronite.

b. Bentonite, dickite and kaolinite clays: Thermal stability curves for the 3 API reference clays bentonite, dickite, and kaolinite are given in Figs. 4-6. It is obvious that dickite and kaolinite clays do not adsorb

large quantities of water which the montmorillonite, nontronite and bentonite clays adsorb. Quantities of structural water lost in the temperature interval 400-600°C (10.2 to 14.3%) are greater than that noted for montmorillonite, nontronite and bentonite clays. These differences reflect structural differences between the clay types. Dickite and kaolinite clays studied under a CO₂ atmosphere lost greater amounts of adsorbed water than samples studied under N₂, indicating an ease of removal of adsorbed water from dickite and kaolinite under a CO₂ or Martian-like atmosphere.

Sulfur-bearing minerals: Gypsum, epsomite, ferric sulfate and ferrous sulfate were examined (Figs. 7-10). Both massive rock gypsum (Fig. 7) and selenite gypsum (Fig. 8) were studied. The 21.1 and 20.8% loss of water from gypsum occurred below 200°C and was essentially equivalent to the theoretical value of 20.9%. Loss of SO₂ was not observed during the heating of massive rock gypsum to 1000°C and 700°C for selenite gypsum. Decomposition of epsomite (MgSO₄·7H₂O) indicated loss of water in two steps below 300°C (Fig. 9). Six waters are lost below 200°C and the final water is lost near 300°C. Decomposition of the sulfate occurs at 870°C under both N₂ and CO₂ atmospheres. The derivative (DTG) of the weight-loss curve for epsomite is given in Fig. 9. Ferric and ferrous sulfates were examined because of the potential of their presence in the Martian regolith (Clark, 1979). The normal form of ferrous sulfate is FeSO₄·7H₂O. At temperatures, below 250°C approximately 42.3 and 43.7% water is lost in three steps when heated under N₂. Decomposition of the sulfate begins at 525°C (26.9% wt. loss). Ferric sulfate, Fe₂(SO₄)₃·nH₂O, lost 22.4% water below 300°C and 47.2% SO₂ at 600°C when heated under 1 atm. N₂. From these measurements it can be seen that ferrous sulfate has a greater water holding capacity than ferric sulfate. It is unclear whether the ferrous or ferric forms of the iron sulfates presently or previously existed on the Martian surface. The iron sulfate salts hydrolyze to form acidic aqueous solutions (Posnak and Merwin, 1923) which are very capable of assisting the weathering of primary silicates. The end-product of such weathering should result in the formation of additional iron-rich clay and sulfur-rich weathering products.

Thermal stability and volatile release measurements of analog minerals are contributing to the data base of potential Martian surface constituents. The understanding of the behavior of these minerals under different conditions determine the parameters under which future flight experiments must operate in order to characterize the volatile components within the Martian regolith.

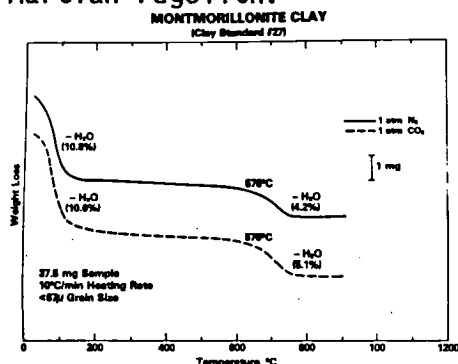


Fig. 1

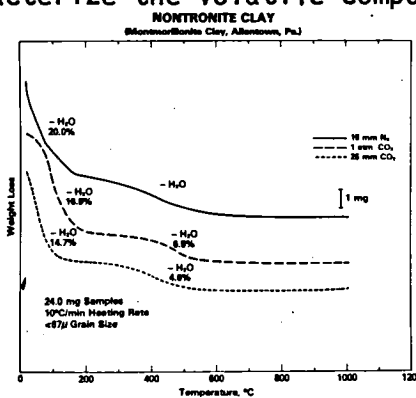


Fig. 2

References: Clark, B.C. (1979) *Science* 124, 1286-1293.
Clark, B.C. (1979) *Earth Planet. Sci. Lett.* (in press).
Clark, B.C. (1979) *J. Geophys. Res.* (in press).
Fassett, J.P. and Cannon, W.A. (1979) *J. Geophys. Res.* (in press).
Gooding, J.C. (1978) *Earth Planet. Sci. Lett.* 43, 483-492.
Posnak, E. and Merwin, H.H. (1923) *J. Am. Chem. Soc.* 45, 1277-1280.
Touret, R. and Naveau, P. (1973) *J. Metamorphic Geol.* 1, 463-474.
Touret, R. et al. (1977) *J. Metamorphic Geol.* 5, 483-493.

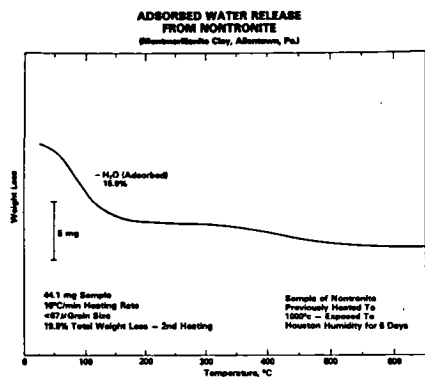


Fig. 3

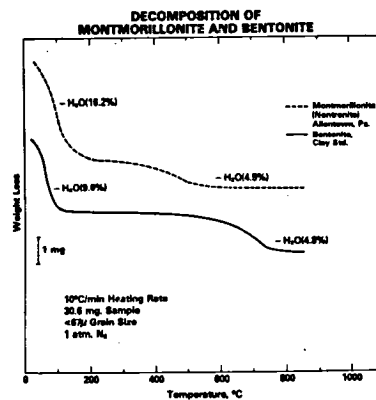


Fig. 4

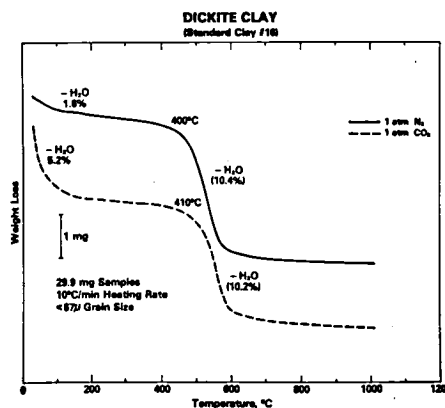


Fig. 5

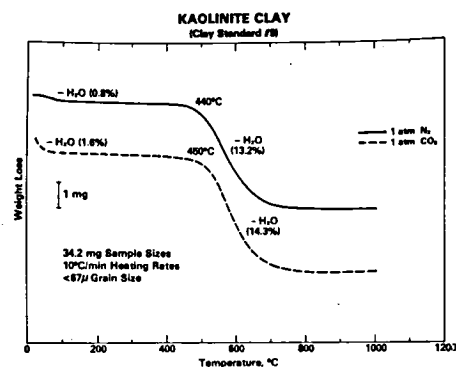


Fig. 6

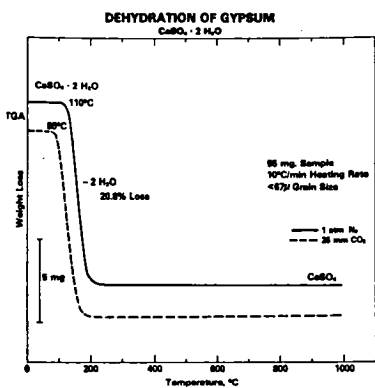


Fig. 7

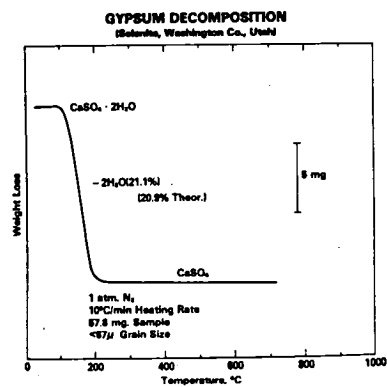


Fig. 8

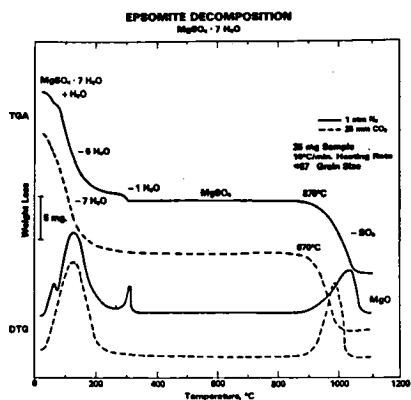


Fig. 9

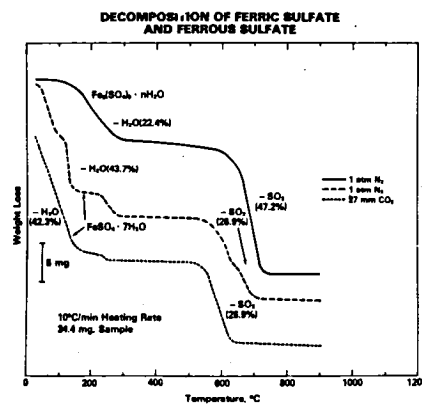


Fig. 10

EXPERIMENTAL EVIDENCE AGAINST THE UV PHOTODEHYDRATION OF GEOTHITE (α -FeOOH)

R.V. Morris, NASA-Johnson Space Center, Houston, TX 77058, and
H.V. Lauer Jr., Lockheed Electronics, Co., Inc., Houston, TX 77058

INTRODUCTION

According to Andersen and Huguenin (1977), goethite (α -FeOOH) is efficiently dehydrated by UV radiation having $\lambda \leq 0.28 \mu\text{m}$. Apparently, this wavelength was selected because of charge transfer bands centered near $0.25 \mu\text{m}$. In any case, UV photodehydration has been subsequently invoked (Huguenin 1976; McCord et al., 1978) in a planetary context to predict that the uppermost surface soils on Mars may be highly dehydrated. However, Andersen and Huguenin (1977) do not cite evidence precluding that the dehydration observed in their laboratory experiments was a thermal effect due to radiant heating. We have, therefore, undertaken a reinvestigation of the kinetics of goethite dehydration in the presence of electromagnetic radiation.

EXPERIMENTAL PROCEDURES

The experimental apparatus used to irradiate the particulate goethite samples with electromagnetic radiation under controlled environmental conditions is described by Morris and Lauer (1979). The irradiance in the near-IR (NIR), visible (VIS), and near-UV (NUV) incident on the samples for each radiation employed and that for solar radiation at 1.5 AU (the orbit of Mars) are given in Table 1. The temperatures as measured by a thermocouple embedded in the goethite samples in the presence of the Xe(A) and Xe(B) radiations were $\sim 540^\circ\text{C}$ and $\sim 80^\circ\text{C}$, respectively. Due to the nature of radiant heating, these temperatures must be considered as lower limits for the actual temperature of the goethite particles. All irradiations were carried out in an O_2 atmosphere at 100 torr total pressure.

After irradiation, the samples were analyzed for structural water (H_2O^+) to determine the extent of dehydration. The analyses were performed in a moisture evolution analyzer where the water evolved by heating the samples to $\sim 900^\circ\text{C}$ was measured; prior to heating, adsorbed water (H_2O^-) was removed with the N_2 stripping gas. We have not yet determined the mean grain size of the goethite used in this study. Thermogravimetric analysis shows that the H_2O^+ is lost from the goethite by 350°C .

RESULTS AND DISCUSSION

The results for irradiation of the goethite with Xe(A) and Xe(B) radiations are shown in Fig. 1 as a plot of structural water remaining after irradiation versus irradiation time t . With the Xe(A) radiation, the goethite lost most of its structural water; the amount of structural water decreased from the initial value of $\sim 9.8 \text{ wt. } \%$ to $0.5 \text{ wt. } \%$ after

~15 hr. irradiation with Xe(A) radiation. Since the minimum temperature of the goethite particles during irradiation is ~540°C and since thermogravimetric analyses showed the goethite was dehydrated thermally by 350°C, radiant heating by the Xe(A) radiation at least in part must have resulted in thermally induced dehydration of the goethite. In contrast, irradiation with the Xe(B) radiation resulted in no detectable dehydration of the goethite. From the null result with the Xe(B) radiation we can conclude the following: (a) the dehydration observed with the Xe(A) radiation can be attributed predominantly, if not entirely, to thermal dehydration since the NUV components of the Xe(A) and Xe(B) radiations are comparable and (b) neither thermal dehydration nor UV photodehydration occurred to a perceptible extent with the UV-rich Xe(B) radiation.

In summary, our experimental results do not show any evidence for the UV photodehydration process proposed by Andersen and Huguenin (1977). Perhaps radiant heating was an unrecognized factor in the work of Andersen and Huguenin (1977) which led to their misinterpretation of experimental results. Thus, although the possibility that UV photodehydration actually occurs cannot be totally eliminated, there is as yet no experimental basis for inferring the process occurs naturally on Mars.

Table 1: Irradiance in W/cm^2

Radiation	NUV	VIS	NIR
	0.25→0.4 μm	0.4→0.7 μm	0.7→1.0 μm
Xe(A)	1.68	5.80	6.56
Xe(B)	0.77	0.080	0.30
Solar, 1.5 AU	0.0054	0.025	0.017

REFERENCES

- Andersen and Huguenin (1977) BAAS 9, 449
Huguenin (1976) Icarus 28, 203
McCord et al. (1978) JGR 83, 5433
Morris and Lauer (1979) NASA TM 80339, 225

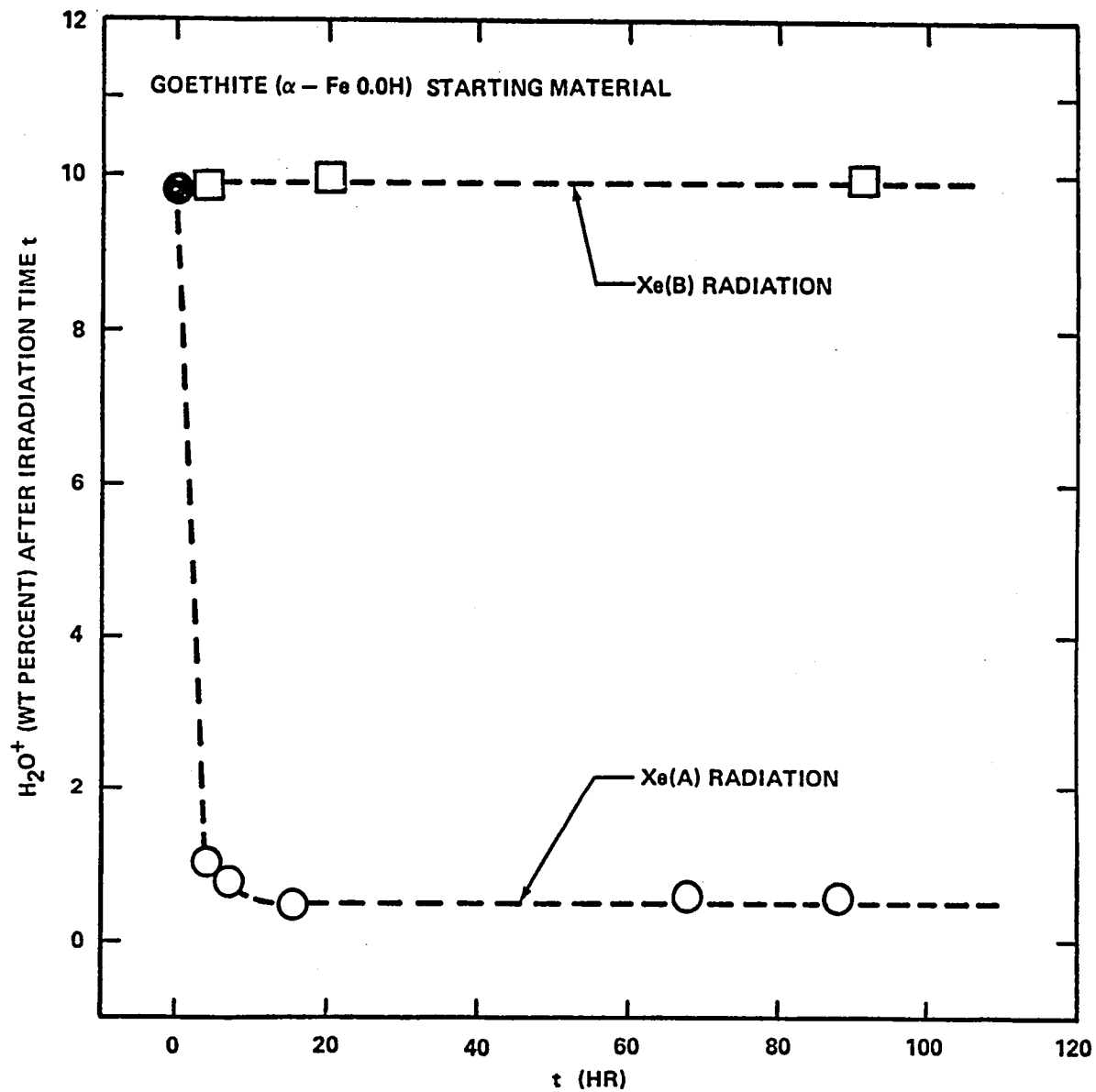


Fig. 1. Weight percentage of structural water (H_2O^+) in goethite starting material after irradiation time t .

THE EVIDENCE AGAINST UV PHOTOSTIMULATED OXIDATION OF MAGNETITE

R.V. Morris, NASA-Johnson Space Center, Houston, TX 77058 and
H.V. Lauer Jr., Lockheed Electronics Co., Inc., Houston, TX 77058

INTRODUCTION

(1,2,3) proposed that photostimulated oxidation of magnetite by UV radiation might be an important process on the surface of Mars and have performed laboratory experiments which investigated this effect. We have conducted additional experiments to investigate this potentially significant process and have studied the kinetics of magnetite oxidation in O₂-bearing atmospheres in the presence of electromagnetic radiation. The data from our experiments constrains us to conclude that perceptable oxidation of magnetite by UV photostimulation did not occur and that previous conclusions to the contrary by (1,2,3) are spurious. Consequently, although the possibility that the process actually occurs cannot be totally eliminated, there is no experimental basis for inferring UV photostimulated oxidation of magnetite occurs naturally on Mars.

EXPERIMENTAL PROCEDURES

The experimental apparatus used to irradiate the particulate magnetite samples with electromagnetic radiation under controlled environmental conditions has been previously described by (4). The irradiance in the near-IR (NIR), visible (VIS) and near-UV (NUV) incident on the samples for each radiation employed and that for solar radiation at 1.5 AU (the orbit of Mars) are given in Table 1. The temperatures as measured by a thermocouple embedded in the magnetite samples in the presence of the Xe(A), Xe(B), and Xe(C) radiations were ~540, ~80, and ~80°C, respectively. Due to the nature of radiant heating, these temperatures are considered as lower limits for the actual temperature of the magnetite particles. Most irradiations were carried out in an atmosphere of O₂ at 100 torr total pressure. The extent of oxidation was determined by measuring changes in the saturation magnetization (J_s) of the samples. The value of J_s for magnetite is 92 emu/g, and those for the oxidation products hematite (α -Fe₂O₃) and maghemite (γ -Fe₂O₃), ~0.5 and ~73 emu/g, respectively. Three synthetic (MTCPS1, MTFSL, and MTMRC1) and six natural (MTCM1A, -B, -D, -G, MTCPN1, and MTMCB1) magnetites having mean grain sizes from 0.4 to 200 μ m were used as starting materials.

RESULTS

The results for irradiation of the MTCM1 series magnetites with the Xe(A) radiation are shown in Fig. 1a. The parameter $J_s(t)/J_s(0)$ is the ratio of the value of J_s after an irradiation time t to its value at time zero. Within the scatter of the data, the values of $J_s(t)/J_s(0)$ for each magnetite starting material have decreased (indicating oxidation) from the value of 1.0 at time zero to a constant value by ~9 hrs. The same observation holds for the other magnetites, but the data were not plotted for clarity. The constant values, denoted by the parameter

$J_S(t>9)/J_S(0)$, were calculated as the average of all values of $J_S(t)/J_S(0)$ for $t>9$ hr. and are plotted versus the mean grain size of the magnetite starting materials in Fig. 2a. The dashed line was calculated assuming the irradiation products were spherical particles having a 20 μm thick, hematite composition shell surrounding a magnetite core; except for MTCPS1, this model very adequately describes the data. That the oxidation product was in fact predominantly hematite (excepting MTCPS1) was confirmed by x-ray and thermomagnetic analyses. For MTCPS1, corresponding analyses indicate the oxidation product was a mixture of hematite and maghemite and thus account for the deviation from the hematite model.

The results for the Xe(B) and Xe(C) radiations, shown in Figs. 1b, 1c, 2b, and 2c, are dramatically different from those for the Xe(A) radiation. All the values of $J_S(t)/J_S(0)$ are close to or within the 3% one standard deviation error of the measurements of being invariant. For the UV-rich Xe(B) radiation, only MTFPS1 may show a statistically significant decrease in $J_S(t)/J_S(0)$ by ~ 300 hr. Note that oxidation is also observed for the UV-absent Xe(C) radiation. The dashed lines in Figs. 2b and 2c were calculated assuming spherical particles and a 0.007 μm thick, hematite composition shell.

THE CASE AGAINST THE UV PHOTOSTIMULATED OXIDATION OF MAGNETITE

The temperature indicated by the thermocouple using the Xe(A) radiation was $\sim 540^\circ\text{C}$. Since this temperature is actually a lower limit for the sample temperature and since independent experiments have shown that thermally-stimulated oxidation occurs by 250°C (e.g., 5), we conclude at this point that the observed oxidation using the Xe(A) radiation must at least in part have been thermally stimulated.

The $\sim 80^\circ\text{C}$ temperature indicated by the thermocouple using the Xe(B) radiation is below that required for thermally-stimulated oxidation. The fact that no perceptible oxidation was observed excepting MTFPS1 demonstrates the following for the remaining magnetites: (a) the actual temperature of the magnetite grains was in fact below the thermal oxidation threshold and (b) UV photostimulated oxidation did not occur either. Since the NUV power in the Xe(A) and Xe(B) radiations are comparable, we conclude the oxidation observed with the Xe(A) radiation was predominantly, if not entirely, thermally-stimulated.

At this point, the small amount of oxidation observed for MTFPS1 using the Xe(B) radiation cannot unambiguously be attributed to either UV photostimulation or thermal-stimulation because the Xe(B) radiation contains an intense UV component and because the $\sim 80^\circ\text{C}$ temperature is a lower limit for the sample temperature. The observation that MTFPS1 oxidized to a comparable degree in both Xe(B) and Xe(C) radiations suggests that in both cases the oxidation was not due to UV photostimulation because the Xe(C) radiation has essentially no NUV component but does give the same temperature measurement of $\sim 80^\circ\text{C}$. However, we cannot conclude unambiguously that the oxidation is thermally stimulated because there may be as yet unidentified mechanism specific to the

synthetic magnetite MTFS1 which results in its oxidation at $\sim 80^\circ\text{C}$.

In summary, our results from experiments utilizing three irradiation conditions constrain us to conclude we have not observed UV photochemical oxidation of particulate magnetite samples having mean grain sizes down to $0.4\ \mu\text{m}$. This conclusion is diametric to that of (1,2,3) who interpreted his results to show that UV radiation ($\lambda \leq 0.35\ \mu\text{m}$) photo-stimulates the oxidation of magnetite and that the oxidation layer is $\sim 1\ \mu\text{m}$ thick. If this were in fact the case, we cannot reconcile why the four magnetites having mean grain sizes $\leq 1.0\ \mu\text{m}$ did not substantially if not completely oxidize using the Xe(B) radiation since its radiant energy in the NUV is at least a factor of 100 higher than that employed by (1). (The spectral irradiance reported by (1) is a factor of 100 too high; Huguenin, pers. comm.). From insights gained during this study, we suggest several factors (1,2,3) apparently failed to recognize and consequently led to misinterpretation of their experimental data. (1) measured temperatures below the thermal oxidation threshold and thus did not consider thermal stimulation to be viable. However, we have pointed out that due to the nature of radiant heating such temperatures **must** be regarded as lower limits for the actual sample temperature and are not therefore an unambiguous criterion for concluding thermally stimulated oxidation did not take place. Per our discussion of magnetite MTFS1, there may be some unknown mechanism by which the magnetite used by (1) is oxidized below the thermal oxidation threshold.

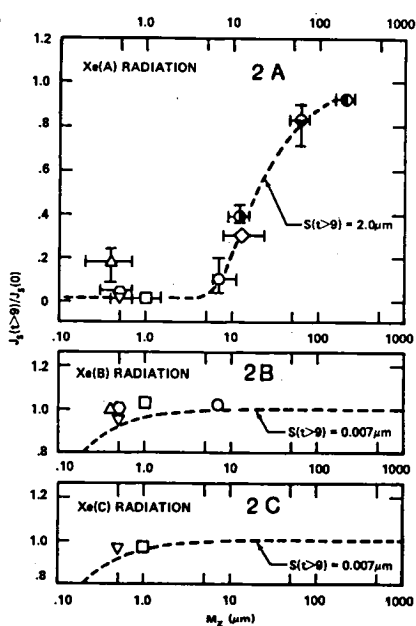
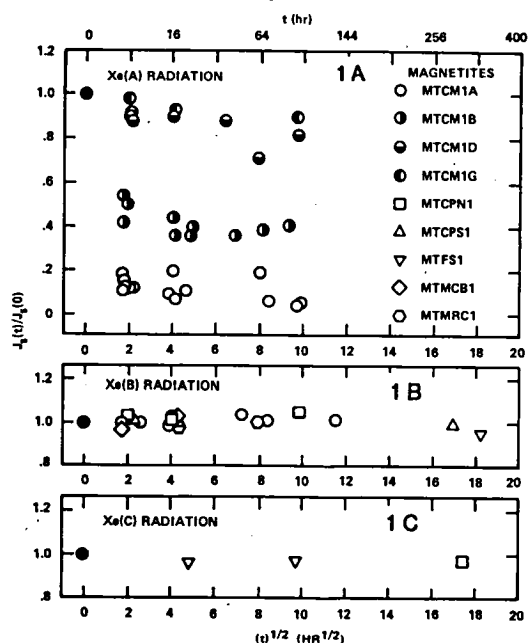


Fig. 1:
 $J_s(t)/J_s(0)$
vs. $t^{1/2}$.

Fig. 2:
 $J_s(t)/J_s(0)$
vs. mean grain
size M_z in μm .

REF.: (1)Huguenin
(1973a) JGR 78,
8481; (2)Huguenin
(1973b) JGR 78,
8495; (3)Huguenin
(1974) JGR 79,
3895; (4)Morris
and Lauer (1979)
NASA TM 80339,
225; (5)Elder
(1965) J. App.
Phys. 36,1012.

Table 1:
Irradiance
(in W/cm^2)

Radi- ation	NUV: .25 +.4 μm	VIS: .4 +.7 μm	NIR: .7 +.1.0 μm	Radi- ation	NUV: .25 +.4 μm	VIS: .4 +.7 μm	NIR: .7 +.1.0 μm
Xe(A)	1.68	5.80	6.56	Xe(C)	<0.0008	0.60	0.74
Xe(B)	0.77	0.080	0.30	1.5 AU	0.0054	0.025	0.014

THE H₂O MASS BALANCE ON MARS: IMPLICATIONS FOR A GLOBAL SUBPERMAFROST GROUNDWATER FLOW SYSTEM.

Clifford, Stephen M., and Huguenin, Robert L., Dept. Physics & Astronomy, U. Massachusetts, Hasbrouck, Amherst, MA.

Viking orbiter water vapor measurements have indicated that a net annual transport of H₂O occurs into the north polar regions of Mars (1). Estimates of the total amount of H₂O deposited, poleward of 60°N, range from $\sim 4 \times 10^{14}$ g H₂O (1) to $\sim 2 \times 10^{15}$ g H₂O (2). Total annual deposition of H₂O over the entire northern hemisphere may actually exceed these estimates based on both Viking 2 lander observations of possible H₂O surface condensate (3) and a tempofrost-to-permafrost conversion process discussed later in this abstract. Retention of an amount of H₂O $\geq 10^{15}$ g/yr in the martian polar regions has significant long term implications for the global H₂O budget. Assuming such a retention rate has been typical of the martian norm, an amount of H₂O equivalent to that contained in the North Polar Cap would accumulate in about 10^5 martian years. Indeed, the entire theoretical inventory of H₂O on Mars (4) could be cold-trapped in as little as 10^7 martian years. Since we fail to observe an accumulation of H₂O of this magnitude and as enough time has elapsed on Mars for this process to have been repeated several hundred times, we conclude that some efficient means for the equatorial replenishment of regolith H₂O probably exists.

Purely atmospheric models of replenishment, such as preferential adsorption and burial of condensates by windblown dust, appear to be too inefficient to account for the resupply of such large quantities of H₂O. Once H₂O has been released from the equatorial regolith it sees the cold polar regions as the dominant sink. Climatic variations on Mars will not substantially alter this process as long as the constraints of temperature and pressure prohibit the stable existence of liquid H₂O at the surface. Therefore, we have proposed a model hydrological cycle for Mars (5), whereby the deposition of dust and condensate on the polar caps produces a layer of insulation which results in the rise of the melting isotherm and the subsequent release of a layer of liquid water at the base of the cap. The weight of the cap might then drive the melted H₂O into a global interconnected groundwater flow system beneath the martian permafrost. The existence of such a global distribution of regolith H₂O is supported by the current interpretation of such features as rampart (or "splosh") craters, patterned ground, fluvial channels and a number of other surface morphologies. Much of this work has been summarized by both Carr and Schaber (1977) and Soderblom and Wenner (1978). Since these features appear to span geologic time (6) it is reasonable to assume that the H₂O responsible for their origin is still present.

The thickness of the polar cap required for the geothermal melting of a basal layer depends on a variety of conditions. Calculations based on a mean surface temperature of 180° K and thermal conductivities for both ice and dust of 2.7×10^5 cal./cm/yr and 3.1×10^3 cal./cm/yr respectively, yield thickness estimates which range from several hundred meters to several

kilometers or more - depending on the dust-to-ice ratio, the salt content of the dust, and the local value of geothermal heat. If ice at the base of the cap constitutes the major volumetric fraction of cap material then it should also provide a significant amount of the cap's structural support. The rise of the melting isotherm into this previously frozen material will result in a removal of this support as the weight of the overburden cap drives the water into the subpermafrost groundwater system. The subsequent structural adjustment of the cap may result in morphological features which can be identified from Viking orbital imagery.

An additional sink for atmospheric H_2O , which may also release water to the subpermafrost system, are the regions of "tempofrost" proposed by Farmer and Doms (1979). The tempofrost-to-permafrost interface is determined by the depth to which the seasonal thermal wave elevates the soil temperature above the frost point. Deposition of a layer of dust over the original surface will result in a corresponding upward displacement of this interface within the soil. Thus, a small portion of the tempofrost which was present prior to the dust layer deposition, will be retained as permafrost. Eventually, the melting isotherm at the base of the permafrost will see the added insulation provided by the deposited layer of dust and will, in response, rise in the regolith. The H_2O released by this rise will then be available to the groundwater system. As much as 10^{15} g H_2O may be cycled by this process each martian year.

Subpermafrost groundwater systems on Earth, such as those in Siberia and in the Dry Valleys of Antarctica, can be found at depths of several kilometers and are often characterized by their high salinities. Such saline groundwater, often rich in calcium chloride, is found with freezing points as low as 220° K. On Mars the existence of various inorganic salts in the regolith is supported by the discovery of a duricrust at both Viking lander sites (7) and by the composition of the soil as determined by the inorganic chemical analysis experiments onboard each spacecraft (8). The salinity of the subpermafrost groundwater can have a significant effect on the thickness of the permafrost layer itself. If the groundwater is pure then the melting isotherm at the base of the permafrost will have a value of 273° K. If we assume a geothermal gradient of $\sim 25^\circ/\text{km}$, the total thickness of the permafrost can exceed two kilometers - even in the comparatively warm equatorial regions of Mars. Depending on the soil porosity and permeability, a two kilometer thick layer of permafrost can act as an enormous sink for regolith H_2O . For this reason, coupled with the low H_2O outgassing estimates of Anders and Owen (1977), Soderblom and Wenner (1978) concluded that groundwater on Mars had only a short existence before being irreversibly taken up as permafrost. However, if we assume the groundwater is saline, then the melting isotherm may be as low as 220° K. Reconsidering our example of the martian equatorial regions, ground ice will occur only in the seasonally active temperature layer of the top six meters of soil - where temperatures, sometime during the martian year, will fall below 220° K. With the added consideration of the more generous H_2O outgassing estimates of Pollack and Black (1979) and Lewis (1972), room still exists for substantial groundwater reserves on Mars.

The stability of permafrost in the martian equatorial region may be called into question by the fact that the mean equatorial surface temperatures exceed the frost point temperature of H₂O by as much as 20° K or more. However, as has been discussed by Smoluchowski (1968) and Farmer (1976), the diffusion-limiting properties of an overlying layer of soil can be such as to allow local water vapor equilibrium to occur within the soil while remaining in disequilibrium with the atmosphere. As the upper surface of permafrost is depleted by evaporation to the atmosphere it is replenished by the diffusion of vapor and the migration of thin films of water towards the freezing front at its base. These processes are efficient even when the vertical distances separating the permafrost from the groundwater are measured in kilometers.

As discussed by Carr (1979), the intense bombardment phase of early martian history resulted in a highly brecciated and permeable regolith extending to considerable depth. Various physical and chemical processes may have modified and sealed the outermost layer of the regolith; however, at depth, it should have retained its porous and permeable nature and thus would prove to be an excellent host for a planet wide interconnected groundwater system. As a result, such a system would be unconstrained by surface topography and would hydrostatically adjust to variations in geopotential. In this respect the martian groundwater system might closely imitate the behavior of terrestrial oceans.

We conclude that one possible solution to the problem of the H₂O mass balance on Mars is a global groundwater system. Such a system would be atmospherically discharged, at the latitudes of maximum annual insolation, by evaporation from near surface brines and ice. The eventual deposition of this H₂O into the polar regions will result in the recharge of the groundwater system by geothermal melting. From the recharged system, the near surface brines and ice are ultimately replenished. (Note that the groundwater system proposed here is not necessarily a steady-state system and may periodically discharge and recharge in response to climatic variations.)

References: (1) Farmer, C.B. and Doms, P.E. (1979) JGR 84, 2881; (2) Pollack *et al.*, (1979) JGR 84, 2929; (3) Wall, S. D, and Jones, K.L., (1979) NASA TM 80339, 222; (4) Pollack, J.B. and Black, D. C. (1979) Science 205, 56; (5) Clifford *et al.* (1979) BAAS 11, 580; (6) Allen, C.C., (1979) Icarus 39, 111; (7) Clark, B.C. (1978) Icarus 34, 645; (8) Clark *et al.* (1976) Science 194, 1283. Also: Carr, M.H. and Schaber, G.G. (1977) JGR 84, 4039; Soderblom, L.A. and Wenner, D.B. (1978) Icarus 34, 622; Anders, E. and Owen, T. (1977) Science 198, 453; Lewis, J. (1972) Icarus 16, 241; Smoluchowski, R. (1968) Science 159, 1348; Farmer, C.B. (1976) Icarus 28, 279; Carr, M.H. (1979) JGR 84, 2995.

ADDITIONAL EXPERIMENTAL EVIDENCE FOR THE PHOTOSTIMULATED OXIDATION OF MAGNETITE ON MARS.

Huguenin, R., Danielson, J., and Clifford S.-U. Massachusetts, Dept. of Physics/Astronomy-Hasbrouck, Amherst, MA 01003

It has been proposed by Huguenin (1,2) that photooxidation of magnetite and Fe^{2+} - silicates may be an important oxidation/weathering process on Mars. Additional experimental results and discovery of an error in the original UV flux estimate suggests that the reaction may be more efficient on Mars than previously estimated.

The original estimate of photoelectric work function, photoelectron quantum yield, and sample temperature have been refined. It was predicted that photoemission from Fe^{2+} in magnetite has a work function of 3.8 - 4.2 eV (1) and a quantum yield of 0.1-1 electrons/photons at 1950Å (3). This has been tested experimentally in 10^{-6} torr O_2 using the technique described by Poole and Huguenin (4). The measured work function was 3.9 ± 1 eV at 1950Å. The measured yield for powdered samples in a vacuum is lower than the actual yield at the grain surface by a factor of 10^{2-3} due to grain-grain reabsorption (5) and even lower in an atmosphere due to collisional losses; thus the yield at the grain surfaces was apparently close to the predicted value. This supports the proposal that photoelectron emission is a principal step in the photooxidation process.

S. Cook (private communication) discovered an error in the original calculation of the experimental UV flux estimate, due to a misinterpretation of the format of the lamp spectral output data provided by the manufacturer. The published fluxes were 1.00×10^2 higher than the actual fluxes and the constant for the kinetic rate equation (1) was consequently too low by a factor of 1.00×10^3 . The corrected kinetic rate equation is:

$$d\alpha/dT = 5.1(\pm 0.6) \times 10^{-22} P_T^{-2} p_{\text{O}_2}^{1/2} \Phi_{0.350}^{3/2} f(\text{H}_2\text{O}) \quad (1)$$

where $d\alpha/dT$ is the formation rate of the alteration layer in microns per minute, P_T is the total atmospheric pressure in torr, p_{O_2} is atmospheric O_2 partial pressure in torr, and $\Phi_{0.350}$ is the photon flux at the reference wavelength of 0.35 μm in photons $\text{cm}^{-2} \text{s}^{-1} \text{\AA}^{-1}$. $f(\text{H}_2\text{O}) = 1$ relative humidities between 1 and 5% and a complex function described by Huguenin (1) for humidities out of this range. The error has interesting ramifications. The lower end of the UV flux range in the original experiment was $6.6 (\pm 0.7) \times 10^{12}$ rather than the published value of $6.6 (\pm 0.7) \times 10^{14}$. This is quite close to the martian flux (at 0.35 μm) of 0.92×10^{12} photons $\text{cm}^{-2} \text{s}^{-1} \text{\AA}^{-1}$; thus the assumption that the kinetic rate equation remains valid down to the martian flux is more certain than previously thought. In addition, since the oxidation rate is proportional to $(\text{flux})^{3/2}$ (see equation 1), the original rate estimate for Mars (10^{-4} - $10^{-1} \mu\text{m yr}^{-1}$) was too low by a factor of 10^3 . The upper limit would still be constrained by the exposure rate of cations by eolian abrasion and H_2O adsorption (cation migration), however (3); thus only the lower limit would probably be affected by the revised flux estimate.

Measurements of sample temperature were refined using (1) several embedded or thinly coated (with magnetite) thermocouple and thermistor probes in a variety of configurations; and (2) a series of magnetite coated and (or) embedded standardized melting point substances. The maximum temperature that was measured (maximum flux, uncooled) was $\sim 230^{\circ}\text{C}$. This was above the thermal oxidation threshold (150°C), and the reaction rate was very high (consistent with the kinetic rate equation). Temperatures were measured at a variety of lower UV fluxes, and over most of the range sample temperatures were below the threshold value. At the lowest flux ($1.74 \times 10^{12} \text{ photons cm}^{-2} \text{ s}^{-1} \text{ \AA}^{-1}$) a sample temperature of $50\text{--}65^{\circ}\text{C}$ (sample was uncooled in air) was measured. This flux was lower than the lower limit of the fluxes in the original experiment, and was within a factor of 2 of the actual martian flux. Discernable reddening of the undisturbed sample was observed after 240 hours of exposure. This was a much higher rate than that predicted by Equation 1, although the equation may not be strictly valid under the uncontrolled ambient conditions under which these temperature measurements were made. Differences may also be due to differences between magnetite samples used in the past and present studies, and this is a subject of current investigation. This finding, however, coupled with the revision of the kinetic rate equation raises the possibility that photooxidation may be more efficient on Mars than previously thought.

References (1) Huguenin, R. (1973) J.G.R. 78, 8495; (2) Huguenin, R. (1974) J.G.R. 79, 3895; (3) Huguenin, R., Prinn R, and Maderazzo, M. (1977) Icarus 32, 270; (4) Poole, C. and Huguenin, R. (1977) BAAS 9, 449; (5) Feuerbacher et al. (1972) Proc. 3rd Lun. Sci. Conf. 3, 2655.

ALTERATION PRODUCTS OF FROST WEATHERING ON MARS

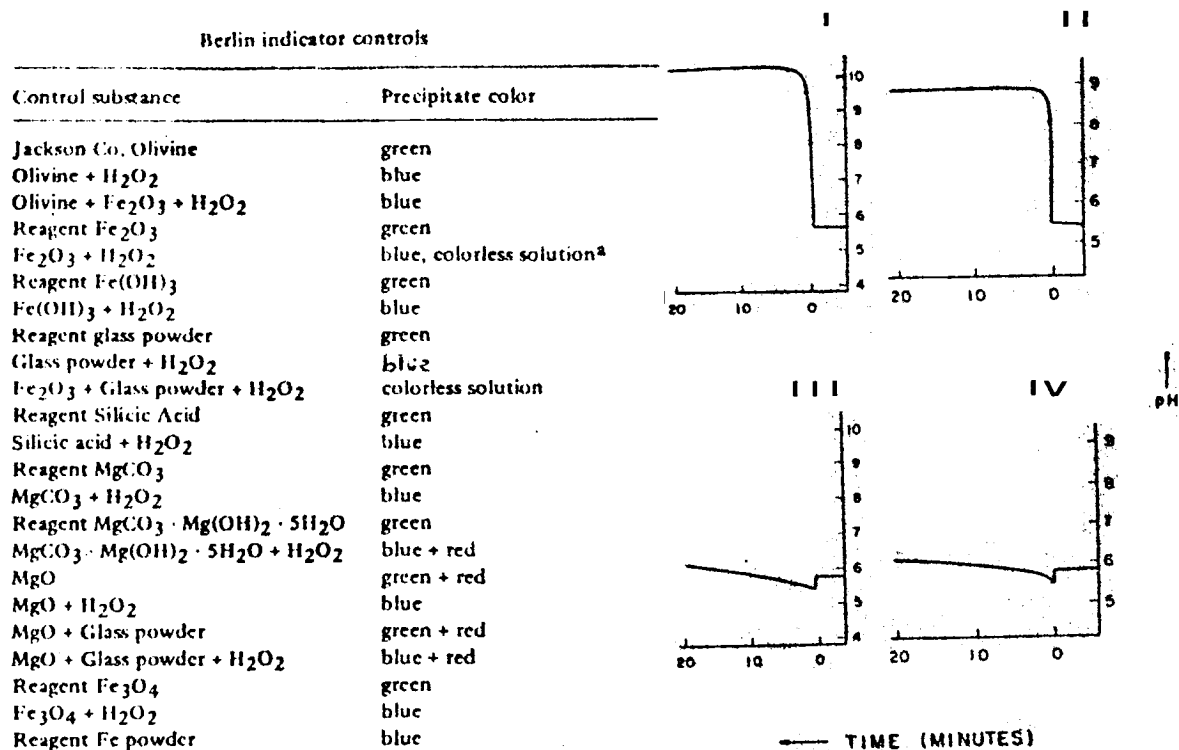
Miller, K.J., Dept. Biochemistry, U. Mass. Amherst 01003, Huguenin, R.L., Dept Physics/Astronomy-Hasbrouck, U. Mass. Amherst 01003, and Danielson, J., Dept Geology, U. Mass. Amherst 01003

It has been proposed by Huguenin et al that the interaction of frost with minerals at the Martian surface may be producing some unusual alteration products. One proposed product is a peroxide species or metal peroxide species of high oxidation potential which may have been derived from the chemical reduction of mafic silicates within the Martian regolith. The minerals olivine, pyroxene (both clino and ortho varieties), and plagioclase are apparently the principal mafic silicates in Martian rocks and were used in our laboratory studies. The proposed peroxide species may be responsible for the unusual chemical activity detected in the Martian soils during the Viking Biology Experiments. Qualitative simulations of the active cycles of the Viking Labeled Release and GEX experiments have been performed in the laboratory, and indicator tests specific for peroxides and/or metal peroxides have been performed in an attempt to identify the precise nature of the active agent. Following frost exposure, the altered mineral was exposed to the Berlin Indicator reagents (the Berlin Indicator test is specific for H_2O_2) and unusual results were obtained (colorless solution, no ppt.). Several controls were performed, and it was discovered that an intimate mixture of Fe_2O_3 , SiO_2 , and H_2O_2 gave the same qualitative results while other controls did not (see table below). We believe that this intimate mixture of Fe_2O_3 , SiO_2 , and H_2O_2 may represent a possible analog of our active agent created during frost exposure. We propose that the metal-peroxide species produced during frost exposure of olivine is also produced in the mixture of Fe_2O_3 , SiO_2 , and H_2O_2 . Fe_2O_3 may become dissolved in the acidic H_2O_2 solution and Fe^{3+} may become incorporated at surface sites on the SiO_2 particles. Fe^{3+} may then react with H_2O_2 to produce FeO_2H^+ and $FeOH^{2+}$ (two species thought to be released to solution when frost altered olivine is exposed to liquid H_2O). The Luminol chemiluminescence test for H_2O_2 was also performed and was negative (no visible chemiluminescence) for our 'analog'. This is interesting because the levels of H_2O_2 within the analog mixture are above the threshold of detection of this test. This may indicate that either our oxidant is not simply H_2O_2 in solution or it may indicate that a quencher is present. Our third indicator test, the Potassium Dichromate test, gave positive support for the production of a peroxide species or a metal peroxide species. Using dilute $K_2Cr_2O_7$ solution, the detection of H_2O_2 and metal hydroperoxy complexes (G. Rossman, private communication) is confirmed by the formation of CrO_5 . The CrO_5 imparts a diagnostic pale blue color when extracted with ether. It is unstable and decomposes on standing, causing the blue color to fade quickly. When 0.1 g of frost weathered olivine was added to the reagent (10ml $K_2Cr_2O_7$), a localized brown coloration was induced in solution. 10ml of anhydrous ether was immediately added, which formed a layer on top

of the $K_2Cr_2O_7$ solution. A faint pale blue coloration was observed in the ether layer (indicating that CrO_5 had formed) which quickly faded to colorless (detection and decay was followed with a spectrophotometer).

We have previously reported pH studies in which pH trends versus time have been compared between frost-altered minerals and minerals not exposed to frost. Typical pH profiles in distilled H_2O for unaltered olivine and pyroxene are shown below in figures I and II respectively. Note the initial rapid increase in basicity. This is consistent with abrasion pH studies indicative of proton incorporation. When these minerals are frost altered prior to pH runs, however, very different profiles result as noted in figures III and IV for olivine and pyroxene respectively. This indicates a marked alteration of the mineral and supports a model where HO_2^- (ads) and H^+ (ads) species are produced. These species may be released into solution upon exposure to liquid H_2O . We have recently begun infrared studies in an attempt to identify these proposed adsorbed species. Inconclusive results have been obtained, however, and it is evident that conventional IR solid sample analysis may not be suitable for these studies. Thus, we are now in the process of designing a cryogenic reflectance IR analysis device for this study.

References: Huguenin et al, J. Mol. Evol. (in press) and Huguenin et al, PGPI abstract (1979 June).



^a With six trials, 5 formed blue ppt and 1 formed a colorless solution

CHEMICAL ENVIRONMENTS OF MARTIAN OASES

Miller, K.J., Dept. Biochemistry, U.Mass., Amherst 01003, Huguenin, R.L. Dept. Physics/Astronomy-Hasbrouck, U.Mass., Amherst, MA 01003

The proposed oases on Mars may have significantly different chemical environments than those of the Viking landing sites. The Viking-sampled soils were found to be highly desiccated. The Gas Chromatograph Mass Spectrometer (GCMS) analyses detected .1-1% by weight of water in regolith samples heated to 350° or 500°C and less than .1% by weight of water in samples heated to 200°C. It was only the Badger rock sample that released approximately .2% by weight of water at 200°C. It is estimated that the amount of H₂O evolved (approx. 10²⁰ molecules g⁻¹) corresponds to the equivalent of only 1 monolayer of adsorbed or inter-layer H₂O for surface areas of only approx. 10¹m²g⁻¹ where adsorption site separation is approx. 4 Å. Surface areas however, may range from 10¹m²g⁻¹ (basalts) to 10²m²g⁻¹ (clays). Thus, samples may have evolved less than a monolayer equivalent of H₂O. This suggests that the surface material probably contained essentially no physically adsorbed or inter-layer H₂O, but contained only the most strongly-bound components (chemisorbed H₂O and water of hydration). In the oases, the uppermost soils (a few mm) are probably similarly desiccated, but the subsurface soils may be more hydrated. This hydrated state may be of the form of H₂O films of varying thickness. The spatial distribution of water may be heterogeneous and range from relatively pure liquid/ice to saturated brines. As reflectance spectra have shown the surface material (in Solis Lacus) to contain less bright dust, more dark basaltic material, and anomalously large fractions of calcic pyroxene (as compared with Viking sites), the brines may consist of high concentrations of calcium salts with potentially great freezing point depression capacities (eg. CaCl₂). Near surface temperatures are significantly higher in the oases than at the Viking sites, varying diurnally from 220-295°K in the summer and from 170-230°K in the winter. Brines could be unfrozen during a portion of each day throughout most of the year while relatively pure H₂O could undergo daily freeze-thaw cycling for approximately 1/2 the year to a depth of several centimeters. Such freeze-thaw cycling may promote the further segregation of saturated brine areas from those of pure water. It is proposed that the relatively high near-surface humidities should inhibit the formation of and promote the decay of the oxidants that were discovered at the Viking sites. This is evidenced by the observed oxidant destruction (O₂ evolution) during humidification of the Viking Soil samples. The relatively high near-surface temperatures at the sites of the oases should also result in a shortened lifetime for these oxidants. (E_{act} for decay of the oxidant is approx. equal to 34 kcal/mole.) (Huguenin et al., Levin and Straat). The absence of oxidants may permit an accumulation of greater amounts of organics by both abiogenic synthesis at the solid particle-atmosphere interface (eg. Hubbard et al) and meteoritic infall (if it is assumed that carbonaceous chondrites comprise a significant fraction of meteoritic material reaching the surface of Mars). Hubbard et al have demonstrated that surface catalyzed synthesis of organic molecules such as formic acid and

glycolic acid may be occurring on Mars. This production of organic material, derived from the surface-dependent conversion of CO and H₂O to organic compounds, involves the excitation of adsorbed CO with UV radiation of wavelengths considerably longer than those adsorbed by gaseous CO. It was concluded that substantial abiogenesis could occur on Mars provided that the surface particles have high surface areas and that adequate levels of water are available. It is believed that the H₂O species involved in the conversion of CO to organics comprises the primary monolayer at surface sites (Hubbard, personal communication). It has also been demonstrated, however, that excess H₂O vapor may be inhibitory to this reaction. From this data, it is difficult to evaluate the production of organic compounds at the sites of the oases. It was discussed above that oxidant levels at the oases could be low due to high near-surface humidities. For this same reason, synthesis of organics may be quite inefficient. We can, however, imagine a gradient of H₂O (dessication to several monolayers) existing within approx. the upper centimeter of surface material. UV radiation may penetrate through this amount of surface material and catalyze such an abiogenic synthesis at appropriate H₂O levels. In order for organics to accumulate, where average rates of synthesis exceed rates of destruction by UV radiation, they must be periodically buried. Dust storms were cited by Hubbard et al as a possible protective burying mechanism. As reported by Huguenin, Clifford, and Greeley (these abstracts), dust storm initiation sites are, in fact, the sites of the proposed oases, and, thus, such a protective mechanism for organic accumulation should be most efficient there.

References Biemann, K. et al, JGR, 82 pp 4641 (1976); Hubbard, J.S. et al, PNAS 68, No. 3 pp 574-578 (1971); Hubbard, J.S. et al, J. Mol. Evol. 2, pp 149-166 (1973); Huguenin, R.L. et al, J. Mol. Evol. (in press); Huguenin, R.L. et al. PGPI Abstract (1977-78).

ADDITIONAL REMOTE SENSING EVIDENCE FOR OASES ON MARS

Huguenin, R.L. and Clifford, S.M., U.Massachusetts Dept. Physics/
Astronomy-Hasbrouck, Amherst, MA. 01003

Huguenin et al. (1979) previously reported remote sensing evidence for anomalous H₂O outgassing from two tropical regions on Mars in Solis Lacus (-25°, 85°) and Noachis-Hellespontus (-30°, 315°), and it was proposed that the outgassing may indicate a near-surface source of ice and liquid H₂O in these regions. Additional remote sensing evidence is discussed here that supports this proposal.

Again the evidence is based primarily on the remote sensing identification of condensates that repeatedly form preferentially in these regions. Condensates act to flatten the steeply sloping (at UV-visible wavelengths) martian reflectance spectra, and they appear as highly reflecting at blue wavelengths. In the previous paper we discussed photometric images of Mars that were obtained during the 1973 dust storm. They showed the Solis Lacus dust cloud to be anomalously bright at blue wavelengths, indicative of condensates being present with the dust. The condensates appeared suddenly at dawn and were restricted to the Solis Lacus cloud on Day 1. On Day 2 condensates also appeared in adjacent regions and continued to reappear in and symmetrically around Solis Lacus throughout the early phases of the storm. Citing the diurnal behavior and distribution of the brightenings, we proposed that Solis Lacus was the principal source for the H₂O.

Extensive examinations of past observational records reveal that the 1973 event was not an isolated occurrence. It has happened near almost every perihelion since observational records have been kept. Indeed in 1977 a nearly identical cloud was photographed by the Viking orbiter several times during the extended mission. The 1977 cloud has essentially the same physical dimensions as the 1973 cloud and it was bright in the violet, indicative of the presence of condensates along with the dust. The past record revealed further that the condensate activity in and around Solis Lacus extends throughout the martian year, with primarily 'blue cloud' activity during southern Fall and Winter ($L_s = 340^\circ$ to 180°) and mixed 'blue' and 'yellow (dust) cloud' activity during Spring and Summer ($L_s = 180$ to 340°). Noachis-Hellespontus shows very similar activity ('blue clouds' from $L_s = 10^\circ$ to 180° and mixed 'blue' and 'yellow clouds' from $L_s = 180^\circ$ to 10°). Both regions have been the major core areas of past dust storms, the core clouds typically appearing suddenly at dawn and fading from white (indicative of the presence of condensates) to yellow by noon (local time).

The Fall and Winter condensates around these regions have generally extended from Solis Lacus upslope into the Tharsis volcanic complex and from Noachis-Hellespontus into the northern portion of the Hellas basin. The Solis Lacus/Tharsis condensates generally brighten toward afternoon, suggesting orographic uplift from upslope winds or active convection as discussed by previous authors. The Noachis/Hellas condensates, on the

other hand, are brightest at dawn, suggesting that they are low-level hazes and possibly frosts. These behaviors have generally been quite repeatable, although during the 1962-1963 apparition ($L_s = 25^\circ - 45^\circ$) there was an unusually intense outburst of condensate cloud activity over Noachis.

The Viking Orbiter 2 color approach map from Soderblom et al (1978) provides an excellent map of the Fall/Winter condensate distribution during 1976 at $L_s = 105^\circ$. Of particular interest is the two-color Red ($0.59 \mu\text{m}$)/Violet ($0.45 \mu\text{m}$) ratio map in which condensates appear as dark grey due to the flatter R/V slope of the reflectance spectrum. The dark Solis Lacus/Tharsis condensate unit extends directly from the northwestern edge of Solis Lacus upslope, consistent with a vapor source immediately downslope in Solis Lacus. The dark Noachis/Hellas condensate unit can be seen emanating from Noachis-Hellespontus ($-35^\circ, 315^\circ$) and being swept into northern Hellas by the prevailing westerly winds. This map appears to confirm the earlier conclusion based on diurnal behavior that the Noachis/Hellas condensates are low-level hazes and frosts: the condensates in Noachis in particular appear to be low-level, as revealed by the filled craters and exposed rims.

Another line of evidence, which we cited in the earlier paper, was the Period 5 water vapor map from the Viking MAWD experiment (Farmer et al., 1977). This map showed striking water vapor anomalies over Solis Lacus and Noachis Hellespontus (10-15 pr. microns compared to the 0-6 pr. micron abundances for the other regions of that latitude). Other period maps don't show these anomalies and it is puzzling why they appeared during Period 5 ($L_s = 140-155^\circ$). The outgassing rate is expected to be highest at the onset of the Spring/Summer dust storms during the morning hours ($\sim 110 \text{ mgH}_2\text{O}/\text{cm}^2/\text{day}$), corresponding to the insolation-driven evaporation of upward-migrating brine/ice melts (Huguenin, Clifford, and Greeley, these abstracts). During the rest of the year the outgassing rates are expected to be much lower and sporadic. During the period of maximum expected outgassing the water vapor signatures would be effectively masked by the associated dust, as clearly demonstrated during the extended mission (Farmer and Doms, 1979). During southern Fall and Winter, when dust activity is at a minimum the small anomalies that might sporadically develop would be at least partially masked by the condensates that preferentially form in these regions. The probabilities of observing anomalies such as those in the Period 5 map would thus seem quite low.

When all the independent lines of evidence, including the Period 5 anomalies, are pulled together, however, a remarkable spatial coincidence of the data occurs. Comparison of these data with those for other nearby sites of dust activity in Claritas and Hellas, for example, show Solis Lacus and Noachis-Hellespontus to be unique in their intimate association with condensates. Purely atmospheric models to explain the diurnal and seasonal condensate behaviors have not satisfied the combined data sets.

References Farmer, C.B. and Doms, P.E. (1979) J.G.R, 84 2881. Farmer, C.B. et al. (1977) J.G.R, 82, 4225; Huguenin, R.L. et al. (1979), NASA TM 80339, 208; Soderblom et al. (1978) Icarus 34, 446.

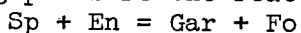
PHASE EQUILIBRIA OF THE MARTIAN MANTLE

Patera, E. S. and J. R. Holloway, Department of Chemistry, Arizona State University, Tempe, Arizona 85281

Bulk density and moment of inertia data for Mars together with models of the internal structure have been used to constrain the density of the Martian mantle between 3.47 and 3.58 g/cm³. One possible reason for the difference between the Earth's mantle density (3.35 g/cm³) and that of Mars is that the Martian mantle is enriched in FeO.

By adding FeO to Pyrolite III the whole-rock density can be increased to that required for the Mars mantle. The amount of FeO added will of course be dependent on the model used for the interior of Mars, therefore an investigation of a range of compositions was done. To obtain a mineralogy for pyrolite + FeO, the system was converted into the CaO-MgO-Al₂O₃-SiO₂ (CMAS) system (O'Hara, 1968). Reactions involving possible minerals in the CMAS system were investigated for their plausibility and to calculate the equilibrium pressures and temperatures. All thermodynamic data except for garnets (pyrope-grossular, almandine) were obtained from Robie and others (1978). Thermodynamic data for pyrope-grossular solid solution were obtained from Newton, Charlu and Kleppa (1977) and Hensen, Schmid and Wood (1975). Grossular-almandine solid solution data was obtained from Cressey, Schmid and Wood (1978).

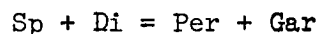
With increasing pressure the reaction is¹:



This reaction is a spinel lherzolite reacting to form a Gar + Sp + Fo + Di wehrlite. This is the same reaction which occurs in the terrestrial mantle, but unlike the terrestrial case, orthopyroxene is consumed before spinel, so spinel remains as a stable phase. The calculated equilibrium pressure is 22 kilobars at 1273 K. The solubility of En in Di is not accounted for in our calculation nor is the solubility of Al₂O₃ in either.

The assemblage Gar + Sp + Fo + Di is stable over the P and T range in which partial melting is thought to occur in the mantle of Mars (150 to 250 Kms in depth) (Carr, 1973, 1974). At approximately 65 kilobars at 1273 C, the following reaction occurs:

¹The symbols used are: Sp, spinel; Fo, forsterite; En, enstatite; Gar, garnet; Di, diopside.



This results in a change from the assemblage Gar + Sp + Fo + Di to the assemblage Gar + Per + Fo + Di. Spinel is consumed and an oxide phase (magnesio-wustite) appears. Our thermodynamic calculations suggest that this assemblage is stable until the olivine-spinel transition pressure is reached.

Modal abundance of the minerals for each of the above mineral assemblages were calculated as a function of the amount of FeO added to Pyrolite III (Table 1). The mole fraction of iron was determined and Fe was distributed to the different phases assuming ideal mixing and distribution coefficients equal to one between each mineral pair. Mineral densities were calculated and together with the modal abundance, whole rock densities were determined. The whole rock densities are plotted versus wt. % FeO added to Pyrolite III in Figure 1. The densities fall within the range of densities predicted by internal structure models for Mars.

The mineral assemblages predicted by the above calculations differ significantly from those of McGetchen and Smyth (1978). This difference is due to the different method of component combination and to the thermodynamic constraints we have used. The consequences of the differences are significant in terms of predicted compositions of partial melts and the amount of FeO needed to produce a given density.

Experiments have been done using Pyrolite III with 12.8 wt. % FeO added as the starting composition. These preliminary experimental data confirm the stability of the olivine, clinopyroxene, spinel and garnet phase assemblage. The reaction boundary between the spinel lherzolite and the wehrlite has been bracketed between 14 and 12 kilobars pressure. The stability of the high pressure oxide phase assemblage has not yet been confirmed.

	<u>ol+cpx+opx+sp</u>	<u>ol+cpx+sp+gar</u>	<u>ol+ox+gar+cpx</u>
Olivine	69.42	74.29	71.35
CPX	15.75	8.26	3.74
OPX	6.95		
Spinel	7.89	2.97	
Garnet		14.49	23.23
Oxide			1.68

Table 1. Modal mineral calculations for Pyrolite III with 12.8 wt. % FeO added. In weight percents.

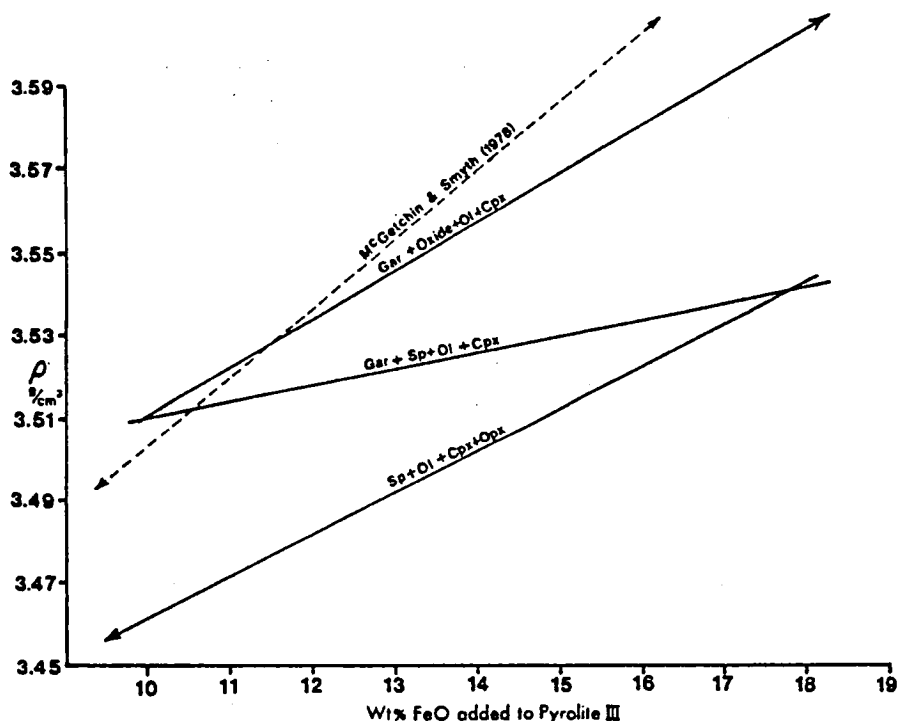


Figure 1. Densities of mineral assemblages as a function of FeO enrichment.

References

- 1) Cressey, O. et al. (1978) Contrib. Mineral. Petrol. 67, 397-404.
- 2) Carr, M. (1973) J. Geophys. Res. 78, 4049-4062.
- 3) Carr, M. (1974) J. Geophys. Res. 79, 3943-3950.
- 4) Henson, F. et al. (1975) Contrib. Mineral. Petrol. 51, 161-166.
- 5) McGetchin, T. and J. Smith (1978) Icarus 34, 512-536.
- 6) Newton, R. et al. (1977) Geochim. Cosmochim. Acta 41, 369-377.
- 7) O'Hara, M. (1968) Earth Sci. Rev. 4, 69-133.
- 8) Robie and others (1978) Geol. Survey Bull. 1452.

ANALOGUE AND SIMULATION STUDIES OF MARTIAN CHEMICAL WEATHERING: THE FORMATION OF EVAPORITE MINERALS

Donna J. Prestel, Lockheed Electronics Co., Inc., Houston, TX 77058 and
David S. McKay, SN6/NASA-Johnson Space Center, Houston, TX 77058

INTRODUCTION

The presence of water on Mars has been clearly demonstrated by many lines of evidence (cf. JGR Viking issue, 1977). Recently, studies of Martian volatile behavior and currently-active meteorological processes have greatly expanded. Some of these have implications for the extent of atmosphere-regolith interactions which are presently occurring. Analysis of data at the Viking 1 lander by Davies (1979) implies that water vapor is uniformly mixed with the atmosphere throughout its lowest 10 km, and is not concentrated near the surface. Davies (1979) also points out that the apparent diurnal variation of the vertical column abundance of water vapor shown from earth-based observations is due to effects of opacity, thereby eliminating the need for transport of large amounts of water between the atmosphere and the regolith. However, observations of the distribution and seasonal variation of Martian atmospheric water vapor reported by Farmer and Doms (1979) are consistent with the vapor being in equilibrium with the regolith over a range of latitudes, where the regolith acts as a sink for vapor during the cold seasons. This water vapor probably evaporates or sublimates to the atmosphere during the warm seasons. Consequently, at least in these regions, atmosphere-regolith interactions involving water are likely.

In spite of the new inferences of surface conditions on Mars, the chemical weathering cycle of Mars is at best only poorly understood. The implied presence of a sulfate-rich duricrust at the Viking lander sites may suggest atmosphere-regolith interactions involving water. In order to understand the chemical weathering cycle of Mars, we have undertaken studies of the process of formation of evaporite crusts under various environmental conditions. We have examined samples from an arid, hot desert environment (Western Desert of Egypt) in detail. We are beginning studies of samples from an arid, cold, permafrost-containing environment (Dry Valleys of Antarctica). Understanding the process of salt crust formation in known terrestrial environments is vital for modeling of the weathering, transportation, and deposition of sulfur and many other elements on Mars. The formation of near-surface evaporites is an important process in some terrestrial environments and may be equally important in parts of the Martian regolith. If an evaporite-forming process has been operating on Mars, the Martian regolith is likely to be exceedingly complex and to contain a variety of evaporite minerals. Investigations of the formation of terrestrial evaporite crusts and their resultant mineral assemblages are useful to define the environmental conditions required for their formation. Laboratory simulation experiments should enable us to place constraints on the formation and mineralogy of crusts likely to be found in the martian environment.

EGYPTIAN EVAPORITES AS ANALOGUES

Viking investigators (Toulmin et al. (1977), Clark (1978)) proposed a possible process for the formation of duricrust. This process consists of the leaching action of a thin film of moisture, with subsequent movement toward the surface by capillary transport, evaporation at the Martian surface, and deposition of a sulfate-rich crust. We have been studying a similar process in Egypt. Subsurface water with dissolved sulfate, chloride, and other species in solution moves upward toward the surface by capillary action. As the water approaches the surface, and begins to evaporate, evaporite minerals begin to crystallize in shallow, loose sands. At the surface, evaporite crusts form during complete evaporation to the atmosphere.

Mineralogy, chemistry, and morphology studies of these crusts by x-ray diffraction and SEM with attached energy dispersive x-ray analysis have been done (Prestel, McKay, and Haynes (1979), and unpublished data). Our results indicate that a seemingly simple chemical environment with the water-induced chemical weathering can lead to decidedly complex mineral assemblages. Even on an annual time scale, stratified mineral assemblages develop from continued evaporation producing new minerals and reactions with preexisting evaporite minerals. In some cases, a single mineral grain has been observed (by SEM-EDAX studies) to have tiny, numerous secondary crystals of different minerals coating its surface.

SAMPLES FROM ANTARCTICA AND PERMAFROST REGIONS

Perhaps the most Mars-like environment on Earth is found in the Dry Valleys of Antarctica. In these regions, lack of precipitation is combined with extremely cold conditions. Permafrost is present at variable depths beneath the surface. Regolith evaporites and salt crusts have been formed in this environment. Evaporite salt grains are found in soil samples as salt encrustations and salt-indurated layers (Bochheim 1978), and from the rims of lakes and ponds (Horowitz et al. 1972). Antarctic soil formation studies (cf. Ugolini 1976), salty permafrost studies — i.e. sulfate, chloride, and nitrate analyses (cf. Cameron et al. 1969, 1970); and detailed characterization of rocks and sediments by DVDP boreholes (McGinnis and Osby 1977) delineate regions which have been postulated to be Martian permafrost analogues.

Using this geologic information and our Egyptian sampling experience as a framework, we have planned a detailed Dry Valleys sample program presently underway in Antarctica by one of our Mars group at JSC (E. Gibson). We also plan to investigate evaporite samples from permafrost regions in Canada and Alaska, in particular, from a Yukon salt marsh where sulfate mineral encrustations have been collected. These regions are more typical of wet, cold environments and will provide a contrast to the Dry Valley samples.

Our intent is to make comparative studies of near-surface evaporites and salt crusts from a variety of terrestrial locations which are analogous to Mars in at least some respects. Mineralogical and morphological data on

these samples will help to constrain models for similar processes in the Martian regolith and will also be used to help design experimental projects.

SIMULATION EXPERIMENTS

Laboratory simulation experiments on salt crust formation are vital to the understanding of Martian chemical weathering processes and are necessary to determine the viability of their formation under Martian conditions. Terrestrial analogue samples build a framework and provide insight into the study of the process of salt crust formation, and Viking chemical data provides the necessary constraints. We are using the JSC Martian Weathering Simulation Facility in collaboration with R.V. Morris in an attempt to understand specific aspects of the duricrust-forming process. We believe that close interaction between analog studies and laboratory simulation experiments will improve both and will provide new insights into complex weathering processes which may be operating on Mars.

References

- Bochheim, J.G., 1978, Antarctic Jour. of the US, Oct. 1978, V. 13, No. 4 p. 36.
- Cameron, R.E. and H.P. Conrow, 1969, Antarctic Jour. of the US. Jan-Feb 1969, V. 4, No. 1, p. 23.
- Cameron, R.E., J. King, and C.N. David, in Holdgate, M.W., ed., Antarctic Ecology, Vol. 2, Academic Press, London (1970).
- Clark, B., 1978, Icarus, V. 34, No. 3, p. 645.
- Davies, D.W., 1979, Jour. Geophys. Res.-Mars Volatiles, V. 84, No. B6, p. 2875.
- Farmer, C.B., and P.E. Doms, 1979, Jour. Geophys. Res.-Mars Volatiles, V. 84, No. B6, p. 2881.
- Horowitz, N.H., R.E. Cameron, and J.S. Hubbard, 1972, Science, V. 176, 21 April 1972, p. 242.
- Journal of Geophysical Research-Viking issue, V. 82, No. 28, 1977.
- McGinnis, L.D. and D.R. Osby, 1977, Antarctic Jour. of the US, Oct. 1977, V. 12, No. 4, p. 115.
- Prestel, D.J., D.S. McKay, and C.V. Haynes, 1979, in Repts. of Planetary Geology Program 1978-1979, NASA TM 80339, p. 200.
- Toulmin, Baird, Clark, Keil, Rose, Christian, Evans, and Kelliher, 1977, Jour. Geophys. Res., V. 82, No. 28, p. 4625.
- Ugolini, F.C., 1976, Antarctic Jour., Dec. 1976, V. 11, No. 4, p. 248.

RECENT (?) SURFACE ALTERATIONS FROM SUBSURFACE SOURCES IN THE OLYMPUS MONS AREA

Morris, Elliot C., U.S. Geological Survey, Flagstaff, Arizona 86001

Twelve dark, irregular-shaped, subcircular patches that range from 2 to 30 km across form an aligned group 130 km long about 150 km west of the base of Olympus Mons (fig. 1). The patches occur on a blanket of eolian material that buries parts of the Olympus Mons aureole. Because their boundaries show no relief, the patches appear as dark stains on the surface material. The fine pattern of pits and grooves that characterizes the surface of the eolian blanket is unaltered within these dark areas. Ridges of the aureole material project through the blanket and cross some of the dark areas but do not affect the color or shape of the areas. Patches in the west half of the aligned group are darker than those in the east half. The largest patch, in the east half, is partly covered by thin layers of eolian material of varied thickness; it has a mottled appearance and is lighter than the other patches.

The patches appear very dark in Viking Orbiter pictures taken with a red filter (614A58) but are very pale or unrecognizable in pictures taken with a violet filter (614A52), indicating a strong blue component in the color of the patches. The patches can be seen in Mariner 9 pictures DAS06823428 and DAS06823708, but because of haze and poor resolution they are not easily recognized.

It is proposed that the origin of the dark patches is due to the eolian deposits having been soaked or saturated by fluids or gases from a subsurface fissure percolating upward through porous, unconsolidated surface materials. Lateral spreading may have occurred by capillary action. The fluids or gases may be volcanic in origin and, if fluids, probably are aqueous solutions enriched in iron and sulfur minerals. Alinement of the patches indicates subsurface structural control: the alinement parallels a major fracture 50 km north in one of the aureole deposits. Absence of vents, mounds, or other landforms resulting from surface disruption indicates *in situ* alteration of the surface materials, and that the fluids or gases were under low pressure.

The dark patches may be very recent additions to the martian scene, as they have formed on some of the youngest sediments on the surface of Mars (1).

REFERENCES

- 1) Scott, D. H., and Carr, M. H., 1978, Geologic Map of Mars, U.S. Geol. Survey Misc. Geol. Inv. Map I-1083.

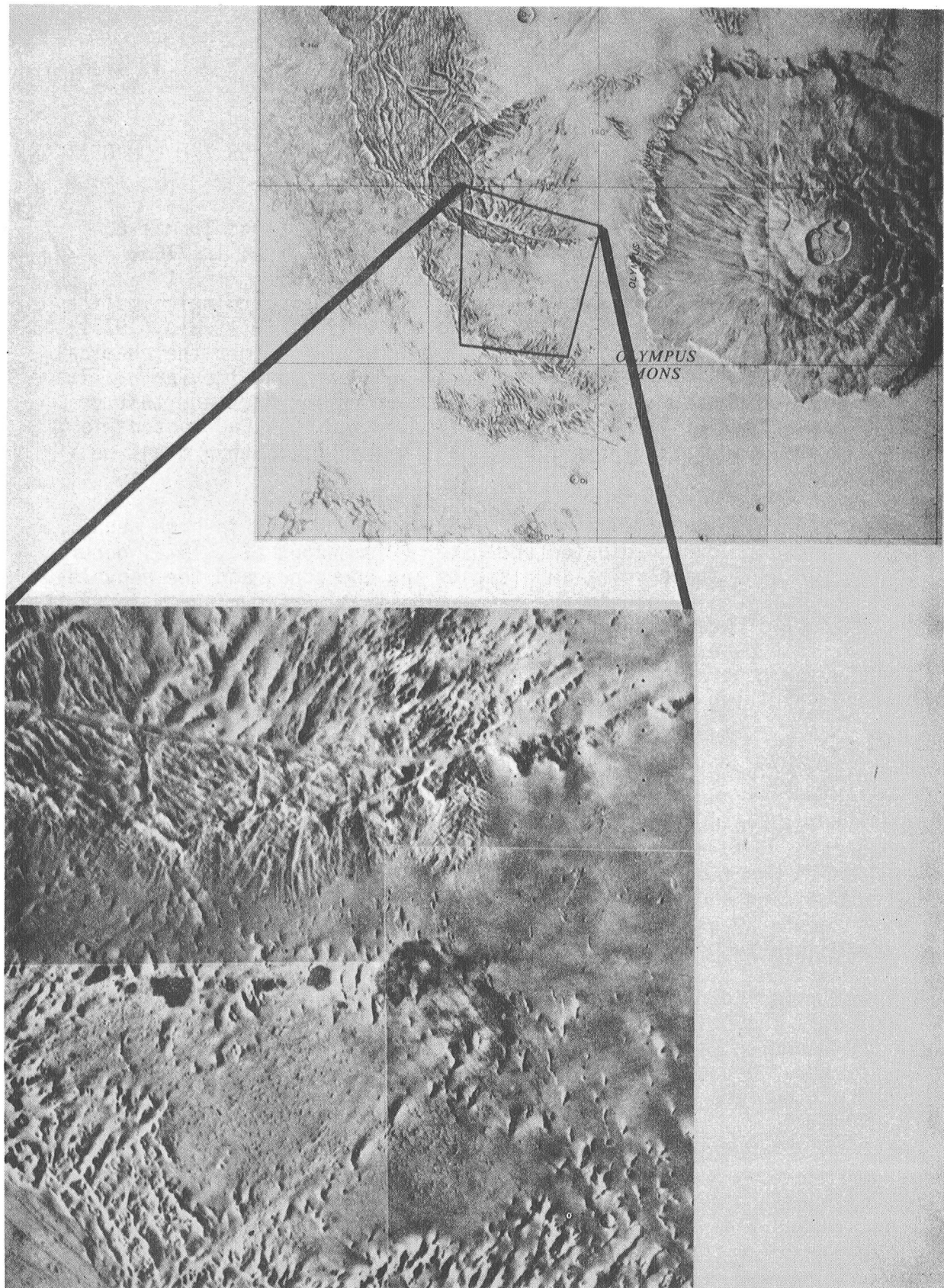


Figure 1. Location of dark stains on young eolian deposits 150Km west of Olympus Mons. The dark areas 2 to 30Km across, form an aligned group of patches 130Km long. (46B21, 46B22, 46B23, 46B24).

CARBOCHLORINATION OF COMMON SILICATES: IMPLICATIONS FOR THE COMPOSITION OF THE MARTIAN SURFACE

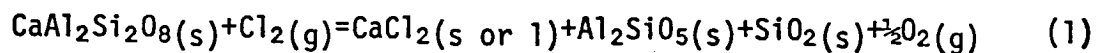
Richard J. Williams, SN7 NASA JSC, Houston, TX 77058 and Thomas E. Erstfeld, Lockheed Electronics Co., Inc., Houston, TX 77058

The chemistry of Martian surface materials and the petrologic implications of that chemistry have been presented by Toulmin et al. (1977); the variation diagrams (Figure 1 in that paper) highlight the chemical differences and similarities among Mars, the Moon, and the Earth. There is a remarkable congruency between the chemistry of Mars and that of rocks from other planets with a single exception, the CaO content is significantly lower in the analyzed Martian materials than might be concluded from the measured SiO₂ content.

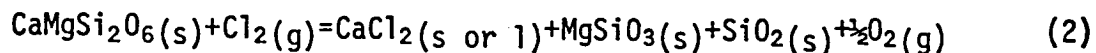
Sulfur and chlorine (Toulmin et al., 1977) are present in high abundances and both carbon dioxide and water (Biemann et al., 1977) occur. The presence of these volatile elements and compounds and the nonvolatile chemistry have lead to the suggestion that Mars surface material is the product of weathering or alteration of mafic rocks (Toulmin et al., 1977). This paper reports on a theoretical investigation of another process for generating calcium-poor compositions: a primary igneous process involving the interaction of chlorine and carbon with common minerals.

The class of reactions investigated are those known industrially as carbochlorination reactions (most recently summarized by Rao et al., 1979). We have used thermodynamics data (Kelly, 1960; JANAF, 1971; Robie et al., 1978) and fugacity coefficients (Ryzenko and Volkov, 1971) to compute reaction constants for the carbochlorination of olivines, pyroxenes, and anorthite for temperatures between 1000 and 1500 K at pressures to 20 kilobars (pressures and temperatures to be expected in magma generating events in planets).

Our analysis indicates that, for C - O - Cl fluids at graphite saturation, only the calcium component of the minerals considered is involved in the reaction; magnesium silicates are refractory, and iron reactions do not occur because of the relative instability of the iron chlorides. Two reactions are particularly important:



and



At graphite saturation (a probably correct assumption for the interior of terrestrial planets according to Sato (1978)), these reactions are functions of temperature, pressure, and chlorine fugacities; the relations are illustrated in Figure 1. At low temperatures, reactions

typified by $\text{CaCl}_2(\text{s or l}) + \text{CO}_2(\text{g}) + \frac{1}{2}\text{O}_2(\text{g}) = \text{CaCO}_3(\text{s}) + \text{Cl}_2(\text{g})$ (curve C on Figure 1) and $\text{CaCl}_2(\text{s, l}) + \text{CO}_2(\text{g}) + \text{H}_2\text{O}(\text{g}) = \text{CaCO}_3(\text{g}) + 2\text{HCl}(\text{g})$ (not shown) intersect the chlorocarbonation reactions. These may provide a sink for calcium chloride, and a mechanism for recycling chlorine.

Our computations suggest relatively modest chlorine fugacities can strip calcium from common silicates under conditions appropriate for magma genesis; this process could produce the anomalously low calcium contents observed in Martian materials. This conclusion must be viewed as highly tentative, because rather large extrapolations of thermodynamic data were used, because it is uncertain whether the quantities of chlorine or rapid recycling mechanisms exist which are necessary to make this process significant on a large scale, and because neither hydrogen nor sulfur species were included in the computations. The carbochlorination reactions and the variations imposed by the inclusion of sulfur and hydrogen will be investigated more thoroughly both experimentally and theoretically in the next year.

References:

- Biemann *et al.* (1977) J. Geophys. Res., 82, p. 4641-4658.
 Toulmin *et al.* (1977) J. Geophys. Res., 82, 4625-4634.
 Kelley (1960) Bureau of Mines, Bull. 584, 232p.
 JANAF (1971) Nat. Stand. Ref. Data Ser., Nat. Bur. Stand. (U.S.), 37, 1141 pages.
 Rao *et al.* (1979) 1977 NASA-Ames Space Settlements Summer Study, Space Resources and Space Settlements, NASA SP-428.
 Robie *et al.* (1978) Geological Survey Bulletin 1452.
 Ryzenko and Volkov (1971) Geochem. International, 37, p. 468-481.
 Sato (1978) Geophys. Res. Letters, 5, p. 447-449.

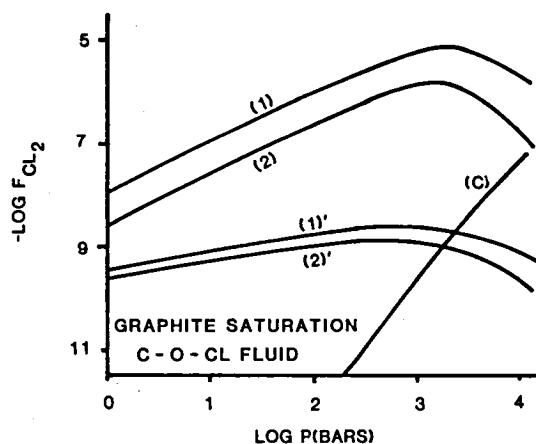


Figure 1. Fugacity of chlorine-temperature-pressure relations for reactions (1), (2), and (C). Curves (1) and (2) are reactions (1) and (2) at 1500 K; curves (1)', (2)', and (C) are reactions (1), (2), and (C) at 1000 K.

VIKING SURFACE SAMPLER DIURNAL TEMPERATURES

Moore, H. J., U.S. Geological Survey, Menlo Park, CA 94025; Hutton, R.E., 1501 Palos Verde Dr., Harbor City, CA 90710; Scott, R. F., Dept. Engr. and Appl. Sciences, Calif. Inst. Tech., Pasadena, CA 91125; Shorthill, R. W., Univ. of Utah Res. Inst., Salt Lake City, Utah 84108; and Spitzer, C. R., NASA Langley Res. Ctr., Hampton, VA 23665

The surface sampler collector heads of Viking Lander 1 (VL-1) and Viking Lander 2 (VL-2) were inserted into the martian surface materials and collector head temperatures monitored throughout diurnal cycles on Sols 343-344 (VL-1), Sols 405-406 (VL-2), and Sols 957-958 (VL-2) (Table 1). Analyses of the temperatures have not been made but plots of the temperatures are given here in the event that others may find a use for them (fig. 1).

Nominal depths of the collector head temperature sensors, which are located on the lower side of the fixed jaw (3), are 5 to 7 cm. The collector heads were inserted into the surface materials with the collector head jaw open so as to surround the sensors with the surface materials. The uppermost parts of the collector heads were uncovered by surface materials. Surfaces were partly to completely shadowed during the VL-2 tests.

Footpad 2 temperatures are included in Figure 1. The sensors of VL-1 are immersed 0.2 to 1.5 cm in the surface material while those of VL-2 are exposed to the atmosphere (8). Because of their locations on the lander, the sensors are subjected to complicated insolation functions.

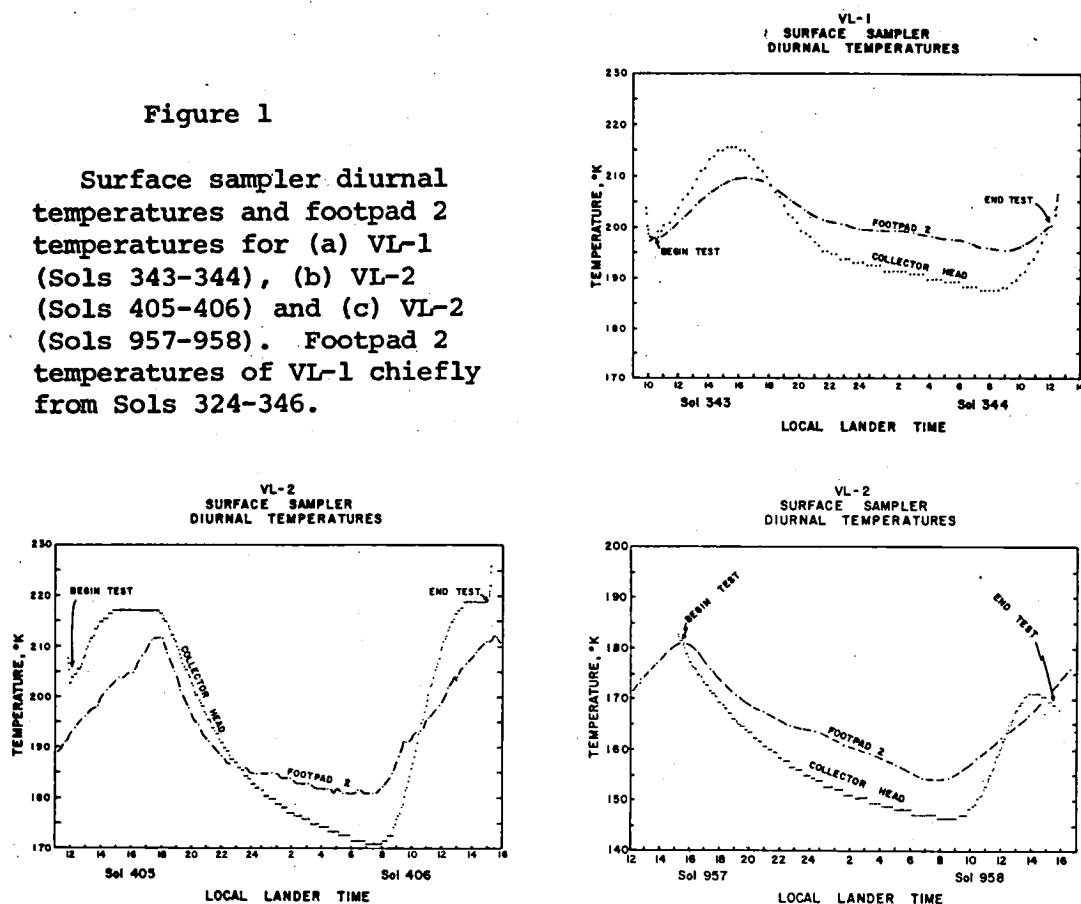
In general, the collector head temperature curves resemble terrestrial and other martian diurnal temperature curves. Temperatures are highest 2 to 4 hrs. after noon and lowest in the early morning (near 8). Peak temperatures are lower than predicted surface temperatures and lows are reasonably close to predicted surface temperatures (5) (Table 1). A smaller range in diurnal temperatures would be expected for a buried probe but a clouded sky could also reduce the range (5, 4).

Lowest temperatures for VL-1 on Sol 344 (fig. 1a) and VL-2 on Sol 406 (fig. 1b) are larger than the CO₂ and CO₂-clathrate sublimation temperatures (1, 7). Highest temperatures correspond to H₂O vapor pressures of 0.015 (VL-1), 0.02 (VL-2, Sol 406), and $\approx 10^{-5}$ (VL-2, Sol 958) mbars (1).

The constant temperatures measured by VL-2 on Sols 405-406 (fig. 1b) may be important and represent a phase change. On Sol 405, the temperature is 217°K from 14:49 to 17:49 and, on Sol 406, the temperature is 218.7°K from 13:28 to 15:03 (end of test). Spacecraft shadowing is an unlikely candidate to explain the constant temperatures because they occur at

Figure 1

Surface sampler diurnal temperatures and footpad 2 temperatures for (a) VL-1 (Sols 343-344), (b) VL-2 (Sols 405-406) and (c) VL-2 (Sols 957-958). Footpad 2 temperatures of VL-1 chiefly from Sols 324-346.



different times in the day. The sensor appears to be working because of the rapid changes in temperatures near the beginning and end of the test. Changes in insolation due to clouds could produce the constant temperatures but the response is the reverse, in part, of what would be expected from opacities measured before and during the periods of constant temperatures (e.g., 4). On Sol 405, opacities changed from 0.96 (11:00) to 0.45-0.58 (16:30-18:00) and, on Sol 406, they changed from 0.37 (12:20) to 0.56 (16:30). Reduced cloud cover would tend to increase the amplitude of the thermal wave.

If the constant temperatures were due to a phase change, the minimum amount of heat required is not large. The Sol 405 peak has been truncated by about 2 or 3°K. If the specific heat of the VL-2 material is $0.14 \text{ cal g}^{-1} \text{ } ^\circ\text{K}^{-1}$, then the heat involved is near 0.28 to 0.42 cal g^{-1} . This is comparable to latent heats of interfacial water on clays (2). Two eutectics have also been considered: (1) $\text{CaCl}_2\text{-MgCl}_2\text{-H}_2\text{O}$ brine

(218°K) (6), and (2) H₂O-H₂O₂ (217°K) (10). Only small amounts of these eutectic compositions would be required. If H₂O-H₂O₂ is responsible for the constant temperatures, the model for H₂O-H₂O₂ in the regolith proposed by Nadeau (9) may be correct.

References

1. Anon., 1957, Handbook of Chemistry and Physics: Chem. Rubber Publ. Co., Cleveland, Ohio, 3213 p.
2. Anderson, D.M. and Tice, A.R., 1971, Low temperature phases of interfacial water in clay-water systems: Soil Sci. Soc. Amer. Proc., v. 35, p. 47-54.
3. Crouch, D.S., 1977, Mars Viking surface sampler subsystem: Proc. 25th Conf. on Remote Systems Tech., Amer. Nuclear Soc., p. 141-152.
4. Ford, A.B. and Anderson, B., 1967, Sorted talus aprons and the movement of debris in Antarctica by repeated thermal contraction and rupture of underlying ice: Jour. Geol., v. 75, p. 722-732.
5. Kieffer, H.H., 1976, Soil and surface temperatures at the Viking landing sites: Science, v. 194, p. 1344-1346.
6. Linke, W.F., 1958, Solubilities of inorganic and metal organic compounds: D. Van Nostrand Co., Inc., v. 1, p. 1487.
7. Miller, S.L., 1973, Nature and occurrence of clathrate hydrates, in Physics and Chem. of Ice, Roy. Soc. Canada, Ottawa, p. 42-50.
8. Moore, H.J., Hutton, R.E., Scott, R.F., Spitzer, C.R., and Short-hill, R.W., 1977, Surface materials of the Viking landing sites: Jour. Geophys. Res., v. 82, p. 4497-4523.
9. Nadeau, P.H., 1977, UV radiational effects on martian regolith water: M.A. Thesis, Dartmouth College, Hanover, NH, 89 p.
10. Schumb, W.C., Satterfield, C.N., and Wentworth, R.L., 1955, Hydrogen Peroxide: Amer. Chem. Soc. Mono, Reinhold Publ. Co., NY, 759 p.

Table 1. Surface sampler diurnal temperatures

	Max Temps (°K) (LLT)	Min Temps (°K)	Predicted (5)		L _s
			Max	Min	
a. VL-1	215.4 (343, 15:13)	187.6 (344, 07:23-07:58)	250	180	296
b. VL-2	217.0 (405, 14:49-17:49) 218.7 (406, 13:28-15:03)	170.9 (406, 06:59-08:30)	240	170	355
c. VL-2	181.5 (957, 15:20-start) 170.9 (958, 13:45-14:35)	146.5 (958, 07:40-09:05)	200	150	289

STUDY OF LIBYAN DESERT GLASS SITE, SW EGYPT: JUNE 1979

James R. Underwood, Jr., Department of Geology, Kansas State University, Manhattan, KS 66506 and Robert Giegengack, Department of Geology, University of Pennsylvania, Philadelphia, PA 19104

In June 1979 the distribution area of Libyan Desert glass was visited, and during a five-day period glass samples were studied in situ and some were collected, bedrock outcrops were studied and sampled, and dune sand and the sand from the interdune corridors was sampled. Close scrutiny of bedrock blocks and of many, many pieces of Libyan Desert glass failed to reveal on any of them a zone of transition from sand or sandstone to glass.

Special attention was focused on outcrop areas of the vaguely elliptical pattern (12 km x 8 km) visible on Landsat images, of dark, iron oxide-enriched Nubian Sandstone that may represent strata disrupted by meteorite impact. Microscopic study of samples of the Nubian Sandstone collected in the area during an earlier expedition (Underwood, 1979) did not reveal conclusively the presence of shock metamorphic features.

The close association of concentrations of large (>500 gm) glass samples and some of the areas of outcrop of large blocks of Nubian Sandstone up to one meter in maximum diameter, suggest that the glass may not have been transported far from its source. It is difficult to imagine just how transport over any significant distance could have been achieved without distributing the larger blocks of Libyan Desert glass more evenly than, apparently, they were. It is possible, however, that the glass fragments, and the larger pieces from which they may have been derived, underwent several episodes of transport.

A small (593 gms) nickel-iron meteorite was found at lat 25° 09.5'N, long 25° 35.1' E within the southern part of the distribution area of the glass. The microscopic ablation ridges on the convex side of the meteorite are delicate features that do not survive weathering on Earth more than a few hundred to a few thousand years (Alexander Bevin and Robert Hutchison, personal communication, 1979). If the age of the glass of 28.5 million years, determined by fission track analysis (Gentner, Storzer, and Wagner, 1969; Storzer and Wagner, 1971) is valid, there can be no connection between this meteorite and the origin of Libyan Desert glass.

Artifacts abound in the region. Most are of Late Paleolithic affinity, and numerous blades and scrapers manufactured in this tradition are concentrated on and around two occurrences of playa lake sediments. A skillfully worked 8 cm-long doubly terminated point of Libyan Desert glass was recovered from the southernmost part of the area of glass occurrence in September 1978.

Although Nubian Sandstone artifacts of Acheulean lithic industry also are common in the region, until this trip no Acheulean artifacts had been discovered that were made of Libyan Desert glass. At Lat 25° 08.0' N and long 25° 35.3' E, near the southern margin of the glass area, a hand axe of Libyan Desert glass and identified as Acheulean (Kenneth Oakley and Derek Roe, personal communication, 1979) was discovered lying on the surface.

References:

- Gentner, W., Storzer, D., and Wagner, G. A., 1969, New fission track ages of tektites and related glasses: *Geochem. et Cosmochem. Acta*, v. 33, p. 1075-1081.
- Storzer, D. and Wagner, G. A., 1971, Fission track ages of North American tektites: *Earth and Planetary Sci. Letters*, v. 10, p. 435-440.
- Underwood, James R., Jr., 1979, Libyan Desert glass; 1978 expedition: *Trans. Kansas Acad. Science*, v. 82, no. 2, p. 101.

Chapter 5

VOLCANIC PROCESSES AND LANDFORMS

THE VOLCANIC RESURFACING HISTORY OF MARS

Spudis, Paul D. and R. Greeley, Department of Geology, Arizona State University, Tempe, Arizona 85281

Mars displays a diversity of geologic units and landforms that, when mapped photogeologically, enable interpretation of geologic history. Recent syntheses of Mariner 9 and early Viking data have given a fairly good understanding of the role of volcanism in the geologic evolution of Mars (1,2). The extensive collection of Viking Orbiter images enable the improved delineation of volcanic units on a nearly planetwide basis. This photogeologic mapping is then correlated with relative age data, based on both superposition relationships and density of medium sized impact craters (3). It is then possible to reconstruct the volcanic history of Mars in terms of *areal resurfacing*; i.e., the percentage of the planets surface that has been modified by volcanic eruptions in a given period of geologic time. Two potential errors in these estimates arise from photogeologic interpretation. The identification of volcanic units is accomplished through established photogeologic criteria: presence of volcanic edifices, calderas, flow fronts and lava tube/channel systems. The presence of wrinkle-ridges is considered a useful criterion for interpretation of a volcanic origin, but is not necessarily a definitive indicator. In addition, some units may be buried or partially buried by younger units so the values of resurfaced areas should be considered minimum estimates.

The distribution of volcanic units on Mars is shown in Figure 1. *Plains* units are the most widespread volcanic units on Mars. The oldest plains are the pl_1 - *lower plateau plains* (intercrater plains) (4, 5) and occupy $26.7 \times 10^6 \text{ km}^2$ (18.6%) of the martian surface. Other plains units include: 1) pl_2 - *upper plateau plains* (Lunae Planum plains) - $5.2 \times 10^6 \text{ km}^2$ (3.6% Mars surface); 2) f_1 - *lower flood lavas* (Syrtis Major epoch) - $9.2 \times 10^6 \text{ km}^2$ (6.4%); 3) f_2 - *intermediate flood lavas* (Chryse epoch) - $8.1 \times 10^6 \text{ km}^2$ (5.6%); 4) f_3 - *upper flood lavas* (Tharsis epoch) - $7.5 \times 10^6 \text{ km}^2$ (5.2%); and 5) Vp - *northern volcanic plains* (identification as volcanic questionable in some areas) - $27.4 \times 10^6 \text{ km}^2$ (19% Mars surface). An additional unit, volcanic materials (?) ($5.9 \times 10^6 \text{ km}^2$; 4.1%) includes such units as aureole material grooved and fractured plains and eroded units peripheral to the Tharsis volcanoes and may be partly or mostly volcanic in origin. The *volcanic constructs* are subdivided into four units: 1) S - shields (large Tharsis constructs) occupy $1.2 \times 10^6 \text{ km}^2$ (0.8%); 2) Sb - shield, partly buried (older Tharsis patera and tholi; see 6) - $1.26 \times 10^6 \text{ km}^2$ (0.9%); 3) Alba Patera (a unique martian construct (6)) - $1.1 \times 10^6 \text{ km}^2$ (0.8%); and 4) II - Old Patera (Tyrhenna Patera-type; see (6)) - $0.2 \times 10^6 \text{ km}^2$ (0.015%). Thus, constructs occupy only $2.65 \times 10^6 \text{ km}^2$ (1.8% Mars surface) strongly suggesting they are minor contributors to the planet's resurfacing history.

These areal data for martian volcanic units are combined with relative age data (2,3) to produce Figure 2. In this depiction of the resurfacing history of Mars, shields and partly buried shields have been combined into one unit. It is seen that extrusion of volcanic material has been more or less continuous throughout martian geologic history but has apparently decreased in volume of extrusion through time. This is consistent with a Moon-like thermal history (i.e., thickening lithosphere - increasing depth to magma source region), albeit active over a longer period of time, as has been postulated elsewhere (1,7).

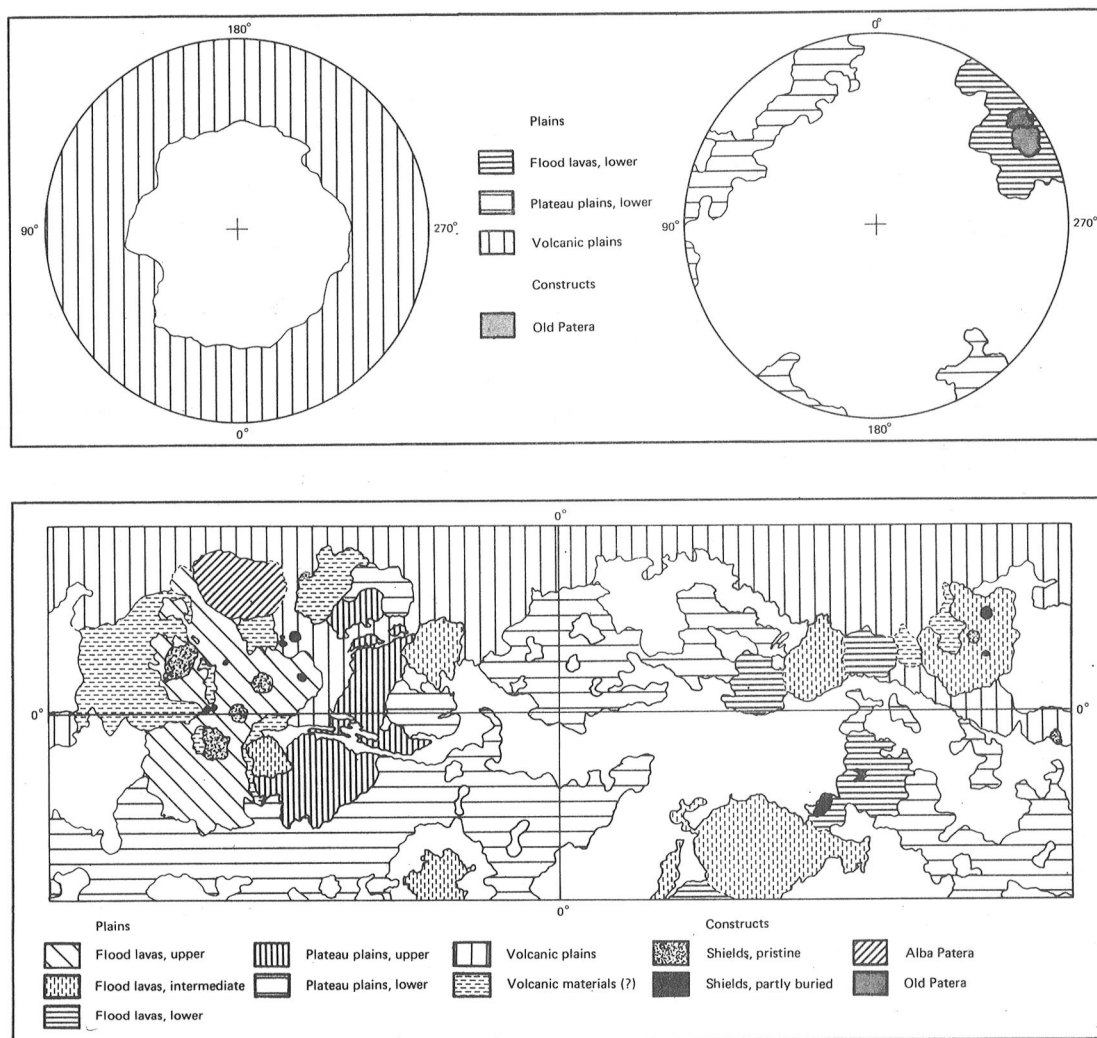


Figure 1. Map of distribution of volcanic units on Mars as defined in text.

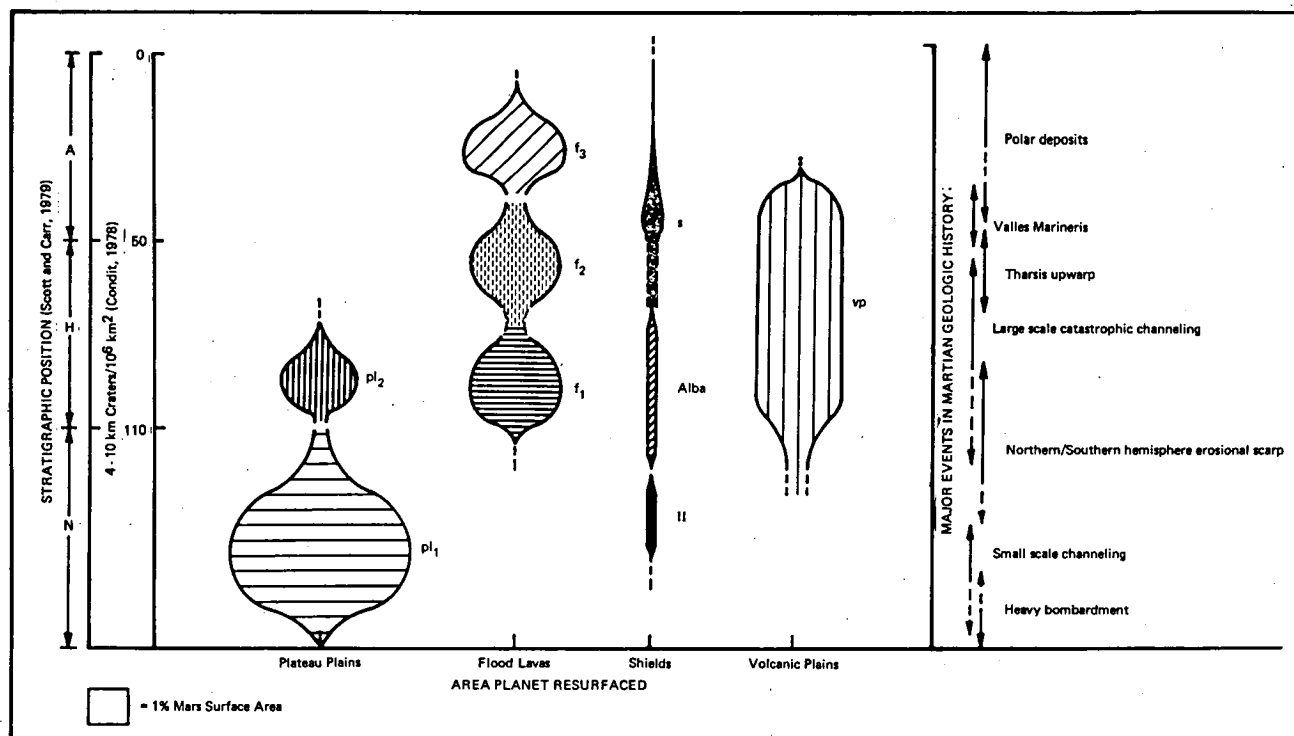


Figure 2. A summary of the volcanic resurfacing history of Mars. Units are defined in text and their distribution is shown in Fig. 1. Relative age correlation utilizes data given in references 2 and 3. The positions of major geologic events are taken primarily from references 1 and 2; the length of arrows represents uncertainty in the placement of the event, not necessarily its duration.

References

1. Mutch, T., et al. (1976). *The Geology of Mars*, Princeton Press.
2. Scott, D. and M. Carr (1978). *USGS Map I-1083*.
3. Condit, C. (1978). *Icarus*, 34, 465.
4. Wilhelms, D. (1974). *JGR* 79, 3933.
5. Greeley, R. and P. Spudis (1978). *GRL* 5, 453.
6. Greeley, R., et al. (1978). *EOS* 59, 310.
7. Carr, M. (1973). *JGR* 78, 4049.

by Rosaly M.C.Lopes and J.E.Guest, University of London Observatory,
Mill Hill Park, London NW7 2QS
and C.J.N.Wilson, Geology Department, Imperial College, London SW7

The base of the Olympus Mons volcano is bounded by a 2 to 6 km high scarp. Extending out from near the foot of the scarp is a distinct terrain characterised by curvilinear ridges and troughs, and distributed around the volcano as a series of overlapping lobes with arcuate outer boundaries. Based on Mariner 9 photography the materials making up this terrain were mapped as aureole materials (Carr, 1975), and shown to extend for hundreds of kilometres from the foot of the volcano.

A number of explanations for the aureole materials and scarp were proposed from Mariner 9 data (Carr *et al.*, 1973; King and Riehle, 1974; Morris and Dwornik, 1978).

Surface features of the aureole materials appear fresher from Viking pictures than was evident from Mariner 9, and show no evidence of extensive erosion of the surface. The aureole materials can be seen in places to overlie the surrounding plains. However, fresh appearing lavas veneer the scarp and extend over parts of the aureole. The sequence of events suggested, therefore, in the formation of Olympus Mons is: (i) formation of pedestal, now exposed in the scarp, (ii) formation of scarp and aureole, (iii) young lava flows and construction of upper part of present mountain.

Viking pictures showed mass movement features some tens of kilometres long associated with the basal scarp which have some characteristics in common with the aureole materials, and Carr *et al.* (1977) suggested that the aureole may also have been formed by mass movements on a much larger scale. This explanation appears to be the most likely based on present evidence. That they were emplaced by outward movement from the volcano is supported by the surface texture which, especially on the outer margins, is indicative of flow. Also, there are strong topographic controls on the areal extent of the units, those lobes of largest extent being to the north and northwest where the terrain slopes away from the volcano into the northern plains; the lobes are less extensive elsewhere as the terrain rises onto Tharsis. This distribution indicates a clear gravity control on the surface extent of the units. However, locally where the materials abut against Tharsis they have climbed uphill by as much as 1 km, over a distance of about 200 km; this requires a flow of considerable momentum such as a rockslide or an ash flow rather than lava flows.

To test this theory, the volume of material present in the aureole lobes has been determined from Viking pictures, using the areal extent of the lobes and their minimum thicknesses estimated from shadow lengths on the ridges. These volumes are compared with estimates for the potential volume of material that could have been removed from the edge of the volcano in scarp formation. This was calculated using the average height of scarp adjacent to each lobe unit, based

on Blasius et al photogrammetric measurements, and an estimate of slope for the flank of the volcano. The present average slope (4° estimated from present diameter and height) was taken for the northeast, east, southeast and southwest flanks. A shallower average slope of 2° was taken for the north, northwest and west flanks; since the local topography shows that Olympus Mons sits on a southeast - northwest slope, therefore indicating a shallower average slope for the northern to western flanks.

The comparison between present volume of material in the aureole and volume available in scarp formation (figure 1) shows a good correlation between the two. The 4° slope is the maximum slope possible and at the time the aureole was formed it may have been shallower, in which case we get an excess of material available; since the estimates of material in the aureole are minimum volumes the results are consistent with the view that the aureole materials are the results of mass movement during scarp formation.

The evidence in favour of aureole materials being of mass movement origin can be summarized as follows:

- (i) Surface features indicate emplacement by flowage away from the volcano,
- (ii) Comparison with small mass movement features at base of scarp,
- (iii) Control of local topography on length of lobes,
- (iv) Highest scarps are adjacent to largest volume lobes,
- (v) Volumes of lobes are consistent with their having been derived from scarp formation.

Assuming the aureole materials were produced by rapid mass movement of material from scarp, we consider that they were emplaced by a series of mega-rockslides rather than as a rock flow or sturzstrom (Hsü, 1975). Surface textures and thicknesses of deposits are more consistent with what would be expected for rockslide products rather than sturzstroms. Also, some of the aureole units have travelled uphill locally, and since the slopes on which the material travelled initially are only 1° or 2° , it is unlikely that sturzstrom type velocities could have been achieved, and the material would most likely have been diverted by topographic highs rather than being carried uphill. However, in the case of a slide mechanism, the non-fragmented material would have been able to transmit a high stress, and assuming a low coefficient of friction at the base, be capable of movement up the slope.

We consider that the emplacement of the rockslides may have been assisted by the development of permafrost in the rocks of the pedestal material of the mountain. Renewal of volcanic activity to produce the present summit cone may well have been accompanied by a general increase in heat flow; this could have caused melting of permafrost and general slope instability of the mountain, leading to breaking up of material from scarp.

It is interesting to note that many workers consider the martian channels to have been formed by floods caused by an increase in the surface temperatures. It may be that the Olympus Mons mega-slides

and the production of at least some of the channels are related, having been formed during a period of widespread melting of permafrost caused by an amelioration of the martian climate.

References:

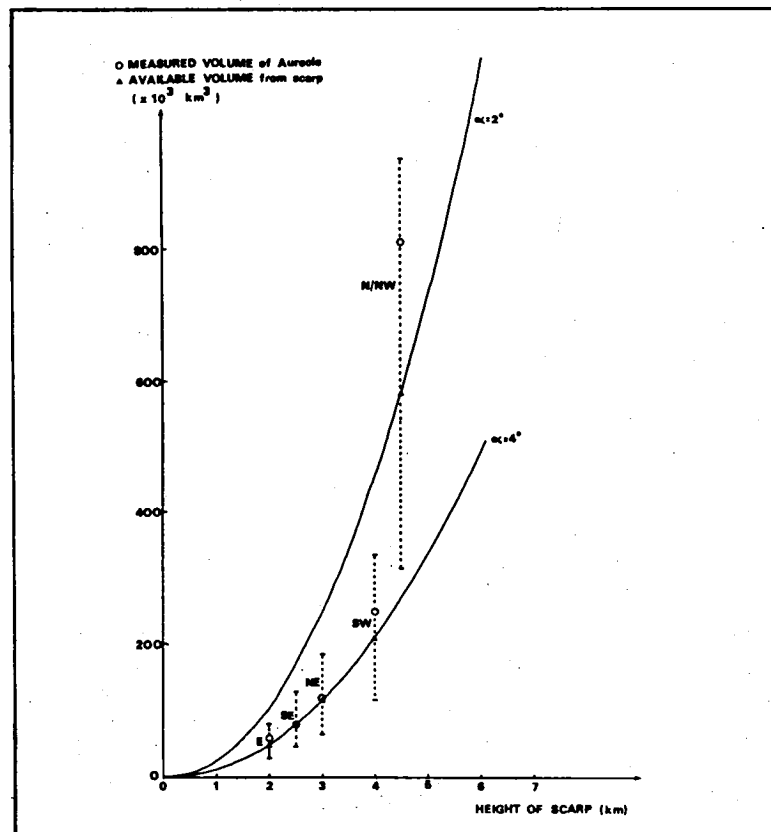
- Blasius, J.R.; Roberts, W.J.; Cutts, J.A.; Duxbury, T.C. and Glacklin, D.L., in press
 Carr, M.H., 1975, U.S. Geol. Survey Map I-893
 Carr, M.H.; Greeley, R.; Blasius, J.R.; Guest, J.E. and Murray, J.B., 1977, Journ. Geophys. Res. **82**, 3985-4015
 Carr, M.H.; Masursky, H. and Saunders, R.S., 1973, Journ. Geophys. Res. **78**, 4031-4036
 Hsü, K.J., 1975, Geol. Soc. Am. Bull. **86**, 129-140
 King, K.J. and Riehle, J.R., 1974, Icarus **23**, 300-317
 Morris, E.C. and Dwornik, S.E., 1978, U.S. Geol. Survey Map I-1049

Figure 1 - Volume of material available from scarp formation (V) calculated as a function of height of scarp (h) and slope of the volcano's flank (α), following the relation:

$$\frac{V}{F} = \frac{h^2}{3 \tan \alpha} (h + 3 r \tan \alpha)$$

where F = part of the volcano's circumference adjacent to each unit,
 r = present radius of volcano (275 km).

The error bars represent error in volume equivalent to a 25% error on estimation of scarp height.



LAVA FLOW MAPS OF THE THARSIS PROVINCE ON MARS

Scott, D. H., Schaber, G. G., Horstman, K. C., and Dial, A. L., Jr.,
U.S. Geological Survey, Flagstaff, Arizona 86001

The systematic mapping of lava flows in the Tharsis volcanic province covers some 18 million square kilometers and is being compiled on a series of 16 maps at 1:2 million scale. Within this province occur the four largest and youngest volcanoes on Mars: Olympus Mons, Arsia Mons, Pavonis Mons, and Ascraeus Mons; the latter three collectively form the large elevated area named Tharsis Montes. Other major physiographic and structural features included in the province are Alba Patera, an ancient low-relief volcano of great size; Acheron Fossae, possibly also a volcano-tectonic structure but older than Alba Patera; and Syria Planum, a very large domical uplift southeast of the Tharsis Montes.

Some of the maps are being made from controlled Viking photomosaics tied to the Viking control net and published as quarter quadrangles in the Atlas of Mars Topographic Series (1). Where these bases are not available, larger scale catalog photomosaics tied to the Mariner 9 control net were used. These maps were subsequently reduced to the 1:2 million scale but slight differences may occur in places between features referred to coordinates on the two types of bases.

Although the geologic investigation was mostly directed toward mapping of lava flows and the determination of their eruptive sequences, structural features such as faults, fractures, and the basal scarp around Olympus Mons were also mapped and dated relative to the flow units. In this way a sequence of tectonic episodes was determined in conjunction with the major volcanic events.

Stratigraphic relations and flow morphology of the major eruptive sequences were the primary means of determining their relative ages. Crater counts on the various units were made to verify these age relations and to obtain some degree of correlation between flows in widely separated areas where overlap relations could not be established. Crater size-frequency distributions were calculated from crater counts on moderate resolution (180-280 m/pixel) frames. Sources of error in crater counts include variations in cloud cover, sun elevation-angle, and resolution in the images. Statistically valid data were gathered by counting craters within large areas of individual flow units; these areas range in size from 36,000 km² to 176,500 km².

Of the 17 major lava flow sequences mapped in the Tharsis region, 11 emanated mostly from two large source volcanoes, Olympus Mons and Arsia Mons. The youngest recognized flows were extruded from large fissures in the high plains east of Olympus Mons. The oldest flows erupted from

calderas and associated fissures in two widely separated localities at Alba Patera and Syria Planum. All flows are similar in morphology to those on Earth and the Moon. They commonly exhibit overlapping, lobate, and crenulated margins and occur chiefly as sheet flows or as channel and tube-fed flows (2). Sheet flows are more common on the plains and on the lower, more gentle slopes of volcanoes. Their surfaces appear flat and smooth at moderate resolution but at high resolution they show concentric ridge-and-trough patterns subparallel to flow margins. Channel and tube flows are more prevalent on the steeper slopes of volcanoes such as Olympus Mons and Arsia Mons, but also occur on relatively low-relief surfaces at Alba Patera and Ceraunius Fossae. High resolution pictures show that younger flows have rougher textures than older ones that have been smoothed by erosion and mantled to various degrees by eolian deposits. The martian flows, like those on Earth, originated from the central vents of volcanoes or from radial fissures on their flanks, or from fissures in plains areas far removed from the volcanic edifices.

The Tharsis lava flow maps will be published as a series by the U.S. Geological Survey as Miscellaneous Geologic Investigations Maps (I-maps). The first map of the series, MC 9-NW, has been submitted for publication.

REFERENCES

- 1) U.S. Geological Survey, 1979, Atlas of Mars Topographic Series.
- 2) Carr, M. H., Greeley, Ronald, Blasius, K. R., Guest, J. E., and Murray, J. B., 1977, J. Geophys. Res., v. 82, no. 28, p. 3985-4015.

TEMPE-MAREOTIS VOLCANIC PROVINCE OF MARS

Carroll Ann Hodges, U.S. Geological Survey, Menlo Park, CA 94025

Perhaps the least ambiguous small-scale volcanic province thus far identified on Mars is in the Tempe-Mareotis Fossæ region, northeast of and aligned with the main Tharsis shields. Approximately 30 topographic features of probable volcanic origin are localized within the intensely fractured terrain along the southwest margin of a highlands plateau remnant. The ragged, discontinuous escarpment of the plateau appears to have receded by erosion and foundering, and lava flows have invaded the lowlands. The area of interest is approximately 200,000 km², covered by high-resolution (≈ 60 m/pixel) Viking imagery obtained during rev 627A (JPL mosaic 211-5813).

Small volcanic vents are primarily, but not exclusively, within the lowland plains. Circular to elongate rimless craters atop low, gently sloping shields are the most common morphologic type. Aprons that terminate in concentric lobate patterns surround many of these craters, so that a direct relation to the lava flows that characterize the lowland plains seems implied. Shields range from about 2 to 6 km across at the base, and summit craters are a few hundred meters to as much as a kilometer in diameter. Two well-developed slot-shaped vents are 2 to 4 km long, 500 m wide.

The gentle slopes of the low shields prevent the use of shadow measurements to estimate heights. However, the depths of summit craters can be so estimated, and a rough guess can thus be made of the relief of the edifice in which a crater occurs. Crater depths obtained by this means are 100 m or so; the low shields appear to be 2 to 3 times as high as the craters are deep and thus stand perhaps 200 to 400 m in relief.

In addition to the conspicuous shields, there is at least one large conical feature with a summit crater. Its unique symmetry in this area where elongate structures predominate lends ambiguity to its interpretation, but it is a good candidate for a cinder cone. It is over 1000 m high and about 3 km across at the base, with a summit crater about 400 m in diameter.

The volcanic features in this province appear to be analogous in morphology and even in scale to basaltic vents characteristic of the Snake River Plain, specifically those classed as low shields (Greeley, 1977a), and similar constructs in Hawaii and Iceland. Shields of the Snake River Plain range from 2 to 20 km in base diameter; summit craters are from 100 to 1000 meters across, with depths of 5 to 60 m (Pike, 1978). Cottrell's Blowout is a linear slot-shaped vent about 1 km long, 40 m

deep, and 170 m wide atop an elongate low shield (Greeley, 1977b) and is identical in appearance to the slot vents in the Tempe-Mareotis region of Mars.

Comparisons of martian dimensional ratios with those of terrestrial counterparts are problematical because of the current lack of topographic data for the martian features. However, preliminary estimates for six low shields yield height to base ratios of about 0.04 to 0.07. An average of ratios for terrestrial low shields, derived from Pike's (1978) tabulation, is about 0.014 ± 0.005 for Snake River Plain shields and $0.020 \pm .005$ for similar low shields in Iceland and Hawaii. The martian estimates are within the same order of magnitude, albeit--like so many other parameters on Mars--higher by a factor of 2 or 3. Estimates based on more reliable topographic data are required in order to validate the comparison.

The Tempe-Mareotis plateau remnant, within the margins of which these volcanic vents occur, is intensely dissected by graben trending predominantly N 40° E, approximately parallel to the alignment of the great shields on the Tharsis ridge. Subsidiary graben trends superposed on this dominant set include slightly west of north and N 60° E; the latter predominates in the western part of the area, and most of the volcanic vents are localized along this N 60° E trend. The lowland plains are much less dissected than the plateau, and lava flows clearly embay and obscure some of the highlands fractures. Circular to elongate collapse pits are numerous along many graben; these may be of volcanic affinity, but there is no clear evidence that eruptions were associated with them. They may be analogous to the collapsed pit craters common in Hawaii. Low rims recognizable along some graben in the lowland suggest that lava may have been extruded from these fissures.

The remarkable morphologic and scale similarities of the prospective volcanic vents in the Tempe-Mareotis area to the numerous fissure-related, basaltic, low shields of the Snake River Plain lend strong support to their analogous interpretation. Prominent structural control is especially characteristic of both the martian and terrestrial examples. The position of the Tempe vents at the northeast end of the Tharsis ridge, where volcanism apparently progressed from southwest to northeast (Carr, 1976; Wood, 1976), suggests that these small constructs may represent simply the last and least product of the Tharsis volcanic episode.

References:

- Carr, M. H., 1976, The volcanoes of Mars: Scientific American, v. 234, p. 32-43.

- Greeley, Ronald, 1977a, Basaltic "plains" volcanism, in Volcanism of the eastern Snake River Plain, Idaho, R. Greeley and J. S. King, eds., NASA, p. 25-44.
- Greeley, Ronald, 1977b, Aerial guide to the geology of the central and eastern Snake River Plain, in Volcanism of the eastern Snake River Plain, Idaho, R. Greeley and J. S. King, eds., NASA, p. 61-111.
- Pike, R. J., 1978, Volcanoes on the inner planets: some preliminary comparisons of gross topography: Proc. Lunar & Planet. Sci. Conf., 9th, Lunar and Planetary Institute, Houston, p. 3239-3273.
- Wood, C. A., 1976, Morphological evolution of shield volcanoes on Mars and Earth: EOS, v. 57, p. 344.

THE DOMES AND ASSOCIATED FLOW LOBES IN ARCADIA PLANITIA, MARS

Carroll Ann Hodges, U.S. Geological Survey, Menlo Park, CA 94025

A group of domical structures that are apparently unique on Mars occurs about 1500 km northwest of Olympus Mons, in Arcadia Planitia. The domes number perhaps 20 to 30 and range from about 1 to 8 km across at their bases. Crude shadow-length measurements, and visual comparisons with crater rim flanks whose heights can be obtained (Pike, 1977), suggest that the largest domes may be as much as 200-300 m high, with height to base ratios on the order of 0.04.

Associated with the domes is a series of crescentic ridges in a distinctly lobate, flowlike pattern covering an area of some 12,000 km². The narrow ridges and troughs have a "wavelength" of about 700 to 800 m and appear fairly evenly spaced. Relief of the ridges relative to the furrows is possibly as much as 100 m. Superposed on this crenulate pattern of narrow ridges is a poorly defined, widely spaced set of larger ridges or "downstream"-facing scarps spaced at about 2- to 8-km intervals.

The "axis" of this lobe is marked by a conspicuous trough in which lies an axial ridge, nearly 200 m high, flanked by leveelike ridges on either side. The ridges of the lobate material fan away from this central ridge and trough in a sort of pinnate pattern, and a genetic relation seems implied by such a configuration.

Viking coverage does not extend far enough south to determine an actual source area for this material that appears to have flowed northward. Areas to the east and west are surfaced by similarly textured, irregular terrain, but the pinnate ridge pattern and associated domes progressively disappear.

The domes are rounded and smooth in general, but the largest ones have slight depressions and radial cracks at their summits, aptly described as "puckers."

The regular pattern of ridges in the debris lobe resembles rather closely the crescentic patterns of terrestrial silicic lava flows like those associated with Glass Mountain and Little Glass mountain at the Medicine Lake Highlands caldera, a similar glass flow at Newberry caldera, or the Chao dacite flow in Peru (Guest and Sanchez, 1969). Adding to this impression is the strong resemblance of the domes to obsidian or rhyolite domes in such localities as Mono Craters, California, and those associated with the glass flows cited above. Unlike these terrestrial cases, however, the lobate ridges in the martian example show no obvious relation to the domes, which appear to be superposed on

the flow pattern. Height to base ratios on Glass Mountain, Little Glass Mountain, and a nearby unnamed dome range from 0.04 to 0.13, so that dimensional ratios appear comparable to those of the martian examples, insofar as they can be estimated.

The spacing of ridges on terrestrial flows on both basaltic and silicic compositions is indicative of flow viscosities (Fink and Fletcher, 1978; Fink, 1979, in press). Using estimates of ridge heights based on shadow measurements, and strain rates consistent with those of terrestrial flows, Fink (1979, in press) estimated a viscosity for this martian lobe of the order of 10^{11} poises, within the range of viscosities of terrestrial rhyolite flows, but far greater than that of terrestrial basaltic flows.

The height of the axial ridge appears to establish a minimum thickness for the entire "flow" of perhaps 200 m, and regional topographic gradient in this vicinity is about 0.002 (U.S. Geological Survey, 1976). Lava flows associated with the Tharsis shields were emplaced on similar gradients, but measured thicknesses ranged only from about 11 to 60 m (Moore and others, 1978). These flows have morphologies and yield strengths characteristic of basalts. The considerably greater apparent thickness of the Arcadia Planitia flow, on a comparable gradient, suggests a higher yield strength possibly related to a more silicic composition.

The height measurements cited here may be high by a factor of 6 or more (D. W. G. Arthur, oral commun., 1979). Estimates based on shadow lengths are dubious at best, but the enhanced contrast of these particular pictures has greatly aggravated the problem. Thus interpretations dependent on these estimates are subject to revision when better topographic data become available. Ridge heights reduced by a factor of 6 would invalidate the conclusions based on viscosity calculations (Fink, oral commun., 1979).

Thus far, persuasive evidence for silicic volcanism on Mars has been notably unreported, although Malin (1978) did suggest that Elysium Mons could be analogous to a composite volcano in the Tibesti province of Chad, Africa. Certainly the most conspicuous volcanoes, like those of the Tharsis region, appear comparable to terrestrial basaltic shields. The province described here, northwest of Olympus Mons, is perhaps the best candidate so far recognized for silicic volcanism. Unlike most terrestrial rhyolite or obsidian domes, however, the domes in Arcadia Planitia show no obvious relation to caldera structures.

Alternative mechanisms that might explain the morphologic characteristics of the Arcadia Planitia domes and flow lobes include mud flows (H. J. Moore, oral commun., 1979) or debris flows of some sort; even if

the ridge heights as estimated are greatly exaggerated, basaltic lava does not seem a likely candidate for the material for several reasons, the most obvious being the distinctly different and very terrestrial-like appearance of presumed basaltic flows emanating from the Tharsis shields. Recessional moraines with associated pingoes are thought unlikely also but have not been entirely discounted.

References:

- Fink, J. H., 1979, Surface folding and viscosity of rhyolite flows: Geology, in press.
- Fink, J. H. and Fletcher, R. C., 1978, Ropy pahoehoe: surface folding of a viscous fluid: Journal of Volcanology and Geothermal Research, v. 4, p. 151-170.
- Guest, J. E. and Sanchez, J. R., 1969, A large dacitic lava flow in northern Chili: Bulletin Volcanologique, Tome XXXIII-3, p. 778-790.
- Malin, M. C., 1977, Comparison of volcanic features of Elysium (Mars) and Tibesti (Earth): Geological Society of America Bulletin, v. 88, p. 908-919.
- Moore, H. J., Arthur, D.W.G., and Schaber, G. G., 1978, Yield strengths of flows on the Earth, Mars, and Moon: Proc. Lunar & Planetary Sci. Conf. 9th, p. 3351-3378.
- Pike, R. J., 1977, Size-dependence in the shape of fresh impact craters on the Moon, in Roddy, D. J., Pepin, R. O., and Merrill, R. B., eds., Impact and Explosion Cratering, Pergamon Press, N.Y., p. 489-509.
- U.S. Geological Survey, 1976, Topographic Map of Mars: U.S. Geol. Survey Misc. Inv. Map I-961, 1:25,000,000.

SMALL VOLCANIC CONSTRUCTS IN UTOPIA PLANITIA

Woronow, A., Lunar & Planetary Lab, U. of AZ., Tucson, AZ 85721

In addition to the large shield volcanos, Mars has many minor volcanic constructs. Hodges (1) describes the settings of many of these minor features. Using tentative diameter/height measurements, she concludes that the constructs are probably similar to the "cinder cones" in Cydonia Mensae described by Wood (2). McGetchen et al (3), using detailed ejection data for an eruption of NE crater on Etna, find that cinder cones on Mars and the Moon should have allometries vastly different from those of terrestrial cinder cones. This naturally results from the differing effects of gravity and atmospheric drag. Remarkably, Wood (2) finds that "cinder cones" on the Earth, Mars, and the Moon all lie on a single trend line!

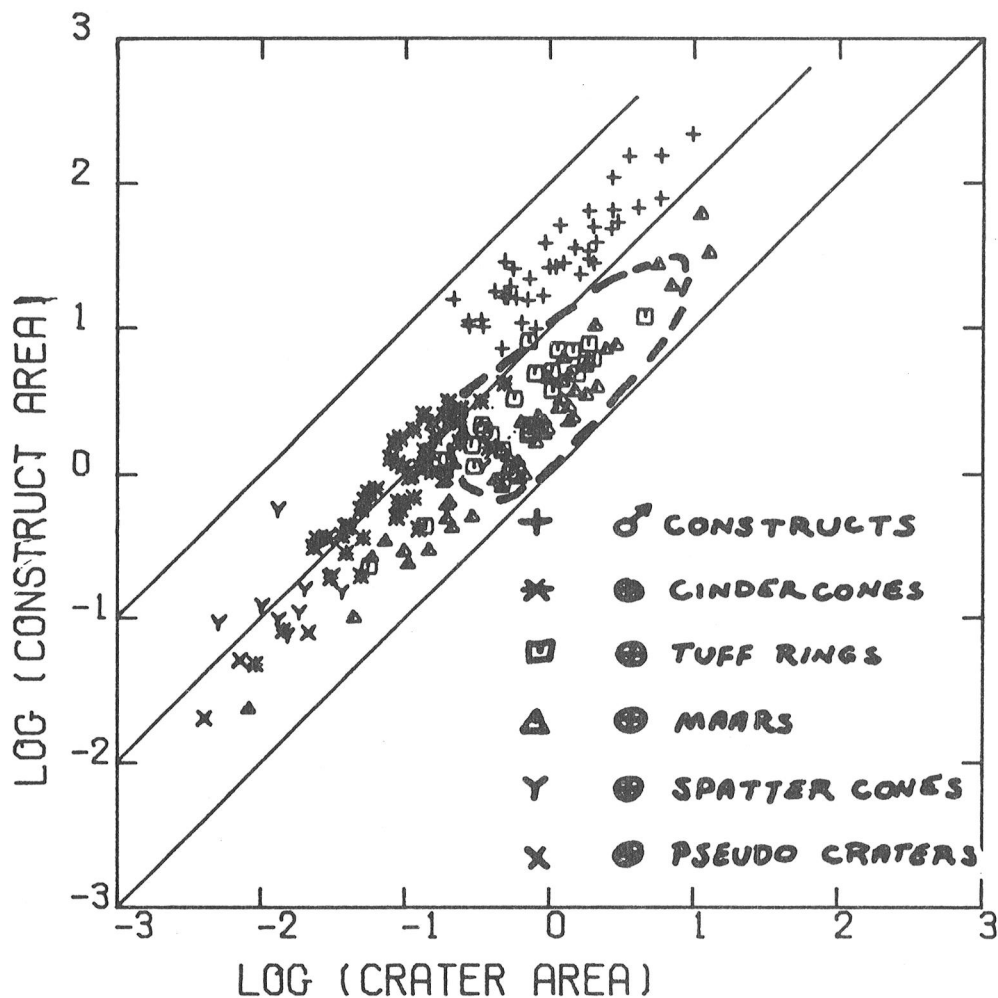
We report here on a new set of martian ballistic-volcanic data which do not support the findings of Wood (2), but exactly fit the models of McGetchen et al (3). We have begun measuring the small constructs in the B3 Viking landing site of Utopia Planitia. Thus far we have about 40 data points with the attributes given below:

	THIS WORK	WOOD (2)
Construct Dia.	~2-14 km	~.4-1.4 km
Crater Dia.	~1-3.5 km	~.2-.4 km
No. Data Pts.	~40	~18
Rel. Scatter	~5x	~1

Figure 1 shows our data set compared to the terrestrial forms of ballistic volcanism cataloged by Pike (4). The dashed region is where our Mars data would lie if the scaling of McGetchen et al (3) were applied. Clearly, the application of this correction is necessary to provide coincidence between the trends of the martian and terrestrial landforms. The most likely analogs of these martian features, because of their size, are maars, tuff rings, and cinder cones; spatter cones and pseudo craters lie below the size range of these martian features.

We suspect, therefore, that because gravity effects are demonstrably important, Wood's (2) study may not have been of true cinder cones or other ballistic volcanics, but of a more effusive form of volcanism.

REFERENCES (1): Hodges, C. A., NASA TM 80339, 247, 1979.
 (2) Wood, C. A., Lunar Sci Conf. X absts., 1370, 1979.
 (3) McGetchen, T. R., et al. JGR, 79, 3257, 1974. (4)
 Pike, R. J., Proc. Lunar Sci. Conf. IX, 3239, 1978.



THE TEMPE VOLCANIC PROVINCE: AN ANALOG TO THE EASTERN SNAKE RIVER PLAINS?

J.B. Plescia, Department of Geological Sciences, University of Southern California, Los Angeles, California 90007 and Jet Propulsion Laboratory, 4800 Oak Grove Drive, Pasadena, CA 91103

There are a number of small scale volcanic provinces on Mars, which have been reported by Hodges (1979) and West (1974). One of these regions, here termed the Tempe Volcanic Province ($+30^{\circ}$ - $+40^{\circ}$, 80° - 90° long.), is of particular interest because of its similarity in scale and form to the eastern Snake River Plain volcanic area of Idaho. A series of high resolution images (60m/pixel) of the Tempe volcanic region was acquired in March, 1978, during Viking orbiter rev 627A (JPL Mosaic 211-5813). Analysis of those images is reported here.

The Tempe Volcanic province lies along the southwest edge of the highly fractured Tempe - Mareotis Plateau. The region surveyed (approx. 200,000 km²) can be divided into two principal geologic - geomorphic units: (1) an older highly fractured plateau region, and (2) a younger smooth volcanic plains unit. This smooth plains unit is directly comparable to the eastern Snake River plains volcanic area. The majority of the volcanic features are developed on the smooth plains, however a few do occur on the plateau material. In several locations pieces of the older plateau protrude through the smooth plains as mesa like structures.

Crater counts on the various units indicate that the fractured plateau can be defined by two crater numbers, an older one indicating the period of formation, and a younger one indicating a period of resurfacing. The period of formation appears to coincide with the development of the extensive Lunae Planum surface. The density of 1 km craters/ 10⁶km² for Lunae Planum is approximately 2500 \pm 80, while the fractured plateau exhibits a density of approximately 2700 \pm 55. The volcanic plains have an average crater number of 1100 \pm 35. The resurfacing of the plateau may be either an early expression of the volcanism of the plains or an independent event.

The part of the volcanic province observed (approximately 45000 km²) contains over 30 volcanic features. These features include low shields, as defined by Greeley (1977), cinder cones, dome-like features and linear depressions. The linear depressions cut across the plains and have large flood basalts emanating from them at various locations.

Most numerous are the low shields, numbering approximately 20. These shields have very gently slopes and appear to have little local

relief. Central calderas are either circular or elongate in shape and may be either singular or multiple in number. Central caldera are generally 400 - 1000m in diameter. The shields all exhibit a radial texture, and long narrow lava flows have been identified on several of the shields. Linear depression, analagous to those developed on other large Tharsis shields, occur on the flanks of several of the low shields. The shields merge gradually with the adjacent volcanic plains and in places may be buried by those plains.

There are also several cinder cones. Cinder cones appear to have steeper slopes and exhibit a sharp contact with the adjacent plains. The cones lack the radial texture exhibited by the shields. Both circular and elongate summit craters have been noted on the cinder cones.

Crossing the volcanic plains are long linear depressions. These features vary in width, but average approximately 1 - 1.5 km at their widest parts narrowing to zero in both directions. The depressions are all aligned along the same strike. In several places flood basalts can be seen to emanate from them.

There is an additional group of features which may be volcanic in nature. These are dome-like hills scattered across the area. These features lack the radial texture of the shields and the conical plan of the cones and lack central craters. They do not exhibit a distinct contact with the adjacent plains.

The rifts and volcanoes exhibit very strong structural control. The linear depressions on the plains, crater chains, elongate craters, and the rifts in the shield flanks all follow 1 orientation, approximately N 60 E. The fractured plateau is dominated by two trends, a major N 40 E and a minor due north trend. The trends of the volcanics are distinctly different from the structural trends of the plateau. The N 60 E trend is also exposed southward on the Tharsis plains units. The difference in orientation between the volcanic trends and the plateau fractures indicates a reorientation of the stress field in the time interval between the fracturing of the plateau and the development of the volcanic plains. The older plateau fractures can be correlated with a fracture system radial to the Syria Planum region, while the younger volcanic trends can be assigned to a radial system centered in the region of Pavonis Mons (Plescia and Saunders, 1979a).

Preliminary crater counts on individual small shields and lava flows, although subject to large statistical errors, indicate that the flows and shields were all active contemporaneously. An average age for the

volcanism of the area can be obtained by combining crater counts on all of that surface. This results in a crater number of 1100 ± 35 . In comparison to other Tharsis area volcanoes, several have similar crater numbers; Arsia Mons 780 ± 135 , Biblis Patera 1400 ± 290 , and Apollinaris Patera 990 ± 150 . The Tempe volcanic province appears to have been active during the small shield building stage of basaltic volcanism, prior to the period of time of the large Tharsis area shield construction (Plescia and Saunders, 1979b). The age of the Tempe Volcanic Province, based on the chronology of Soderblom (1977), is approximately 1 b.y.

There are a number of similarities between the volcanic features of the Tempe region and those of the Snake River Plains of Idaho. Greeley (1979) has reviewed the geologic features of the Snake River Plains and many of the features described there are nearly identical to those found in the Tempe region of Mars. Both areas are dominated by flood basalts and coalesced low shields. Low shields, cinder cones and fissures occur in both examples. The low shields of both areas can be capped by either singular or multiple summit craters, which can be circular or irregular in outline.

The volcanic features in both examples are very strongly structurally controlled. Crater chains, fissure orientation, and distribution of vents all follow one trend, with very little deviation. In summary the Tempe Volcanic province appears to be one of the few Martian geologic features which has a terrestrial analog of comparable form and scale.

References:

- Greeley, R. (1977) In Volcanism of the Eastern Snake River Plain, Idaho: A comparative planetary geology guidebook, 23-44.
- Hodges, C.A. (1979) NASA Technical Memorandum 80339, Reports of the Planetary Geology Program, 1979-1979, 247-249.
- Plescia, J.B. and Saunders, R.S. (1979a). (in press) Proc. of the Tenth Lunar and Planetary Science Conference.
- Plescia, J.B. and Saunders, R.S. (1979b). NASA Technical Memorandum 80339, Reports of Planetary Geology Programs, 1978-1979, 47-49.
- Soderblom, L. (1977) In Impact and Explosion Cratering, 629-633.

QUANTITATIVE MORPHOLOGY OF VOLCANOES: RECENT RESULTS FOR EARTH AND MARS

R. J. Pike, R. Jordan, and F. J. Schafer, U.S. Geological Survey, Menlo Park, CA 94025 and Flagstaff, AZ 86001

New work on the descriptive geomorphology of planetary volcanoes includes photogrammetry of Martian edifices, geometric models for additional classes of terrestrial volcanoes, and updating a file of topographic measurements (Pike, 1978). The new topographic results are being incorporated into improved multivariate comparisons of terrestrial and extraterrestrial edifices, the goal of which is a better geologic interpretation of the Martian volcanoes.

Three separate photogrammetric models have been set up on the AS-11 plotter thus far, and some of the results are shown in Figure 1 and Table 1. The data in Table 1, which follow the format used in Pike (1978), come from averages of several different stereo profiles rather than from elevation readings. Comparison of the photogrammetric results with results of shadow-length relief measurement (Pike, 1978) reveals significant differences for Uranus Patera, Ceraunius Tholus, and Uranus Tholus (data on Albor Tholus are all new, but do not come from photogrammetry). Although superior to the older data, most of the new results are affected by tilt in the stereo models.

Cratered seamounts recently were discovered and mapped in the Pacific Ocean (Hollister et al., 1978; Lonsdale and Spiess, 1979). Topographic data for 11 seamounts and the resulting preliminary geometric model are given in Table 2 and in Figure 2, respectively. Comparison of the averaged dimensions with those for other classes of terrestrial edifices (Pike, 1978, Table 2 and Figure 2) indicates that cratered seamounts as a group may be either the largest monogenetic volcanoes on Earth, or the smallest polygenetic volcanoes. Each has about the same base diameter as Icelandic shields, but twice the height and a much larger crater. The relatively large sizes of the summit depressions suggest that they are calderas and that the seamounts probably are polygenetic edifices. In overall geometry, disregarding size, the cratered seamounts closely resemble none of the 20 classes of terrestrial volcanoes described previously (Pike, 1978, Figure 2).

The data file on 655 volcanoes (Pike, 1978, Appendix) has been enlarged by 30 edifices (Table 2) including the 11 cratered seamounts. Additionally, topographic measurements for 4 other volcanoes (last four entries in Table 2) have been revised.

References:

Hollister, C. D., Glenn, M. F., and Lonsdale, P. F., 1978, Morphology of seamounts in the Western Pacific and Philippine Basin from

- multi-beam sonar data: Earth & Planetary Sci. Letts., v. 41, p. 405-418.
- Lonsdale, P. F., and Spiess, F. N., 1979 A pair of young cratered volcanoes on the East Pacific Rise: Jour. Geol., v. 87, p. 157-173.
- Pike, R. J., 1978, Volcanoes on the inner planets: some preliminary comparisons of gross topography: Proc. 9th Lunar Planet. Sci. Conf., p. 3239-3273.

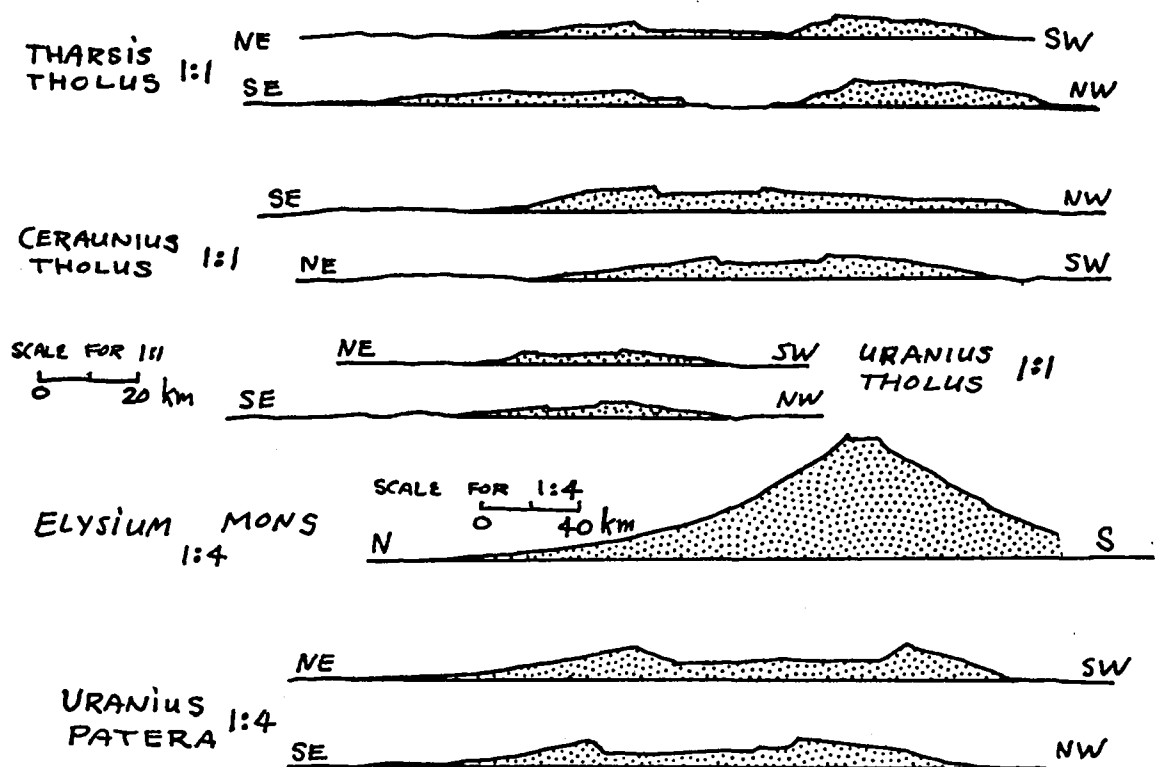


Figure 1. Some stereophotogrammetric profiles for volcanoes on Mars. Vertical exaggeration 1:1 or 1:4 as indicated.

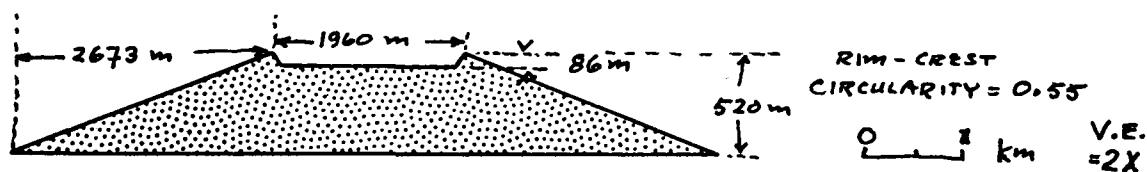


Figure 2. Geometric model for cratered seamounts in the Pacific Ocean. Linear dimensions are geometric means for 11 seamounts (Table 2). Circularity index is area of circle inscribed within crater rim-crest divided by area of circumscribed circle. Compare with other models in Pike (1978, Table 2, Figure 2).

TABLE 1

NEW MEASUREMENTS FOR SIX MARTIAN VOLCANOES

CLASS	NAME	SOURCE	DIAM.	DEPTH	HEIGHT	WIDTH	CIRC
MM	ELYSIUM MONS	846A18, 844A17	14600.	1000.	12500.	200000.	.81
MP	URANIUS PATERA	701A08, 816A09	98500.	900.	1630.	71400.	.39
MT	URANIUS THOLUS	701A08, 816A09	19900.	350.	2450.	20000.	.74
MT	CERAUNIUS THOLUS	701A08, 816A09	25400.	1130.	5150.	44200.	.70
MT	THARSIS THOLUS	858A23, 857A51	47800.	4100.	4100.	42100.	.51
MT	ALBOR THOLUS	846A21	32400.	2600.	5000.	62000.	.74

TABLE 2

NEW AND REVISED DATA FOR CATALOG OF TERRESTRIAL VOLCANOES

CLASS	NAME	LOCATION	NB	DIAM.	DEPTH	HEIGHT	WIDTH	CIRC
SC	YOTEI	JAPAN, SW HOKK.	1	730.	100.	1625.	6900.	.56
SC	SAKURAJIMA	JAPAN, SO, KYUSHU		595.	120.	1125.	5000.	.55
SC	MT. TONGARIRO (NORTH)	NO. IS., N.Z.	1	1070.	100.	1200.	11000.	.74
KA	EMURUANGOGOLAK (II)	NO. KENYA RIFT	1	4100.	75.	700.	10500.	.58
KCS	OSOREYAMA	JAPAN, N, HONSHU	1	6100.	300.	500.	6500.	.54
KCS	LAGUNA DE AYARZA	S.W. GUATEMALA	1	6150.	735.	600.	10000.	.44
AP	CERRO GALAN	NW ARGENTINA	1	32000.	1000.	1500.	25000.	.38
KT	ISLA TORTUGA	GULF OF CALIF.		1550.	150.	1535.	10000.	.74
KT	EAST SEAMOUNT	E. PACIFIC RISE		2100.	130.	1250.	5500.	.51
O	N.W. PACIFIC BASIN "A"	NORTHWEST PACIFIC	1	2320.	45.	870.	4090.	.30
O	N.W. PACIFIC BASIN "B"	NORTHWEST PACIFIC	1	1525.	115.	615.	3235.	.69
O	N.W. PACIFIC BASIN "J"	NORTHWEST PACIFIC	1	2815.	220.	935.	3470.	.53
O	N.W. PACIFIC BASIN "P"	NORTHWEST PACIFIC	1	2300.	160.	650.	1975.	.75
O	PHILIPPINE BASIN "C"	W. PHIL. BASIN	1	2850.	55.	650.	3075.	.63
O	PHILIPPINE BASIN "F"	W. PHIL. BASIN	1	2950.	215.	1140.	4775.	.26
O	PHILIPPINE BASIN "F.1"	W. PHIL. BASIN	1	1445.	195.	285.	1525.	.54
O	PHILIPPINE BASIN "V"	W. PHIL. BASIN	1	2800.	55.	591.	3350.	.70
O	PHILIPPINE BASIN "V.1"	W. PHIL. BASIN	1	1000.	24.	148.	1250.	.47
O	PHILIPPINE BASIN "Z"	W. PHIL. BASIN	1	1000.	27.	100.	1065.	.64
C	HALALII	MAUI, HAWAIIAN I		210.	49.	66.	170.	.71
C	PUU NAUE	MAUI, HAWAIIAN I		235.	55.	95.	213.	.70
C	PUU O MAUI	MAUI, HAWAIIAN I		210.	42.	136.	315.	.71
C	PENGUIN ISLAND CONE	SO. SHETLAND IS.		350.	35.	155.	370.	.61
E	MALPAIS TANK MAAR	SE ARIZONA, USA	1	2500.	35.	13.	875.	.74
E	PARAMORE CRATER	SE ARIZONA, USA		2440.	115.	55.	1280.	.60
E	WELLS TANK MAAR	SE ARIZONA, USA		1530.	52.	17.	600.	.66
E	LAKE SIMBI EXPLOSION CR	S.W. KENYA		700.	25.	10.	200.	.55
E	PETREL CR. (PENGUIN I.)	SO. SHETLAND IS.	1	305.	55.	10.	220.	.61
U	T' IEN CH' IH (PAEKTUSAN)	SO. MANCHURIA	1	5750.	715.	1350.	22000.	.59
U	MT. EDGE CUMBE	NO. IS., N.Z.	1	70.	64.	595.	1370.	.28
SC	MT. FUJI	JAPAN, C. HONSHU	1	700.	100.	3700.	19000.	.62
SC	COTOPAXI (1903 CRATER)	NO. ECUADOR		625.	215.	2500.	11500.	.61
KC	AGRIHAN IS.	CEN. MARIANA IS.		2200.	400.	3350.	22000.	.55
AA	SUSWA CALDERA	KENYA, CEN. RIFT		9500.	235.	315.	5250.	.42

Sources are Viking Orbiter frames for stereo models. Measurements in meters, except circularity index (defined in Figure 2). Class codes for Mars: MM (mons), MP (patera), MT (tholus). Codes for Earth: SC (stratocone); KA, KC, KCS (caldera on stratocone); AP, AA (caldera in ash-flow plain); KT (tholeiitic shield with caldera); O (seamount); C (cinder cone); E (maar); U (uncertain); complete classification given by Pike (1978).

PROBLEMS ASSOCIATED WITH THE IDENTIFICATION OF MAGMA COMPOSITION FROM VOLCANIC LANDFORMS

Whitford-Stark, J.L., Dept. of Geological Sciences, Brown Univ.,
Providence, RI 02912.

Terrestrial volcanologists are able to analyze the composition of volcanic products from in situ samples and, on the basis of these analyses, it has been generally believed that different magma compositions result in the production of morphologically distinct landforms. Were this in fact true, photogeological analysis would be an extremely powerful tool in determining the chemistry of a planetary surface without the need to obtain surface samples or to employ orbital spectral remote sensing.

On the only other solar system body which has been sampled, an early hypothesis¹ that the maria were possibly basalt was confirmed. A recent synthesis² of lunar remote sensing data has shown that there are, however, significant areal and temporal variations in lunar basalt compositions. Further volcanic constructs have been reported from Venus,³ Mars,⁴ and Io.⁵ The Venus constructs were identified on the basis of low resolution radar imagery, the Mars volcanics were interpreted⁴ to be similar to terrestrial basalts on the basis of their inferred rheological properties, while very low resolution spectral data and morphological data have led to the interpretation of Io flows as sulfur⁶ or possibly sulfur and basalt.⁵

The identification of rock composition on the basis of morphology and color alone is not possible since it is both the magma composition and the mechanism of the eruption, which determines eruptive morphologies. The following examples have been chosen to illustrate why photogeologists should proceed with caution when interpreting the chemistry of non-terrestrial volcanic products solely on the basis of morphology and color.

Volcanoes

The classic subdivision of terrestrial volcanoes on the basis of shape is that of shield volcanoes and cones.⁷ Shield volcanoes are commonly believed to be of basaltic composition while the large, symmetrical composite cones are thought of as being andesitic or more silicious. This is a gross oversimplification in that, for example, the classic cone-shaped Mt. Fuji is predominantly composed of basalts while shield volcanoes composed of trachyte, phonolite, and ignimbrite have been reported.⁸ Likewise, maars, tuff-rings, and diatremes are not found to be associated with a specific magma type; magmas forming such structures including tholeiite, alkali-basalt, carbonatite, and acidic rocks.⁹

Flows

The general belief is that areally extensive flows are basaltic while short stubby flows are silicic. In general, this is true, but there

IDENTIFICATION OF MAGMA COMPOSITION FROM VOLCANIC LANDFORMS

Whitford-Stark, J.L.

are exceptions. For example, the flood-type lavas in Kenya are phonolites¹⁰ while a 35 km long rhyolite flow has been reported from Texas.¹¹ Furthermore, flows of ash have been interpreted to have travelled great distances.¹² A similar morphology argument has been employed to interpret the lunar and mercurian plains deposits as being of volcanic origin. In the lunar case, the return of samples from one of the plains sites showed that, at that site, the plains were impact breccias.¹³

Pahoehoe surfaces are commonly interpreted as being found only on basaltic lavas. Photographs of the 1977 Niragongo lava,¹⁴ however, show it to have a pahoehoe-type surface though in composition it is a melilite nephelinite. In addition, pahoehoe structure has been reported from the surface of liquid sulfur flows.¹⁵

Pillow lavas are also commonly thought to be exclusively associated with basaltic magmas, largely because basalt is the predominant terrestrial subaqueous magma type. Pillow lavas are, however, not exclusively basaltic; dasitic andesite pillows have been described.¹⁶

The presence of levees and channels on flows does not even necessarily imply that those flows are lava. Such structures are quite common on lahars (mud flows), impact melt deposits¹⁷ and have even been found on ash flows.¹⁸

Lava flows need not be silicic or even contain silicates. The discovery of volcanism on Io has highlighted the existence of eruptions of liquid sulfur on both andesitic¹⁵ and basaltic volcanoes,^{19,20} alkali carbonates with both pahoehoe and aa surfaces have been reported from East Africa, while flows of iron oxide exist on Chilean volcanoes.^{22,23}

Finally, color is not a diagnostic criterion of composition. Although basalts tend to be blackish and silicic rocks whitish when erupted, weathering and hydrothermal alteration can produce a variable color assemblage. Likewise, silicic tephra can be white but also occurs in yellows, reds, browns and greens. Carbonatite lavas are dark grey to white while sulfur flows can exhibit a variety of colors.⁶

To summarize, it is not possible to identify the composition of volcanic rocks by morphology and color alone. Photogeology can enable elucidation of some of the parameters of eruptions, such as yield strength, but spectral remote sensing or in situ analysis is required before the composition of the surface rocks can be characterized. An example of the usefulness of a combined morphological-spectral analysis is that of Head and McCord²⁴ who showed the lunar Gruithuisen domes were not mare basalts but were distinct from the highlands. The martian flows may have the rheological characteristics of basalts but that does not mean they are basalts. Likewise, although the color and low resolution

IDENTIFICATION OF MAGMA COMPOSITION FROM VOLCANIC LANDFORMS

Whitford-Stark, J.L.

spectral characteristics of Io flows can be satisfied by their being sulfur, other materials such as realgar (AsS) have similar color and spectral characteristics.^{25,26} Our understanding of volcanism and volcanic products can be improved if there are 1) a more complete inventory of terrestrial volcanic features and compositions, 2) better modeling of volcanic eruption processes, 3) samples from extraterrestrial volcanoes, and 4) high resolution geochemical and spectral data.

References:

- ¹Coblentz, W.W. 1905, Carnegie Publ. No. 65, Pts. IV & V.
- ²Pieters, C. et al. 1979, Submitted to J. Geophys. Res.
- ³Malin, M.C. 1974, Reports of Planetary Geology Program, 1978-1979, 94-96.
- ⁴Carr, M.H. et al. 1977, J. Geophys. Res. 82, 3985-4015.
- ⁵Strom, R.G. et al. 1979, Nature 280, 733-736.
- ⁶Sagan, C. 1979, Nature 280, 750-753.
- ⁷Whitford-Stark, J.L. 1975, In Volcanoes of the Earth, Moon and Mars (ed. G. Fielder and L. Wilson), 66-88.
- ⁸Wood, C.A. 1977, In Abstracts for the Planetary Geol. Field Conf. on the Snake River Plain, Idaho, NASA TM-78,436, 34-39.
- ⁹Lorenz, V. 1973, Bull. Volc. 37, 183-204.
- ¹⁰Baker, B.H. et al. 1971, Tectonophysics 11, 191-215.
- ¹¹Gibbon, D.L. 1969, Bull. Volc. 33, 438-474.
- ¹²Miller, T.P. and Smith, R.L. 1977, Geology 5, 173-176.
- ¹³Wilhelms, D.E. 1976, Icarus 28, 551-558.
- ¹⁴Tazieff, H. 1977, Bull. Volc. 40, 189-200.
- ¹⁵Watanabe, T. 1940, Japan J. Geol. Geog. 17, 289-310.
- ¹⁶Macdonald, G.A. 1977, Volcanoes, Prentice-Hall, Inc., 510 pp.
- ¹⁷Hawke, B.R. and Head, J.W. 1977, in Impact and Explosion Cratering (ed. D.J. Roddy et al.), p. 815-841.
- ¹⁸Davies, D.K. et al. 1978, Geol. Soc. Amer. Bull. 89, 369-384.
- ¹⁹Skinner, B.J. 1970, Pacific Sci. 24, 144-145.
- ²⁰Colony, W.E. and Nordlie, B.E. 1973, Econ. Geol. 68, 371-380.
- ²¹Dawson, J.B. 1962, Nature 195, 1075-1076.
- ²²Park, C.F. 1961, Econ. Geol. 56, 431-436.
- ²³Rogers, D.P. 1968, Econ. Geol. 63, 700.
- ²⁴Head, J.W. and McCord, T.B. 1978, Science 199, 1433-1436.
- ²⁵Dana, E.S. 1964, A Textbook of Mineralogy.
- ²⁶Fanale, F.P. et al. 1979, Nature 280, 761-763.

Are Calc-alkalic Volcanic Rocks Unique to Earth? W.E. Elston, J.C. Aubele¹,
L.S. Crumpler¹ and D.B. Eppler², Department of Geology, University of New
Mexico, Albuquerque, NM 87131

Earth is unique among planetary bodies examined to date in its dichotomy of continents and ocean basins and in its system of moving lithospheric plates. Calc-alkalic igneous rocks are characteristic of continents and many modern occurrences closely correlate with convergent plate margins. It could therefore be concluded that calc-alkalic rocks are unique to Earth. However, such a conclusion may be premature, because terrestrial calc-alkalic rocks also exist in regions of tensional tectonics not directly related to plate convergence (e.g. late Tertiary rocks of the Banks Peninsula of New Zealand and of coastal eastern Australia, near the New South Wales-Queensland border). Data for this study are from North America, from Oligocene-Miocene rocks of the transition zone from the Colorado Plateau to the Basin and Range province (Mogollon-Datil volcanic field, Elston and Bornhorst, 1979); Pliocene rocks from the south side of the Colorado Plateau (Mount Taylor volcanic field, Crumpler, 1977) and Pliocene rocks of the Rio Grande rift (Cerro del Rio, Aubele, 1977, 1979; Taos Plateau, Eppler, 1976).

Compared with volcanic rocks associated with convergent plate margins, the calc-alkalic rocks of tensional regimes are higher in FeO^* and darker in color. They tend to look "basaltic" but are, in fact, a complex series ranging from about 50 to 68 percent SiO_2 . Basaltic andesite is a major component. Characteristically, $^{87}\text{Sr}/^{86}\text{Sr}$ increases with increasing SiO_2 , from about 0.704 to 0.709. Some rocks in the andesite range have partly resorbed quartz and oligoclase grains in an olivine- and labradorite-bearing matrix; it is uncertain whether these grains are xenocrysts or relict high-pressure phases. The most mafic members of the

Current Addresses: ¹ Department of Planetary Sciences ² U.S. Army
University of Arizona
Tucson, Arizona

of the Oligocene-Miocene Mogollon Plateau rocks plot on the alkaline side of the dividing line between Hawaiian tholeiitic and alkaline rocks (Macdonald and Katsura, 1964); more siliceous members plot on the tholeiitic side. These rocks erupted during a stage of predominantly ductile extension, prior to Basin and Range block faulting. The Pliocene rocks of the Cerros del Rio, which erupted in the most mobile part of the Rio Grande rift, plot in a similar manner. The Pliocene calc-alkaline rocks of the more stable Taos Plateau plot on the tholeiitic (subalkaline) side of the Macdonald-Katsura line. The Pliocene rocks are younger than the main stage of rifting and Basin and Range faulting. During this stage, calc-alkaline rocks erupted concurrently with an alkaline series (Mount Taylor and Cerros del Rio fields). In alkaline rocks of the Mount Taylor field, $^{87}\text{Sr}/^{86}\text{Sr}$ tends to decrease with increasing SiO_2 , from alkali basalt to trachyte.

The origin of these calc-alkaline rocks is a subject for future studies. To date, chemical and isotopic constraints suggest a predominant mantle component but crustal contamination cannot be ruled out. Zimmerman and Kudo (1979) proposed an origin by partial melting of upper mantle materials containing perthitic hornblende, to account for hydrous magmas enriched in light rare-earth elements. A crucial question from a planetological point of view concerns the degree of subsequent contamination by siliceous crustal materials, concomitant with crystal fractionation. If there were little or no contamination, fractionation within this rock series would indicate a possible mechanism for generating sialic crustal materials on terrestrial planets less mobile than Earth and less subject to sedimentary differentiation. If contamination turns out to be an essential part of differentiation, rocks of this type could exist on other planets only if these planets had an independent source of siliceous crustal contaminants. The data of Zimmerman and Kudo (1979) permitted, but did not demand, contamination of some of the lavas by as much as 20 percent crustal materials.

Even if our knowledge of these terrestrial rocks were complete, extrapolation to other planetary bodies would be uncertain, because of differences in bulk composition, especially of volatile constituents (McGetchin and Smyth, 1978; Morgan and Anders, 1979). However, the tensional tectonic setting of the terrestrial rocks has counterparts on Mars and other planetary bodies.

- Aubele, J.C., 1978, Geology of the Cerros del Rio volcanic field, Santa Fe, Sandoval, and Los Alamos Counties, New Mexico: Unpubl. M.S. thesis, Univ. N. Mex., 136 p.
- Aubele, J.C., 1979, The Cerros del Rio volcanic field: N. Mex. Geol. Soc. Guidebook of Santa Fe country, 30th Field Conf., p. 243-252.
- Crumpler, L.S., 1977, Alkali basalt-trachyte suite and volcanism, northern part of the Mount Taylor volcanic field, New Mexico: Unpubl. M.S. thesis, Univ. N. Mex., 131 p.
- Elston, W.E. and Bornhorst, T.J., 1979, The Rio Grande rift in context of regional post-40 m.y. volcanic and tectonic events, in Rio Grande Rift: Tectonics and Magmatism (R.E. Riecker, Ed.): Am. Geophys. Union, p. 416-438.
- Eppler, D.B., 1976, The geology of the San Antonio Mountain area, Tres Piedras, Taos and Rio Arriba Counties, New Mexico: Unpubl. M.S. thesis, Univ. N. Mex., 77 p.
- Macdonald, G.A. and Katsura, T., 1964, Chemical composition of Hawaiian lavas: Jour. Petrology, v. 5, p. 82-133.
- McGetchin, T.R., and Smyth, J.R., 1978, The mantle of Mars: some possible geologic implications of its high density: Icarus, v. 34, p. 512-536.
- Morgan, J.W. and Anders, Edward, 1979, Chemical composition of Mars: Geochim. et Cosmochim. Acta, v. 3, p. 1601-1610.
- Zimmerman, Charles and Kudo, A.M., 1979, Geochemistry of andesites and related rocks, Rio Grande rift, New Mexico, in Rio Grande Rift: Tectonics and Magmatism: (R.E. Riecker, Ed.): Am. Geophys. Union, p. 355-381.

ESTIMATES OF LAVA-FLOW VELOCITIES USING LAVA TREES

Moore, H. J. and Kachadoorian, R., U.S. Geological Survey, Menlo Park, California 94025

Lava trees and molds produced by the chilling of lava as it flows around trees may provide a means of estimating the peak velocities of the flow when the yield strength, plastic viscosity, and density of the lava are known. Lava tree molds can be used to estimate the present thickness of the now-stationary flow (h_y) and the maximum thickness at the time of flow (H_f) as well as the direction of flow (8,4) (fig. 1). The present thickness (h_y) of the flow allows an estimate of the yield strength (τ_y) of the flow, assuming that it behaved as a Bingham plastic (1,6,2). An estimate of the plastic viscosity (η_p) can be obtained using an assumed model relating yield strengths and plastic viscosities to the volume fraction of solids in the flowing lava (figs. 8 and 9 of ref 7). The maximum thickness at the time of flow (H_f), as determined from the lava trees and molds combined with the density of the flow (ρ), the topographic gradient ($\sin \theta$), and the acceleration of gravity (g) allows an estimate of the stress at the base of the flow (τ_b). Using reasonable values of these parameters, maximum average-flow velocities can be estimated using suitable equations (equations 5, 6 and 7 of ref. 7, where $H_f = H$).

Lava trees and molds of the July 1974 flow just south of the Kilauea caldera of Hawaii are used to estimate thicknesses at the time of flow in order to calculate the maximum average velocities of that flow along a segment south of the vent area and extending to a point just west of Kokoolau Crater (Fig. 2).

Using the thickness of the tip of the flow, topographic gradient near the tip, and a bulk density of $2,200 \text{ kg/m}^3$, we estimate a yield strength of 620 N/m^2 (6200 dyn/cm^2), which corresponds to a volume fraction of solids near 0.41 (fig. 8 of ref 7). The volume fraction of solids, in turn, implies a plastic viscosity of $\approx 2 \times 10^4$ poise. Calculated maximum average velocities vary along the length of the flow from 5.7 km/hr to as low as 0.5 km/hr (table 1). The maximum average velocity occurs at the center of section B (fig. 2), where the flow is narrow. Velocities downstream from B are smaller (table 1), as would be expected in a flow that was thinning because of cessation of lava extrusion at the vent and spreading of the flow. In the Bingham plastic model, the upper part of the flow moves as a slab whose velocity is higher than the average velocity (3,7). The slab velocity (V_s) at B is 7.7 km/hr. Slab velocities for the other parts of the flow are given in table 1.

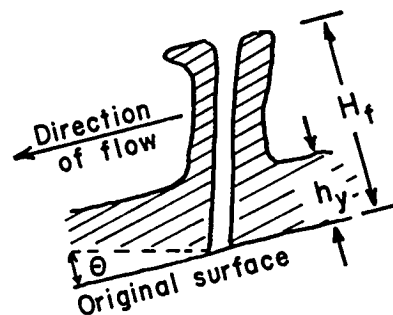


Fig. 1. Profile of lava tree and mold

Applying the values of yield strength (1×10^3 dyn/cm²) and plastic viscosity (7×10^3 poise) derived from measurements at Makaopuhi Lava Lake (10), the maximum average velocity at the center line of B (fig. 1) comes out to be 22 km/hr and the slab velocity, 33 km/hr (table 1). The predicted flow thickness (0.2 m) is smaller than the observed thickness (≈ 1.2 m).

We know of no field observations of actual velocities of the July 1974 flow. Velocities of basalt flows as great as 100 km/hr have been observed, but velocities a few km/hr are more common (9, p. 358). Viscosities calculated using estimates of velocities and thicknesses at the time of flow range from 3×10^3 to 4×10^4 for basalts of Mauna Loa (5). Thus, data on other flows do not permit selection of the correct values of viscosity of the July 1974 flow. The agreement between the calculated and measured values of the present thickness of the July 1974 flow (h_y) suggests that the lower velocities are more likely than the higher ones. If the lower values of velocity are correct, then both the yield strength and plastic viscosity of the July 1974 flow would appear to be greater than those measured in Makaopuhi. Larger values could result from lower temperatures and/or more entrained solids.

We have tried to estimate instantaneous maximum velocities at a number of locations near the center of the flow. The velocities do not apply to flow during the initial stages of eruption, near the flow edges, or during the late stages of flow. Velocities near the center are greater than those near the edges where the thickness at the time of flow (H_f) is less than in the center. During the late stages of flow, velocities will decrease as the flow thins, cools, and acquires more solids.

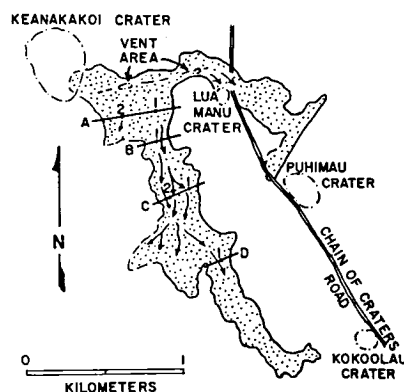


Fig. 2. July 1974 lava flow showing locations of velocity estimates. Letters and numbers correspond to those of table 1.

References

1. Bingham, E. C., 1922, Fluidity and Plasticity: McGraw-Hill, New York, p. 215-226.
2. Hulme, G., 1974, The Interpretation of lava flow morphology: Geophys. J. Roy. Astron. Soc., v. 39, p. 361-383.
3. Johnson, A. M., 1970, Physical Processes in Geology: Freeman, Cooper, and Co., San Francisco, 577 p.
4. Lockwood, J. P. and Williams, I. S., 1978, Lava trees and tree moulds as indicators of lava flow direction: Geol. Mag., v. 115, p. 69-74.

5. Macdonald, Gordon A., 1959, Activity of Hawaiian volcanoes during the years 1940-1950: Bull. Volcanologique, Ser. II, v. 15, p. 119-179, 27 plates.
6. Moore, H. J., 1974, A note on the Imbrium flows and Bingham plastics: U.S. Geol. Survey Prof. Paper 900, 209 p.
7. Moore, H. J. and Schaber, G. G., 1975, An estimate of the yield strength of the Imbrium flows: Proc. Lunar Sci. Conf. 6th, v. 1, p. 101-118.
8. Moore, J. G. and Richter, D. H., 1962, Lava tree molds of the September 1961 eruption, Kilauea Volcano, Hawaii: Geol. Soc. Amer. Bull., v. 73, p. 1153-1158.
9. Press, Frank and Siever, Raymond, 1974, Earth, 2nd Ed., W. H. Freeman and Co., San Francisco, Calif., 649 p.
10. Shaw, H. R., Peck, D. L., Wright, T. L., and Okamura, R., 1968, The viscosity of basaltic magma: an analysis of field measurements in Makaopuhi Lava Lake, Hawaii: Amer. Jour. Sci., v. 226, p. 225-264.

Table 1. Observations and Calculations for July 1974 flow.

Location ^{1/}	Sin θ	h_y (measured) (m)	h_y (Calc) (m)	H_f ^{2/} (m)	\bar{V} km/hr	V_s km/hr
A 1.	0.018	1.56 ± 0.65	1.7	5.2	3.5	4.5
2.	0.029	≈ 1.1	1.0	3.2	2.1	2.7
B 1.	0.029	≈ 1.2	1.0	4.7	5.7	7.7
	(0.029) ^{3/}	≈ 1.2	(0.2)	(4.7)	(22.5)	(33.1)
C 1.	0.029	1.11 ± 0.47	1.0	4.0	3.8	5.0
2.	0.029		1.0	2.0	0.5	0.6
	(0.029) ^{3/}		(0.2)	(2.0)	(3.8)	(4.3)
D 1.	0.017	1.33 ± 0.22	1.7	3.7	1.1	1.3
E (tip)	0.017	1.68 ± 0.24	1.7	-	-	-

^{1/} Locations indicated by letters and numbers on fig. 1.

^{2/} H_f measured at thickest parts of flow.

^{3/} Numbers in parenthesis apply to calculations using yield strength and viscosity obtained from measurements at Makaopuhi Lava Lake (10).

VISCOSITY OF BASALTIC LAVAS: COMPARISON OF THEORETICAL MODELS AND EXPERIMENTAL MEASUREMENTS

Mark Settle, Dept. of Geological Sciences, Brown Univ., Providence, RI 02912

Photogeological investigations have revealed that extrusive volcanic eruptions on the Moon and Mars commonly produced lava flows which were capable of advancing over distances of several hundred kilometers.^{1,2} The morphometry and morphology of these very long flows suggest that they are predominantly basaltic in composition. Individual flows of comparable length are inferred to form on the earth during flood basalt eruptions. As part of a larger study of emplacement mechanisms involved in the construction of very long lava flows, this abstract describes an investigation of basalt viscosity models. The purpose of this investigation is to develop a means of estimating the bulk viscosity of basaltic lavas of varying composition at subliquidus temperatures.

Naturally occurring volcanic lavas are complex, three phase mixtures consisting of liquid silicate melt, solid crystals, and gaseous bubbles. Lavas behave as open chemical systems during the process of flow emplacement, losing volatile phases by degassing and crystalline phases by sedimentation and flotation. In addition, crystallization phenomena alter the chemical composition of the liquid melt phase as a lava cools. The dynamic interplay of crystallization and degassing processes can be quite complicated within natural lavas. Consequently, it is quite difficult to quantitatively characterize the rheological properties of flowing lava during extrusive eruptions.

Field observations and sample analyses reported by Swanson and Fabbri³ indicate that volatile phases entrained in basaltic lavas are effectively removed by lava flowage. These observations tentatively suggest that the influence of entrained bubbles upon basalt viscosity may be largely restricted to areas near a flow's source vent. Basaltic lavas travelling over distances of 50 km or more may be accurately characterized as two phase (crystal-liquid) suspensions over the major portion of their flow length.

Theoretical studies of two phase solid-liquid suspensions performed by Einstein and Roscoe predict that the bulk viscosity of solid-liquid mixtures is given by:

$$\eta_s = \eta_l (1 - 1.35c)^{-2.5} \quad \text{for uniform spheres}$$
$$\eta_s = \eta_l (1 - c)^{-2.5} \quad \text{for spheres of diverse size}$$

where η_s is the bulk suspension viscosity, η_l is the viscosity of the liquid phase, and c is the total volume fraction of admixed crystalline

VISCOSITY OF BASALTIC LAVAS

Settle, M.

phases.⁴ Shaw⁵ has previously proposed that these expressions could be used to estimate the bulk viscosity of natural lavas provided that crystal content and liquid silicate viscosity were known at successive stages of crystallization.

Wright and Okamura⁶ have recently documented variations in crystal content, crystal composition, and residual melt chemistry that occurred during the cooling and solidification of the 1965 Makaopuhi lava lake, Hawaii. These measurements describe the near-equilibrium crystallization of a naturally occurring, tholeiite basalt at 1 atmosphere pressure. The Makaopuhi data can be used to determine residual melt composition at successive cooling stages by removing elements from the liquid melt phase in accordance with observed changes in crystal content at progressively lower temperatures. Residual melt composition has been calculated at sub-liquidus temperatures assuming: (i) modal proportions of crystalline phases generalized from the data of Wright and Okamura with a constant 6.0 wt% olivine below 1180°C (i.e., no mechanical separation of olivine crystals), and (ii) constant composition for crystalline phases over the temperature range 1205°C to 1080°C (olivine Fo75, clinopyroxene En45Fs18Wo37, plagioclase An60).

The viscosity of liquid silicate melts can be calculated using models developed by Bottinga and Weill⁷ and Shaw.⁸ These models estimate liquid melt viscosity on the basis of the mole fractions of various component oxides within a silicate liquid. Silica (SiO₂) and alumina (Al₂O₃) components form strong intermolecular bonds in the liquid state which serve to increase melt viscosity; whereas oxides containing large metallic or alkali cations such as FeO, MgO, TiO₂, Na₂O, and K₂O tend to disrupt intermolecular bonds, serving to decrease melt viscosity. Both the Bottinga and Weill and the Shaw models employ empirical additive relations to calculate the viscosity of a liquid silicate melt.

Estimates of suspension viscosity for the 1965 Makaopuhi basalt using the Bottinga and Weill and the Shaw models agree with one another to within a factor of three over the temperature range 1205°C-1080°C. Suspension viscosity estimates based upon the Bottinga and Weill model are consistently greater than those based upon the Shaw model. This discrepancy may be due to several factors (for example, the Bottinga and Weill model does not account for the influence of nongaseous H₂O upon liquid silicate viscosity; whereas the Shaw model does provide for an H₂O melt component).

Laboratory measurements of the bulk viscosity of Makaopuhi basalt reported by Shaw⁵ consistently fall between suspension viscosity estimates based upon the Bottinga and Weill and Shaw models. These laboratory measurements have absolute accuracies of ±10°C in temperature and ±20% to ±50% in viscosity over the temperature range 1300°C to 1150°C.

VISCOSITY OF BASALTIC LAVAS

Settle, M.

Laboratory measurements agree with calculated suspension viscosities to within a factor of two in most cases (agreement is actually better than this if experimental error estimates are taken into account).

The results of this investigation imply that: (i) the Einstein-Roscoe relations accurately predict variations in the bulk viscosity of natural basalts resulting from crystal nucleation and growth, and (ii) liquid silicate viscosities derived by averaging Bottinga and Weill and Shaw model estimates may provide a more accurate description of melt phase viscosity than either individual model. These results are currently being employed in studying the emplacement histories of very long lava flows.

References:

- ¹Schaber G. (1973) Proc. Lunar Sci. Conf. 4th, p. 73.
- ²Carr M. et al (1977) J. Geophys. Res. 82, 3985.
- ³Swanson D.A. and Fabbri B.P. (1973) J. Res. USGS 1, 649.
- ⁴Roscoe R. (1952) Brit. J. Appl. Phys. 3, 267.
- ⁵Shaw H.R. (1969) J. Petrology 10, 510.
- ⁶Wright T.L. and Okamura R.T. (1977) USGS Prof. Paper 1004.
- ⁷Bottinga Y. and Weill D.F. (1972) Am. J. Sci. 272, 438.
- ⁸Shaw H.R. (1972) Am. Jour. Sci. 272, 870.

SCALE MODEL SIMULATION OF LAVA FLOWS

Womer, Michael B. and Ronald Greeley, Department of Geology, Arizona State University, Tempe, AZ; James D. Iversen, Department of Aerospace Engineering, Iowa State University, Ames, IA; and Jeffrey Kremer, Department of Geology, University of Texas, Austin, TX.

The dynamics of lava flow emplacement is a complex and poorly understood problem that may be studied through observation of active flows, theoretical modelling and laboratory simulations. A properly designed scale model has the advantage of allowing systematic investigation of the effects of any number of parameters. The design of a scale model for use in laboratory simulation requires geometric, kinematic and dynamic similarity between prototype and model (1). According to the Buckingham Pi Theorem, $S = N - B$; where S is the number of dimensionless parameters required to define a system, N is the number of variables in the system, and B is the number of basic dimensions in which the variables are measured (2). The variables in a single phase (liquid) system are: fluid density (ρ), gravitational acceleration (g), fluid velocity (V), characteristic horizontal length (L), characteristic vertical length (H), all other horizontal lengths (l), all other vertical lengths (h), viscosity (μ), Bingham Fluid yield stress (T_y), surface tension (σ), specific heat (C_p), thermal conductivity (k), temperature (T), temperature difference (ΔT), heat transfer coefficient (h_c), heat of fusion (Q_f), pressure (p), and time (t). These variables have the dimensions of mass, length, time, and temperature. The following 14 dimensionless parameters are therefore derived: horizontal geometric scaling (l/L), vertical geometric scaling (h/H), Reynolds number (VL/γ) where $\gamma = \mu/\rho$, Froude number (V^2/Lg), Weber number ($\rho V^2 L/\sigma$), Peclet number ($\rho C_p VL/k$), Prandtl number ($\rho \gamma C_p/k$), Grashof number ($g \Delta T L^3/T \gamma^2$), effective Reynolds number ($1/(\mu/LVO + (T_y/(\rho VL \partial V/\partial \gamma)))$), fusion number ($Q_f/C_p T$), temperature ratio ($\Delta T/T$), and dimensionless time ($t^2 g/L$) (gravity based). For a model to satisfy similitude requirements each of these Pi terms for both systems must be equal, respectively. Average values for the above variables are listed in Table 1. A comparison of model and prototype Pi terms is given in Table 2 when Carbowax 4000 is used as modelling material. Note that the Weber number indicates greater relative surface tension effects in the model and the Prandtl number indicates greater convective heat loss in the model. Other parameters match moderately well.

Carbowax 4000 was extruded at various eruption rates and temperatures (viscosities) onto a flat, variable slope surface. Extrusion rates varied from 3.6×10^{-2} cc/sec ($4.2 \times 10^3 \text{ m}^3 \text{ sec}^{-1}$) to 3×10^0 cc/sec ($3.5 \times 10^5 \text{ m}^3 \text{ sec}^{-1}$), viscosity was varied from 0.45 poises (1.2×10^6 poises) to 2.15 poises (5.7×10^6 poises) and slope was varied from 0° to 20° (0° to 4°). The figures in parentheses are equivalent prototype values for the Carbowax model values listed. The first and third variables correlate closely to Mare Imbrium flows (3,4,5) whereas the second variable, viscosity, correlates poorly (6,7,8). In attempting to define the controlling parameters of lava flow morphology, the aspect ratios (depth of flow/width) and flow lengths were compiled and plotted against slope, temperature (viscosity), extrusion rate and flow volume. Aspect ratio increases with increasing slope in all cases examined. This results from higher slopes creating longer, narrower flows. Flow thickness decreased with increasing slope, but at a much slower rate. An inverse relationship between aspect ratio and extrusion rate is also evident. This trend is less well developed

and results from flow thickness decreasing with increasing eruption rate. No relationship between aspect ratio and viscosity was apparent when plotted with respect to various slopes, volumes and extrusion rates. It is concluded that the effect of viscosity is insignificant compared to the other parameters as has been found in "real" flows (9). In comparing length and extrusion rate, a general trend is evident, with length increasing with extrusion rate. This relationship holds for all slopes investigated, higher slopes correlating with increased flow length. The effects of viscosity and flow volume on length are not evident, and considered insignificant compared to the effects of slope and extrusion rate. Though scaled to simulate lunar flows, these model flows qualitatively confirm the results of Walker (1973).

REFERENCES:

1. Hubbert, M. K., 1937, *Geol. Soc. Amer. Bull.*, 48, 1459-1520.
2. Hodgson, G. W., 1969, An experimental investigation of simulated lava flows using Carbowax materials: Master of Science Thesis, Air Force Institute of Technology, Wright-Patterson A. F. B., Ohio.
3. Hulme, G., and G. Fielder, 1977, *Phil. Trans. R. Soc. Lond. A.*, 285, 227-234.
4. Schaber, G. G., J. M. Boyce, and H. J. Moore, 1976, *Proc. Lunar Sci. Conf. 7th*, 2783-2800.
5. Moore, H. J., and G. G. Schaber, 1976, *Proc. Lunar Sci. Conf. 6th*, 101-118.
6. Provost, A., and Y. Bottinga, 1972, *Earth and Planet. Sci. Letters*, 15, 325-337.
7. Murase, T., and A. R. McBirney, 1970a, *Science*, 170, 165-167.
8. Murase, T., and A. R. McBirney, 1970b, *Science*, 167, 1491-1493.
9. Walker, G. P. L., 1973, *Phil. Trans. R. Soc. Lond. A.*, 279, 107-118.
10. Schaber, G. G., 1973, *Proc. Lunar Sci. Conf. 4th*, 73-92.
11. Bullard, B. W., 1968, An experimental study of the mode of emplacement of lava flows: Unpublished thesis, Wright-Patterson A. F. B., Ohio.
12. Macdonald, G. A., 1953, *Amer. J. Sci.*, 251, 169-191.
13. Sakuma, S. and T. Nagata, 1957, *Handbook des Physik, Geophysics II*, 48, 982-1011.
14. Union Carbide Corp, 1978, *Carbowax Polyethylene Glycols*: New York, 36 p.

TABLE 1

	Lunar lava*	Terrestrial Basic Lava**	Carbowax 4000***
L	1000 cm	2500 cm	.25 cm
V _{min}	50 cm sec ⁻¹	10 cm sec ⁻¹	.3 cm sec ⁻¹
V _{max}	400 cm sec ⁻¹	400 cm sec ⁻¹	.3 cm sec ⁻¹
ρ	3.0 g cm ⁻³	2.0 g cm ⁻³	1.07 g cm ⁻³
C _p	.2128 cal g ⁻¹ °C ⁻¹	.20 cal g ⁻¹ °C ⁻¹	0.55 cal g ⁻¹ °C ⁻¹
k	1.5 x 10 ⁻³ cal cm ⁻¹ sec ⁻¹ °C ⁻¹	7.0 x 10 ⁻³ cal cm ⁻¹ sec ⁻¹ °C ⁻¹	0.8 x 10 ⁻³ cal cm ⁻¹ sec ⁻¹ °C ⁻¹
QF	~100 cal g ⁻¹	~200 cal g ⁻¹	43 cal g ⁻¹
σ	300 d cm ⁻¹	300 d cm ⁻¹	65 d cm ⁻¹
γ	50 to 1000 poise	~1000 poise	~1 poise
l	1000 m	1000 m	1 cm
H	5000 m	5000 m	5 cm
h	10m	25 m	0.05 cm
g	167 cm sec ⁻²	980 cm sec ⁻²	980 cm sec ⁻²
T	1473 °K	1473 °K	373 °K
ΔT	1200 °K	1200 °K	100 °K
t	--	--	--
h _c	--	--	--

* Values as given by 3,4,5,6,7,8,10

** Values as given by 2,11,12,13

*** Values as given by 2,14

TABLE 2

	Lunar Flows	Terrestrial Basic Flows	Carbowax 4000*
Width Ratio (l/L)	0.20	0.20	0.20
Depth Ratio (h/H)	0.002	0.005	0.01
Reynolds Number (VL^*/γ)	5×10^1 to 8×10^3	2.5×10^1 to 1×10^3	7×10^{-2}
Froude Number (V^2/L^*g)	1.5×10^{-2} to 9.9×10^{-1}	4.1×10^{-5} to 6.5×10^{-2}	4×10^{-3}
Weber Number ($\rho V^2 L^*/\sigma$)	2.5×10^4 to 1.6×10^6	1.7×10^3 to 2.7×10^6	4×10^{-4}
Nusselt Number ($h_c L^*/k$)	6.7×10^5 (h_c)	3.6×10^5 (h_c)	6×10^3 (h_c)
Prandtl Number ($\rho \gamma C_p/k$)	2.1×10^4 to 4.3×10^5	5.7×10^4	7×10^2
Eckert Number ($V^2/C_p T$)	8×10^{-4} to 5.1×10^{-2}	3.2×10^{-5} to 5.4×10^{-2}	3×10^{-7}
Fusion Number ($QF/C_p T$)	0.3	0.7	0.2
Temperature Difference ($\Delta T/T$)	0.8	0.8	0.2
Grashof Number ($g \Delta T L^3 / T \gamma^2$)	5.4×10^7 to 1.4×10^5	1.2×10^7	4.1×10^2
Peclet Number ($\rho C_p V L^*/k$)	2.1×10^7 to 1.7×10^8	1.4×10^6 to 5.7×10^7	5.5×10^1
Dimensionless Time ($t^2 g/L^*$)	1.7×10^{-1} (t^2)	9.8×10^{-1} (t^2)	(t^2) 3.9×10^3

*Carbowax 4000 values calculated assuming 5X vertical exaggeration on test model.

SCALE MODEL SIMULATION OF MARE BASALTS

Womer, Michael B. and R. Greeley, Department of Geology, Arizona State University, Tempe, Arizona 85281; J.D. Iversen, Department of Aerospace Engineering, Iowa State University, Ames, Iowa 50010

To further investigate the conditions and mechanics of mare basalt emplacement in lunar impact basins, a series of scale model simulations has been initiated. The project consists of extruding Carbowax 4000, a viscous liquid with a freezing point of 56°C (1), onto a 3 m square topographic model of an idealized pre-mare lunar impact basin. To satisfy modelling constraints of the Carbowax, the model was constructed with a 5X vertical exaggeration. The basin was scaled to the approximate diameter of the basin Schrodinger (~ 300 km) and consists of inner basin, inner ring, outer basin, outer ring and extra-basin topography. Data for generation of the model were derived from limb profiles across Orientale basin (2). The profiles were adjusted to fit the generalized geology (2) and geometry of Schrodinger Basin, with correction for fill by mare basalts. A solid of revolution was generated by the adjusted profile and then altered to fit the outcrop pattern of massif and plains seen in Schrodinger.

Design of the experimental apparatus allows precise control of both extrusion rate and temperature (and therefore viscosity) of the Carbowax. In addition, from one to seven vents of either circular or fissure type may be used, and the entire model may be tilted up to 5° in any direction. Extrusion rate may be varied from $4200 \text{ m}^3 \text{ sec}^{-1}$ lava. The scaled viscosity is variable between 1.0×10^6 poise and 5.7×10^6 poise (at 140°C and 60°C , respectively). Clearly, this represents a distortion of the model, being a better approximation of intermediate lavas than mare basalt lava (3,4,5). Primary effect of the high viscosity is exaggerated thickness of model flows, which is overcome by the vertical exaggeration of the model. Scaled thicknesses of the model flows average approximately 40 m.

Two preliminary runs were conducted at scaled viscosity of 2.5×10^6 poise and scaled extrusion rate of $\sim 40,000 \text{ m}^3 \text{ sec}^{-1}$ from a single circular vent 500 m in diameter. Both runs resulted in complex, channel flow formation (Fig. 1). Infilling was restricted largely to the inner basin, individual flows seldom retaining sufficient mobility to fill the outer basin. Early flow profiles (<20 years, scaled duration) exhibit very low gradients, typically less than 7 m/km from vent to flow margin, the result of ponding against the inner wall of the first ring. Later profiles become increasingly shield-like as some material flows into the outer basins. A third preliminary run, conducted with scaled values of $\sim 2.0 \times 10^6$ poise and $430,000 \text{ m}^3 \text{ sec}^{-1}$ from a central vent yielded strongly contrasting results. Material was emplaced as a single cooling unit,

gradually filling the inner basin, then flowing outward into the outer basin. Relief on the flow was essentially zero, and filling of the outer basin much more complete (Fig. 2). Transition from sheet flow to channel flow occurred at approximately the inner ring, with filling of the outer basin episodic. The result is a complex accumulation of flow units averaging 20 to 50 m thick in the outer basin. The thicknesses agree moderately well with the results of Gifford and El-Baz (6). Additionally, roofing over some of the channels occurred with continued activity as lava tubes for as long as ~150 days (scaled duration).

In conclusion, these preliminary runs exhibit profound differences in morphology due to extrusion rate, and display many features seen in both lunar and terrestrial basic lavas. Future runs with more realistic vent configurations are expected to yield insight into the mechanisms and parameters of basin flooding.

REFERENCES:

1. Union Carbide Corp., 1978, *Carbowax Polyethylene Glycols*: New York, 36 p.
2. Howard, K. A., and D. E. Wilhelms, 1974, Lunar basin formation and highland stratigraphy: *Rev. of Geophys. Space Phys.*, 12(3), 309-327.
3. Hodgson, G. W., 1969, An experimental investigation of simulated lava flows using Carbowax materials. Master of Science Thesis, Air Force Institute of Technology, Wright-Patterson AFB, Ohio.
4. Murase, T. and A. R. McBirney, 1970, Viscosity of lunar lavas, *Science*, 167, 1491-1493.
5. Provost, A. and Y. Bottinga, 1972, Rates of solidification of Apollo 11 basalt and Hawaiian tholeiite, *Earth Planet. Sci. Letters*, 15, 325-337.
6. Gifford, A. W. and F. El-Baz, 1978, Thickness of Mare flow fronts: *Proc. Lunar Planet. Sci. Conf. 9th*, 382-384.

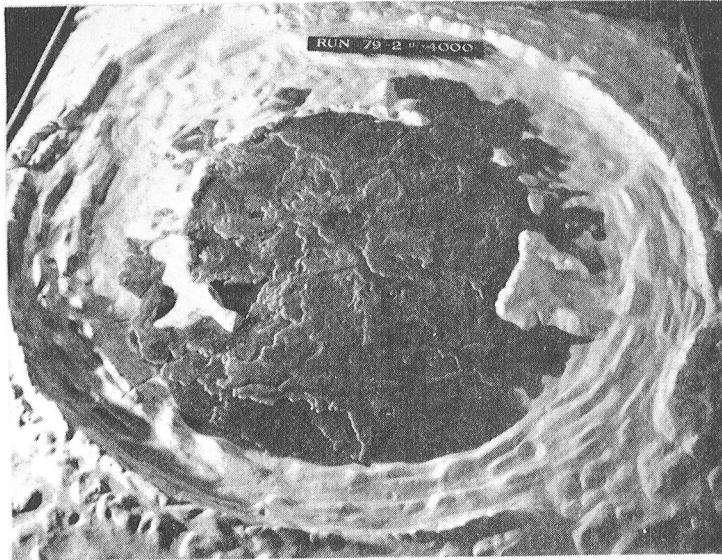


Figure 1. Extent of simulated lava flows in Schrodinger-sized (300 km) basin using a constant extrusion rate of $\sim 4.0 \times 10^4 \text{ m}^3 \text{sec}^{-1}$ (scaled). Note the complex interlayering of flow units and incomplete filling of outer basin.

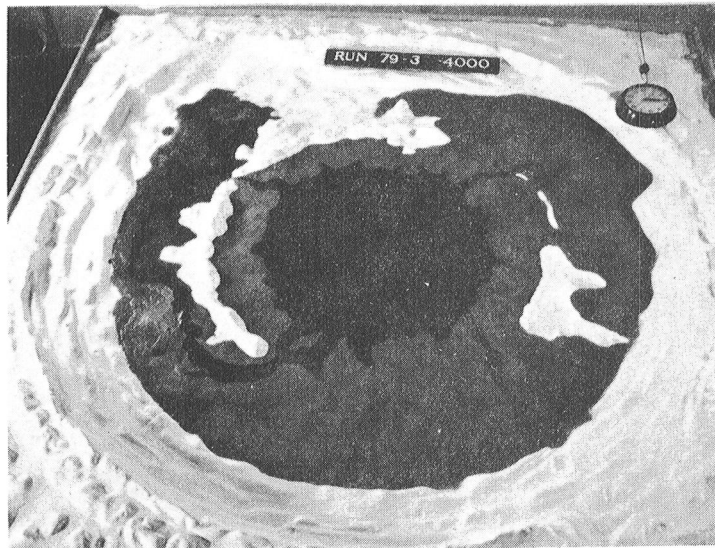


Figure 2. Extent of simulated lava using a constant extrusion rate of $\sim 4.0 \times 10^5 \text{ m}^3 \text{sec}^{-1}$ (scaled) lava. Note the lack of flow lobes and large sheet of liquid material in the center. Filling of outer basin is relatively complete.

Chapter 6
AEOLIAN PROCESSES AND LANDFORMS

MARS: ORIGIN OF THE GLOBAL DUST STORMS

Huguenin, R.L., Clifford, S.M., U.Massachusetts Dept. Physics/Astronomy-Hasbrouck, Amherst 01003, and Greeley, R., Arizona State U., Tempe, AZ

Huguenin et al. (1979) and Huguenin and Clifford (these abstracts) presented evidence for outgassing of H_2O in two regions, Solis Lacus (-25° , 85°) and Noachis Hellespontus (-30° , 315°). Associated with this outgassing during Southern Spring and Summer is dust cloud activity in these two regions, occurring during nearly every martian year since observational records have been kept. The dust clouds have generally appeared suddenly near dawn as brilliant white features and faded to yellow toward noon (LT). In addition to spawning local storms, these two regions have also been primary core areas for the past global storms. We don't think it is a coincidence that the onsets of the local and global storms in these regions were immediately preceded by or coincident with the sudden increase in condensate (blue and white cloud) activity.

We have proposed (Huguenin and Clifford, these abstracts) that the condensate activity is produced by the evaporation of a subsurface brine/ H_2O ice layer. As pointed out by several authors the diffusion of H_2O vapor out of the soil is inhibited by the overburden soil (in a manner similar to that of a gas chromatograph column). We propose that the sudden increase of outgassing occurs near perihelion (as evidenced by the sudden increase in condensate activity) as a result of the melting and upward migration of H_2O brine films into the drier overburden. As the moisture approaches the surface, evaporation becomes less diffusion-inhibited and the vapor can escape at higher rates. In addition the moisture experiences higher heating rates and higher daytime temperatures near the surface. The maximum outgassing rates for the near-surface H_2O should occur during the period of maximum heating rate ($\sim 15^\circ \text{ hr}^{-1}$) after dawn. For H_2O that is sufficiently confined (eg by duricrust or at ~ 1 cm depth in unconsolidated soil) the outgassing could be explosive when temperatures rise above $\sim 273^\circ\text{K}$, since the equilibrium H_2O vapor pressure of H_2O at that temperature exceeds the mean martian atmospheric surface pressure (~ 6 mbar). Near the daily maximum surface temperatures ($\sim 295^\circ\text{K}$) confined H_2O could achieve vapor pressures of up to ~ 26 mbar. We are proposing that the outgassing H_2O may inject dust into the atmosphere and initiate the dust storms in the 'oasis' regions.

This is supported by pilot laboratory experiments using dampened 'soils' in both a bell jar and a low atmospheric pressure wind tunnel (Greeley and Leach, 1979). The 'soils' included: fine silt ($10 \mu\text{m}$), talc ($13 \mu\text{m}$), quartz ($23\text{--}44 \mu\text{m}$), walnut shells ($61\text{--}88 \mu\text{m}$), and poorly sorted calcite grains ($12\text{--}1000 \mu\text{m}$). During the bell jar experiments it was found that as the atmospheric pressure was reduced below 10 mb at 24°C the moisture in the soil vaporized and ejected particles into the atmosphere. Vent holes and fissures developed, followed by a fountainlike spray of particles as high as 20 cm above the surface. In addition, violent 'eruptions' occurred in a manner similar to boiling. Smaller grain sizes produced more violent eruptions. Activity was observed with water

contents as low as 0.75% by weight. During the wind tunnel experiments similar effects were observed with dampened silt when the pressure was dropped to ~ 10 mb. Dust injection at pressures near ~ 10 mb could also be 'triggered' when a low velocity wind ($\sim 25 \text{ ms}^{-1}$) was passed over the surface. As the pressure was reduced to 10 mb the surface developed irregular fissures from the outgassing H_2O and when subjected to the 25 ms^{-1} wind, the fissured surface began to erode. By comparison, the normal threshold wind speed for eroding dry undisturbed silt is in excess of 250 ms^{-1} .

The results of these experiments suggest that a similar dust injection process could be 'triggered' by the rapid increase in evaporation rate that would occur when the upward migrating liquid H_2O /brine melt approaches the surface. The observed sudden outbursts of cloud activity near dawn may result from the sudden melting of a brine ice layer formed at the cold nighttime surface. Such an ice layer could inhibit the escape of vapor during the night from the relatively warm subsurface brines and enhance the supply of H_2O for morning evaporation.

The dust storms in Solis Lacus and Noachis Hellespontus occur at different L_S dates each year, spanning Spring and Summer. These observed yearly variations might be explained as a consequence of the small expected yearly differences in the depth and salinity of the brine/ice layer, since the L_S date on which the thermal wave would penetrate to and melt the brine/ice layer would correspondingly vary. Such variations may also explain why the local clouds don't always develop into global events. In particular, it has been proposed by several authors that around southern Summer Solistice (and perihelion) atmospheric columns of strong vertical uplift develop within approximately 1000 km of the 'oasis' regions as a result of interactions of the diurnal thermal tide and large-scale martian topography. It is possible that the global obscuration may result from the pumping of dust into the atmosphere from the core (oasis) areas by these columns of strong vertical uplift. The dust which is carried aloft could be moved great distances before settling out, and result in global scale obscuration. If the development of the atmospheric 'pumps' does not coincide with the period of brine/ice melting and dust activity, then the global obscuration may not develop and the activity might remain in the vicinity of the 'oasis'.

It should be stressed that we are only proposing that the dust storms in the Solis Lacus and Noachis-Hellespontus regions may be produced by H_2O outgassing. Other dust clouds which are not accompanied by condensates, e.g. in Claritas and Hellas, are probably generated by other processes. Dust clouds near Isides, which are accompanied by condensates and which form core clouds of global storms may also be produced by H_2O outgassing, however, and this will be discussed in a later paper.

References Greeley, R. and Leach, R. (1979) NASA TM80339, 304;
Huguenin et al. (1979) NASA TM80339, 208.

THE EFFECTS OF TOPOGRAPHY, ALBEDO AND THERMAL INERTIA VARIATIONS ON
THE GENERATION OF MESOSCALE MARTIAN WIND PATTERNS: A COMPARATIVE
STUDY OF THE SNAKE RIVER PLAIN, IDAHO AND THE MARTIAN SURFACE.

Rankin, Robert L., Arizona State University, Department of Aerospace
Engineering and Engineering Science, Tempe, Arizona 85281

Peterfreund, Alan, Arizona State University, Department of Geology,
Tempe, Arizona 85281

Greeley, Ronald, Arizona State University, Department of Geology,
Tempe, Arizona 85281

Eckerman, Greg, Arizona State University, Department of Aerospace
Engineering and Engineering Science, Tempe, Arizona 85281

Introduction: Mesoscale surface winds are important in the study of
aeolian processes. In the absence of any significant synoptic scale
weather phenomenon many regions exhibit regular diurnal variations in
surface winds which appear closely tied to diurnal temperature varia-
tions. Depending on local topography, surface heating and cooling
characteristics and albedo variations these surface winds may be a
significant factor in altering surface features and in the formation
of mesoscale atmospheric disturbances.

The diurnal rotation of the winds at the Viking Lander sites are
primarily the product of mesoscale surface winds due to slope heating
[Hess et al., 1977]. Mesoscale surface winds are also a major factor
in the initiation of particle saltation and the generation of local
dust storms on Mars. The driving mechanism for these winds are
spatial and temporal variations in the temperature. Due to the
transfer of heat between the ground surface and the adjacent air, a
temperature gradient is formed in a direction normal to the inclined
surface. The differences in the horizontal components of these
gradients generate an upslope wind when the surface is being heated
and a downslope wind when the surface is being cooled. A model has
been developed [Rankin, 1979] based on these concepts. This model
is used to compare a region of the Snake River Plain in Idaho with a
portion of the Claritas Fossae region of Mars. These regions were
chosen because they are topographically similar and exhibit similar
albedo variations. The Claritas Fossae region is the site of numerous
local dust storms observed in 1977 [Peterfreund and Kieffer, 1979].

The Model: The governing equations for surface winds are derived from
the principles of conservation of momentum and mass. In order to
simplify the analysis we look only for the average hourly horizontal
velocity components at a height of 10m in a surface layer of uniform
thickness. The vertical structure of this layer is assumed to be

in hydrostatic equilibrium. In a mesoscale theory the effects of planetary curvature can be neglected and, in order to simplify the viscous stresses, the viscous force is assumed to be directly proportional to velocity. Coriolis accelerations are included, however it is assumed that material rates of acceleration can be neglected in order to filter out wave phenomenon.

The atmosphere is assumed to behave like a perfect gas. Using the above assumptions it is possible to eliminate pressure and density in favor of temperature and topographic variations in the governing equations. This is an extremely important feature of this approach since both temperature and topographic data are readily available.

The Data: The data collection for this project consists of two parts. Topographic, temperature, albedo and wind velocity data must be obtained for both the Snake River Plain (SRP) region of Idaho and for the Viking Lander 1 (VL-1) site on Mars. Model validation will be carried out by comparison of measured and predicted surface winds between the SRP and VL-1 site. Once a validated Martian model is available it will be used to study the Claritas Fossae region of Mars.

Topographic data is readily available from U.S. Geological Survey maps for the SRP. Temperature, albedo and wind data have also been obtained from direct field measurements at that site. For the Martian sites, topographic data is available from the radar altimeters aboard the Viking Landers and the Viking Infrared Thermal Mapper will be used to obtain albedo and thermal inertia data.

The Output: Four periods from the Martian seasons will be chosen to look for seasonal variations in surface winds due to solar insolation and to determine the seasonal dependence of surface winds as a function of latitude. These periods will be chosen to coincide with locally observed dust storms to determine if threshold velocities for the saltation of particles are exceeded.

The actual output of the model is in the form of computer generated hourly wind maps where wind velocity is plotted as a vector over an evenly spaced rectangular grid. These maps will be studied to see if any significant trends in wind speed and direction can be related to albedo and thermal inertia variations.

References:

1. Hess, S. L., et al., 1977, J. Geophys. Res., V82, N28, 4559-4574.
2. Rankin, R., 1979, ASU Research Center, ERC-R-79026.
3. Peterfreund, A., and H. Kieffer, 1979, J. Geophys. Res., V84 NB6 2853-2864.

Mars: Some Mechanisms of Contrast Change Inferred from Behavior of Wind Streaks. P. Thomas, J. Veverka, Cornell University, Ithaca, New York.

The seasonal behavior and geographic distribution of wind streaks on Mars provide much information on the occurrence of sediment transport by saltation and suspension and on the mechanisms responsible for the retention of dark albedo markings.

The occurrence of several mechanisms of changing or retaining albedo contrasts, as inferred from windstreaks, are shown in Figure 1. Areas of unit 1 are subject to widespread dust storm fallout, local erosion of dust shortly after duststorms, and widespread erosion of the dust at the start of the next dust storm.

Many areas (2, 3, Fig. 1), however, retain most or all of their contrast with their surroundings after dust storms. Dark dune fields are some of the most prominent of these areas. In regions with a relatively thick dust mantle (2, Fig. 1), only dune fields and some small associated streaks retain their contrast with the brighter surroundings. In regions of thinner dust mantling, such as Oxia Palus and some canyons and plains areas, large areas downwind of dune fields also remain relatively dark after dust storms. We infer that most of these dune fields are currently active and that saltation of sand-sized particles prevents deposition of significant amounts of dust. It is also concluded that some material deflated from the dunes is present downwind in sheets or stringers, and prevents significant accumulation of dust by saltation "cleaning" of the substrate.

Other large, dark areas (4, 5) have some dust deposition concentrated in bright streaks. However, these areas are also subject to some uniform dust blanketing and erosion, even at high northern latitudes.

Some dark streaks (area 1) repeat forms precisely from year to year, although most do not. Other dark streaks seen only once at very high resolution have sharp boundaries (less than 20 m) and follow local topography. These dark streaks strongly indicate that there can be some ground level control of streak formation such as surface roughness. Some large dark areas may be subject to minimal dust deposition and preferential erosion caused by their evident rough topography.

Dust may be accumulating on perennial polar ice (6). The source areas are so large, and include significant areas of thick mantle, that little or no erosion of bedrock need contribute to building up polar deposits.

Other areas on Mars, which include both landing sites, are subject to a variety of processes transporting and depositing dust, but the overall patterns are not clear.

The wind streaks show dust storms do not cause uniform dust deposition or erosion over Mars. Most activity, both deposition and erosion occurs in bright areas and may be concentrated near the margins of large dark areas. Thus, much of the dust raised in storms may be trapped in a closed loop.

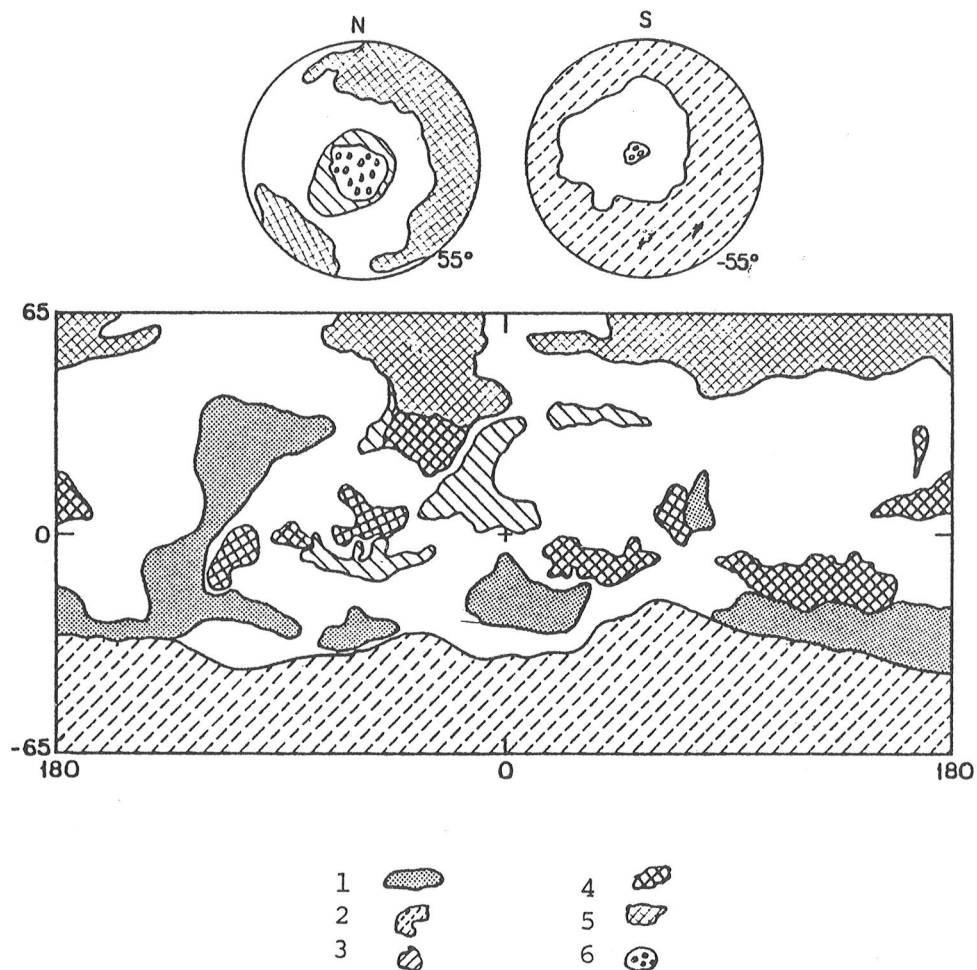


Fig. 1

1. Widespread erosion and deposition of dust.
2. Scattered dune locations in generally thick dust mantle.
3. Significant dune influence--continuous dunes or thin dust mantle.
4. Dust deposition in bright streaks, some areas of uniform dust deposition and erosion.
5. Dust deposition in scattered bright streaks; some dark streaks are formed in more widespread dust deposits.
6. Polar dust deposition.
7. (Blank) Variety of dust deposition and erosion on bright areas; includes both Viking landing sites.

SURFACE CHARACTERIZATION OF WIND STREAKS ON MARS

Peterfreund, Alan R., Department of Geology, Arizona State University,
Tempe, Arizona 85281

Visual, color and infrared data are useful in defining characteristics of the particular wind streaks and the environment in which wind streaks form. Visual and color data is derived from Mariner 9 and Viking images and albedo and thermal infrared data from the Viking Infrared Thermal Mappers (IRTMs). Infrared observations of the martian surface are sensitive to the thermal inertia (I) of the surface material (Kieffer et al., 1977).

In a study of the Oxia Palus region of Mars (350°W to 20°W , 0°N to 25°N), three distinct surface units are defined by correlating color (Soderblom et al., 1978) and thermal inertia data. The low I regions correspond to the bright red surfaces, the high I regions correspond to the blue, low albedo units and the intermediate albedo, red unit matches the moderate values. Mixed-toned wind streaks emanate from dark deposits within craters in this region, and exhibit variability of size and shape over seasons and years (Thomas and Veverka, 1979). These features are present almost exclusively in the intermediate unit. Histograms (Fig. 1) of the three color units plotted against milli-inertia values ($10^{-3} \text{ cal cm}^{-2} \text{ s}^{-1/2} \text{ K}^{-1}$), using $2^{\circ} \times 2^{\circ}$ cells in the study area, shows the strength of these correlations. Those features found to be variable are located exclusively between the two brackets.

The bright red, low I surface is blanketed by fine eolian debris. The high region contains a greater proportion of exposed rocks or coarser material on the surface, with the dark blue color resulting from a less oxidized material (Singer et al., 1979). Thus, an exposed surface is most probable. The intermediate zone, where the streaks are most prevalent is considered to be transitional between the two end members. A global extension of this type of correlation is in progress.

High resolution IRTM ($<20 \text{ km}$) observations of the wind streaks and the surrounding region provide constraints on the size sediments involved in streak formation. Large dark streaks emanating from intracrater deposits of Mesogaea (190°W , 8°N) and Pettit (174°W , 12°N) occur in regions of high albedo (0.28) and low I, ~ 3 milli-inertia. The streaks have an albedo of ~ 0.20 , and I between 4 and 6. The bright material is interpreted as particles being $<80 \mu\text{m}$ in diameter and similar in albedo and spectra as the material involved in the atmospheric dust activity (Singer et al., 1979). The streaks are inferred to be either deposits of material with mean particle size between $100 \mu\text{m}$ and $300 \mu\text{m}$, or regions where rocks, ranging in size from 3 cm to bedrock, are exposed or cover up to 20% of the surface with the distinction between these two models unresolvable. In the Cerberus (203°W , 12°N) and Hesperia (243°W , 17°S)

regions, the bright streaks occur in regions of albedo = 0.16 to 0.18 and $I = 7$ to 9. In the Syrtis Major Planitia, bright streaks occur where the albedo is less than 0.15, and I ranges from 6 to 9. The bright streaks of Syrtis Major are in fact darker than the background of Cerberus and Hesperia. Thus, having all bright streaks classified as deposition of fines raises problems that concern the ratio of how much fines are being mixed with the primary surface.

This work was supported by NASA Mars Data Analysis Program grant NSG 7548.

References

- Kieffer et al., 1977. J. Geophys. Res., 84, 4249-4291.
 Singer et al., 1979. J. Geophys. Res., in press.
 Soderblom et al., 1978. Icarus, 34, 446-464.
 Thomas and Veverka, 1979. J. Geophys. Res., in press.

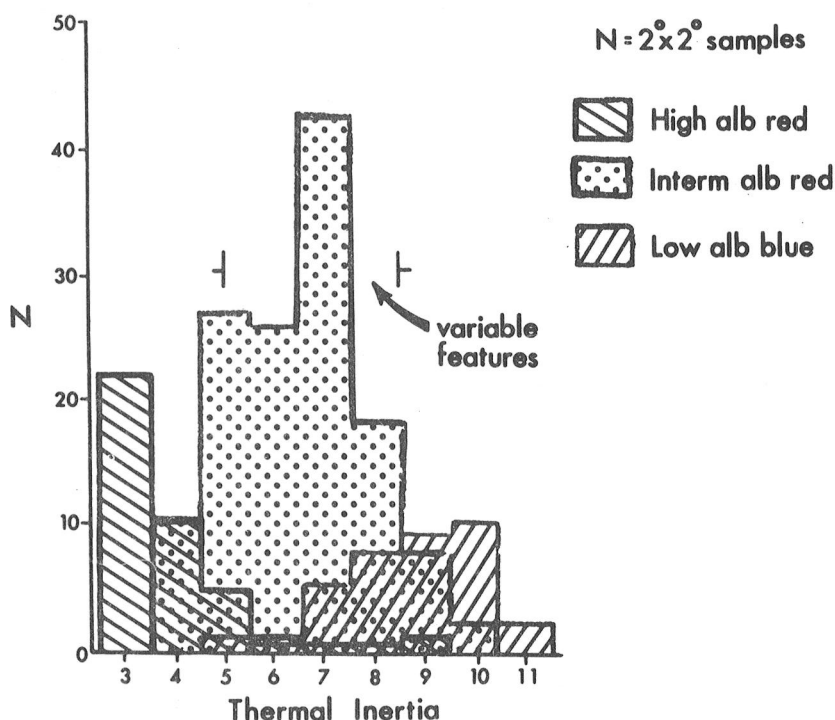


Figure 1. Thermal inertia histograms of color in Oxia Palus.

DISTRIBUTION OF EOLIAN MANTLE ON MARTIAN CANYON RIMS.

Mouginis-Mark, P.J. and Head, J.W., Dept. of Geological Sciences, Brown Univ., Providence, RI 02912

Viking images indicate that a spectrum of rim deposits exists on the walls of Valles Marineris and bounding canyon systems. These deposits have markedly different albedoes than the surrounding plains material and extend from a few kilometers to a few tens of kilometers from the edge of the canyon rim. Multiple views of individual features (e.g., frames 57A43, 58A70, 64A19, and 65A12), and the presence of dark halo ejecta deposits surrounding craters excavated in light-colored surface material (Fig. 1) demonstrate that these rim deposits are not artifacts of the camera system. Rim deposits have been observed on images acquired with clear, violet and red filters at resolutions between 60-250 m/pixel.

We attribute these rim deposits to a local mantling unit of eolian origin, and are attempting to interpret them in terms of the erosional/depositional environment of the canyon system. Five types of deposit have been identified: 1) a plain rim with no albedo variations; 2) a bright, thin deposit at the edge of the canyon wall; 3) a wide, bright rim unit with distal plains material; 4) a narrow bright rim, followed first by darker material, then "normal" plains units; 5) bright, filamentary material with no pronounced boundary. The spatial distribution of these deposits is displayed in Fig. 2.

Correlations of deposit types with rim morphology,¹ the local surface air-flow pattern (derived from adjacent wind streaks^{2,3}) and canyon wall orientation⁴ were made for 512 wall segments sampled at 25 km intervals along the canyon rim. Fig. 3A illustrates that, except for the small number of segments on crater chains, rim morphology plays only a minor role in the distribution of the deposits. Only the filamentary material displays a marked relationship to wall morphology, occurring almost twice as often on tributary canyon¹ segments as other wall units. Dividing air-flow regimes into areas where wind streaks indicate air 1) enters; 2) possibly enters; 3) leaves; 4) possibly leaves the canyon; and 5) an indeterminate class (Fig. 3B) reveals that segments with no albedo variations most commonly correlate with net outward flow of air. Conversely, the thin bright (and to a lesser extent the wide bright) rim is almost exclusively found where air enters the canyon. Other deposits (types 4 and 5) occur almost as often where air enters or leaves the canyon. Wall orientations (Fig. 3C) indicate that the aspect of the wall also influences the deposit distribution. Type 4 deposits are most common on NW facing walls, Type 2 are virtually absent from walls facing 30-180° from north, and Type 3 deposits are least numerous on SE facing walls.

EOLIAN MANTLE ON MARTIAN CANYON RIMS

Mouginis-Mark, P.J. and Head, J.W.

Further data analysis is currently in progress, with the data base expanded to contain values of wall height, canyon width and wall material for each wall segment.

REFERENCES: ¹Lucchitta B.K. 1978, Jour. Res. USGS 6, 651-662. ²Mutch T. A. et al. 1976, The Geology of Mars, Princeton Univ. Press, pp. 235-261. ³Mouginis-Mark P.J. unpubl. data. ⁴USGS Map I-976.

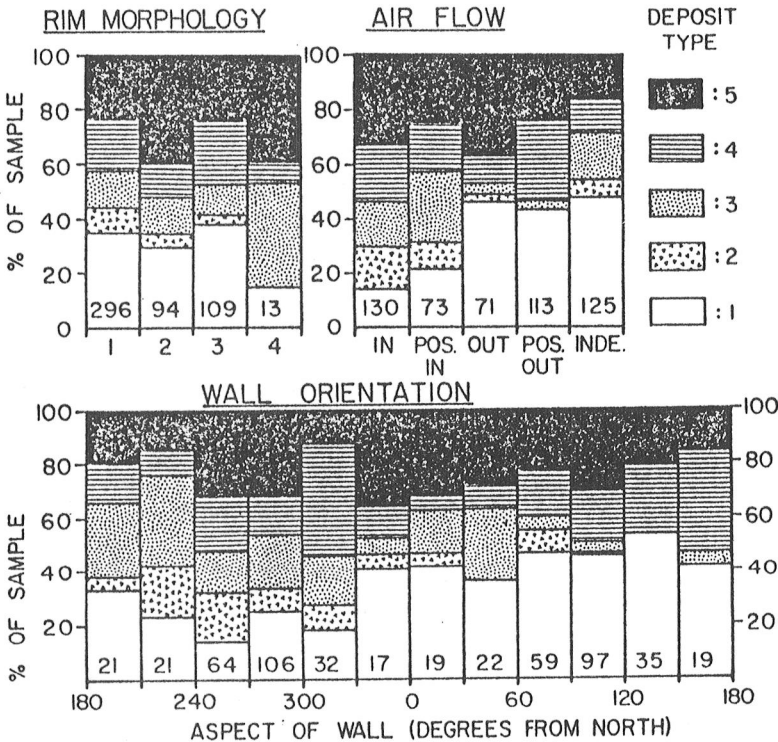
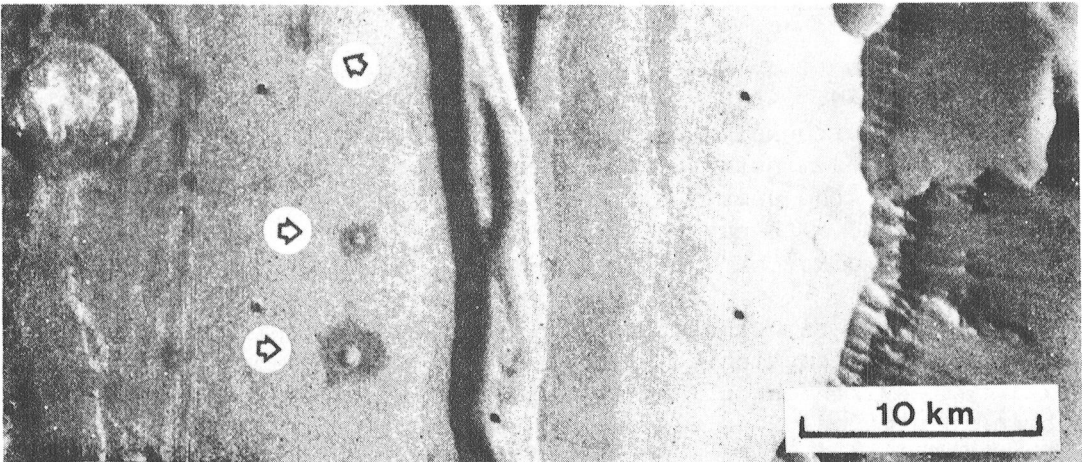


Fig. 1 (above): Dark-halo craters (arrowed) and a bright rim unit exposed in the canyon wall indicate a surface mantling that is inferred to be eolian in origin. Illumination from left, Viking frame 66A15.

Fig. 2 (next page).

Fig. 3 (left): Distribution of rim deposits as a percentage of total occurrence, numbers in bottom box give size of each sample.

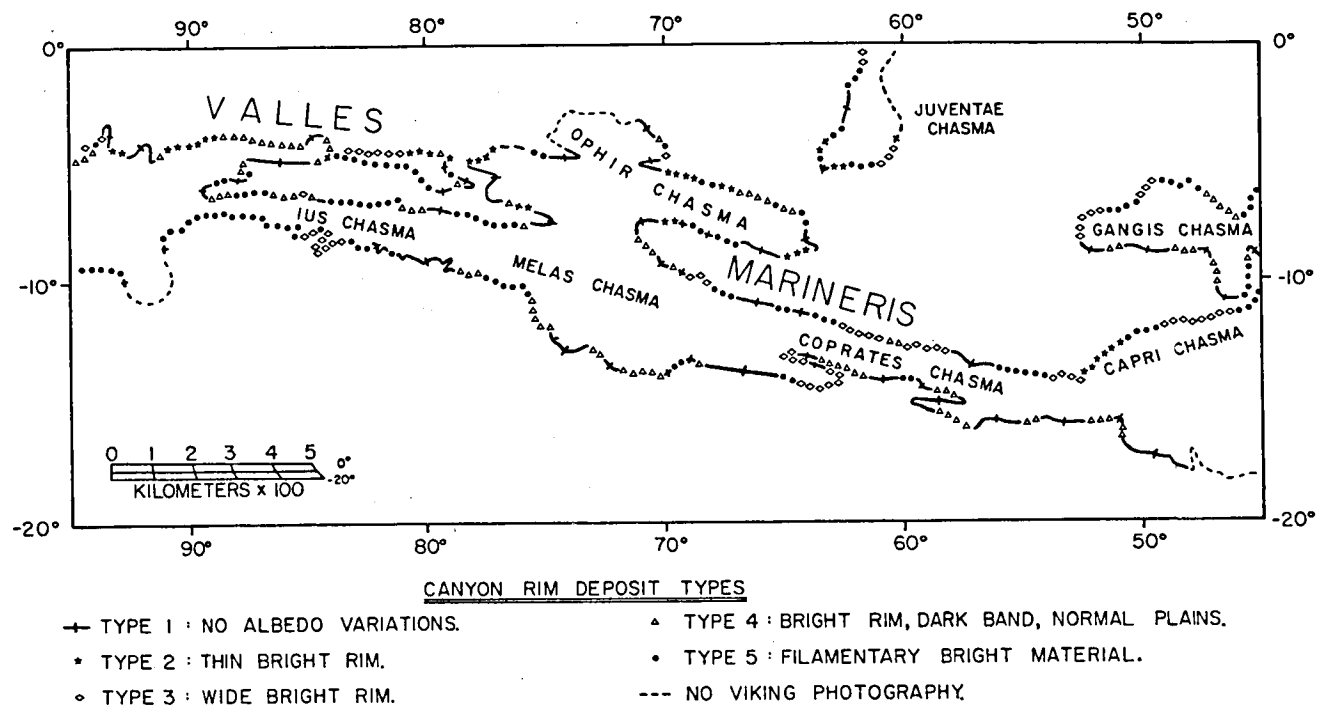
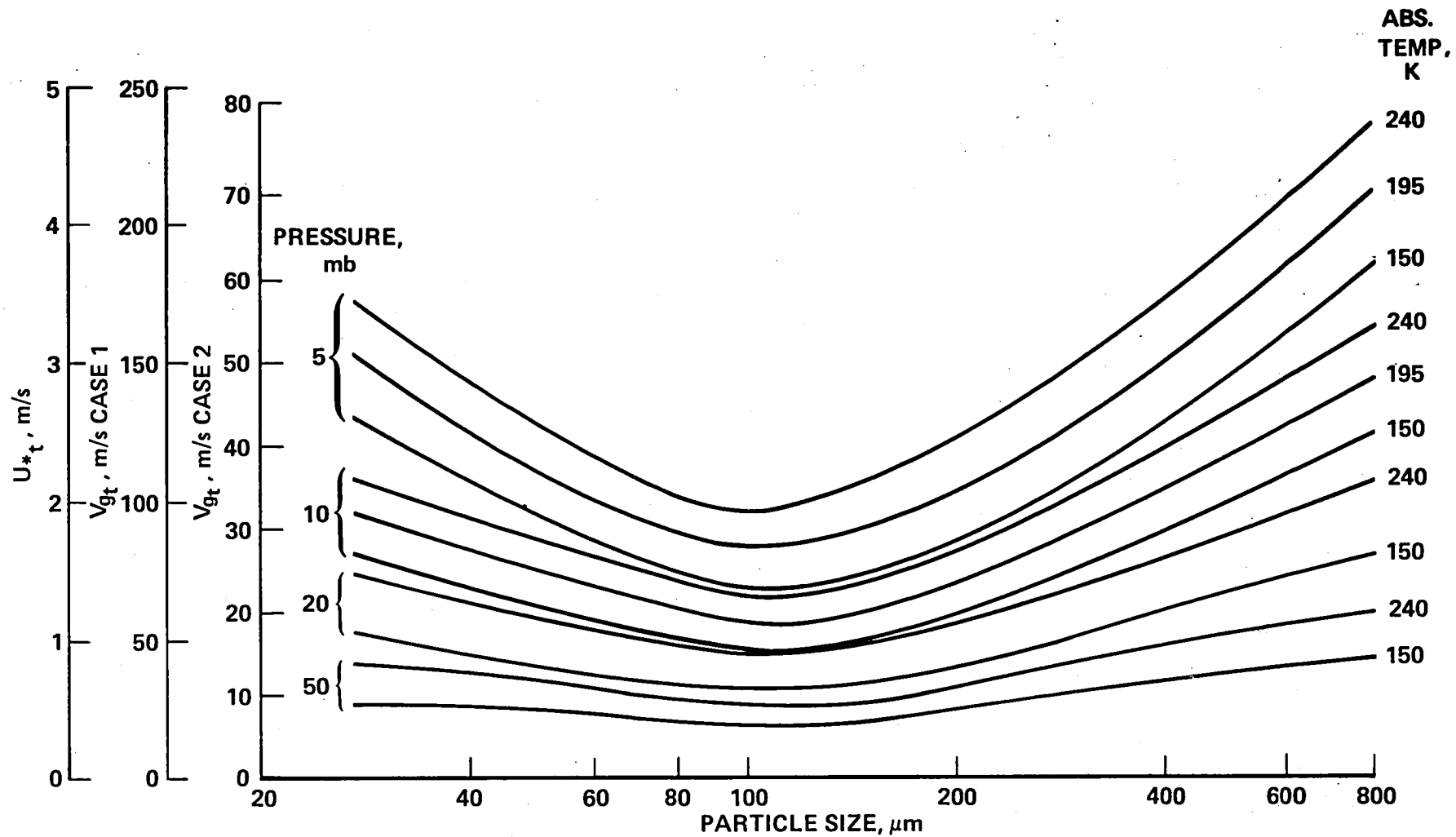


Fig. 2: Spatial distribution of rim deposits sampled at 512 localities spaced 25 km apart along the canyon rim crest.

THRESHOLD WINDSPEEDS FOR SAND ON MARS: WIND TUNNEL SIMULATIONS

Greeley, Ronald, Center for Meteorite Studies, Arizona State University, Tempe, AZ 85281; Rodman N. Leach, University of Santa Clara and NASA-Ames Research Center, Moffett Field, CA 94035; Bruce R. White, Department of Mechanical Engineering, University of California at Davis, Davis, CA 95616; James D. Iversen, Department of Aerospace Engineering, Iowa State University, Ames, IA 50011; and James B. Pollack, Space Sciences Division, NASA-Ames Research Center, Moffett Field, CA 94035

A great deal of attention has been given to the problem of windblown particles on Mars, beginning with a paper by Sagan and Pollack (1969). Most investigations have involved estimations of wind speeds needed to initiate movement of particles of different sizes and densities based on the work of Bagnold (1941). Extrapolations were made to Mars by substituting the appropriate parameter values for Mars in the equations derived by Bagnold for Earth (Sagan and Pollack, 1969, Arvidson, 1972, Iversen *et al.*, 1973, and others). Some studies (Chang *et al.*, 1968, Adlon *et al.*, 1969) incorporated data from laboratory simulations of some of the conditions on Mars. An extrapolation taking inter-particle force into account, more appropriate for martian pressures, was obtained by Iversen *et al.* (1976). To provide better simulations, an open circuit wind tunnel (MARSWIT) was constructed at NASA-Ames Research Center (the facility is described in Greeley *et al.*, 1977). Experiments yielded estimates of wind friction speeds for particle movement on Mars in which nearly all the important parameters were physically simulated or otherwise taken into account. Two of the most important parameters for martian simulations are gravity and the atmospheric conditions at the surface. For simulations of Mars on Earth the primary effect of gravity may be accounted for partly by using proportionately lower density particles than those expected on Mars. The atmosphere is more difficult to simulate. Although MARSWIT is capable of operating down to about 3 mb pressure, the experiments presented by Greeley *et al.* (1976, 1977) were run not in a CO₂ atmosphere, but rather in 'Earth' air. Extrapolations were made to the martian atmospheric composition by taking into account the differences in molecular weight between CO₂ and 'Earth' air. However, because the dynamics of CO₂ at low pressures and at the relatively low Reynold numbers involved with the martian aeolian environment are so poorly understood, these extrapolations were open to question. Consequently, MARSWIT was modified to enable experiments to be run in a 95 percent CO₂ atmosphere. The experiments described earlier (Greeley *et al.*, 1976) were duplicated in the CO₂ atmosphere and wind friction threshold speeds (u_{*t}) for saltation were determined. The relationship between friction speed (u_*) and free-stream velocity (u_∞) was extended to the critical case for Mars of momentum thickness Reynolds numbers (Re_θ) between 425 and 2000. It was determined that the dynamic pressure required to initiate saltation is nearly constant for pressures between 1 bar (Earth) and 4 mb (Mars) for atmospheres of both air and CO₂; however, the threshold friction speed (u_{*t}) is about 10 times higher at low pressures than on Earth. For example, the u_{*t} (Earth) for particles 210 μm in diameter is 0.22 m s^{-1} and the u_{*t} (Mars, 5 mb, 200 K) is 2.2 m s^{-1} . These values agree with the Viking meteorology recordings of sustained wind speeds of 18 m s^{-1} and gusts of up to 28 m s^{-1} (Ryan *et al.*, 1978), and speculations on particle movement (Sagan *et al.*, 1977, Jones *et al.*, 1979).



Particle threshold curves as a function of particle size for martian surface pressures and higher, and for representative martian temperatures. Case 1 scale is free stream velocity (above boundary layer) for winds blowing over a flat surface of erodible grains; Case 2 surface containing cobbles and small boulders.

EFFECT OF INTERPARTICLE FORCE AND REYNOLDS NUMBER ON WIND THRESHOLD SPEED

J. D. Iversen, Iowa State University, Ames, Iowa 50011, B. R. White, Univ. California at Davis, Davis, CA 95616, R. Greeley, Center for Meteorite Studies, Arizona State Univ., Tempe, AZ 85281, R. Leach, NASA Ames Research Center, Moffett Field, CA 94035, J. B. Pollack, NASA Ames Research Center, Moffett Field, CA 94035

Data collected from the MARSWIT low-atmospheric-density wind tunnel have been used to determine new and improved expressions for the threshold friction speed of wind-blown particles.

Estimates of threshold speed on Mars and Venus were presented in Ref. 1. These estimates were based primarily on data taken at atmospheric pressure (Ref. 2), except for 4 points available from Ref. 3. Since then, the MARSWIT facility has been completed and a great deal of data at low atmospheric pressure has been compiled (Refs. 4 & 5).

The data from the MARSWIT facility used to determine the new friction speed correlation covers the following ranges of values:

Particle Diameter - 37 to 673 microns
Particle Density - 1100 and 2650 kg/m³
Atmospheric Density - 0.006 to 1.22 kg/m³
Gas Composition - air and carbon dioxide

The effect of Reynolds number was eliminated by cross-plotting data at constant values of Reynolds number $B = u_{*t} D_p / \nu$. The effect of

interparticle force was then determined by multiple regression analysis of the resulting data. The effect of interparticle force can then be eliminated from the original data and the curve shown in Fig. 1 results. This curve displays the dimensionless threshold friction speed $u_{*t} (\rho/\rho_p g_p)^{1/3}$ as a function of the Reynolds number B as it

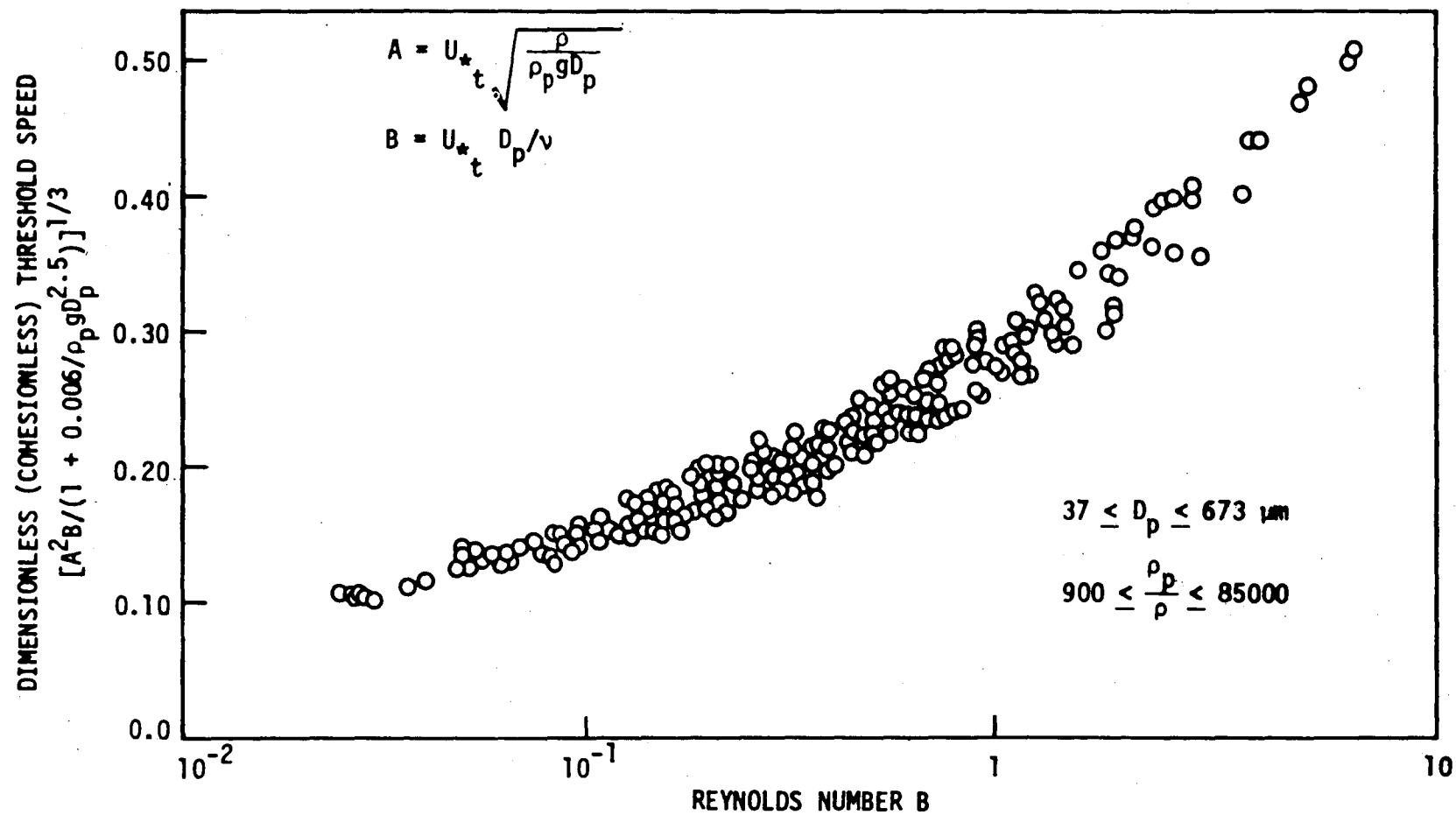
would appear if the interparticle forces of cohesion were absent. That the data fairly well coalesce to a single curve illustrates the accuracy of the interparticle force function.

Expressions for the dimensionless friction speed $A = u_{*t} / (\rho_p g_p D_p / \rho)^{1/2}$

as a function of Reynolds number B and interparticle force derived from the curve of Fig. 1 can be used to determine threshold speed accurately for large ranges of particle densities and diameters and for a variety of atmospheric conditions.

References:

1. J. D. Iversen, R. Greeley, J. B. Pollack 1976. Windblown Dust on Earth, Mars, and Venus. J. Atmospheric Sciences, 33, 2425-2429.
2. J. D. Iversen, J. B. Pollack, R. Greeley, B. R. White 1976. Saltation Threshold on Mars: The Effect of Interparticle Force, Surface Roughness, and Low Atmospheric Density. Icarus, 29, 381-393.
3. R. K. Weinberger, G. L. Adlon 1971. Particle dislodgement and entrainment by low density airstream flowing over a surface. NASA CR 111924.
4. R. Greeley, B. R. White, R. Leach, J. D. Iversen, J. B. Pollack, 1976. Mars: Wind friction speeds for particle movement. Geophysical Research Letters, 3, 417-420.
5. R. Greeley, R. Leach, B. R. White, J. D. Iversen, J. B. Pollack, 1979. Threshold windspeeds for sand on Mars: Wind tunnel simulations. To be published.



PITTED AND FLUTED ROCKS - VIKING COMPARISONS

*McCauley, John F., *Breed, Carol S., *Grolier, Maurice J.,
+Whitney, Marion I., and X*Ward, A. Wesley, *U.S. Geological
Survey, Flagstaff, Arizona 86001, +Central Michigan
University, Mount Pleasant, Michigan 48859, XGeology Depart-
ment, Arizona State University, Tempe, Arizona 85281

The pitted and fluted rocks of the Western Desert of Egypt described in previous reports (refs. 1, 2, 3, 4) bear a striking resemblance to the pitted and fluted rocks seen by the Viking Landers. Although much has been written on wind-faceted stones such as dreikanter, descriptions of pitted and fluted rocks in desert regions are scarce. Sharp (5) provides one of the most complete accounts of wind-produced pitting, fluting, and grooving of Pleistocene ventifacts east of the Big Horn Mountains, Wyoming. These ventifacts are lithologically diverse, and are composed of chert, quartz, quartzite, quartzitic sandstone, gneiss, hornfels, pegmatite, diabase, and many varieties of granite. They were eroded by northwesterly winds similar in direction to present-day areal winds. The erosion observed was ascribed to sand blasting, but the possibility that finer material caught in small vortices might have aided in the wind cutting process was considered. The multiple faces on these ventifacts were explained by shifting of the stones with time, because of strong evidence that the wind has blown consistently from one direction in this area since Pleistocene time.

Higgins (6) described small, faceted Late Pleistocene ventifacts from Ocean Cove, California. He recognized that fine abrasives in suspension are probably important in wind erosion and that scour by suspended particles can be almost as effective on the leeward side as on the windward side of a ventifact. Thus, shifting of a rock with time is not necessary to explain leeward erosion.

Whitney and Dietrich (7) show from field and experimental studies that suspended dust is an important factor in ventifact sculpture. As a consequence of this work, the definition of a ventifact is expanded from a stone or pebble that has been faceted, cut, shaped or worn by sandblast action to include "any rock or mineral fragment which has been shaped, worn, or polished by wind-promoted activities." They also point out that many of the fine erosional structures seen on ventifacts are too small or too fragile to have been produced by sandblast action. Experimental evidence indicates that all rock surfaces can be eroded simultaneously, but at different rates, when subjected to prolonged impingement by directed airstreams. Another suggestion by Whitney and Dietrich, which may have application to

the pitted and fluted rocks from the Western Desert of Egypt and to the Viking Lander rocks, is that slower winds carrying only dust particles may account for more overall erosion than the less frequent winds of sand-moving strength.

Whitney (8) emphasizes the importance of vorticity and the role of positive, negative, and secondary flow in the production of small wind erosion features such as pits, flutes, and grooves. Negative (reverse flow in the upwind direction) and secondary flow (transverse to either the positive or negative flow) in the lee of a ventifact results in erosion by dust-laden air in close contact with the rock surface. Negative and secondary flow also controls the distribution of small vortices that form normal to the surface and produce circular erosion pits. In general, the more irregular the shape of the rock the more the negative and secondary flow and the greater the degree of erosion. We think the highly irregular, pitted and fluted rocks previously described from Egypt represent an important but neglected type of ventifact. Some solution has probably occurred on these sandstone and quartzite ventifacts, primarily during the many periods of semi-aridity that punctuate the history of the region, but these effects are miniscule and cannot explain the complex surface textures observed.

To test the hypothesis that the pitted and fluted rocks of the Western Desert are ventifacts formed by northerly winds and that sand blasting is not necessarily the process by which they formed, we conducted a series of wind tunnel simulation studies on oriented specimens at Arizona State University (2). Visualization of air flow below the saltation velocity of sand was provided by a bubble generating device produced by Sage Action Inc., Ithaca, New York. At tunnel velocities of about 1 to 2 meters per second, the 2 to 3 mm bubbles simulate (in a general way) the behavior of atmospheric dust as it moves over and around a ventifact.

Air flow separation and negative flow was observed behind rock faces inclined from 35° to 50° to windward. Secondary flow was also observed. Vorticity normal to specimen faces occurred in the lees and on the sides of most of the irregular and apparently non-streamlined rocks. Bubbles impacted on the windward faces, or were pulled from the separated air flow behind the specimen and then moved in a reverse direction. Some of these bubbles moving in the reverse direction hovered behind, or spiralled into pits, flutes, and irregular erosional concavities on the lee surfaces of the specimens. When the specimens are aligned with the air flow as they were collected in the field, bubble motions can be related to the overall erosional pattern on each rock. In other orientations

the bubble pattern became disorganized, lost contact with the specimen, and had no relation to the surface morphology. From these experiments we conclude: 1) that the pits and flutes on all sides of these rocks can be explained by winds blowing predominantly from the north and 2) that abrasion by dust and silt, carried by everyday winds at velocities less than the threshold velocity for sand, is probably responsible for most of the erosional patterns observed.

The view of the martian surfaces obtained by the Viking Landers show a variety of pitted and fluted rocks, much like those from the Western Desert of Egypt. Figure 1a is a view of a typical pitted quartzite boulder from the Western Desert of Egypt and Figure 1b shows "sponge rock" at the Viking 1 site. The similarities are obvious, even to the presence of a deflational moat in the loose sediments on the upwind sides of both specimens. Viking investigators have commented that the pits in the martian rocks are larger and more widespread than those from any known terrestrial localities, but have generally interpreted these features as vesicles only slightly modified by wind erosion. We think that the Egyptian data, the work of Whitney and Dietrich, and our wind tunnel experiments indicate that most of the rocks and boulders at both landing sites are ventifacts, and that the overall degree of wind erosion on the surface of Mars has not been fully appreciated. Recognition of the Viking rocks as ventifacts cut by windblown dust alleviates many of the problems concerning active wind erosion on Mars raised by the fact that saltation velocity was not recorded by the Viking Landers. In our interpretation, saltation is not necessary for wind erosion to occur. Low wind velocities and the dust entrained in the Martian atmosphere are sufficient to account for all of the erosion features seen.

References:

- 1) McCauley, J. F., Breed, C. S., Grolier, M. J., and El-Baz, Farouk, Pitted rocks and other ventifacts in the Western Desert of Egypt, NASA TM 80339, 286-287.
- 2) McCauley, J. F., Breed, C. S., Grolier, M. J., Whitney, M. I., Ward, A. W., and Greeley, Ronald, Wind tunnel simulation studies of airflow patterns around pitted and fluted ventifacts from the Western Desert of Egypt, NASA TM 80339, 288-289, 1979.
- 3) El-Baz, Farouk, Haynes, Vance, Boullos, Loutfi, Issawi, Bahey, McHugh, William, Maxwell, T. A., McCauley, J. F., Breed, C. S., Embabi, N. S., Grolier, M. J., El-Etr, Hassan, Dardeer, A., Dowidar, H., Imbrahim, M., Ramadan, A., and Yousif, M., Journey to the Gilf Kebir and Oweinat, southeast Egypt, 1978, Geographical Journal, in press, 1979.

- 4) McCauley, J. F., Breed, C. S., El-Baz, Farouk, Whitney, M. I., Grolier, M. J., and Ward, A. W., Pitted and fluted rocks in the western desert of Egypt - Viking comparisons, J. Geophys. Res., in press, 1979.
- 5) Sharp, R. P., Pleistocene ventifacts east of the Big Horn Mountains, Wyoming, J. Geol. 57, 175-195, 1949.
- 6) Higgins, C. G., Formation of small ventifacts, J. Geol., 64, 5, 506-516, 1956.
- 7) Whitney, M. J., and Dietrich, R. V., Ventifact sculpture by windblown dust, Geol. Soc. America Bull. 84, 2561-2582, 1973.
- 8) Whitney, M. J., The role of vorticity in developing lineation by wind erosion, Geol. Soc. America Bull. 89, 1-18, 1978.

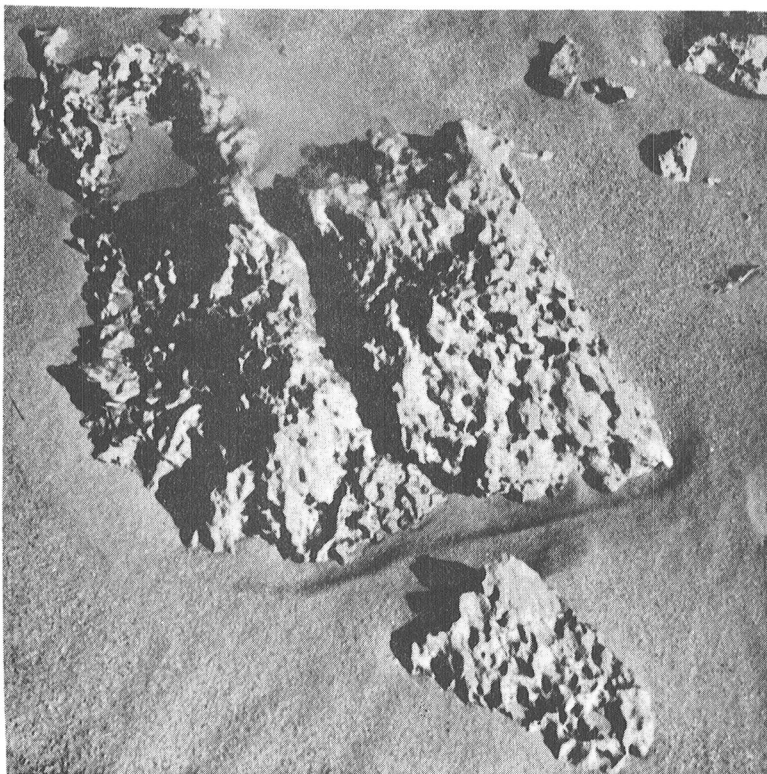


Figure 1a. Pitted and fluted quartzite boulder about 40 cm across from top of Gilf Kebir plateau in southwestern Egypt.

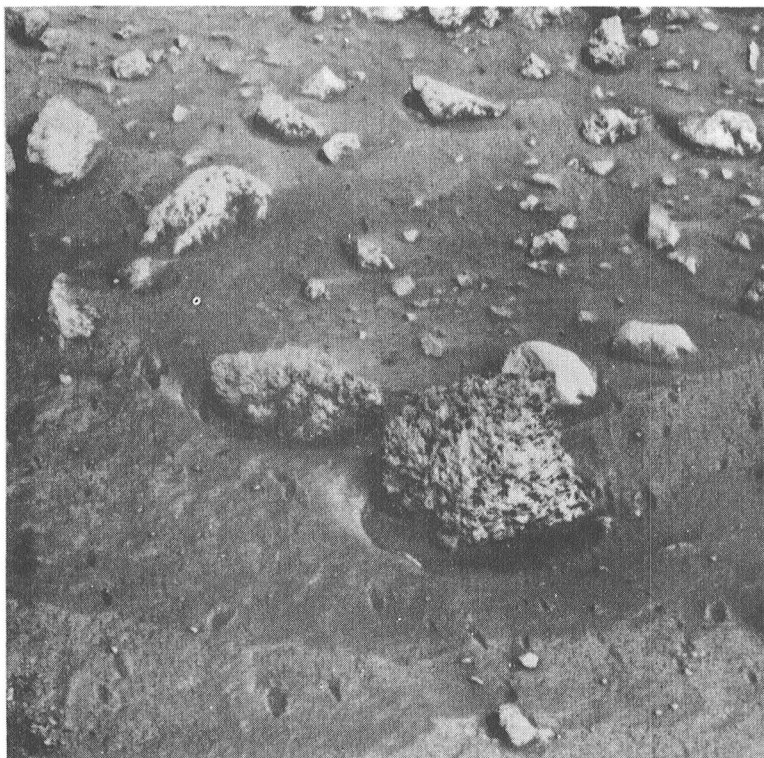


Figure 2b. "Sponge rock" from Viking 1 lander site. Rock is about 20 cm across.

VENTIFACTS: MODELS FOR WIND EROSION ON ANY SCALE

Whitney, Marion I., Central Michigan University, Mount Pleasant,
Michigan 48859

Both field and laboratory studies indicate that ventifacts are eroded by aerodynamic and vorticity processes (Whitney and Dietrich, 1973 and Whitney, 1978 and 1979), as well as by grain impact, and that suspended particles such as dust, silt and ice crystals may act as tools in the interfacial flow lines (Dietrich, 1977a, 1977b and Whitney, 1979). The history of most individual ventifacts can be discerned accurately and relatively simply. It can be shown that they constitute convenient models of wind systems around all sorts of objects both large and small. That is, the aerodynamic concept based on my study of ventifacts provides a universal tool for the understanding of the origins of features eroded by wind, regardless of their scale. In other words, the form of the resultant wind eroded feature reflects, in large measure, the history of development of the feature. For instance, from the distortion on the rim of a vortex pit, it is possible to determine the dominant wind direction involved in shaping the pit--the score and rays associated with the pit denote the direction of turning of the gyre.

Examples include the following: the origin of a triquetrous ventifact can be extended to apply to the origin of a yardang. The origin of wind eroded flutes on ventifacts may help elucidate history of the origin of a flute on a Martian canyon wall.

Much of our original analysis was based on several hundred wind sculptured, former beach pebbles that occur sporadically around Lake Michigan where the typical original pebble forms are well known and where every gradation in form from unmodified beach pebbles to highly modified triquetrous ventifacts may be found. To supplement these observations, we have conducted eighteen years of diverse laboratory research in which flow patterns around various shapes have been examined and the results of prolonged wind blast and dust blast tests have been investigated. Also by studying ventifacts from many additional localities--including such regions as Wind River, Wyoming; Garnet Ridge, California; Egypt; and both valley and mountain ridge localities in Antarctica--our analyses have been expanded even further.

Analyses of ventifacts formed in a two, three or four wind direction system are possible. Where one wind direction is highly dominant, as in parts of Egypt, assessment of ventifact history can be quite simple. Where ventifacts are more complicated, as in parts of Antarctica where they have undergone reorientation by ice action, the task is more difficult--for example, there may be evidence of an original shaping direction that is in marked contrast to that of later wind-sculpturing

directions. Nonetheless, in nearly all cases assessment of the history of ventifact formation is possible. This is true because under aerodynamic influence, erosional features typically develop in sets and consequently there are sets of undercut facets, flutes, pits, keels and other features belonging to both the older and the more recent ventifact-to-wind orientations.

Illustrations that demonstrate how the shape of an object influences the dispersal of wind flow around it and thus, its sculptural patterns will be shown. Ventifacts from several regions--such as Michigan, California, Egypt and Antarctica--will be compared and contrasted in order to illustrate diverse degrees of complexity.

References:

- Dietrich, R. V. 1977a, Impact abrasion of harder by softer materials: *Journal of Geology*, v. 85, p. 242-246.
- _____. 1977b, Wind erosion by snow: *Journal of Glaciology*, v. 18, no. 78, p. 148-149.
- McCauley, J. F.; M. J. Grolier and C. S. Breed, 1977, Yardangs of Peru and other desert regions: The United States Geological Survey Interagency Report: Astrogeology 81, p. 1-177.
- _____. ; C. S. Breed; M. J. Grolier; M. I. Whitney; A. W. Ward; R. Greeley, 1979, Wind tunnel simulation studies of airflow patterns around pitted and fluted ventifacts from the western desert of Egypt: Reports of Planetary Geology Program 1978-1979, NASA Technical Memorandum 80339, p. 388.
- _____. ; C. S. Breed; F. El Baz; M. I. Whitney; M. J. Grolier; A. W. Ward: in press, Pitted and fluted rocks in the western desert of Egypt--Viking comparisons: *Journal of Geophysical Research Special Issue Mars Colloquium*.
- Whitney, Marion I., 1978, The role of vorticity in developing lineation by wind erosion: *Geological Society of America Bulletin*, v. 89, p. 1-18.
- _____. 1979a, Electron micrography of mineral surfaces subject to wind blast erosion: *Geological Society of America Bulletin*, Pt. I, v. 90, 917-934.
- _____. 1977b, Aerodynamic and vorticity erosion of Mars: Part I, The formation of channels: *Geological Society of America Bulletin*, Pt. I, v. 90, p. 1111-1127, in press.
- _____. 1977c, Aerodynamic and vorticity erosion of Mars: Part II, Vortex features, related systems, and some possible global patterns of erosion: *Geological Society of America Bulletin*, Pt. I, v. 90, p. 1128-1143, in press.
- _____. and R. V. Dietrich, 1973, Ventifact sculpture by windblown dust: *Geological Society of America Bulletin*, v. 84, p. 2361-2582.

STUDIES OF THE COATINGS ON SAND GRAINS FROM THE GILF KEBIR, SOUTHWEST EGYPT

Donna J. Prestel and John E. Wainwright, Lockheed Electronics Co., Inc./ Johnson Space Center, Houston, TX 77058 and Farouk El-Baz, NASM Smithsonian Institution, Washington, D.C. 20560

INTRODUCTION

Field investigations have established that the red color of desert sand is due to the presence of iron-oxide coatings on individual grains (Van Houten 1973, Folk 1976, Walker 1967). True color earth-orbital photographs of the Egyptian desert show distinct variations in desert color. Sand grains become redder as the distance from their source increases. Based on color, El-Baz (1978) recognized three relative-age zones which do not correspond to boundaries of geological formations. We have initiated an investigation of sands from the Egyptian desert to determine what minerals are contributing to the color, and whether the observed geographic variations in color are due to varying thicknesses and mineralogy of the coatings on individual sand grains.

MINERALOGY & MORPHOLOGY OF THE COATINGS

The sand grains examined were collected from a dune in Wadi Bahkt, a valley in the southeast corner of the Southern Gilf Kebir plateau in the Egyptian desert. This region is included in El-Baz's zone 3, the area displaying the darkest color. Heavily-coated quartz sand grains and those with coatings concentrated in pits or cracks were chosen for X-ray powder diffraction study using the Gandolfi camera. The coating was gently scraped from many individual grains in order to concentrate sufficient material for analysis. Hematite and kaolinite (7Å clay mineral) were identified in the scrapings. Diffraction lines from kaolinite suggest a well-crystallized material. In contrast, hematite displayed diffuse lines inferring poor crystallinity and very fine grain size. Additional grains were fractured under liquid freon to expose the interior of the grains and a cross section of the coating. The grains were examined by SEM at magnifications from 100X-200,000X. Energy dispersive x-ray analysis (EDXA) was used to qualitatively determine the chemistry of the coating and attached crystals. EDXA indicates that the coating is much richer in Al than Fe. This suggests that the coating is predominantly a clay material with very finely disseminated hematite.

All of the grains studied had an irregular, pitted surface with a ubiquitous coating of fine-grained material. The coating has a well-defined contact with the underlying quartz surface (Fig. 1) and conforms closely to grain morphology. Its thickness varies from 0.5 μm to 4.5 μm over the surface of a single grain. The coating exhibits a complex morphology and is composed of randomly-oriented particles ranging in size from a few hundred angstroms to about 2 micrometers. Many of the particles are hexagonal platelets (Fig. 2). Individual platelets have a

grainy surface, with small platelets occurring on the surfaces of the larger plates. This may indicate that books of platelets are formed as the result of in-situ growth of small platelets on larger, preexisting ones. Additionally, we have observed incipient growth of coating crystals on a quartz grain surface (Fig. 1). The coating shows no evidence of successive layers of deposition over most of the surface area of the grain. No systematic changes in morphology (crystal size or orientation), mineralogy, or chemistry were observed. However, in a few pitted regions, some preferred orientation of platelets in response to grain morphology was seen. Twisted platelets and oriented platelets occur within pits and in areas surrounding pits. Recognized abrasion features include extensive grooving, cracking, and degrading of the coating, and polishing of protruding ridges on the grains. Additionally, secondary crystals of gypsum and halite, and small areas plastered with silica were noted.

DISCUSSION

The occurrence of small platelets on the surfaces of larger platelets, and the growth of coating crystals directly on the quartz grain surface are consistent with in-situ nucleation and growth processes. The lack of layering also suggests gradual growth on a preexisting coating. These features imply that nucleation and in-situ growth processes are the predominant mechanisms for coating formation, rather than a mechanical plastering of clay particles on the quartz substrate.

We propose to examine grains from El-Baz's other color zones and the parent rock (Nubian sandstone) from Egypt to determine where and how the coating originates. We are seeking microscopic evidence relevant to the hypothesis that the coating develops during aeolian transport. We have compared the mineralogy of the coating to desert varnish. Work by Potter and Rossman (1977, 1979) on desert varnish indicates that clay minerals (montmorillonite and mixed-layer illite) comprise more than 70% of the varnish, and are necessary for varnish formation. They also note that both clays and Mn and Fe oxides are always found in varnish. The importance of clay and Fe oxides in varnish is in accordance with our results on sand grain coatings. However, Potter and Rossman have observed no crystallinity in their varnish materials (Rossman 1979, pers. comm.). The reason for this difference is as yet unresolved; however, it likely results from different conditions of formation. For example, in extremely arid environments the coating on desert sands may develop by slow growth which allows crystal development, while the desert varnish studied by Potter and Rossman develops in a more humid environment at the soil-water interface involving successive rewetting episodes and a complex chemical environment. Therefore, the processes involved may not be directly comparable.

The study of the mineralogy and morphology of these coatings is necessary to evaluate their effect on the spectral characteristics of deserts as observed in satellite photographs. Results discussed here

may have significant implications to the signatures of planetary regoliths obtained by spectral reflectance measurements. In fact, the fine dust on Mars could coat grain surfaces and might be thick enough to strongly affect the observed spectral characteristics.

References

- El-Baz, F. (1978) The Meaning of Desert Color in Earth Orbital Photographs, *Photogramm. Eng. Rem. Sens.*, 44:1, 69-75.
- Folk, R.L. (1976) Reddening of Desert Sands: Simpson Desert, N.T., Australia, *Jour. Sed. Petrol.*, 46, p. 604-615.
- Potter, R.M. and G.R. Rossman (1977) Desert Varnish: The Importance of Clay Minerals, *Science*, 196, p. 1446-1448.
- Potter, R.M. and G.R. Rossman (1979) The Manganese-and Iron-oxide Mineralogy of Desert Varnish, *Chem. Geology*, 25, p. 79-94.
- Van Houten, F.B. (1973) Origin of Red Beds: A review, *Ann. Rev. of Earth & Planetary Sci.*, 1, p. 39-61.
- Walker, T.R. (1967) Formation of Red Beds in Modern and Ancient Deserts, *Geol. Soc. Amer. Bull.*, 78, p. 353-368.

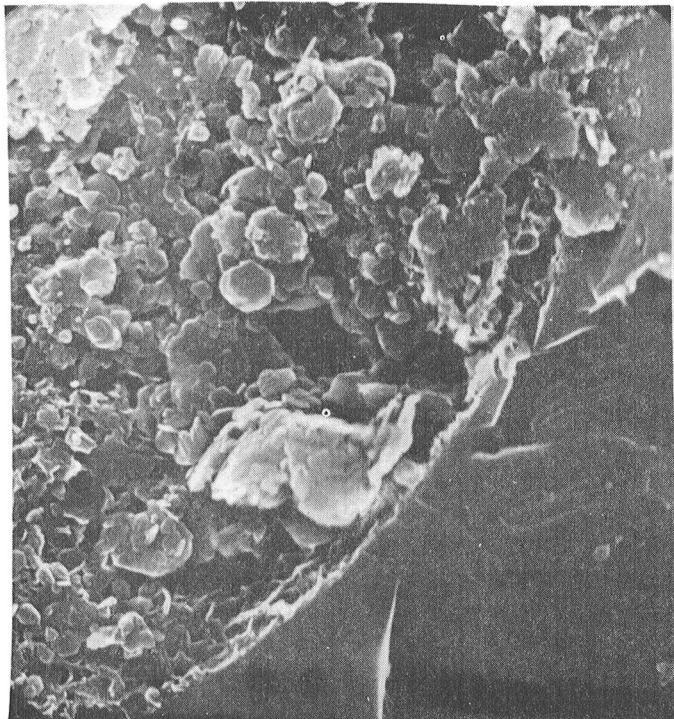


Figure 1. Coating crystals growing along the contact with the quartz grain surface. At 10,000X, width of field of view is 9 micrometers.



Figure 2. At 30,000X, Randomly-oriented books of hexagonal platelets. Width of field of view is 3 micrometers.

MARS: SIMULATION OF SURFACE WIND ABRASION

Greeley, Ronald and Steven H. Williams, Department of Geology, Arizona State University, Tempe, Arizona 85281

Prior to Viking results, wind erosion on Mars was thought to be very effective and to occur at a high rate (1). Although the Viking landers represent only two sites on the planet, and the total time of observation since landing is very short geologically, it would appear that wind abrasion is not as effective as once conceived (2,3).

The strategy for accurately determining the rate of aeolian abrasion is as follows. The three primary parameters are:

- 1) The susceptibility to abrasion of various rock materials and other substances under simulated martian conditions.
- 2) The flux of saltating particles under martian wind conditions.
- 3) The frequency of occurrence of saltation strength winds on Mars.

The latter parameter can be estimated from Viking meteorological observations; the saltation flux can be estimated by wind tunnel studies, Earth observations and numerical analyses (4); and the susceptibility of different rocks and minerals to abrasion can be determined in the laboratory. Abrasion measurements from a first-generation erosion machine (RAMED) have been previously reported (Fig. 1; ref. 5). However, subsequent high speed motion pictures of RAMED have revealed that some of the impacting material is prevented from striking the target by other impactors. This effect would yield a value for the susceptibility to abrasion that is too low. An abrasion machine that avoids this problem was developed at the Argonne National Laboratory to study metal wear. The blocking of impactors is greatly reduced by slinging the impactors from a rotating arm at stationary targets (Fig. 2), rather than have a moving target intersect a sand stream, as in RAMED. Some modifications were made to the Argonne design to facilitate abrasion study, and the Martian Rotating Erosion Device (MRED) was fabricated. It has the capability of abrading targets at pressures ranging from <1 mb to atmospheric and at any impact angle with impact velocities ranging from <5 to 120 meters per second. Preliminary runs on basalt (Fig. 1) show that the MRED results are compatible with the trial runs at Argonne, both of which yield a slightly higher value for the susceptibility to abrasion than RAMED did. Future tests will be conducted to determine the susceptibility to abrasion for a variety of materials under these variable conditions.

REFERENCES:

1. Sagan, C. (1973), *JGR*, 78, 4155-4161.
2. McCauley, J. F. (1973), *JGR*, 78, 4123-4137.
3. Arvidson, R. et al. (1979), *Nature*, 278, 533-535.
4. White, B. (1970), *JGR*, 84, 4643-4651.
5. Greeley, R. and Williams, S. H. (1979), *Lunar & Planetary Sci. Conf.* X, 461-463.

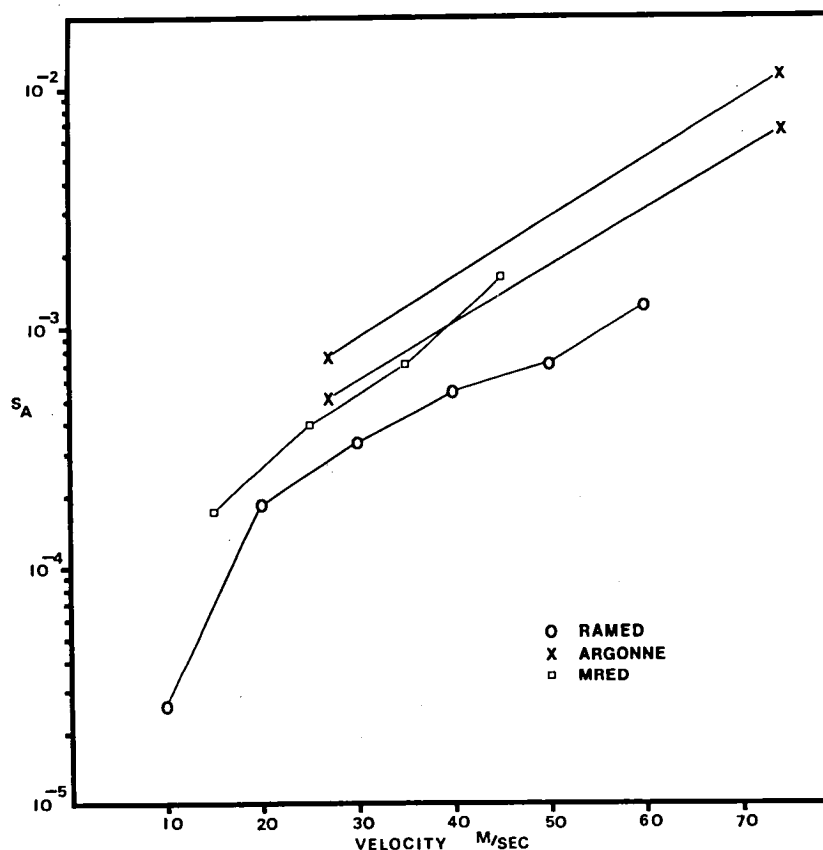


Figure 1: Susceptibility to abrasion (S_A) for Basalt.

This graph compares values from different abrasion machines for the susceptibility to abrasion of basalt. All runs were done at approximately martian pressure (1-10 mb) on similar but not identical basalt samples. Quartz sand (125-175 micron diameter) was used as the impacting material. All impacts were normal to the target. The units for susceptibility to abrasion are mass lost from target (g) divided by mass of impactors striking target (g).

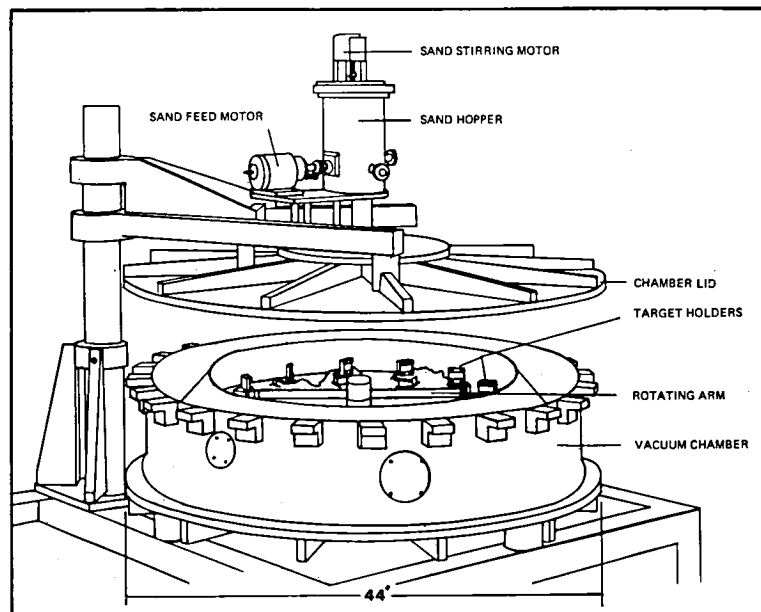


Figure 2: MRED (Martian Rotating Erosion Device)

Sand feeds from a hopper through the vacuum chamber lid into the hub of the rotating arm. It travels down the hollow arm, from which it is slung at a target sample. Steel wool in the bottom of the chamber traps sand after impact.

Krinsley, D.H., Fillers, T. and Patera, E. Dept. of Geology, Arizona State University, Tempe, AZ 85281

Viking photographs show evidence of vast aeolian action on Mars including dune fields and dune forms. However, it has been suggested that the high velocity winds which presumably exist on Mars will cause the destruction of sand sized particles, leaving only silt and clay (Sagan, 1977; Krinsley and Leach, 1979; see also Toon et al., 1977; Toulmin et al., 1977; Baird et al., 1976; Huck et al., 1977). In order to account for the presence of aeolian features on Mars, which involves saltation of sand sized particles (Cutts and Smith, 1973), Greeley (1979) postulated that sand sized agglomerates of small particles form, held together via electrostatics. Krinsley et al. (1979) describe laboratory experiments in which olivine aggregates were formed at various velocities and list some of their properties.

In a further series of experiments, olivine aggregates were created as described in Krinsley, et al. (1979) at 8, 20, 30 and 40 m sec⁻¹. After removal from the abrasion device (Krinsley, Greeley and Pollack, in press), the material was aggitated in a sonic sifter for 5 minutes to create the maximum number of aggregates; this was done because material taken directly from the abrasion device contains few aggregates and these are weak and easily disintegrate. This aggitation is similar to what would occur in nature, for as winds of high velocity decrease in intensity, gentle motion will produce numerous aggregates and strengthen them.

Size frequency studies were made of the material produced in the abrasion device after the aggregates had been manually crushed and destroyed. The percentage of aggregates to remaining material, the axes lengths of the largest and smallest aggregates, shape, internal structure, relative strength and the ratio of sand sized particles to clay (ommitting aggregates) was made at each of the velocities indicated above, after sifting. In addition, mosaics across aggregates (with the scanning electron microscope [SEM]) were made at low magnification to study orientation and packing.

No aggregates were produced at velocities of 8 m sec⁻¹, while aggregates comprised only 1% of the total amount of material at 20 m sec⁻¹; however, 25% at 30 m sec⁻¹ and 50% of the material at 40 m sec⁻¹ consisted of aggregates. At 8 m sec⁻¹ hardly any of the abraded material was less than 37 μm in diameter, at 20 m sec⁻¹, 18%, at 30 m sec⁻¹, 63%, and finally at 40 m sec⁻¹, 73% was less than 37 μm. Thus the production of silt and clay and the destruction of sand sized olivine appears to parallel the increased production of aggregates with increasing wind velocity.

Smaller aggregates which have a lower size of about 300 μm tend to be spherical, and are produced over the entire range of velocities. The maximum aggregate diameter increases with increasing velocity to about 620 μm at 40 m sec⁻¹; the larger sizes tend to be egg shaped, are layered and are stronger than the smaller forms. With increasing velocity, all aggregates tend to become stronger and more stable, but there obviously is some limiting velocity at which breakdown occurs.

Photographs taken with the SEM demonstrate that the olivine aggregates are composed of flat, elongated particles, about 10 to 50 μ m in diameter in a matrix of very fine silt to clay sized particles. Occasionally, large particles of silt (>50 μ m) are observed oriented irregularly in the larger aggregates; frequently large cracks appear around them. Most of the larger particles are observed with their flat faces parallel and in some cases overlapping. Aggregates lose their charge after a few months at earth pressures and temperatures; films of water are absorbed from the atmosphere and probably substitute for electrostatic charges, holding the aggregates together.

Strong wind should produce violent breakage of sand sized particles on Mars, reducing the material to silt and clay. Simultaneously, aggregates will form and disintegrate, reaching various steady states at given velocities. As winds of high velocity decrease in intensity, aggregate formation should increase and should reach figures of at least 25% of the total material, depending on a number of factors, such as the distribution of mineralogy in the initial sand-silt-clay source, the density of the cloud, the velocity and fetch of the wind, etc. Since the charge on clay particles probably lasts for long periods of time on Mars due to the low temperatures and pressures on that planet, weak wind gusts and/or updrafts, if above threshold velocity for movement of fine particles, would tend to create additional aggregates. Since aggritation increases strength, with time aggregates will acquire increased cohesion and will be more likely to form eolian structures. It appears that the type of wind action which occurs in nature on Mars is just what would be expected to produce the maximum aggregate number and strength.

References:

- Baird, A. K., Toulmin, P., III, Clark, B. C., Rose, H. J., Keil, K., Christian, R. P., and Gooding, J. L. (1976) *Science* 194, 1288-1293.
- Greeley, R. (1979) *J. Geophys. Res.*, in press.
- Huck, F. O., Arvidson, R., Jobson, B., Park, S., Patterson, W., and Wall, S. (1977) *J. Geophys. Res.* 82, 4401-4411.
- Krinsley, D. H. and Leach, R. (1979) *Repts. Planet. Geol. Program*, 1978-1979, NASA TM 80339, 311-312.
- Krinsley, D. H., Leach, R., Greeley, R. and McKee, T. R. (1979) *Repts. Planet. Geol. Program*, 1978-1979, NASA TM 80339, 313-315.
- Krinsley, D. H., Greeley, R. and Pollack, J. (1979) *Icarus*, in press.
- Sagan, C., Pieri, D., Fox, P., Arvidson, R. E. and Guinness, E. A. (1977) *J. Geophys. Res.* 82, 4430-4438.
- Toon, O. B., Pollack, J. B. and Sagan, C. (1977) *Icarus* 30, 663-696.
- Toulmin, P., III, Clark, B. C., Baird, A. K., Keil, K., and Rose, H. J. (1976) *Science* 194, 81-83.

INVENTORY OF WIND-FORMED FEATURES ON MARS: AN EOLIAN ATLAS

Breed, Carol S., Ward, A. Wesley, McCauley, John F., and Witbeck,
Nanci, U.S. Geological Survey, Flagstaff, Arizona 86001

An inventory of wind-formed features on Mars, utilizing data from Earth-based telescopes and from the Mariner 9 and Viking images is in progress, in preparation of an Eolian Atlas of Mars. The regional distribution of yardangs, grooved and fluted terrain, deflation pits, dark streaks, light streaks, dunes, and "sand" sheets will be shown on geomorphic maps utilizing the U.S.G.S. 1:250,000 mosaics as a base. Key images that illustrate types of eolian features on Mars will be accompanied by full-page captions that will summarize the interpretations of these features by various investigators. Possible analogs of martian features in terrestrial deserts will be presented in a separate section. The early history of investigations of eolian processes and landforms on Mars will be described in an introductory chapter. Subsequent chapters will synthesize results from Mariner 9 and Viking. The summary chapter will include an assessment of the role of the wind as a geologic agent on Mars. The Atlas will also include a comprehensive bibliography.

References:

- Arvidson, R. E., 1972, Aeolian processes on Mars: erosive velocities, settling velocities, and yellow clouds: Geological Society of America Bulletin 83, p. 1503-1508.
- Baum, W. A., Martin, L. J., Briggs, G. A., and Barnes, J., 1979, A review of martian dust clouds and storms: U.S. National Aeronautics and Space Administration Conference Publication 2072, p. 6.
- Breed, C. S., 1977, Terrestrial analogs of the Hellespontus Dunes, Mars: Icarus, v. 30, p. 326-340.
- Breed, C. S., Grolier, M. J., and McCauley, J. F., 1979, Morphology and distribution of common "sand" dunes on Mars: comparison with Earth: Journal of Geophysical Research (in press).
- Breed, C. S., McCauley, J. F., Grolier, M. J., and Witbeck, N., 1979, Eolian depositional features in the Western Desert of Egypt: comparison with Mars: U.S. National Aeronautics and Space Administration TM 80339, p. 382-385.
- Breed, C. S., Ward, A. W., and McCauley, J. F., 1978, Windform patterns on Earth and Mars: implications for similarities of eolian processes on two planets: U.S. National Aeronautics and Space Administration TM 79729, p. 228-229.
- Cutts, J. A., Blasius, K. R., Briggs, G. A., Carr, M. H., Greeley, R., and Masursky, H., 1976, North polar region of Mars: imaging results from Viking 2: Science, v. 194, no. 4271, p. 1329-1337.

- Cutts, J. A., and Smith, R. S. U., 1973, Eolian deposits and dunes on Mars: *Journal of Geophysical Research*, v. 78, no. 20, p. 4139-4154.
- El-Baz, F., Breed, C. S., Grolier, M. J., and McCauley, J. F., 1979, Eolian features in the Western Desert of Egypt and some applications to Mars: *Journal of Geophysical Research* (in press).
- Greeley, R., Iversen, J. D., Pollack, J. B., Udovich, N., and White, B., 1974, Wind tunnel studies of Martian aeolian processes: *Royal Society of London Proceedings*, v. 341, p. 331-360.
- Greeley, R., Papson, R., and Veverka, J., 1977, Crater streaks in the Chryse Planitia region of Mars: early Viking results: U.S. National Aeronautics and Space Administration TM X-3511, p. 157-158.
- Greeley, R., White, B., Pollack, J. B., Iversen, J. D., and Leach, R. N., 1977, Dust storms on Mars: Considerations and simulations: U.S. National Aeronautics and Space Administration TM 78423, 29 p.
- Grolier, M. J., McCauley, J. F., Breed, C. S., and El-Baz, F., 1979, Yardangs of the Western Desert of Egypt: U.S. National Aeronautics and Space Administration TM 80339.
- Grolier, M. J., Ward, A. W., and McCauley, J. F., 1976, Wind trends in Peru and on Mars, in *Reports of Accomplishments of Planetology Programs, 1975-1976*: U.S. National Aeronautics and Space Administration, TM X-3364, p. 115-116.
- McCauley, J. F., 1973, Mariner 9 evidence for wind erosion in the equatorial and mid-latitude regions of Mars: *Journal of Geophysical Research*, v. 78; no. 20, p. 4123-4137.
- McCauley, J. F., Breed, C. S., Grolier, M. J., and Collins, P. S., 1979, The eolian features of the north polar region of Mars: *International Colloquium on Mars, 2nd Abs.* Pasadena, CA, Jan. 1979: U.S. National Aeronautics and Space Administration Conference Publication 2072, p. 55.
- McCauley, J. F., Breed, C. S., Grolier, M. J., and MacKinnon, D. A., 1980, The U.S. dust storm of February 23-25, 1977: *Geological Society of America Memoir*, T. Péwé, ed., (in press).
- McCauley, J. F., El-Baz, F., Grolier, M. J., Breed, C. S., Whitney, M. I., Ward, A. W., and Greeley, R., 1979, Pitted and fluted rocks in the Western Desert of Egypt - Viking comparisons: *Journal of Geophysical Research* (in press).
- McCauley, J. F., Grolier, M. J., and Breed, C. S., 1977, Yardangs: *Annual Geomorphology Symposium, 8th*, Binghamton, New York, Proceedings, Morisawa, M., ed., p. 233-269.
- McCauley, J. F., Grolier, M. J., and Breed, C. S., 1977, Yardangs of Peru and other desert regions: U.S. Geological Survey Interagency Report, Astrogeology 81, 176 p.

- Peterfreund, A. R., 1978, Dust storms on Mars: visual and thermal observations from Viking: U.S. National Aeronautics and Space Administration TM 78,455, p. 37-39.
- Sagan, Carl, 1973, Sandstorms and eolian erosion on Mars: *Journal of Geophysical Research*, v. 78, no. 20, p. 4155-4161.
- Sagan, Carl, and Bagnold, R. A., 1975, Fluid transport on Earth and aeolian transport on Mars: *Icarus*, v. 26, p. 209-218.
- Sagan, Carl, Veverka, J., Fox, P., Dubisch, R., French, R., Gierasch, P., Quam, L., Lederberg, J., Levinthal, E., Tucker, R., Eross, B., and Pollack, J. B., 1973, Variable features on Mars II, Mariner 9 global results: *Journal of Geophysical Research*, v. 78, no. 20, p. 4163-4196.
- Thomas, P., 1979, Seasonal and secular behavior of crater-related streaks on Mars: a study of Mariner 9 and Viking Orbiter data: U.S. National Aeronautics and Space Administration, Conference Publication 2072, p. 82.
- Thomas, P., and Veverka, J., 1979, Seasonal and secular variations of wind streaks on Mars: U.S. National Aeronautics and Space Administration TM 80339, p. 302-303.
- Toon, O. B., 1979, History of the Martian climate: U.S. National Aeronautics and Space Administration, Conference Publication 2072, p. 84.
- Veverka, J., 1975, Variable features on Mars 5, evidence for crater streaks produced by wind erosion: *Icarus*, v. 25, no. 4, p. 591-605.
- Veverka, J., Goguen, J., and Cook, K., 1977, A statistical study of ragged dark streaks in the Southern Hemisphere of Mars: U.S. National Aeronautics and Space Administration TM X-3511, p. 156.
- Veverka, J., Thomas, P., and Bloom, A., 1978, Classification of Martian wind streaks: U.S. National Aeronautics and Space Administration TM 78,455, p. 46-47.
- Veverka, J., Thomas, P., and Sagan, Carl, 1977, On the nature and visibility of crater associated streaks on Mars: U.S. National Aeronautics and Space Administration TM X-3511, p. 155.
- Ward, A. W., 1978, Windforms and wind trends on Mars: an evaluation of martian surficial geology from Mariner 9 and Viking spacecraft television images: Ph.D. thesis, University of Washington, Seattle, Washington, 201 p.
- Ward, A. W., 1979, Yardangs on Mars, evidence for recent wind erosion: *Journal of Geophysical Research*, (in press).
- Ward, A. W., McCauley, J. F., and Grolier, M. J., 1979, The yardangs at Rogers Playa, California: U.S. National Aeronautics and Space Administration TM 79729, p. 209-210.

EOLIAN FEATURES OF THE NORTH POLAR REGION ON MARS: COMPARISON WITH EARTH

Breed, Carol S., McCauley, John F., and Grolier, Maurice J.,
U.S. Geological Survey, Flagstaff, Arizona 86001

Massed crescentic ridges are the most common dunes on Mars; they are similar in plan to dunes that are typical of many desert basin ergs and dune fields on Earth. This correspondence implies that the dynamics of dune formation are similar on the two planets, despite martian constraints on dune formation that include much higher velocity winds required to move "sand" in saltation, the possible inhibition of "sand" movement by adsorbed water vapor, the seasonal "snow" cover in the north circumpolar erg, and a probably sparse "sand" supply. Scale ratios derived from measurements of martian dunes are almost identical to scale ratios for much smaller gypsum dunes at White Sands, New Mexico (fig. 1). Isolated, scattered barchan dunes along the southern margin of the north circumpolar erg may indicate a diminished sand supply or deflation of parts of the region by high-speed winds. A complex dune formed by the apparent collision of barchans suggests that dunes of different sizes on Mars, as on Earth, migrate at different rates (fig. 2). The present activity of the martian dunes, however, is not known and they must be at least seasonally inactive.

Uniform dune patterns in areas of "sand" accumulation on Mars, as on Earth, reflect the long-term adjustment of eolian bedforms to wind regimes, sand supply, and topographic variations. Boundary ridges of sand delineate many topographically controlled dune fields and ergs on Mars, as on Earth. Complex akle patterns on both planets probably reflect locally complex wind regimes. Possible wind erosion grooves and the apparent superposition of some dune patterns in the north circumpolar erg may record changes in the martian eolian regime. Preservation of these features implies considerable cohesion of the dune sands.

Large through-going longitudinal dune belts, common on Earth, are not seen on Mars. Both the absence of such "sand-passing" dunes, and the restriction of "sand-trapping," massive crescentic dunes to a few sites, suggest that much of the available "sand" has been removed from the martian plains. Mars may have a long eolian history in which much of the "sand" suitable for saltation has already been transported to the north polar erg and crater-floor dune fields. On Earth, the formation of "mature" ergs is estimated to require 2×10^6 years or more. By analogy, the massive dunes on Mars probably required as much or more time to accumulate. The age of their formation is not known; it may extend to periods when climatic conditions were possibly more Earth-like than at present.

References:

- Breed, C. S., Grolier, M. J., and McCauley, J. F., 1979, Morphology and distribution of common "sand" dunes on Mars: comparison with Earth: *Journal of Geophysical Research* (in press).
- Breed, C. S., McCauley, J. F., Grolier, M. J., and Witbeck, N., 1979, Eolian depositional features in the Western Desert of Egypt: comparison with Mars: U.S. National Aeronautics and Space Administration TM 80339, p. 382-385.
- Grolier, M.J., Breed, W. J., McCauley, J. F., and Breed, C. S., 1979, Eolian processes in the polar regions, Earth and Mars: Colloquium on Planetary Water and Polar Processes, 2nd, Hanover, New Hampshire, Proceedings, October 1978, p. 203-204.
- McCauley, J. F., Breed, C. S., Grolier, M. J., and Collins, P. S., 1979, The eolian features of the north polar region of Mars: International Colloquium on Mars, 2nd, Abs., Pasadena, CA, Jan. 1979: U.S. National Aeronautics and Space Administration Conference Publication 2072, p. 55.

Figure captions:

1. Massed crescentic dune ridges: a) at latitude 72°N, longitude 53° in the north circumpolar erg on Mars, and b) at White Sands, New Mexico show a close correspondence of pattern elements. Ratios of measured dune segment widths, lengths, and wavelength are identical for both dune fields, although the martian dunes at this locality are about five times larger than those at White Sands (Breed et al., in press).
2. Barchan dunes in collision: a) at latitude 73°N, longitude 39°50' on Mars, and b) in the Sechura Desert, Peru. The larger segment of the martian dune at (A) is about 500 m wide and 200 m long. The larger segment of the Peruvian dune (B) is about 100 m wide and 50 m long (Breed et al., in press).

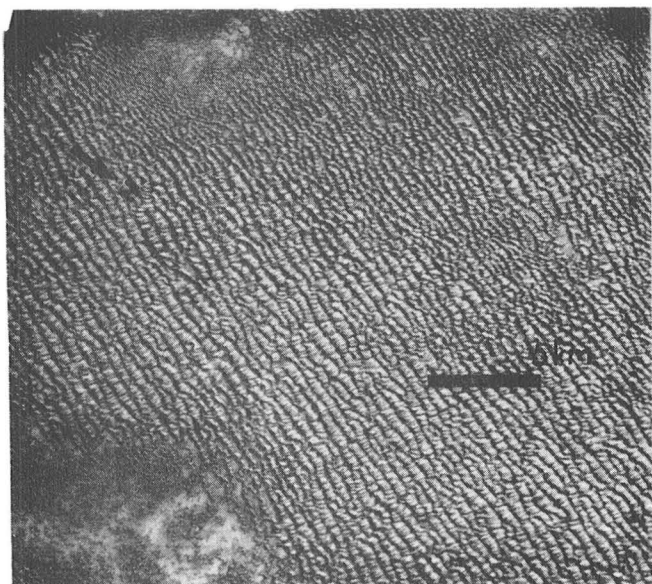


Figure 1a

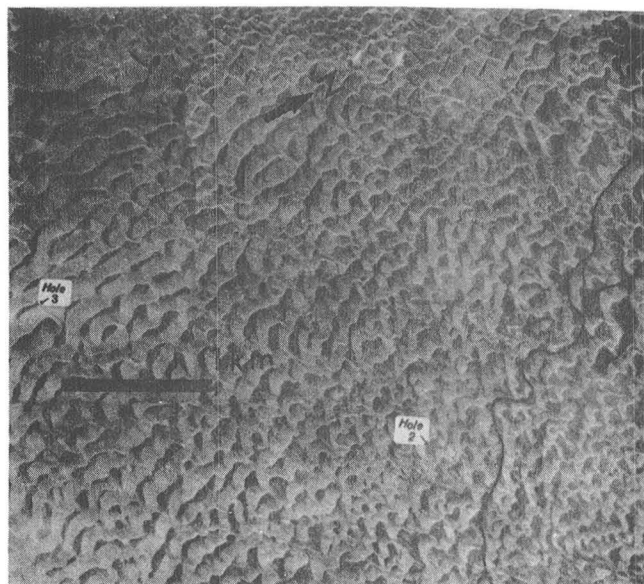


Figure 1b

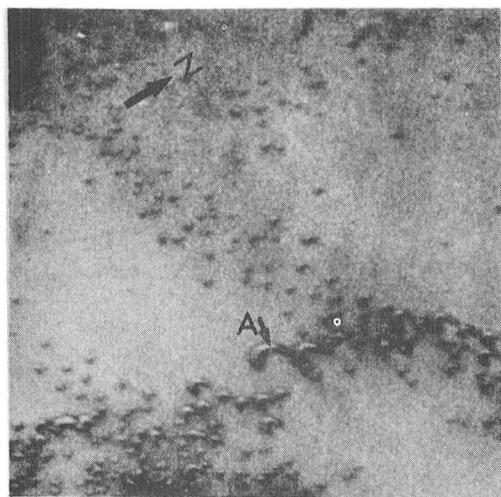


Figure 2a

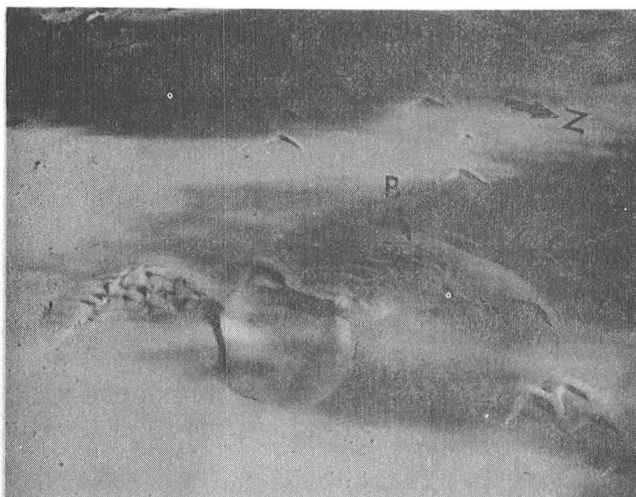


Figure 2b

"ZIG-ZAG" DUNES ON MARS AND EARTH

Smith, Roger S. U., Geology Department, University of Houston,
Houston, Texas 77004

"Zig-zag" transverse dunes are common in the north-polar dune fields on Mars but uncommon on Earth and easily mistaken for barchan dunes at the scale of orbital imagery. If these martian dunes behave like their terrestrial counterparts, they may be diagnostic of a regime of mostly diametrically-opposed winds balanced roughly in intensity over a year's time. Thus winds blowing towards the north pole of Mars may locally balance those blowing away from the pole and any viable model of martian meteorology must account for this reversal.

"Zig-zag" dunes differ from barchans in that: 1) their plan is angular rather than rounded; 2) they are made of nearly-straight, parallel-sided segments, unlike the tapering horns of barchans; 3) the junction angle between segments is acute and individual forms are connected laterally into transverse features, unlike the en echelon arrangement typical of barchans; and 4) individual segments are roughly symmetrical in cross section, at least on Earth.

The best terrestrial example of "zig-zag" dunes yet found is in northern Death Valley, California, a NW-trending graben 2000 meters below confining mountains. Most of the dunes are 2-4m tall and made of segments about 25m wide by 50-250m long joined at angles of 60-90°, but some are single triangular pyramids. These dunes adjoin a field of NE-trending transverse dunes and incipient star dunes, where Clements et al (1963) documented seasonal reversal of form and migration from NW to SE and little net annual movement. The martian "zig-zag" dunes are similar to these "zig-zag" dunes in proportions but tend to join at sharper angles and be several times larger in plan view.

Reference Cited

Clements, Thomas, Mann, J.F., Jr., Stone, R.O., and Eymann, J.L., 1963,
A study of windblown sand and dust in desert areas: U.S. Army
Natick Labs., Earth Sci. Div., Tech. Rep. ES-8, 61p.

MAINTENANCE OF BARCHAN SIZE IN THE SOUTHERN ALGODONES DUNE CHAIN,
IMPERIAL COUNTY, CALIFORNIA

Smith, Roger S.U., Geology Department, University of Houston, Houston,
Texas, 77004

Barchans may maintain steady size because of fixed sand supply and not because of any characteristic wind conditions. Within the southern Algodones dune chain, barchans maintain steady size despite large fluctuations in the intensity and duration of the winds that blow along their axes. During two intervals, June 1968 through May 1978 and January 1976 to January 1978, most dunes were the same height at the end of each interval as at the beginning and growing dunes roughly offset shrinking dunes. Winds recorded at the junction of the All American and Coachella canals, 8km west of the dunes, were generally much weaker and less persistent during 1976-7 than during the 1968-78 interval. Velocity and persistence over different intervals can be compared by using a characteristic shear velocity $U_{*c} = \frac{(\sum U_*^3)^{1/3}}{n}$, where U_* is shear velocity measured hourly and n is number of hours. U_* is herein computed from velocity exceeding 500cm/sec at 400cm height by assuming that upwind roughness is controlled by 1cm pebbles and that wind is measured within a fully-developed turbulent layer above this surface; little sand moves across the surface upwind (W&NW) of the instrument to complicate velocity profiles. For winds aligned with the dunes (W&NW) during 1963-78, $U_{*c} = 41.5$ cm/sec and $n = 467$ hrs/yr; these are strongest and most persistent during April ($U_{*c} = 47.2$ cm/sec and $n = 95$ hrs/mo), weakest during July ($U_{*c} = 32.0$ cm/sec) and least frequent during August ($n = 7$ hrs/mo). During June 1968-May 1978, $U_{*c} = 44.7$ cm/sec and $n = 427$ hrs/yr, but during January 1976-January 1978, $U_{*c} = 32.8$ cm/sec and $n = 245$ hrs/yr. For comparison, calculations by Bagnold's (1941) methods suggest that impact and fluid threshold shear velocities for the dune sand are 19.1 and 23.0cm/sec, respectively, and that shear velocities above 33.4cm/sec represent "strong" winds capable of moving sand across a surface of 1cm pebbles. These data suggest that barchans, once established, maintain steady height both under conditions of a balance between "strong" and "gentle" winds (1976-7) as well as under predominant "strong" winds (1968-78).

Barchan shrinkage during January 1978 to January 1979 was pronounced and was probably caused by sand storage on the interdune floor behind small plants that sprouted following frequent heavy rains during the 1977-8 winter and spring season. Winds were unusually light and infrequent during 1978 ($U_{*c} = 34.4$ cm/sec, $n = 210$ hrs/yr), but dunes maintained steady size during the 1976-7 years of comparable conditions. If a constant volume of sand is available within the dune field and some of it is stored on interdune flats, then each dune must shed sand and shrink until the interdune sand cover thickens to equilibrate with wind

conditions. As annual plants shrivel and release the sand trapped behind them, the dunes should grow to their former sizes unless unusually-heavy rainfall causes new plants to sprout. Average or unusually-intense or persistent winds during and following plant sprouting would probably minimize sand buildup between the dunes, and dunes would probably shrink less under these conditions than under 1978 conditions.

Reference Cited

Bagnold, R.A., 1941, The physics of blown sand and desert dunes:
London: Methuen, 265p.

TOPOGRAPHICALLY CONTROLLED DUNE SYSTEMS ON EARTH AND MARS

Mc Cauley, Camilla K. and William J. Breed, Museum of Northern Arizona, Flagstaff, Az., 86001

Viking Orbiter pictures have revealed numerous topographically controlled dune fields as well as depositional streaks that lie downwind from craters on Mars (Fig. 1). Many of these streaks emanate from intra-crater dune deposits and probably represent climbing dunes.

An instrumented field study is being conducted on the dynamics of climbing dunes and the influence of topography on mobile through-going sand systems along the western end of the Painted Desert in northern Arizona. Climbing, falling, barchan and dome dunes are all well represented here and occur in a wide variety of topographically controlled environments.

This is one of the most windswept regions in the southwestern United States due to the upwind topographic effects of the San Francisco Peaks and surrounding volcanic cinder cones. Sediments are blown onto terraces northeast of the Little Colorado River by the prevailing southwesterly winds and form numerous fields of barchan dunes. Within this area, active and inactive dunes up to 10 meters in height have accumulated at the base of, around, and on top of a 60 meter high escarpment that extends along the margin of the Painted Desert. The actively migrating dunes lose their distinctive barchanoid forms as they near the base of the escarpment. There they form climbing dunes and ridges that funnel up a series of former watercourses to surmount nearly vertical cliffs. Trailing sand sheets from the climbing dunes supply sand for the formation of transverse, falling and dome dunes on top of the escarpment. Sand grains comprising these dunes have climbed 165 meters over a distance of 15 km from their source in the Little Colorado River floodplain.

Topography plays an important role on through-going sand systems. Strong local funnelling effects occur in this area which in turn have caused local increases in wind velocity of as much as 50% as measured in the field. Resulting air-borne sand plumes and gravitational cascades combine to form the morphology of climbing dunes and sand ridges on the escarpment periphery.

This area has been subjected to multiple periods of dune formation of unknown age and to episodic sweeping away of eolian deposits during periods of fluvial activity. Archeologic evidence such as datable artifacts found among the dune sands and interbedded volcanic cinders in the dunes may provide some ideas of the rates and intensity of pluvial and eolian cycles within this region.

Recent investigations of selected sites within the area have included long term, in situ field measurements of annual and seasonal wind regimes at various elevations above the sand surface, both below and on top of the scarp. Three wind recording systems were installed at various locations within the dune field. Two of the systems record wind velocity and direction at variable heights up to 10 meters above the surface. This instrumentation permits simultaneous comparison of the local wind regime at various locations and elevations.

In addition to monitoring the wind regime, sand samples from more than 100 sites within the dune field have been analyzed to determine the relationship between sand movement and grain size parameters.

The major objective of this study is to quantitatively analyze topographic control of sand accumulation, dune formation and sand migration on sloping surfaces. Such measurements of terrestrial analogs are expected to lead to a better understanding of the relationships between local topography, wind regime and surficial sediment distribution on Mars.

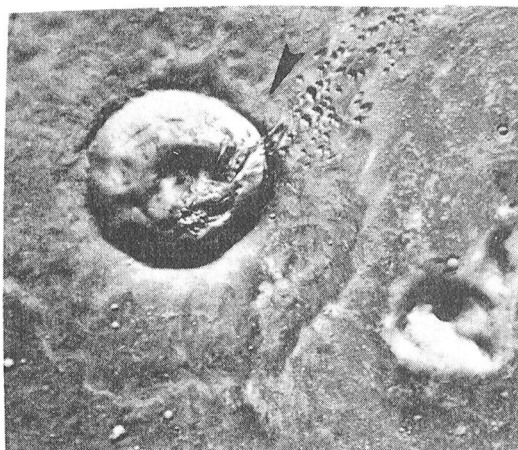


Fig. 1 Barchan dunes approaching a crater on Mars (Viking 2, frame 571B53). The dunes are surmounting the crater rim as climbing dunes and then descend onto the crater floor as falling dunes. Movement is in the direction of the arrow.

DUNES RELATED TO OBSTACLES ON EARTH AND MARS: OBSERVATION AND SIMULATION

Tsoar, Haim and R. Greeley, Department of Geology and Center for Meteorite Studies, Arizona State University, Tempe, Arizona 85281

Most terrestrial dunes occur in the big ergs of Northern Africa and Asia (Wilson, 1973). These ergs are within large flat basins or playas which serve as good potential sources for sand, and are developed independently of fixed surface features (Bagnold, 1954). Terrestrial sand dunes are rarely found in areas of high relief because of the lack of potential sources of sand. Except for the northern plains and some large impact basins (e.g. Hellas), Mars lacks large smooth basins. Many dunes on Mars occur within craters or encounter crater slopes which change the flow patterns of the dunes. Eddies on the lee side of single dunes result from flow separation and play an important role in the evolution of the dune (Tsoar, 1978). Where dunes encounter obstacles, the lee eddies are interrupted and change their magnitude, form, and direction; dunes located in the lee of obstacles are affected by the eddies and gusts generated by the obstacle. Understanding the typical morphology of these dunes is important in the determination of the associated wind directions. Study of dune types (windward and leeward obstacles) is being conducted through simulations in the wind tunnel and through field studies. Preliminary results show that sand and dunes on the windward side of an obstacle can create two distinct features depending on the slope of the obstacle. When the slope angle is less than 35° , the eddies between the dune that is approaching the slope and the slope itself are not strong enough to cause a strong reverse flow. The result will be a destruction of the dune form and a creation of a blanket of sand that covers the slope and moderates its angle. This form is a *climbing dune* found in the deserts of Northern Arizona (Breed *et al.*, in press) and Mojave in California (Evans, 1962) and along coastal cliffs. When the angle of the obstacle is between 40° to 90° , large eddies develop between the dune and cliff which appears to increase the wind velocity in the opposite direction to the general wind flow. The result will be a movement of sand from the slip face of the dune to the brink, deposition over the brink, and preservation of a V-shaped trough between the dune and the cliff. This form is an *echo dune* that cannot climb the slope, but is maintained some distance from it, although in some cases the edges of echo dunes become climbing dunes. When the wind flow encounters the brink line of the echo dune obliquely, a helical vortex causes flow along the axis of the eddy. Figure 1 shows a dune field within a crater in the north polar region of Mars that creates an echo dune, and apparently is a result of eddies between the inside crater slope and the dune slip face. According to the V-shaped trough between the dune front and the crater rim, and to the swelling of the dune brink in the north side we conclude that the prevailing strong winds were from south to southwest, corresponding to the general wind direction found in the area for this time of the year (Tsoar *et al.*, in press). Wind that changes direction and flows to the reverse way, i.e. from the obstacle to the echo dune, will lower the dune brink as a result of reverse flow eddies that carry sand to the V-shaped trough, as seen in the southwestern part of the echo dune in figure 1. When sand is moved to the lee side of an obstacle it creates an elongated dune form that is linked and

evolved from the obstacle slope (figure 2). This form is a *lee dune* and is a result of a slight deflection of the wind in areas where the obstacle rim has a projection into the wind. Although resembling longitudinal (seif) dunes, the lee dune is quite different in formational processes, mechanism of advance, and relation to wind direction.

References

- Bagnold, R. A., 1954, *The Physics of Blown Sand and Desert Dunes*, Methuen, London.
- Breed, C. S., McCauley, J. F., Breed, W. J., McCauley, C. K., and Cotera, A. S., Eolian (wind-formed) landscapes, in: *Landscapes of Arizona - The Geologic Story*, University of Arizona Press, Tucson, in press.
- Evans, J. R., 1962, Falling and climbing sand-dunes in the Cronese ('Cat') Mountain, San Bernardino County, California, *J. Geol.*, 70, 107-113.
- Tsoar, H., 1978, *The dynamics of longitudinal dunes*, final technical report, Eur. Res. Office, U.S. Army, London.
- Tsoar, H., Greeley, R., and Peterfreund, A. R., Mars: The north polar sand sea and related wind pattern, *J. Geophys. Res.*, in press.
- Wilson, I. G., 1973, Ergs, *Sediment. Geol.*, 10, 77-106.

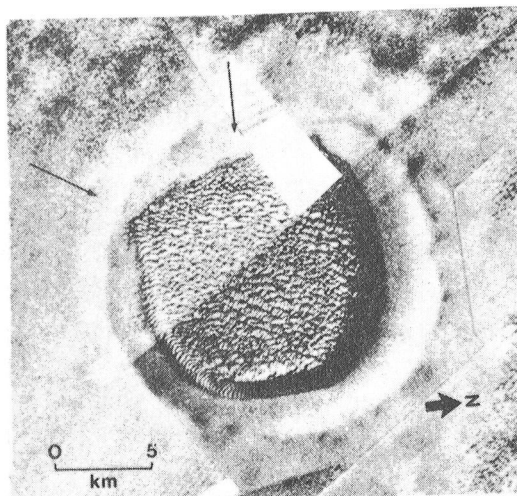


Figure 1. Echo dune within a crater in the north polar region of Mars (71°N, 51°W). Arrows indicate main wind directions (Mosaic of VO frames 487B14, 30 & 32).

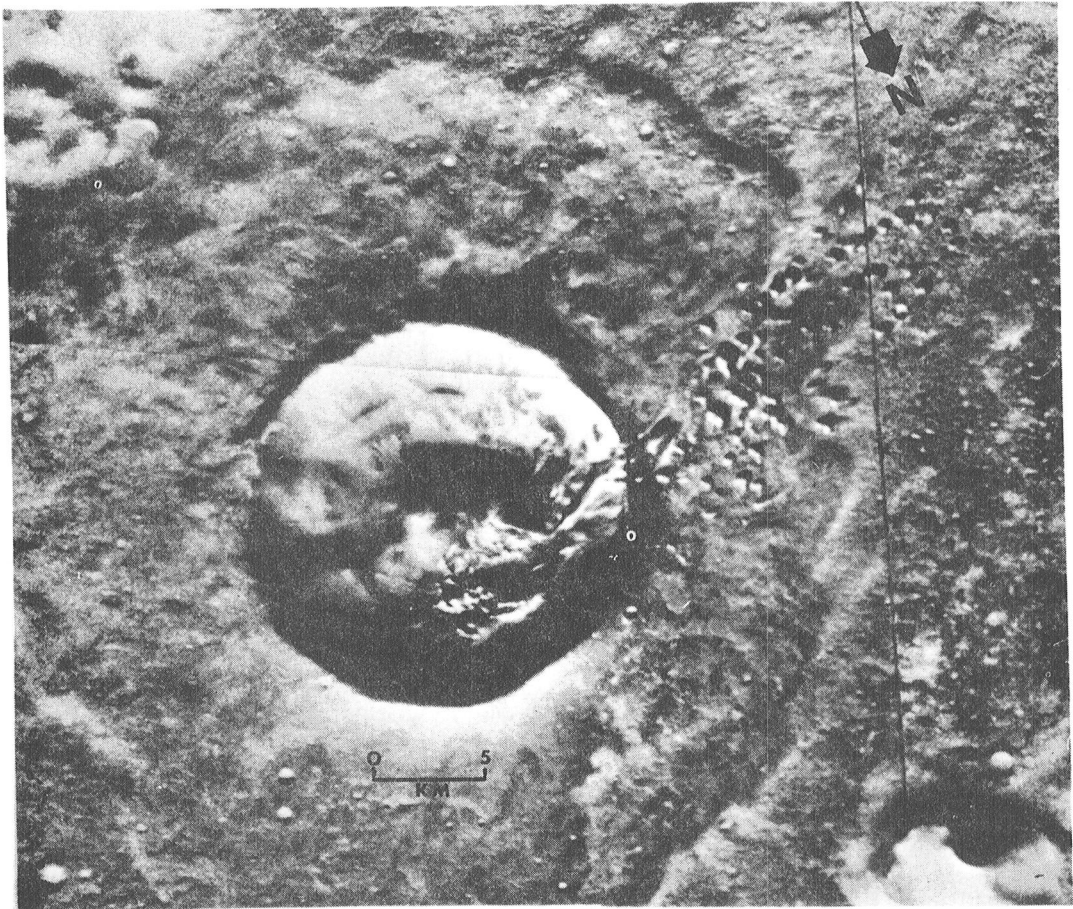


Figure 2. Lee dunes related to a crater rim in the southern hemisphere of Mars (51°S , 9°W). Some of the lee dunes move from the rim inside the crater, others move outside, which indicates two opposite wind directions (ASU mosaic #52).

EXPERIMENTAL MODELING OF EROSIONAL WINDFORMS II

*Ward, A. Wesley, and Greeley, Ronald, Arizona State University, Tempe, AZ 85281 *(Present address, U.S.G.S., Flagstaff, AZ 86001)

This paper presents a discussion of experiments into the evolution of the streamlined form of yardangs. Because yardangs evolve on a greater time scale than can be observed, we turned to theoretical and scale-modeling studies to further our understanding of their genesis. With reasoning from basic physics and a wind tunnel, we conducted a controlled study on the evolution of model yardangs. Our objectives were to detail the reasons, methods, types and sites of activity, evolutionary sequences, and forms of evolving yardangs and to compare these forms with those of natural yardangs.

The theoretical formation of yardangs by wind erosion can be modeled with a few principles from fluid mechanics. A body immersed in a moving fluid will have three ambient flow regions. Upstream (or upflow), where the flow is essentially undisturbed, is the ideal flow region. Near the body, the fluid develops a frictional shear layer called the boundary layer. Separation of the boundary layer from the immersed body creates the third flow region, the wake. The wake is the source of some of the drag on the body. The other component of drag is roughness or skin friction. The sum of these two equals the total drag.

The form of the boundary layer is dependent upon the pressure gradient $\frac{\Delta P}{\Delta X}$. When pressure decreases in the direction of flow (i.e., $\frac{\Delta P}{\Delta X} < 0$), the gradient is said to be favorable, aiding the transport of a particle. Conversely, the gradient is adverse if pressure increases in the direction of flow. By Bernoulli's principle, velocity and pressure vary along an immersed body of variable cross section. The pressure gradient can be completely reversed, which causes separation of the boundary layer. Air particles near the surface will experience a decrease in momentum and come to rest. These will deflect following particles out and away from the surface, which is the actual separation. The following particles will be drawn down to the new pressure gradient, and will reverse their course and begin to move upstream because the pressure gradient locally goes the other way. This reverse flow has also been termed backflow and negative flow (Whitney, 1978).

The shape of the immersed body determines the form of pressure drag and much of the total drag. Elongating and tapering (or streamlining) an initially cylindrical immersed body reduces the pressure drag and also the total drag. However, as a consequence, skin friction drag becomes more critical because the surface area is increased. But, the total drag on an immersed body is at a minimum (and the two drag

components are of equal value) at a thickness/length ratio of approximately 1:4. On such a streamlined form, the flow is ideal completely around the body except for a thin boundary layer and a thin wake.

Because pure wind erosion of natural samples in the wind tunnel requires apparently several hundreds to perhaps thousands of hours before streamlining fully develops, synthetic samples were constructed that duplicated the characteristics of natural yardangs. Samples and scale models were constructed from a mixture of 33% fine and medium silica sand, 33% hominy grits, and 33% moist coffee grounds. Earlier experiments with this type of sample are described in McCauley et al. (1977a) and Ward (1978). These materials could be molded into moderately indurated models with the same micro-roughness as natural samples, yet with loose grains that could be eroded several times faster than natural samples. Models up to 25 cm by 25 cm by 5 cm, with initial shapes including square, rectangular, circular, cylindrical, and pyramidal were individually tested at low velocities (5-10 m/sec) for up to 220 hours.

The dominant types of overall yardang shapes and several morphologic variations were produced. Most models evolve through the sequence of: a) erosion of windward corners, b) erosion of the front slope and upper surface, c) erosion of the downwind upper surface, and d) erosion of the rear flanks.

The region of highest shear stress (highest velocity) is immediately downwind of the nose on a three-dimensional model. Downwind portions of the model are eroded in an upwind direction by inward-rotating currents of reverse airflow. The shape ratios achieved are close to that of an ideal form and similar to those of many yardangs. The evolution of the streamlined form seems to proceed asymptotically with time. Large volume losses are observed early in most experimental runs. Later, as an equilibrated form develops (and changes in width, for example, must be accompanied by changes in length), less material is lost per unit time. The ideal form was not always achieved and actual drag coefficients were probably much higher than in theory because of inhomogenetics, protruberances, and other irregularities in each model.

An important consideration for the genesis of refinement of the overall yardang shape can be made from theoretical modeling. Abrasion (including saltation) and deflation are the dominant processes acting on a yardang. However, contrary to earlier speculation (e.g., McCauley et al., 1977b), abrasion and deflation are most effective at the same places. Where the velocity is greatest, abrading particles will have their highest kinetic energy, but this is also the region of lowest ambient pressure, aiding deflation. Thus, arguments that abrasion dominates over the

upwind portion of yardangs (except for saltation low on the bows) while deflation dominates along the downwind portions, are hard to substantiate. Deflation is most effective at forward, high-velocity sites and downwind abrasion can occur as fine particles are carried into and forward along rear flanks.

References:

- Fox, R. W., and McDonald, A. T., 1973, Fluid mechanics, Wiley, New York, 630 p.
- Hughes, W. F., and Brighton, J. A., 1967, Fluid dynamics, Schaum, New York, 265 p.
- McCauley, J. F., and others, 1977a, Experimental modeling of wind erosion forms, in Reports of Planetary Geology Program, 1967-1977: U.S. National Aeronautics and Space Administration Technical Memorandum X-3511, p. 150-152.
- McCauley, J. F., and others, 1977b, Yardangs: Annual Geomorphology Symposium, 8th, Binghamton, New York, Proceedings, Morisawa, M., ed., p. 233-269.
- Ward, A. W., 1978, Windforms and wind trends on Mars: an evaluation of martian surficial geology from Mariner 9 and Viking spacecraft television images: Ph.D. thesis, University of Washington, Seattle, Washington, 201 p.
- Ward, A. W., (in press) Yardangs on Mars, evidence for recent wind erosion: Journal of Geophysical Research.
- Ward, A. W., and others, 1979a, The yardangs at Rogers Playa, California: U.S. National Aeronautics and Space Administration Technical Memorandum 79729, p. 209-210.
- Ward, A. W., and others, 1979b, Experimental modeling of erosional windforms I: U.S. National Aeronautics and Space Administration Technical Memorandum 80339, p. 326-327.
- Whitney, M. I., 1978, The role of vorticity in developing lineation by wind erosion: Geological Society of American Bulletin 89, p. 1-18.

Chapter 7

**MASS MOVEMENT, FLUVIAL, PERIGLACIAL, AND
OTHER SURFACE PROCESSES AND LANDFORMS**

SURVEY OF MARTIAN FLUVIAL FEATURES

Michael H. Carr, U.S. Geological Survey, Menlo Park, CA 94025

A survey of the distribution of channels on the surface of Mars has been completed. Approximately 7000 frames covering the area between 65°N and 65°S were examined. The frames chosen were the "moderate resolution mapping frames," those taken within 5,000 to 12,000 km of the surface, with resolutions between 125 and 300 meters/pixel. The entire belt was mapped except for the northern part of Amazonis, eastern Elysium Planitia, and part of the belt south of 30°S between 180° and 0° for which moderate resolution mapping frames were not available. Three broad classes of channels were mapped that roughly correspond to the "runoff channels," "fretted channels" and "outflow channels" of Sharp and Malin (1975). Runoff channels are mostly smaller than those of the other two classes, being generally no more than a few tens of kilometers long and less than 2 km wide. They start small, increase in size upstream, and commonly have tributaries. Most are probably not true channels but are more analogous to terrestrial river valleys. Outflow channels start full size either in areas of chaotic terrain or in steeply walled alcoves, and tributaries are rare. They may be very large, as much as 200 km across and 3000 km long. Fretted channels are broad flat-floored valleys with steep walls that commonly intersect features of the surrounding terrain as if the channel had been widened by scarp retreat. Tributaries are relatively common. Fretted channels are transitional with the other two channel types, but runoff and outflow channels can be readily distinguished.

Outflow channels. Outflow channels are almost totally within the old cratered terrain. All sinuous linear features were mapped as channels, and some small percentage (<< 1%) almost certainly are tectonic or volcanic in origin. The small number of channels mapped in the sparsely cratered terrain may be mostly this non-fluvial component. Within the old cratered terrain, the density of channels varies considerably according to location. This variation may partly reflect differences in the character of the old terrain, which can be coarsely divided into two units, (1) an older, intensely cratered, dissected and commonly fractured unit, here called cratered plateau, and (2) a younger, more sparsely cratered plains unit with wrinkle ridges, termed ridged plateau plains (Greeley and Spudis, 1978). The ridged plateau plains are only sparsely dissected and commonly transect channels in the cratered plateau. The simplest explanation of these relations is that most runoff channels formed very early, mostly before deposition of the ridged plateau plains. The part of the old cratered terrain that extends north of the equator between 280°W and 20°W is relatively sparsely channeled, especially between 330° and 20° where the number of channels barely exceeds that of the sparsely cratered plains. Most craters in

this area are surrounded by ridged plateau plains; very little of the cratered plateaus is exposed at the surface other than the crater rims. The scarcity of channels may thus simply reflect the absence of exposure of the oldest component of the density cratered terrain. A similar explanation may hold for the region around Argyre and the part of Memnonia between 140° and 160° in which runoff channels are also relatively scarce. In the more extensive areas of ridged plains within the heavily cratered hemisphere, such as Hesperia Planum, Syrtis Major Planitia, and the floor of Argyre, runoff channels are totally absent. Several large channels occur within Hellas. These are probably not runoff channels, but their origin is somewhat ambiguous.

Although most runoff channels are only a few tens of kilometers long, larger channel networks are occasionally found. Some of the largest and best integrated tributary networks occur in Margaritifer Sinus, southwest of the main regions of chaos at the head of the large Chryse outflow channels. Here the drainage of much of the runoff channels is northwest toward the chaos region. In Sinus Meridiani and Sinus Sabeus, the drainage is mostly to the west, also in the direction of the chaos region. North of these two areas, however, drainage is mainly to the north where no chaos regions occur. Drainage is also mainly northward, toward the plains/upland boundary, between longitudes 260° and 180°. In other areas no regional pattern in drainage is obvious. Even where a regional pattern is obvious, very few larger integrated channel systems are present. The regional pattern is made up of short segments with preferred orientations.

Outflow channels. Outflow channels occur in five main regions: (1) Circum-Chryse: Numerous large channels start in box canyons north of Valles Marineris, and in chaos regions to the east of the canyon, then drain northward ultimately to cross Chryse Planitia, and disappear around 40°N in Mare Acidalium. (2) Several large channels start in graben-like features northwest of Elysium Mons and drain northwestward for about 1000 km before disappearing in Utopia Planitia, southwest of the VL-2 landing site. (3) A large channel can be traced from the equator northward, approximately along the 170° meridian, in the west of Amazonis Planitia, until it is lost at around 30°N. (4) Mangala Vallis starts instantaneously at one of the large graben of the Memnonia Fossae. (5) Several large channels start instantaneously on the northeast rim of Hellas and drain into the basin floor. All the outflow channels cut the ridged plateau plain of the old cratered terrain, and the plain of the sparsely cratered hemisphere. They therefore appear to be younger than runoff channels which rarely, if ever, cut the plains of the sparsely cratered hemisphere of Mars.

Fretted channels. Fretted channels occur along the plains/upland boundary between 280°W and 0°, around Argyre, and possibly along the plains/upland boundary between 180° and 210°W, although the latter channels are somewhat questionable. Most fretted channels can be traced upstream into channels that resemble the runoff variety. In the area of fretted channels (except between 180° and 210°W), debris flows are common at the bases of steep slopes, and the pattern of erosion suggests that processes of escarpment retreat are particularly effective (Sharp, 1973). The flows of the fretted channels are mostly devoid of craters as are debris flows around massifs. Patterns within the channel flows suggest that mass wasting has been particularly active. Crater counts within these channels probably measure the mass-wasting rates, not channel age. At the mouth of some fretted channels, faint linear striations suggest mass flow of material out of the channel. Fretted channels are interpreted as runoff or outflow channels enlarged by mass-wasting processes.

The next stage in this work will be correlating channel densities with other properties of the surface such as color, albedo, elevations, and geologic units by means of the various data bases assembled by the Mars Consortium. Crater counts will also be made on individual channels and on dissected units to define more accurately the times of formation of the different channel types.

References

- Greeley, R. and Spudis, P. D., 1978, Volcanism in the cratered terrain hemisphere of Mars: *Geophys. Res. Letters*, v. 5, p. 453-455.
Sharp, R. P., 1973, Mars: fretted and chaotic terrains: *J. Geophys. Res.*, v. 78, p. 4073-4083.
Sharp, R. P. and Malin, M. D., 1975, Channels on Mars: *Geol. Soc. America Bull.*, v. 86, p. 593-609.

ORIGIN OF MARS FLUVIAL FEATURES: ANALYSIS FOR FLUIDS OF STRESS AND TEMPERATURE DEPENDENT RHEOLOGY

Thompson, David E., and Julie E. Laity, Jet Propulsion Lab, Caltech, Pasadena, CA, 91103

Fluid instability analysis for the origin of longitudinal grooving in Tiu Vallis, Mars, has been developed. The results have shown that for fluids of exponentially stratified viscosity, those similar to mudflows or debris flows have the best chance of developing longitudinal helicoidal flow patterns which might be able to erode groove patterns on channel bottoms of the large Martian outflow channels (Thompson, 1979a, 1979b). This analysis has dealt only with flow of arbitrarily varying viscosity. A separate program is now aimed at relating required sediment or debris transport to the specific variable viscosity distribution used in the theoretical analysis. Parallel to that analysis, a second project has been established which deals with the flow behavior and erosion capabilities of fluids whose viscosities are explicitly dependent on the flow strain-rate field and the temperature distribution within the fluid. This analysis is being developed as a modified version of an original stability analysis for glaciers and ice sheets (Thompson, 1976, 1978, 1979c). The quasi-plastic rheology exhibited by glaciers and ice sheets is not meant to be representative of fluid flow in the large Martian outflow channels; rather the slow viscous flow of debris laden ice or viscous lavas are being modelled under analysis more compatible to their actual flow characteristics than that used in the limit-case models of the previous longitudinal grooving analysis for the Tiu Vallis features. In addition, flow under explicit stress or temperature dependent rheology allows calculation of the initial behavior and surface collapse of chaotic terrain. Thus the analysis addresses massive debris flows representative of material conditions just prior to liquefaction and fluid separation.

The analysis for this project is part theoretical, part field oriented. The theoretical analysis is an extension of surface wave stability analysis on glaciers and includes 1) growth and decay of large scale surface fluctuations in fluids of power-law stress-dependent viscosity, and 2) development of kinematic waves as a response of the fluid to changes in environmental conditions. The temperature dependence and its variation due to changing flow conditions needs to be incorporated into the stability analysis whereby shear heating effects can be examined. The actual behavior of stress-dependent viscosity fluids is being examined by a field study on the flow and climatic response of large rock glaciers in the Sierra Nevada, California. Specifically, air photos of Sierran rock glaciers taken in 1962, 1972, 1973, and 1974 are being analyzed for changes in snout position and collapse features. One large rock glacier of about 2 km long, at an elevation of between 11600-13000 feet, was surveyed extensively this summer from permanent bedrock stations, and

a strain net of over 50 stations was established on the rock glacier surface. The strain net consisted of stations along the longitudinal central flow line of the rock glacier and stations along six transverse profiles. Roughly the upper two thirds of the rock glacier is covered by this net as below this point, the bedrock gradient steepens appreciably and flow may not be as a rheological continuum. The central survey profile bifurcates roughly 300 m from the upper end of the rock glacier in order to measure local lateral flow input from the surrounding cirque glacier. The stations along both the longitudinal and transverse profiles are roughly 40-50 m apart. The locations of these stations have been accurately surveyed with a Wild T-2 theodolite, and will be resurveyed again both in early summer (as soon as the surface is snow free) and again in the fall. The total yearly surface strain-rates of the rock glacier can thus be separated into winter and summer components, and the response of the rock glacier to seasonal temperatures and mass variations can be detected. It is expected that the measured strain-rates will be very small, but they should be within the resolution errors of the theodolite. The particular rock glacier selected exhibits extensive pressure ridges and lateral surface variations which seem to indicate flow activity. Other rock glaciers will be surveyed and monitored as the project continues.

The strain rate data and gross long-term flow changes on Sierran rock glaciers will help isolate the rheological characteristics of massive ice-charged debris movements. Models of constitutive relations can be tested against actual field conditions so that the concurrent theoretical analysis will be constrained by measured surface strain rates. In this way, realistic viscosity laws for fluids of stress-dependent rheology can be established and incorporated in the surface wave stability analysis. The thermal profiles will be hypothetical insofar as very few rock glaciers have been drilled or cored (none to great depth) and monitored by thermistors. The sensitivity of debris-laden ice mixtures can then be tested against climatological fluctuations or local heating perturbations which might initiate collapse and liquefaction flow on Mars.

Thompson, D.E., 1976, Application of fluid-instability analysis to glacier flow: PhD dissertation, U.C.L.A.

Thompson, D.E., 1978, Stability of glaciers against long-wavelength surface perturbations: EOS, Trans. American Geophys. Union, vol. 59, no. 4, p. 274

Thompson, 1979a, Origin of longitudinal grooving and fluting under converging channelized flow in Tiu Vallis, Mars: Reports of Planetary Geology Program 1978-1979, NASA Tech. Mem. 80339, p. 334-336

Thompson, D.E., 1979b, Origin of longitudinal grooving in Tiu Vallis, Mars: isolation of responsible fluid types: Geophys. Res. Lett., vol. 6, no.9, p. 735-738

Thompson, D.E., 1979c, Stability of glaciers and ice sheets against flow perturbations: Jour. Glaciology, vol. 24, no. 90, in press.

MARTIAN OUTFLOW CHANNELS SCULPTURED BY GLACIERS

Lucchitta, B. K., U.S. Geological Survey, Flagstaff, Arizona 86001
and Anderson, D. M., State University of New York at Buffalo,
Buffalo, New York 14260

Several hypotheses have been advanced for the origin of martian outflow channels (1), but catastrophic flooding (2,3) remains the leading one principally because of the morphologic similarity with features observed in the flood-scoured scablands of Washington (4). This paper will show that martian channel morphologies are equally well explained by glacial origin.

Morphology: (a) Martian outflow channels widen, constrict, anastomose and become incised in places. Glaciers on Earth widen and constrict with topographic changes; glaciers in Antarctica anastomose around ice rises; deeply incised valleys in Yosemite, in northern Canada, and in fjords in Greenland and Scandinavia are typical of glacial landscapes. (b) Where martian channels constrict, they acquire a U-shaped cross profile. This shape, on Earth, is most distinctive for glacial erosion. (c) Hanging valleys occur on Mars where distributaries and tributaries merge with the main channel. Hanging valleys are a classic landform of terrestrial glacial regions. (d) Long, even terraces (scour marks) occur on valley walls and islands in martian channels. Similar even and continuous terraces are seen on Landsat images in glacial valleys in Alaska, and terraces are recorded by radio-echo sounding on the subglacial scarp of the Fletcher ice rise in Antarctica (5). (e) Longitudinal ridges and grooves are conspicuous on martian valley floors; they are also characteristic of terrestrial glacial landscapes. They abound as scour marks under the former Laurentide ice sheet (6), they are found in thin morainal blankets at the transition zone between continental glacial erosion and deposition (7), and they are seen on Landsat images on the floor of large, glacial valleys in Alaska and Iceland. (f) Channel islands on Mars have been compared with flood-islands in the scablands by Baker (4); their dimensions were shown to lie on a common regression line. Five ice rises in Antarctica have been measured and plotted on Baker's (4) diagrams. They fall on his regression line, and indicate that glacial erosion could have sculptured the martian islands. The lemniscate k-factor (4) has been calculated for the Antarctic ice rises; it, also, lies near that of the scabland and martian islands. (g) The width of martian outflow channels varies widely. Kasei Vallis' grooved terrain reaches 160 km, but is generally less, and deeply incised troughs are a few kilometers to 20 km wide. Most of the other channels surrounding the Chryse basin only locally exceed a few tens of kilometers in width. Glacial valleys in Alaska with grooved floors are up to 20 km wide and merge to form a grooved flat plain 80 km wide, incised ice streams in Antarctica are up to 50 km wide (8). (h) Steep scarps on channel sides and islands on Mars are as much as 2000 m

in height (based on shadow measurements); the bedrock scarps on ice streams and ice rises in Antarctica locally are 1000 to 3000 m high (5,8).

In summary, it appears that glacial erosion may have sculptured the channels on Mars and is a process resulting in morphologic forms whose dimensions are similar on both Mars and Earth.

Theoretical considerations: Glaciers may be either cold-based or warm-based (9). Cold-based glaciers are frozen to the ground, movement occurs by slippage within the ice, and erosion is usually slight. Warm-based ice moves mostly by sliding of the glacier over the ground either by pressure melting or slipping over a water layer. Most terrestrial glaciers are warm-based (9), and powerful erosion is usually associated with them (6). By analogy if the martian channels were sculptured by ice, the grooves on their floors suggest that they were probably warm-based.

Shear strain within cold-based ice in terrestrial glaciers commonly occurs if the basal shear stress is between .5 and 1.5 bars (9). Preliminary calculations indicate that under martian conditions basal shear stress of 1 bar corresponds to an ice-surface slope of 1° and an ice thickness of 1.5 km; for gradients below 0.2° the ice thickness required for basal shear strain exceeds 4 km (at .5 bar shear stress). The overall gradient of martian outflow channels ranges from less than 0.1° to 0.25° (10). If one assumes an ice-surface gradient parallel to the ground gradient, cold-based flow appears unlikely for the entire distance, but could have occurred along steeper stretches. Also, ponding and build-up of ice caps could have increased local ice-surface gradients to allow cold-based flow.

Warm-based ice must have a basal temperature near 273° K. Preliminary calculations [using Fanale's (11) heatflow values for Mars and Glen's (12) thermal conductivity value for ice], and disregarding complicating factors such as changes of state indicate that the 273° K isotherm in pure ice lies at a depth of 4.5 to 6 km beneath the surface in the present martian environment. Since the origin of martian channels has been linked to geothermal heating (3), a heatflow equivalent to terrestrial Cenozoic volcanic areas (14) would raise the 273° K isotherm to 1.5 km below the surface. Under this condition, glaciers on Mars could be warm-based, which would facilitate flow. Warm-based glaciers also could have existed if the martian climate was warmer in the past. Glaciers on Mars, however, may have been entirely different from terrestrial ones and consisted of ice caps over rivers as postulated by Wallace and Sagan (15). These ice caps may have been thick enough to cause some of the glacial features observed in the channels. Even though thick river ice would not account for all the glacial morphologies observed, its formation may have led to thick ice masses that eventually produced glaciers in the martian channels.

REFERENCES

- 1) Sharp, R. P., and Malin, M. C., 1975, *Geol. Soc. Amer. Bull*, 86, p. 593-609.
- 2) Sharp, R. P., 1973, *J. Geophys. Res.*, v. 78, p. 4073-4083.
- 3) Baker, V. R., and Milton, D. J., 1974, *Icarus*, v. 23, p. 27-41.
- 4) Baker, V. R., 1978, *Lunar and Planet. Sci. Conf. 9th*, Houston, Tx., *Proc.* p. 3205-3223.
- 5) Swithinbank, C., 1977, *Phil. Trans. R. Soc. London B.*, v. 279, p. 161-183.
- 6) Sugden, D. E., 1978, *J. Glaciology*, v. 20, p. 367-391.
- 7) Bird, J. B., 1967, *The Physiography of Arctic Canada*, John Hopkins Press, Baltimore, 336 p.
- 8) Morgan, V. I., and Budd, W. F., 1975, *J. Glaciology*, v. 15, p. 103-111.
- 9) Sugden, D. E., and John, B. S., 1976, *Glaciers and Landscape*, Edward Arnold Publishers, London, 376 p.
- 10) U.S. Geological Survey, 1976, *Topographic map of Mars: U.S. Geol. Survey Misc. Geol. Inv. Map I-961*.
- 11) Fanale, R. F., 1976, *Icarus*, v. 28, p. 179-202.
- 12) Glen, J. W., 1974, *The Physics of Ice: Cold Regions Sci. and Engin. Mono. II-C2a*, Cold Regions Res. and Engin. Lab., Hanover, NH, 82 p.
- 13) McCauley, J. F., Carr, M. H., Cutts, J. A., Hartmann, W. K., Masursky, Harold, Milton, D. J., Sharp, R. P., and Wilhelms, D. E., 1972, *Icarus*, v. 17, p. 289-327.
- 14) Stacey, F. D., 1969, *Physics of the Earth*, Wiley, New York, 324 p.
- 15) Wallace, David, and Sagan, Carl, 1979, *Icarus*, v. 39, p. 385-400.

MARS CATASTROPHIC FLOODING ANALOG: ANALYSIS OF DEBRIS TRANSPORT IN
VARIABLE VISCOSITY FLUIDS

Thompson, David E., Jet Propulsion Lab, Caltech, Pasadena, CA 91103

Recent fluid instability analysis on the origin of longitudinal grooving in Tiu Vallis, Mars, has shown a tendency for growth of longitudinal helicoidal flow patterns in fluids of exponentially stratified viscosity, representative of debris laden fluids such as mudflows or debris flows (Thompson, 1979a, 1979b). It has been assumed that such secondary flow fields, once developed, can erode the pervasive longitudinal grooving and fluting observed in several of the large Martian outflow channels. To date, however, this analysis has assumed an arbitrary but spatially variable viscosity distribution which has not been tied physically to particular sediment transport mechanisms. In an effort to understand the erosion processes and debris transport mechanisms which operate during a catastrophic flood and then to relate this debris transport to a variable viscosity distribution in fluids, a field program has been established to study sediment transport hydraulics both on active catastrophic floods and on remnant catastrophic fluvial features.

During the summer of 1979, field work was carried out on two localities in the St. Elias Mountains, Yukon. This project is a collaboration with Dr. G.K.C. Clarke, Geophysics, University of British Columbia. Steele Glacier is currently ablating following an intense surge in 1966-1967 (Stanley, 1972). The margin of Steele Glacier, at a point 15 km upstream from the terminus, blocks the drainage of Hazard Creek. Each spring, Hazard Creek flows with meltwater from glaciers to the interior of Steele, and the drainage ponds along this margin. The thickness of Steele Glacier at present is such that Hazard Lake must reach a depth of about 80m to 90m before it can drain out an upper spillway along the margin of Steele. Immediately following the surge, Steele Glacier was thick enough that it did not respond to the 90m deep lake along its flank, and the lake drained along the spillway. Now, due to ablation of the ice surface, Steele Glacier is only a few tens of meters thicker than the lake depth at this point, and when Hazard Lake fills completely, it begins to float portions of Steele Glacier. Water then channels under the ice, connects with extensive drainage networks within Steele Glacier, and the intense water flow forms a subglacial tunnel which allows catastrophic drainage of Hazard Lake on about 1 August each year. This drainage leaves behind gross current ripples and channel grooves in the lake bottom and also forms huge erosional features and islands beyond the glacier snout due to the intense increase in discharge along the normal glacial outwash plain. These features are being studied according to their debris content and formation with respect to the degree of flooding observed during the ice dam break-up. The lake drainage has been filmed. In addition, the response of the glacier to the intense tunnelling and rather instantaneous removal of hydrostatic support of the 90m deep lake is being monitored both seismically and by induced polarization methods.

The second aspect of the field program has been initiated at a 3x5 km gravel bar located along the Alsek River drainage in the St. Elias. This bar, and many other bars up to 110 km upstream, are covered with giant current ripples of 5m amplitude and 100m wavelength formed of gravel and very coarse debris. These bar sets are created and reworked during catastrophic break-up of the Lowell Glacier ice dam and drainage of Glacial Lake Alsek. The Lowell Glacier surges and blocks the Alsek River drainage about once every 70-100 years, with some partial closures on shorter time scales. Within 6 months of closure, Lake Alsek is formed and reaches about 110 to 130 km upstream with depths of several hundred meters. Analogous to the Steele Glacier case, the lake floats the snout end of Lowell Glacier, tunnels under it, and then catastrophically breaks up the ice dam. The resulting drainage of Lake Alsek forms and modifies the huge current ripple sets in the Alsek valley. During the summer of 1979, many of these large dunes were sectioned, sampled, and studied according to weight fraction and number fraction of the size of the gravel constituents. Results of this sampling (over 29000 samples) are being compared statistically with respect to variances within location on a given ripple, variances between ripples of different sizes and locations on the bar, and variances in peak weight fraction with respect to peak number fraction for a given sample in an effort to determine the hydraulics active during formation of the dunes and ripples. In addition, several profiles of the dune and ripple sets of up to 1.5km in length are available in the sampled locations so that theoretical analysis of the transport and migration of gravel waves during flooding can be tied to actual data.

The bulk of the data collected at both field sites is still under analysis so that only speculative results are available. Further analysis should not only provide initial ideas of the differences between sediment and debris transport in catastrophic flooding as opposed to that in alluvial streams, but should also guide the focus of the field program in successive seasons so that a reasonable process analog for erosion and debris transport on Mars can be developed and related back to the completed theoretical analysis.

Stanley, A.D., 1972, Observations on the surge of Steele Glacier:
Arctic Institute of North America, Icefield Ranges Research Project
Scientific Results, vol. 3, p. 61-69.

Thompson, D.E., 1979a, Origin of longitudinal grooving and fluting under converging channelized flow in Tiu Vallis, Mars: Reports of Planetary Geology Program 1978-1979, NASA Tech. Mem. 80339, p.334-336.

Thompson, D.E., 1979b, Origin of longitudinal grooving in Tiu Vallis, Mars: isolation of responsible fluid types: Geophys. Res. Lett., vol. 6, no. 9, p. 735-738.

AN ANALYSIS OF THE MODES OF SEDIMENT TRANSPORT IN RIVERS WITH APPLICATION TO THE EROSION OF THE MARTIAN OUTFLOW CHANNELS

Komar, Paul D., School of Oceanography, Oregon State University,
Corvallis, Oregon 97331

A reexamination of the criteria that are employed to distinguish between bed-load, suspension and wash load transport in rivers has been undertaken for the purpose of application to the analysis of sediment transport in the large martian outflow channels. Included in this examination is a review of the comparable criteria used in the pipe flow of suspensions where the terms heterogeneous flow and homogeneous flow are analogous to suspension and wash load transport. This review of pipe flow has led to the possibility of new criteria that might be employed in rivers, especially for the distinction between suspension and wash load, which has been poorly studied in rivers.

Application of these new criteria to the martian outflow channels refines my previous analysis (Komar, 1979), but does not alter the main conclusions. The calculations still indicate that water flows that may have eroded Mangala and Ares Channels would have been capable of transporting basalt pebbles and cobbles in suspension and any sand size material as wash load. A further analysis of the threshold of motion under water flows on Mars indicates that even the smaller expected flows would have been competent to move boulder-size material ($D \approx 1$ meter). All indications are then that the channels could have been eroded by water flows within a few days. Exact calculations are difficult because of the uncertainties in evaluating the transport rates of wash load without knowing the proportions of the different grain sizes present on Mars.

References

- Komar, P.D.(1979) Modes of sediment transport in channelized water flows with ramifications to the erosion of the martian outflow channels: Reports of Planetary Geology Program, 1978-1979, NASA Tech. Memo. 80339, p. 344-5.

FLUVIAL AND GLACIAL PROCESSES, CENTRAL ARCTIC SLOPE, ALASKA

Jon Boothroyd, Department of Geology, University of Rhode Island, Kingston, RI 02881; Barry S. Timson, The Mahoosuc Corporation, Augusta, ME 03240

Field studies, coupled with detailed geomorphic mapping, of the Central Arctic Slope region of Alaska, are being carried out to gain a better understanding of processes that may be analogous to those that formed the upper reaches of the martian outflow channels. The area under study is in between the Colville River on the west, the Sagvanirktok River (Sag) on the east, and extends from the Brooks Range to the Beaufort Sea. Figure 1 is a Landsat image (scale 1:1,000,000) of the area; Figure 2 is a geomorphic map originally constructed at a scale of 1:250,000 from Landsat images and topographic maps.

The erosional remnant hills (unit R), composed of upper Cretaceous and Tertiary partially-consolidated sandstone, siltstone, and claystone, rise 200 m above the presently-active fluvial systems (unit F) and older Pleistocene fluvial-deltaic terraces (unit T). The only structural control of remnant location appears a major southwest-northeast trending lineament that bounds one side of each remnant and is defined by the Colville River floodplain in the southeast (Albert, 1978). Contacts of Cretaceous and Tertiary units (Beikman, 1978) cut across the remnants and play little role in remnant shape.

The fretted and etched plains units (E) that bound the remnants on the south consist in part of drained thaw lakes that were probably active during the late Pleistocene and early Holocene (Péwé, 1975). This terrain is bounded on the south by the foothills of the Brooks Range (Uf). Tongues of glacial terrain (unit C) extend out of the valleys of the foothills and have been dissected by presently-active streams. Hamilton (1978), in a summary map, indicates the existence of glacial lakes dammed behind the Pleistocene moraines.

The present rivers are underfit with respect to valley and floodplain width. The older Holocene terraces and deltaic plain are blanketed by loess in which wind-aligned thaw lakes are present. The terrace scarps along the Sag River are undergoing degradation by permafrost melting and solifluction processes. These observations suggest that remnant-forming events occurred at times of increased runoff during periods of deglaciation, perhaps augmented by flooding from moraine-dammed lakes.

REFERENCES CITED

- Albert, N. D., 1978, Landsat mosaics of eastern North Slope petroleum province, Alaska, with preliminary interpretation of observed features: U. S. Geol. Survey Map MF-928V.
- Beikman, H. M., 1978, Preliminary geologic map of Alaska: U. S. Geol. Survey Map.
- Hamilton, T. D., 1978, Surficial geologic map of the Phillip Smith Mountains quadrangle: U. S. Geol. Survey Map MF-879A.
- Péwé, T. L., 1975, Quaternary geology of Alaska: U. S. Geol. Survey Prof. Pap. 835, 145 p.

EXPLANATION FOR GEOMORPHIC MAP

FLUVIAL SYSTEMS

- F_a** ACTIVE
- F_i** INACTIVE
- F_b** ABANDONED
- F_u** UNDIFFERENTIATED

DELTA SYSTEMS

- D_a** ACTIVE
- D_i** INACTIVE
- D_b** ABANDONED
- D_u** UNDIFFERENTIATED

FLUVIAL-DELTAIC TERRACES

- T₃** YOUNGEST
- T₂**
- T₁** OLDEST
- T_u** UNDIFFERENTIATED

FRETTED ETCHED PLAINS

- E₂** YOUNGEST ?
- E₁**

ALLUVIAL FAN

- A** ALLUVIAL FAN

EROSIONAL REMNANTS


- R₄** YOUNGEST SURFACE
- R₃**
- R₂**
- R₁** OLDEST SURFACE

GLACIAL TERRAIN

- C_n** ICE DISINTEGRATION TOPOGRAPHY
- C_i** MORaine TOPOGRAPHY
- C_s** SMOOTH TOPOGRAPHY

UPLAND

- U_m** MOUNTAINS
- U_f** FOOTHILLS


 HEADCUTS

 DISINTEGRATION DEPRESSIONS

 MORaine AXES

 SWALE AXES

 FRETTED SLOPE MARGINS

 STREAM CHANNEL (ACTIVE)

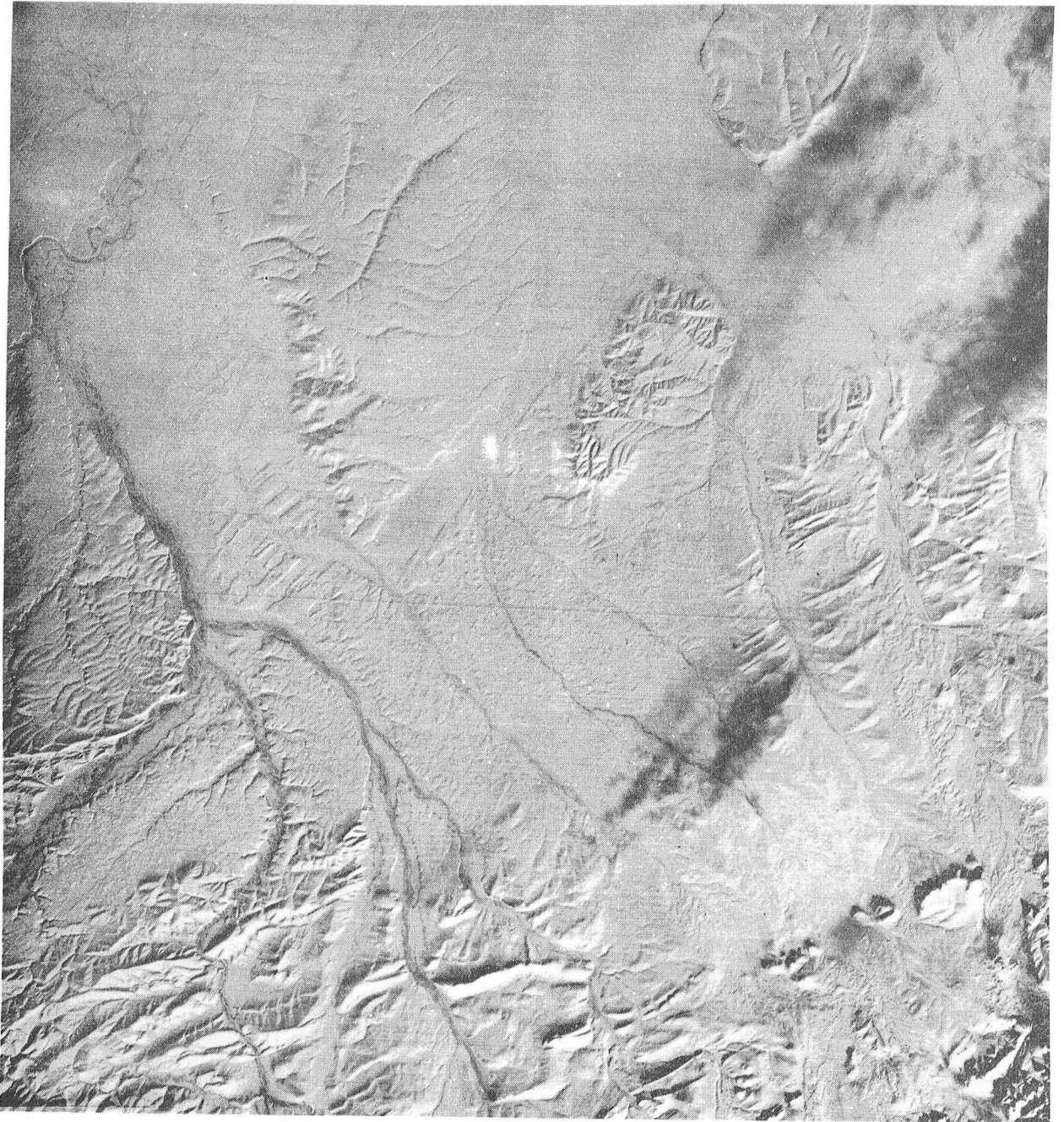


Figure 1. Landsat Band 5 image (E-1217-21235-501). Scale: 1:1,000,000.

[illegible]

GLOBAL INVENTORY OF GLACIAL AND PERIGLACIAL FEATURES ON MARS, A PROGRESS REPORT

Lucchitta, B. K., U.S. Geological Survey, Flagstaff, Arizona 86001,
and Mohr, E. T., Kent State University, Kent, Ohio

A major objective of the inventory is to recognize and map the features on Mars whose origin could be attributed to permafrost and ice. The study comprises the identification of possible ice-related features, the determination and evaluation of the processes, and an assessment of their role in landscape evolution. A classification of features has been developed, which will be modified as new discoveries are made and new insights are gained. Major morphologic entities are (a) mass-wasting features (talus slopes, gullies, slumps, landslides, debris flows, possible rock glaciers, and possible glaciers and their deposits); (b) patterned ground (polygonal, circular and curvilinear, having troughs with or without raised margins); (c) apparent collapse structures possibly due to thermokarst (chaotic terrain, reentrants on scarps, circular or irregular depressions, and deep troughs in craters and along grabens); (d) forms resulting from the interaction of volcanism and ice (table mountains); and (e) hills with central depressions that could be pingoes.

We have plotted on maps the locations of identified features and outlined areas that contain clusters of individual features. Additionally, we have developed a table in which are recorded for each plotted feature its location by quadrangle, subquadrangle, latitude and longitude, number of the best image, its trend and dimensions where applicable, the geologic unit on which the feature occurs, and its elevation. This data collection can eventually be computerized.

All Viking images are being screened during a systematical investigation of the 1:2,000,000 scale orthophotomosaic subquadrangles. A pilot study of the Memnonia quadrangle (MC16) showed that conspicuous mass-wasting features are scarce in this area. Only high-resolution images showed talus slopes clearly and a few minor lobes that could be debris flows. In places low hill slopes are gullied, and fields of small channels occur locally. Short, stubby channels of the fretted type (1) line the highland border that traverses the quadrangle in the north (2). No patterned ground was seen other than a few reticulate networks of deep troughs and mesas bounded by orthogonal scarps. Collapse features that may be related to thermokarst are common. Prominent are beaded depressions and elongate oval troughs in grabens that traverse the MC16 SE subquadrangle in an east-northeast direction. Also occurring locally, especially in association with the grabens, are craters whose interiors are dissected by networks of deep troughs. Small patches of chaotic terrain (3) occur in circular reentrants along

the outflow channel of Mangala Vallis. The highland border locally is paralleled by mesas and buttes (hummocks) of the fretted terrain (3), but prominent flow forms on valley floors, like those seen in Deuteronilus, Protonilus and Nilosyrtris Mensae (4) were not observed. Scalloped scarps similar to those attributed to alas formation in the Chryse area (5) are seen north of the highland boundary on the ejecta blanket of crater Nicholson. The Chryse scarps also occur near the large crater Wahoo; it may be that the scalloped scarp form preferentially develops in ejecta deposits. A thick sedimentary blanket covers the northern lowlands in Memnonia. In it occur many flat-topped hills, some with depressions at the top. These hills are more probably buried and reexcavated craters than pingoes or volcanic table mountains.

Overall, the Memnonia quadrangle shows few features that could be attributed to glacial or periglacial action, with the exception of apparent collapse features that could be related to thermokarst. The quadrangle lies in the equatorial belt, and our preliminary survey indicates that this belt has fewer possible glacial or periglacial features than do the higher northern and southern latitudes.

REFERENCES

- 1) Sharp, R. P., and Malin, M. C., 1975, *Geol. Soc. America Bull.* 86, p. 593-609.
- 2) Mutch, T. A., and Morris, E. C., 1979, *U.S. Geol. Survey Misc. Geol. Inv. Map I-1137*.
- 3) Sharp, R. P., 1973, *J. Geophys. Res.*, v. 78, p. 4073-4083.
- 4) Squyres, S. W., 1978, *Icarus*, v. 34, p. 600-613.
- 5) Carr, M. H., and Schaber, G. G., 1977, *J. Geophys. Res.*, v. 28, p. 4039-4054.

THERMOKARST ON MARS

Rossbacher, Lisa, and Sheldon Judson, Department of Geological and Geophysical Sciences, Princeton University, Princeton, N.J. 08540

No direct observations or measurements exist to demonstrate the presence of water ice beneath the martian surface. Yet many workers, including ourselves, have appealed to ground ice to account for several different features of the landscape. On Earth, the degradation of ground ice can lead to surface collapse and the creation of topographically closed depressions. We believe that some closed depressions on Mars are best explained by such a process; the resulting topography would be a form of thermokarst.

One of the most abundant ice-degradation features on Mars appears to be a roughly circular depression; these are flat-floored, generally less than 5 km across, and without raised rims. These pits may be either isolated or linearly aligned. In some instances the latter appear to coalesce along surface fractures to form elongate valleys. The pit forms have limited areal distributions and are concentrated near Olympus Mon and the equatorial Valles Marineris region (Fig. 1).

We support the suggestion by Carr and Schaber (1977) that these are ice-degradation features. The geographic association of pits with Olympus Mons and its nearby volcanic region may be a clue to their genesis. Volcanism could provide a heat source for ice degradation. Similarly, the pitted terrain in the plains around 25°N, 220°W is adjacent to the Elysium volcanic region. The size of the pits suggests that ice was present not as pore ice alone, but that significant volumes of ice-segregated masses were involved. Other depressions which we believe may reflect wastage of ground ice occur in curvilinear arrangements. Curvilinear features on Mars are of several types: 1) Some are discontinuous arcs of ridges and depressions. The features may change between positive and negative relief along their length but the variations show no consistent pattern. The ridges and depressions are roughly equal in width, approximately 1 km. 2) Other curvilinear features are steep-sided, flat-floored depressions lying below a generally level surface. 3) The remainder of the features have no discernible topographic expression and may reflect albedo variations.

Each group of curvilinear features occurs as arcs concentric around a central point. Maximum radii range between 12 and 120 km, and the maximum observable arcs are 20° to 105°. Preliminary analysis indicates a relationship between the average maximum radii of curvilinear features and their location on the planet; for

example, two groups for which we have data, those centered at 48°N, 288°W and at 48°N, 350°W, have average maximum radii of about 70 km and 20 km, respectively. The curvilinear features are found in the 40-50°N latitude belt, generally along the escarpment between the southern cratered upland and the lower plains to the north.

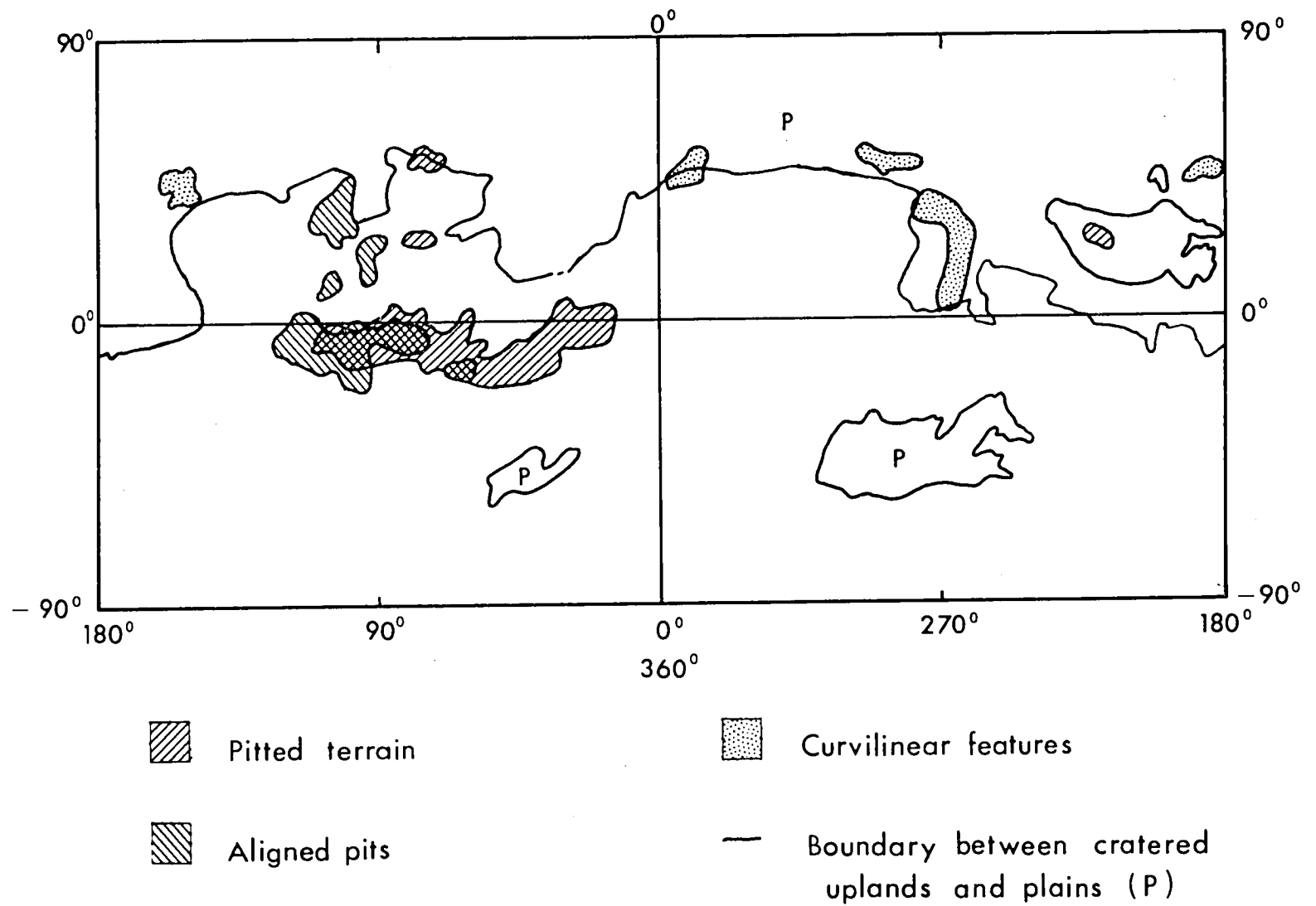
We do not know the precise age of these features, or even whether they are of the same general age. The scarcity of observable impact craters makes crater counts suspect. Thermokarst features are apparently not forming at the present; the pits and curvilinear features are younger than the plains, and probably contemporaneous with the Tharsis events.

These proposed thermokarst features provide one of the rare instances in which martian features occur at the same scale as a terrestrial analog. The flat-floored depressions without raised rims which are found in permafrost regions on Earth are called alases, and they are similar to the martian pits. These terrestrial landforms may range from 0.1 to 15 km in diameter (Soloviev, 1962, p.48 as quoted in Washburn, 1973, p. 238) dimensions comparable to the martian features.

REFERENCES CITED

- Carr, M.H., and G.G. Schaber, 1977, Martian permafrost features: *Journal of Geophysical Research*, v. 82, p. 4039-4054
- Soloviev, P.A., 1962, Alasnyy relyef Centralnoj Jakutii i ego proiskhozhdeniye: p. 38-53 in Mnogoletnemerzlyye porody i sputstvuyushchiye yim Yavleniya na territorii JASSR, Moskva, Izdatel'stvo AN SSSR.
- Washburn, A.L., 1973, Periglacial Processes and Environments: St. Martin's (New York) 320 p.

Fig. 1. Distribution of some thermokarst features on Mars



Some Terrestrial Analogs to Dry Valley Systems on Mars. Victor R. Baker, North Australia Research Unit, Australian National Univ., P.O. Box 39448, Winnellie, N.T. 5789 Australia, and Dept. Geological Sciences, Univ. of Texas, Austin, TX 78712.

The dry valley systems discussed here comprise those Martian channel systems classed as "runoff" and "fretted" channels by Sharp and Malin (1). These are distinguished from the very large troughs, termed "outflow channels", that appear to have been largely inundated by the fluids responsible for their genesis (2). The terminology is still not precise, however, because many outflow channels have experienced extensive "postdiluvian" wall modification by mass movement processes (3).

Undermining and sapping along steep escarpments has been argued for the origin of fretted channels (4). Many of the "runoff channels" also display features more consistent with sapping processes than with surface runoff (5). These include (a) the relatively low drainage density, (b) the abrupt, cirquelike valley heads, (c) the abnormally long high order stream valleys contrasting with very short first order tributaries, (d) the occurrence of hanging valleys, (e) the morphology of relatively smooth valley floors in contrast to steep valley walls characterized by mass movement effects. Steep escarpments appear to play an important role in the development of all the Martian dry valley systems.

Terrestrial scarp recession by sapping occurs most readily where a massive, resistant lithology overlies a relatively weak incompetent one. Undermining of the resistant layer occurs by weathering and groundwater flow along the contact between the two lithologies. Where scarp steepness is maintained, scarp recession will leave a smooth, nearly flat surface, often termed a "pediment". Because sapping is favored along certain zones of structural weakness, scarp recession is often differential, forming great embayments. Residual areas of upland may be isolated to form outliers, or "inselbergs" in the pediplain that is produced by scarp retreat.

Valley development by sapping was studied in the sandstone plateau country of southeastern Utah, the jointed sandstone plateau of Arnhem Land, Northern Territory, Australia, and in the volcanic terrains of Hawaii. The southeastern Utah region illustrates classic headward recession of steep-walled valleys by spring sapping at the base of massive sandstone caprocks. The valleys have long high order segments and terminate headward in steep, cirquelike scarps. They also display hanging tributaries which enter the main canyon at waterfalls. Mass movement processes characterize the steep valley walls.

The Arnhem Land Plateau of northern Australia is an extensive surface of resistant sandstone surrounded by a steep escarpment from 30 to

330 meters in height. The Middle Proterozoic Kombolgie Formation provides the resistant caprock for the escarpment. Since the Cretaceous, erosion has been attacking a variety of weaker rocks at the base of the escarpment, undermining the caprock and inducing retreat. Spring sapping, cavernous weathering, and rock spalling produce debris from the sandstone cliffs. This debris mantles slopes, inhibiting further erosion until it is reduced in size and removed by wind or sheetwash. The escarpment assumes a variety of active or stable configurations depending on the jointing in the sandstone, exposure of weak rocks at the scarp base, and faulting of scarp boundary (6). Local enhancement of erosion along joints, faults, and anticlines has produced large embayments into the escarpment and many sandstone outliers on the broad, flat pediplain that was left by scarp retreat.

In the Hawaiian Islands valley development by fluvial action is inhibited by the extremely high permeability of the lava flows comprising individual shield volcanoes. Volcanic ash and deep weathering may allow the initiation of some fluvial dissection, as along the Hamakua Coast of Hawaii. Penetration of this low permeability layer, however, will again result in rapid infiltration by surface water into the highly permeable lavas.

The youngest Hawaiian volcanoes, Kilauea and Mauna Loa generally lack surface streams. A temporary perching of small arroyos occurs on the 1790 Keanakakoi Ash of the Kau Desert. Mauna Kea's northeastern slopes show long, parallel valleys eroded through the mantle of Pahala Ash. The characteristic valley form for the older volcanoes is U-shaped in cross section and ends in an abrupt amphitheater-like head (7, 8). Valley sides are steep-walled and subjected to mass movement processes (9). Headward valley growth occurs by spring sapping. Hanging valleys may be created when deep, headwardly receding valleys intersect and capture perched fluvial valleys.

Excellent amphitheater-headed valleys occur on the northeastern slopes of Kohala and in West Maui. The biggest valleys have eroded back into the central dike complex of the old volcanoes to tap groundwater held in interdike compartments. On Haleakala volcano (eastern Maui) two large amphitheater-headed valleys eroded headward into the central caldera of the volcano. These valleys were subsequently partly filled by lava flows.

These examples of large-scale valley development and scarp recession have not received much attention in the geomorphic literature. Further study appears warranted because of the abundance on Mars of dry valleys displaying an assemblage of landforms characteristic of sapping processes.

References: Sharp R.P. and Malin M.C. (1975) Geol. Soc. Amer. Bull. 86, p. 593-609. (2) Baker V.R. and Milton D.J. (1974) Icarus 23, p. 27-41. (3) Baker V.R. and Kochel R.C. (in press) J. Geophys. Res. (4) Sharp R.P. (1973) J. Geophys. Res. 78, 4073-4083. (5) Pieri D. and Sagan C. (1979) N.A.S.A. Tech. Memo. 80339, p. 349-352. (6) Galloway R.W. (1976) C.S.I.R.O. Land Research Series 38, p. 52-70. (7) Stearns H.T. and Vaksvik K.N. (1935) Hawaii Div. Hydrography Bull. 1, 479p. (8) Wentworth C.K. (1928) Jour. Geol. 36, p. 385-410. (9) Wentworth C.K. (1943) Geol. Soc. Amer. Bull. 54, p. 53-64.

DEBRIS FLOWS AND DEBRIS AVALANCHES IN THE LARGE MARTIAN CHANNELS

Nummedal, Dag, Department of Geology, Louisiana State University, Baton Rouge, Louisiana 70803

It has already been proposed that a debris flow mechanism could account for the formation of the large channels debouching into Chryse Planitia from the adjacent southern uplands (Nummedal, 1979). The debris is thought to have originated through a mechanism of collapse producing the chaotic terrains which exist at the head of these channels. Collapse through localized excess pore water pressure (Carr, 1979), or subsurface liquefaction (Nummedal, 1978), are two mechanisms both capable of producing the debris. The proposed debris flows are based on the numerous morphological similarities between the Mars channel source areas and the heads of both subaerial and subaqueous terrestrial debris flows.

The purpose of this paper is to present evidence that the debris flow gained mobility as it moved downstream, turning into a catastrophic debris avalanche through a mechanism of strain-dependent viscosity decrease. This would have been aided by two factors: (1) melting of ice particles in the debris by friction-generated heat, and (2) increase in buoyancy of large particles due to the production of an increased number of fine particles by the debris movement.

When the debris reached the margin of Chryse Planitia, the movement had changed from the pattern of a shearing debris flow to a highly turbulent debris avalanche, carrying cobble and boulder-sized rocks highly dispersed in a medium of fine dust and vapor. The Huascarán debris avalanche (sturzstrom), triggered by a Peruvian earthquake in 1970, had such a composition and moved at a maximum velocity of above 400 km/h (Erickson *et al.*, 1970). The material carried by the debris avalanche would have been deposited as a thin blanket over a large area of the

Chryse Planitia basin, creating virtually no depositional relief.

Southern Chryse Planitia, where the 5 large channels discussed in this paper debouch, is characterized by numerous streamlined remnants, with long-axes oriented parallel to inferred flow direction, anastomosing channel patterns, extensive fields of linear grooves, and some erosional scour depressions upstream of remnants in the inferred flow paths. These features are strongly suggestive of erosion by catastrophic flows (Carr et al., 1976). It is argued that these catastrophic flows were the distal parts of the debris flows of the Chryse channels. The morphology of the basin floor, the inferred thickness of any sedimentary deposit and the clast size distribution of the Viking Lander 1 site support this contention.

REFERENCES

- Carr, M. H., Formation of martian flood features by release of water from confined aquifers, J. Geophys Res. 84, p. 2995-3007, 1979.
- Carr, M. H., H. Masursky, W. A. Baum, K. R. Blasius, G. A. Briggs, J. A. Cutts, T. Duxbury, R. Greeley, J. E. Guest, B. A. Smith, L. A. Soderblom, J. Veverka, and J. B. Wellman, Preliminary results from Viking orbiter imaging experiment, Science, 193, 766-776, 1976.
- Ericksen, G. E., G. Pflaker and J. V. Fernandez, Preliminary report on the geological events associated with the May 31, 1970, Peru earthquake, U.S. Geological Survey Circular 639, 25 p., 1970.
- Nummedal, D., The role of liquefaction in channel development on Mars (abstract), Reports of the Planetary Geology Program, 1977-78, NASA Tech. Memo, 79729, 257-259, 1978.

Nummedal, D., Mechanics of fluid release on Mars,
(abstract), Second International Colloquium on Mars,
NASA Conf. Publ. 2072, 63, 1979.

SAPPING: NETWORK STRUCTURE IN TERRESTRIAL AND MARTIAN VALLEYS

Pieri, David C.¹, Michael C. Malin², and Julie E. Laity¹

1. Jet Propulsion Laboratory, Pasadena, CA, 91103

2. Department of Geology, Arizona State University,
Tempe, AZ, 85281

Martian valleys exhibit a range of network patterns from which the classic dendritic pattern is notably absent (figure 1.) (Pieri, 1979). Martian networks are generally characterized by a tendency for major trunk segments to coalesce near system mouths and by strong parallelism between network segments. Intervalley areas within networks consist of undissected plateau surfaces with no evidence of intra-network competition for the undissected terrain: no drainage divides are visible. Martian valleys exhibit steep walls and flat floors. On Mars, small low-magnitude tributaries possess cross-sections comparable in area to main trunk segments and enter them at typically low junction angles. Further, a detailed analysis of the overall systematics of network junction angles in martian networks reveals little organization of the kind present in terrestrial dendritic networks formed predominantly by rainfall-supplied overland flow. From the point of view of both morphology and planimetric form, there is little compelling evidence to suggest that martian valley networks formed by overland flow fed by rainfall. Rather, based in part on the observations above, we infer martian valley formation and network growth to have occurred by sapping processes.

An investigation of valley planimetric form and morphology is underway for both terrestrial and martian valley networks in an effort to quantify the aspects of process, structure, and materials which are influential in the development of both of these factors. Parameters include junction angle systematics (after Pieri, 1979), link length and directionality statistics, degree of intervalley competition and overall network character. As part of this investigation, field studies are underway in southeastern Utah in the canyons of the Colorado Plateau (Laity et al. and Malin et al., this report). Preliminary reconnaissance indicates that these canyon networks are analogous to martian valley systems (often termed "small channels"), of the type dealt with extensively by one of the authors (Pieri, 1976; 1977a,b; 1978; 1979a,b; Pieri and Sagan, 1978; 1979) and recently by Carr (1979), in both morphology, planimetric form, and, to a lesser degree, scale. As is pointed out in Laity et al. (this report), from Landsat images, aerial photographs, and topographic maps, Colorado Plateau networks often display a modified trellis pattern (e.g. Iceberg and Forgotten Canyons at Lake Powell),

similar to martian rectilinear valley systems (Pieri, 1979). This pattern tends to occur where the main valley system elongation is perpendicular to major NE-SW structural trends. More strongly aligned parallel valley systems (e.g. Cow Canyon at Lake Powell) develop when the main system elongation is in the same direction as regional structural trends. All canyon systems in the Lake Powell area have a digitate character in that major trunk links intersect near the canyon mouths as is very common in martian valley networks (Pieri, 1979; Pieri and Malin, in preparation). Several of these systems have been reconnoitered (Iceberg, Escalante River, and Moki Canyons). All appear to be extending or to have extended at one time by headward sapping into sandstone, with active seeps observed in several sapping alcoves (Laity et al., this report). Amphitheater terminations typically occur and many low magnitude tributaries have roughly similar cross-sections to main trunk segments. Thus, the analogy to martian valley networks with characteristically similar morphology and planimetric form is strong.

Many obvious questions arise as to the mode of formation and history of the Colorado Plateau canyons and as to their suitability as martian analogs. With regard to network structure, there are at least several: (1) what are the factors influencing bifurcation?; (2) are first magnitude tributaries preferentially elongated as on Mars? (Pieri, 1977a); (3) does the gross canyon network planimetric pattern show a systematic character with regard to tributary junction angles as do dendritic fluvial systems or is it more like martian networks (i.e. more random)?; (4) can link length and link directionality be correlated with regional structural trends?; and (5) most generally, what can planimetric form and morphology tell about the underlying structure, constituent materials, and formation processes for both terrestrial and martian valleys?

- Carr, M.H., 1979, Distribution of small channels on Mars, in Reports of Planetary Geology Program, 1978-79, p.337, NASA TM-80339, 461p.
- Laity, J.E., D.C.Pieri, and M.C.Malin, this report, Sapping processes in tributary valley systems
- Malin, M.C., J.E. Laity, and D.C.Pieri, this report, Sapping: Analog studies on Earth and Mars
- Pieri, David C., 1976, Distribution of small channels on the martian surface, Icarus, 27, p.25-50.
- _____, 1977a, Small channels in the Margaritifer Sinus region: Implications for climatic change, abstr., Bull. Amer. Astron. Soc., 9, p.539
- _____, 1977b, Preliminary statistical analysis of some martian channel networks, in Reports of Planetary Geology Program, 1976-77, p.168 NASA TM-X3511, 294p.
- _____, 1978, Small channels on Mars from Viking Orbiter, in Reports of Planetary Geology Program, 1977-78, p.267, NASA TM-79729, 356p.
- _____, 1979a, Global distribution of martian valley networks, in Reports of Planetary Geology Program, p.353, NASA TM-80339, 461p.
- _____, 1979b, Geomorphology of Martian Valleys, doctoral thesis, Cornell University, 288p.

SAPPING PROCESSES IN TRIBUTARY VALLEY SYSTEMS

Laity, Julie E. and David C. Pieri, Jet Propulsion Laboratory, Pasadena, CA, 91103, and Michael C. Malin, Dept. of Geology, Arizona State University, Tempe, AZ, 85281

Sapping has been proposed as an important mechanism for valley extension on Mars and in some terrestrial valley systems which exhibit similar network pattern and morphology. Sapping is defined as a process by which valleys extend headward or slopes retreat owing to the collapse of valley walls following the undermining of basal support. Valley systems which evolve predominantly by sapping differ considerably from fluvially eroded systems in morphology, network pattern, and in process of formation. Nevertheless, few studies have addressed the role of sapping in drainage evolution. Those few workers who have examined this process in detail have aimed their research at small-scale features such as seepage lines in the soil profile. The function of sapping in determining the form of certain large valleys is not fully understood, although it is generally recognized that seepage lines related to the groundwater table are highly significant in the formation of the escarpment dry valleys in Europe (Small, 1964), in steep-walled box canyons in basalts of the Hawaiian Islands (Hinds, 1925; Wentworth, 1928), in the wadis of the Libyan desert (Peel, 1941), and in numerous tributary canyons of the Colorado Plateau (Gregory, 1917; Bryan, 1928; Campbell, 1973).

Field work has been initiated to investigate sapping and canyon formation on the Colorado Plateau. Numerous steeply descending, box-headed tributaries enter the main channel, incised throughout much of the region into the Glen Canyon Group - Navajo, Kayenta, and Wingate sandstones. Tributary valley systems on the Colorado Plateau are morphologically analogous to martian valley systems (Pieri, 1979), based on a similarity of network pattern, amphitheatre terminations of first order tributaries, large scale, and evident structural control. Seepage and sapping along the canyon walls operates largely as a mass movement phenomenon, similar to scarp retreat, but may exploit zones of structural weakness such as joints. Only local rainfall events contribute to the intermittent flow of the tributary canyons and sapping is at least as important as fluvial erosion in extending and modifying the valleys.

The role of sapping in valley development is dependent on many lithologic, structural and climatic controls. The weathering process involved in sapping is primarily one of slow grain release resulting from the interaction of chemical weathering, hydraulic action, freeze-thaw action, and salt efflorescence and crystallization. Chemical weathering is probably the most significant process. Grain release is facilitated by water carrying in solution the local cementing agent. Alcoves commonly mark the sites of groundwater emergence, and may range in size from centimeters to many tens of meters.

An important structural control is the jointing pattern which modifies canyon morphology in two important ways. The spatial relations of the regional joint set exert considerable control on the drainage pattern and an elongation along the structural trends is clearly evident on topographic maps and on aerial photographs, often appearing as a modified trellis pattern. These large-scale regional joint sets increase the permeability of the sandstone, and serve as pipes for laterally flowing subsurface water (Campbell, 1973). The water emerges at a seepage point in the cliff face, commonly at an alcove, and the canyon migrates headward along the joint lines as sapping undermines the steep cliff faces and causes the collapse of massive sandstone slabs. Canyon cutting along this main regional jointing system stimulates exfoliation joint development in response to relief of pressure along a topographic surface (Bradley, 1963; Bjerrum, 1968). The joints develop generally parallel to the canyon walls and thereby help maintain steep walls through vertical cliff recession in the form of slab failures (Robinson, 1970). Factors which affect the stability of the cliff include the strength of the rock mass, the development of water pressures within joints, the degree of sapping, and the rate of removal of talus beneath the free face.

The persistence of cliff forms and headcuts is a function of the weathering and transportation processes. On the Colorado Plateau, the accumulation of talus is generally very small. Experimental evidence (Schumm and Chorley, 1966) and observations during field reconnaissance of the area suggest rather rapid weathering rates. Fresh cross-sections of talus cones exposed by slumping show a large percentage of fine material. Mechanically weak sandstones shatter readily upon impact and are further reduced by active weathering processes. The means by which material is removed from talus cones into the stream channel is not well documented and is presently under investigation. It is likely, however, that the finer material is moved from the cone by a combination of surface wash, subsurface flow and undermining, gravity fall, and wind action. Flash floods and strong winds remove debris accumulation in the stream bed.

Our research into the development of tributary valley systems on the Colorado Plateau and other areas stresses the similarities and differences in sapped- and fluvially-derived systems in an effort to understand processes operating in valley systems on Mars. The rates and means of erosion and headcut retreat are being examined, the sediment budget estimated by determining weathering and transportation rates and mechanisms, and instrumentation developed to monitor the hydrologic regime of surface and subsurface flow and to measure the physical environment of canyon alcoves.

References

- Bjerrum, L. and Jørstad, F., 1968, Stability of rock slopes in Norway: Norwegian Geotech Inst, Pub, 79, p. 1-11
- Bradley, W.C., 1963, Large-scale exfoliation in massive sandstones of the Colorado Plateau: Geol. Soc. Amer. Bull., v. 74, no. 5, p. 519-527
- Bryan, K., 1928, Niches and other cavities in sandstone at Chaco Canyon New Mexico: Zeitschr, für Geomorph., v. 3, p. 125-140
- Campbell, I.A., 1973, Controls of canyon and meander forms by jointing: Area, v. 5, no. 4, p. 291-296
- Gregory, H.E., 1917, Geology of the Navajo Country: U.S. Geol. Survey Prof. Paper 93, 161 p.
- Hinds, N.E.A., 1925, Amphitheater valley heads: J. of Geology, v. 33, p. 816-818
- Peel, R.F., 1941, Denudational landforms of the central Libyan Desert: Jour. Geomorphology, v. 4, no. 1, p. 3-23
- Pieri, D.C., 1979, Geomorphology of martian valleys, Doctoral Thesis, Cornell University, 288 p.
- Robinson, E.S., 1970, Mechanical disintegration of the Navajo Sandstone in Zion National Park, Utah: Geol. Soc. Amer. Bull., v. 81, p. 2799-2806
- Schumm, S.A., and Chorley, R.J., 1966, Talus weathering and scarp recession in the Colorado Plateau: Zeitschr. für Geomorph., v. 10, P. 11-36
- Small, R.J., 1964, The escarpment dry valleys of the Wiltshire Chalk: Inst. Brit. Geog. Trans., Pub. No. 34, p. 33-52
- Wentworth, C.K., 1928, Principles of stream erosion in Hawaii: J. of Geology, p. 385-410

SAPPING: ANALOG STUDIES ON EARTH AND MARS

Malin, Michael C.¹, Julie E. Laity² and David C. Pieri²

- 1) Department of Geology, Arizona State University, Tempe, AZ 85281
- 2) Jet Propulsion Laboratory, Pasadena, CA 91103

From the earliest analyses of Mariner 9 images of the surface of Mars (1-5), it has been recognized that many features there resembled those produced on Earth by processes known collectively as "sapping". Sapping refers principally to headward growth, by undermining and collapse; cliff recession and transverse (as distinguished from longitudinal) valley enlargement are two additional aspects worthy of note. Although such diverse features of the martian landscape as fretted terrain (5) and the south-rim canyons "tributary" to the Valles Marineris (4) have been attributed to sapping processes, our emphasis has been on understanding the formation of the so-called "small channels" or valley networks on Mars.

A multi-faceted approach to the assessment of sapping is currently underway (see, e.g. 6,7). This approach includes:

- a) field studies in the Colorado Plateau, examining sapping in sandstones (6)
- b) field studies in Iceland, examining valleys formed by headward erosion in palagonites and basaltic tephra mantles (8)
- c) laboratory analyses of specimens collected from field areas, including scanning electron microscopy
- d) photogeological studies of valley morphology on Earth and Mars
- e) photogeological studies of valley network systematics on Earth and Mars (7).

Initial field studies will begin in 1980. Reconnaissance visits were conducted in 1977 and 1979. Of specific interest are quantitative measurements of the various processes that contribute to sapping, the effects of material on these processes, and the rates at which the processes work.

Preliminary results suggest that constraints may be placed on the physical properties of martian surface layers, on the role of liquid water and eolian deflation, and on the timescales for erosion, relative to the formation of the martian valley networks. Specifically, variations in canyon wall morphology within Glen Canyon and its Iceberg and the Moki Canyon tributaries suggest that subtle variations in material coherence may strongly affect outcrop expression. Further, evolution of talus deposits from coarse to fine debris seems, in some instances, to be a controlling factor in producing the overall gross

morphology of sapped canyons. Implications for these and other findings for Mars valleys are currently under study.

References

- 1) Sharp, R. P. (1972) Personal communication and memoranda to Mariner 9 Imaging Team, March-April, 1972.
- 2) McCauley, J. F., M. H. Carr, J. A. Cutts, W. K. Hartmann, H. Masursky, D. J. Milton, R. P. Sharp, and D. E. Wilhelms (1972) Preliminary Mariner 9 report on the geology of Mars. *Icarus* 17(2), 289-327.
- 3) Milton, D. J. (1973) Water and processes of degradation in the martian landscape. *J. Geophys. Res.* 78(20), 4037-4047.
- 4) Sharp, R. P. (1973a) Mars: Troughed terrain. *J. Geophys. Res.* 78(20), 4063-4072.
- 5) Sharp, R. P. (1973b) Mars: Fretted and chaotic terrains. *J. Geophys. Res.* 78(20), 4073-4083.
- 6) Laity, J. E., D. C. Pieri, and M. C. Malin (1980) Sapping processes in tributary valley systems (abstract). Reports of Planetary Geology Program, 1979-1980 (this volume).
- 7) Pieri, D. C., M. C. Malin, and J. E. Laity (1980) Sapping: Network structure in terrestrial and martian valleys (abstract). Reports of Planetary Geology Program, 1979-1980 (this volume).
- 8) Malin, M. C. (1980) Studies of fluvial, eolian and sapping processes in Iceland (abstract). Reports of Planetary Geology Program, 1979-1980 (this volume).

STUDIES OF FLUVIAL, EOLIAN, AND SAPPING PROCESSES IN ICELAND

Malin, Michael C., Department of Geology, Arizona State University,
Tempe, AZ 85281

Where on Earth would one look for features formed by processes operating on materials comparable to those on Mars? The search for reasonable analogs to martian landforms has led to the Antarctic Dry Valleys (1) and an analysis of eolian and periglacial processes; to the coastal deserts of Chile (2,3) and further studies of eolian features; to Alaska (4) and an analysis of "thermokarst"; and to Iceland (5,6,7) and examination of subglacial volcanism, the landforms thus produced, and related catastrophic flood features.

Iceland is, perhaps, the best locale to study Mars analogs, because its interior deserts are remarkably Mars-like: cold, relatively dry (most precipitation is snow and infiltration rates are high), entirely volcanic materials (including basaltic lavas, palagonites, and large amounts of basaltic tephra) acted upon by strong, often unidirectional seasonal winds, catastrophic floods, and ground water sapping. Features developed within these deserts resemble those on Mars not only in form, but occasionally in scale.

The study currently underway is designed to examine each of the processes active in shaping the Icelandic deserts individually, and more importantly, in areas where they collaborate. The approach is four-fold:

- 1) photogeological study of landforms and analysis of multi-spectral data of the selected area, including aerial photographs, airborne remote sensing scanner data, and Landsat and Seasat data;
- 2) field mapping of the stratigraphic relationships of volcanic materials and the chronology of the geomorphic changes produced by erosion and deposition;
- 3) field "test plot" observations to acquire quantitative measurements of the amounts and rates of material transport;
- 4) laboratory analyses of selected samples to gain understanding of the effects of transport on the volcanic materials (and vice versa).

The field area to be examined during the summer of 1980 includes the Holuhraun, Vikursandur and Grjóf deserts in mid-eastern Iceland, north of Vatnajökull, south and east of Askja Caldera, and bounded on the east by the Jokulsá á Fjöllum - the area is part of the great east-central desert, Oðafahraun.

Preliminary photogeologic studies suggest a series of catastrophic floods have traveled in excess of a hundred kilometers to the north through relatively constricted paths between mobergs ("tablemountains" formed by subglacial volcanism). Both large (several km) teardrop-shaped islands and zones of smaller longitudinal grooves attest to the scale and power of these floods. Pre-existing basalt flows show unusual surface textures, perhaps resulting from plucking by the floods. In several areas, flood plain deposits and large tracts of eolian deposits cover basalts both eroded and not eroded by floods. Later basalts can be found overlying these deposits. Continuing eolian and flood activity has modified, both by erosion and deposition, all of these units. Ground water sapping appears to have played an important role in the evolution of pyroclastic and palagonite deposits. Deep gullies extending headward and terminating in steep, box- or U-shaped head-walls are found in hills of "soft", rounded morphology interpreted to be palagonite deposits supporting no discernable over-land drainage. Similar but smaller features are found in tephra deposits, as on the flank walls of Askja Caldera. The results of the action of these processes is to produce extremely diverse landforms much like those seen on Mars.

References

- 1) Morris, E. C., T. A. Mutch and H. E. Holt (1972) Atlas of geologic features in the Dry Valleys of South Victoria Land, Antarctica. U.S. Geological Survey Interagency Report: Astrogeology 52, 156 pp.
- 2) Grolier, M. J., G. E. Erickson, J. F. McCauley and E. C. Morris (1973) The desert landforms of Peru: A preliminary photographic atlas. U.S. Geological Survey Interagency Report: Astrogeology 57, 146 pp.
- 3) McCauley, J. F., M. J. Grolier, and C. S. Breed (1977) Yardangs of Peru and other desert regions. U.S. Geological Survey Interagency Report: Astrogeology 81, 177 pp.
- 4) Gatto, L. W. and D. M. Anderson (1975) Alaskan thermokarst terrain and a possible martian analog. *Science* 188, 255-257.
- 5) Nummedal, D. (1975) personal communication.
- 6) Hodges, C. A. and H. J. Moore (1978) Tablemountains on Mars (abstract). *Lunar and Planetary Science IX*, 523-525.
- 7) Allen, C. A. (1979) Subglacial volcanism (abstract). Reports of Planetary Geology Program, 1978-1979 (NASA TM 80339), 251-253.

Chapter 8

REMOTE SENSING OF PLANETARY SURFACES: INTERPRETATION AND TECHNIQUES

RADAR, VISUAL AND THERMAL CHARACTERISTICS OF THE THARSIS-MEMNONIA-AMAZONIS LAVA FLOWS ON MARS*

Schäber, Gerald G., U.S. Geological Survey, Flagstaff, Arizona 86001

The early, high-periapsis Viking images provided excellent synoptic coverage of the entire region of Tharsis Montes, Memnonia, and Amazonis, and clearly delineated a great profusion of overlapping lava sequences (1,2). As in the case of Mariner 9, however, the moderate resolution (200-400 m/pixel) of the early Viking Orbiter frames was insufficient to resolve any morphologic details on the flow surfaces. Following the lowering of both Viking Orbiter spacecrafts' periapsis to 300 km, image sequences were uplinked to the spacecrafts to obtain very high resolution (as few as 10 m/pixel) for targets of geologic interest. The resulting pictures are spectacular and of significant importance in assessing the validity of radar-derived surface roughness information and in interpreting the thermal characteristics of the surface materials (figs. 1, 2).

Surface morphology portrayed on approximately 70 high-resolution (10-20 m/pixel) Viking Orbiter images of the Tharsis-Memnonia-Amazonis region is compared to root mean square slope and surface grain sizes obtained from earth-based radar and Viking thermal data, respectively. The Viking Orbiter images contain information on surface roughness at 25 m and larger lateral scale, whereas earth-based radar observations are sensitive to surface undulations at lateral scales generally between 1 m and 30 m, sometimes more (3,4). Information on surface thermal conductivity and grain sizes can be inferred directly from measurements of thermal inertia or pre-dawn temperature residuals (5,6). Analysis of these data sets indicates a good correlation between visually observed roughness and radar-derived rms slopes at these scale lengths. Variable but generally high rms slopes predicted for the Tharsis-Memnonia-Amazonis volcanic plains from the radar observations are qualitatively confirmed with the Viking image data.

The lava flows of the Tharsis-Memnonia-Amazonis region vary greatly in surface roughness at the 1 to 200 m lateral scale and 1 to 5 m vertical scale. The great majority of these flows appear to be mantled with at least a thin layer of fine-grained material. A possible exception may occur just southeast of Arsia Mons, described by Kieffer et al. (5) as an area of elevated pre-dawn temperature residuals or higher thermal inertia. A similar thermal anomaly (similar in plan, not in magnitude) was reported by Zimbelman and Kieffer (6) in the same relative location southeast of Ascræus Mons. The exact nature of these surfaces is unknown because of the lack of any currently available

*Manuscript with slightly modified title submitted Nov. 1979 to Icarus.

high-resolution Viking Orbiter image data; however, no distinct surface features can be seen on the moderate-resolution Viking images. A possible explanation is eolian erosion: fine-grained material in these regions may be kept at a minimum by downslope westerly winds driven by differences in thermal gradient (7).

The strong thermal contact marking the south boundary of the 22×10^6 km² Tharsis-Memnonia-Amazonis region of low thermal inertia (5,6) appears to represent a transition between surfaces with a recent, dynamic mantle of fine-grained (10 to 100 microns) eolian material (lower inertia) and surfaces with an older, more stable mantle (higher inertia) (figs. 1, 2).

The presence or absence of a recent mantle of fine-grained eolian material on the volcanic surfaces studied was determined by the visibility of fresh impact craters smaller than 50 m in diameter. Lava flows south and east of Arsia Mons (within the large region of low thermal inertia centered on Tharsis Montes) were found to have such a recent mantle. At pre-dawn residual temperatures at or above -10° K (the south boundary of this low-temperature region), lava flows were found to have relatively old eolian mantles (abundant impact craters < 50 m in diameter).

This analysis of young volcanic planar surfaces shows that the earth-based radar observations of rms slope can be satisfactorily assessed by extrapolating information from Viking Orbiter images with high resolution between 10 m/pixel and 20 m/pixel. In addition, high-resolution images contain important clues (that is, the presence or absence of small impact craters) that aid in interpreting pre-dawn temperature residuals and thermal inertia. There appears to be little correlation between the thermal data and earth-based radar returns in regard to inferences that can be made as to the nature of the surficial materials. This lack of correlation is significant and emphasizes the different scales of surface roughness to which each sensor is sensitive. Together, the thermal, visible, and radar data contain mutually complementary geologic information.

REFERENCES

- 1) Carr, M. H., Greeley, Ronald, Blasius, K. R., Guest, J. E., and Murray, J. B., 1977, J. Geophys. Res., 82, p. 3985-4015.
- 2) Schaber, G. G., Horstman, K. C., and Johnson, D. A., 1979, Lunar and Planetary Sci. Conf., X, Houston, Tx., Proc., p. 1058-1060.
- 3) Downs, G. S., Goldstein, R. M., Green, R. R., Morris, G. A., and Reichley, P. E., 1973, Icarus, 18, p. 3-21.
- 4) Simpson, R. A., Tyler, G. L., and Campbell, D. B., 1978, Icarus, 33, p. 102-115.

- 5) Kieffer, H. H., Martin, T. Z., Peterfreund, A. R., Jakosky, B. M., Miner, E. D., and Palluconi, F. D., 1977, J. Geophys. Res., 82, p. 4249-4291.
- 6) Zimbelman, J. R., and Kieffer, H. H., 1979, J. Geophys. Res., Mars II volume, in press.
- 7) Peterfreund, A. R., Kieffer, H. H., and Palluconi, F. D., 1977, Lunar Science, VIII, Houston, p. 765-767.



Figure 1

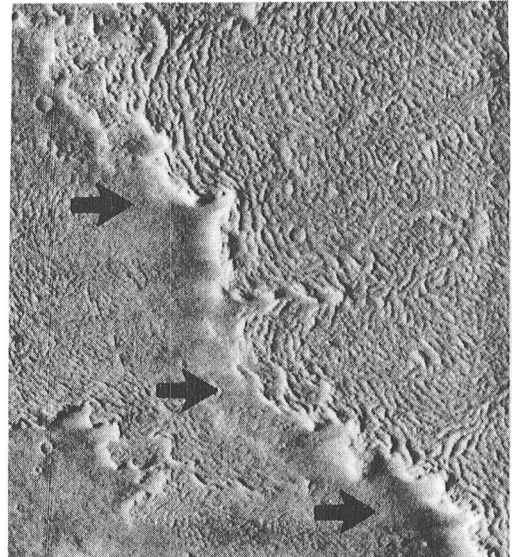


Figure 2

Figure 1.--Viking Orbiter frame 769A09 (10 m/pixel) showing knobby, 35-m-thick lava flow overlying surface with greatly subdued relief. Location is 22.7° S; 119.9°. Frame height is 13 km, frame width 12 km. Solar illumination angle is 5.4°. Presence of many small (< 50-m-diameter) impact craters on both surfaces implies absence of a recent eolian mantle. This surface lies outside the Tharsis-Memnonia-Amazonis region of low thermal inertia at about 0° predawn temperature residual (5). North is up.

Figure 2.--Viking Orbiter frame 731A41 (15 m/pixel) showing three stratigraphic flow levels north of Memnonia Fossae at 2.8° S; 138.2°. Frame height is 17 km, frame width 16 km. Solar illumination angle is 16°. Thickness of eolian mantle increases with increasing age of underlying units. Curvilinear, parallel ridges and troughs are well developed. Note concentration of eolian fine-grained material against 50-m scarp of upper flow (arrows). No small (< 50-m-diameter) impact craters are visible; all are mantled. This surface lies within the Tharsis-Memnonia-Amazonis region of low thermal inertia at about -16° K predawn temperature residual (5). North is up.

CORRELATIONS BETWEEN EARTH-BASED RADAR AND MARTIAN LANDFORMS IMAGED BY THE VIKING ORBITERS

Mouginis-Mark, P.J., Dept. of Geological Sciences, Brown Univ., Providence, RI 02912; Zisk, S.H., NEROC Haystack Observatory, Westford, MA 01886; and Pettengill, G.H., Dept. of Earth and Planetary Sciences, Mass. Inst. of Technology, Cambridge, MA 02139

As part of a program to characterize the surface units of Mars by remote sensing techniques, we are attempting to correlate features illustrated in Viking Orbiter photographs with the 1973 opposition 70 cm radar data derived at Arecibo Ionospheric Observatory by Pettengill *et al.*¹ Similar attempts to locate radar data have been made using Mariner 6, 7, and 9 images and the Arecibo or Goldstone radar data.²⁻⁵ The improved resolution of Viking images, however, provides the opportunity to correlate specific radar profiles and surface features to a sufficiently high accuracy that the measured radar reflectivity and other parameters can be used to aid in the characterization of observed geological units.

The Arecibo data base consists of 1379 point measurements of: 1) surface elevation; 2) surface roughness (a measure of the mean randomness of radar scattering facets); and 3) reflectivity (a function of the dielectric constant of the surface material). Each sample represents a superposition of several point measurements. A combination of the measuring technique and the best previous planetary ephemeris provides the latitudes and longitudes of the radar points.

We have found in our attempts to match radar topography with surface features shown on Viking images and the topographic map⁶ that a problem exists in matching the two data sets.

To date, the "best fit" of the data reveals an offset of 0.3° latitude and 0.7° longitude (radar = control net + offset). We illustrate the correlation between radar and topographic features in Fig. 1 with four profiles across an area in the Margaritifer Sinus Quadrangle,⁷ centered close to the morphologically fresh crater Jones (19°S, 20°W). This area is interpreted⁸ to be predominantly hilly and cratered material.

Viking images reveal an undulating rugged terrain with many degraded craters larger than 30 km diameter and numerous dendritic channel systems⁹ 60-350 km in length and 3-12 km wide.

Fig. 2 displays the associated elevations, surface roughness (c-factor) and inherent reflectance values for each profile. The topography indicates a gently eastward sloping surface that has been dissected by a channel system ~2.5 km deep. Several craters showing 200-500 meters of relief are also evident. Note the generally good negative correlation between c-factor and reflectivity values. As a measure of surface roughness, the c-factor is related to rms surface slope θ_{rms} by¹⁰

Mouginis-Mark, P.J. *et al.*

$$\theta_{\text{rms}} = c^{-1/2}$$

for $c \gg 1$. Also, the inherent radar reflectivity ζ is related to the mean surface dielectric constant, ξ , by (e.g.,¹⁰)

$$\xi = \left[\frac{1 + \zeta^{1/2}}{1 - \zeta^{1/2}} \right]^2$$

The above-mentioned correlation, therefore, implies that smooth areas are composed of low reflectance (= dielectric constant) material, e.g., terrain mantled by fine particles or other poorly compacted material; whereas the rougher areas, with their higher dielectric constant, are likely to be exposed or nearly exposed rock.

In many places, the smooth areas are also topographically low, which tends to confirm the picture of eolian material collecting in low, sheltered areas. Some profiles, on the other hand, show the quasi-mantled radar character at higher elevations (e.g., pt. A in Fig. 2), but still lie in an area with relatively flat topography. Conceptually, there could exist areas with low dielectric constant and high roughness (e.g., a very thick mantling layer with surficial dunes or hummocks) and also high dielectric constant and low roughness (e.g., a smooth bedrock layer or a massive pahoehoe lava flow). Examples of the former type are certainly evident from Viking photography^{11,12,13} and are being investigated at present.

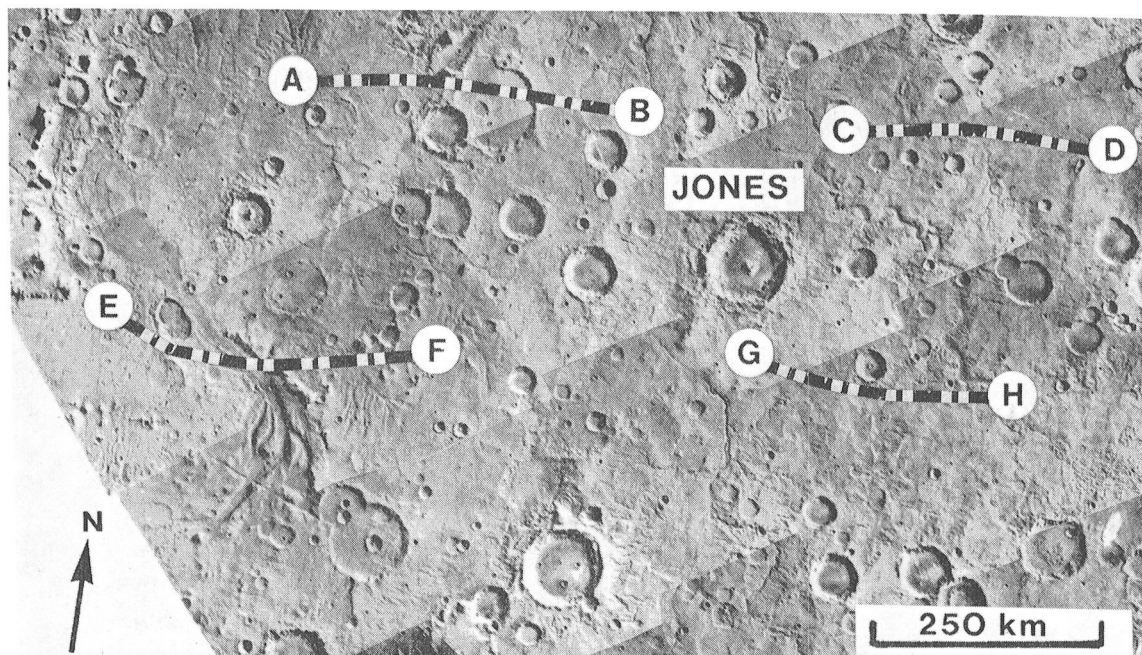


Fig. 1: Location of the four radar swaths discussed in text. IPL mosaic 211-5821.

CORRELATIONS BETWEEN EARTH-BASED RADAR AND MARTIAN LANDFORMS

Mouginis-Mark, P.J. et al.

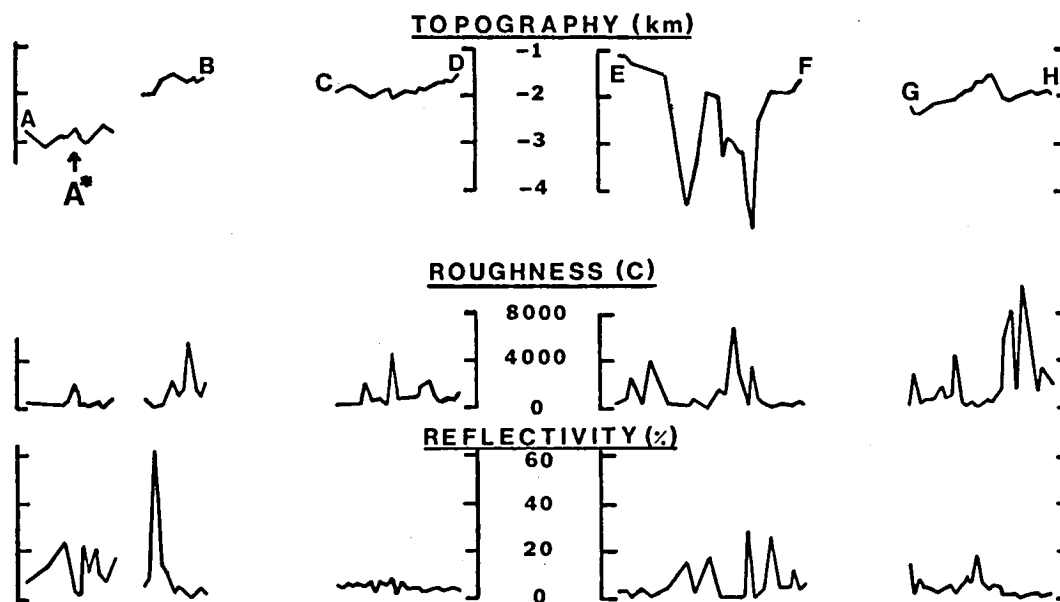


Fig. 2: Topography, roughness, and reflectivity values derived from radar data. For location of each profile, see Fig. 1.

References: ¹Pettengill G.H. et al. 1975, pers. comm. ²Pettengill G.H. et al. 1971, Science 174, 1321-1324. ³Pettengill G.H. et al. 1973, Icarus 18, 22-28. ⁴Downs G.S. et al. 1975, Icarus 26, 273-312. ⁵Roth L.E. et al. 1979, NASA TM-80339, 436-437. ⁶USGS Map I-961. ⁷USGS Map I-975. ⁸Scott D.H. and Carr M.H. 1978, USGS Map I-1083. ⁹Pieri D. 1978, NASA TM-79729, 267. ¹⁰Evans J.V. and Hagfors T. 1968, Radar Astronomy, McGraw-Hill, NY. ¹¹Breed C.S. et al. 1979, NASA TM-80339, 282-285. ¹²Tsoar H. et al. 1979, NASA TM-80339, 316-318. ¹³Mutch T.A. et al. 1976, Science 194, 87-91.

Scattering of Light from Particulate Surfaces. V. A Simple, Approximate Photometric Function for Surfaces of Arbitrary Albedo. J. Goguen and J. Veverka, Cornell University.

We have developed a photometric function for particulate surfaces of arbitrary albedo which is simple in form, yet soundly based in radiative transfer theory. For light incident from an angle i ($\mu_0 = \cos i$) and viewed from an angle ϵ ($\mu = \cos \epsilon$) relative to the normal, the ratio R of the intensity scattered from the sample surface to that from a reference surface at a fixed geometry is

$$R = A\phi(\alpha, g) \frac{\mu_0}{\mu + \mu_0} \{B(\mu + \mu_0) + B^2\mu\mu_0 + S(\alpha, D)\}$$

where α is the phase angle, ϕ the single particle phase function and S the shadowing function derived by Irvine (1966) and Hapke (1963). The four parameters characterizing the scattering are A , a normalization factor dependent on the single particle albedo; B , the degree of multiple scattering; g , the mean value of $\cos \alpha$ describing the degree of forward/backward scattering; and D , determined by the average particle separation. Derivation of this scattering law uses three approximations: 1) mutual particle shadowing is important only on the first scattering and obeys the description of Irvine (1966); 2) second and higher order scattering is independent of the single particle phase function and can be replaced by isotropic scattering (Chandrasekhar, 1960); 3) the H -functions comprising the isotropic scattering solution are linear in μ and μ_0 (Goguen, 1979).

To test the ability of this theoretical photometric function to match laboratory data, we have least squares fit the model to goniometry of mixtures of MgO and charcoal powders (Veverka et al., 1978; Goguen and Veverka, 1979). The results are shown in Figure 1 where the agreement between data (points) and model (lines) is good, even though the surface range in normal reflectance from 0.04 to 0.69 and phase angles up to 120° are included. One set of parameters generated all the curves shown for each sample and fit points along the mirror meridian ($i = \epsilon$, not shown) as well. Considering that the surfaces are binary mixtures of two radically different particle types, one black and one white, the agreement is excellent.

References

- Chandrasekhar, S. (1960). Radiative Transfer. Dover, New York.
- Goguen, J. (1979). Ph.D. Thesis, Cornell University, Ithaca, New York (in preparation).
- Goguen, J., and Veverka, J. (1979). (Abstract) Reports of Planetary Geology Program, 1978-79, NASA Tech. Mem. 80339, 405-406.
- Hapke, B. W. (1963). J. Geophys. Res. **68**, 4571-4586.
- Irvine, W. M. (1966). J. Geophys. Res. **71**, 2931-2937.
- Veverka, J., Goguen, J., Yang, S., and Elliot, J. L. (1978). Icarus **33**, 368-379.

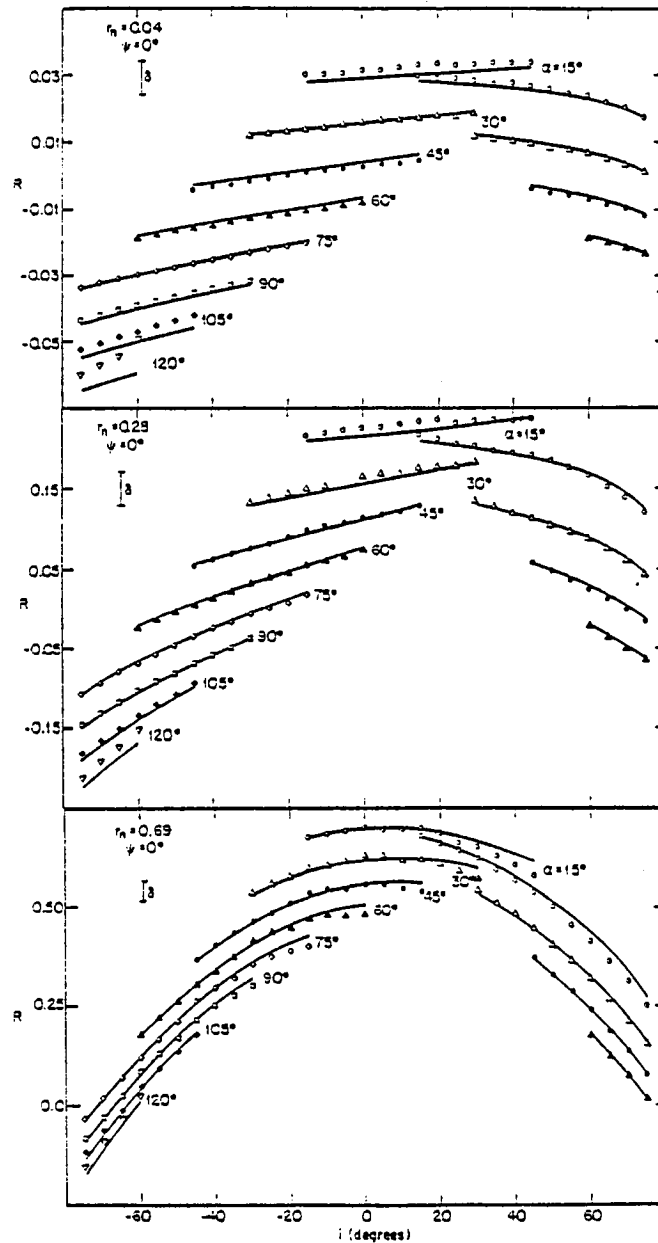


FIGURE 1. A comparison of our theory-based photometric function with goniometry of MgO/charcoal mixtures. R , the intensity relative to a reference surface at a fixed geometry, is plotted against i , the angle of incidence, for points lying along the photometric equator ($\psi = 0^\circ$) at a fixed phase angle α ($\alpha = \epsilon - i$). Surfaces with normal reflectances r_n of 0.04 (top), 0.28 (middle) and 0.69 (bottom) are shown. Successive curves have been displaced downwards by δ for clarity with the magnitude of δ shown at the upper left in each figure.

THE PHOTOMETRIC FUNCTION OF THE NEW DUST DEPOSIT AT THE VIKING LANDER 2 SITE

Guinness, Edward A., Department of Earth and Planetary Sciences,
Washington University, St. Louis, Missouri 63130

The presence of condensates on the surface surrounding the Viking 2 Lander during the northern winter has been reported by Jones *et. al.* (1979). Color changes were detected at both Viking landing sites during the following spring season. The color changes were attributed to a blanketing of the landing sites with a thin layer of bright red dust, probably only a few microns in thickness (Guinness *et. al.*, 1979). In order to characterize the spectral reflectance of the soil at the landing sites before and after the dust deposition, a study of the soil photometry has been started. The intent is to determine how the reflectance of the material at the landing sites compares with other measurements of martian surface reflectance, particularly the bright and dark areas observed from Earth. The determination of the soil spectral reflectance along with the observations of the pattern of dust deposition made from the Viking Landers may provide information on the mechanisms of formation of bright and dark areas. Presented here are the preliminary photometric results for the new dust deposited at the Viking 2 site.

A major problem in working with lander photometry is the calibration of the camera. One method of calibration is to use the lander reference test charts (RTC) (Huck *et. al.*, 1977). The other approach is to use the pre-flight calibrations (Huck *et. al.*, 1975). As a test of the validity of the RTC calibrations, an "apparent optical depth" of the atmospheric aerosols was estimated from RTC data. The apparent optical depth for the blue and green channels is consistently about one half the optical depth measured by imaging the sun (Pollack *et. al.*, 1977), while the apparent optical depth for the red channel is near zero. The results for the blue and green channels are expected because scattered light reaching the surface was not taken into account in the calculation of the apparent optical depth. The values for the red channel may result from the combination of grazing incidence on the RTC, scattered skylight and a large component of light reflected from dust covering the lander deck. Therefore, reflectances for the red channel estimated using the RTC calibration may be systematically too small, thus affecting the shape of spectral reflectance curves. As a result, the pre-flight calibrations were used in this study.

The brightness of a shadow was subtracted from the brightness of a nearby sunlit patch of soil to correct for scattered skylight. Atmospheric optical depth data taken from Pollack *et. al.*, (1979) were used to account for the attenuation of the direct sunlight. It was assumed as a first approximation that there was no wavelength dependence to the optical depth. The reflectance data corrected for scattered skylight were fit with the new Hapke photometric function (Hapke (1979a)). This model was

adapted because Hapke (1979b) used it to obtain a good fit for the soil at the Viking 1 site. The free parameters in the Hapke function were chosen based on minimizing the sum of the squared difference between the data and the function (Figure 1). The reflectance of the new dust deposit at VL2 at a phase angle of 5 degrees is estimated at: 0.07 for the blue channel; 0.12 for the green channel; and 0.39 for the red channel. The new dust deposit data appear to have a steeper slope between 0.5 and 0.67 microns than Earth based data for martian bright areas (McCord and Westphal, 1971). The slope of the new dust data is similar to a sample of maghemite (E. N. Wells, unpublished data) which has a sharp reflectance drop at the edge of the ultraviolet absorption band. The photometric function derived for the Viking Lander data has a wavelength dependence and reproduces the increase in red to blue ratio with increasing phase angle observed for the new dust at VL2 by Guinness et. al. (1979).

These conclusions are to be considered preliminary. At present, more data is being reduced in order to test the goodness of fit to the Hapke model, along with trying other photometric functions to see if there is a better model. This research was supported by Mars Data Analysis Grant NSG-7545.

References

- Guinness, E. A., et. al. 1979. Color Changes at the Viking Landing Sites Over the Course of a Mars Year. Journ. Geophysical Res., in press.
- Hapke, Bruce, 1979a. Bi-directional Reflectance Spectroscopy. I. Theory. Journ. Geophysical Research, in press.
- Hapke, Bruce, 1979b. The Photometric Function of Martian Soil in the Vicinity of Viking Lander 1 (Abstract). in Reports of Planetary Geology Program, 1978-1979, NASA TM-80339, p. 410.
- Huck, F. O., et. al., 1977. Spectrophotometric and Color Estimates of the Viking Lander Sites. Journ. Geophysical Res., Vol. 82, pp. 4401-4411.
- Huck, F. O., et. al., 1975. Radiometric Performance of the Viking Mars Lander Cameras. NASA TM X-72692, 50p.
- Jones, K. L., et. al., 1979. One Mars Year: Viking Lander Imaging Observations. Science, v. 204, pp. 799-806.
- McCord, T. B. and J. A. Westphal, 1971. Mars: Narrow-band Photometry, From 0.3 to 2.5 Microns, of Surface Regions During the 1969 Apparition. The Astrophysical Journal, v. 168, pp. 141-153.
- Pollack, J. B., et. al., 1979. Properties and Effects of Dust Particles Suspended in the Martian Atmosphere., Journ. Geo. Res., v. 84, pp. 2929-2945.
- Pollack, J. B., et. al., 1977. Properties of Aerosols in the Martian Atmosphere, as Inferred From Viking Lander Imaging Data., Journ. Geo. Res., v. 82, pp. 4479-4496.

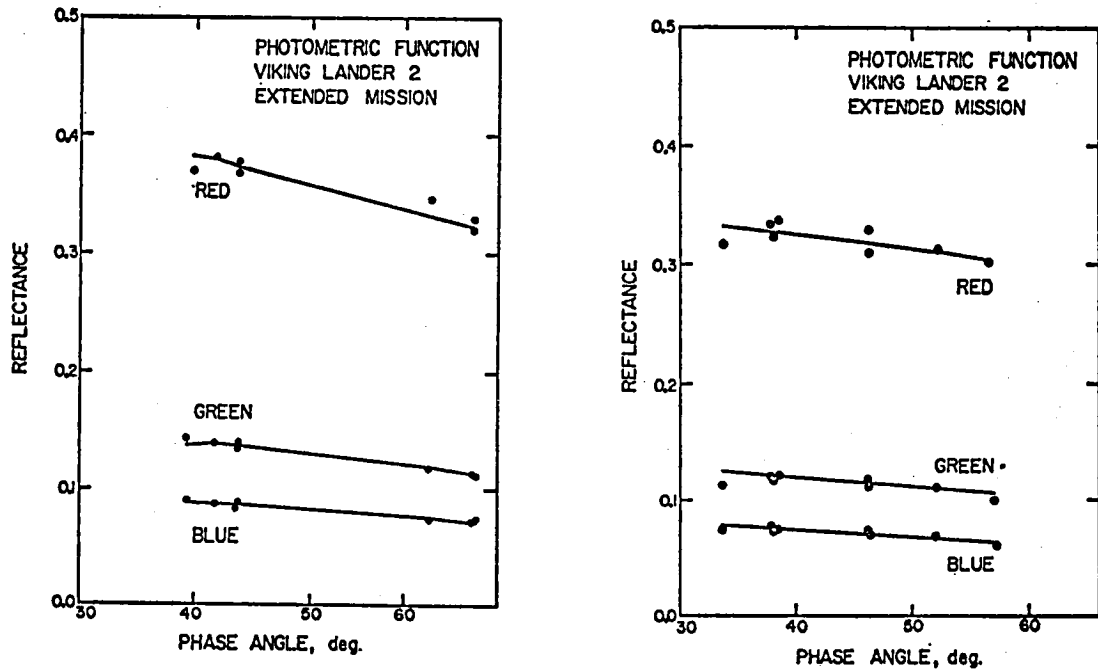


Figure 1. Reflectance data of the new dust deposit at VL2 (circles) and the Hapke photometric function fit to the data (solid lines) are plotted for the three Viking Lander color channels. The blue, green and red channels have effective center wavelengths of 0.500, 0.556 and 0.669 microns, respectively. Each graph is a slice through incidence, emission and phase angle space with the incidence (i) and emission (e) angles kept approximately constant. (left: $i=31$ deg. $e=72$ deg.; right: $i=31$ deg. $e=58$ deg.)

LUNAR GEOCHEMICAL ANOMALIES DETECTED BY ORBITAL REMOTE SENSING

Hawke, B. Ray, Planetary Sciences Division, Hawaii Inst. of Geophysics,
Univ. of Hawaii, Honolulu, HI 96822, P. D. Spudis, Dept. of
Geology, Arizona State Univ., Tempe, AZ 85281, P. E. Clark,
Chemistry Dept., Univ. of Maryland, Coll. Park, MD 20742

I. Introduction

The orbital geochemistry data have shown that some lunar regions have unusual abundances of certain elements relative to surrounding or adjacent areas or have a surface chemistry unlike that which would be anticipated from the examination of local geologic relationships. Investigation of the formation of these geochemical anomalies can provide important clues to understanding impact and volcanic processes operative during the early phases of lunar evolution. For example, such studies have proven useful in outlining the history of KREEP volcanic activity in the western maria (1,2,3,4). The purpose of this study was to investigate the geology and geochemistry of selected anomalous highland regions and attempt to understand the processes responsible for their formation. This study expands on previous work relating to geochemical anomalies on the lunar farside (5) and presents results of mixing model studies for the Van de Graaff region.

II. Causes of Geochemical Anomalies

There has been an increasing tendency in recent years to relate geochemical anomalies and many variations in lunar surface chemistry to lateral heterogeneities produced by the chemical differentiation of the global magma ocean. While this explanation is probably valid for large-scale variations, it must be recognized that other processes are capable of producing geochemical anomalies in the lunar highlands. These include: 1) Basin-forming impacts - Large objects impacting near the end of crustal formation may have produced localized melting and lateral chemical heterogeneities; 2) Highland volcanism - Very early (>4.0 - 4.1 b.y.) highland volcanic deposits were probably destroyed during the terminal bombardment of lunar surface but may have left geochemical and mineralogic signatures; and 3) Ancient mare volcanism - Mare volcanic deposits emplaced considerably before the end of the terminal bombardment would have been thoroughly reworked and mixed with highland material (6,7,8). The magnitude of these effects probably vary for different regions of the lunar surface and are dependent on the local geologic history of the areas investigated.

III. Geologic and geochemical studies of specific lunar anomalies.

A. Light plains with associated dark halo craters - Numerous light plains regions on the moon exhibit high concentrations of dark halo craters where buried low albedo material has apparently been excavated (8). Where these regions have been overflowed by orbital geochemical

instruments, mafic anomalies have been recorded. One region where this is best displayed in the area near the east limb, crater Langemak; Hubbard et al. (9) pointed out the rather striking variations in Mg/Si and Al/Si intensity ratios which occur in this vicinity. The lowest average Al/Si ratios (~ 1.0) and the highest average Mg/Si ratios (~ 0.8) are found around 115°E . In addition, Clark et al. (10) noted that an adjacent highland area immediately northeast of Pasteur crater was defined by the unusual combination of high Fe and high Al/Si values, an exception to the general inverse correlation of orbital Fe and Al/Si values. No apparent radioactivity anomaly has been identified in this general region (11). This highland region is characterized by the presence of several craters that exhibit broad, diffuse low albedo ejecta deposits (8). The existence of these dark-haloed craters with associated geochemical anomalies strongly suggest the presence of a buried ancient basalt layer. The existence of other dark-haloed craters in the region demonstrates that this unit is not limited to the immediate vicinity of Langemak and may, in fact, underlie some or most of the Imbrian and Nectarian light plains units in the region. The correspondence of an area of geochemical anomalies with an area of probable ancient mare volcanic activity suggests that early volcanism may be an important process in the production of regional chemical anomalies elsewhere on the lunar surface.

B. Mare Marginis region - The results of Th deconvolution modeling studies allowed the identification of a region north of Mare Smythii with Th concentrations well above highland levels (1). This region is dominated by Mare Marginis, and the mare-flooded crater Neper but also contains highland units including light plains deposits in Babcock crater and just east of Marginis. While Haines et al. (1) reported a Th concentration of 3.4 ppm for this region as a whole, they noted that when the model was modified by decoupling the Mare Marginis-Neper and highland portions, the resulting fit was equally as good; the resulting highland Th concentration was 2.3 ppm and the mare concentration was 5.4 ppm. The high Th concentrations are clearly associated with the mare material and hence there appears to be a mare basalt unit on the eastern limb with a Th concentration of at least 3.4 ppm and perhaps as high as 5.4 ppm; both values are considerable in excess of those associated with the Apollo mare samples (12). The high Th content of the Mare Marginis basalts suggests that they are intermediate in composition between mare and KREEP basalts and may be similar to the Apollo 17 KREEPy basalt (13). Estimates of Apollo 17 KREEPy basalt Th concentrations based on reported K_2O values range from ~ 4 to 6 ppm and are comparable to those for the Mare Marginis-Neper region. In addition, the MgO values for Neper (~ 8 -9%) (14) are similar to the average composition of Apollo 17 KREEPy basalt (~ 8 %) (13). This observation suggests KREEP-like volcanism was active in the lunar eastern hemisphere in Imbrian time, a result significant for lunar volcanic history (15).

C. Van de Graaff region - Several major geochemical anomalies have been located in the Van de Graaff region. The region contains relatively high Th, K, and Fe concentrations and low Ti content (16). A basic question is whether the chemical anomalies are related to: 1) material excavated by the various basins in the region (17); 2) exotic material transported from some distant source (18); or 3) a local episode of volcanism. A major objection to the last of these has been the limited areal extent of mare-like basalts (18). A partial explanation may involve thinly covered basaltic units. The region is antipodal to Imbrium basin and any pre-imbrian volcanic deposits could easily have been covered by the extensive mass-wasting caused by seismic waves associated with Imbrium (19). Dark-haloed craters have been identified in the region (8) and suggest the presence of buried basalt units, favoring a volcanic explanation (15). Mixing calculations indicate this region can be modeled as 60.8% anorthositic gabbro, 4.8% LKFM basalt and 34.4% Apollo 17 KREEPy basalt (13). These results suggest an episode of extensive pre-Imbrian KREEPy volcanism in the Van de Graaff region (5,15).

References

- (1) Haines E. et al. (1978) PLPSC 9, 2985.
- (2) Spudis P. (1978) PLPSC 9, 3379.
- (3) Hawke B. and Head J. (1978) PLPSC 9, 3285.
- (4) Metzger A. et al. (1979) PLPSC 10, in press.
- (5) Hawke B. et al. (1979) Conf. Lunar Highlands, 56.
- (6) Ryder G. and Taylor G. (1976) PLSC 7, 1741.
- (7) Ryder G. and Spudis P. (1979) Conf. Lunar Highlands, 132.
- (8) Schultz P. and Spudis P. (1979) PLPSC 10, in press.
- (9) Hubbard N. et al. (1978) Mare Crisium, 13.
- (10) Clark P. et al. (1978) PLPSC 9, 3015.
- (11) Frontispiece (1977) PLSC 8
- (12) Taylor S. (1975) Lunar Science, 372 p.
- (13) Ryder G. et al. (1977) EPSL 35, 1.
- (14) Andre C. et al. (1979) PLPSC 10, in press.
- (15) Spudis P. (1979) Conf. Lunar Highlands, 157.
- (16) Bielefeld M. et al. (1976) PLSC 7, 2661.
- (17) Schonfeld E. (1977) PLSC 8, 1149.
- (18) Stuart-Alexander D. (1978) USGS Map I-1047.
- (19) Schultz P. and Gault D. (1975) Moon 12, 159.

APPLICATION OF THE G-MODE CLUSTER ANALYSIS TECHNIQUE TO MULTISPECTRAL DATA SETS

Poscolieri, Maurizio,* McDonnell Center for the Space Sciences,
Washington University, St. Louis, Missouri 63130

* permanent address: National Research Council, Rome, Italy

G-mode is a new cluster analysis technique developed by Gavrishin (1968,1974) and adapted for computer classification of chemical trends in rocks and soils by Coradini *et. al.* (1976,1977). We have further adapted the G-mode technique to search for clustering of image data in color space. Basically, the brightness of a given set of objects in a scene can be plotted in n dimensional space if there are n spectral channels imaging the objects. The G-mode technique and other multivariate cluster analyses attempt to: (1) identify clusters or groupings of the brightness values, (2) determine into which cluster, if any, a given object should be placed, and (3) plot the results as a 2 dimensional image display with classes shown in a gray level or color-coded form. The uniqueness of G-mode is that the resultant classes or clusters are not given as linear combinations of the original data, as they are in linear multivariate discriminant function analyses. Rather, through the transformations discussed below of the original N by M data matrix, one obtains a G-vector, which is quasi-Gaussian in distribution and capable of being used to search for clusters in an interactive fashion. N refers to the number of pixels in the image and M to the number of channels. We have tested the utility of G-mode on two multispectral data sets - (1) The Viking Lander camera 6-channel data, where color differences from place to place are rather small, and (2) LANDSAT 4 channel multispectral data over the Meadig Dome in eastern Egypt, where color differences are appreciably more dramatic. In the G-mode program the data matrix with N samples (pixels) and M variables (channels) is first normalized as follows:

$$x_{ij}^{12} = \frac{(x_{ij} - x_j)^2}{\sigma_j^2}$$

where: x_{ij} are the original data elements; x_j is the mean and σ_j^2 the variance for each channel. This procedure simply normalizes the data matrix so that each column has a mean of zero and a standard deviation of one.

Next each row (pixel) of the standardized data matrix is summed, as follows:

$$Z_j^2 = \sum_{j=1}^m x_{ij}^{12}$$

This procedure collapses the matrix to a Z^2 vector. If the original data

are randomly selected and each variable is independent of any other variable, then the Z^2 vector will follow a chi-square distribution with N degrees of freedom. In the more likely case, where the variables are not independent of one another, the correlation coefficient matrix provides a measure of the amount of information lost due to non-independence between pairs of variables.

For ease of computation, the Z^2 vector can be transformed to a G^2 vector, based on the degrees of freedom and on the degree of independence between the variables. The G^2 vector obeys a standardized Gaussian distribution with a mean of zero and a standard deviation of unity.

Initially, a G^2 vector for all samples is computed. The three samples with smallest G^2 values are used as the core of the first class. A new G^2 vector for samples is computed based on the mean and variance of the initial three samples. Each sample is checked to see if statistically there is a high probability of its being drawn from the population defined by the three initial samples. Iteration of the procedure produces the first class, which consists of data that have a high probability of being drawn from the same population. A new G^2 vector and population parameters are then computed from the remaining data to define the 2nd class, and on the next iteration, the 3rd class, etc.. The second part of G-mode includes statistical procedures that provide information on: (a) the importance of each variable in driving the classification, and (b) the closeness of one class relative to all the others.

Results of using the G-mode technique for the ratioed Viking Lander and LANDSAT data are shown in Figures 1 and 2. For the Lander data the classes consist of a soil unit, and a number of rock units, including several shadow units. Basically, the classes reflect a fairly homogeneous soil in terms of color, together with a variety of rock colors. The rock colors may be photometrically controlled. By way of contrast, the LANDSAT classes reflect varying degrees of redness within the wadis of the Meadig Dome. In particular, the soils become brighter and redder toward the center of the wadis within the dome, while sediment-filled wadis elsewhere are not discernably different than the surrounding rocks. The reason for such a trend remains unknown at this point. Computing time for this research was supported in part by Planetary Geology Grant NSG-7087.

References

- Coradini, A., Fluchignoni, M. and Gavrishin, A. I., (1976), Classification of lunar rocks and glasses by a new statistical technique. The Moon 16, pp. 175-190.
- Coradini, A., Fulchignoni, M., Fanucci, O., Gavrishin, A. I., (1977), A FORTRAN V program for a new classification technique: the G-mode central method. Computer and Geosciences 3, pp. 85-105.

Gavrishin, A. I., (1968), Kriteri videlenia geochimitsheskich anomalii, osnovanny na funkzii pravdapodobia. Litochimitsheskie poiski rudnich mestorogdeni. Alma Ata, ANSSSR, pp. 53-60.

Garvishin, A. I., (1974), Gidrogeochimitsheskie issledovaniia s primenenien matematitsheskei statistiki i EWM. Nedra, Moscwa, 145 p.

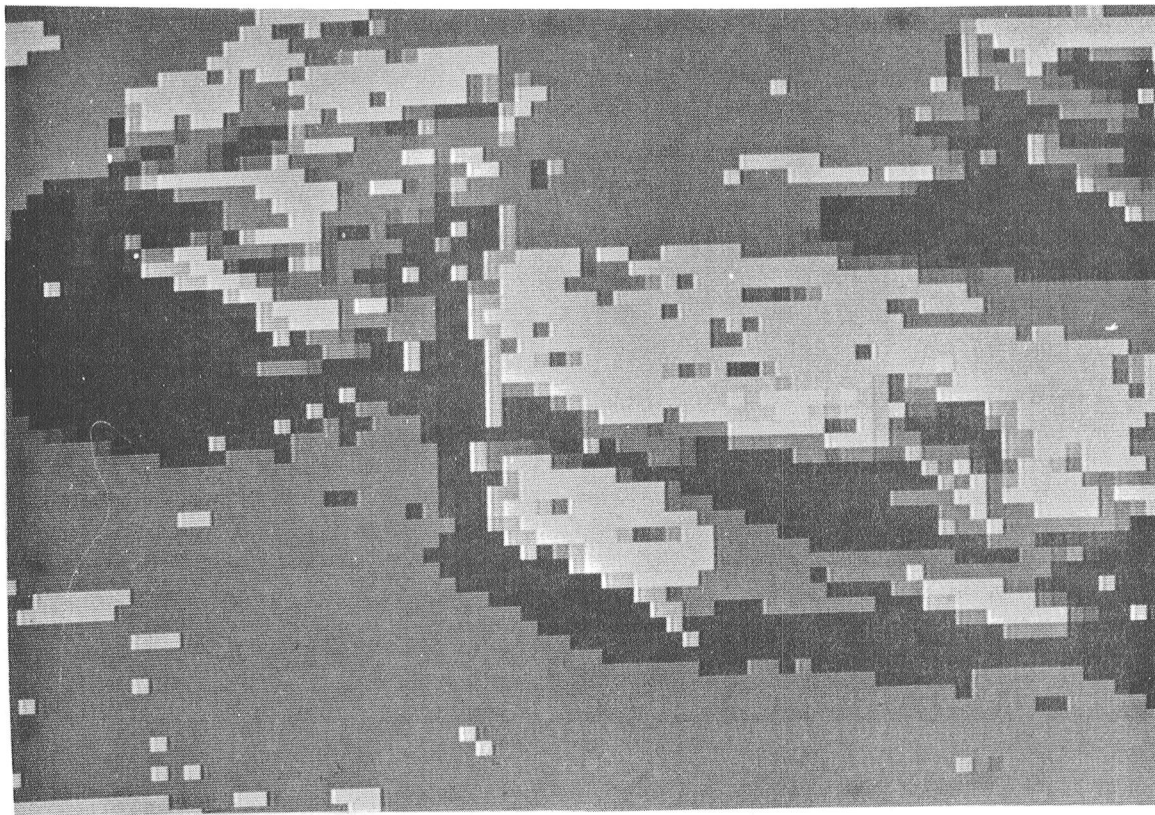


Figure 1 - An approximately 50 x 50 pixel view of a portion of Viking Lander 2 frame 22A190. This rendition is the result of using the G-mode cluster technique to show 6 channel multi-spectral data on a 2 dimensional display. Seven classes are shown coded in 7 gray levels, with the brightest gray levels corresponding to the top of rocks and the darkest to shadows on rock sides. The important point is that the soil corresponds largely to one class - the middle gray level.

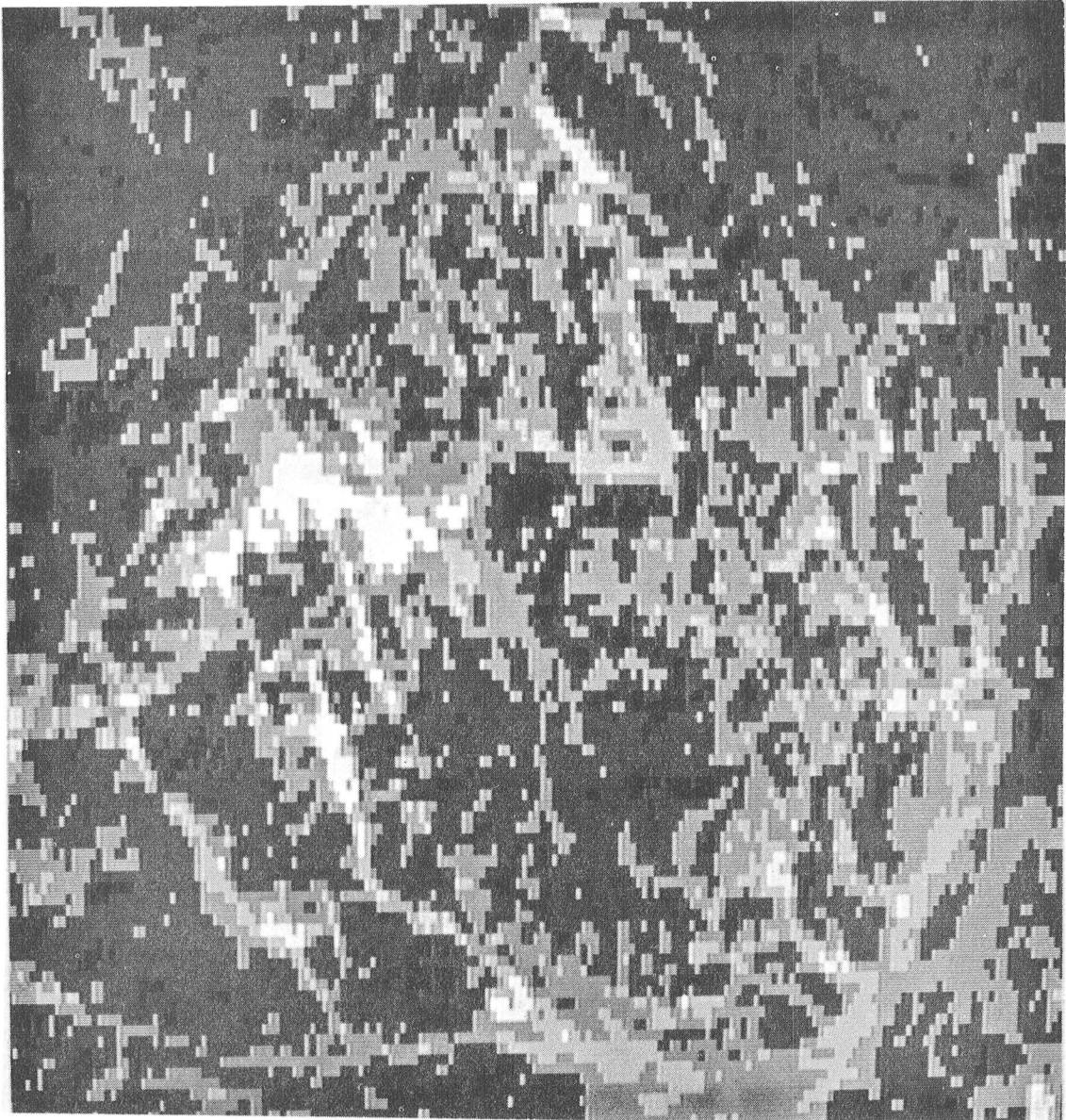


Figure 2 - Gray level coded G-mode image of a portion of the Meatig Dome, Egypt. The brightest gray level corresponds to a class with the brightest and reddest spectral radiance signature. The brighter gray levels are located within wadis (arroyos) in the Dome. In fact, the wadi sediment apparently becomes brighter and redder toward the wadi centers, according to the distribution of gray levels in the G-mode image. The Dome is located at 26° N. lat., 34° E. long. and the view shown is ~15km across. G-mode classes were derived from 4 channel LANDSAT data.

OPTICAL POWER SPECTRUM ANALYSIS OF MARTIAN TERRAINS

R.W. Wolfe, National Air and Space Museum,
Smithsonian Institution, Washington, D.C. 20560

Many landforms and geologic material units on Mars exhibit repetitive patterns that appear to be fairly regularly spaced. Some examples include the fossae to the north and east of Tharsis, dune fields on crater floors and in sand seas encircling the north polar region, the elaborate network of horsts and grabens in Noctis Labyrinthus, the aureole surrounding Olympus Mons, and periglacial features in the northern mid-latitudes.

The orientation and spacing of these features may be related to geologic processes. For example, the pattern of fossae to the north and east of Tharsis is related to the crustal forces that created the Tharsis uplift. Dune patterns of various types are related to effective wind directions. However, the origins of the patterns exhibited by other terrains, particularly the Olympus Mons aureole, are uncertain.

Manual methods of measuring such parameters as spacing between features, or their orientations, are time consuming, subject to error, and as some investigators have shown (e.g., Podwysocki et al., 1975) lack objectivity. Optical data processing techniques, on the other hand, provide a quick and accurate measure of orientation and spacing of linear patterns.

We are beginning a program that aims to develop a sophisticated method of terrain analysis as a basis for more precise, objective comparisons of landforms on Mars than heretofore possible. Such methods as optical diffraction pattern analysis are now practical because of the extremely high resolution of the Viking Orbiter images.

The use of optical data processing in photogeologic studies is still in its infancy and has not yet resulted in a large number of published papers. Among the most useful applications of optical data processing have been the analysis of directional features ranging in scale from photolinears in Landsat imagery (e.g., Pincus and Doe, 1974) to grain orientations in thin section (Power and Pincus, 1974). Another set of applications has dealt with the extraction of signatures for different terrain types with the aim of developing techniques for automatic terrain type recognition in

classification and for change detection (e.g., Gramenopoulos, 1973).

Optical diffraction patterns can be obtained easily with a simple optical bench set-up (Fig. 1). Basically, if an image transparency is placed in the front focal plane of a lens and illuminated by a beam of parallel, coherent light (preferably monochromatic), the Fraunhofer diffraction pattern of the image will be formed at the back focal plane of the lens. The diffraction pattern is essentially the amplitude of the Fourier transform of the image. Phase information (the complex part of the transform) is lost. Unlike manual interpretation of images (which is subject to subjective selection or rejection of features), the optical diffraction pattern contains all spatial information found in the original image. This may be, at times, a hindrance as well as advantageous.

Interpretation of optical diffraction patterns may range in sophistication from simple "eyeball" measurements and comparisons to digitally sampling the pattern and analysis by complex algorithms. As an example of the former method, let us consider the diffraction pattern (Fig. 3) of the grooved terrain shown in Figure 2. Spots or streaks in the diffraction pattern reveal the azimuthal and spatial distribution of linear elements in the original image. In addition, the diffraction pattern indicates the regularity or periodicity of the terrain.

Another method in the analysis of complex diffraction patterns is diffraction plane sampling (Lendaris and Stanley, 1970) in which the pattern is sampled quantitatively over many (up to 64) integrated regions in both frequency and azimuthal spaces (Fig. 4). Plots of data (Fig. 5) obtained from the grooved terrain of Fig. 2 reveal the orientation and spacing of individual elements of terrain and provide an indication of the variability of these parameters. Algorithms have been developed for the complex tasks of pattern recognition based on such diffraction plane sampling (Kasdan, 1977). With these techniques, it is possible to differentiate and characterize terrains with precision and without subjective biases.

Gramenopoulos, N. (1973) NASA SP-351; Kasdan, H.L. (1977) Proc. SPIE, 117, pp. 67-74; Lendaris, G.G. and Stanley, G.L. (1970) Proc. IEEE, 58, pp. 198-216; Pincus, H.J. and Doe, T.W. (1974) Proc. 1st Conf. Basement Tectonics, pp. 423-436; Podwysoki, M. H. et al. (1975) NASA TM X-70951; Power, P.C., Jr. and Pincus, H.W. (1974) Science, 186, pp. 234-239.

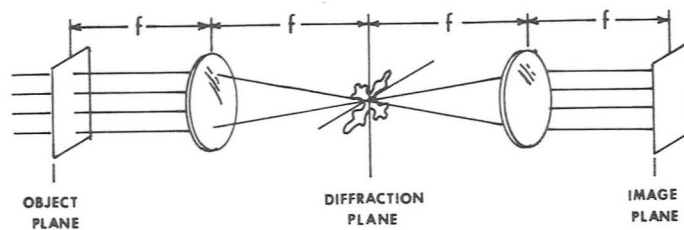
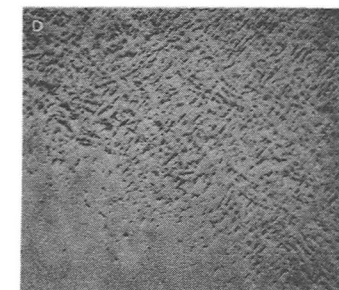
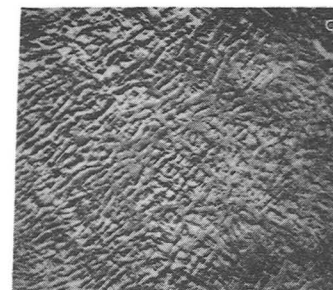
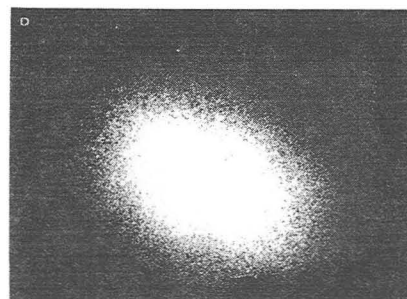
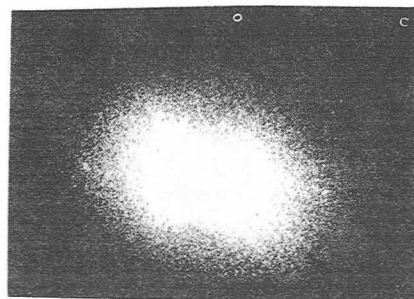


Fig. 1.



↑ Fig. 2. 34B38 (left);
44B25 (right)



← Fig. 3. 34B38 (left);
44B25 (right)

↓ Fig. 5. Spatial fre-
quencies refer to 35 mm
transparency

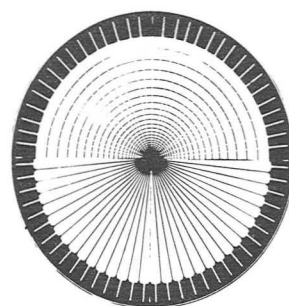
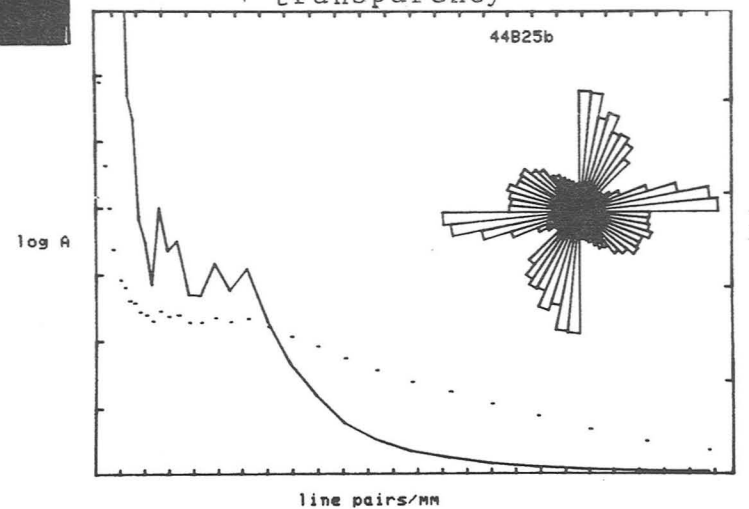


Fig. 4.
Diagram
of wedge-ring
detector.

Chapter 9
GALILEAN SATELLITES

THERMAL EVOLUTION OF EUROPA, GANYMEDE AND CALLISTO

Reynolds, Ray T. and Cassen, Patrick M., Theoretical and Planetary Studies Branch, NASA-Ames Research Center, Moffett Field, CA 94035. Stanton J. Peale, Dept. of Physics, University of California, Santa Barbara, CA 93106.

Thermal evolution calculations for the icy Galilean satellites, based on known densities and conducting thermal models, showed that they are most probably differentiated objects, with rocky cores and mantles composed of H₂O (Lewis, 1971, Consolmagno and Lewis, 1976, Fanale, et al., 1977). Calculations which include the effects of solid convection in the ice crusts indicate that (for radioactive heat sources similar to those for the Earth, moon and meteorites) large liquid layers would solidify early in the evolution of those bodies. Large scale convective motions would be expected which could have produced plate-tectonic like surface features (Reynolds and Cassen, 1979). Also, diapirism would act rapidly to remove large density inversions early in the evolutionary process (Parmentier and Head, 1979).

For Europa, density modeling of a differentiated body yields an estimate for the thickness of an outer H₂O layer of about 100 km. The contribution of tidal dissipation (Peale et al., 1979) to Europa's energy balance was considered within the framework of convecting thermal model calculations and two possible thermal configurations were identified (Cassen et al., 1979a). In the first, the H₂O layer is frozen, with solid convection removing the internally generated heat (from both radioactive and tidal sources). In the second, a liquid H₂O region is maintained below a thin (≤ 10 km) ice crust that is heated by tidal dissipation. The dissipation in the thin ice crust could provide about 20 times the total heat generated by radioactives in the satellite. In order for this configuration to exist, Europa's H₂O layer could never have been completely frozen. This would imply that the three-body orbital resonance involving Io, Europa, and Ganymede was established very early in the history of the Jovian system, thereby maintaining Europa's orbital eccentricity from very early times. The thin ice crust in this model could be fractured periodically by tidal stresses, thus providing an active resurfacing mechanism. Analysis of ground based and spacecraft observations suggest that Europa's surface may be younger than those of Ganymede and Callisto. More evidence will probably be required, however, in order to determine the thermal configuration of Europa's crust.

A detailed study of Ganymede and Callisto indicates that tidal dissipation is unlikely to have been important during their thermal evolutions (Cassen et al., 1979b). It was suggested, however, (on the basis of convective thermal calculations) that differences in radioactive heat sources within these bodies, although relatively small, could nonetheless have significantly influenced the time at which internal activity ceased to affect

the surface morphology. Since the early rate of impact crater production is strongly time dependent, such a difference might have caused the differences in surface appearance observed by the Voyager imaging experiment. Surface tectonic activity on Ganymede could have been prolonged beyond the early period of high impact flux rate, in contrast to Callisto where the production of features resulting from such activity could have ceased earlier. Thus any evidence for tectonic activity on Callisto could have been removed by the cratering process.

References

- Cassen, P., R.T. Reynolds and S.J. Peale, Is there Liquid Water on Europa? Geophysical Research Letters, 731-739, 1979a.
- Cassen, P., S.J. Peale and R.T. Reynolds, On the comparative evolution of Ganymede and Callisto (Submitted to Icarus, 1979b).
- Consolmagno, G.J. and J.S. Lewis, Structural and thermal models of icy Galilean satellites, in Jupiter, T. Gehrels, ed., U. of Arizona Press, Tucson, 1035-1051, 1976.
- Fanale, F.T., T.V. Johnson and D.L. Matson, Io's surface and the histories of the Galilean satellites, Planetary Satellites, J. Burns, ed., U. of Arizona Press, Tucson, 379-405, 1977.
- Lewis, J.S., Satellites of the outer planets: thermal models, Science, 172, 1127-1128, 1971.
- Parmentier, E.M. and J.W. Head, Internal processes affecting surfaces of low-density satellites: Ganymede and Callisto, Journal of Geophysical Research (in press).
- Peale, S.J., Cassen, P. and R.T. Reynolds, Melting of Io by Tidal Dissipation, Science, 203, 892-894, 1979.
- Reynolds, R.T. and P.M. Cassen, On the Internal structure of the major satellites of the outer planets, Geophysical Research Letters, 6, 121-124, 1979.

VOLCANIC ERUPTIONS ON IO

Strom, Robert G., University of Arizona, Tucson, AZ, Terrile, R. J., JPL, Pasadena, CA, Masursky, H., USGS, Flagstaff, AZ, and Hansen, C., JPL, Pasadena, CA.

Nine volcanic eruption plumes were observed over a period of 6 1/2 days during the Voyager 1 flyby of Io (1). During the Voyager 2 encounter, four months later, at least 7 of these plumes were still active at about the same intensities. The largest plume (Plume 1, 280 km high and 1000 km wide) viewed by Voyager 1 was not active during the second encounter. Plume 4 was not viewed near enough to the limb during the second encounter to confirm whether or not it was still active. However, a major eruption occurred at 340° longitude and 45° N latitude (Site 10, Table 1) sometime between the two encounters and deposited an ejecta blanket comparable in size to that associated with Plume 2. The source area was not viewed near enough to the limb on the second encounter to confirm whether or not it was still active. This new eruption is associated with a caldera about 80 km in diameter and is responsible for major changes in surface markings first seen by Voyager 1. The main effects of this eruption seem to have been the flooding of the caldera by a black extrusive, and the mantling of previously bright areas with a layer of dark pyroclastic material. Other changes in surface marking have occurred between the two encounters or during the first encounter. Two of these changes are associated with Plumes 1 and 2, and are probably primarily the result of pyroclastic deposition which accumulated during the four month interval between the two encounters. One short-term change (5 1/2 hours) occurred during the first encounter in an area located primarily north of Plume 4. This change in the surface appearance may be the result of (1) an intense short-term eruption, (2) a transient increase in the intensity of the eruption associated with Plume 4, or (3) a phase effect due to a difference in the scattering properties of the material in this region. Another surface change has been noted between color pictures taken 6 hours apart during the first encounter. A bluish semi-circular area, not present 6 hours earlier, occurs on the northern floor of a caldera about 50 km in diameter. This bluish area may be specular reflections or more likely a venting of gases on the caldera floor. During the first encounter Plume 2 consisted of two components: a large diffuse cloud about 210 km high emanating from the west end of a 175 km long black strip, and a very small plume probably less than 40 km high associated with the east end of this black strip. During the second encounter the smaller plume (now called Plume 9) had about doubled in size.

Most plumes are stronger forward scatterers than back scatterers indicating they consist of very small particles. The detection of gaseous SO₂ in Plume 2 by Voyager 1 IRIS experiment (2) suggests that it may be the principal volatile driving the eruptions.

The geometry and source regions of the plumes suggest they are associated with both long fissure and pipe vent eruptions. Vertical and oblique photographs of Plume 2 show a curtain of pyroclastics being ejected to a height of about 100 km along a 25 km length of the western end of a black strip. This is certainly a fissure eruption and may account in part for the diffuse nature of the plume. The very symmetrical, umbrella-shaped plumes (Plume 1 and 3) contain a narrow central fountain together with a very small circular source suggesting they may be pipe vent eruptions.

The source regions at all active plumes are characterized by a dark diffuse core surrounded by bright and dark diffuse rings. Many other areas showing similar characteristics are almost surely the sites of recent eruptions. The global deposition rate of about 0.1 mm/yr estimated by Johnson, et al. (3), together with the great frequency of eruptions indicated by the appearance of a new eruption during a four month period, suggest that the other eruption sites are very young; perhaps 10 years old or less. All active plumes and the sites of the larger recent eruptions are concentrated within 45° of the equator, but are more or less randomly distributed in longitude. This suggests that the frequency and/or intensity of eruptions, and therefore deposition rate, is greater in the equatorial regions than in the polar regions. It follows that, on the average, the equatorial regions are younger than the polar regions. This, at least in part, may account for the differences in albedo and color between the equatorial and polar regions. This large eruption which took place sometime between the two encounters and its resultant surface changes strongly suggest that major large-scale (several hundred kilometers) changes in color and albedo patterns take place over short periods of time (on the order of months or less).

Volcanic eruptions on Io differ significantly from those on Earth. Although volcanoes on Earth can remain active for many years or even centuries, violent activity is periodic and short-lived (a few hours or days). On Io at least 6 eruptions have continued at a high level of activity for at least four months and probably longer. This suggests that at least in these cases large reservoirs of volatiles (e.g. SO_2) are available to sustain continuous violent activity over long periods of time.

References:

1. Strom, et al., 1979, Nature, Vol. 280, No. 5725, pp. 733-736
2. Pearl, J., et al., 1979, Nature, Vol. 280, No. 5725, pp. 755-758
3. Johnson, et al., 1979, Nature, Vol. 280, No. 5725, pp. 746-750

Table 1. Io Plume Observations

Plume No.	Location lat/long	Plume (a) width(km)	Plume (a) height(km)	Central Fountain (a) width(km)	Voyager 1 (b) activity	Voyager 2 (b) activity
1	-19.4/526.8	1000(c1)	280(c1)	35(uv)	active	inactive
2	18.9/305.3	210(c1)	100(c1)	-	active	active
		585(uv)	210(uv)	-	-	-
3	-2.9/153.0	250(c1)	70(c1)	15(c1)	active	active
4	21.6/176.8	75(v)	95(v)	20(v)	active	?
5	27.2/118.7	200(c1)	80(c1)	?	active	active
6	18.9/122.4	250(c1)	80(c1)	60(c1)	active	active
7	-28.0/209.7	180(c1)	120(c1)	?	active	active
8	-42/50	150(c1)	70(c1)	15(c1)	active	active
*9 + 2	17/300 (Plume 9)	340(c1)	170(c1)	-	active	active
Site 10	45/340	?	?	?	inactive	?

(a) Except for Plume 9, all measurements are from Voyager 1 images.

(b) Plumes designated as inactive were not observed at the resolutions at which these sites were photographed. If plumes were present, they were less than 40km high in the case of Plume 1, and less than 10km high in the case of Plumes 9 and 10.

c1 - clear filter measurement
uv - ultraviolet filter measurement
v - violet filter measurement

* The height and width measurements are for the diffuse halo surrounding both Plumes 2 and 9 on Voyager 2.

VOLATILE EVOLUTION: THE SO₂ REGIME OF IO

Fanale, Fraser P., Jet Propulsion Laboratory, California Institute of Technology, Pasadena, California 91103

We have been able to demonstrate that the puzzling deep 4.08 μm absorption feature observed in Io's infrared reflectance spectrum is due to frozen SO₂ molecules (1). This identification is compatible with and provides a unifying explanation for a large and ever-growing list of key Voyager and earth-based observations of Io. These apparently include: 1.) the supply of S to the Io-surrounding torus, 2.) the precise atomic and molecular species in the torus, 3.) the driving of Io's volcanoes, 4.) the observation of trace quantities of gaseous SO₂ over one of the large calderas, and 5.) the mechanism of crater erasure and erosion in the presence of rapid deposition.

We are currently attempting to solve several outstanding remaining problems. Three of the most difficult are: 1.) How much of the frozen SO₂ is present as free surface frost, how much as adsorbate, how much as SO₂ dissolved or occluded in surface material, and how much as gas? 2.) Does the fact that the local basal pressure observed by the Voyager IRIS experiment near the subsolar point resembles the equilibrium pressure at 130°K mean that the atmosphere is well buffered in equilibrium by surface SO₂ frost all over the disc? Alternatively, could the pressure at most points simply reflect a dynamic equilibrium between local volcanism and the "feeding" of Io's torus on its atmosphere? 3.) How do the kinetic factors such as condensation/sublimation kinetics or global gas migration affect the "Io meteorology"? 4.) Do the "white patches" on Io consist of or contain SO₂ frost, and why are the color variations distributed as they are?

Operationally we have several tools at our disposal. We are currently conducting observations with the International Ultraviolet Explorer. By constructing the UV spectrum with Io's orbital position and time (for repeated observations at the same orbital position) we hope to learn about the spatial and temporal distribution of UV-active substances on Io's surface. However, this also requires considerable laboratory work since our library of UV spectra is sparse. We are thus in a similar state with respect to understanding Io's UV spectrum and its variations to that we were in with respect to its infrared absorption features a year ago. We have recently discovered that while almost all other frosts such as NH₃, H₂O etc. have spectra that are quite flat from 0.2 μm to 0.6 μm , the SO₂ frost spectrum has an exceedingly sharp absorption edge ~ 0.3 μm , a maximum at 0.4 μm , decreasing slightly toward the red (2). We are currently examining the spectral effects of condensing SO₂ frost on various allotropes of sulfur in order to better understand the IUE spectra.

Another important use for the new data will be in the interpretation of the "wideband" spectral data on individual pixels from the Voyager images. We have found the spectral reflectance of SO₂ frost to be suffi-

ciently unusual that its presence should be recognizable in even the "wideband" data, and therefore will serve to aid in the identification of small areas as being rich in frozen SO₂, in the disentangling of the spectral signatures of the various main surface components and in the ultimate production of compositional maps.

In all this interpretive procedure, we will attempt to avoid interpretations which fail to reconcile the depth of the 4.1 μ m band with any recognizable features in the UV. One very interesting result of our attempts to reconcile the various bands we attribute to surface SO₂ with the longer wavelength SO₂ gas bands observed by the Voyager IRIS team is this: Our preliminary results suggest that the Near Infrared Mapping Experiment (NIMS) on Galileo ought to be able to map the atmospheric SO₂ distribution as distinguished from the surface SO₂ distribution since the offset in wavelength of bands from the two coupled with some possible anticorrelation in space suggests that the spectral resolution and sensitivity of NIMS may in fact allow such "atmospheric mapping" in addition to its original surface phase mapping mission on Io.

We intend to tie all the above lines of investigation into a physically plausible model of the SO₂ regime on Io, consistent with both equilibrium and kinetic considerations and the dynamic mass balance between degassing, deposition and the supply of material to the magnetosphere.

(1) F. P. Fanale, R. H. Brown, D. P. Cruickshank and R. N. Clark, Nature, 280, 761-763, 1979.

(2) D. B. Nash, F. P. Fanale and R. N. Nelson, Bull. Am. Ast. Soc., 3, 1979.

Photometric Studies of the Satellites of Jupiter Using Voyager Imaging Data.
J. Veverka, S. Squyres, P. Thomas, D. Simonelli, Cornell University;
D. Morrison, University of Hawaii.

In conjunction with other Voyager investigators we have initiated a systematic program of photometric studies of Jupiter's satellites which includes:

a) Photometry of Ganymede. Initial results indicate that all major units (cratered terrain, grooved terrain, and bright ray craters) have photometric functions which, at least up to phase angles of 30° , are lunar-like, and definitely not Lambertian. We estimate that the mean geometric albedo of the bright ray craters is .53; that of the grooved terrain .47, and that of the cratered terrain, .41. Data up to phase angles of $\sim 110^\circ$ are currently being analyzed.

b) Photometry of Europa. In spite of very high albedo of this satellite (0.64 in the visible), and the fact that near IR spectroscopy indicates a surface largely covered by water frost (Pilcher *et al.*, 1972), the photometric properties are definitely non-Lambertian suggesting a significant admixture of impurities within the frost.

c) Photometry of Amalthea. The photometric properties of this dark red object are lunar-like. For example, essentially no limb darkening is observed at opposition (Figure 1). No significant albedo difference between the trailing and leading side of the satellite is evident in the Voyager data. Such differences occur on the Galilean satellites and have been invoked by some investigators for Amalthea in the past (see Veverka, 1971 for a review).

d) Photometry of Io. We are beginning to match the spectral reflectance properties of various regions on Io and their photometric functions with those measured for sulfur and sulfur compounds at various wavelengths and temperatures in our laboratory.

e) Search for Post-Eclipse Brightening on Io. Binder and Cruikshank (1964) and some other observers have reported occasional anomalous brightenings of Io by some 10% as the satellite reappears from eclipse by Jupiter. Such anomalies apparently last 10 to 15 minutes and have been attributed to the condensation of an atmospheric constituent during the eclipse. We have analyzed data on two such eclipse reappearances obtained by Voyager 1. The sequences consist of violet ($0.41 \mu\text{m}$) frames taken every 96 seconds for 32 minutes after reappearance (Sequence 1) and for 15 minutes (Sequence 2). None of the surface markings visible in these frames changed its albedo during the reappearance (Figure 2). These negative results from Voyager have important implications for the SO_2 budget on Io and for the existence of extensive areas of free sulfur on the satellite.

References

- Binder, A., and Cruikshank, D. (1964). Icarus 3, 299.
Pilcher, C. B., Ridgeway, S. T., and McCord, T. B. (1972). Science 178, 1087-89.
Veverka, J. (1977). Photometry of satellite surfaces. Chapter 9 in Planetary Satellites (J. Burns, ed.), Arizona.

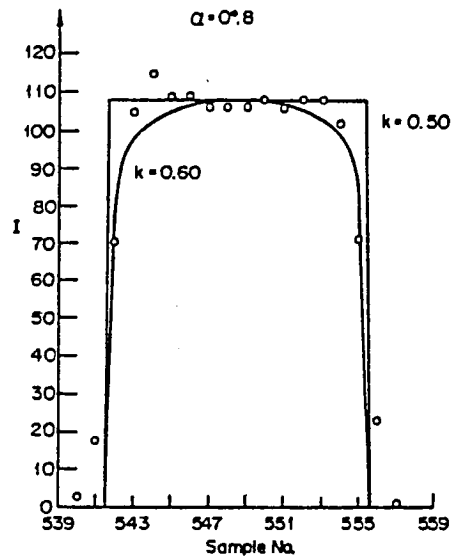


FIGURE 1. A plot of the intensity of scattered light along the photometric equator of Amalthea (points) at a phase angle of 0.8 . The solid lines represent a scattering law of the form $I \propto \mu_0^k \mu^{k-1}$ where $\mu_0 = \cos i$, $\mu = \cos \epsilon$, and i and ϵ are the angles of incidence and emission, respectively. Since all the data points fall between $k = 0.5$ and $k = 0.6$ we conclude that Amalthea shows almost no limb darkening at opposition. Note that no MTF correction has been applied, explaining some of the blurring at the limbs.

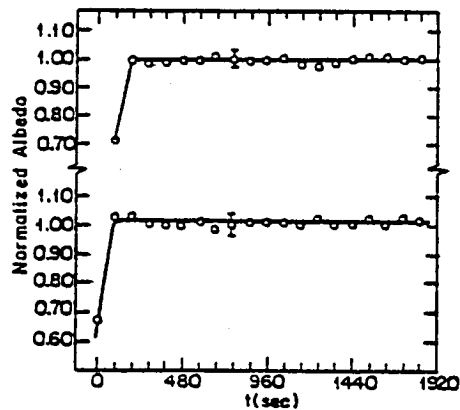


FIGURE 2. Brightness as a function of time of two sample regions on Io during the first eclipse reappearance observed by Voyager I. No anomalous brightening was detected.

Phase Functions of Water Frosts and Ice. Norman G. Purves and Carl B. Pilcher, Institute for Astronomy, University of Hawaii, Honolulu.

The phase functions in visible light of various water frosts and ices grown under low pressure (≤ 1 torr) at Galilean satellite temperatures were measured. The radiation reflected from the samples can largely be resolved into two components: one diffuse and one specular. For illumination within $\sim 20^\circ$ of the surface normal, the reflection of most frosts is largely diffuse. At larger angles of incidence the specular component becomes prominent, appearing at an emission angle somewhat larger than the incident angle. This angular difference is probably caused by the range in orientation of surface ice facets and the rapid increase in reflection with increasing angle of incidence above about 45° , as described by Fresnel's laws. The reflection of ice, on the other hand, is dominated by the specular component, which emerges at an angle equal to the angle of incidence, as expected for a planar surface. "Fairy-castle" frosts show a significantly different phase function from closely packed fine-grained frosts. The former show a much stronger specular component, but lower spherical reflectance. These different optical characteristics might be used to distinguish these frost structures from one another on the surfaces of solar system objects.

Basin Peak-Ring Spacing on Ganymede and Callisto:
Implications for the Origin of Central Peaks and Peak Rings
Joseph M. Boyce*, U.S. Geological Survey, Flagstaff, AZ 86001

The origin of interior mountain peaks and mountain rings in large impact craters has been a matter of controversy. Wood and Head (1976) have shown that there is a morphologic progression, with increased diameter, from the occurrence of central peaks, to peak rings to multiple rings. Some observers have suggested that this sequence is controlled by a single dominant factor. But the specific controlling factor for this morphologic sequence is unknown with other factors playing only minor roles. In an effort to understand the factors that control formation of these features, Head (1978) compiled the peak ring - rim diameter data for the Moon, Mercury and Mars. He discovered that there is a similar linear relationship between the two parameters for all three planets. He noted that the onset diameters for peak-rings for each planet was different and that the difference could be related to differences in impact velocities. Also, from these data Head (1978) concluded that peak-ring formation was dominated by kinetic energy and not the gravitational potential energy. Croft (1979) added additional planetary and Earth data to those compiled by Head. He noted that earth basin peak-rings diameter are systematically larger than those on other planets, but show a similar functional dependence. He suggested that peak-rings represent broken surface materials rebounding just within the gravity controlled transient cavity wall.

The purpose of this paper is to examine the relationship of peak-ring diameters and rim diameters of craters on Callisto and Ganymede and to compare them with previous data to better understand peak-ring formation.

Peak-ring diameters and rim diameters have been measured for craters on Callisto and Ganymede. To account for the effect of topographic flattening due to viscous flow of the icy surface materials measurements of the rings were made from the center of the mountains on each side of the ring instead of at the interior edge of the mountain scarp.

Ganymede - The relationship of peak-ring diameters to rim diameters of craters on Ganymede is shown in Figure 1 and is similar to that discovered by Head (1978) for terrestrial planet craters other than Earth. Peak-ring diameters occur over a range of from 33 km to 124 km.

*Present Address: NASA Headquarters, Washington, DC 20546

Callisto - The relationship of peak-ring diameter to rim diameter of craters on Callisto is shown in Figure 2. Like the Earth, the functional relationship is similar to that of the other planets and Ganymede but like the earth there is a systematic increase (about 1.4 x for Callisto) in peak-ring diameters for comparable rim diameters. Peak-ring diameters on Callisto occur over the range of from 26 km to 98 km.

The new data presented here and that summarized by Head (1978) and Croft (1979) indicate that, except for Callisto and the Earth, all planets investigated show nearly the same peak-ring diameter versus rim diameter relationship. The Callisto and Earth peak-ring craters exhibit a functional relationship that is directly proportional to that for the other planets but with systematic increases in diameter of the peak-rings in relation to the rim diameter. Additionally, onset diameters for Callisto and Ganymede are larger than that for the Earth but smaller than those for the other terrestrial planets.

The fact that the peak-ring diameter is not a functional invariant directly related to rim diameter, as suggested by Head (1978), is indicated by the Callisto and Earth relationship. Their relationship is slightly different from the other terrestrial planets which shows that this relationship is affected by environmental factors. Some of those factors were evaluated by Head (1978) and in the light of the new data will be reevaluated herein.

The new data suggest there is no correlation between the peak-ring diameter relationships and the gravity of the planets supporting the suggestion of Head (1978) that gravity differences only play a minor role in affecting peak-ring formation. Additionally, the new data suggests that there is no correlation between the peak-ring spacing or onset diameter relationships and the impact velocity at the planets surface. Therefore, this lack of correlation suggests that impact velocity plays only a small role in controlling onset diameter or the peak-ring to rim diameter relationship.

Cintala et al (1977) has suggested that substrate structural characteristics related to impact brecciation (megaregolith) may play a major role in crater morphology development. However, the new data indicate that substrate structural characteristics play only a minor role in peak-ring diameter spacing as suggested by the necessity for unrealistic requirements such as (1) the megaregolith of the rocky planets

which have stable ancient crusts and Ganymede which has a dynamic crust would have to be structurally similar; (2) the near surface structure of all terrains on both icy satellites would have to be different; and (3) the near surface structure would have to be similar for the Earth (dynamic crust) and Callisto (ancient stable crust). Additionally, for the same reason the new data suggest that other target material characteristics such as composition also play only a minor role in controlling the peak-ring diameter to rim diameter relationships. The new data also suggest that meteoroid material characteristics (e.g. density) difference throughout the solar system play only a minor role in controlling peak ring - rim diameter relationships. This is indicated by the large distance (from Mercury to Ganymede) between bodies with similar peak-ring relationship and short distances (Ganymede to Callisto; Earth to Moon) between some bodies with different peak-ring relationships.

In conclusion, the peak-ring diameter - rim diameter data indicate that previous simple hypotheses that involve only one dominant factor as controlling ring spacing can be rejected. Other factors that could effect peak-ring formation have yet to be proposed and it is difficult to imagine likely new candidates. Therefore, we suggest that none of the previously mentioned factors dominate over the others, but combine (gravitational potential energy, impact velocity, or a single target or meteoroid characteristic) to produce the observed relationship, with effects of factors adding and cancelling. However, precisely how this is done is difficult to access because the effects of individual factors are unknown. But using knowledge of how these factors effect related cratering parameters (in particular rim diameter) and which geologic factors dominate on a particular planet we can speculate how the factors work in concert to produce the observed relationship. For example, to make a preliminary test of this hypothesis the following simple assumptions have been made: (1) increased impact velocity decreasing the relationship; (2) increased gravity decreasing the relationship; (3) increased megaregolith brecciation decreasing the relationship; (4) increased amount of rocky component to target material decreasing the relationship; and (5) increased density of meteoroid material decreasing the relationship. A matrix was constructed using these assumed parameters and their effects added and subtracted. The results showed that the Earth and Callisto would be expected to have decreased peak-ring diameter to rim diameter relationships compared to the other bodies investigated.

References

- Cintala, M. J., Wood, C. A., and Head, J. W., 1977, The effects of target characteristics on fresh crater morphology: Preliminary results for the Moon and Mercury, Proc. Eighth Lunar Sci. Conf., Houston, Texas, v. 3, p. 3409-3426.
- Croft, S. K., 1979, Interplanetary basin ring spacing: Consequence of gravity vs. Strength Scaling: (abs) Lunar and Planet. Sci. Conf. 10th, Houston, Texas, v. 1, p. 245-247.
- Head, J. W., 1978, Origin of central peak rings: Evidence from peak-ring basis on Moon, Mars, and Mercury; (abs) Lunar and Planet. Sci. Conf. 9th, Houston, Texas, v. 1., p. 485-487.
- Wood, C. A., and Head, J. W., 1976, Comparison of impact basins on Mercury, Mars, and the M oon, Proc. Lunar Sci. Conf. 7th, Houston, Texas, v. 3, p. 3627-3651.

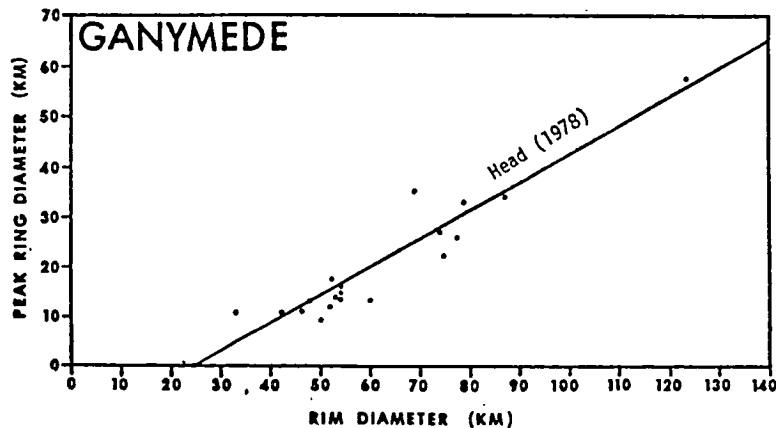


FIGURE 1

Relationship of peak-ring diameter and rim diameter of craters on Ganymede. The relationship for craters on the Moon, Mercury and Mars (Head, 1978) is included for comparison.

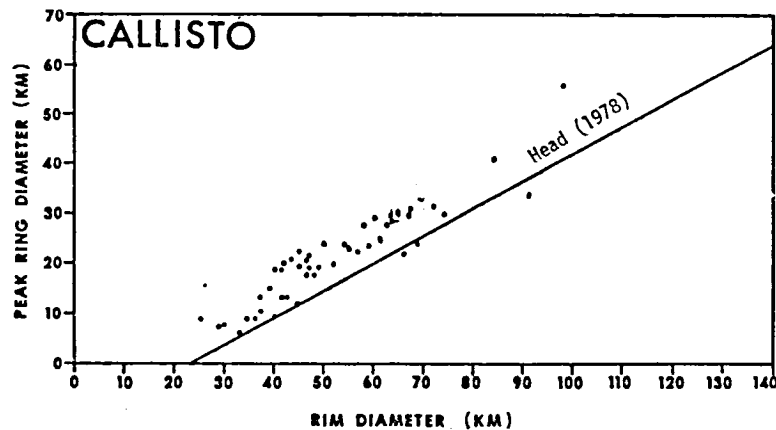


FIGURE 2

Relationship of peak-ring diameter and rim diameter of craters on Callisto. The relationship for craters on the Moon, Mercury and Mars (Head) is included for comparison.

Amalthea: Analysis of Voyager Imaging Data. J. Veverka, P. Thomas, J. Gradie, Cornell University; D. Morrison, University of Hawaii; M. Davies, RAND Corporation.

Several sequences of observations of Amalthea were carried out during the recent Voyager encounters with Jupiter over a variety of orbital longitudes, solar phase angles, and wavelengths. The last images, obtained from a range of 425,000 km, have a resolution of 8 km/line pair.

Amalthea turns out to be a dark, irregular object whose dimensions are 270 ± 10 , 165 ± 15 and 153 ± 5 km (Figure 1), values which compare well with the estimate of the mean diameter by Rieke (Icarus, 25, 333, 1975) of 240 ± 60 km, based on infrared observations from Earth. The satellite is locked in synchronous rotation (period = 12 hours), with the longest axis pointing toward Jupiter.

Amalthea's normal reflectance is about 5%, consistent with the upper limit quoted by Millis (Icarus, 33, 319, 1978). Spectrally the satellite is very red. Mixtures of sulfur and carbonaceous material have similar colors, suggesting that the surface of Amalthea may be contaminated by sulfur ultimately derived from Io.

The Voyager images reveal a number of albedo markings on the satellite (scale: 20-30 km), which are brighter by a factor of 2 than the average surface, and less red.

A few large craters are visible in the best images (Fig. 2); the three most prominent have diameters ranging from about 50 to 90 km. The surface density of craters in the 20 to 90 km range is consistent with that recorded in the lunar uplands.

Since g on Amalthea is about 10 cm/sec^2 , a value about one order of magnitude larger than g on Phobos and Deimos, but an order of magnitude smaller than on the Moon, higher resolution images of the surface of Amalthea on future missions would provide a sensitive test of the effects of gravity on crater morphology.

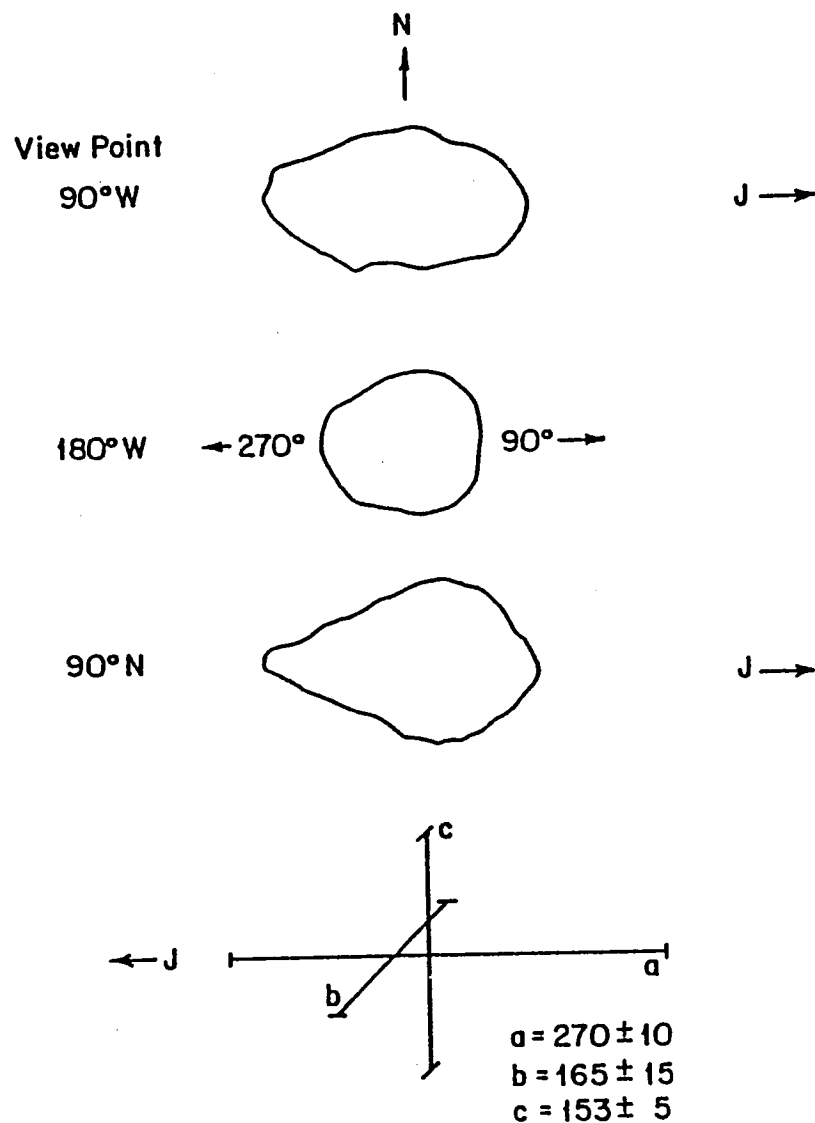


FIGURE 1. Silhouettes of Amalthea based on Voyager data. The satellite is definitely not ellipsoidal. The dimensions given below are the maximum diameters in three orthogonal directions.

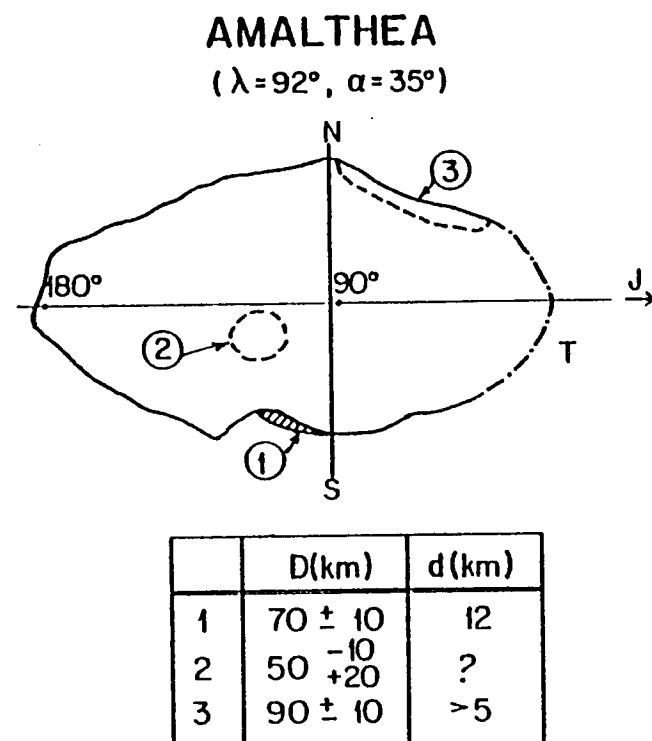


FIGURE 2. Sketch of Amalthea based on a Voyager I image obtained from a range of 695,000 km (resolution 13 km/lp). Subspacecraft longitude = 92° ; solar phase angle = 35° .

The three largest craters are indicated. D is the crater diameter; d is an estimate of crater depth.

Volume Changes in Ganymede and the Origin of Grooved Terrain. S. Squyres, Department of Geological Sciences and the Laboratory for Planetary Studies, Cornell University, Ithaca, New York; E. M. Shoemaker, U.S. Geological Survey, Flagstaff, Arizona.

The geological relationships of grooved terrain on Ganymede suggest that the grooved terrain formed by extensional deformation. No convincing evidence of major zones of compressional deformation has been recognized, however. Therefore, it appears that Ganymede expanded during grooved terrain formation. Crater densities on the grooved terrain indicate that most of the expansion took place near the end of heavy bombardment, probably in the time range of 4.0 to 3.5 Gy.

Changes in the mean specific volume of Ganymede may have occurred as a result of various phase changes at different times in its thermal evolution. If Ganymede accreted homogeneously, a substantial expansion might have occurred during differentiation. Assuming thermal histories like those proposed by Consolmagno and Lewis (1976), the formation of a silicate core, water mantle, and a thin ice I crust from an initially homogeneous body at 100°K would result in a surface area increase of 5.7 to 7.2 percent. These figures are based on the known phase relationships of pure H₂O and the assumptions that all H₂O migrating to the mantle and crust was initially in the form of H₂O ice and that the silicate density was in the range of 2.5 to 3.7 g cm⁻³. Expansion occurs because the high density polymorphs ice II ($\bar{\rho} = 1.18 \text{ g cm}^{-3}$), ice VI ($\bar{\rho} = 1.34 \text{ g cm}^{-3}$) and ice VIII ($\bar{\rho} = 1.66 \text{ g cm}^{-3}$) melt to form water with a mean compressed density in the range 1.10-1.25 g cm⁻³.

If the postulated water mantle of Ganymede refroze after differentiation, due to solid state convection in the lower part of the ice I crust (Reynolds and Cassen, 1979), the resultant volume change may have been small. The net surface area change for complete refreezing would have been a decrease of less than 0.5 percent. With silicates occupying the high pressure region at the core, only ice VI, II, and I would crystallize in significant amounts; their proportions yield a mean ice density close to that of compressed liquid water.

Because the freezing temperature of ice has a minimum at the ice I--ice II transition, increasing from that point for both lower and higher pressures, refreezing of a liquid water mantle would proceed from the core upward and the crust downward simultaneously. Contraction would occur continuously through most of this process, with the volume decrease from freezing of high pressure polymorphs at depth more than compensating for the volume increase from freezing of ice I. The only expansion that could take place during refreezing would be during the final simultaneous freezing of ice I and ice III, amounting to a surface area increase of less than 0.1 percent. These calculations are valid for nearly pure H₂O. Other plausible constituents in solution in the melt may have had considerable effect both on the phase relationships and the densities of specific phases.

Other possible phase changes of interest that may have taken place in Ganymede include replacement of olivine by serpentine (and decomposition of serpentine to olivine and water) and the crystallization or decomposition of clathrates. Too few clues are available at present, however, to assess the importance of these changes.

Our understanding of the accretion history and thermal history of Ganymede is not yet sufficient to identify with confidence the cause of expansion at the time grooved terrain was formed. If Ganymede accreted heterogeneously, first from silicates and later from ice, expansion due to melting of the ice probably was small (comparable in magnitude to the decrease in volume accompanying freezing of a water mantle). Accretional heating and heating by relatively short-lived radionuclides (e.g., Al^{26}), moreover, may have led to melting of ice at much earlier times than found from the thermal histories calculated by Consolmagno and Lewis. Hence, expansion due to initial melting and differentiation may have occurred prior to the development of any surface now preserved on Ganymede. In this case, expansion accompanying formation of the grooved terrain probably must be explained by phase changes other than melting of dense H_2O ice.

S. Squyres' participation in the project is supported in part by NASA grant NSG 7156.

References

- Consolmagno, G. V., and Lewis, J. S. (1976). Structural and thermal models of icy Galilean satellites, in Gehrels, T. (ed.), *Jupiter*. Univ. of Arizona Press, Tucson, pp. 1035-1051.
- Reynolds, R. T., and Cassen, P. M. (1979). On the internal structure of the major satellites of the outer planets. *Geophys. Res. Lett.*, v. 6, pp. 121-124.

IMPACT HEATING OF H₂O ICE TARGETS: APPLICATIONS TO OUTER PLANET SATELLITES

Cintala, M.J., Head, J.W., and Parmentier, E.M., Dept. of Geological Sciences, Brown Univ., Providence, RI 02912

Voyager photography of the Galilean satellites of Jupiter demonstrates that impact cratering has been an important process in the development of the surfaces of Ganymede and Callisto.¹ Various lines of evidence indicate that at least the outer crust of each of these bodies is rich in H₂O ice.² While many of the details of the cratering process in the more familiar silicate targets are applicable to similar events in ice, there are some important differences. Perhaps foremost of these is the partitioning of projectile kinetic energy into heating both the meteoroid and the impacted target material. This report is directed toward an evaluation of impact heating in H₂O ice targets, a comparison with similar calculations for basalt targets, and application of the results to some specific planetary problems.

Method of Calculation - The procedure outlined by Gault and Heitowit³ was applied in evaluating shock attenuation and target heating as a function of distance from the impact point. This method assumes that the energy contained within the affected volume of target material is constant throughout the duration of shock propagation. In addition, release adiabats are approximated by the Hugoniot of the target material; multiple wave structures are not taken into account. While this technique might underestimate the quantities of melt generated by specific impact events,⁴ application of the same procedure to both target types minimizes the relative discrepancy. Hugoniot data for H₂O ice and basalt used in these calculations are from (5) and (6), respectively.

Projectile Types and Impact Velocities - In order to bracket a range of possible meteoroid compositions, calculations were carried out for projectiles with the shock properties of iron, basalt (to simulate ordinary chondrites and/or achondrites), lunar regolith (carbonaceous chondrite), and H₂O ice, impacting over a range of 5 to 30 km/s in 5 km/s increments.

Results - The results of these computations are summarized in Figure 1. A number of observations can be made: (1) more projectile kinetic energy is expended as heat during impacts into the basalt targets, (2) denser projectiles partition less of their kinetic energy into heat, and (3) the much larger kinetic energy densities of the denser projectiles imply that, although the fraction of the initial kinetic energy partitioned into heating is smaller, the total energy dedicated toward this end is generally higher than that of the less dense projectiles. Weaker shock attenuation in basalt and its greater density (hence, affected mass) account for (1), while more gradual (therefore, thermodynamically more efficient) projectile-target coupling, which arises from the density

IMPACT HEATING OF H₂O ICE TARGETS

Cintala, M.J. et al.

contrast in favor of the projectile, results in (2). Nevertheless, since it is energetically closer to its fusion and vaporization points than is basalt in most realistic cases, greater volumes of H₂O ice will undergo shock-induced phase transitions under a given set of impact conditions.⁷

Applications - (1) Silicate/H₂O Differentiation: The large volumes of low viscosity melt formed by impacts into H₂O ice would allow effective segregation of silicate particles sufficiently large to settle through convecting melt sheets. This mechanism could have made an important contribution to large-scale differentiation of Ganymede and/or Callisto early in their histories, particularly in allowing silicates to migrate through a relatively rigid outer crust into a liquid mantle.⁸ (2) Mass Loss through Vapor Escape: Preliminary calculations assuming ideal gas behavior indicate that temperatures high enough to allow the escape of H₂O vapor from Ganymede or Callisto would be realized predominantly during the highest velocity impact events. Insofar as this portion of the target would be ejected at the greatest velocities by the impact process itself, it appears that the effects of thermal escape of H₂O would be minimal in terms of mass loss from these bodies. (3) Maximum Ballistic Range of Solid Ejecta: On the basis of this approach, the maximum distance to which a solid/liquid H₂O mixture can be ejected on Ganymede (45° ejection angle) would be ~1300 km, with a similar figure applicable to Callisto. Since lunar material ejected the same distance at the same angle would have its temperature raised only by ~100°K, secondary cratering phenomena on icy bodies are expected to differ somewhat from those on the more familiar silicate-crust planets. (4) Crater Interior Morphology: Provided that a large fraction of melt remains inside the final cavity as in the case on the terrestrial planets, comparisons of interior morphologies of craters formed in ice-rich crusts with those on the inner planets might be hindered by the greater melt volumes associated with the impacts into ice. Indeed, the fact that pure gravity-scaling yields craters in ice with volumes only ~2.4 times greater than those formed in basalt by similar energy events, coupled with the possibility that melt volumes could be 3-5 times larger in ice,⁷ serves to underscore the need for caution in interpreting the observational data.

Efforts are underway to refine these approaches and to evaluate the partitioning of energy into comminution, ejecta, and other forms of work during impacts into H₂O ice.

References: ¹Smith B.A. et al. (1979) Science 204, 951-972. ²Johnson T.V. (1978) Ann. Rev. Earth Planet. Sci. 6, 93-125. ³Gault D.E. and Heitowit E.D. (1963) Proc. 6th Hypervel. Impact Symp., 419-456. ⁴O'Keefe J.D. and Ahrens T.J. (1977) Proc. Lunar Sci. Conf. 8, 3357-3374. ⁵Anderson G.D. (1968) CRREL Res. Report 257. ⁶Lombard D.B. (1961) Lawrence Rad. Lab. Report UCRL-6311. ⁷Cintala M.J. et al. (1979) Lunar Planet Sci. X, 207-209. ⁸Parmentier E.M. and Head J.W. (1979) J. Geophys. Res., in press.

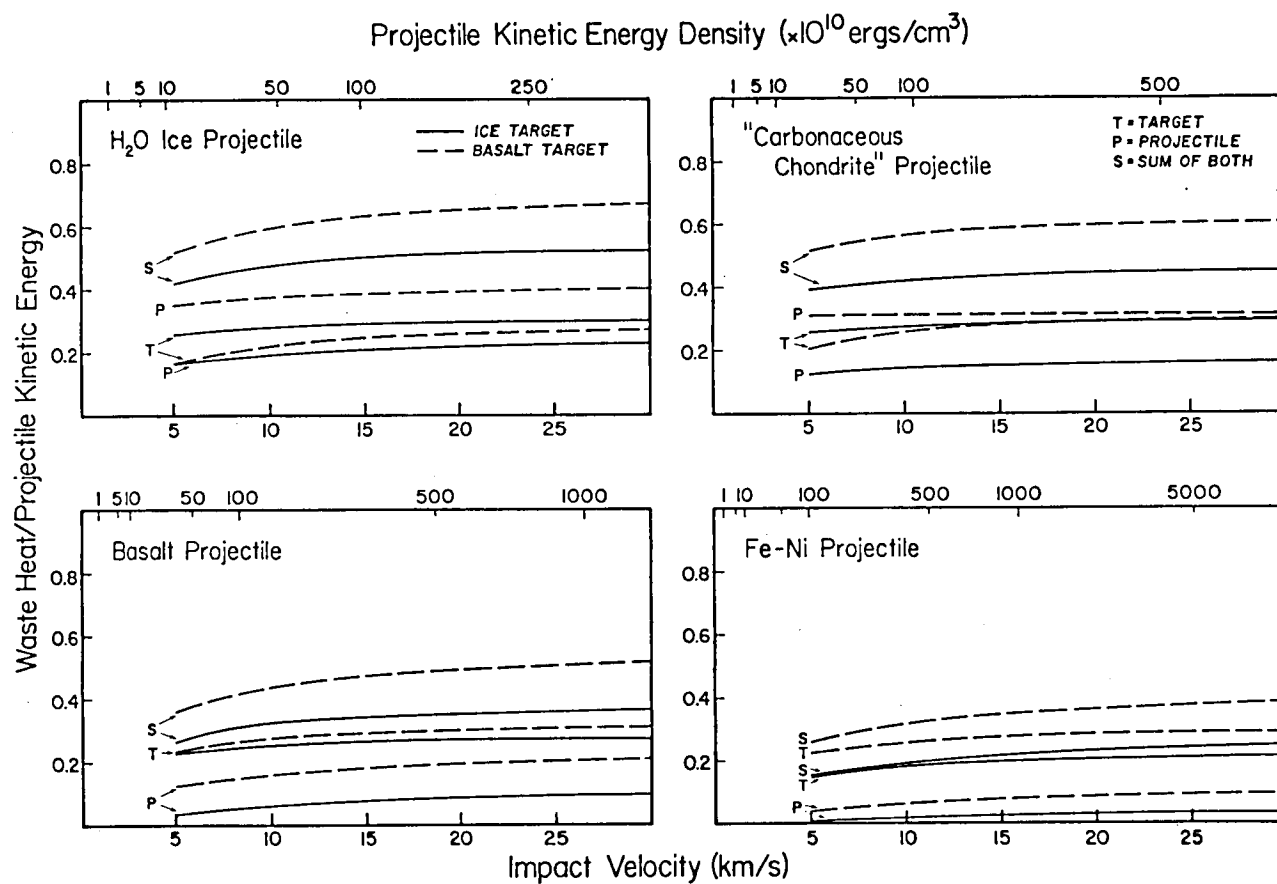


Figure 1. Projectile kinetic energy partitioned into heating both meteoroid and target material as a function of impact velocity and projectile kinetic energy density.

Chapter 10

**PLANETARY CARTOGRAPHY, GEODESY, AND
GEOLOGICAL MAPPING**

IMPROVED ACCURACY OF COORDINATES OF FEATURES ON MARS

Davies, Merton E., The Rand Corporation, Santa Monica, California 90406

The objective of this program is to improve the accuracy of the control points on Mars in the region around the Viking 1 landing site and to tie this area to the small crater Airy-0 with a photogrammetric strip of pictures. Airy-0 defines the longitude system on Mars; thus this strip should yield an improved value for the longitude of the Viking 1 landing site and, since the strip is tied to the planetwide control net, it will improve the accuracy of all of the coordinates. The latitude of the landing site has been determined very accurately by the Lander Radio Science Team.

In the region of the Viking lander, the study started with three high resolution pictures (2-pixel resolution ~ 20 m) and four additional pictures to provide stereo. The 32 control points were measured on 2 to 6 frames. The triangulation was performed using the GIANT program. The standard errors of the latitudes of the control points lay between 73 m and 289 m, with a median of 163 m. The standard errors of the planetary radii at the control points which were on stereo pairs lay between 459 m and 983 m, with a median of 558 m. The area of the triangulation block has now been expanded to include 32 pictures, with the result that the standard errors increase when the points lie farther from the landing site. Additional pictures will be added to improve the stereo coverage and overdetermination.

In the region around Airy-0, the study has started with two high resolution pictures (2-pixel resolution ~ 36 m) and six additional pictures. Vertical measurements of the control points were not possible as the stereo angles were too small.

A minimum of 50 pictures will be required to tie the Viking landing site to Airy-0; the resolution of these pictures will lie between 600 m and 800 m (2-pixel resolution). The entire strip will be tied to the planetwide control net and strengthen the horizontal solution throughout.

THE CONTROL NETWORKS OF THE GALILEAN SATELLITES

Davies, Merton E., The Rand Corporation, Santa Monica, California 90406

Geodetic control networks are being computed for all of the Galilean satellites using pictures from the Voyager 1 and 2 encounters at Jupiter. The satellite coordinate systems have been established to conform with IAU recommendations. Points have been identified on the satellites and their coordinates have been computed by single-block analytical triangulations. The status of the control nets is summarized in the following table.

<u>Satellite</u>	<u>Points</u>	<u>Pictures</u>	<u>Measurements</u>	<u>Normal Equations</u>	<u>Overdeterminations</u>	<u>σ(mm)</u>
Io	192	81	1760	627	2.81	0.02057
Europa	45	35	534	195	2.74	0.01407
Ganymede	190	71	1874	593	3.16	0.03285
Callisto	242	95	2152	770	2.79	0.02477

The mean radii of the satellites determined by the analytical triangulations are very close to those computed from limb measurements,¹ as may be seen below.

<u>Satellite</u>	<u>Radius (km)</u>	
	<u>Limb Measurements¹</u>	<u>Analytical Triangulations</u>
Io	1820	1819
Europa	1565	1563
Ganymede	2640	2638
Callisto	2420	2410

¹Smith, B. A., et al., "The Jupiter System Through the Eyes of Voyager 1," Science, Vol. 204, 1 June 1979, p. 951

Photogrammetric Application To Planetary Mapping, Sherman S. C. Wu, U.S. Geological Survey, Branch of Astrogeologic Studies, Flagstaff, Arizona 86001

The planetary mapping of Mars, Venus, the Moon, etc., involves many unprecedented problems; the lack of primary ground control points, the definition of the topographic datum, data acquisition and representation (imaging and nonimaging), and characteristics of the data itself. These unconventional factors require new concepts for the development of new methodology and new equipment.

Without water and therefore sea level, the most appropriate way to define the topographic datum, the zero-elevation reference surface, for a planetary body, is as a gravity level surface. The topographic datum of both the Moon and Mars have been defined using their gravity fields in terms of spherical harmonics (Wu, 1975, 1978a, 1979b). The application of analytical photogrammetric methods is considered the best way to establish a ground control network of the planetary bodies using the position and orientation parameters of the orbiting spacecraft. This method becomes especially promising because of the advancements in computerized image processing techniques where unconventional imaging geometry, line scans or parabolic surfaces, can be digitally corrected and enhanced by means of both off- and on-line processing.

Mariner 9 acquired photographic coverage of the entire surface of Mars. The Mariner 9 data, together with Earth-based radar have enabled a quantitative representation of Mars topography on a global scale (Wu, 1975, 1978a). Fifty thousand photographs from the Viking mission have opened up Mars to intensive investigation in many fields. Despite the fact that the photographs have extremely narrow fields of view, special photogrammetric techniques have been developed which allow stereo models to be set up for photogrammetric compilation. This makes it possible to use these high quality photographs, of various ranges of resolution, to systematically map the planet Mars. High altitude orbital photographs ranging up to 37,000 km are used to produce a planet-wide control network in three bands. One band is an equatorial belt and the other two will pass through the two martian poles. Medium range photographs (14,000 km to 24,000 km) are used for the compilation of a 1:2 million series of Mars maps. Four subquads (MC17-NW, MC18-NW, MC22-WN and MC8-NE) have been compiled and ten more covering the entire Tharsis dome are planned. Special topographic maps of prominent features, or features of geologic interest on Mars are compiled at larger scales (1:1,000,000 to 1:50,000) using high resolution orbital photographs. A map of the martian canyon-land has been completed. Maps of Arsia Mons and Olympus Mons are being completed. Contour intervals vary from 500 meters to as little as 20 meters. By assembling various newly derived topographic data, together with additional Earth-based radar observations of Mars, the existing Mars global topographic map is being revised, but the scale of the revised map will be 1:15 million instead of 1:25 million.

Two solutions to the problem of stereo-mapping from Viking lander imageries, which are virtually equivalent to images on a spherical surface, have been developed. The first is to rectify the pictures through image processing. Applying this approach, two topographic contour maps of areas surrounding the two landers on the martian surface have been compiled (Wu, 1976, 1979b). The second solution, which involves correction and rectification in real-time on the AS-11A analytical plotter, has also been accomplished. This latter is the most accurate means possible for the compilation of topographic maps of the two Viking landers.

A global topographic map of the Moon is under compilation based on the concepts, approach, and techniques that were used for the global topographic map of Mars. Topographic data include existing large scale contour maps, topographic information derived from Apollo and Lunar Orbiter photographs, laser altimetry, lunar radar sounder, as well as Earth-based observations. The global map is referenced to a new topographic datum (Wu, 1979a) which is defined as a potential surface of the lunar gravity field expressed in terms of spherical harmonics of sixth order and sixth degree. The map scale is 1:5,000,000 with a contour interval of 500 meters.

Using radar altimetry data along flight paths of Pioneer Venus, a preliminary contour map of Venus up to latitudes of $\pm 70^\circ$ has been completed. For this map a spherical figure of Venus is assumed. The surface of Venus can only be imaged by radar and stereo imagery will not be available until the VOIR mission. Map compilation using stereo-radar imagery has been previously attempted. But because of the unique radar geometry, topographic contour maps cannot be directly compiled on conventional stereo-photogrammetric equipment. VOIR photogrammetry is a research project for the extraction of three-dimensional topographic information of terrain features of Venus from VOIR stereo radar imagery. Using current technology of digital image processing, radar imagery is rectified so that maps are compiled on the presently available analytical plotters (Wu, 1978b). For real-time rectifications and corrections, the design and the manufacture of an interface of a digital computer to a radar plotter is being developed. The development of a full capability of radar mapping is expected to be accomplished well in advance of the VOIR mission.

References

- Wu, S. S. C., Topographic mapping of Mars, U.S. Geological Survey Inter-agency Report, Astrogeology 63, 193 p., 1975.
- Wu, S. S. C., Stereo mapping with the Viking lander imagery, presented at the XIII International Congress of the International Society of Photogrammetry, Helsinki, Finland, July 11-23, 1976.
- Wu, S. S. C., Mars synthetic topographic mapping, Icarus 33, no. 3, pp. 417-440, 1978(a).

- Wu, S. S. C., Stereo mapping with side-looking radar imagery, in abstract book, The International Symposium of the Problem of Accuracy Improvement of Photogrammetric Models, International Society for Photogrammetry, Commission IV, Moscow, USSR, July 31 - August 5, 1978(b).
- Wu, S. S. C., Topographic mapping of the Moon, NASA Technical Memorandum 80339, pp. 429, 1979(a).
- Wu, S. S. C., Photogrammetric Portrayal of Mars Topography, Journ. of Geophys. Res., Mars Colloquium special publication, Dec. 1979(b).

PRECISE MARS RELATIVE ALTITUDES

Arthur, D. W. G., U.S. Geological Survey, Flagstaff, Arizona 86001

Stereo coverage of the martian surface by Viking Orbiter is limited and heights in some areas must be obtained by non-photogrammetric methods. Shadow lengths are easily transformed into relative altitudes. The only real problem is the extraction of useful shadow lengths from electronic imagery. The lengths of large shadows are estimated quite successfully from pixel counts along the appropriate line across the shadow. Such counts are however useless for shadows of about one pixel length and an entirely different technique is necessary. This has been devised and depends on integrating the light within the shadow. In this integration method the brightness of the Mars atmosphere has a critical role and the estimation of this background radiance sets a limit to the precision of the shadow estimate. Whereas the pixel count technique usually has a precision of ± 0.5 pixels, the integration method has errors ranging from ± 10 per cent to ± 20 per cent, depending on the uniformity of the background illumination and the proximity of reference areas of known brightness.

Experience with crater depth estimates indicate that these are useful only when accompanied by other dimensions and remarks on the class or type of the crater: this point is given full weight in current work.

The third problem, involving shadows of 2 to 12 pixels, calls for Fourier methods but these are not economic and modelling techniques are under consideration. In these, one works from assumed lengths and brightnesses to arrive at photometric profiles matching the real profiles.

REFERENCE

- 1) Arthur, D. W. G., 1980, Some martian crater depths from shadows, in press.

An Interactive Computer System for Extracting Topographic Data from Viking Orbiter Stereo Digital Imagery, Steven W. Lee*, McDonnell Center for the Space Sciences, Washington University, St. Louis, Missouri 63130.

An interactive hardware/software system for computing relative positions and elevations of surface points in Viking Orbiter stereo digital imagery has been developed. The hardware consists of a PDP-11/34 computer, a video display, and a joy-stick driven dual cursor control unit. The software provides split-screen display of image pairs, interactive selection of surface points for ranging, and display of range data (Lee, et. al., 1979). No scaling, rectification, or rotation of individual images is required.

Corresponding points are identified in both images by the independently moveable cursors. A series of selected points defines a traverse across the surface (not necessarily confined to a straight line). An example of a split-screen display and a typical traverse is shown in Figure 1.

The orientation of the image planes in space is defined by specifying, for each image, the latitude and longitude of the sub-spacecraft point and central image point intercept on the surface of Mars, the spacecraft range from the center of Mars, and the azimuth of the sub-spacecraft point in the image plane. These quantities are tabulated in the SEDR data set.

Each image of an Orbiter stereo pair is acquired from a different location in space. A sequence of matrix coordinate rotations is applied to the image coordinate systems to align them with an areocentric system. First, the image plane is oriented so the scan lines parallel the great circle connecting the sub-spacecraft point and central image intercept. Rotating through the emission angle at the central image intercept (calculated from the given SEDR data), the image plane is made perpendicular to the surface normal at the intercept. A further rotation through the angle between the sub-spacecraft point/central intercept great circle and the circle of longitude through the sub-spacecraft point (also a calculated angle) aligns the scan line direction parallel to Mars' equatorial plane. Subsequent rotations through the central intercept point's areocentric latitude and longitude results in final alignment of the image coordinates with the areocentric system at 0° latitude, 0° longitude. The described rotations differ from those of Benesh (1978); the spacecraft and scan platform pointing vectors used by the JPL routines are not readily accessible data.

The stereobase, or spatial separation between the right and left image coordinate systems, is determined from the spacecraft positions relative to Mars at the time each image was shuttered. Standard photogrammetric equations can then be employed to compute X,Y,Z coordinates relative to one image coordinate system (Tewinkel, et. al., 1966). Translation of origin to the center of the areocentric system yields values of latitude, longitude, and range from the center of Mars for the selected points. Elevations and distances are displayed relative to one of the surface points selected by the user.

A profile along the traverse of Figure 1 is shown in Figure 2. Comparison is made to a vertical profile drawn from a USGS topographic map (Wu, 1979); good agreement is evident. The technique developed allows rapid extraction of relative topographic information from digital stereo imagery, and requires access to only modest computer facilities.

References:

- Benesh, M., 1978, Viking Orbiter Stereophotogrammetry, Photogrammetric Engineering and Remote Sensing, 44, pp. 265-271.

Lee, S.W., Guinness, E.A., Bolef, L.K., and Arvidson, R.E., 1979, A Simple Interactive System for Extraction of Topography from Stereo Digital Images, abstract in Reports of Planetary Geology Program, 1978-1979, NASA TM-80339, pp. 403-404.

Tewinkel, G.C., Schmid, H.H., Hallert, B., and Rosenfield, G.H., 1966, Basic Mathematics of Photogrammetry, in Manual of Photogrammetry, Amer. Soc. of Photogram., Falls Church, Va., Vol. 1, pp. 19-65.

Wu, S.S.C., 1979, Mars Photogrammetry, abstract in Reports of Planetary Geology Program, 1978-1979, NASA TM-80339, pp. 432-435.

* Present address: Laboratory for Planetary Studies, Cornell University, Ithaca, New York 14853.

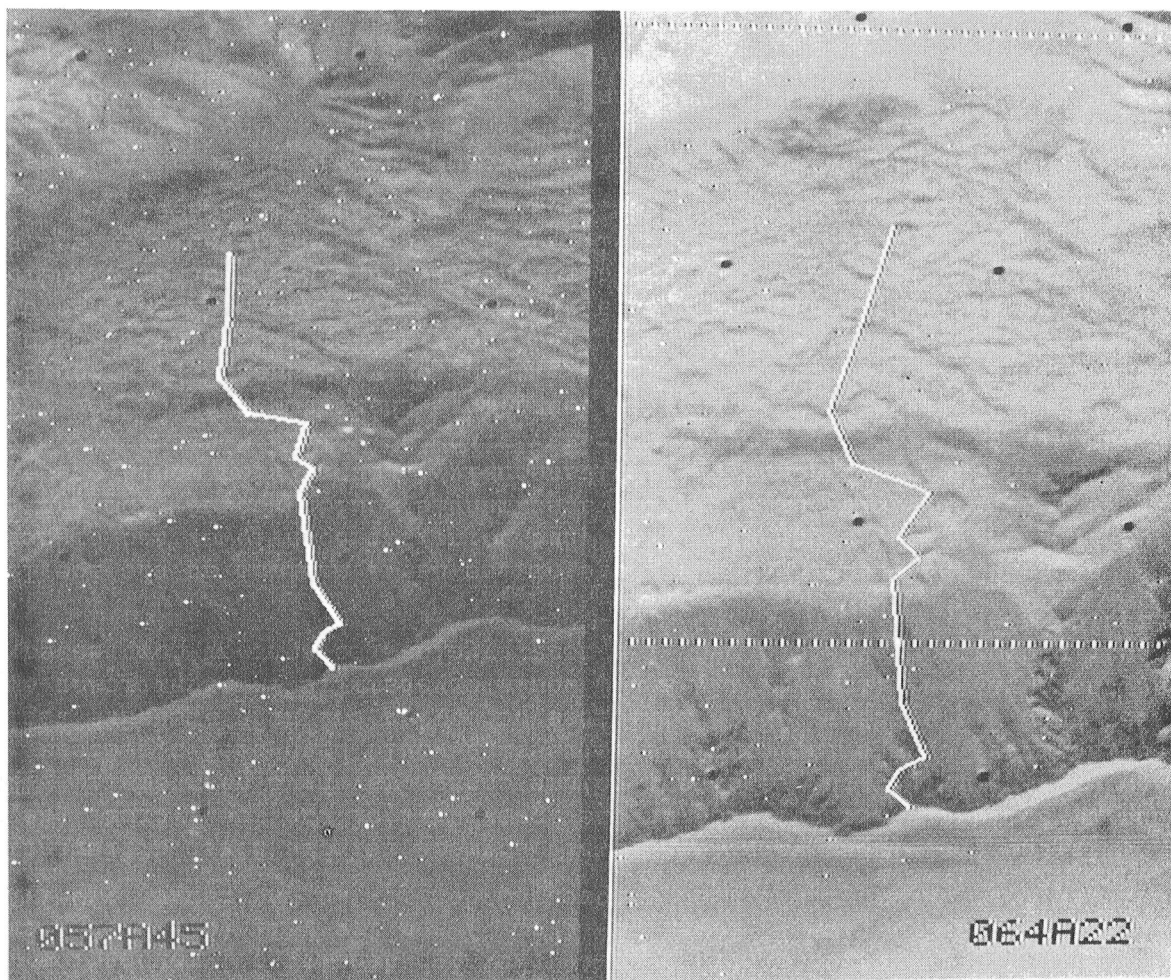


Figure 1: Split-screen video display of Orbiter stereo pair of Tithonium Chasma. The white traces mark the traverse discussed in the text.

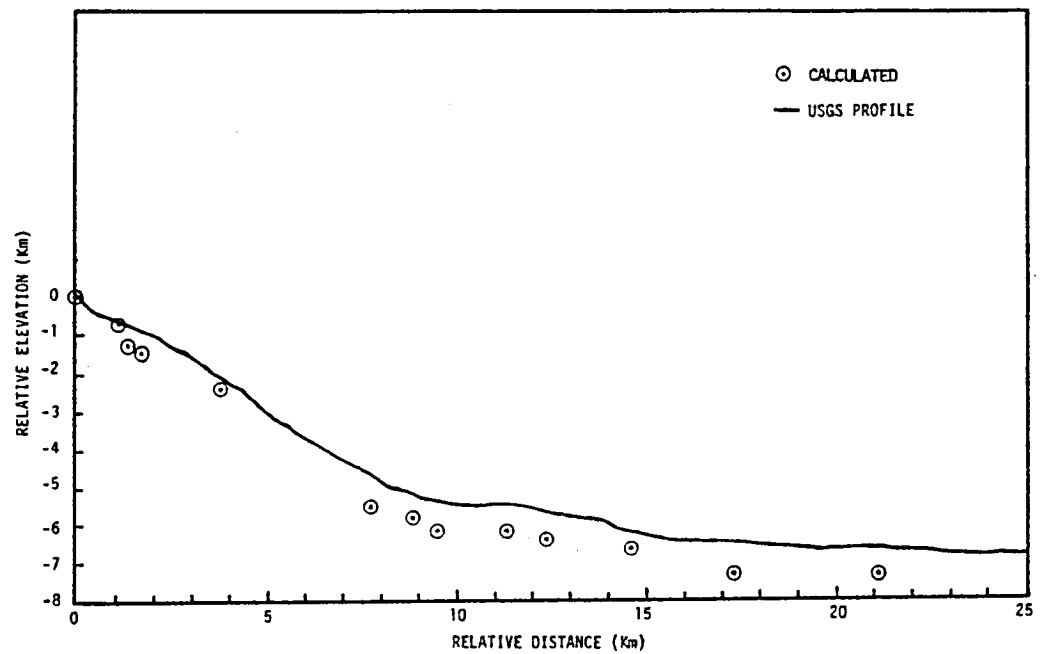


Figure 2: Comparison of calculated elevations and distances to a vertical profile from Wu (1979). All calculated values are relative to a point chosen to be on the rim of the chasm.

RELATIVE ELEVATIONS IN THE VALLES MARINERIS CHAOS

Roth, L. E., Downs, G. S., and Saunders, R. S., Jet Propulsion Laboratory, California Institute of Technology, Pasadena, CA 91103;
Schubert, G., Dept. of Earth and Space Sciences, University of California, Los Angeles, CA 90024.

Chaotic terrain [1] constitutes a substantial fraction of the floor of the extended hollow that marks the transition from the Coprates to the Eos and Capri Chasmae (i.e. from the East Central Troughs to the Eastern Canyons [2]). To the N and NW, the hollow is bounded by steep scarps. The remaining boundaries are less sharply defined and locally may involve a gradational change from the cratered plains to the chaotic material, with spots of the cratered plains preserved inside the hollow. The scans by both the Haystack [3,4] and Goldstone [5,6] radars indicate a negative relief of as much as 6 km inside the hollow, in contrast to the negative relief of about 2 km derived from the Mariner 9 UVS data (cited in [2]).

The Goldstone observations are summarized in Fig. 1. The large scatter in the range measurements over the hollow is caused by the fact that the ranging algorithm selects the peak in power reflected by the area closest to the earth, hence favoring the higher elevations. However, when a particular region at high elevations becomes too rough to be detected, a lower elevation, if sufficiently smooth, will be selected by the algorithm. In this manner, as the planet rotates, the range can jump from the chasm rim (or from an intermediate plateau within the chasm) to the chasm floor. This has prompted separation of the measured elevations into two groupings. The intermediate elevations are presented in Fig. 1a, while the extreme negative elevations are presented in Fig. 1b. The plains surrounding the chasm are situated at average elevations between -1.0 and -2.0 km relative to the reference areoid. In the interval between -2.0 km and about -4.8 km (the intermediate elevations in Fig. 1a), the incidence of the elevation measurements is fairly uniform, and it declines below the lower boundary of that interval. This trend is reversed near -6.0 km, with about 135 elevation readings between -6.0 and -8.0 km [7]. These measurements form the extreme negative elevations grouping (Fig. 1b). Several factors, viz. the large number of the data points in the latter group, their repeatability, wide occurrence within the chasm, and favorable signal/noise ratios [7], coupled with the good areal resolution of the Goldstone data (about 1000 km² [6]) seem to indicate that sizable portions of the chasm floor are situated about 6 km below the level of the surrounding plains. Isolated floor segments may be situated at even greater depths.

Elevation differences of this magnitude, if confirmed by other means, pose new questions as to the mechanism of the chaos formation and the

disposition of the materials involved. Chasm material in various stages of subsidence can be anticipated to produce a wide range of elevations. The scarp retreat along the chasm boundaries and at various localities within the chasm might, perhaps, be associated with the fluvial activity (e.g., deterioration or melting of the ground ice, and subsequent cliff undermining [1]) that resulted in establishment of the intermediate elevations of Fig. 1a. On the other hand, the collapse of the chasma floor has been difficult to reconcile with both the austere planetary volatile budget [8], and with the more generous allowance for the water content of the Martian permafrost [1]. The observed elevation contrast in the chasm (Fig. 1b) makes the ground subsidence due to the wholesale withdrawal of the supporting volatile agent even less likely, while increasing the attractiveness of other mechanisms, such as the withdrawal of magmatic support at depth [1]. It thus appears that, apart from a possible tectonically triggered beginning, at least two different mechanisms participated in the chaos formation, each responsible for a different part of the observed elevations spectrum.

References

- [1] Sharp, R. P. (1973). J. Geophys. Res. 78, 4073-4083.
- [2] Blasius, K. R., Cutts, J. A., Guest, J. E., Masursky, H. (1977). J. Geophys. Res. 82, 4067-4091.
- [3] Pettengill, G. H., Rogers, A. E. E., Shapiro, I. I. (1971). Science 174, 1321-1324.
- [4] Pettengill, G. H., Shapiro, I. I., Rogers, A. E. E. (1973). Icarus 18, 22-28.
- [5] Downs, G. S., Goldstein, R. M., Green, R. R., Morris, G. A., Reichley, P. E. (1973). Icarus 18, 8-21.
- [6] Downs, G. S., Reichley, P. E., Green, R. R. (1975). Icarus 26, 273-312.
- [7] Roth, L. E., Downs, G. S., Saunders, R. S., and Schubert, G. (1979). Submitted to Icarus.
- [8] Woronow, A. (1972). Science 178, 649-650.

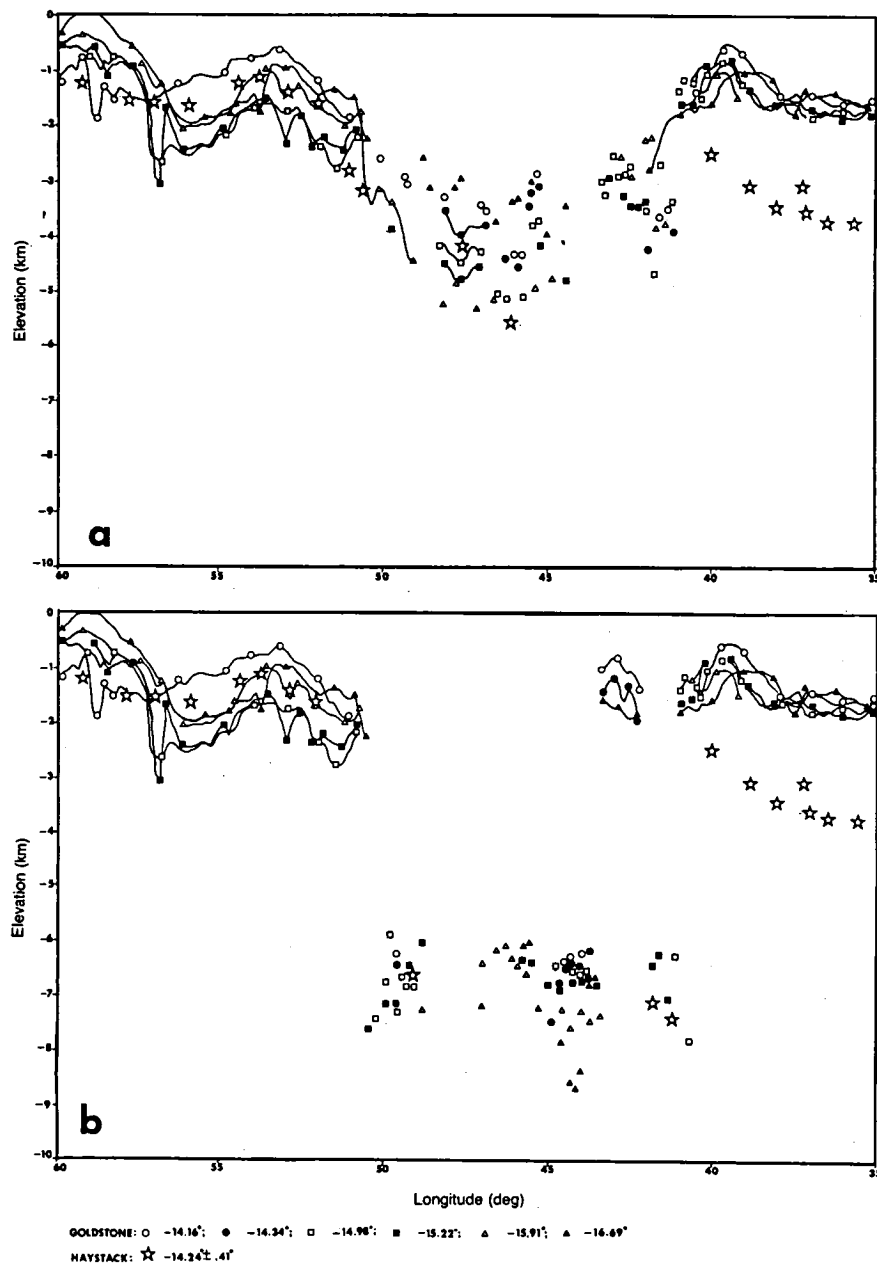


Fig. 1

Relative elevations in the chaotic terrain at the junction of the Coprates, Eos, and Capri Chasmae. (a) Intermediate Elevations. (b) Extreme Elevations. (6 Goldstone radar scans between the latitudes -14.16° and -16.69°. Haystack data points taken from [4]).

VIKING LANDER INTERACTIVE COMPUTERIZED VIDEO STEREOPHOTOGRAMMETRY:
Accomplishments and Prospects

Sidney Liebes, Jr, Artificial Intelligence Laboratory, Department of Computer Science, and Elliott C. Levinthal, Department of Genetics, Stanford University, Stanford, CA 94305.

The abstracts for the previous PGPI Conference described the general goals of this effort and, very briefly, the operation of the Stereo Station.

The work, now in progress, is based on the topographic analysis of the entire stereoscopically mappable surroundings of the two landers. It consists of publishable map material for the following:

1. Systematic contour map data (intersections with Mars of planes oriented perpendicular to the local Martian zenith), extending from the immediate foreground to the remote limits of ranging capability, in excess of 100 m range, for the front and back of both landers.
2. Systematic vertical profiles (intersections with Mars of planes radiating out from the lander and containing the local Mars zenith), at 5 degree azimuth intervals, from the immediate foreground to the remote limits of ranging capability, for the front and back of both landers.

It should be noted that the systematic map data, derived as it is from two cameras located approximately 0.8 m apart and 1.3 m above the nominal Martian surface, is quite unorthodox in character. The ranging accuracy is approximately quadratically dependent upon range, with the absolute single point ranging accuracy varying from ± 1 cm near the lander to ± 20 m at 100 m range. Relative accuracy of the data is judged to be approximately ten times better than these figures. The contour interval spacing varies from a few centimeters in the foreground to a meter at 100 or more meters range. Furthermore, since stereophotogrammetry is only possible for those portions of the relief that can be imaged in common by both cameras, only the facing masks of rocks and the more remote slopes can be developed. It is additionally to be noted that image intensity binary encoding quantization noise, camera angular resolution and spatial pointing direction sampling establish a theoretical limit to the accuracy with which points and extended features can be ranged. It is believed that the accuracy of the raw map data that we have generated approaches the theoretical limit.

There is an additional quantization issue. The 3-dimensional curves that we generated for the profile and contour lines are recorded digitally as a connected sequence of elemental vectors. The fineness of the quantization steps for these vector elements was range dependent and automatically selected in the course of range data set (RDS) generation. These steps were generally selected to be somewhat finer than the absolute local point ranging accuracy. There were two principal reasons

for adopting this practice. First, we did not wish the quantization to degrade the potential for point ranging accuracy below the theoretical limit of absolute point ranging capability. Second, the potential for relative range accuracy for larger features exceeds by roughly an order of magnitude that for point ranging accuracy. This results from the ability of a human operator, doing the visual correlation, to sense an integrated mean range over an extended surface patch that is many resolution elements across.

Bearing in mind that the ranging accuracy of the map data is highly range dependent, the policy adopted in producing the contour maps has been to ensure that somewhere in the collection of delivered map materials there will be found, for any location, a sheet that is of such scale that a reader can visually examine the data to the limit of meaningful resolution for that location. This policy has led to the production of contour maps at eleven different scales: 1:1, 1:2, 1:5, 1:10, 1:20, 1:50, 1:100, 1:200, 1:500, 1:1000, and 1:2000. The map grids are all standardized to a 50 cm square, thus, for example, the single sheet at 1:2000 records RDS data out to 500 m in all directions from the centrally located lander. Multiple sheets are required at the smaller scales. The total complement of delivered sheets will be roughly 70 in number for each lander. The lander 1 contour maps have been completed, and we are now into production of the contour maps for lander 2.

All of the maps are formatted within and produced by computer. The output device is a Varian Statos 4222 electrostatic printer/plotter, with 4224 styli spaced at 0.005 inch intervals over the 21.12 inch writing width. It is a straight forward matter to command production of map sheets at any scale for any location.

It is anticipated that at least one and perhaps the only set of vertical profiles will involve non-linear scaling, in order to economize on the number and size of the sheets required to portray the data.

It is to be emphasized that all of the map data that has been generated is stored in computer accessible RDS's. This material constitutes a Martian surface topographic resource available in principle for any desired investigative purposes. The potential exists for conducting specific geometrical or statistical analyses of the topographic information contained in these RDS's.

The underlying data base for creating the RDS are the ten high resolution mosaics of the Martian surfaces produced by each of the Viking camera. This digital data is now available, as are the Optronics negatives and photoprints. In collaboration with Dr. Elliot Morris of the U.S. Geological Survey, sets of large format lithographic sheets, derived from these negatives, are being prepared.

Examples of the graphic map products and the large format mosaic half-tone products will be available for inspection at the meeting.

The Stereo Station has been returned to Stanford University. Grinnell display equipment is on order. The Grinnell is a solid state memory display device. It is being purchased with 36 bit planes of 512x512 pixel, up to 16 of which can be used to support a 6-8 bit stereo image pair for the Stereo Station. Up to three planes can be used as graphics overlay planes for each image as a 3-dimensional cursor. The Stereo Station, together with the Grinnell equipment, will be coupled into the PDP-10 computer facilities of the Artificial Intelligence Laboratory of the Computer Science Department at Stanford via a minicomputer, to be operated as a shared resource.

A first task for the system will involve working in collaboration with Prof. Raymond Arvidson of Washington University. The system will be employed to establish surface normals to be used in the reduction of Viking lander multispectral data sets for the determination of normal albedos and photometric functions.

The interactive video computer-based stereo capability, developed in support of Viking, has proven to be a powerful, versatile and highly accurate means for quantifying the landing site topography. This system has the potential for continued use for any kind of topographic analysis, be the imagery derived from Viking lander or any other camera sources. In particular, with regard to Viking lander data, the system could be used, for specialized detailed feature studies of rocks, underlying surfaces and for rock size distribution analysis, etc. We invite expressions of interest in scientific collaboration involving the further use of the RDS's and the Stereo Station.

GEOLOGIC MAPPING IN THE SOUTHWEST EQUATORIAL REGION OF MARS

King, John S. - State University of New York at Buffalo

Geologic mapping has been initiated in the southwestern equatorial region of Mars and data are now being assembled on a new mosaic of Viking imagery at a scale of 1:15,000,000. This region is covered by the 1:5,000,000 Mariner IX maps MC-16, 17, 18, 19, 24, 25 and 26. Data are being assembled from 1:1,250,000 and 1:2,000,000 medium and high resolution Viking mosaics where available as well as individual Viking images. Major lava flow fronts are being identified and related back to source wherever possible thus establishing superposition relationships and developing relative ages. Some small conical-shaped prominences with summit craters which are possible source vents have been identified. Structure is locally dominated by fractures in the central part of the area and cross cutting relationships with some offset has allowed the definition of discrete fracture sets. Units are also being defined in the older basement which makes up a large part of the crust of the southern highlands. These will be adapted to units being identified in other parts of the planet. No craters less than 150 km in diameter will be included on the final map which will emphasize unit distribution and structure.

EVOLUTION OF THE GEOLOGICAL MAP OF KUIPER QUADRANGLE OF MERCURY

James R. Underwood, Jr., Department of Geology, Kansas State University, Manhattan, KS 66506, D. H. Scott, U.S. Geological Survey, Flagstaff, AZ 86001, and R. A. DeHon, Department of Geosciences, Northeast Louisiana University, Monroe, LA 71209

The first meeting of the mapping teams for the mercurian quadrangles was at the First International Colloquium on Mercury in Pasadena in June 1975. Mapping materials in the form of images and mosaics of Kuiper quadrangle were received in late 1975 and early 1976; at Flagstaff in June 1976, the Kuiper quadrangle team selected tentative geologic mapping units and symbols. A third of the quadrangle, which was subdivided latitudinally with 5° overlap north and south, was assigned to each member of the team for geologic mapping, and various parts of the text were assigned as follows: Underwood - Introduction, Methods and Materials, Description of Units, and Correlation Chart; Scott - Stratigraphy; DeHon - Structure, and Scott and DeHon - Geologic History and lunar comparison. By late summer DeHon, as team coordinator, had compiled the preliminary maps and text from other team members, and by November 1976 when the Symposium on Comparisons of Mercury and the Moon convened at the Lunar Science Institute, a preliminary geological map and text were ready for display.

This map included two terra units (rough and smooth), two plains units (cratered and smooth). Four classes of craters were mapped; basins and associated materials were mapped separately. In the west part of the quadrangle, where image resolution is reduced because of high solar illumination angles, plains-terra undifferentiated and plains undifferentiated were mapped. Originally it was planned to use overlays to show the fields of secondary craters and crater chains, but this was abandoned in the belief that the map would be too cluttered.

At a conference of Mercury mappers following the Moon-Mercury symposium, Michael Malin suggested that an appropriate mapping strategy would be to map units delineated by age on the basis of the oldest craters superimposed on the units and the youngest craters underlying the units. He suggested using five crater classes; basins were not to be differentiated from craters in this scheme. Following considerable discussion, it was suggested that all mapping teams use this approach and that it would be evaluated at the PGPI meeting at Washington University, St. Louis in June 1977.

A geologic map and text were ready for review by the time of this meeting, during which there was vigorous debate on mapping strategy and philosophy by the Mercury mapping team members. Newell Trask and Daniel Dzurisin reported that they had used the Malin system successfully in their mapping of the Discovery quadrangle. A major concern was that this system of determining relative ages of surface material units presumes an accuracy that does not exist, e.g. that all craters of a given class were

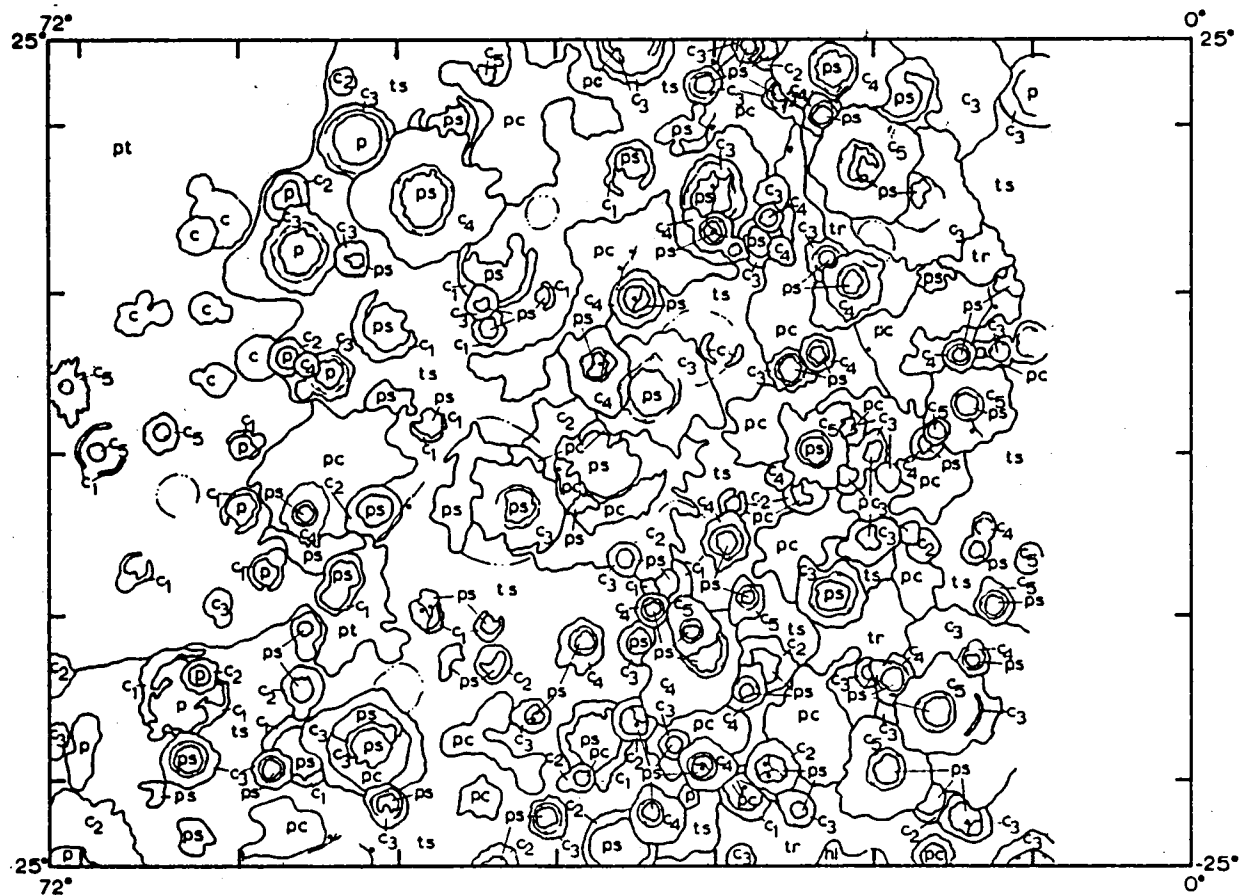
formed at about the same time and that they would evolve similarly no matter what their size nor what materials compose the craters. Furthermore, at the resolution of Mariner 10 images, it is not always possible to determine accurately the superpositional relationships of small-and medium-size craters and associated materials. Nevertheless, it was suggested that all mappers use five crater classes and use the Malin system to subdivide plains materials.

During the summer of 1977, the geologic map and text of Kuiper quadrangle were revised following a review by Trask. On this map there were five classes of craters, smooth and cratered plains units, smooth and rough terra units, and undifferentiated plains units and an undifferentiated plains-terra unit. A small area of hilly and lineated terrain was shown along the south margin, and several irregular patches of dark material (young lava flows?) were mapped in the western part of the quadrangle. The map and text were submitted to the mapping coordinator for review in the fall of 1977.

Mercury mapping teams did not meet at the PGPI meeting in Tucson in early summer, 1978, but later that year and in early 1979 the map of Kuiper quadrangle was modified slightly to conform with mapping in adjacent quadrangles. Minor changes were made in the map and text during the summer of 1979 following completion of the review by the Mercury mapping coordinator; the map and accompanying text were scheduled to be sent to the U. S. Geological Survey Technical Review Unit in September 1979. Although the three mapping team members never worked together at one locality after June 1976, the team coordinator circulated each draft of the map and text to the other team members for review and editing. The final map, in generalized form, is shown in Figure 1.

References:

- Scott, D. H., DeHon, R. A., and Underwood, J. R., Jr., 1976, The geology of the Kuiper quadrangle of Mercury in Papers Presented to the Conference on Comparisons of Mercury and the Moon, Lunar Science Institute Pub. 262, p. 31.
- DeHon, R. A., Underwood, J.R., Jr., and Scott, D. H., 1977, Geology of the Kuiper quadrangle of Mercury: NASA TMX-3511, p. 242-246.
- DeHon, R. A., Scott, D. H., and Underwood, J. R., Jr., 1978, Geologic history of Kuiper quadrangle, Mercury: Geol. Soc. America Abstracts with Programs for 1978, v. 10, no. 1, p. 4.



PLAINS MATERIALS

TERRA MATERIALS

CRATER AND BASIN MATERIALS

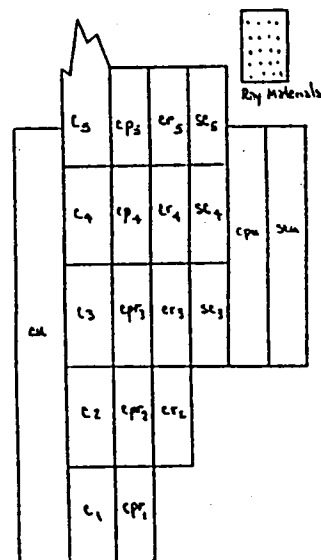
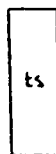


Figure 1

MARS GEOLOGIC MAP, 1:15 MILLION SCALE

Scott, D. H., U.S. Geological Survey, Flagstaff, Arizona 86001

Geologic maps using Viking images are being compiled in the western hemisphere of Mars on the new 1:15 million-scale base. Work in this region is being done by J. S. King, University of New York at Buffalo, and D. H. Scott, U.S. Geological Survey, Flagstaff, Az. Mapping extends from the northern plains into the highlands south of Tharsis Montes and includes parts of six quadrangles. The mapping is much more detailed than that shown on the previous map of Mars at 1:25 million scale (1). It includes, for example, 10 of the 17 major flow units in the Tharsis Montes-Olympus Mons region (2) and subdivided rock units in the walls and floors of Valles Marineris and some of their related larger chasmata. Many areas previously mapped in the general category of smooth plains or plains materials are being reclassified and differentiated according to their probable eolian, volcanic, or alluvial origin.

Mapping in the eastern hemisphere is being conducted by Ronald Greeley, Arizona State University at Tempe, and J. E. Guest, University of London Observatory. They have completed studies in the Casius quadrangle using Viking photomosaics of subquadrangles at 1:1.25 million scale. The plains material in this area that they previously mapped as eolian deposits (3), are now thought by them to be primary volcanic features that show different morphologic characteristics from place to place. The stratigraphic positions of these flows are difficult to determine from geologic considerations such as overlap and embayment relations. The mottled plains in the northern part of the quadrangle are presently the most difficult to subdivide, as even high-resolution Viking images show little variation in their appearance from place to place.

As work on this map progresses, many relations can be studied between geologic units and remote sensing data on such attributes as gravity, thermal inertia, albedo, and color.

REFERENCES

- 1) Scott, D. H., and Carr, M. H., 1978, U.S. Geol. Survey Misc. Geol. Inv. Map I-1083.
- 2) Scott, D. H., Schaber, G. G., Horstman, K. C., and Dial, A. L., Jr., (in this publication).
- 3) Greeley, Ronald, and Guest, J. E., 1978, U.S. Geol. Survey Misc. Geol. Inv. Map I-1038.

Chapter 11

WORKSHOPS AND SPECIAL PROGRAMS

PLANETARY STUDIES AT THE HAWAIIAN VOLCANO OBSERVATORY

Dzurisin, Daniel, U. S. Geological Survey, Hawaiian Volcano Observatory, Hawaii National Park, HI 96718

The planetary research program at the Hawaiian Volcano Observatory consisted of two distinct parts during FY 1979. The first was continuing co-ordination of an active guest investigator program designed to promote research in Hawaii by interested planetary scientists. Victor Baker of the University of Texas at Austin and Henry Moore of the U.S. Geological Survey were the designated visitors to the observatory this year. Baker concentrated on valley development during erosive dissection of Hawaiian shield volcanoes. His work included aerial surveys of Kilauea, Mauna Loa, Mauna Kea, and Kohala volcanoes on the island of Hawaii, and Haleakala on Maui. Moore studied the dimensions and morphologies of several historic Kilauea lava flows in order to explore the validity of the Bingham plastic lava flow model. One goal of this work is to infer from remote imaging observations certain rheologic, and perhaps compositional, characteristics of lunar and martian lava flows.

A second part of the planetary program at HVO is an ongoing study of the structure and stratigraphy of Kilauea caldera, initiated in FY 1979 by the author in collaboration with observatory staff member T. Casadevall. A 150 m section through the northern caldera wall has been measured, and will be extended laterally by photogeologic techniques. Selected lava flows have been sampled for chemical analysis, to investigate chemical evolution of Kilauea lavas with time.

In addition, more detailed studies are underway of intrusive rocks and a major tephra accumulation exposed in the caldera wall. More than 20 dikes have been mapped and sampled to date, and a generalized stratigraphy of the Uwekahuna tephra deposit has been developed. The volatile content of shallow intrusive rocks at Kilauea provide information on the degassing efficiency of basaltic magma in Hawaii (and presumably on other planets). This in turn has implications for the contribution to planetary atmospheres made by volcanic outgassing. Work on the Uwekahuna Ash will complement a recent study of the character and remote sensing implications of the Keanakakoi tephra deposit at Kilauea (Malin, Sharp, and Dzurisin, in preparation). Early results suggest that explosive, tephra-producing eruptions may be relatively common at Kilauea, so that their potential significance should not be overlooked in studies of volcanic landscapes on other planets.

SAR INTERPRETATION COURSE FOR VOIR PHOTOGEOLOGISTS

LaPrade, George L., Goodyear Aerospace Corporation,
Litchfield Park, Arizona 85340

The SAR Interpretation Course for VOIR Photogeologists is designed to introduce project personnel to basic radar interpretation and data extraction techniques that can effectively exploit VOIR data. It is intended primarily for those with photo interpretation experience but limited or no exposure to radar imagery.

The first of four such courses in the series sponsored by NASA headquarters was conducted September 10 through 14, 1979.

An attendee critique was very useful for determining the following as desirable course revisions:

- 1) make course length four days
- 2) introduce several practical exercises
- 3) place more emphasis on tradeoffs of parameters such as wavelength, polarization, and beam depression angles
- 4) introduce additional examples of comparative imagery--particularly radar photography--to assist in understanding the similarities and dissimilarities between radar imagery and air photos.

The primary text for the course will continue to be "Radar Imagery Interpretation Adaptable to Planetary Investigations." Course content includes a general review of side-looking radar and the VOIR system; radar imaging principles that are pertinent to an understanding of synthetic aperture radar image formation; and utilizing the imagery for analysis of rock type and structure, soils, and surface configuration.

Basic radar mensuration concepts for both planimetric and stereo applications are covered. While it is beyond the scope of the course to develop detailed map compilation procedures for the Venus surface, the essentials of radar mensuration required for cartographers to develop such procedures will be covered.

THE PLANETARY GEOLOGY ASSOCIATES PROJECT: A PROGRESS REPORT

D'Alli, Richard E., Department of Geology, Arizona State University,
Tempe, Arizona 85281

The Planetary Geology Associates Project was initiated on March 1, 1979. The primary objective of the project is to increase communication and cooperation between the principal investigators in the Planetary Geology Program and the general community of geologists (D'Alli, 1979). During the first eight months of operation, the following tasks were completed toward implementing the project's objectives:

- 1) A summer Institute in Planetary Geology was conducted at Arizona State University June 18 - 23, 1979. The Institute, announced by brochure, was a six-day intensive introduction to the fundamentals of planetary geology. Most participants came from geology departments in southwestern colleges and universities. The Institute format was one of formal lectures interspersed with "hands-on" laboratory activities, concluding with a two-day field trip, including an aerial survey of northern Arizona, and ground study of Meteor Crater and volcanic terrain. The instructional staff was assembled from active planetary geologists from academic institutions and NASA facilities; most were planetary geology principal investigators. The response of the participants was highly favorable. Monitoring of their use of the experience will continue.
- 2) A nationwide Speakers Bureau was formalized to begin operation early in 1980. The speakers are all principal investigators who have agreed to deliver colloquia at the request of colleges and universities. Interested host institutions will contact the Associates Project office for speaker availability and scheduling. The host will pay all expenses associated with the speaker's travel and accommodations and may provide a discretionary honorarium. The Associates Project will coordinate, monitor, and evaluate the Speakers Bureau.
- 3) The prototype in a forthcoming series of videotapes was produced to demonstrate the efficacy of the medium for planetary geology instruction. The demonstration tape suggests that geologists can gain quick and highly visual access to reviews of topics of current research in planetary geology. The tapes could be used for graduate or undergraduate instruction as well as brief overviews for instructors. Introductory or summary sessions of the January, 1980, Planetary Geology Principal Investigators meeting will be taped to provide additional material for this project.

REFERENCE:

- D'Alli, R.E. (abstract), 1979. Information Transfer in Planetary Geology: The Planetary Geology Associates Project, Rep. Plan. Geol. Pgm., 1978-1979, NASA TM 80339, p. 450.

APPLICATION OF BIRP (AUTOMATED PICTURE SEARCH) TO VIKING ORBITER DATA - THE UBIQUITY OF MARTIAN DUNES

Arvidson, Raymond E., Bolef, Lawrence K., Guinness, Edward A., McDonnell
Center for the Space Sciences, Department of Earth and Planetary Sciences,
Washington University, St. Louis, Missouri 63130

BIRP consists of a number of FORTRAN IV + computer programs designed for: (1) interactive interrogation of image engineering data, such as picture latitude, longitude, slant range, filter position, etc.; (2) print-out of engineering data for pictures that fulfill search requirements, and (3) near real-time display of desired pictures by use of an automated microfiche system or a videodisk player. A flow diagram for BIRP, updated from Arvidson (1979) is shown in Figure 1. The main user options are: (1) DESCRIBE, which prints a description of the searchable parameters. Table 1 shows the result of use of the DESCRIBE option for the Viking Orbiter data set (39,757 pictures - all VO II pictures, VO I pictures through rev. 964); (2) SEARCH, which allows the user to specify values or ranges for the searchable parameters listed in the DESCRIBE option; (3) PRINT, which allows the user to print-out any combination of parameters for pictures that fall within search requirements, along with display of the pictures; (4) RESTORE, which is used before starting a new search on the entire set of pictures; (5) SAVE, which allows the user to save the results of a search in a file for future use; and (6) HELP, which tells the users what options are available to them.

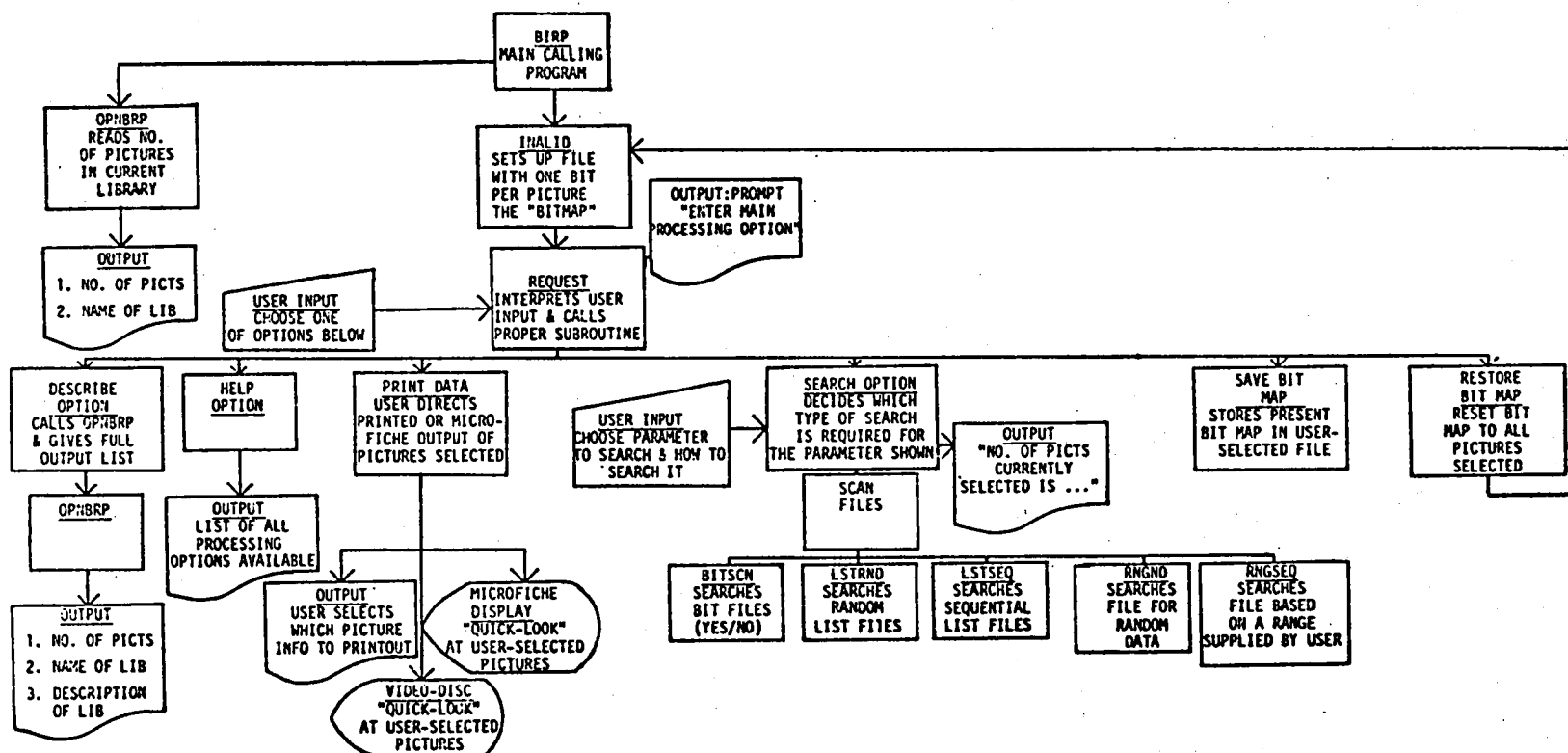
During testing of BIRP, we performed a set of searches to determine the areal distribution of dune fields on Mars. A vast dark dune erg circles the north polar layered deposits (Cutts, 1976, Breed *et. al.* 1978). However, observations by Sagan *et. al.* (1977) show that sand-sized material is rare at both landing sites, suggesting that Mars may be deficient in dune-forming particle sizes, as compared to Earth's sand deserts. Very few dunes can be found in the equatorial to mid-latitudes in either Mariner 9 image data or Viking Orbiter primary mission image data, perhaps because of insufficient resolution. To test whether or not dunes become more abundant with increasing resolution, we used BIRP to cull-out the highest resolution Viking Orbiter pictures, those with 01 to 10 meters/pixel. The search, on a PDP-11/34 with a floating point processor, took 52 seconds to examine the 39,757 picture entries and to come up with 1354 pictures that have the appropriate resolution limits. Next, we chose to further restrict the list by specifying "clear" as the QUALITY parameter. This search, done on the 1354 pictures, took 10 seconds, and left us with 121 pictures. Finally, we used the TARGET parameter to restrict the search to Mars. This search took 2.5 seconds and produced 116 pictures. The final picture list contains frames that are dominantly located in a 30° to 50° N. Latitude band. An automated microfiche search, backed-up by examination of prints, shows that about 10% of these pictures have discernable dune forms. The dunes are located principally within depressions - craters, graben, or against ridges. These dunes, in contrast

to the dark circumpolar dunes, have about the same albedo as the surrounding terrains (see for example, 448B07). Examination of albedo data for these regions suggest that these terrains are dominated by bright to intermediate albedoes. The only dark dunes were found in Sinus Sabaeus, a region with a distinctly low albedo. In summary, our search of high resolution, high quality pictures suggests that dunes may be ubiquitous to regions on Mars with sharp relief. A partial print-out of pictures used in the dune search is shown in Table 2.

A copy of the BIRP user's guide, system's programmer's guide, and the source code can be obtained through the authors. This research was supported by Planetary Geology Program Grant NSG-7087.

References

- Arvidson, R.E., 1979, BIRP - An Interactive System for Interrogation of Lunar and Planetary Image Engineering Data, NASA TM -80339, pp. 398-399.
- Breed, C., A. Ward, J. McCauley, 1978, Windform patterns on Earth and on Mars: Implications for Similarities of Eolian Processes on the two Planets, NASA TM - 79729, pp. 228-229.
- Cutts, J. et. al., 1976, North Polar Region of Mars: Imaging Results from Viking 2, Science, v. 194, pp. 1329-1337.
- Sagan, C., D. Pieri, P. Fox, R. Arvidson, E. Guinness, 1977, Particle Motion on Mars Inferred From the Viking Lander Cameras, J. Geophys. Res., v. 82, pp. 4430-4438.

Figure 1 - BIRP SIMPLIFIED, USER-ORIENTED FLOWCHART

BETTER IMAGE RETRIEVAL PROGRAMS

YOU ARE ACCESSING THE VIKING ORBITERS 1 AND 2 MISSION LIBRARY
IN WHICH THERE ARE 39757 PICTURES

PARAMETERS

BOXNO 10 DEGREE BOX NUMBER CONTAINING CENTER OF PICTURE. [RANGE: 1 - 648]
CAMERA CAMERA USED: WHICH CAMERA OF ORBITER TOOK PICTURE. [VALUES: A OR B]
CLAT LATITUDE OF PICTURE CENTER: +90=N.POLE,-90=S.POLE [RANGE:-90.0 TO +90.0]
CLONG WEST LONGITUDE OF PICTURE CENTER: [RANGE:10-360.0]
CRAFT SPACECRAFT: WHICH VIKING ORBITER. [VALUES:1 OR 2]
EMANG EMISSION ANGLE: NORMAL TO SURFACE = 0 DEGREES [RANGE:10-90.0]
FILTER FILTER USED [RANGE:BLUE, MINUS (BLUE), VIOLET, CLEAR, GREEN, OR RED]
INANG INCIDENCE ANGLE: NORMAL TO SURFACE = 0 DEGREES [RANGE:10-90.0]
LS AEROCENTRIC LONGITUDE OF THE SUN: POSITION OF SUN [RANGE:10-360.0]
MCNO MARS CHART NUMBER: MARS MAPPING CHART (USGS QUADRANGLE) [RANGE:1 TO 30]
PHANG PHASE ANGLE:ANGLE BETWEEN EMISSION AND INCIDENCE ANGLES [RANGE:10-180.0]
PICHT PICTURE HEIGHT: HEIGHT OF PICTURE FRAME IN KILOMETERS. [RANGE:12-2000]
PICNO PICTURE SEQUENCE #: REVOLUTION, SPACECRAFT, PICTURE COUNT IN ORBIT.
STANDARD PICTURE SEQUENCE NUMBER: XXXYZZ, WHERE XXX=ORBIT OR REVOLUTION
NUMBER, Y=SPACECRAFT(A=VIKING 1, B=VIKING 2, S=VIKING 1 SURVEY MISSION)
ZZ=PICT COUNT WITHIN ORBIT
PICWD PICTURE WIDTH: WIDTH OF FRAME IN KILOMETERS. [RANGE:12-2000]
QUAL PICTURE QUALITY (DEGREE OF HAZINESS) [RANGE:CLEAR,SLIGHT,MODERATE,DENSE]
RES RESOLUTION: SIZE OF A PICTURE ELEMENT (PIXEL) IN METERS.[RANGE:1-1500]
REVNO REVOLUTION NUMBER: ORBIT NUMBER OF SPACECRAFT [RANGE:10-999]
SLANTR SLANT RANGE: SPACECRAFT TO PICTURE CENTER ON MARS(KM). [RANGE:1250-30000]
TARGET SUBJECT: [RANGE:PHOBOS, DEIMOS, MARS, STAR, TERM(INATOR) OR LIMB]

TABLE 1- BIRP OUTPUT FROM "DESCRIBE" OPTION

ENTER NEXT COORD: PRI 7

PICNO	BOXNO	CAMERA	CLAT	CLONG	CRAFT	EMANG	FILTER
	INANG	LS	MCNO	PHANG	PICHT	PICNO	PICWD
	QUAL	RES	REVNO	SLANTR	TARGET		
448B02	189	B	34.68	82.18	2	33.24	CLEAR
	57.48	2.16	3	37.82	9.90	448B02	12.60
	CLEAR	8	448	358.0	MARS		
448B03	189	A	34.86	82.22	2	31.78	CLEAR
	57.52	2.16	3	38.82	9.80	448B03	12.10
	CLEAR	8	448	352.0	MARS		
448B04	189	B	34.72	82.30	2	27.46	CLEAR
	57.44	2.16	3	39.84	9.40	448B04	11.10
	CLEAR	8	448	338.0	MARS		
448B05	189	A	34.90	82.34	2	25.80	CLEAR
	57.48	2.16	3	40.86	9.40	448B05	10.80
	CLEAR	8	448	334.0	MARS		
448B06	189	B	34.78	82.32	2	21.62	CLEAR
	57.46	2.16	3	41.92	9.00	448B06	10.20
	CLEAR	8	448	326.0	MARS		
448B07	189	A	34.94	82.34	2	19.90	CLEAR
	57.54	2.16	3	42.90	9.00	448B07	9.90
	CLEAR	8	448	322.0	MARS		
448B21	189	A	35.34	82.32	2	26.48	CLEAR
	57.92	2.16	3	70.62	9.80	448B21	11.10
	CLEAR	8	448	350.0	MARS		

TABLE 2 - BIRP OUTPUT FROM "PRINT" OPTION.

"PRINT 7" means print SEDR data for
the next 7 pictures in the active
picture list.

AUTHOR INDEX

Alfvén, H., 3
Anderson, D. M., 271
Andrawes, F. F., 135
Arthur, D. W. G., 108, 358
Arvidson, R. E., 114, 378
Aubele, J. C., 198
Baker, V. R., 54, 286
Bianchi, R., 86
Blasius, K. R., 93
Bolef, L. K., 378
Boothroyd, J., 277
Boyce, J. M., 339
Breed, C. S., 231, 246, 249
Breed, W. J., 255
Brook, G. A., 57
Bus, S. J., 8
Carey, D. L., 105
Carr, M. H., 265
Carusi, A., 86
Cassen, P. M., 329
Chaiken, A. L., 43
Chapman, C. R., 5, 14
Cintala, M. J., 125, 128, 347
Clark, P. E., 316
Clifford, S. M., 144, 147, 153, 215
Coradini, A., 86
Coradini, M., 86
Crumpler, L. S., 198
Cutts, J. A., 63, 93
D'Alli, R. E., 377
Danielson, J., 147, 149
Davies, G. F., 77
Davies, M. E., 343, 353, 354
Davis, D. R., 5, 14
De Hon, R. A., 28, 34, 41, 369
Dial, A. L., Jr., 179
Downs, G. S., 74, 362
Dzurisin, D., 375
Eckerman, G., 217
El-Baz, F., 43, 238
Elston, W. E., 198
Eppink, J. F., 66
Eppler, D. B., 198
Erstfeld, T. E., 164
Fanale, F. P., 134, 334
Federico, C., 86
Fillers, T., 244
Flamini, E., 86
Fulchignoni, M., 86
Funciello, R., 83

Garvin, J. B., 51
 Gault, D. E., 95
 Gibson, E. K., 135
 Giegengack, R., 169
 Gifford, A. W., 111
 Goguen, J., 12, 311
 Golombek, M. P., 19
 Gradie, J., 12, 343
 Greeley, R., 95, 173, 207, 210, 215, 217, 226, 228, 241, 257, 260
 Greenberg, R., 5, 14
 Grinspoon, D., 51
 Grolier, M. J., 231, 249
 Guest, J. E., 95, 176
 Guinness, E. A., 313, 378
 Hansen, C., 331
 Hawke, B. R., 316
 Head, J. W., 51, 71, 223, 347
 Helfenstein, P., 51
 Helin, E. F., 8
 Hiller, K., 119
 Hodges, C. A., 181, 184
 Holloway, J. R., 156
 Horstman, K. C., 179
 Housen, K., 14
 Howard, A. D., 60
 Huguenin, R. L., 144, 147, 149, 151, 153, 215
 Hutton, R. E., 166
 Iversen, J. D., 207, 210, 226, 228
 Jones, K. L., 48
 Jordan, R., 192
 Judson, S., 283
 Kachadoorian, R., 201
 King, J. S., 368
 Komar, P. D., 276
 Kremer, J., 207
 Krinsley, D. H., 244
 Laity, J. E., 268, 292, 295, 298
 LaPrade, G. L., 376
 Lauer, H. V., Jr., 138, 141
 LaVoie, S. K., 48
 Leach, R. N., 226, 228
 Leake, M. A., 31
 Lee, S. W., 359
 Levinthal, E. C., 365
 Liebes, S., Jr., 365
 Lopes, R. M. C., 176
 Lucchitta, B. K., 271, 281
 Lucey, P., 51
 Magni, G., 86
 Malin, M. C., 292, 295, 298, 300

Masursky, H., 331
 Maxwell, T. A., 43
 McCauley, C. K., 255
 McCauley, J. F., 231, 246, 249
 McGill, G. E., 19, 80
 McKay, D. S., 159
 Mendis, D. A., 3
 Milkowski, G., 122
 Miller, K. J., 149, 151
 Mohr, E. T., 281
 Moore, H. J., 166, 201
 Morris, E. C., 162
 Morris, R. V., 138, 141
 Morrison, D., 336, 343
 Mougini-Mark, P. J., 51, 99, 105, 223, 308
 Mutch, P., 96, 102
 Neukum, G., 119
 Nummedal, D., 289
 Parmentier, E. M., 347
 Parotto, M., 83
 Patera, E. S., 156, 244
 Peale, S. J., 329
 Peterfreund, A. R., 217, 221
 Pettengill, G. H., 308
 Phillips, R. J., 79
 Pieri, D. C., 292, 295, 298
 Pike, R. J., 108, 192
 Pilcher, C. B., 338
 Plescia, J. B., 68, 189
 Pollack, J. B., 133, 226, 228
 Poscolieri, M., 86, 319
 Prestel, D. J., 159, 238
 Purves, N. G., 338
 Rankin, R. L., 217
 Reynolds, R. T., 329
 Ritke, S., 79
 Roberts, W. J., 93
 Robinson, E. A., 51
 Roddy, D. J., 108
 Rossbacher, L., 283
 Roth, L. E., 68, 74, 362
 Salvini, F., 83
 Saunders, R. S., 66, 68, 74, 134, 362
 Schaber, G. G., 179, 305
 Schafer, F. J., 192
 Schelte, J., 8
 Schubert, G., 74, 362
 Schultz, P. H., 95
 Scott, D. H., 28, 34, 40, 179, 369, 372
 Scott, R. F., 166

Sekanina, Z., 11
 Settle, M., 204
 Shoemaker, E. M., 8, 345
 Shorthill, R. W., 166
 Simonelli, D., 336
 Sisson, V., 95
 Smith, J. C., 79
 Smith, R. S. U., 252, 253
 Snyder, D. B., 95
 Solomon, S. C., 71
 Spitzer, C. R., 166
 Spudis, P. D., 173, 316
 Squyres, S., 336, 345
 Stephens, J. B., 134
 Strickland, E. L., III, 46
 Strom, R. G., 331
 Terrile, R. J., 331
 Thomas, P., 12, 219, 336, 343
 Thompson, D. E., 268, 274
 Timson, B. S., 277
 Tsoar, H., 257
 Underwood, J. R., Jr., 28, 34, 169, 369
 Urbancic, M. A., 135
 Valsecchi, G., 86
 Veverka, J., 12, 219, 311, 336, 343
 Viglienzzone, L., 51
 Wainwright, J. E., 238
 Ward, A. W., 231, 246, 260
 Watkins, J. A., 37
 Weidenshilling, S. J., 5, 14
 Whipple, F. L., 11
 White, B. R., 226, 228
 Whitford-Stark, J. L., 22, 195
 Whitney, M. I., 231, 236
 Wilhelms, D. E., 25
 Williams, J. G., 8
 Williams, R. J., 164
 Williams, S. H., 241
 Wilson, C. J. N., 176
 Winnellie, N. T., 286
 Wise, D. U., 83, 122
 Witbeck, N., 246
 Wolfe, R. W., 323
 Womer, M. B., 207, 210
 Wood, C. A., 111
 Woronow, A., 96, 102, 187
 Wu, S. S. C., 355
 Zisk, S. H., 308

ABSTRACTS RECEIVED AFTER DEADLINE

INTRA-CRATER FORMATIONS AS REVEALED IN SURVEY MISSION IMAGING DATA

Evans, Nancy, Jet Propulsion Laboratory, Pasadena, California 91103.

The imaging data obtained during the Survey Mission, revolutions 1122 through 1224 of the Viking I Orbiter have revealed a profusion of intra-crater formations. Those which have been observed include: dunes (two types), scoured rock (at least three types of formations), concentric slumps (one or two rings), lobate slumps, scarps, chaos, and finally filled craters around which the rims appear to have been entirely removed. The randomness of the process by which craters were selected for alteration prompted this study.

The unique data set (Survey Mission) provides an ideal base from which to develop a study. It is all of a similar resolution, having been obtained at slant ranges between 800 and 2000 Km; it provides sufficient diversity in latitude, longitude, and terrain type; and it is self limiting (102 revolutions).

The variety of formations included for study and the range of crater size, 1 Km to 60 Km, requires that the classification system be simple, while the randomness of the occurrence pattern requires that the classification parameters be complete. If the findings of this study are ever to be applicable planet-wide, the system must be computer compatible (computer assistance may be necessary to sort this small data set.) Present crater conditions including size, location, state of degradation, and intra-crater formation must be recorded for comparison, as well as an indication of any original crater morphology such as a central peak, layering, terracing, ejecta blanket, etc..

It is hoped that by correlation of some or all of this data a relationship can be established between intra-crater formations and some pre-existing condition. A secondary goal of this study is to seek means of identifying these structures in images of lesser resolution in order to study the phenomena on a global, or at least greater, scale. The ulterior motive is, however, White Rock which defies all attempts to understand it!

PLOTS AND MOSAICS OF SURVEY MISSION COVERAGE

Evans, Nancy; Dueck, Sandra; Johnston, Gordon; and Scribner, Paul,
Jet Propulsion Laboratory, Pasadena, California, 91103.

Viking Orbiter I Survey Mission imaging data (Revs 1122 - 1224) consist of strips of 24-28 frames obtained on a daily basis from slant ranges starting at 800 km and increasing to 2000 km. The goal of the Survey Mission was to obtain a swath of contiguous coverage through the ancient cratered terrain for study as a possible landing site for future Mars exploration. Coverage obtained from Rev 1149 through 1224 provides a continuous swath of coverage which extends northwestward from $250^{\circ}\text{W}/10^{\circ}\text{N}$ to $25^{\circ}\text{W}/36^{\circ}\text{N}$. The swath width varies from about 5° to slightly more than 8° . Earlier sequences obtained at lower altitudes are not contiguous; they, however, provide a splendid overview of the cratered terrain just to the south of the equator, Isidis Planitia, and Syrtis Major Planitia.

Gravity anomalies lying directly under the ground track at periapsis and difficult orbit solutions combined to cause timing errors of sufficient magnitude to "misplace" the data blocks from the predicted locations. High resolution imagery is, of course, more useful when the location of the data is precisely defined.

As the Survey Mission data is reduced and images made available, they are mosaicked, located, and foot-print plotted on an appropriate base map. This effort will yield for publication a complete documentation of the Survey Mapping Mission activities. It is presumptuous to anticipate that these location and documentation procedures will be completed prior to the January meeting or that all of the mission imaging data will have been reduced by that time. We will, however, display much of the coverage and report on the progress of this task at that meeting.

TRANSPORTATION AND DEPOSITION OF PARTICULATE MATERIAL ON THE SURFACE
OF MARS: INFERENCES FROM SAND SHEET DEPOSITS IN THE WESTERN DESERT
OF EGYPT.

Ted A. Maxwell and Farouk El-Baz, National Air and Space Museum,
Smithsonian Institution, Washington, D.C. 20560

As shown by Mariner and Viking images of the surface of Mars, dunes and other eolian features have suggested the presence of a significant population of saltation-size particles that are available for eolian transport and deposition (Cutts and Smith, 1973; Greeley et al., 1974). Observations of martian duststorms indicate that material in the 1 μ m range is extensively redistributed on a planet-wide scale (Arvidson, 1972). In contrast to these observations, however, Viking lander images indicate an apparent deficiency of surficial material in the 1.75 - 2.5 ϕ size range (Patterson et al., 1977), and theoretical calculations of wind velocities needed for eolian entrainment suggest that sand-size material should not be an important constituent in the martian eolian regime. According to Greeley (1979), three possible explanations for the presence of sand-size material are: 1) the dunes are remnants of a previous episode of a denser atmosphere, 2) the calculations suggesting that sand-size material is in saltation are incorrect, and 3) the eolian features may be formed of agglutinates of smaller grains that act as sand-size material during transport. Based on the size characteristics of sediments from the Western Desert of Egypt, however, it is also possible that these seemingly conflicting lines of evidence are the result of the heterogeneity of eolian depositional environments.

Source materials for many present-day terrestrial deserts are found in previously consolidated sedimentary deposits, which have been subject to fluvial reworking during Pleistocene and Recent times (Folk, 1968). Eolian sands of the Western Desert present one example of this process in that they were derived from highlands to the south, and transported northward by rivers only to be blown back southward by the prevailing winds (El-Baz and Maxwell, 1979). In the Western Desert, however, there is an additional local source of sand grains in the widespread Nubia sandstone that underlies the surficial deposits. Consequently, there is a continuum of particle sizes present that are available for eolian sorting. The characteristics of source materials for martian deposits are much more difficult to specify. The effects of impact, thermal and chemical weathering, and possible fluvial erosion may all play an important role in generation of sand- and silt-size material. Because of our limited knowledge on the nature of martian bedrock, however, the grain size of source materials on that planet remains unknown.

On both Earth and Mars, the size distributions of wind-transported material can be divided into two fractions: 1) Unimodal, saltation-size grains that make up the dune-forming population, and

2) A bimodal population of sand and coarser grains that composes the sand sheet deposits. Locally, material derived from an immediate source will modify both populations in the form ofserir deposits. As shown by comparisons of textural parameters, the deposits of these two desert subenvironments can be distinguished on the basis of size and sorting characteristics. Although both the gravity and atmosphere differ on Mars, the basic processes of eolian sorting are likely to be the same. Differences in the martian environment suggest that the size of the saltation fraction may be greater than the Earth's (Sagan and Bagnold, 1975), and that both wind speeds and net sediment transport rates are greater (Arvidson, 1972; White, 1979). Because of the differing modes of sand sheet deposition (both traction and suspension are likely), these environmental effects may be represented more by sand sheet and associated deposits rather than by relatively homogeneous dune deposits.

Unfortunately, data from the Viking landers are inconclusive with respect to particle size variations at the two locations on the martian surface. Limitations on pixel size and sampling rate of the lander cameras make it impossible to see surface particles finer than about 2.5 ϕ . Based on an absence of false low frequency components in surface imaging, Patterson et al. (1977) suggested that there is a deficiency in the medium to fine sand size range (1.75 to 2.3 ϕ). On the basis of grain counting in the footpad of Viking Lander 2, Zimmer et al. (1977) also suggested a depletion of fragments less than -1 ϕ in diameter. Consequently, there is an apparent bimodal sediment distribution among the < 5mm size material at both sites. Grains greater than a few millimeters are abundant on the surface, with finer material (less than ~ 2.5 ϕ) forming intervening areas, and possibly the drifts.

The deficiency of sand-size material has been explained as the result of particle break-up due to reduced atmospheric density (the so-called "Kamikaze" particles of Sagan et al., 1977), or a debris-flow origin for material near the landers (Shultz et al., 1979). Based on sorting characteristics of Western Desert sands, however, it is also possible to consider this size distribution as the result of the sand-sheet mode of deposition transferred to the martian environment. On Mars, the larger gap between modes of granules and fine silt-size material may be the result of the much higher wind speeds and wind speed variations present at the martian surface.

References

- Arvidson, R.E. (1972) Aeolian processes on Mars: Erosive velocities, settling velocities, and yellow clouds. *Geol. Soc. America Bull.*, v. 83, p. 1503-1508.
- Cutts, J.A. and Smith, R.S.U. (1973) Eolian deposits and dunes on Mars. *Jour. Geophys. Res.*, v. 78, p. 4139-4154.

- El-Baz, F. and Maxwell, T.A. (1979) Eolian streaks in southwestern Egypt and similar features in the Cerberus region of Mars. In Proc. of the Tenth Lunar and Planetary Science Conf., in press.
- Folk, R.L. (1968) Bimodal supermature sandstones: Product of the desert floor. In 23rd Session Intern. Geol. Cong., Proc. Sect. 8, Prague, Academia, p. 9-32.
- Greeley, R., Iverson, J.D., Pollack, J.B., Udovich, N., and White, B. (1974) Wind tunnel simulations of light and dark streaks on Mars. Science, v. 183, p. 847-849.
- Greeley, R. (1979) A model for the formation of windblown sand-size particles and related structures on Mars. In Second Intl. Colloquium on Mars, NASA Conf. Pub. 2072, p. 32.
- Patterson, W.R., Huck, F.O., Wall, S.D., and Wolfe, M.R. (1977) Calibration and performance of the Viking Lander cameras. Jour. Geophys. Res., v. 82, p. 4391-4400.
- Sagan, C. and Bagnold, R.A. (1975) Fluid transport on Earth and aeolian transport on Mars. Icarus, v. 26, p. 209-218.
- Sagan, C., Pieri, D., Fox, P., Arvidson, R., and Guinness, E. (1977) Particle motion on Mars inferred from the Viking Lander cameras. Jour. Geophys. Res., v. 82, p. 4430-4438.
- Shultz, A., Suttner, L.J. and Basu, A. (1979) Terrestrial debris flow deposits as analogs martian strewn fields. In Second Intl. Colloquium on Mars, NASA Conf. Pub. 2072, p. 74.
- White, B.R. (1979) Soil transport by winds on Mars. Jour. Geophys. Res., v. 84, p. 4643-4651.
- Zimmer, H., Moore, H.J., Shorthill, R.W., and Hutton, R.E. (1977) Grain size distribution of the martian soil inside the Viking Lander 2-footpad 3. Paper presented at Twentieth Plenary Mtg., COSPAR, June 7-18, 1977.

CONDENSATES AT THE VIKING 2 LANDER SITE

Wall, Stephen D., Jet Propulsion Laboratory, Pasadena, Calif. 91103

The Viking 2 lander has observed a white surface condensate during both of its two winters on Mars. In each case the condensate appeared near $L_S = 235^\circ$. Isolated patches of the first winter's condensate remained for approximately 250 sols (to $L_S = 15^\circ$). Dust storms over the lander accompanied the appearance both years. While the condensate existed multispectral imagery, optical depth, air temperature and pressure were recorded by the lander. Spectral reflectance and photometric function of the condensate have been derived from these. The amount of condensate on the surface can be indirectly measured by change in surface albedo and color.

Data taken during the first year's deposition phase show that air pressure slowly rose to meet the CO_2 saturation pressure as nighttime temperature fell to minima of 150°K ; then temperature and pressure both stabilized and the surface began to turn white. Figure 1 shows VL-2 meteorology diurnal minimum temperature and pressure during this period. The condensate's photometric phase function (figure 2) shows a strong backscatter peak which indicates either that dust is present in the condensate or that it is not optically thick. The former conclusion supports the idea that the condensate fell already condensed onto dust particles¹. The presence of water is not required to explain the deposition phase, but it may be required to account for the slow removal. Results of an investigation into the kinetics of the removal period will be reported.

This work was sponsored by the Mars Data Analysis Program, and was done at the Jet Propulsion Laboratory under NASA Contract NAS7-100. Preliminary analysis was sponsored by the Viking Program Office.

1. Jones et al, Science 204, 1979.

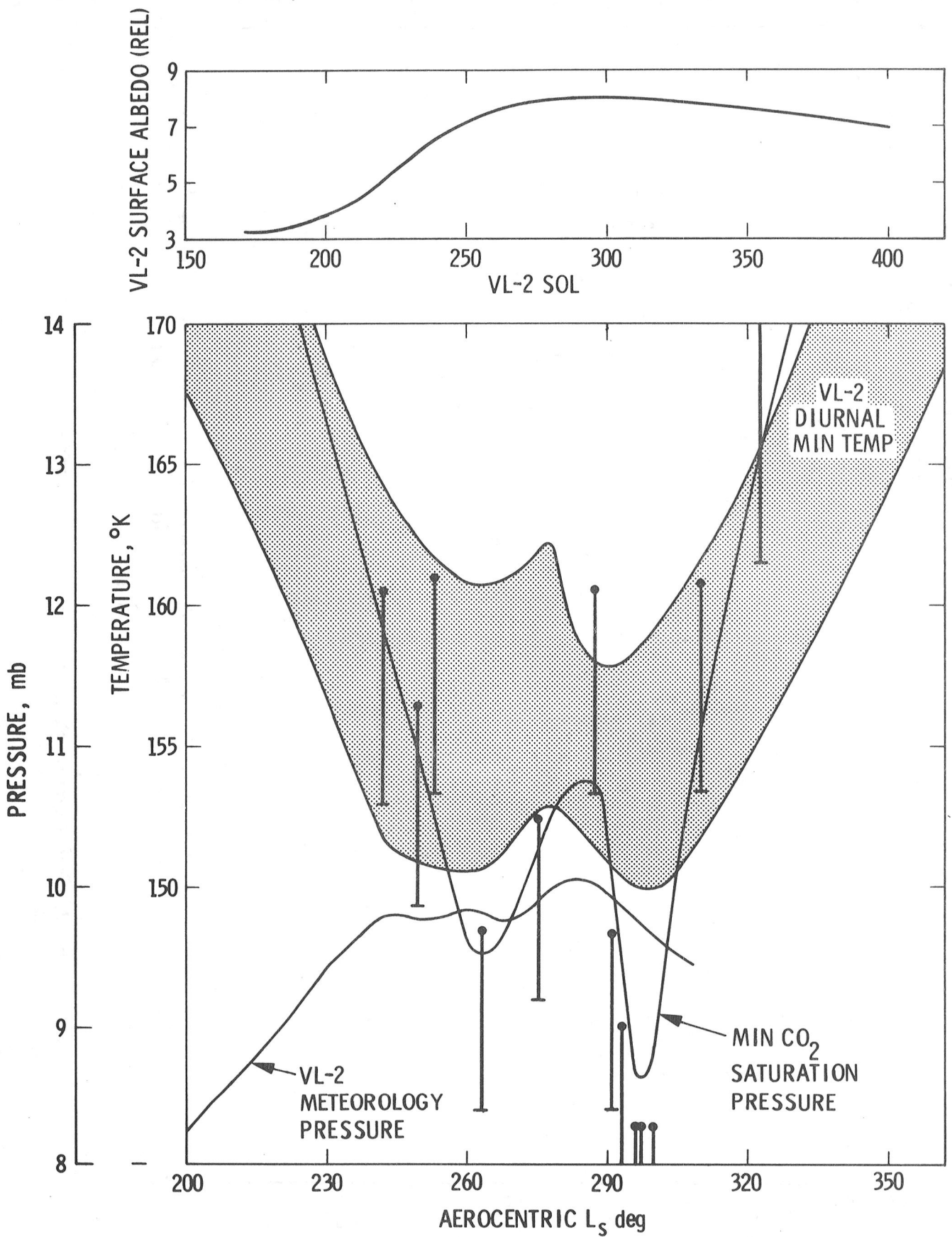


Figure 1.-Pressure, temperature and surface albedo at the lander

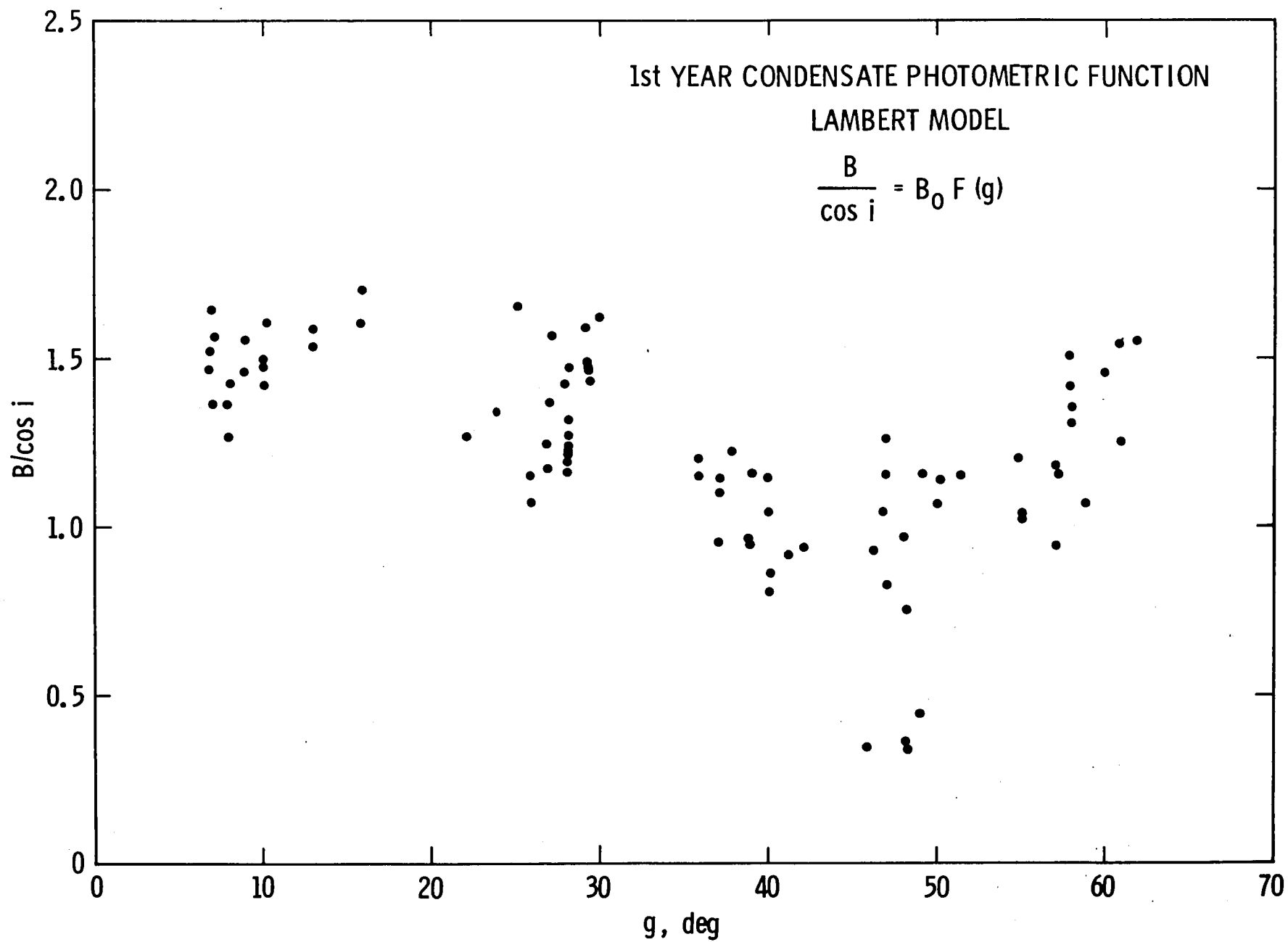


Figure 2.- Photometric phase function of the condensate.

POLAR ICE INVENTORY - A PROGRESS REPORT

Masursky, Harold; Dial, A.L.; and Strobell, M.H.; U.S. Geological Survey, Flagstaff, Arizona 86001

Mapping and profiling of the residual polar caps is continuing; stereo models have been constructed and topographic contours derived for one area on the north polar ice and one in the south polar region. From these models, volume of the residual ice has been calculated to be more than two million cubic kilometers at the north pole, estimating a thickness of 2.2 kilometers for the ice cap (fig. 1). Viking IRTM and MAWD data show the north polar cap to be comprised of water ice. Observations made by these instruments of the south polar cap indicate it may be comprised of carbon dioxide ice. Preliminary estimates of the south polar residual cap, based on stereophotogrammetric profiling indicate a thickness similar to the northern cap and a volume of about 400,000 cubic kilometers (about 1/5 of the volume of the northern cap).

In the north polar region, patches of residual ice occur as a discontinuous aureole near latitude 75° north, between 120° and 290° longitude. These patches of ice are severely etch-pitted by sublimation; layers within the ice are shown clearly in images of this material that have been specially computer enhanced. The main polar cap has also been strongly modified by sublimation or wind erosion, or both process, so that layers in the residual ice are clearly displayed here also.

Horizontal alternating dark and light layers can also be seen in the deposits which fringe the permanent continuous ice cap and which underlie it. Absence of craters larger than a few kilometers in diameter attests to the relative youthfulness of these deposits. The layers have probably been preserved by binding of the discrete dust particles that comprise each layer by interstitial ice. The continuity of these layers may indicate a lack of thick layers of wind deposited clastic ice grains or snow layers that lie between the dominantly mineral fragment layers. Volume of the ice contained within the layered deposits has not yet been computed.

Between 75° and 80° latitude, material similar to the mantle which probably covers the cratered plains to the south has been reworked by wind erosional and depositional processes. Large areas of longitudinal dunes abut against horizontal sedimentary deposits that have been complexly eroded by wind action; strongly divergent patterns are shown by the dune and eroded units. The spiral pattern of residual ice records the anticorolis flow directions of wind moving downward and outward. Farther south the patterns recurve into the coriolis direction. Simarly patterns are visible in satellite pictures of the

earth's polar cloud patterns.

The dunes may be made of medium sand, size grains that can be shaped into dune forms; these grains probably are composite grains of water or ice cemented silt and clay. Similar dunes of composite grains were observed in Nevada playas (Grass Valley of; Guilluly and Masursky, 1963).

Lat: 81.1°
Lon: 95.5°

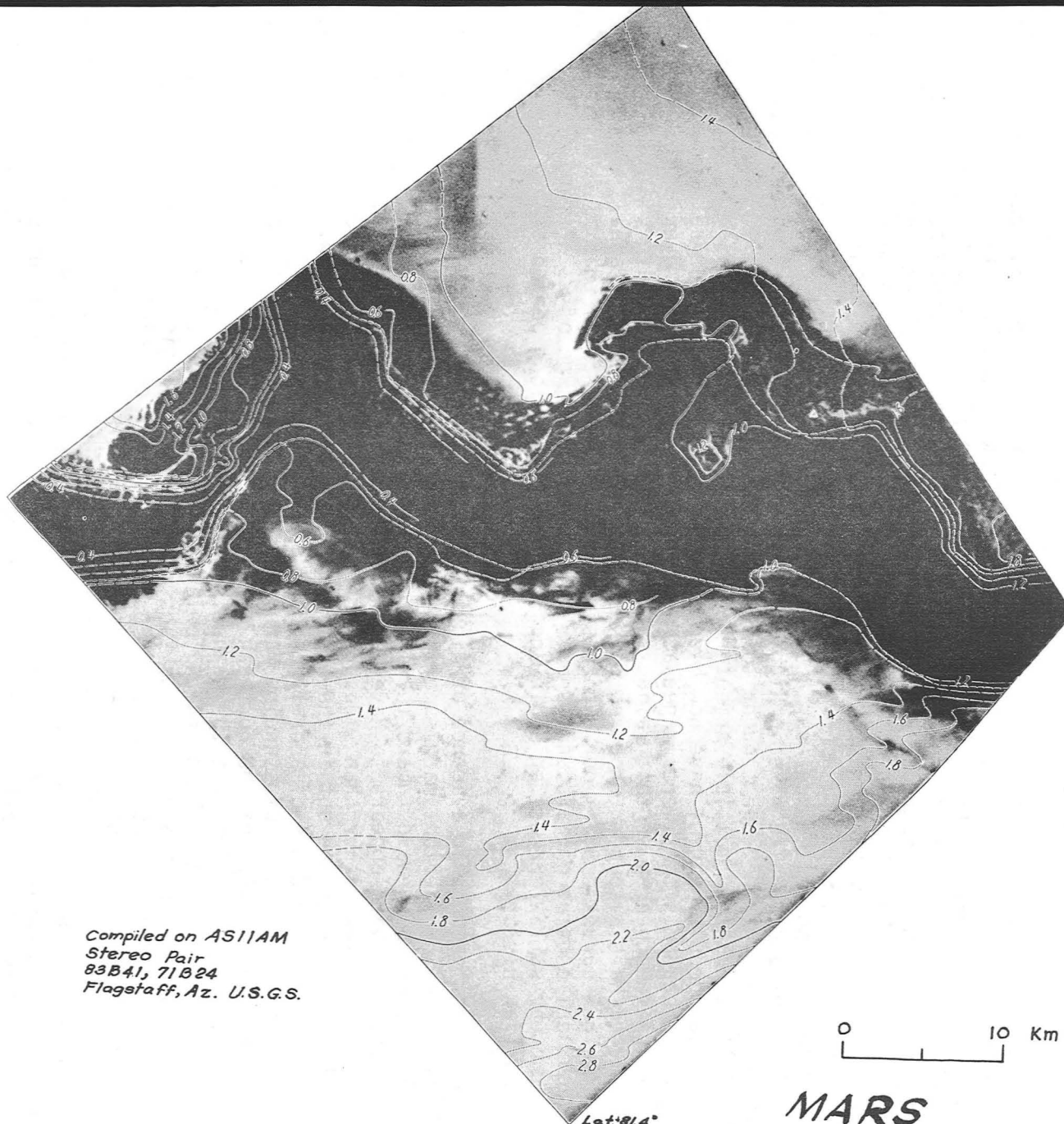
Lat: 81.4°
Lon: 87.2°

Compiled on ASIIM
Stereo Pair
83B41, 71B24
Flagstaff, Az. U.S.G.S.

0 10 Km

Lat: 81.4°
Lon: 94.7°

MARS
NORTH POLE



FLUVIAL HISTORY OF THE CHRYSE BASIN - A PROGRESS REPORT

Masursky, Harold; Dial, A.L.; and Strobell, M.E.; U.S. Geological Survey, Flagstaff, Arizona

The Chryse basin is an extension of the lowland volcanic plains province of Mars which embays the northeastern flank of the Tharsis plateau; aerial extent of the basin is almost two million square kilometers. The largest channels on Mars, as well as several somewhat smaller, sinuous channels, rise in the cratered highland terrain which fringes the basin to the west, south and east. The large channels originate in areas of chaotic terrain that probably formed when localized heat sources, emplaced in the mantle, heated overlying materials and melted near-surface ice. Sinuous channels that are intermediate in size rise in highland areas west and, in one case, east of the basin; they are thought to have been cut by runoff which collected in the multiple tributaries seen at their source areas. Crater density curves have now been obtained for all of the Chryse basin channels that were imaged at high enough resolution and over a large enough area so that valid statistics were obtained. Crater curves have also been produced for most geologic units in the area. The new curves confirm our hypothesis, reported earlier (1) that channel cutting on Mars and, specifically, the discharge of water into the Chryse lowland was episodic and occurred over a long period of martian history.

Abundant geomorphic evidence of fluvial erosion has been recognized in the alluvial piedmont margins of the basin and for several hundred kilometers northward toward the center of the basin. The regional slope northward appears to have been steep enough to promote rapid, confined flow rather than widespread flooding in these areas although the channels spread out in the central flatter part of the basin. However, no evidence of shorelines, or deposits that might have collected in a body of standing water has been recognized in photographs and mosaics of the northern part of the basin, at 35° north latitude. Water that cut the channels is therefore thought to have flowed outward onto the northern lowland, where it dispersed and then evaporated or sank into the substrata. Photogeologic interpretation of the features seen in the northern part of the basin thus strengthens our hypothesis, developed from analysis of the crater density curves, that channel flow was episodic. Although large floods did occur, the basin does not appear to have ever been overwhelmed by flooding because discharge of water from the several channels occurred at different times rather than simultaneously. Numerical analysis of individual flood volumes and probable evapotranspiration rates along the channel courses is continuing. Final results for the study must await completion of a controlled photomosaic map of the Chryse basin region, and topographic contour values and long profiles for the

for the individual channels and their source areas; preparation of both data sets is currently in progress.

CONSTRAINTS ON THE DENSITY OF THE MARTIAN MANTLE

Goettel, Kenneth A., Dept. of Earth and Planetary Sciences, and
McDonnell Center for the Space Sciences, Washington University,
St. Louis, Missouri 63130

The mean density of Mars, $3.933 \pm 0.002 \text{ g/cm}^3$ (1), is well determined by the observed mass and mean radius. The estimated moment of inertia factor, which Mars would have if Mars were in hydrostatic equilibrium, is 0.365 (2,3); this value may still be model dependent. These data provide the most direct constraints on the density distribution within Mars, but do not define it uniquely: the estimated zero pressure density of the Martian mantle, which is of considerable petrologic and geochemical interest, varies as a function of the assumed core density and as a function of the elastic data chosen as representative of the Martian interior. Johnston and Toksöz (4) computed zero pressure mantle densities ranging from 3.58 to 3.47 g/cm^3 , for cores from $\text{Fe}_{85}\text{S}_{15}$ to FeS . Okai and Anderson (5) computed core zero pressure mantle densities from 3.415 to 3.328 g/cm^3 , for core densities from 8.145 to 5.389 g/cm^3 .

The purpose of the present study was to define as rigorously as possible the present bounds on the density of the Martian mantle by: a) fully utilizing existing high pressure, high temperature elastic data, and b) systematically investigating the sensitivity of the computed density models to uncertainties in the thermal and structural state of Mars and to uncertainties in the elastic data required for the calculations. 79 models for the density distribution within Mars were computed by numerical integration of the equations of hydrostatic equilibrium, using the Murnaghan equation of state. Mars was modeled with several main zones: crust, upper and lower mantle (above and below the olivine to spinel phase change), and core (with a phase change, if appropriate). Each of these zones was characterized by: zero pressure density, bulk modulus (K), pressure derivative of the bulk modulus (K'), temperature derivative of the bulk modulus (dK/dT) and thermal expansion coefficient (α). Temperatures were taken from the thermal model of Toksöz et al. (6). The results shown in Table 1 for representative core compositions were computed using estimates of the elastic data for each zone (Table 2).

The range of zero pressure mantle densities shown in Table 1, computed for the range of geochemically plausible core compositions and densities, provides a minimum estimate of the present uncertainty in the density of the Martian mantle. Uncertainties in the moment of inertia factor, thermal state, and structural state of Mars and uncertainties in the experimentally determined or estimated high pressure and high temperature elastic data all affect the computed mantle densities shown in Table 1.

The effects of these uncertainties on the computed density of the Martian mantle are summarized in Table 2. The variations in the input parameters,

listed in Table 2, were chosen principally to investigate the magnitude of the effect of these variations on the computed mantle density; these variations are not intended to be rigorous estimates of present uncertainties in each input parameter. Plausible uncertainties in several of the input parameters have a significant effect (0.02 - 0.05 g/cm³) on the computed mantle density: moment of inertia factor, temperature profile, crust density, mantle dK/dT and thermal expansion coefficient, and bulk modulus of the upper mantle. The high pressure polymorph of FeS (FeS III) is very poorly characterized; uncertainties in the FeS parameters result in substantial uncertainties in the mantle density of Mars models with substantial amounts of FeS in the core. The effects of uncertainties in the elastic parameters for an Fe core (and for Ni and Fe₃O₄ cores) and of uncertainties in several of the mantle parameters are minor. Effects of uncertainties in the elastic parameters of the crust are negligible.

Conservatively, the numerical results presented in Table 1 should be regarded as preliminary, subject to revision by selection of more accurate input parameters. Also, calculations to assess the effect of using different equations of state, and calculations to assess the uncertainties introduced by the several approximations inherent in the numerical integration are in progress. Assessment of the implications of these results with respect to constraints on the bulk composition of Mars is also in progress.

References

- (1) Bills and Ferrari, 1978, *J. Geophys. Res.* 83, 3497-3508.
- (2) Reasenber, 1977, *J. Geophys. Res.* 82, 369-375.
- (3) Kaula, 1979, *Geophys. Res. Lett.* 6, 194-196
- (4) Johnston and Toksöz, 1977, *Icarus* 32, 73-84.
- (5) Okal and Anderson, 1978, *Icarus* 33, 514-528.
- (6) Toksöz, Hsui, and Johnston, 1978, *Moon and Planets* 18, 281-320.

TABLE 1

core composition	core density ¹ (g/cm ³)	core mass (wt.% of Mars)	mantle density ² (g/cm ³)
Ni	8.90	13.1	3.467
Fe	8.09	14.8	3.460
Fe ₃ O ₄	5.06, 6.37	25.4	3.424
FeS	5.77	26.3	3.409

¹Zero pressure density of the relevant high pressure phase: Ni, γ -Fe, Fe₃O₄ before and after the 250 kb phase change, and FeS III.

²Computed zero pressure mantle density.

TABLE 2			
input parameter	model value	(+) parameter variation	(+) effect on mantle density (g/cm ³)
moment of inertia factor	0.365	0.002	0.027
temperature profile	-----	500 °C	0.039
<u>crust</u>			
thickness (km)	30	10	0.008
density (g/cm ³)	3.0	0.5	0.026
K (megabars)	1.0	0.2	<0.001
K'	5	1	<0.001
dK/dT (megabars/°C)	-2.5×10^{-4}	1×10^{-4}	<0.001
α (per °C)	2×10^{-5}	1×10^{-5}	<0.001
<u>mantle</u>			
K (upper mantle)	1.25	0.20	0.029
K' (upper mantle)	5	1	0.005
K (lower mantle)	1.90	0.20	0.005
K' (lower mantle)	4	1	0.002
dK/dT	-2×10^{-4}	1×10^{-4}	0.027
α	3×10^{-5}	1×10^{-5}	0.046
phase change pressure	117 kb	30	0.016
<u>Fe core</u>			
density	8.09	0.10	0.001
K	1.86	0.20	0.002
K'	4	1	0.001
dK/dT	-2×10^{-4}	1×10^{-4}	0.003
α	7.3×10^{-5}	2×10^{-5}	0.006
<u>FeS core</u>			
density	5.77	0.20	0.018
K	1.00	0.25	0.034
K'	4	1	0.012
dK/dT	-2×10^{-4}	1×10^{-4}	0.031
α	10×10^{-5}	5×10^{-5}	0.033

1. Report No. NASA TM 81776		2. Government Accession No.		3. Recipient's Catalog No.	
4. Title and Subtitle Reports of Planetary Geology Program, 1979 - 1980				5. Report Date January 1980	
				6. Performing Organization Code	
7. Author(s) Compiled by P. Wirth, R. Greeley, and R. D'A111				8. Performing Organization Report No.	
9. Performing Organization Name and Address Office of Space Science Planetary Division Planetary Geology Program				10. Work Unit No.	
				11. Contract or Grant No.	
12. Sponsoring Agency Name and Address National Aeronautics and Space Administration Washington, DC 20546				13. Type of Report and Period Covered Technical Memorandum	
				14. Sponsoring Agency Code	
15. Supplementary Notes					
16. Abstract <p>This is a compilation of abstracts of reports from Principal Investigators of NASA's Office of Space Science, Division of Lunar and Planetary Programs, Planetary Geology Program.</p> <p>The purpose is to provide a document which succinctly summarizes work conducted in this program. Each report reflects significant accomplishments within the area of the author's funded grant or contract.</p> <p>No attempt has been made to introduce editorial or stylistic uniformity; on the contrary, the style of each report is that of the Principal Investigator and may best portray his research. Bibliography information will be included in a separately published document.</p> <p>Full reports of selected abstracts were presented to the annual meeting of Planetary Geology Principal Investigators at Arizona State University, Tempe, Arizona, January 14-16, 1980.</p>					
17. Key Words (Suggested by Author(s)) Planetary Geology Solar System Evolution Planetary Geologic Mapping				18. Distribution Statement Unclassified - Unlimited	
19. Security Classif. (of this report) Unclassified		20. Security Classif. (of this page) Unclassified		21. No. of Pages 421	
				22. Price* \$13.25	

* For sale by the National Technical Information Service, Springfield, Virginia 22161



National Aeronautics and
Space Administration

Washington, D.C.
20546

Official Business
Penalty for Private Use, \$300

SPECIAL FOURTH CLASS MAIL
BOOK

Postage and Fees Paid
National Aeronautics and
Space Administration
NASA-451



NASA

POSTMASTER: If Undeliverable (Section 158
Postal Manual) Do Not Return
